Porphyrin Probes for Xanthine Oxidase

By

Elizabeth Gibson

A thesis submitted for the degree of Doctor of Philosophy

Department of Chemistry

University of York

September 2007

Declaration

The following results were obtained by or with the assistance of other researchers:

1. Computer simulations were performed with the assistance of C. Verma.
2. Synthesis of $[Ru(bpy)_2$(2-methoxy-4-nitro-*N*-(1,10-phenanthrolin-5-yl)benzamide)$]^{2+}$, **8**, performed by C. Albrighton at the University of York.
3. Mass Spectrometry performed by T. Dransfield at the University of York.
4. X-ray crystallography performed by A. Whitwood at the University of York.
5. NMR spectroscopy (600 MHz) performed by S. Matthews at the University of York.

All other work was performed by the author.

Abstract

The molybdo-enzyme xanthine oxidase (XO) accelerates hydroxylation of a range of planar aromatic substrates such as purines. The enzyme has been associated with a number of medical conditions including hyperuricemia (gout), therefore screening for possible clinical inhibitors is being actively pursued. This thesis is concerned with the design and preparation of luminescent probes to investigate metallo-enzymes.

Luminescent probes have been prepared, based on a water-soluble zinc porphyrin derivative, an aromatic linker and a simplified substrate. The synthesis was performed initially with tetraphenyl porphyrin (TPP) rather than the water-soluble derivatives. TPP was monofunctionalised by nitration followed by reduction to give the corresponding amine. DCC mediated amide coupling was used to link the porphyrin to 2-methoxy-4-nitrobenzoic acid, the linker. The nitro substituent was reduced selectively using indium and ammonium chloride to give the corresponding amine. A second 2-methoxy-4-nitrobenzoic acid unit was coupled and reduced in the same way to give probes of different lengths. The spectroscopic properties of the TPP compounds were dependent on solvent and the nature of the terminal substituents (nitro vs. amine).

The trismethyl pyridinium (TMPyP) analogues were synthesised by coupling the linker followed by the substrate, isonicotinic acid anhydride. The compounds were characterised by ^{1}H, ^{13}C NMR (COSY, HMQC, HMBC), FTIR, UV-Vis spectroscopy, ESI-MS and fluorimetry. A $[Ru(bpy)_2(phen)]^{2+}$ analogue was crystallographically characterised in order to demonstrate the presence of an intramolecular hydrogen bond between the amide proton and the methoxy oxygen on the neighbouring ring.

Enzyme affinity bioassays were carried out and IC_{50} values were calculated for potential substrates, substrate-linker compounds and probes and were converted to K_i values. In order for the probe to be displaced by a potential inhibitor, a moderate affinity is required. This was achieved for the isonicotinic acid derivative K_i =31.9 ± 0.3 μmol (allopurinol K_i = 1.37 ± 0.36 μmol), appropriate for this application. Binding of the probes to the enzyme caused a red shift in the porphyrin absorption and quenching of the luminescence.

Contents

Abbreviations and Notation

Abbreviations

A	Acceptor
Å	Ångström(s)
Ac	Acetate
Ad	Adamantane
ADP	Adenine Diphosphate
AMP	Adenine Monophosphate
ATP	Adenine Triphosphate
B	Bridge
br	broad
bpy	Bispyridyl
BSA	Bovine Serum Albumin
C(prefix)	Centi
°C	degrees Celsius
CD	Cyclodextrin
d	doublet
D	Donor or Dansyl
Da	Dalton(s)
DCC	Dicylcohexylcarbodiimide
DIEA	Diisopropylethylamine
DMAP	4-Dimethyl Amino pyridine
DMF	Dimethylformamide
DMSO	Dimethylsulfoxide
EB	Ethylbenzene
EI–MS	Electron-Impact Mass Spectroscopy
ESI-MS	Electrospray Ionisation Mass Spectroscopy
EtOH	Ethanol

FAB	Fast Atom Bombardment
FAD	Flavin Adenine Dinucleotide
FB	Free-Base
FTIR	Fourier-Transform Infrared spectroscopy
FYX-051	4-(5-Pyridin-4-yl-1*H*-[1,2,4]triazol-3-yl)pyridine-2-carbonitrile
g	gram(s)
h	hour(s)
HABA	4′-Hydroxyazobenzene-2-carboxylic Acid
Hz	hertz
IL	Intraligand (charge transfer)
Im	Imidazole
J	coupling constant
K_m	Michaelis constant
K_d	Equilibium dissociation constant
LAS	Light Absorbing Photosensitiser
LES	Light Emitting Photosensitiser
m	metre(s)
m	multiplet (spectroscopy)
m(prefix)	milli
M	metal
M(prefix)	Mega
M^+/M^-	cationic/anionic Molecular ion
MeI	Methyl Iodide
min	minute(s)
mol	mole(s)
m/z	mass/charge
MLCT	Metal to Ligand Charge Transfer
MoCo	Molybdenum Cofactor active site
NAD^+	Nicotinamide Adenine Dinucelotide
NADH	Nicotinamide Adenine Dinucleotide (reduced form)
NMR	Nuclear Magnetic Resonance

NOS	Nitric Oxide Synthase
NsCl	Nosyl Chloride
OAc	acetate
OTf	triflate
P	Porphyrin
PET	Photoelectron Transfer
ppm	parts per million
py	Pyridine
q	quartet
Q	Quinone
Q	Quaternary (spectroscopy)
s	singlet
SCE	Standard Calomel Electrode
t	triplet
^{t}Bu	tertiary-butyl
TEA	Triethyl Amine
TEI-6720	2-(3-cyano-4-isobutoxyphenyl)-4-methyl-5-thiazolecarboxylic acid
TFA	Trifluoroacetic Acid
THF	Tetrahydrofuran
TPP	Tetraphenyl Porphyrin
TRIR	Time-Resolved Infra-Red (spectroscopy)
UV-Vis	Ultraviolet-Visible (spectroscopy)
V_{max}	The limiting maximal velocity that would be observed in an enzyme catalysed reaction when all the enzyme is present as ES.
XDH	Xanthine Dehydrogenase
XO	Xanthine Oxidase
XOR	Xanthine Oxidoreductase
Y-700	1-[3-Cyano-4-(2,2-dimethylpropoxy)phenyl]-1H-pyrazole-4-carboxylic acid
δ	chemical shift
μ(prefix)	micro
°	degrees

Notation

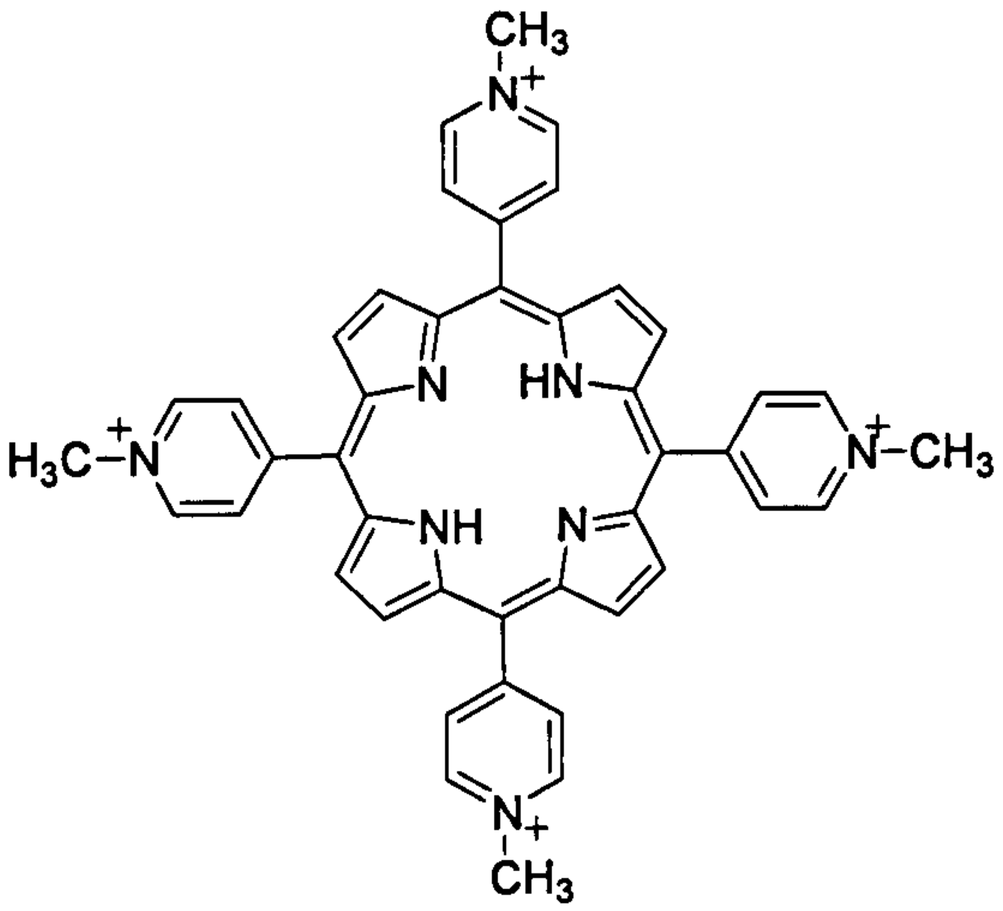

TMPyP

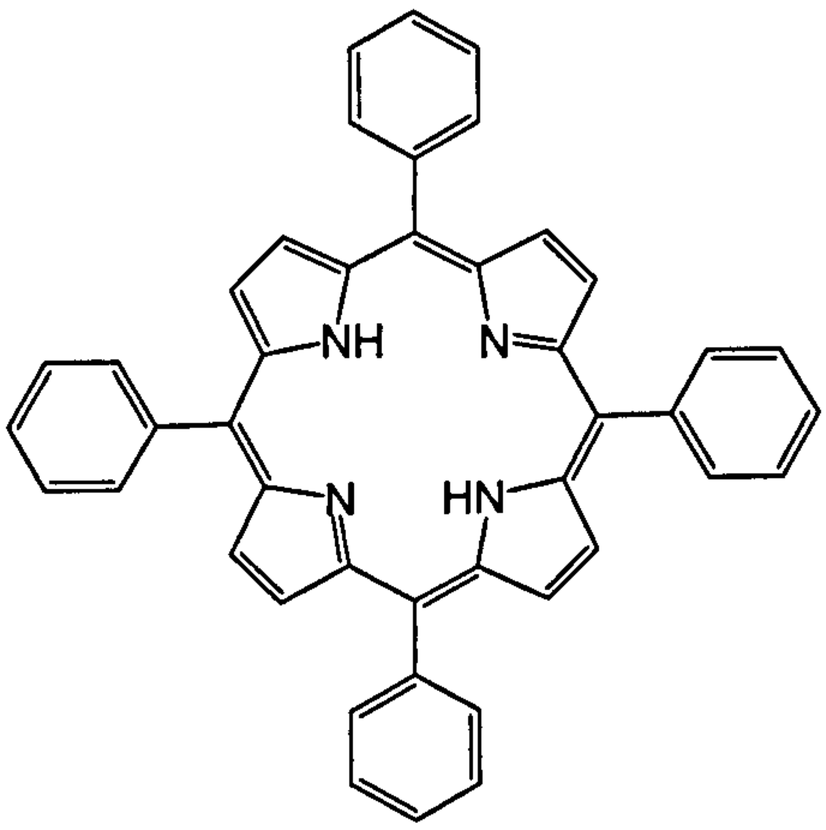

TPP

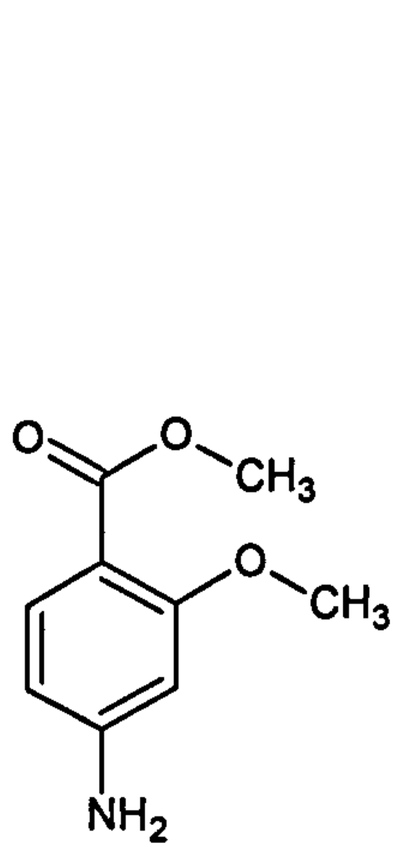

1

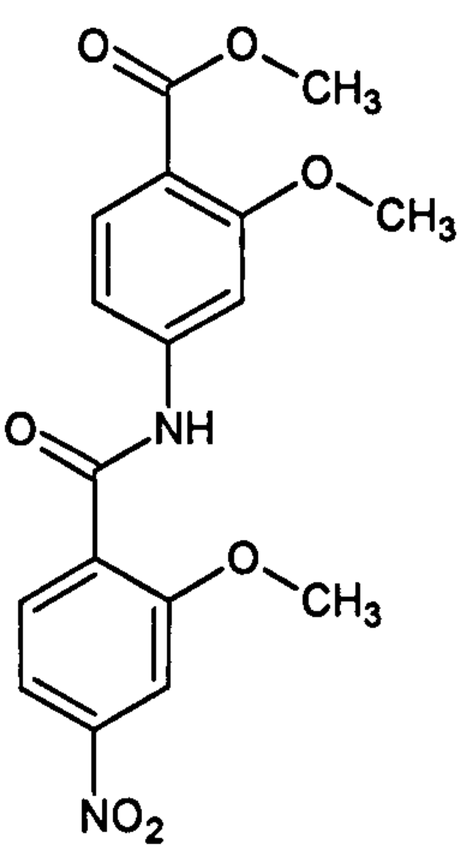

2

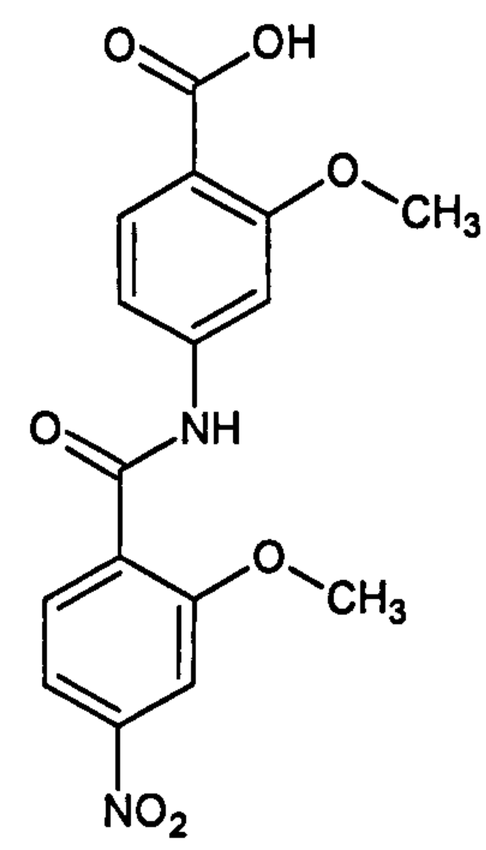

3

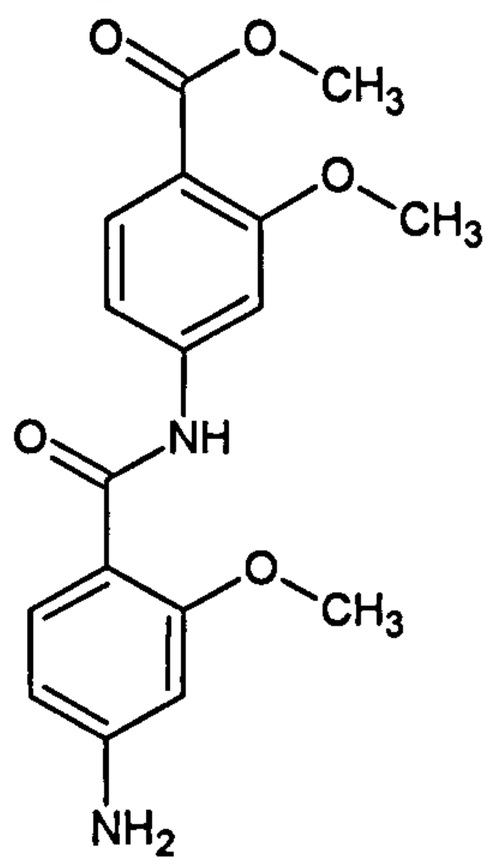

4

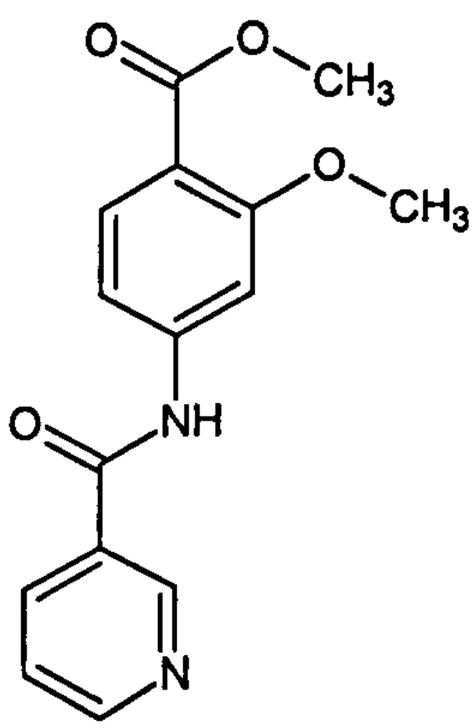

5

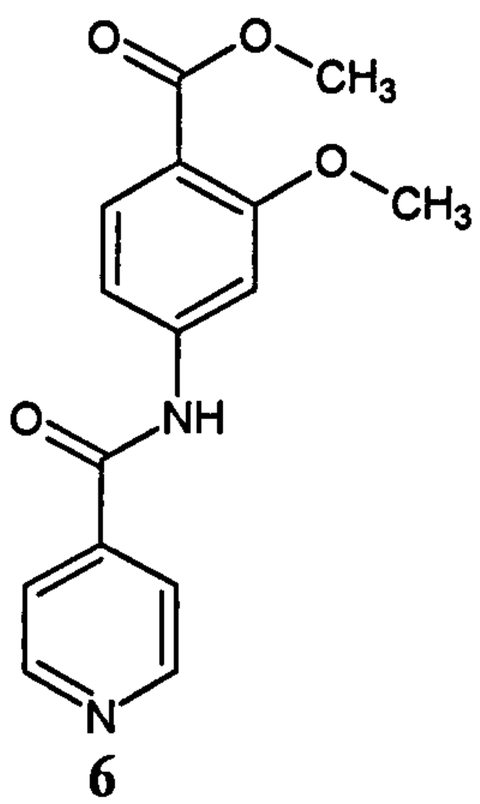

6

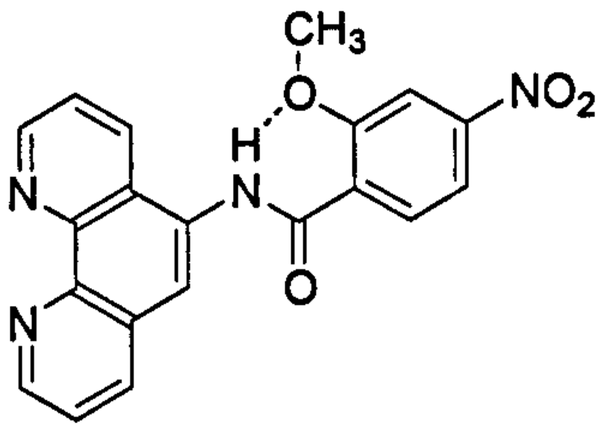

7

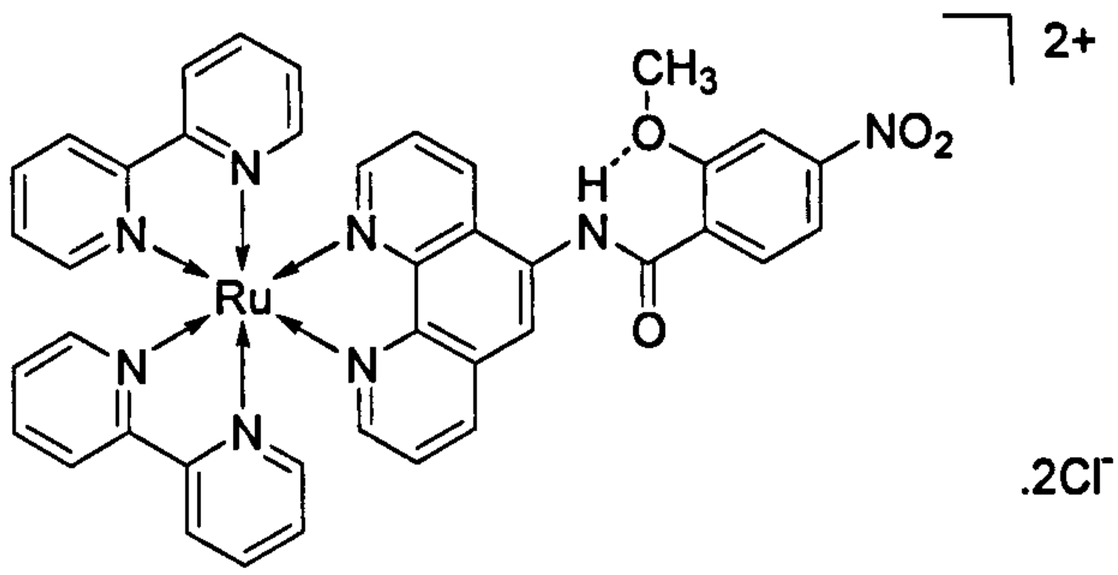

[8][Cl]$_2$

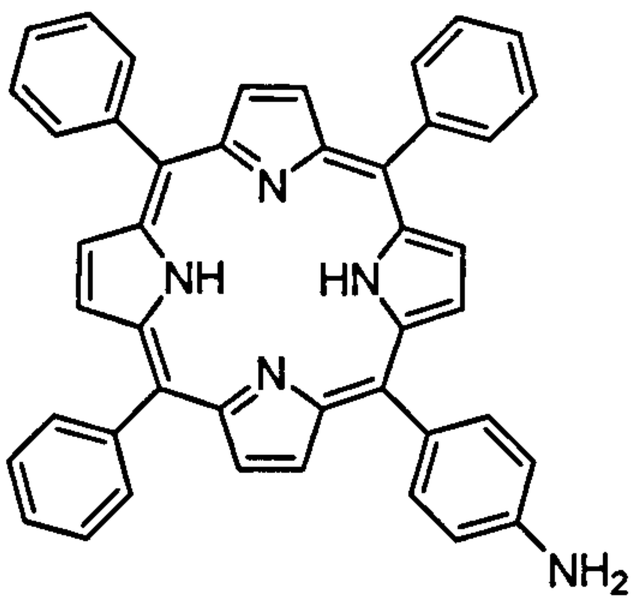

9

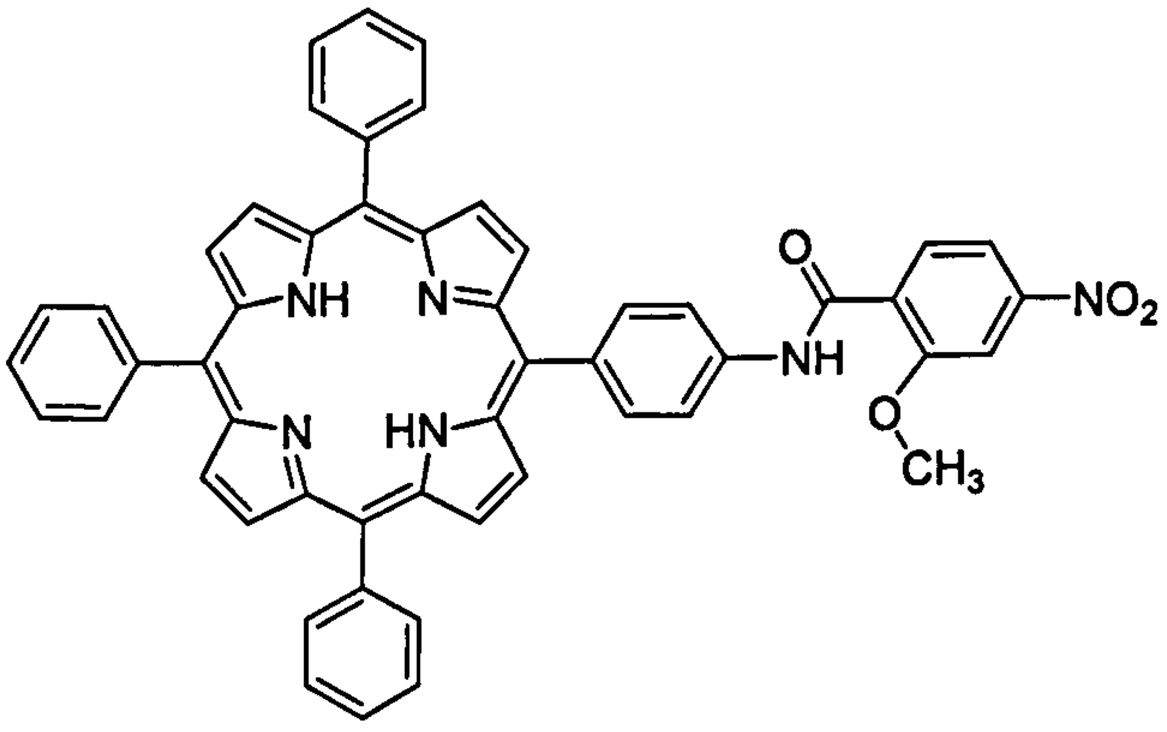

10

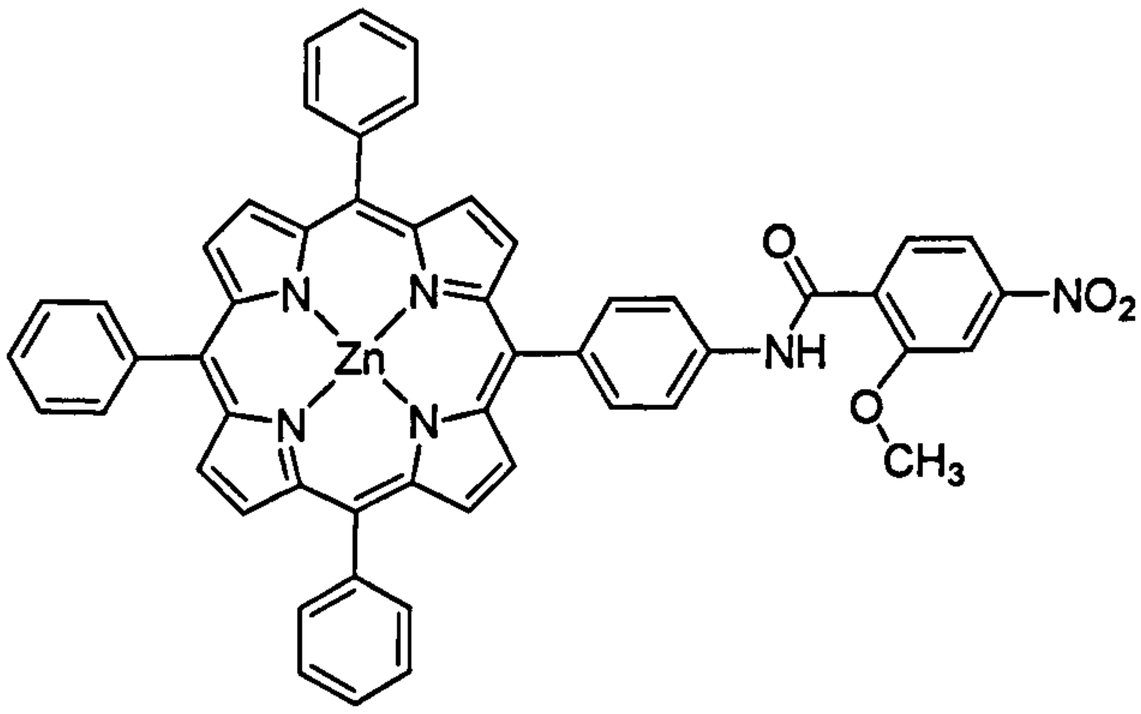

11

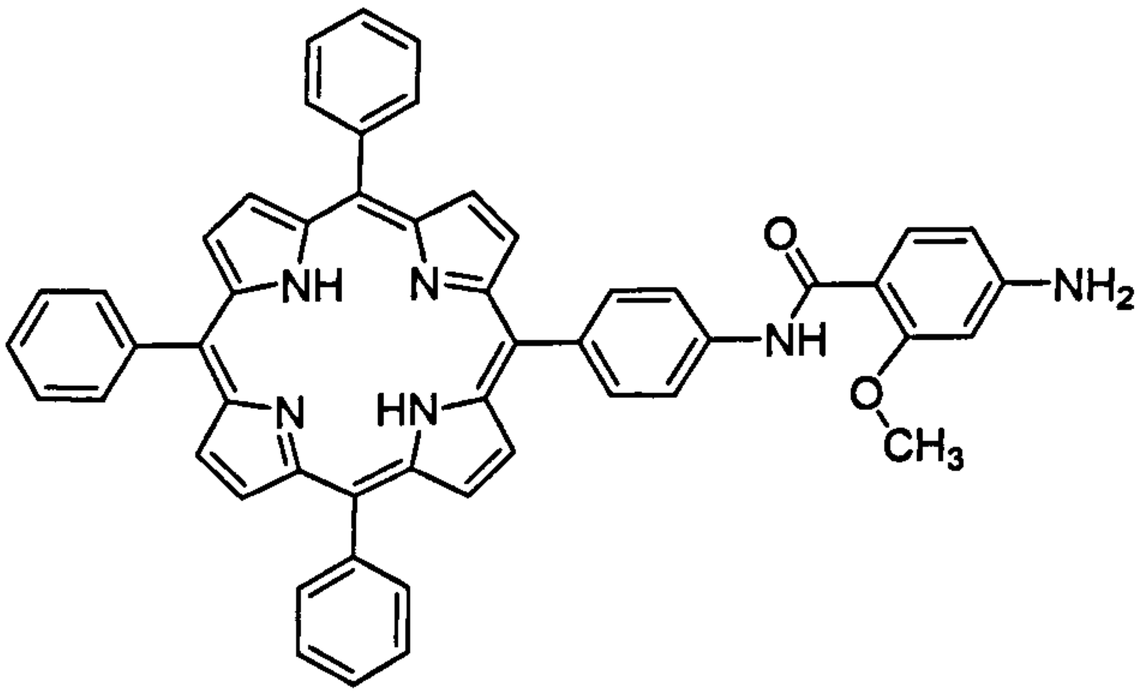

12

XIV

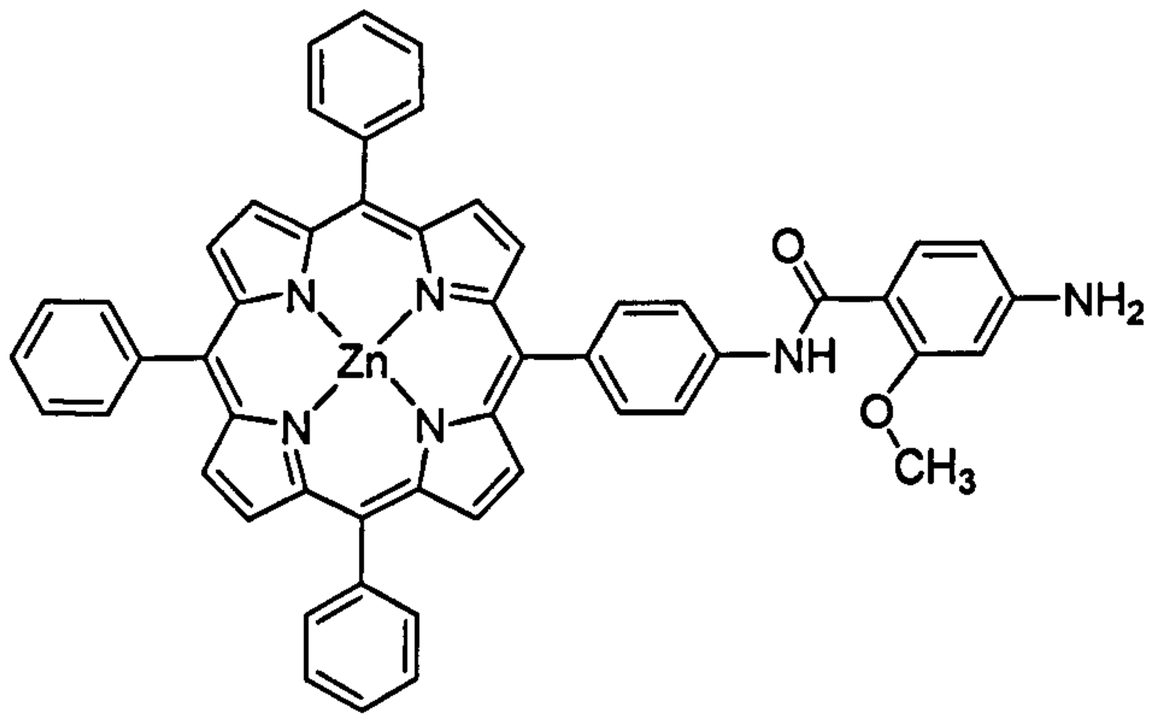

13

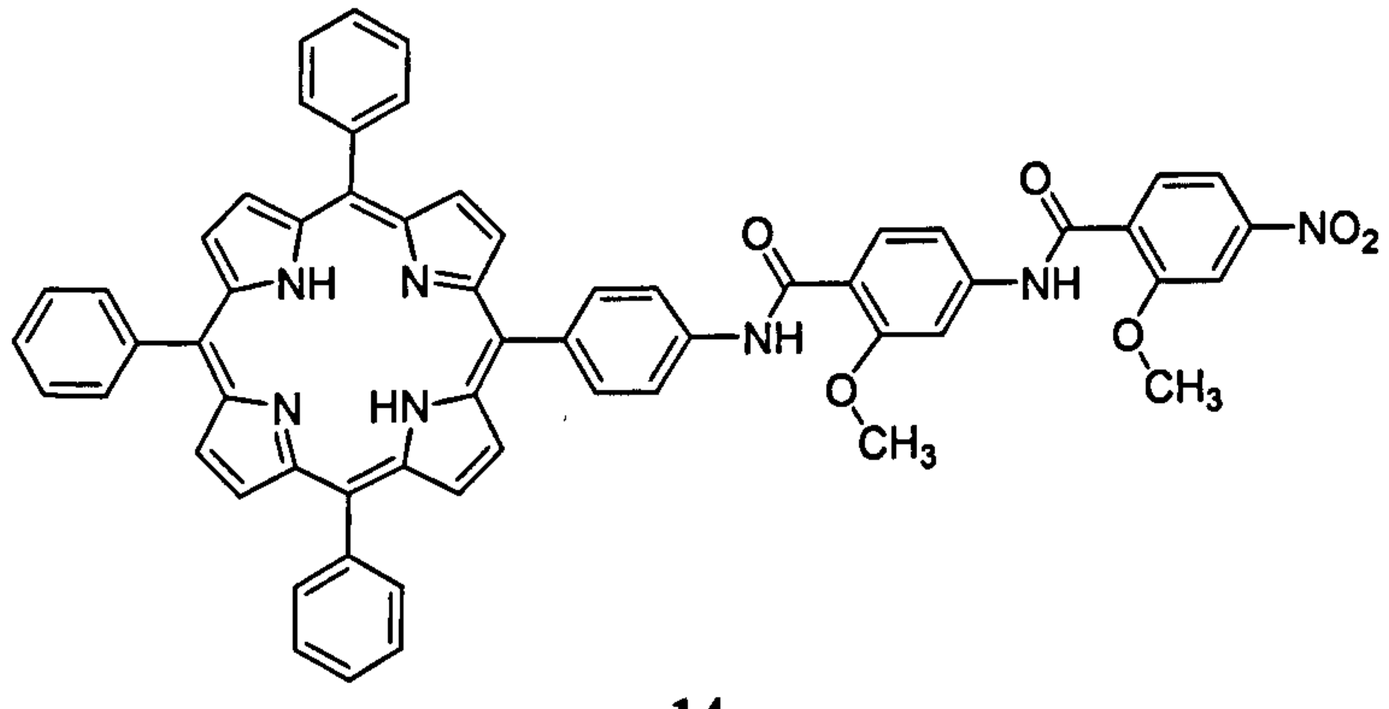

14

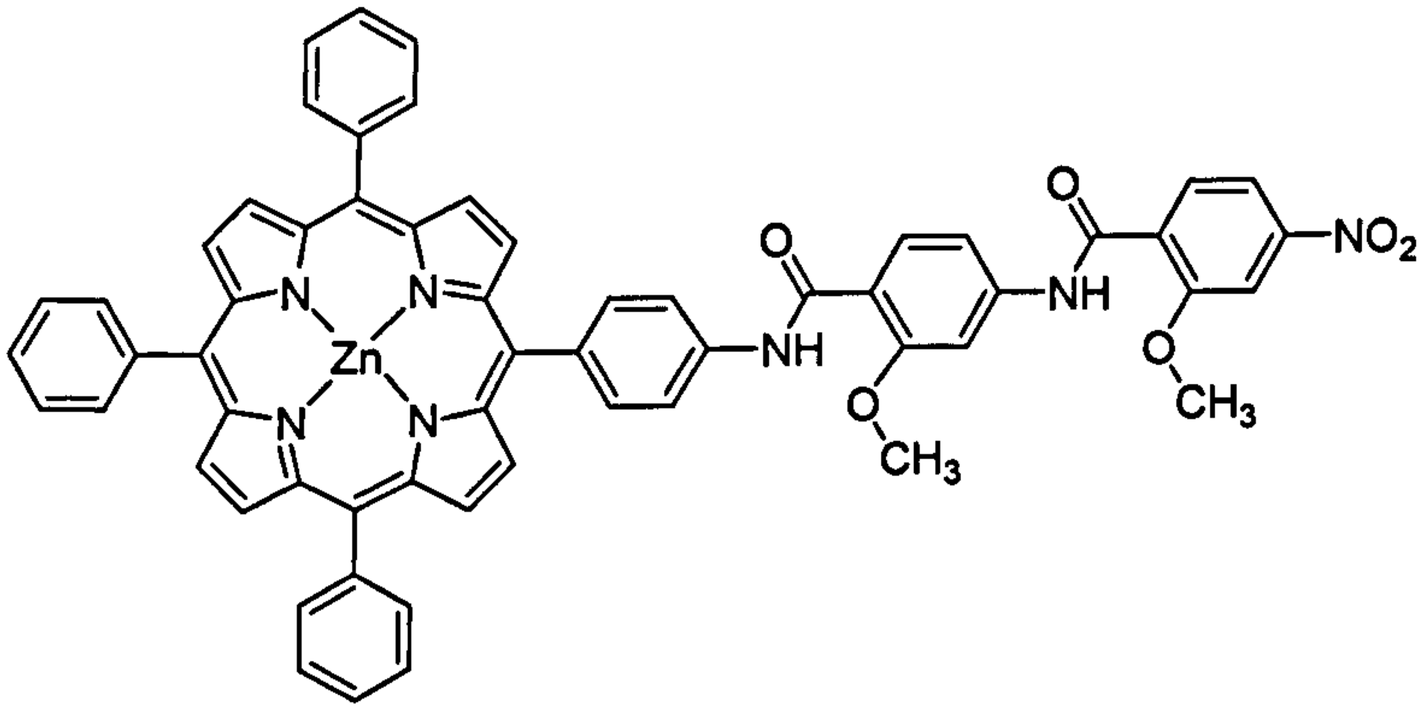

15

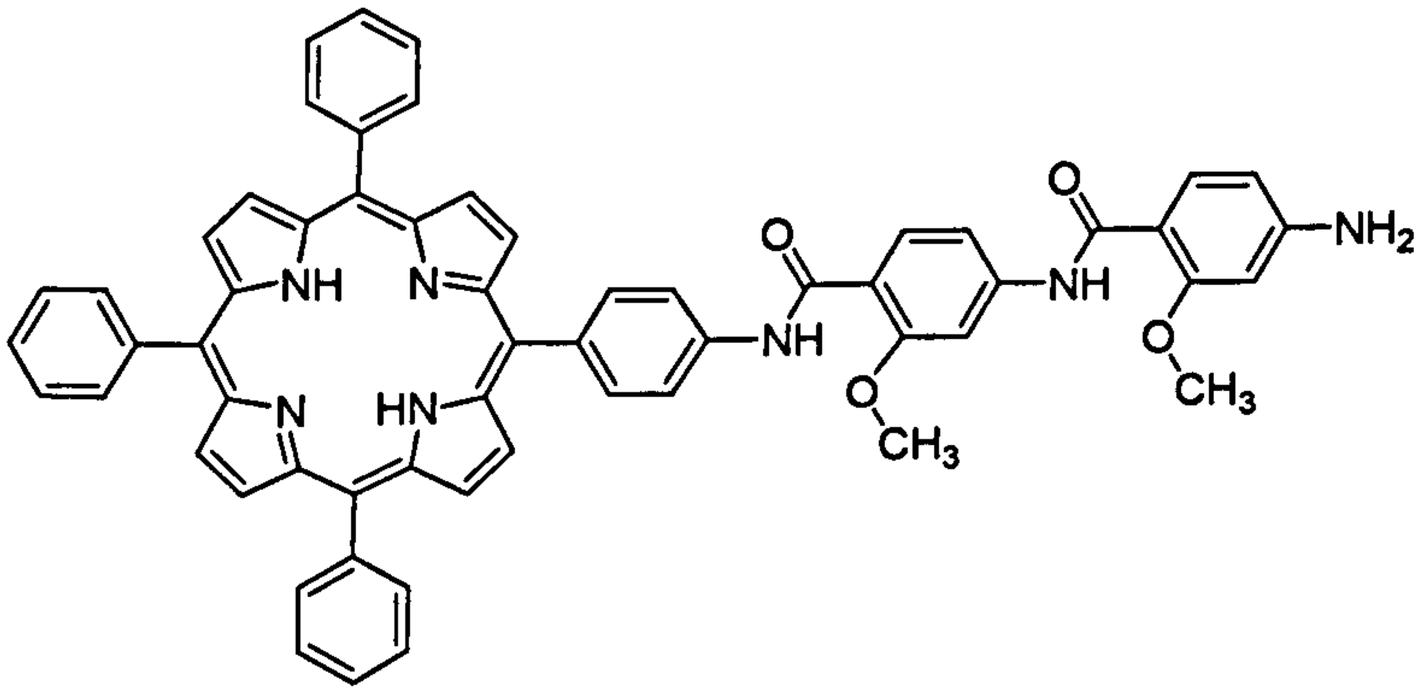

16

XV

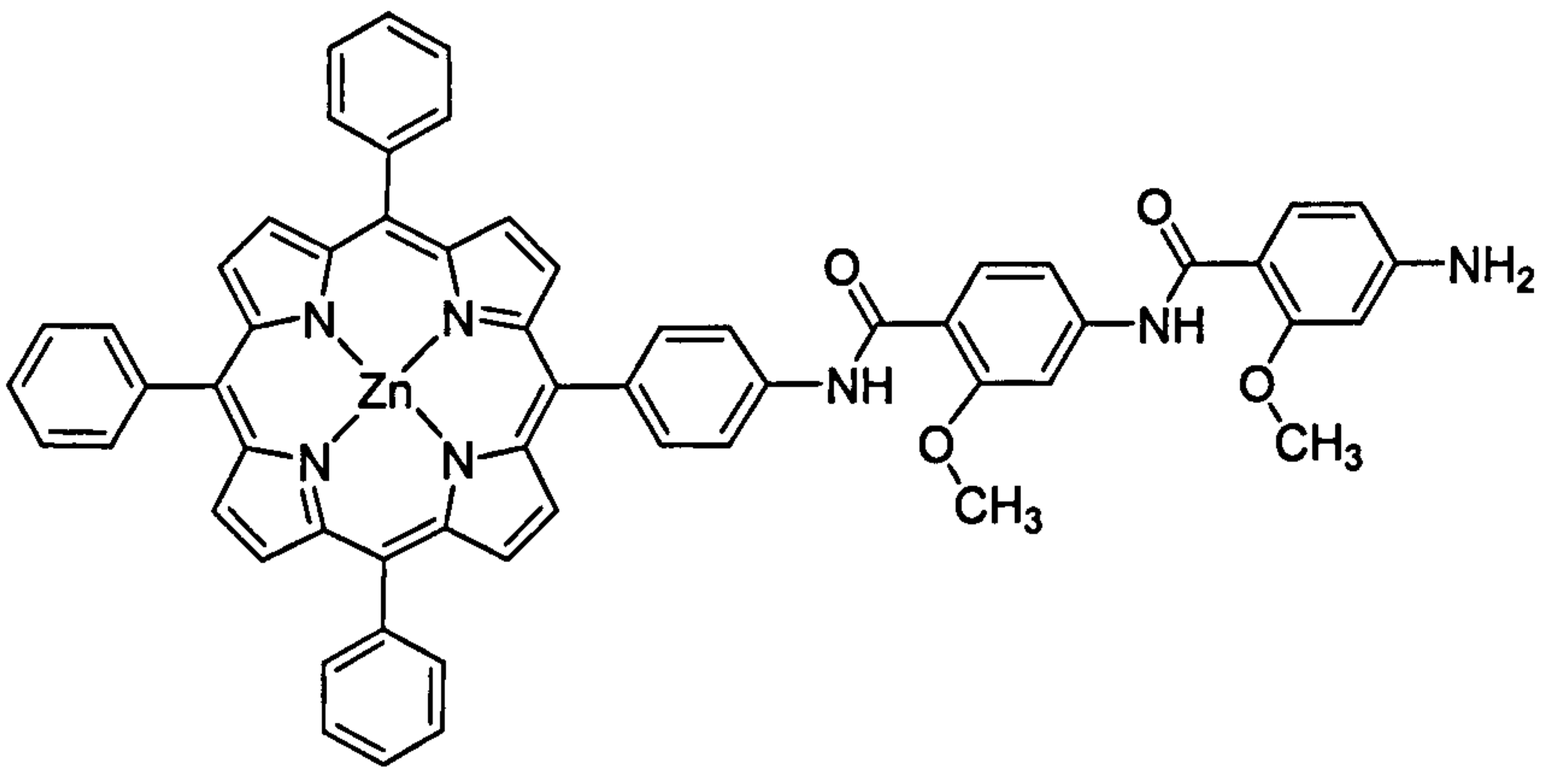

17

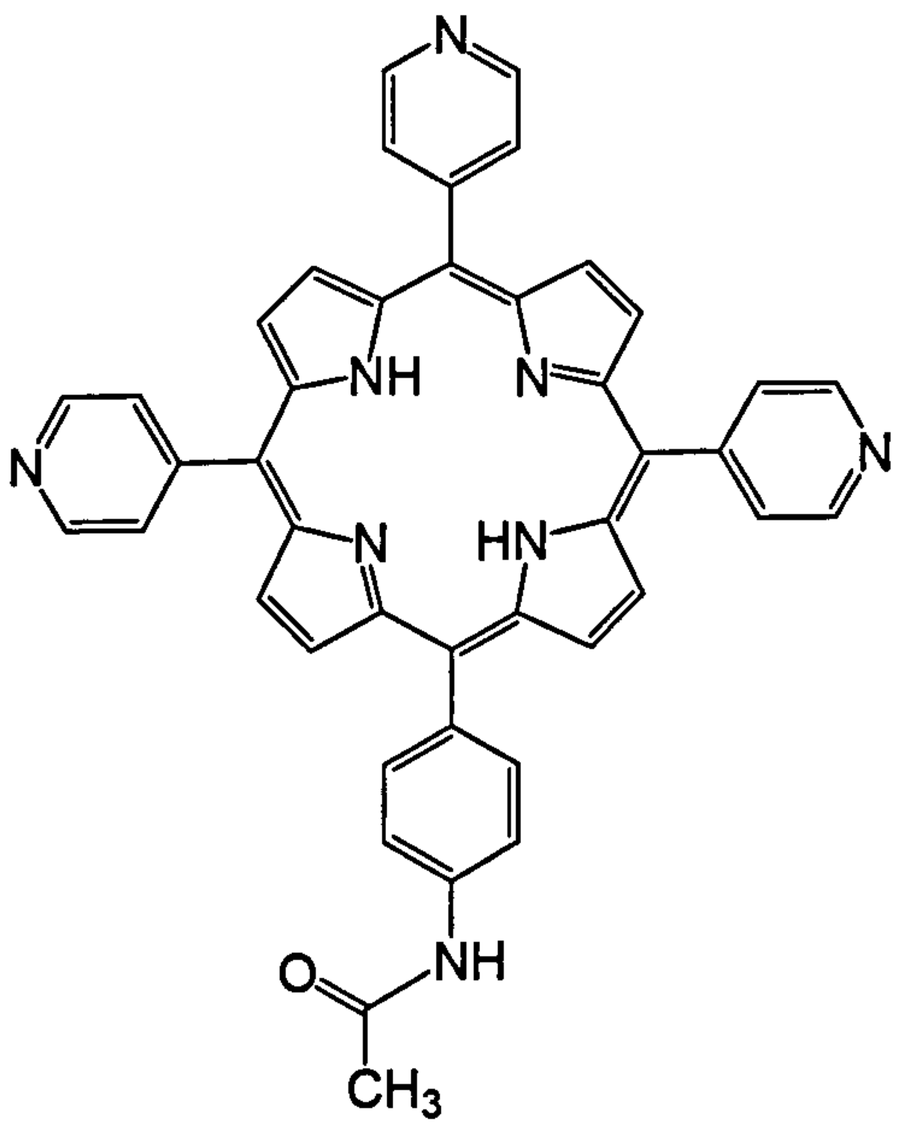

18

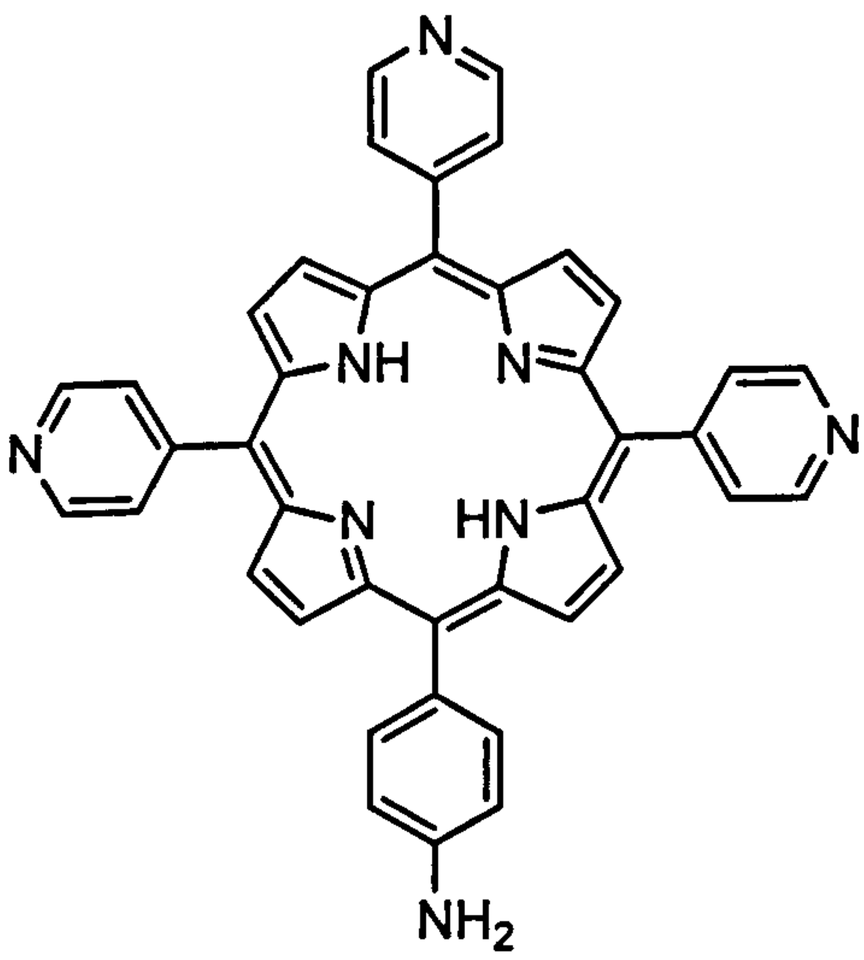

19

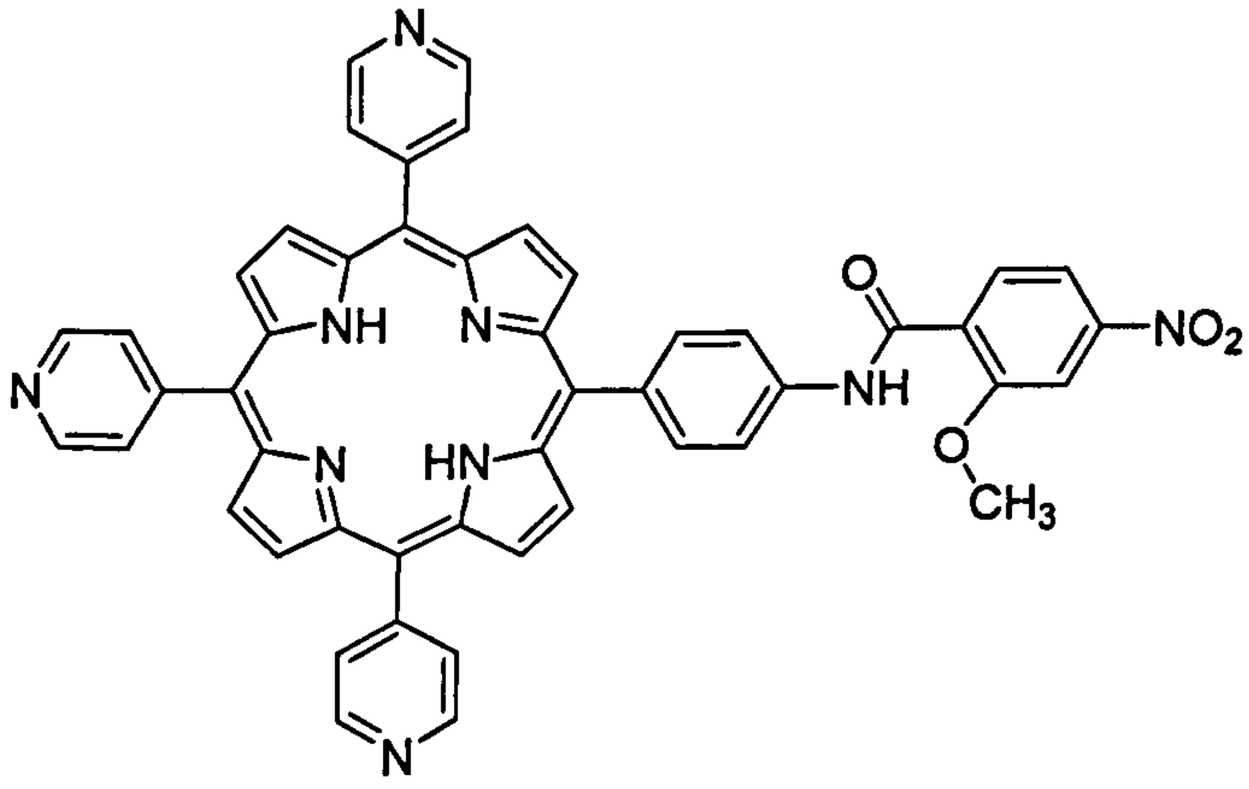

20

XVI

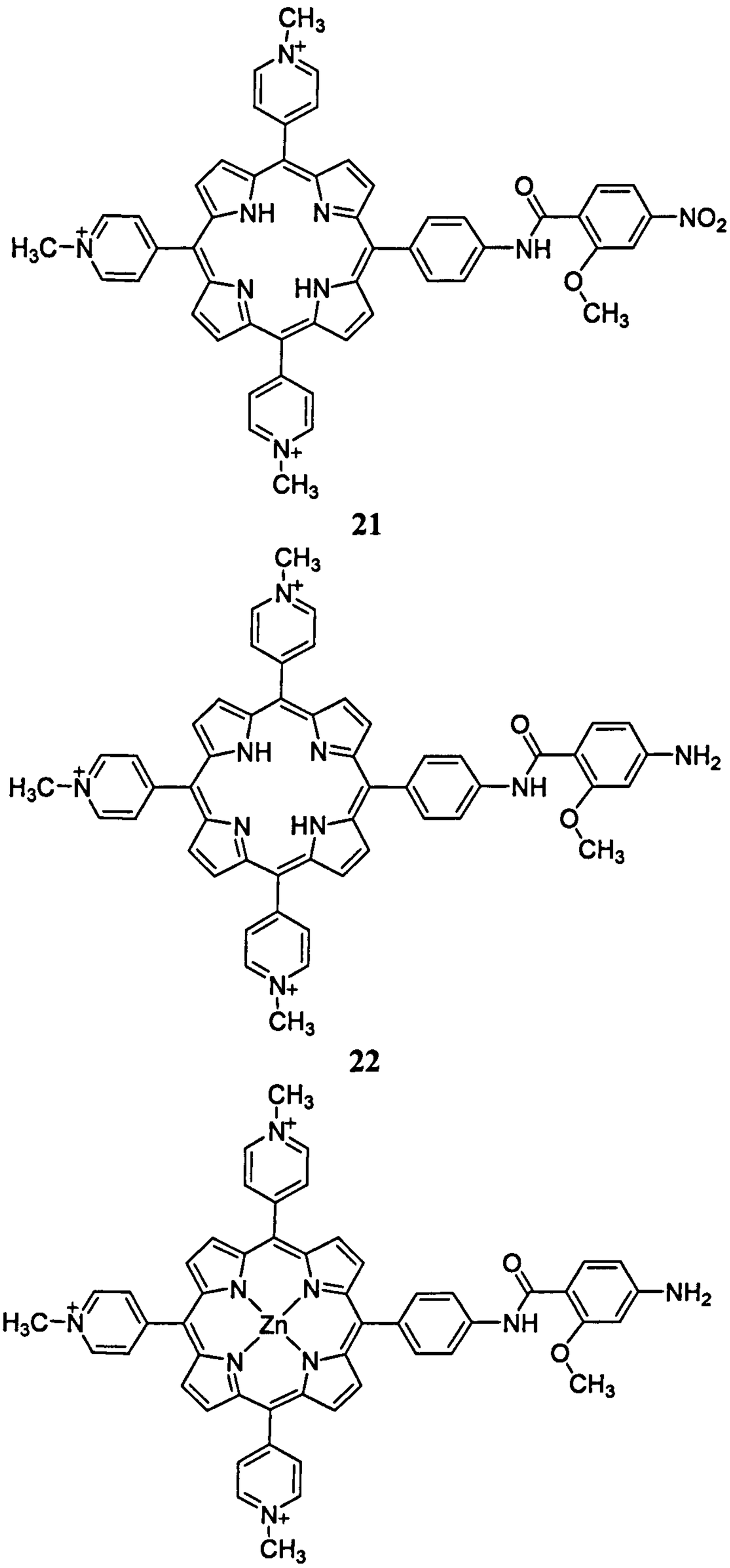

21

22

23

XVII

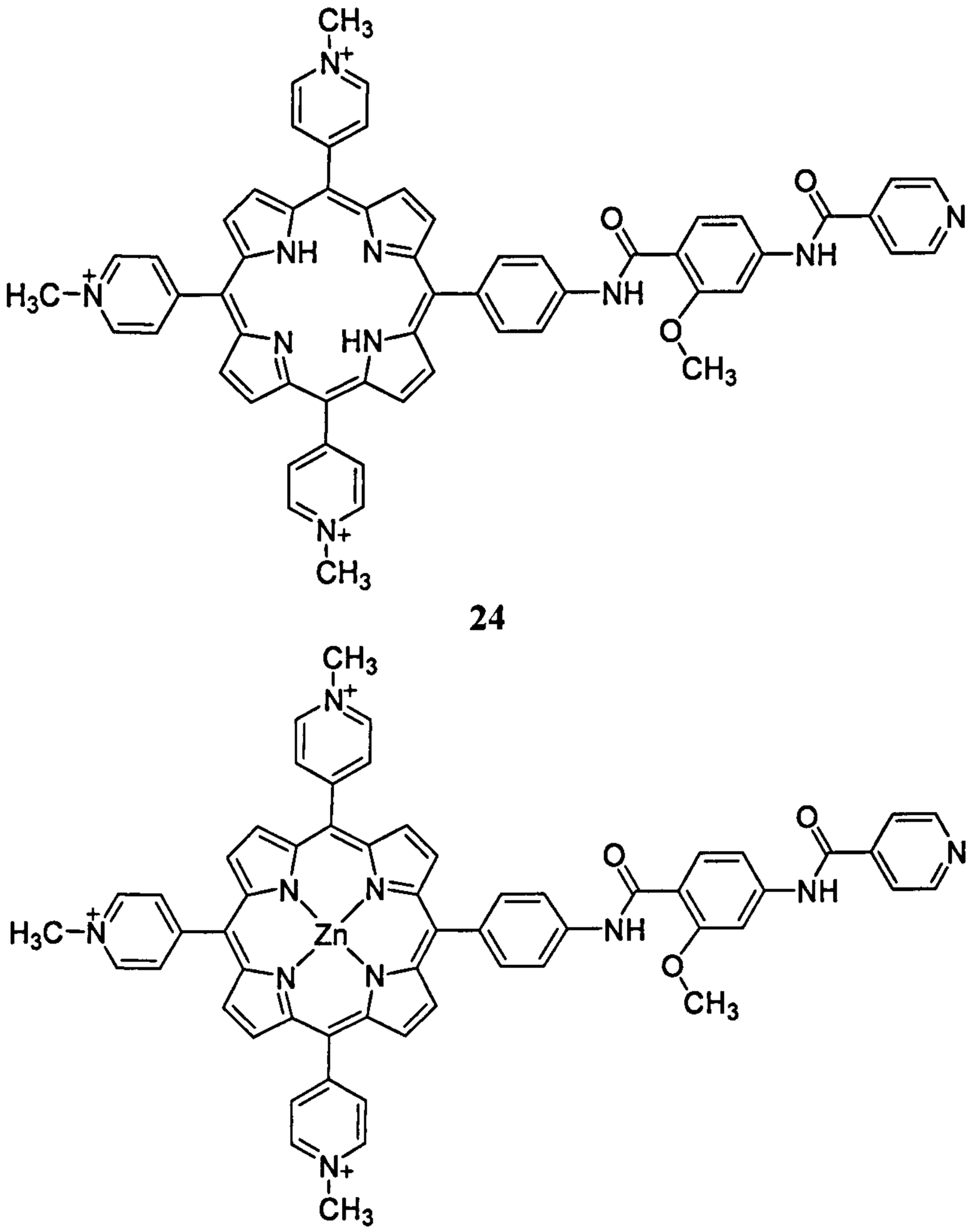

24

25

Acknowledgements

There are many people without whom this work would not have been possible. I'd like to thank my supervisors, Robin Perutz and Anne Duhme-Klair who gave me the opportunity to carry out this project. Both have been very supportive and encouraging throughout. I'd also like to thank the students, postdocs and technicians I have had the fortune to work with at York; 'Team Snail' past and present (Naser, Rich, Charlotte, Jake (dis)Grace, 'dangerous' Mike, 'Des', Steve 'Snail', Tracy, Vicki, Nick, Marius, Nicole ('the German'), Claire, Danielle, James, David and David) and team Duhme-Klair (Nicola, Siti and Catherine); the organometallic group (including Grumpy Steve, Pat, Gav, Ralph, Paul, Joaquin, Juan, Jon, JC, John, Stuart, Cyril, Anna, Rathika, Catherine, Simon and Richard); Jim, Áine, Kirby, Jess and Iman; as well as the former supramolecular group. Thanks to Chandra for the molecular modelling and calculations. Thanks to the technical staff, especially Trevor, Heather and Adrian, the stores staff and the workshop staff for all their help.

Many thanks to my amazing family, who inspire me every day (even though none of you have a clue what any of this is about!). Thanks to Julie for helping me escape once in a while. Most of all, I need to thank 'my boys', Chris and Kai, for all their love and support throughout.

CHAPTER 1

INTRODUCTION

1. Introduction

1.1. Xanthine Oxidase

1.1.1. Structure and Reactivity

Xanthine oxidase[1] is a multifunctional enzyme occurring across a diverse range of species, from bacteria to humans, and tissues, ranging from the liver to the brain. It belongs to a family of hydroxylase enzymes which catalyse hydroxylation of otherwise stable carbon centres using oxygen derived from water. Within this class are the xanthine oxidoreductases (XORs), xanthine dehydrogenase (XDH) and xanthine oxidase (XO). XDH uses NAD^+ as the terminal electron acceptor, XO uses molecular oxygen. The human form of XO is converted from the native form, XDH, by proteolysis of the enzyme polypeptide chain or oxidation of sulfhydryl residues. This results in a conformational change at the electron acceptor binding site so that NAD^+ can no longer fit[2,3].

The crystal structure of XDH (**Figure 1.1**) reveals a 300 kDa homodimer[4]. Each monomer functions as an independent catalytic unit containing one flavin adenine dinucleotide (FAD), one molybdenum-pterin centre and two iron-sulfur clusters. Modification of the cysteine residues causes a structural rearrangement around the FAD site which alters the reactivity towards the substrate at that active site[2]. However, the substrate specificity at the molybdenum centre is unaffected. Since this is the active site of interest for the purpose of this work, it will be XO activity which will be further discussed. However, the principles outlined will apply equally to the oxidoreductases in general.

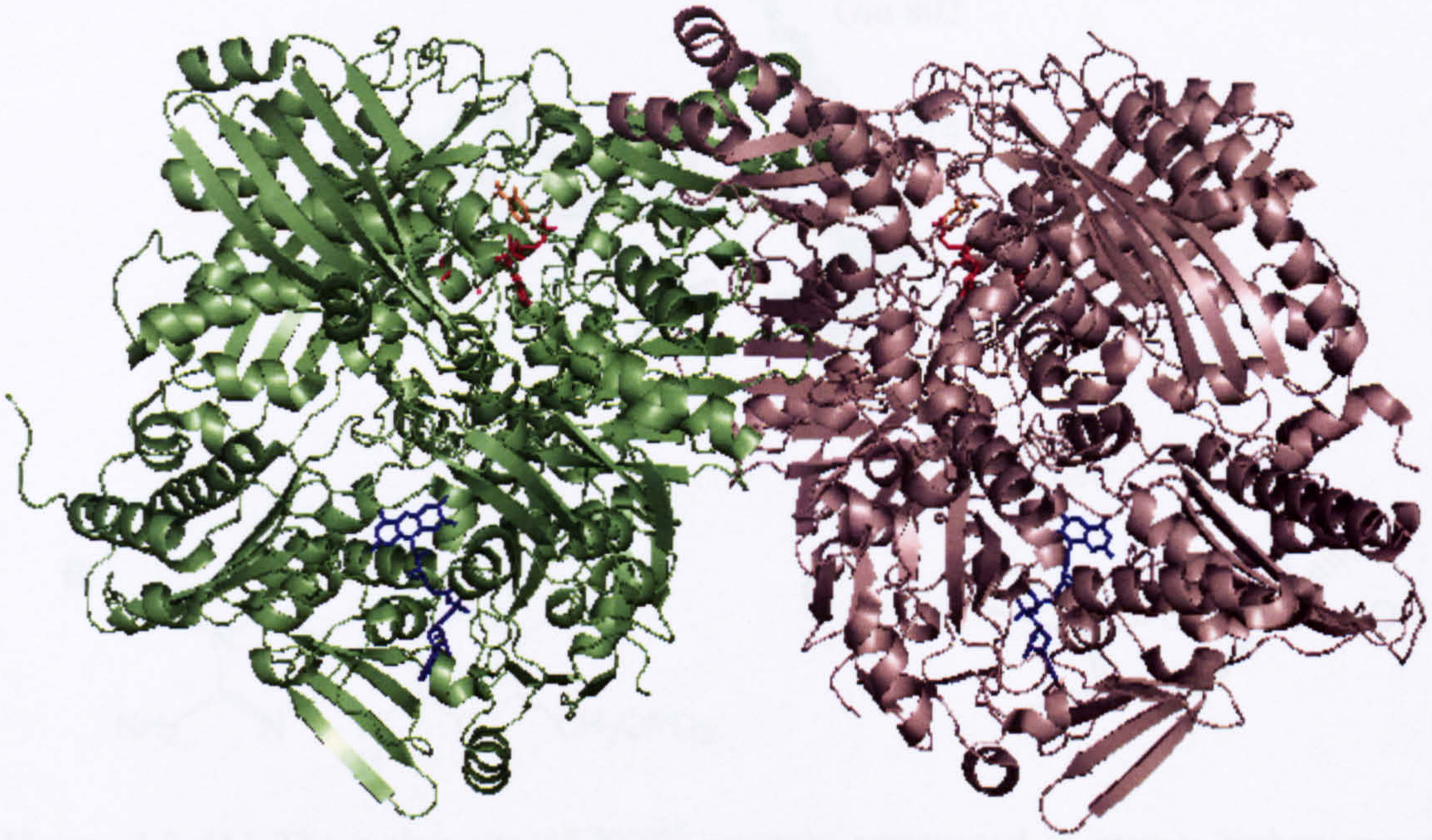

Figure 1.1: Crystal structure of the xanthine dehydrogenase homodimer[5]; colours correspond to structure types: protein scaffold (green, pink), FAD (blue), molybdenum-pterin centre (red) and salicylate (orange). Original in colour.

The enzyme catalyses the hydroxylation of aromatic heterocycles, such as purines, pteridines and aromatic aldehydes[1]:

$$RH + H_2O \longrightarrow ROH + 2H^+ + 2[e^-]$$

This reaction occurs at a molybdopterin active site, which contains oxygen and sulfur ligands coordinated to the Mo centre as shown in **Figure 1.2**[6] . A recent report by Doonan *et al.*[7] confirms that the Mo=O is apical and the Mo=S is in the equatorial position (**A**) and that the remaining ligand is OH rather than OH_2. It is thought that the Mo=S group participates in catalysis as a proton or a hydride acceptor[1].

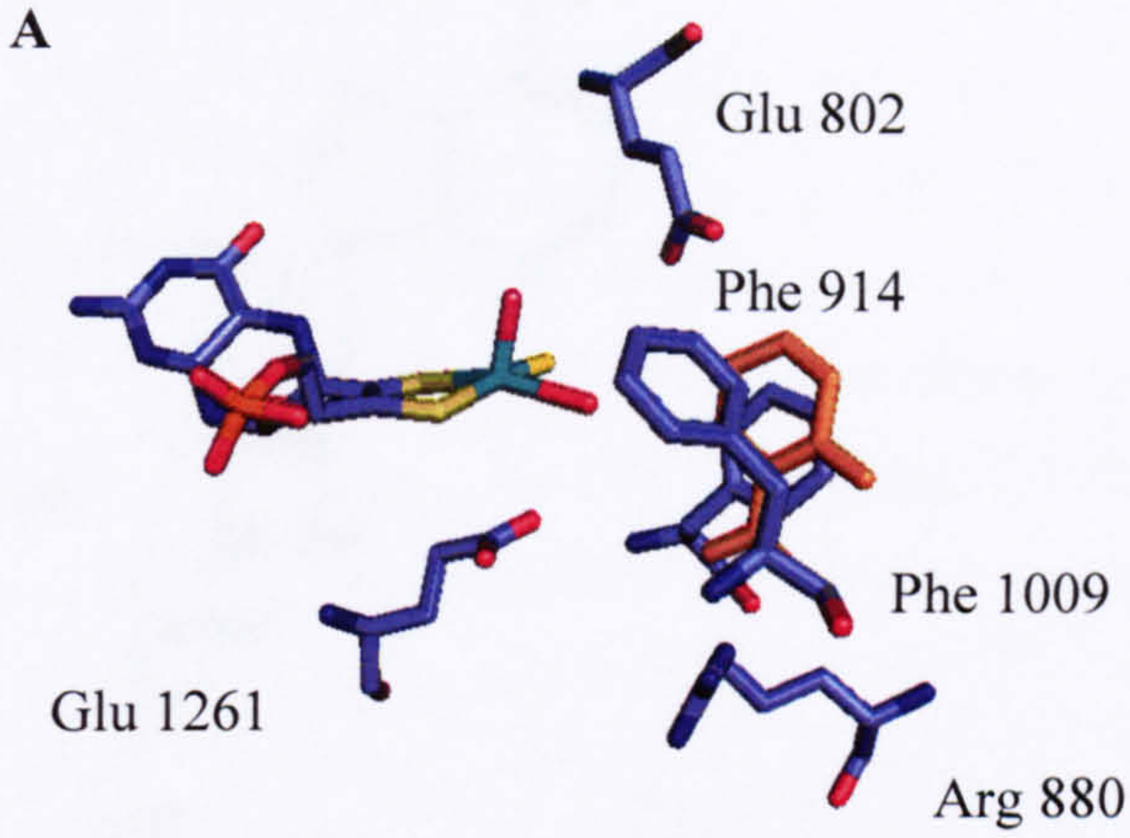

B

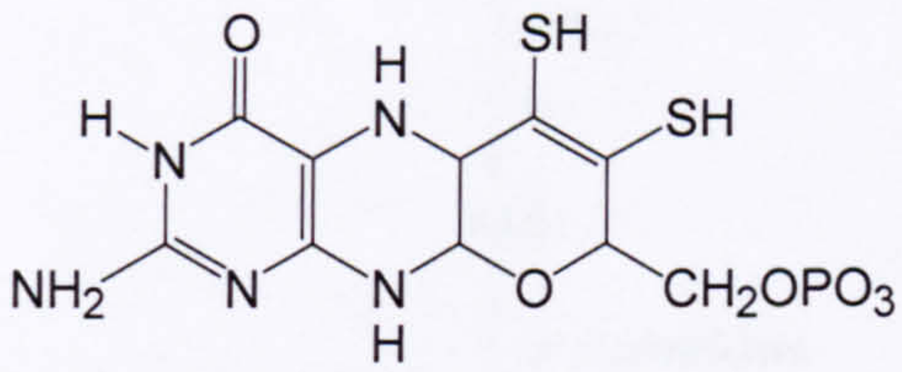

C

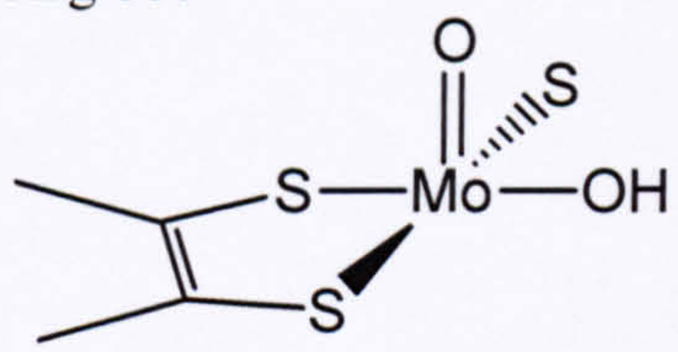

Figure 1.2 (A) The active site of XOR[8], colours correspond to atoms: carbon: mauve; nitrogen: blue; oxygen: red; sulfur: yellow; molybdenum: green; phosphorus: orange; bound salicylate: orange; **(B)** structure of the pterin cofactor, **(C)** structure of the Mo centre: approximately square planar coordination geometry, with M=O at the apical position, the bidentate enedithiolate ligand form Mo=S and Mo-OH groups in the equatorial plane. Original in colour.

The oxidation of xanthine to uric acid is particularly important in the catabolism (energy-releasing breakdown) of ATP as shown in **Figure 1.3.**

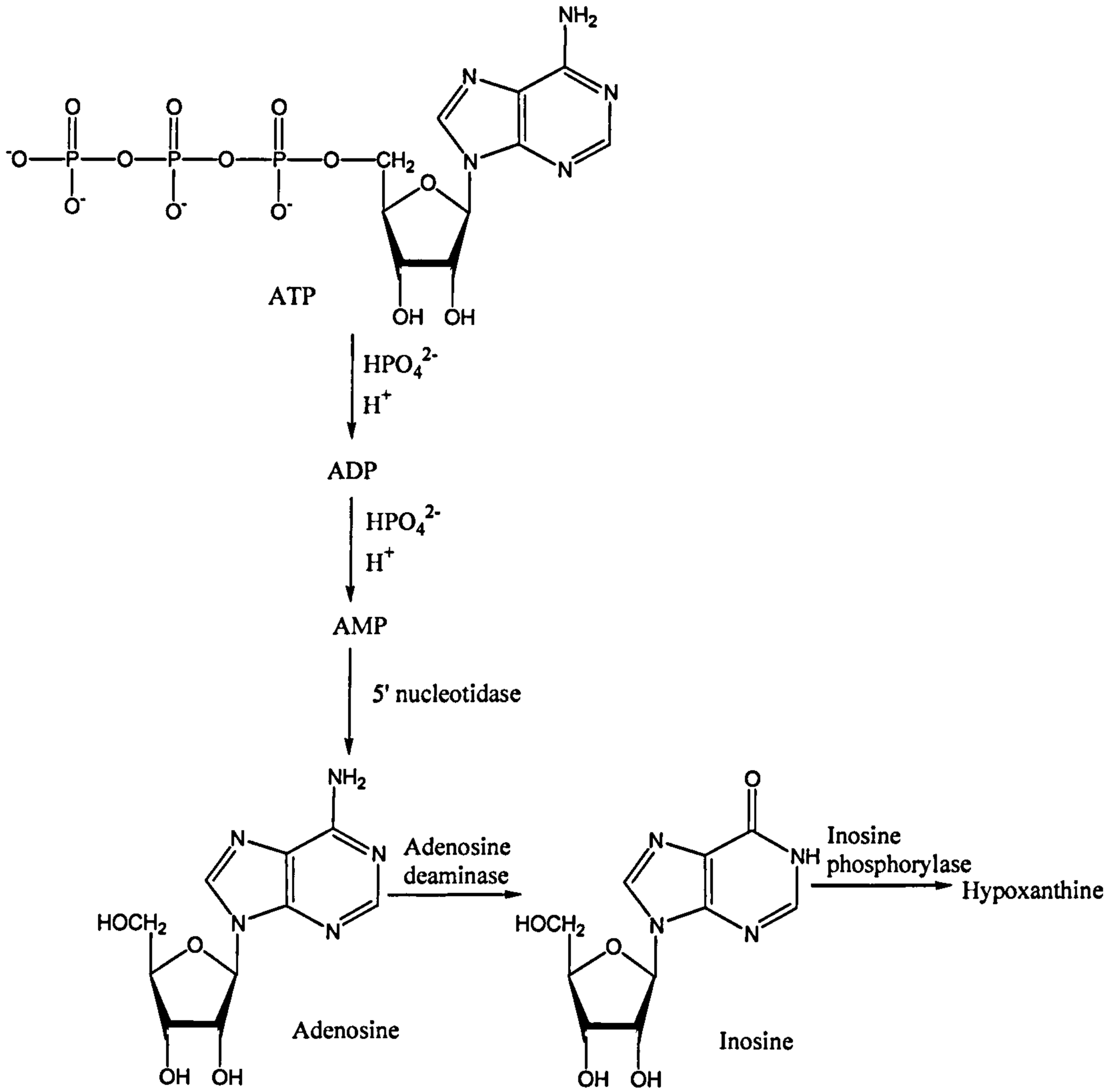

Figure 1.3 Catabolism of ATP to uric acid.

The reaction is likely to proceed via discrete two electron steps, as illustrated in **Figure 1.4**. The Mo active site is reduced from Mo(VI) to Mo(IV), coupled with hydride transfer. The oxidised Mo(VI) site is regenerated by two sequential one electron transfers to a second

active site, an FAD, via 2 Fe_2S_2 clusters, where a second substrate, NAD^+ in XDH but molecular oxygen in XO, is reduced[9]. The initial step is base catalysed by Glu1261, generating Mo-O^- which attacks the C-8 position of xanthine, which is intercalated between the phenylalanine residues. This is followed by hydride transfer to yield LMo(IV)O(SH)-P (L = pyranopterin cofactor). Isotope-labelling studies have shown that a catalytically labile site (Mo-OH) donates the oxygen atom which is incorporated into the product. This site is regenerated with oxygen from neighbouring water when the product is displaced[10].

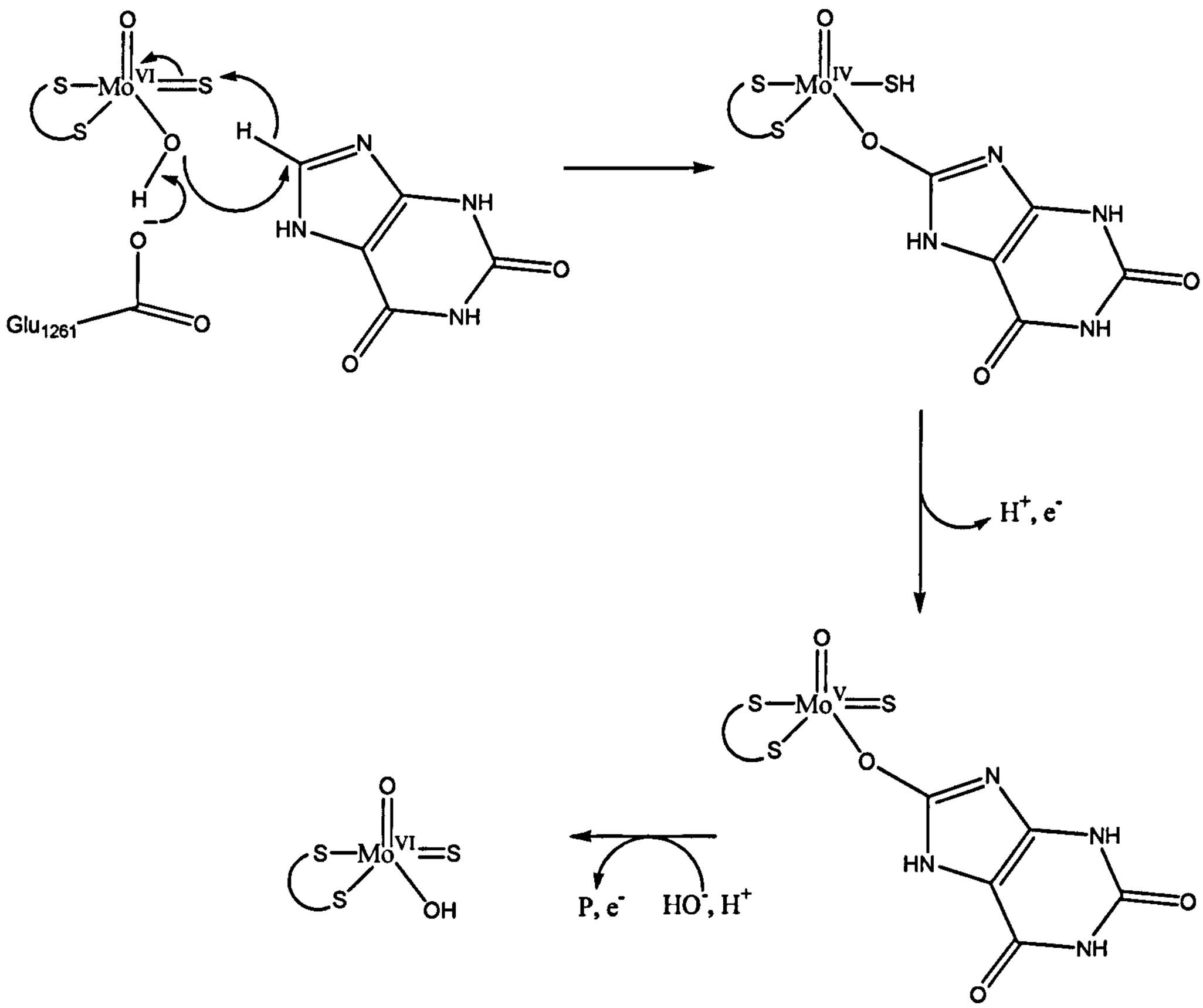

Figure 1.4 Postulated catalytic mechanism for XO[10], P = uric acid.

1.1.2. Associated Medical Conditions and XOR Inhibitors

A number of medical conditions are associated with XO. It is released into the circulation from XO rich organs (such as the liver or intestine) at times of metabolic stress and during a number of pathological states. A build up of uric acid as a result can cause conditions such as hyperuricemia or gout. The release of oxygen-derived free radicals leads to tissue damage. This has also been linked to NO activity resulting in vascular constriction or combination of the superoxide radical with NO directly to form the even more reactive species $ONOO^{\bullet-}$. Increased concentrations of XO have been found in tumours and it is believed that XO is associated with heart failure, cancers, and vascular problems. A build up of uric acid as a result can cause conditions such as hyperuricemia or gout. Therefore, there are a host of potential medical applications for XOR inhibitors to block the activity of the enzyme, the most commonly used being allopurinol.

Allopurinol is a suicide inhibitor of XOR. It is likely that the conformation of the nitrogen atoms in xanthine is crucial to the hydride transfer mechanism. In the case of allopurinol, the substrate is oxidised to alloxanthine, which binds tightly to the molybdenum as illustrated in **Figure 1.5**. Despite being successfully used for several decades as a clinical inhibitor of XOR for the prevention of gout, regular, high doses are required, and unpleasant side affects are known. For this reason there is a prevailing push to discover new, effective clinical inhibitors of XOR.

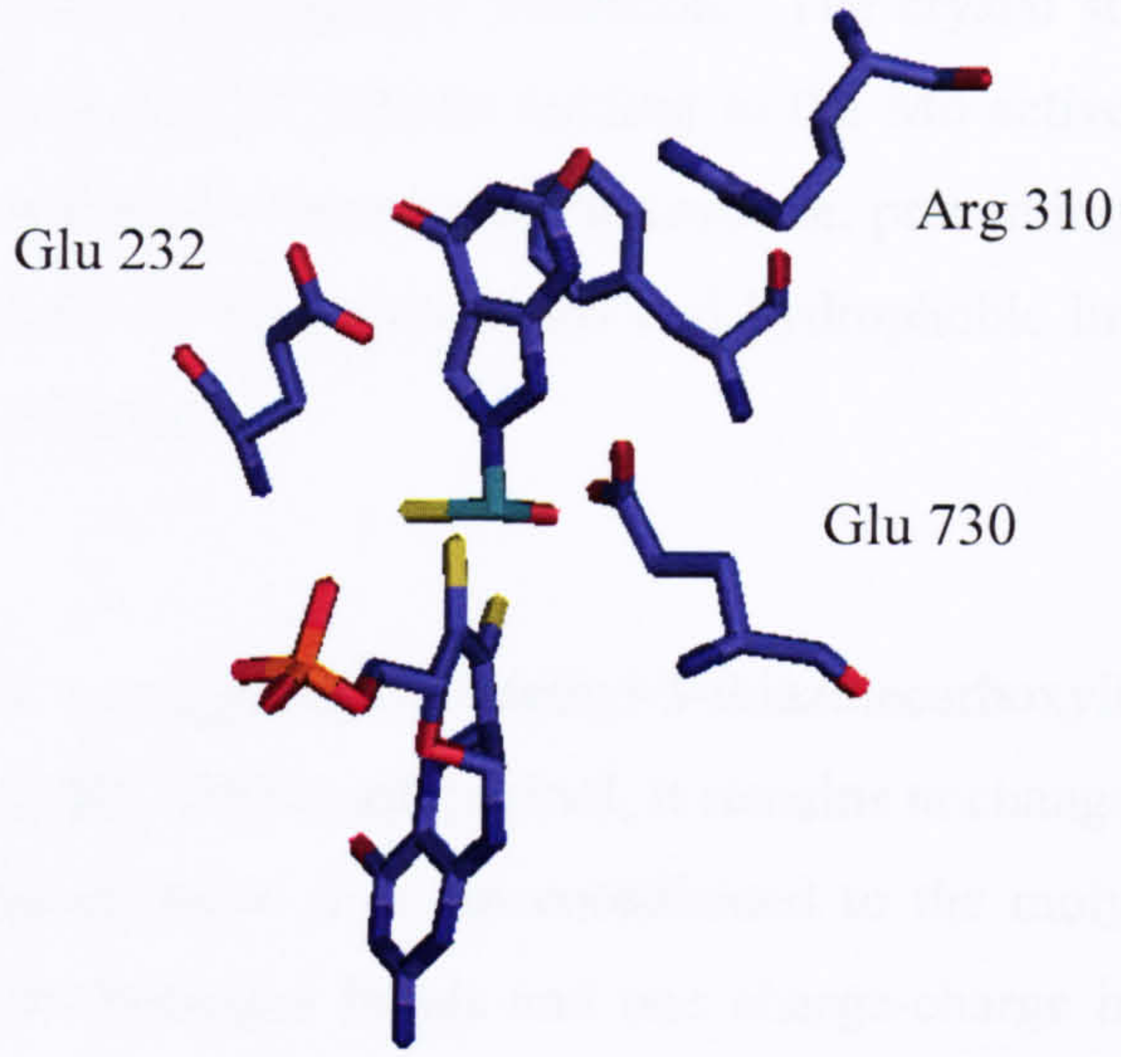

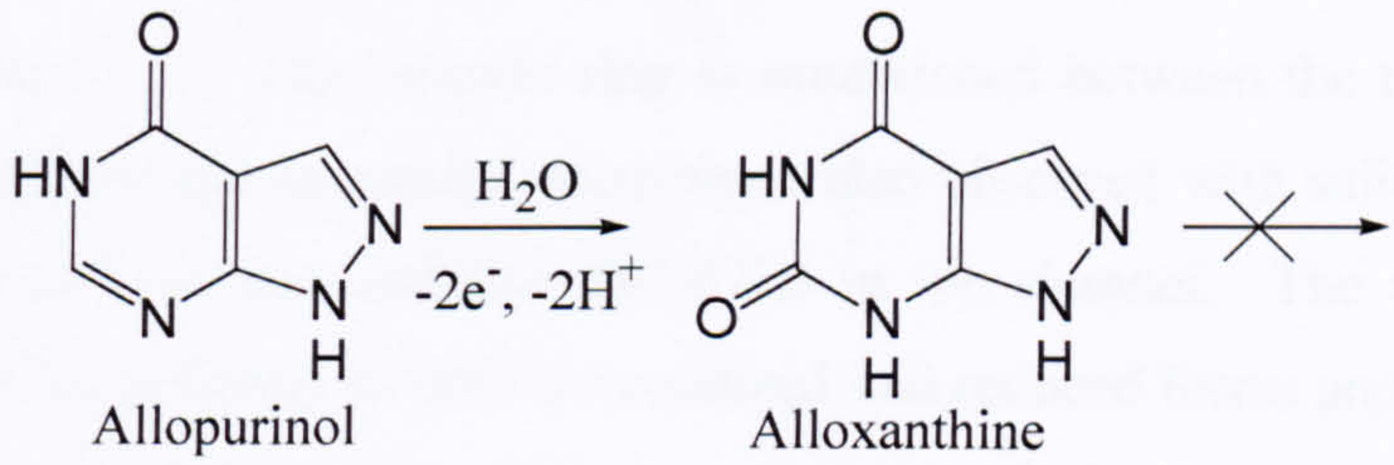

Allopurinol Alloxanthine

Figure 1.5 The active site of XO bound by allopurinol, colours correspond to atom types: carbon: mauve; nitrogen: blue; oxygen: red; sulfur: yellow; molybdenum: green; phosphorus: orange. Original in colour.

A thorough review of XOR inhibitors by Borges, Fernandes and Roliera[11] lists a range of compounds which bind near the molybdenum cofactor (MoCo) active site. The scope of the review highlights the low specificity of the enzyme, binding a range of heterocyclic systems containing one to three rings. The most potent inhibitors are planar aromatic systems with hydrogen bonding substituents, which are stabilised in the active site by corresponding hydrogen bonding residues and π-stacking.

Okamoto *et al.*[12] have investigated a number of non-purine inhibitors. Each has similar binding characteristics, exhibiting mixed-type inhibition. The crystal structures show that the inhibitors bind in the long, narrow channel leading to the Mo active site. Inhibition is achieved by filling the immediate environment of the cofactor, preventing substrate binding. The inhibitors are held in place by hydrogen bonds and hydrophobic interactions, without directly binding to the molybdenum.

TEI-6720 (2-(3-cyano-4-isobutoxyphenyl)-4-methyl-5-thiazolecarboxylic acid) is an extremely potent inhibitor of XO. Unlike allopurinol, it remains unchanged when recovered from XO (i.e. no hydroxylation) since it is not coordinated to the molybdenum cofactor. The inhibitor is bound by six hydrogen bonds and one charge-charge interaction, **Figure 1.6**. The carboxylate group is the most tightly bound, located in the same position as that of salicylate in **Figure 1.1**[4]. The thiazole ring is sandwiched between the two phenylalanine residues providing aromatic/aromatic interactions also observed with salicylate. A host of hydrophobic interactions also stabilise TEI-6720 in the channel. The advantage of this inhibitor is that it binds tightly to both the oxidized and reduced forms and is not influenced by the oxidation state of the metal, whereas oxypurinol only binds to the reduced form and the oxypurinol inhibited enzyme can be reactivated at $t_{1/2}$ = 300 min by spontaneous reoxidation of the molybdenum cofactor. TEI-6720 is now in clinical use as Febuxostat[13].

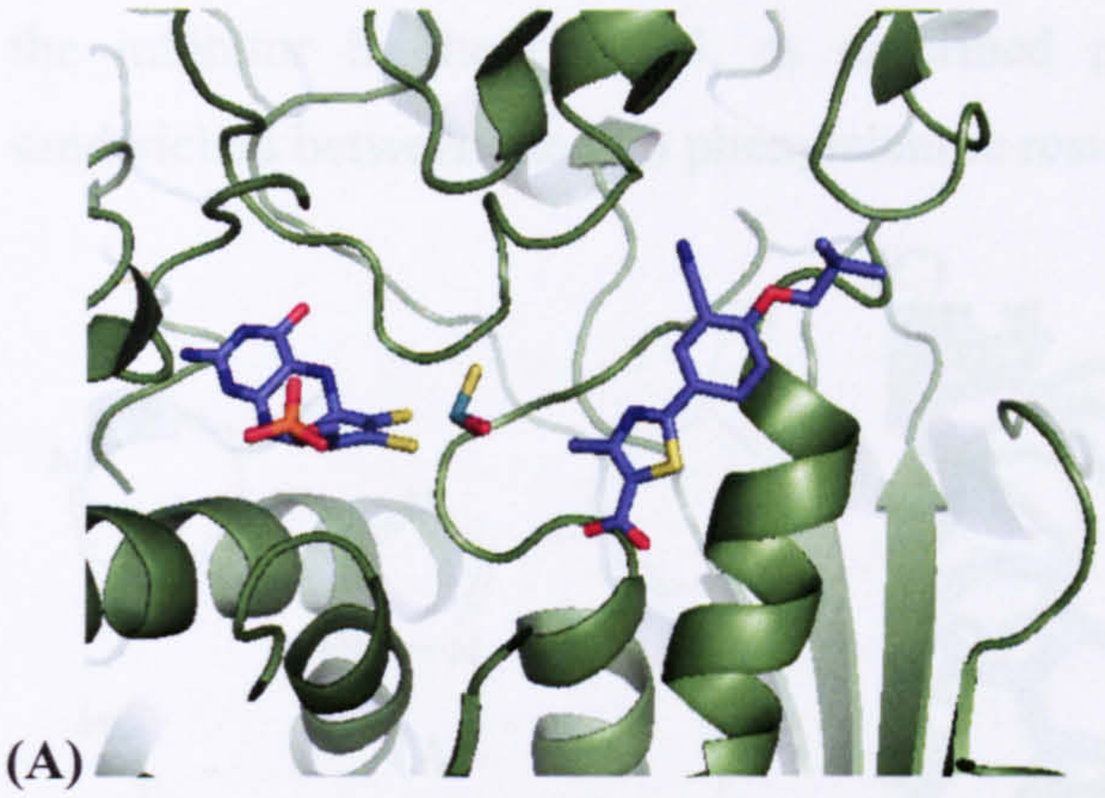

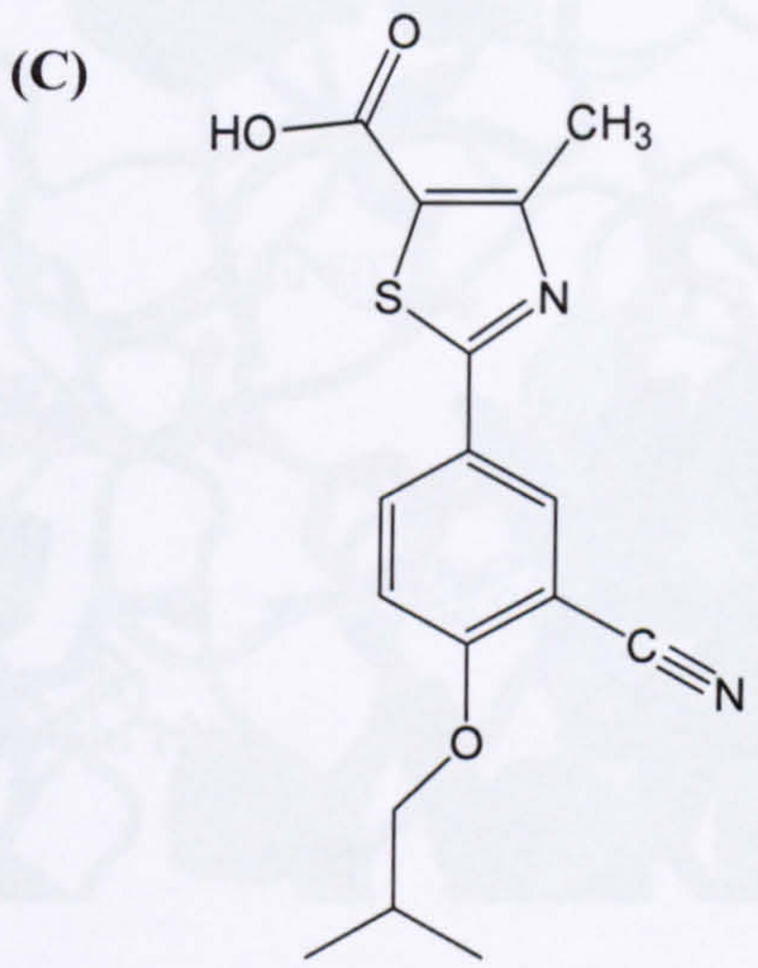

Figure 1.6 (A) Crystal structure of TEI-6720 bound in the XO active site[14]; **(B)** Interaction of TEI-6720 with residues lining the access channel to Mo-pterin, colours correspond to atoms: carbon: mauve; nitrogen: blue; oxygen: red; sulfur: yellow; molybdenum: green; phosphorus: orange; **(C)** chemical structure of TEI-6720. Original in colour.

In contrast, the inhibitor FYX-051[15], **Figure 1.7**, is slowly hydroxylated by the enzyme. This reaction is accompanied by an increase in absorption at 640 nm and a decrease at 430 nm, corresponding to the formation of a charge transfer complex between the reduced Mo centre and the hydroxylated inhibitor. As previously, the inhibitor is bound in the solvent access channel to the molybdenum active site. In this instance, electron density is observed between the Mo centre and the pyridine ring, suggesting a covalent bond to the C2 of FYX-051, which is hydroxylated. Several hydrogen bonds and electrostatic interactions stabilise

the inhibitor in the channel, as dercribed previously. Similarly the triazole ring is sandwiched between the two phenylalanine residues.

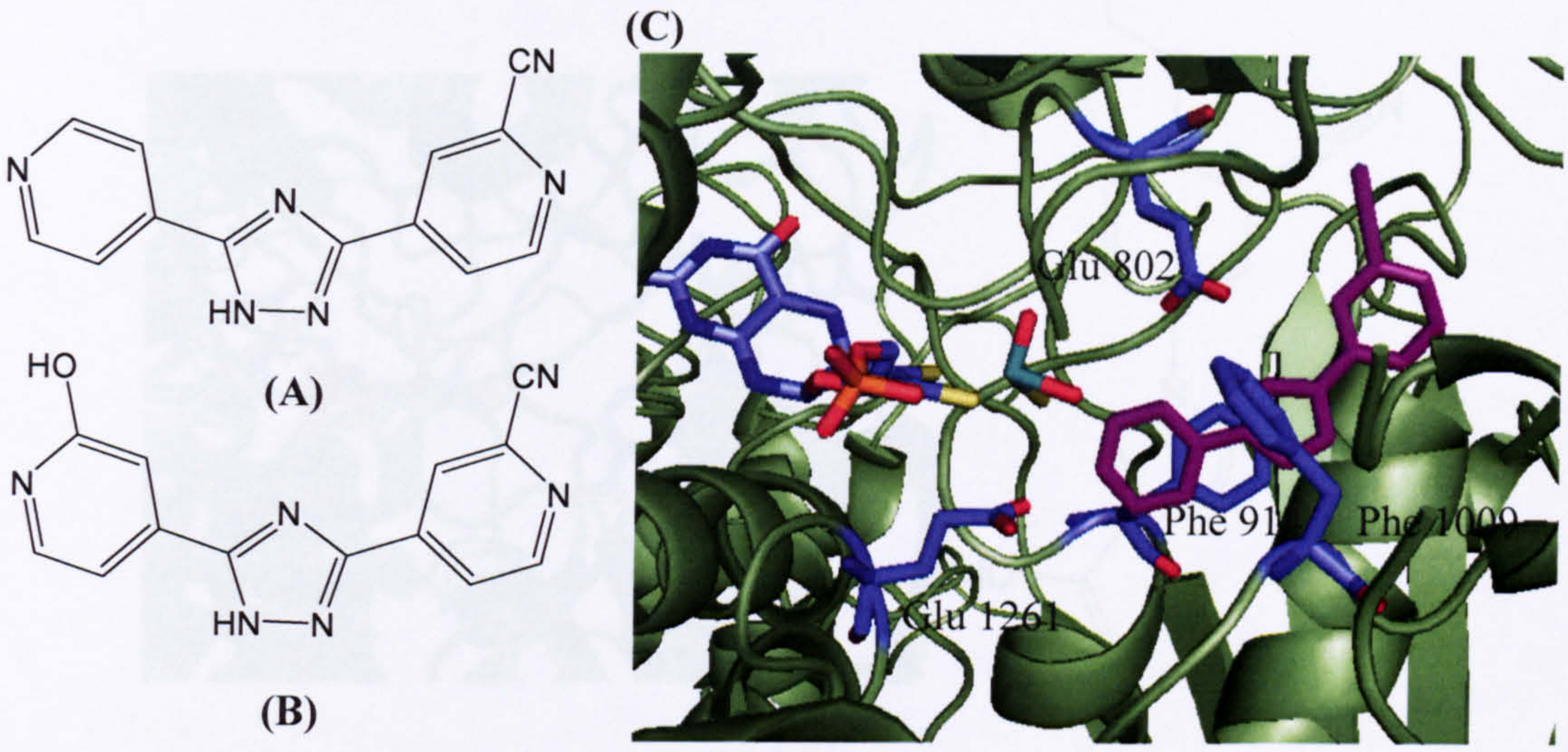

Figure 1.7 (A) FYX-051, **(B)** and 2-OH-FYX-051 produced by hydroxylation by the enzyme, **(C)** bound FYX-051 (purple) in the active site of XO[16], colours correspond to atoms: carbon: mauve; nitrogen: blue; oxygen: red; sulfur: yellow; molybdenum: green; phosphorus: orange. Original in colour.

Y-700 (1-[3-Cyano-4-(2,2-dimethylpropoxy)phenyl]-1H-pyrazole-4-carboxylic acid)[17] is a newly synthesized inhibitor of XO. Titration experiments showed that Y-700 bound tightly to the active site of the enzyme. Like TEI-6720, Y-700 closely interacts with the channel leading to the molybdenum-pterin active site but does not directly coordinate to the molybdenum ion. Y-700 is currently being investigated for its potential in clinical treatment of hyperuricemia and a number of other XOR-associated diseases.

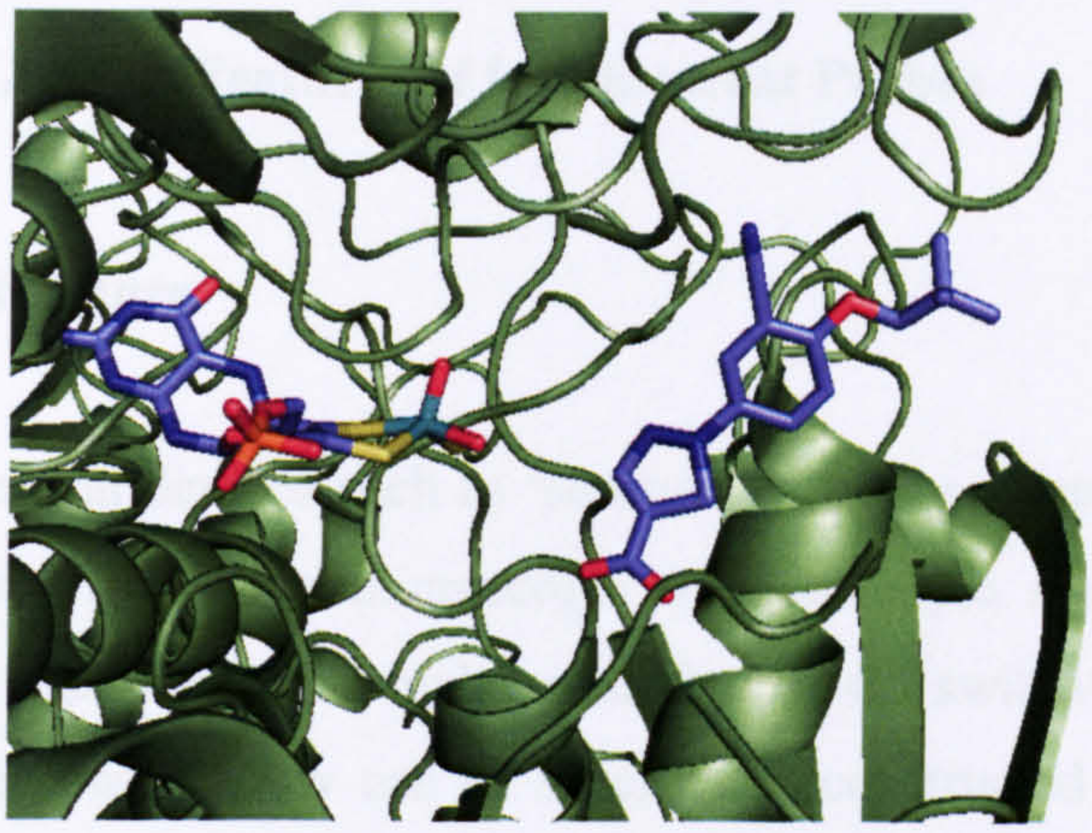

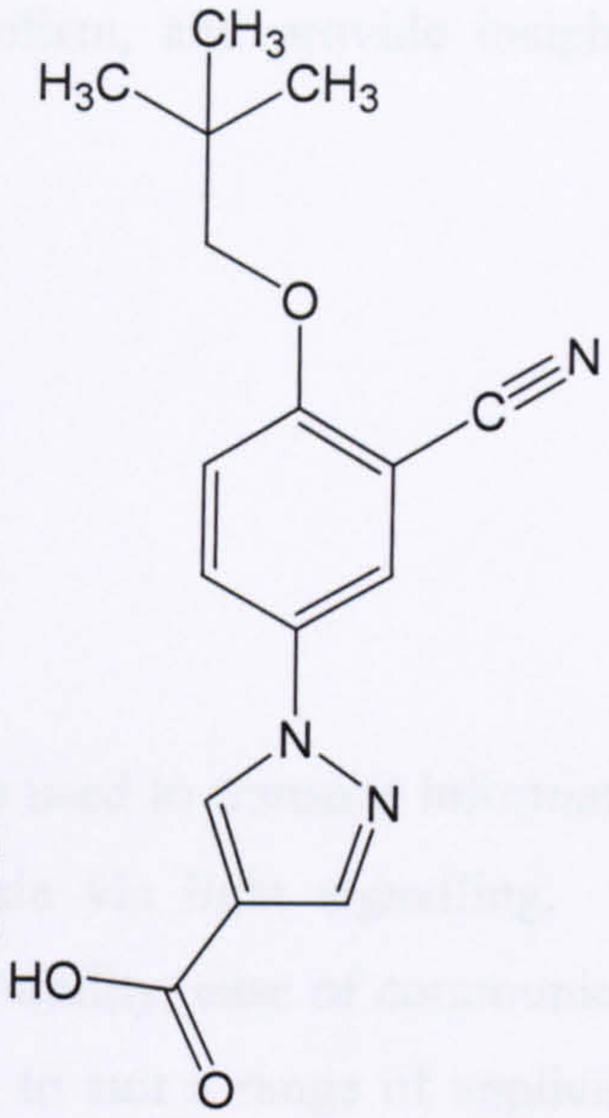

Figure 1.8 Left: Crystal structure of XO bound Y-700[18]; **Right**: Y-700. Original in colour.

Recently Krenitsky has demonstrated that XORs are useful for designing and utilising pro-drugs[19]. Drugs which are not easily absorbed by the body can be administered in an inactive but easily absorbed form, which is converted (e.g. by XO) to the active drug. For example acyclovir {9-[(2-hydroxyethoxy)methyl]guanine}, an antiherpetic agent commercially known as Zovirax, has limited absorption in humans after oral administration. 6-Deoxyacyclovir {2-amino-9-[(2-hydroxyethoxy)methyl]-9*H*-purine}, a congener, is 18 times more water soluble but lacks the required activity. However, deoxyacyclovir is readily oxidised to acyclovir by XO and may therefore be used as a prodrug suitable for oral administration.

In summary, XORs have enormous biological significance, which may be both beneficial and detrimental. It would be useful to study the molybdenum cofactor active site in detail to obtain further information on the structure, function and reaction mechanisms of these multi-substrate, multi-functional enzymes. Such information could include studying the reaction mechanisms, development of possible clinical inhibitors, substrate selectivity,

cooperativity, mechanisms of drug action and metabolism, and provide insight into the circulatory and antibacterial activity of XORs.

1.2. General Features of Luminescent Probes

1.2.1. Structure

Photochemical devices such as 'sensors' or 'probes' are used to transmit information about events occurring on a microscopic or nanoscopic scale via light signalling. They are designed to perform with high sensitivity, on-off switch-ability, ease of communication and a rapid response. They can be specifically constructed to suit a range of applications and target analytes[20,21].

The general principle is to attach a signalling unit (luminophore) covalently to the binding unit via a bridge which will enable communication between the two[22]. Binding of a substrate to the receptor unit is communicated to the signalling unit by energy transfer or electron transfer and the information is reported as a change in the luminescent properties. Each of these distinct components can be specifically designed according to the intended application to maximise supramolecular interactions, tune the spectroscopic properties and redox potentials of the components and to achieve the required solubility of the molecule.

A simple example reported by de Silva[23] is the azacrown ether shown in **Figure 1.9.**

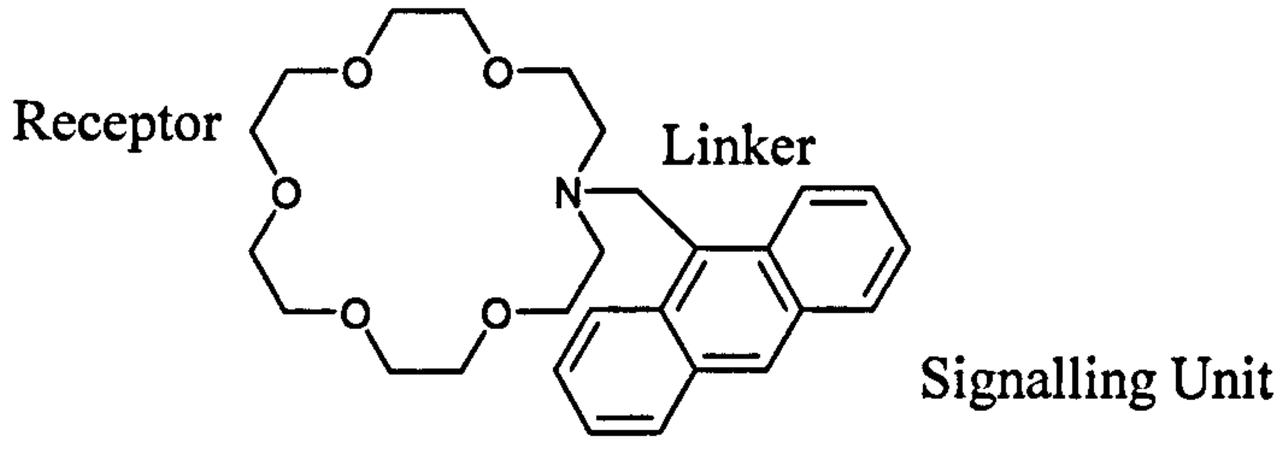

Figure 1.9 A potassium ion sensor reported by de Silva[23].

This molecule shows large fluorescence enhancements when 'switched on' by incorporation of alkali metal ions, because quenching of the anthracene fluorescence by the nitrogen lone pair is prevented on binding of sodium or potassium ions. The sensor was selective as it did not respond to lithium ions.

1.2.2. Mechanism of Communication

Photochemical molecules often operate by means of photoinduced energy transfer[24]. The luminophore (L) absorbs a photon which promotes it to an excited state (1).

$$L + h\nu \rightarrow {}^*L \qquad (1)$$

*L is a high energy species, which can decay by a number of pathways, such as photochemical reaction, radiative decay (emission of light or luminescence), non radiative decay (conversion of excitation energy to heat) or quenching processes by interaction with another molecule. The emission can be described as fluorescence or phosphorescence depending on whether it originates from an excited state of the same (spin allowed) or different (spin forbidden) spin as the ground state. Quenching of the luminescence can occur by energy transfer (2), which can be radiative or non-radiative, or electron transfer (3).

$$^*L + Q \rightarrow L + {}^*Q \qquad (2)$$

$$^*L + Q \rightarrow L^+ + Q^- \qquad (3)$$

Radiative energy transfer (4) may occur over any distance, the emitted photon is simply intercepted:

$$*L \rightarrow L + h\nu'$$
$$h\nu' + Q \rightarrow *Q \qquad (4)$$

Non-radiative energy transfer can occur when there is an interaction between *L and Q where (*L + Q) is isoenergetic (i.e. at resonance) with (L + *Q). This mechanism is subdivided into electron exchange (Dexter mechanism[25]) and coulombic energy transfer (Förster mechanism[26]) which are illustrated in **Figure 1.10**.

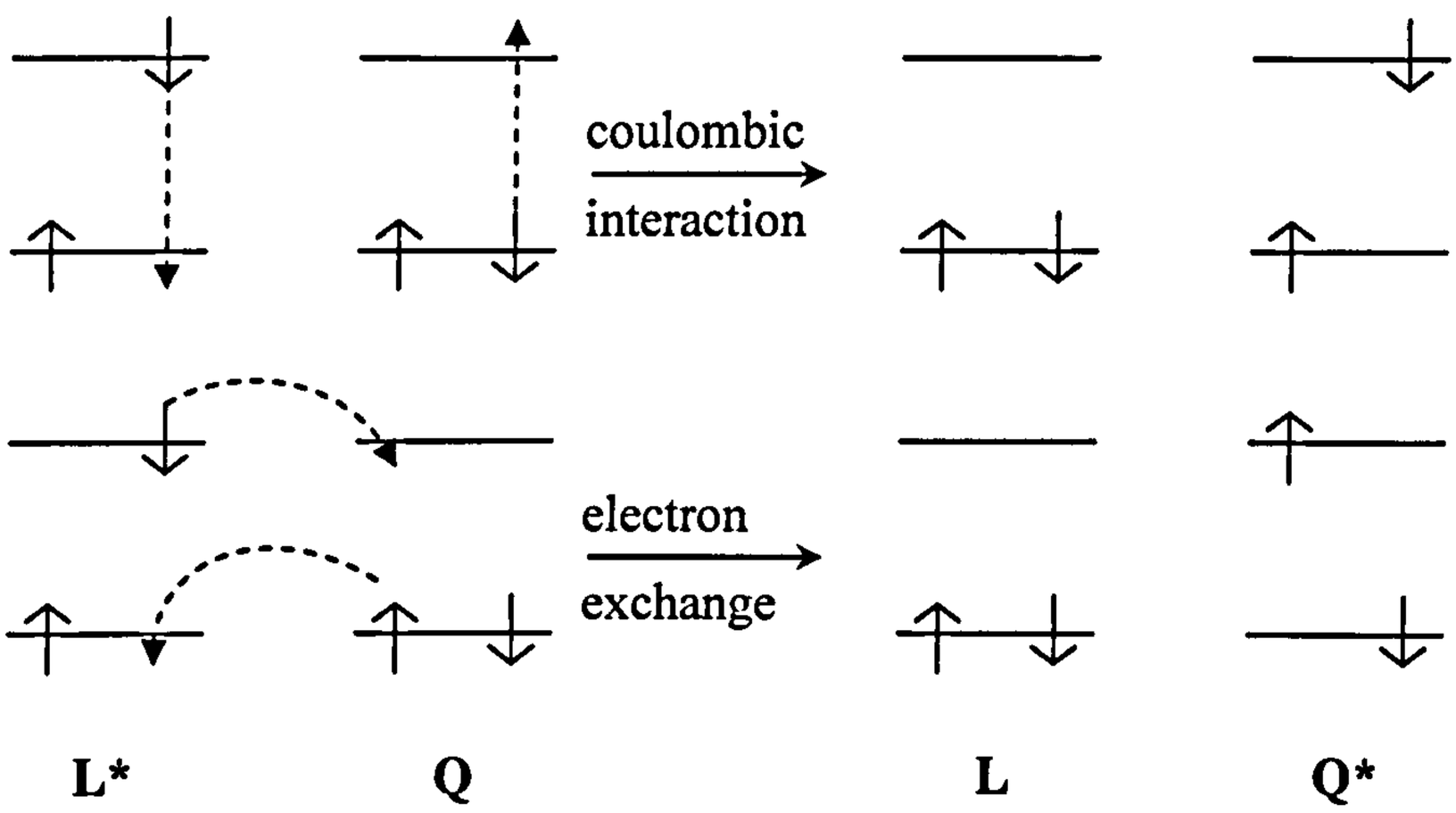

Figure 1.10 A schematic representation of the the Förster mechanism (top) and the Dexter mechanism (bottom) for a non-radiative energy transfer mechanism[24].

The electron exchange mechanism requires short donor-acceptor distances, i.e. contact, between *L and Q since it depends on orbital overlap. The electrons are simultaneously transferred when favourable overlap of the corresponding orbitals takes place on collision[24]. In order to compete with diffusion, long-lived excited states are required. Therefore, this is a common mechanism for energy transfer from inorganic chromophores for which the first

triplet excited state is sufficiently long lived[22]. Since overall spin is conserved, this mechanism enables processes to occur that would be spin-forbidden by direct conversion.

The coulombic or electrostatic mechanism takes place via the electromagnetic field, so no contact between *L and Q is required, i.e it is a long range process. In simple terms, the electrons in *L cause a perturbation in the electrons in Q. Energy transfer then takes place when relaxation of the electron in *L occurs with corresponding excitation of an electron in Q[24]. The same selection rules apply as would for the independent relaxation of the individual chromophores. Therefore this mechanism is common for singlet-singlet energy transfer between aromatic molecules with high oscillator strength (such as chlorophylls) [22].

This mechanism depends on distance according to (5).

$$\beta_e = \frac{\mu_L \mu_Q}{r^3} \qquad (5)$$

Where β_e = the electronic coupling in cm^{-1}, μ_L and μ_Q are the dipole moments of *L and Q and r is the distance between them[24].

The final process is outer-sphere electron transfer from *L to Q to give e.g. L^+ and Q^- for oxidative electron transfer shown in **Figure 1.11.** A molecule in its excited state is simultaneously a better oxidising and reducing agent than the ground state molecule because it is at higher energy. Therefore a photo-excited chromophore can subsequently transfer an electron to a second species, Q[22].

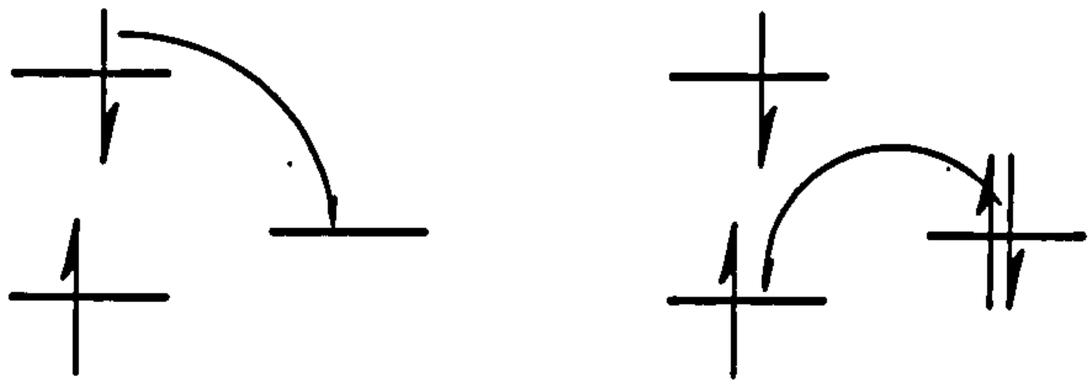

Figure 1.11 Photoinduced electron transfer. (Left) Oxidative electron-transfer and (Right) reductive electron-transfer.

Therefore *L may decay by a unimolecular pathway, radiative or nonradiative deactivation, or a bimolecular pathway, such as a chemical reaction or energy transfer. Following energy transfer *Q decays following the pathways described for *L. These are known as energy transfer sensitization processes[24]. Sensitization may induce bimolecular electron transfer reactions. Sensitizers may be chosen with the correct spectroscopic, redox and excited state properties to drive photochemical reactions, which may be thermodynamically unfavourable, i.e. they convert light energy into chemical energy. A light absorption sensitizer (LAS) absorbs light, promoting it to its excited state which reduces or oxidizes a reactant. The oxidized or reduced sensitizer then completes the redox reaction as it returns to its ground state (6). A light emission sensitizer (LES) uses the chemical energy to produce light. For example, if LES is oxidised by one of the reactants and the subsequent oxidised form then oxidises another reactant, the resulting excited state *LES can undergo radiative deactivation to the ground state, i.e. it luminesces (7).

LAS

$$A + B + h\nu \rightarrow A^{+} + B^{-} \qquad (6)$$

LES

$$A^{-} + B^{+} \rightarrow A + B + h\nu \qquad (7)$$

Both LAS and LES require a species which has sufficient stability to withstand the reaction without being consumed and the appropriate redox potentials in its ground and excited states for the process. An LAS requires a chromophore with intense absorption bands, whereas an LES requires a chromophore which has a high quantum yield of luminescence. The spectroscopic, energetic and redox properties are thus important in selecting the appropriate chromophore for a sensing device.

1.2.3. Choice of Signalling Unit

The properties which are of particular importance in choosing the relevant chromophore include the spectroscopic properties of the ground state: the frequency and molar absorption coefficient of the absorption. Similarly, the spectroscopic properties of the excited state must be considered: the efficiency of formation of the active excited state, the lifetime of that state (τ) and the quantum yield of emission (Φ).

$$\tau = 1/(k_r + k_{nr} + k_p) \quad (8)$$

$$\Phi = k_r \tau \quad (9)$$

where k_r is the rate constant for radiative decay, k_{nr} is the rate constant for radiationless decay and k_p is the rate constant for chemical reaction[22].

The redox behaviour of the system is defined by the redox potentials for oxidation (E_{ox}) and reduction (E_{red}) of the ground and excited state of the components and the energy of the exited state (E_{00}). For electron transfer, a one electron redox reaction between the ground state donor and the excited state acceptor component occurs. Therefore

$$\Delta G = E_{ox}(D) - E_{red}(A) - E_{00} \quad (10)$$

1.2.3.1. Metal Complexes

Metal complexes with aromatic ligands, such as polypyridyls, are frequently chosen as luminescent signalling units[27, 28]. $[Ru(bpy)_3]^{2+}$, an example which has been extensively studied, is shown in **Figure 1.12**[30].

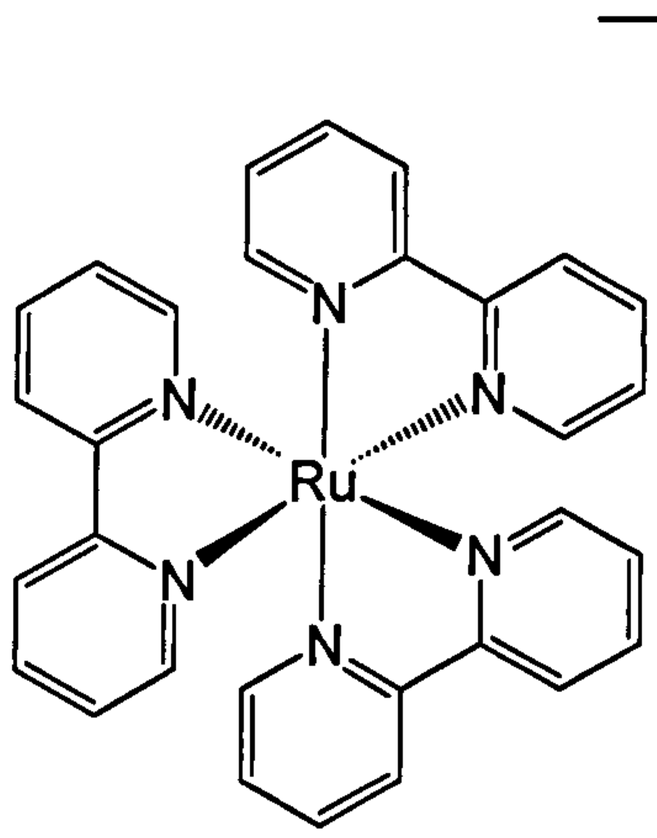

Figure 1.12 $[Ru(bpy)_3]^{2+}$

Metal complexes are suited to these applications because they exhibit metal-to-ligand charge transfer bands at relatively low energies (the MLCT is 2.1 eV above the ground state in the case of $[Ru(bpy)_3]^{2+}$)[27]. This means that they absorb in the visible and near UV region of the spectrum (e.g. 450 nm). The heavy metal atom leads to spin-orbit coupling which enables fast and efficient population of the lowest exited state (S1 → T1)[29]. This is normally spin forbidden in organic molecules. In addition, the lowest excited state is usually luminescent in solution at room temperature. The metal complexes possess distinct redox centres. Each of these properties may be chosen or tuned for a specific process, such as signalling of the binding of a substrate by a sensor, by altering the metal or ligands.

However, these types of complexes usually emit in the visible region. Since the absorption spectrum of XO is dominated by the strongly absorbing flavin and iron sulfur clusters, a photosensitiser with a high extinction coefficient is required[1].

1.2.3.2. Porphyrins

Another well documented class of luminophores is formed by free-base or metal containing porphyrins. Abundant in nature as chromophores[31] and in electron transfer mechanisms[32] they are incorporated in enzyme active site models[33, 34]. Porphyrin-based electron transfer systems are widely studied with respect to charge separated intermediates for possible photosynthesis mimics[35]. One of the most common systems is the porphyrin-quinone dyad due to its biological significance[36]. An example is that reported by Connolly *et al.*, illustrated in **Figure 1.13**[37].

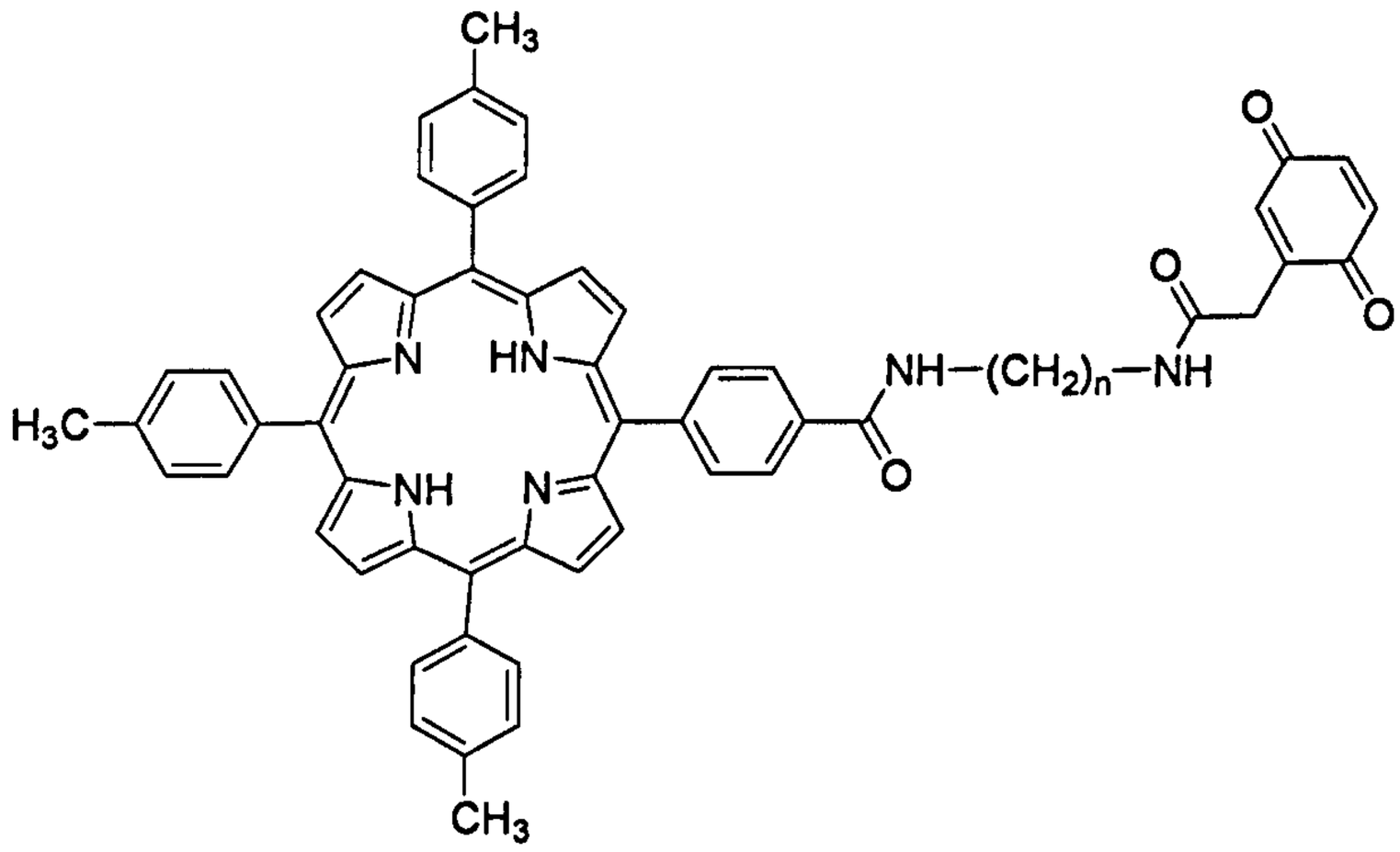

Figure 1.13 Porphyrin-quinone dyad reported by Connolly *et al.* n = 2, 3, 4[37].

Biradical ion pairs ($P^{\bullet+}$-$Q^{\bullet-}$) are generated upon irradiation, and can be observed by EPR. Photochemical electron transfer (> 10^{-8} s^{-1}) occurs, in moderately polar solvents, from the excited singlet state and is quenched by up to 40 % upon attachment of a quinone compared to porphyrins without attached quinone, with hydroquinone or dimethyl benzene attached. In these flexible systems, the quinone moiety may fold over to interact with the π-system of the porphyrin causing broadening of the Soret band in the absorption spectra, but no other absorption spectral changes are observed. In these cases, broadening and red shifting of the emission bands and reduction of the quantum yields is attributed to enhanced radiationless decay. A long lived component (~ 9 ns) of the decay is attributed to the 'extended' conformer; a shorter lived component (~ 2 ns) is attributed to the 'folded' conformer. For

the optimal system, (fully oxidized quinone, n = 3) the fluorescence yields and lifetimes are as short as 1.7-1.9 and 7.5 ns. Quenching diminishes with lowering of temperature since rotation to give optimum orbital overlap is slowed and no longer occurs within the lifetime of the excited singlet state.

The carotenoid-porphyrin-quinone triad[38] in **Figure 1.14** was shown to mediate photoinduced proton transfer across a lipid membrane, mimicking conversion of light energy into ATP chemical potential by photosynthetic bacteria[45].

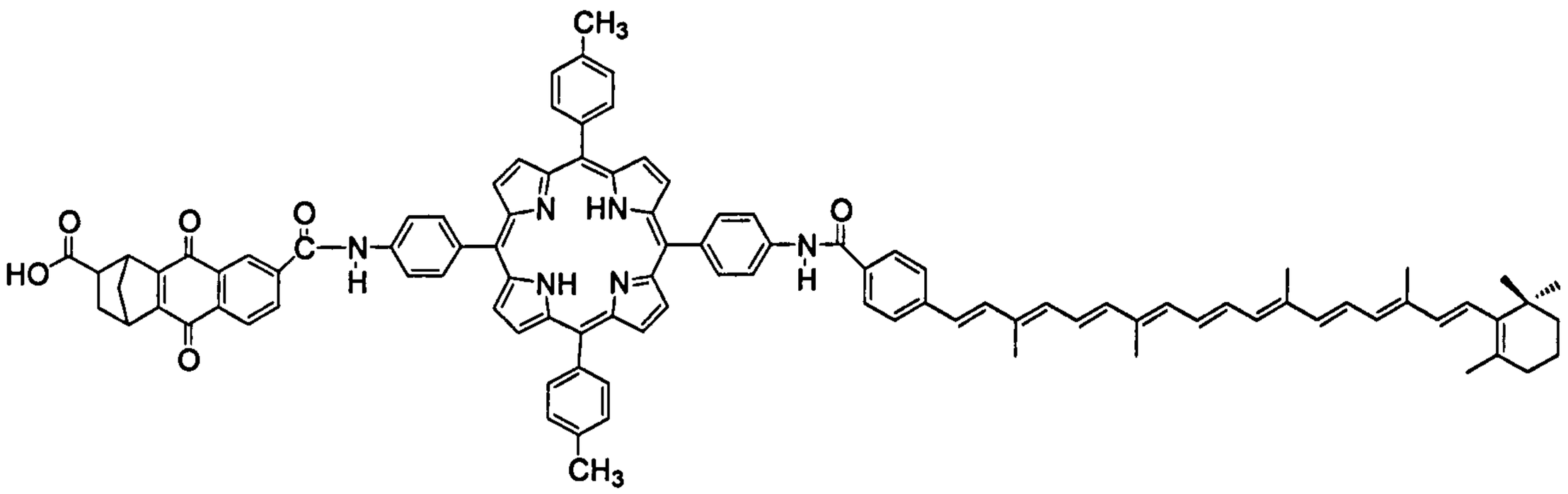

Figure 1.14 Above: Carotenoid-porphyrin-quinone triad reported by Gust, Moore and Moore[38]; Below: photoactive compounds for active transport of Ca^{2+} across a lipid membrane.

The group have modified the system to create a system which mimics active transport of calcium ions across a lipid membrane[38]. Ca^{2+} may bind to the quinone and hydroxyquinone

compounds in **Figure 1.14** on the outer side of the membrane enabling it to diffuse across to the inner surface. Photoinduced electron transfer of the porphyrin triad produces a carotenoid radical cation which oxidises the complex releasing Ca^{2+} to the inner aqueous phase and diffuses back across where it can pick up another cation.

Since fullerenes have first reduction potentials comparable to that of benzoquinone, small reorganisation energies (λ) due to their rigidity, and ability to form short Van der Waals contacts with porphyrins (2.7-3.0 Å), porphyrin-fullerene electron transfer has been extensively studied[39,40,41]. Fullerenes are capable of accepting up to six electrons reversibly which makes these systems of particular interest for potential solar energy conversion and storage devices[42]. Such electron transfer may occur intermolecularly from the porphyrin triplet excited state to the C_{60} or C_{70}, or intramolecularly from the porphyrin singlet state to the fullerene components in a supramolecular dyad, triad or larger assembly. The following examples serve to illustrate the different mechanisms by which porphyrins may coordinate to a second species, such as a fullerene, and the resulting changes in luminescence.

A host of axially coordinated porphyrin-fullerene systems have been studied such as that in **Figure 1.15 (A)**[43]. Coordination to the metal is indicated by a red-shift in the absorption spectra of the porphyrin. The electron transfer rate is smaller in such systems than in the equivalent covalently bonded systems **(B)**. Electron transfer occurs from the porphyrin excited singlet state in non-coordinating solvents or the excited triplet state in coordinating solvents. By covalently attaching the fullerene to one of the phenyl substituents as shown in **Figure 1.15 (B)**, control over the distance and orientation between the donor and acceptor components can be achieved[44]. This can be used to tailor the electron transfer rates, lifetimes and higher order structures.

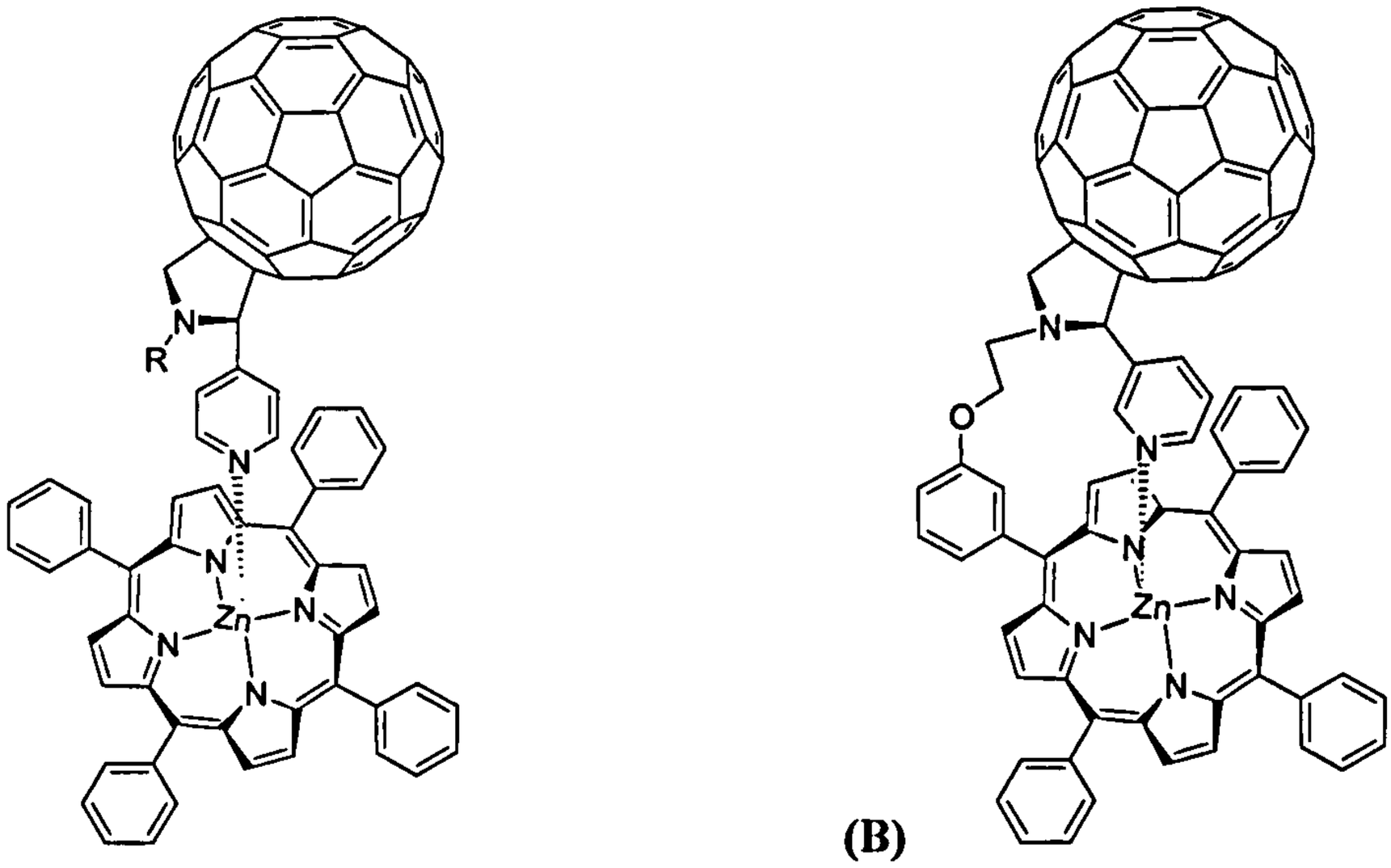

Figure 1.15 Porphyrin-fullerene dyads reported by D'Souza *et al*[43,44].

Stevenson and coworkers have used supramolecular interactions to construct the self-assembled supramolecular porphyrin-fullerene dyad shown in **Figure 1.16**[41]. Self assembly in non-coordinating solvents gave rise to a decrease in the fluorescence emission of the porphyrin with increasing concentration of fullerene. Watson-Crick hydrogen bonding between a porphyrin-appended cytidine and a fullerene-appended guanine brings the donor and acceptor moieties sufficiently close for through space electron transfer. Restoration of the fluorescence was observed on addition of a hydrogen bond disruptor (hexafluoro-2-propanol). Time resolved fluorescence studies revealed biexponential decay with a component for the uncomplexed porphyrin excited state (τ_1 = 2.1 ns) and for the photoelectron transfer (PET) quenching of the porphyrin by the hydrogen bonded fullerene (τ_2 = 0.6 ns).

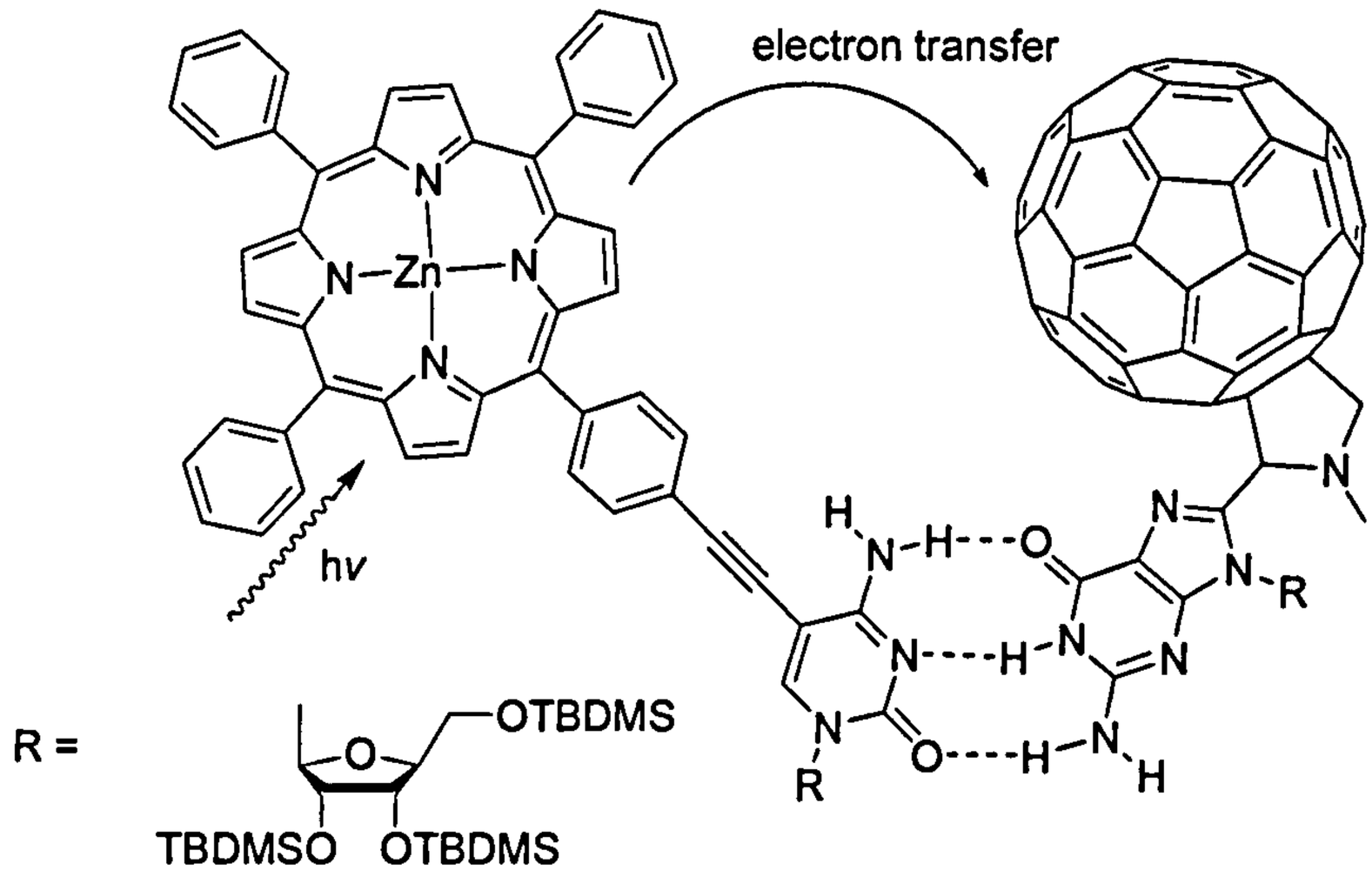

Figure 1.16 Watson-Crick hydrogen bonded porphyrin fullerene dyad reported by Stevenson *et al.*

Time-resolved infra-red spectroscopy (TRIR) can be used to study the photophysics of these systems as fullerenes have characteristic singlet-singlet and triplet-triplet absorptions in the visible and near infra red region. π-Radical anions ($C_{60}^{\bullet-}$, $C_{70}^{\bullet-}$) show narrow bands in the near-IR (1080, 1380 nm) which serve as a diagnostic tool in porphyrin-fullerene systems where the visible region is dominated by the porphyrin. The fullerene radical anion was observed at 1000 nm and the charge separated radical anion pair had a lifetime of 2.02 μs.

In summary, porphyrins are able to report binding to a redox centre via direct coordination through the porphyrin metal centre, covalent attachment, or supramolecular interactions such as hydrogen bonding or π-stacking. Porphyrins are suitable signalling units since their absorption and luminescence spectra are altered by such binding.

1.2.3.3. Applications of Water Soluble Porphyrins

For a biological application, such as the XO studies, water solubility is essential. Water soluble porphyrins have been investigated for their potential biological importance. Cationic porphyrins have been found to chelate to DNA[45, 46, 47]. Polar porphyrins with long organic chains appended may interact with lipid membranes[48, 49, 50] and can be used in small molecule sensing due to their luminescent properties[51].

The most widely documented potential application of water soluble porphyrins is in photodynamic therapy[52]. A free base porphyrin acting as a photosensitiser may generate singlet oxygen by energy transfer from its excited state to molecular oxygen. The reactive oxygen species causes oxidative damage to biological material. Therefore this process may be utilized for antibiotic, antiviral and anticancer purposes in photodynamic therapy. If the photosensitiser accumulates in tumours cells, the surrounding area may be irradiated by visible light, selectively building up lethal reactive oxygen species which destroy the tumour. Retention of the sensitizer in tumour cells occurs as a result of its faster removal from healthy tissue than the malignant tissue.

Lang *et al.*[53] comment on the photophysics involved and the requirements for the photosensitiser. Porphyrins are well suited to this purpose since they typically absorb at the required wavelengths (below 800 nm, avoiding competition from water, and above 400 nm, avoiding photosensitization of the skin). Fluorescence provides a means of detection. Porphyrin compounds are sufficiently stable to withstand the conditions and photochemical processes involved.

Tailoring of the peripheral groups of the macrocycle to suit a particular host increases the selectivity. Charged groups introduce water solubility: cationic porphyrins such as TMPyP **(Figure 1.17)** are well documented[54] due to their potential to intercalate between the guanine-cytosine base pairs in DNA. Negatively charged porphyrins such as TPPS[55] interact with proteins with positively charged side chains such as protonated nitrogen atoms while

neutral sensitizers such as OEP may accumulate in lipid membranes[56]. A carrier such as a cyclodextrin[57, 58] may be required to administer the compound.

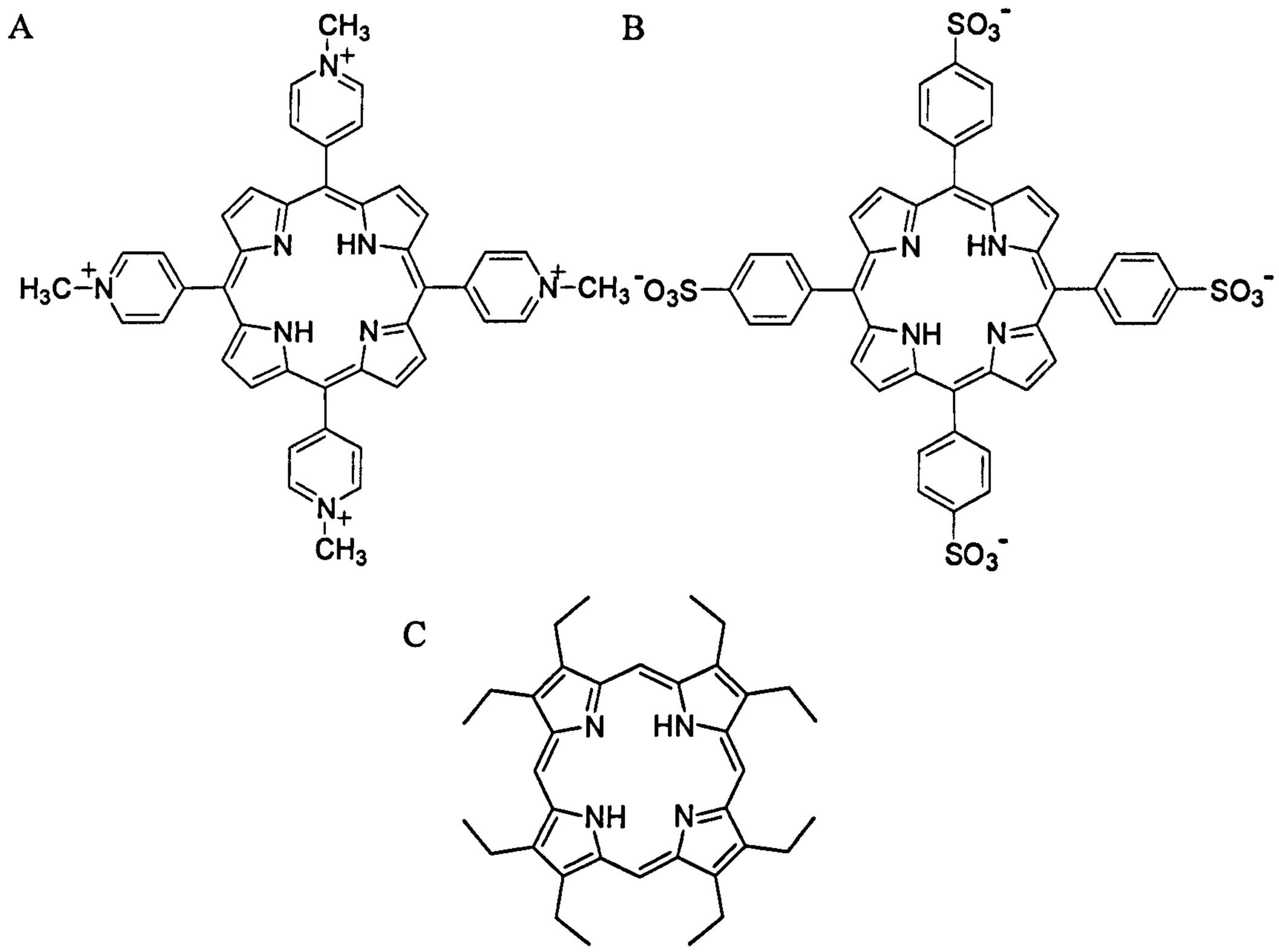

Figure 1.17 **(A)** Free base 5, 10, 15, 20 Tetrakis(*N*-methylpyridinium-4-yl)porphyrin, TMPyP; **(B)** Free base meso-tetra(4-sulfonatophenyl)porphine, TPPS; **(C)** Free base octaethyl porphyrin, OEP.

One of the advantages of using porphyrins in this way is that information may be gathered about the types of interactions involved between the photosensitiser and its local environment since they are capable of reporting host-guest interactions as described previously. In particular there are characteristic differences between absorption and emission spectra of monomeric porphyrins and those of aggregates, where the energy is dissipated, causing a reduction in fluorescence lifetimes and quantum yields. In some cases porphyrin aggregation is disrupted on interaction with a host, while in others aggregation is

caused by self-stacking on the host exterior[59] or incorporation into a liposome[60]. The resulting shift in absorption maxima, for example, would report the corresponding mechanism.

Cyclodextrins (CDs) are frequently used to demonstrate host-guest interactions in aqueous media because of their hydrophobic interior and water soluble periphery, as illustrated in **Figure 1.18**. The cavity can incorporate a range of guests, including some porphyrins. This makes cyclodextrins potential carrier molecules to transport hydrophobic compounds into the body[61, 62]. They are also known to disrupt aggregation of porphyrins[53], demonstrated by a red-shift of the Soret band and fluorescence emission bands. The intensity of the emission bands varies according to the porphyrin substituents and the nature of the connecting link between βCDs. Excited triplet state lifetimes are increased because collisional quenching by solvent and diffusion-controlled quenching by oxygen is reduced by encapsulating the porphyrin within the CD.

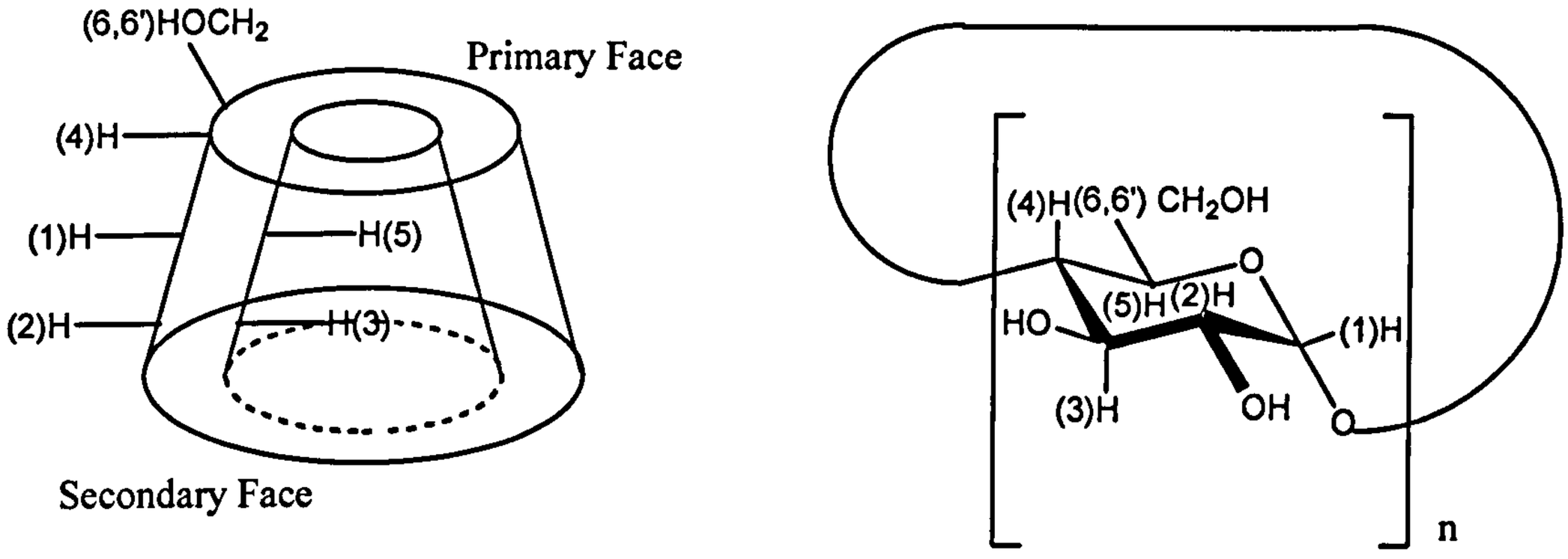

Figure 1.18 Schematic representation of cyclodextrins described by Lang *et al.*; αCD: n=6; βCD: n=7; γCD: n=8[53].

1.2.4. The Bridge

For bimolecular processes of excited states, the lifetimes of the excited chromophores must be sufficiently long lived (>10 ns) to overcome the kinetic restrictions (i.e. diffusion). For applications in supramolecular devices, such as sensors and luminescent probes, the luminophore and binding unit are not discrete, but tethered for efficient communication, as demonstrated by the examples so far. At the very least, the bridge serves to hold the components sufficiently close to enable communication by energy/electron transfer[63]. As in the previous examples, the linker may be anything from a covalent bond to a supramolecular interaction, but it defines the rigidity, length and conformationl behaviour of the system. A suitable choice of linkage may enable such rapid energy transfer that the first singlet and higher excited states may be quenched (8)[22].

$$*D–B–A \rightarrow D–B–A* \qquad (8)$$

In order for long-range communication of events occurring at one site, the other must ideally be electronically coupled via the bridge. A certain degree of orbital overlap or electronic interaction is required for electron transfer or electron exchange. Consequently, the bridge may provide a through bond mechanism for the transfer of energy and therefore information.

Examples of energy transfer systems, in which electron transfer is mediated by the bridge, have been investigated by Albinsson *et al.* The group have studied electron transfer within 25 Å 'donor-bridge-acceptor' systems in order to monitor the influence of the bridging chromophore on the photoinduced electron/energy transfer[64]. In these systems, two porphyrins are incorporated: a zinc porphyrin is the donor and a gold(III) porphyrin is the acceptor. A third chromophore, the 'bridge', makes up the triad.

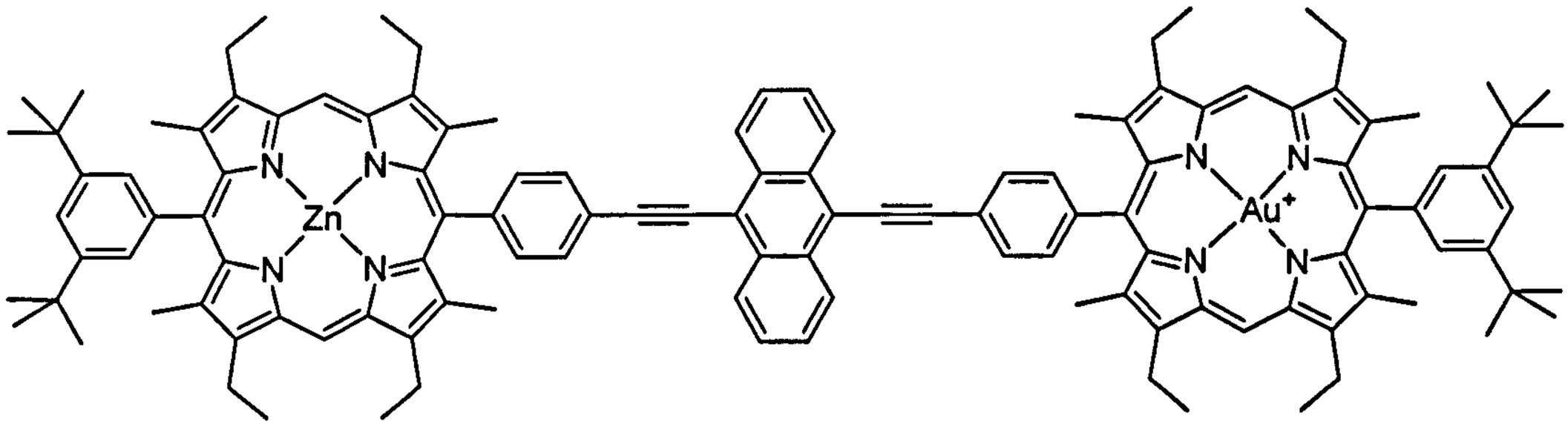

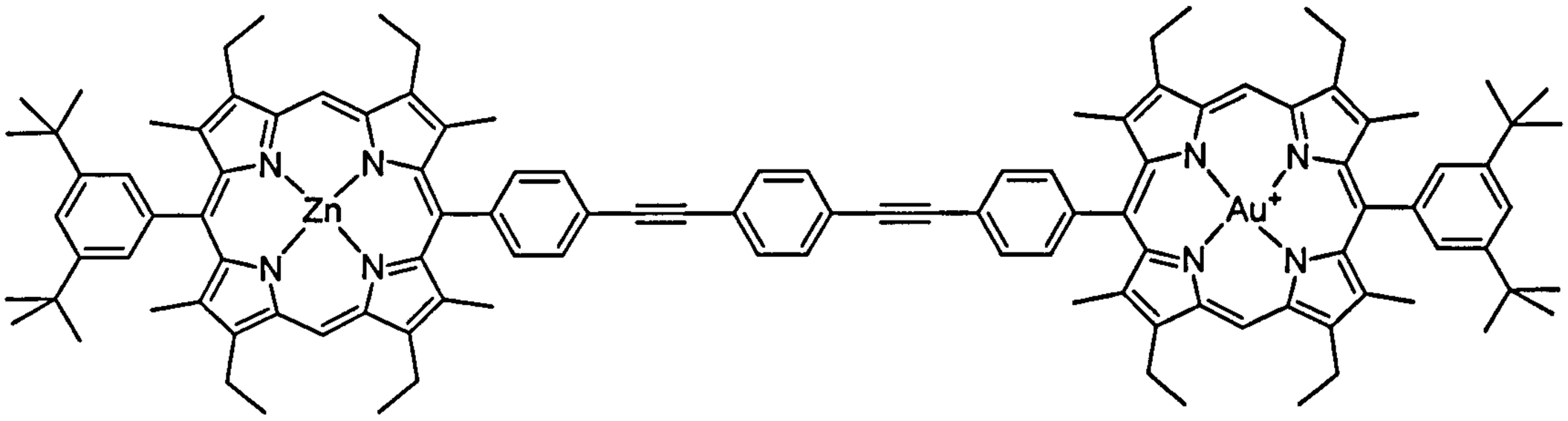

Figure 1.19 Benzene and anthracene bridged porphyrin triads (ZnP-B-AuP$^+$) triads studied by Albinsson *et al*[64].

The largest quenching effect is observed in the anthracene bridged systems. In these examples long-range direct superexchange-mediated electron transfer processes[65] compete independently with sequential electron transfer in polar solvents. In weakly polar solvents, such as 2-methyltetrahydrofuran, only direct electron transfer occurs[66]. It is believed that the electron tunnels through unoccupied orbitals, or 'virtual low-lying excited states', of the bridge rather than travelling through space. The alternative, sequential electron transfer is said to go via a 'hopping' mechanism[67]. The key difference between the two mechanisms is that superexchange mediated electron transfer results directly in the charge-separated state ($D^{\bullet+}BA^{\bullet-}$), whereas the sequential mechanism goes via a charge-separated intermediate ($D^{\bullet+}B^{\bullet-}A$) where the electron is temporarily localised on the bridge, which in turn gives the charge separated state ($D^{\bullet+}BA^{\bullet-}$) (**Figure 1.20**). Both of these processes are widely discussed with respect to molecular wires[68, 69, 70]. In these various bridging systems the superexchange phenomenon is often evaluated in terms of a distance-dependent 'attenuation factor', β (Å).

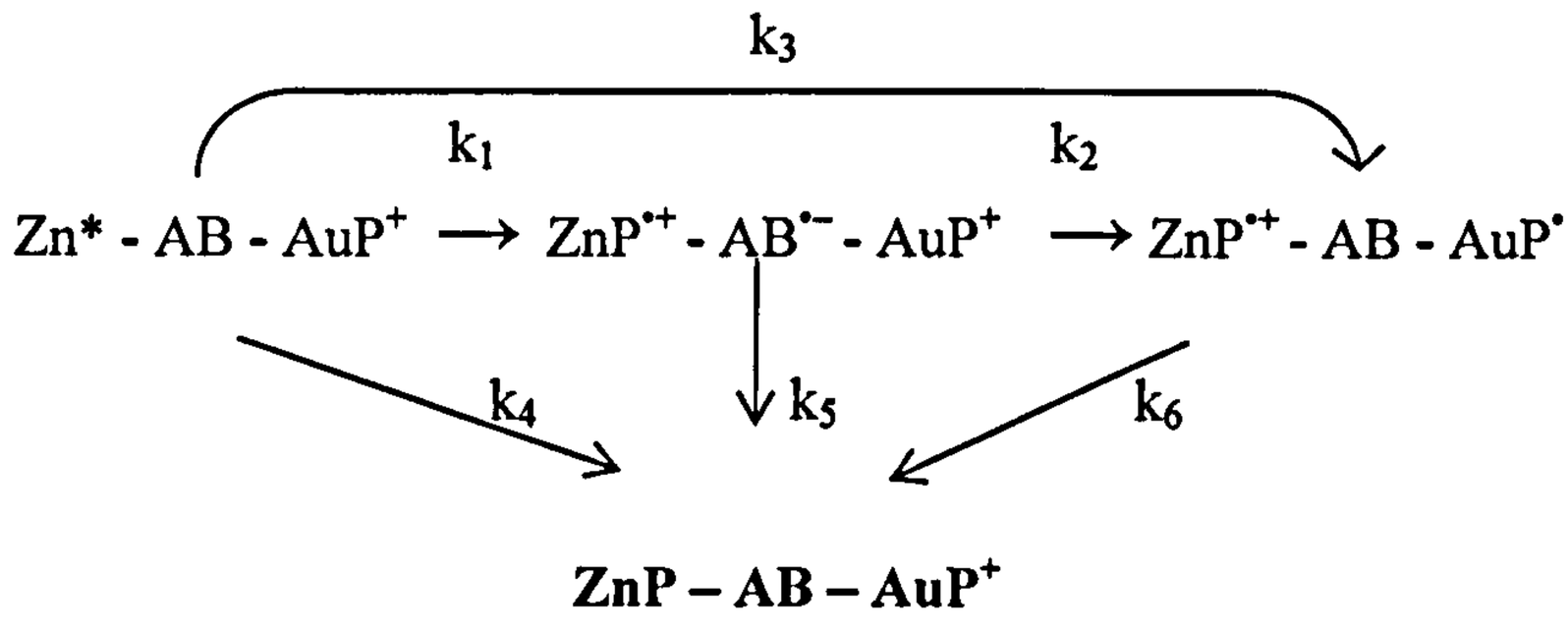

Figure 1.20 The competing deactivation processes: sequential and superexchange-mediated electron transfer[65]. $k_1 - k_6$ are rate constants for each of the processes illustrated.

It has been demonstrated that the mechanism can be controlled by tuning the energy gaps between the D-B-A primary excited state and the charge separated states[71, 72]. Such systems are therefore sensitive to temperature, solvent, the metals coordinated within the porphyrins and the nature of the bridging chromophore. Consequently, the choice of bridge for a probe molecule may affect the mechanism and rate of communication (e.g. electron or energy transfer) between the binding unit and the signalling unit.

1.3. Probing Enzyme Active Site

Lo *et al.* have reported luminescent probes for indole-binding proteins which show protein-induced emission enhancement on binding to tryptophanase and bovine serum albumin (BSA) (**Figure 1.21**)[73]. Tryptophanase is a bacterial pyridoxal 5-phosphate (vitamin B_6) dependent lyase that catalyses the breakdown of of L-tryptophan to indole, pyruvate and ammonia as well as a variety of α,β-elimination and β-replacement reactions on a number of other β-substituted L-amino acid residues[74]. BSA is a large water-soluble globular protein which binds and transports lipids, fatty acids, amino acids and other small molecules[75]. Metal complexes were chosen over organic luminophores since the poor spectral overlap and mis-matched electrochemical properties with the enzyme prevent quenching by resonance energy transfer to the protein.

The dpqa/dpq and pyridine ligands have intense absorption bands at 259-298 nm due to spin allowed $\pi \rightarrow \pi^*$ intraligand (^{1}IL) transitions and less intense bands at 355-393 nm due to metal-to-ligand charge-transfer (^{1}MLCT) transitions. The absorption due to the indole is less intense. The luminescence wavelength (500-570 nm) depends on the nature of the ligand and the solvent. The emission of tricarbonylrhenium(I) indole complexes is concentration dependant (weak in polar solvents, e.g. aqueous buffer, stronger in less polar solvents, e.g. dichloromethane) and the presence of the indole lowers quantum yields and shortens lifetimes. This indicates self quenching of the rhenium(I)dipyridoquinoxaline by indole.

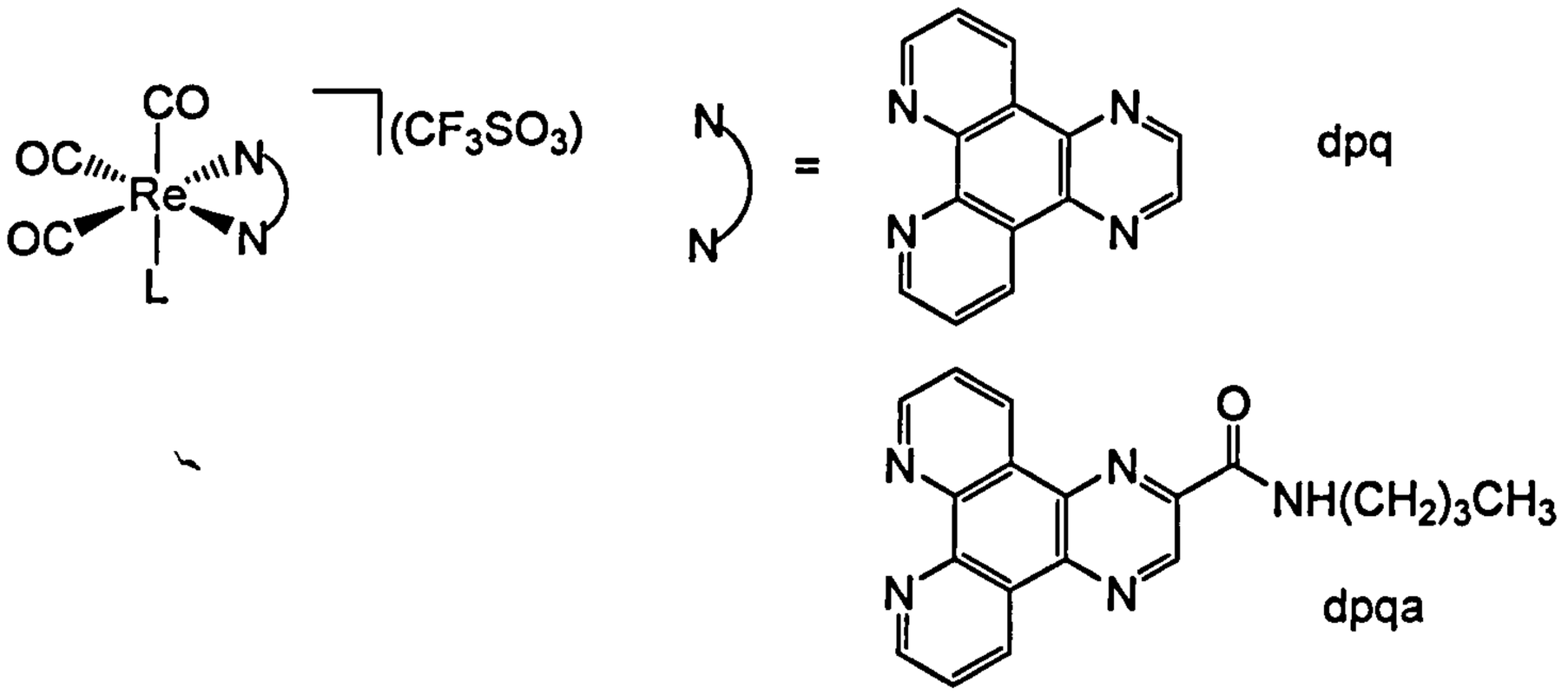

Figure 1.21 Tricarbonylrhenium(I) dipyridoquinoxaline complexes reported by Lo *et al.*[73]

Lo *et al.* suggested that the quenching occurs by intermolecular electron transfer (9). Evidence for reductive quenching by indole comes from the redox potentials of the indole

free complexes and indole ($E^{O}[Re^{+*/0}]$ = +1.43, +1.48 V; $E^{O}[indole^{+/0}]$, +1.06 V vs. SCE) and the self-quenching rate constants of the indole complexes ($3.3 - 6.8 \times 10^{9}$ $dm^3 mol^{-1} s^{-1}$) which are similar to the bimolecular quenching rate constant of the emission of the indole free complexes by indole ($1.3 - 1.9 \times 10^{10}$ $dm^3 mol^{-1} s^{-1}$).

$$Re^{+}* + indole \rightarrow Re^{0} + indole^{+\cdot} \quad (9)$$

On titration with BSA, the absorption spectra for the tricarbonylrhenium(I) indole complexes were unchanged whilst the emission intensities and lifetimes were enhanced substantially. The decay remained single exponential. The emission for the indole free complexes remained unchanged. This suggests that the indole moiety binds to the protein, increasing the emission due to the hydrophobic environment and preventing intermolecular electron transfer between the complexes. The binding constant for the complexes with the longer alkyl chain (spacer) were larger than for those with a shorter spacer.

Enzyme inhibition assays were carried out with tryptophanase. The conversion of L-serine to pyruvate was inhibited in the presence of indole (48 %, K_m = 328 mM) and the tricarbonylrhenium(I) indole complexes (64-68 %, K_m = 298 – 389 mM) in a non-competitive fashion. The binding affinity was not greatly affected by the length of the spacer. No inhibition was observed in the presence of the indole free complex with the dpq ligand, whereas inhibition was observed for the dpqa complex (44 %) possibly due to interaction of the amide substituent with the enzyme.

Lo *et al.* have also developed luminescent biotin conjugates which bind to avidin. This tetrameric protein can bind up to four biotin molecules at two pairs of binding sites on each side of the structure, with a first dissociation constant $K_d \sim 10^{-15}$ M[78]. Because of this strong affinity, the system is a widely used biochemical tool for detection and isolation of biotinylated molecules.

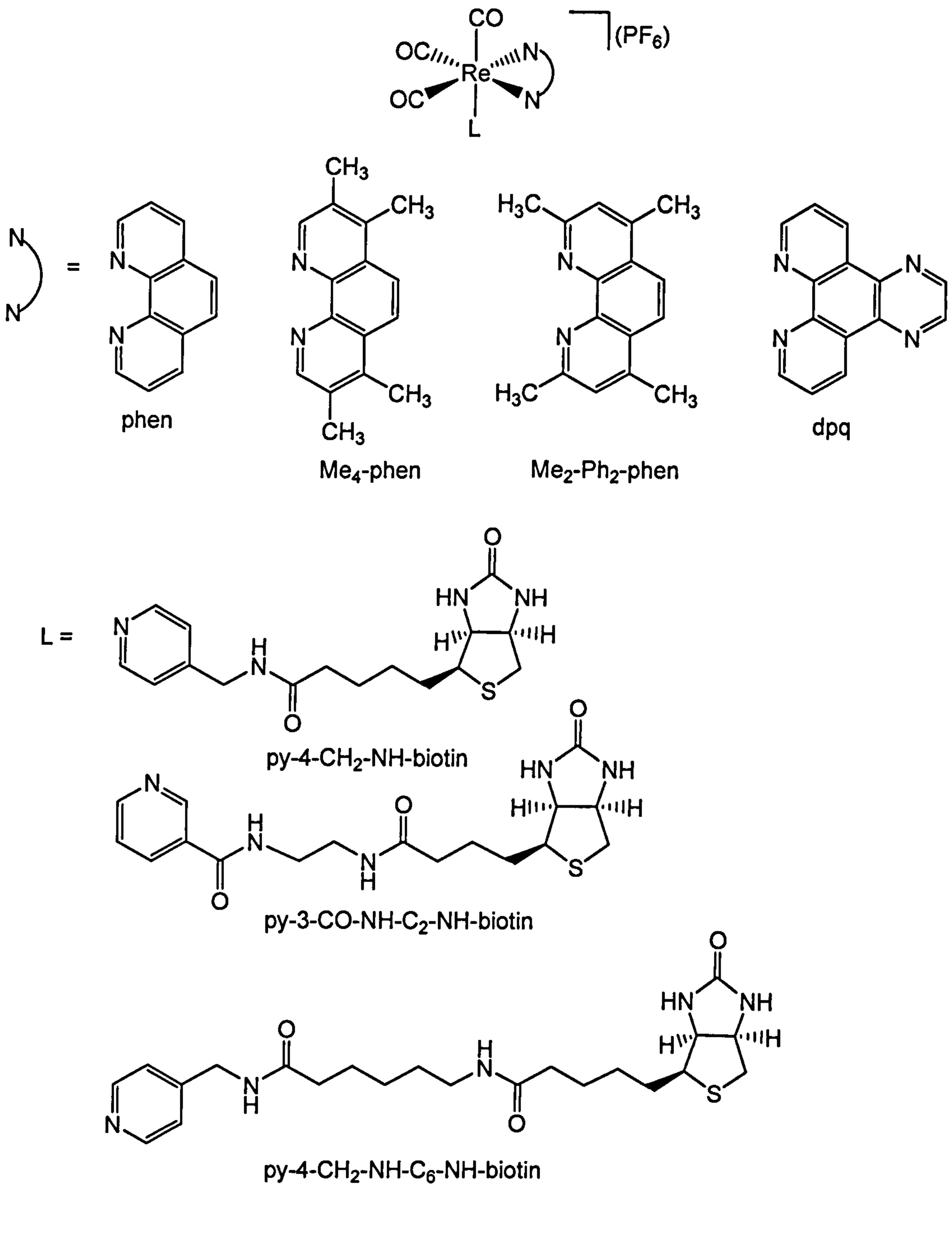

Figure 1.22 py-spacer-biotin complexes reported by Lo *et al*.[76]

Each of the probe complexes in **Figure 1.22** exhibited solvent dependant triplet MLCT ($d\pi(Re) \rightarrow \pi^*$ (N-N)) emission (500-570 nm) as observed for the indole systems. The exception was the Me_4-phen complex, which exhibited long lived emission (7.3-14 ns) due to the low lying ^{3}IL (Me_4-phen) emissive state. The emission intensities were enhanced and the lifetimes extended on binding to avidin. As for the tricarbonylrhenium(I) indole complexes with BSA, the emission enhancement can be explained by increased rigidity and hydrophobicity of the protein binding pocket. The binding was investigated using a standard HABA (4′-hydroxyazobenzene-2-carboxylic acid) assay whereby absorption at 500 nm corresponding to avidin-bound-HABA decreases on addition of the rhenium(I)-biotin complexes, indicating that HABA had been displaced by the probes. Each of the complexes bound with 4:1 stoichiometry, as for biotin itself. The more hydrophobic (Me_4-phen, Me_2-phen) complexes showed greater enhancement than the others (phen, dpq) as did the complexes with the shorter spacer (py-4-CH_2-NH-biotin). However, the binding was stronger for the complexes with the longer spacers.

Similarly, the iridium complexes in **Figure 1.23 (A)** exhibited solvent dependant, long-lived (ns) ^{3}MLCT ($d\pi(Ir) \rightarrow \pi^*$ (bpy-CH_2-NH-C2-NH-biotin)) luminescence (550-590 nm in degassed solution). The complexes in **Figure 1.23 (B)** exhibited even longer-lived (ms) luminescence (528-712 nm in degassed solution) with structured emission bands corresponding to ^{3}IL ($\pi \rightarrow \pi^*$) (N-C$^-$) with some mixing of ^{3}MLCT ($d\pi(Ir) \rightarrow \pi^*$ (N-C$^-$)). On addition of avidin the emission is enhanced as for the rhenium complexes and the binding was investigated by HABA assays as described above. The complexes with the most hydrophobic ligands exhibited the most enhancement as for the rhenium(I)-biotin complexes. The complexes with the most significant emission enhancement and therefore greatest sensitivity were the biphenyl and naphthyl complexes in (**B**). The iridium complexes each bound several orders of magnitude more weakly ($K_d \sim 10^{-10}$ to 10^{-8} M) than biotin itself.

A

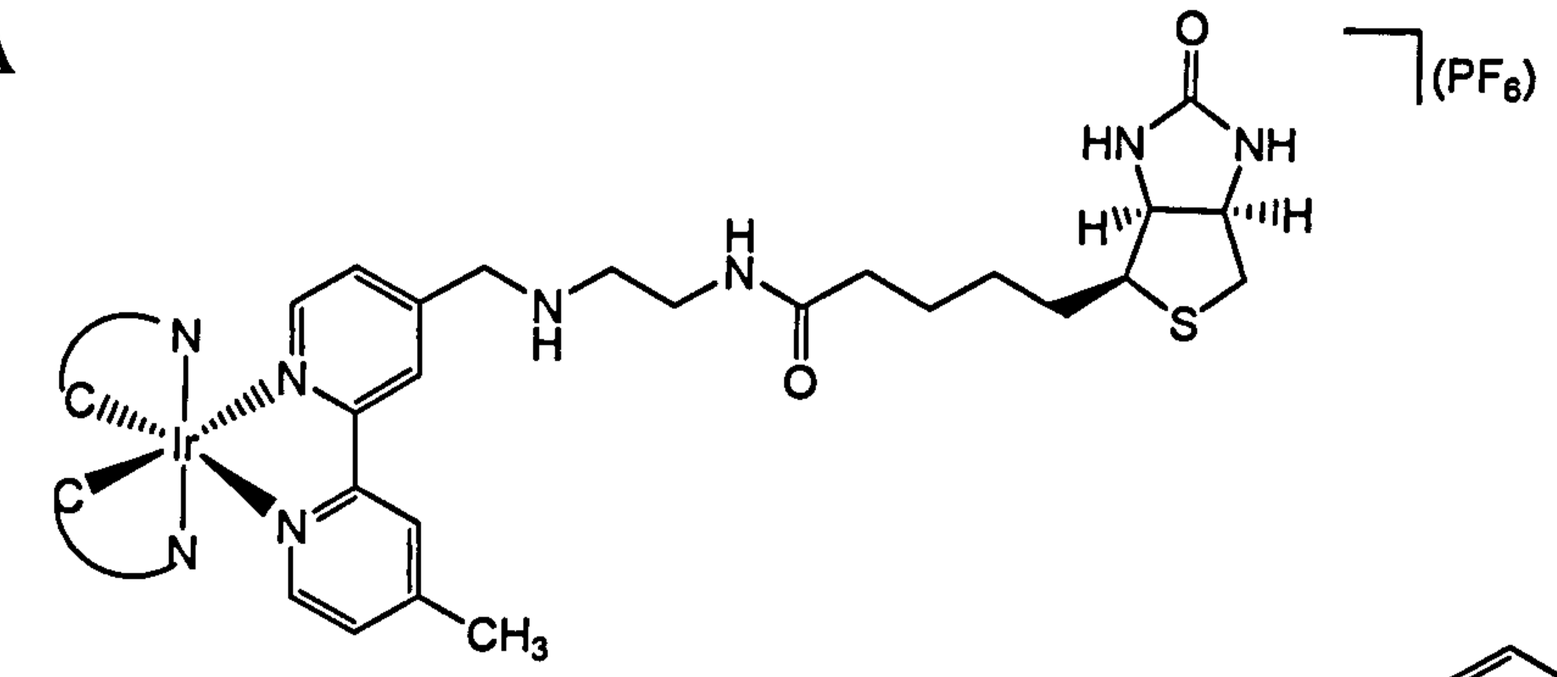

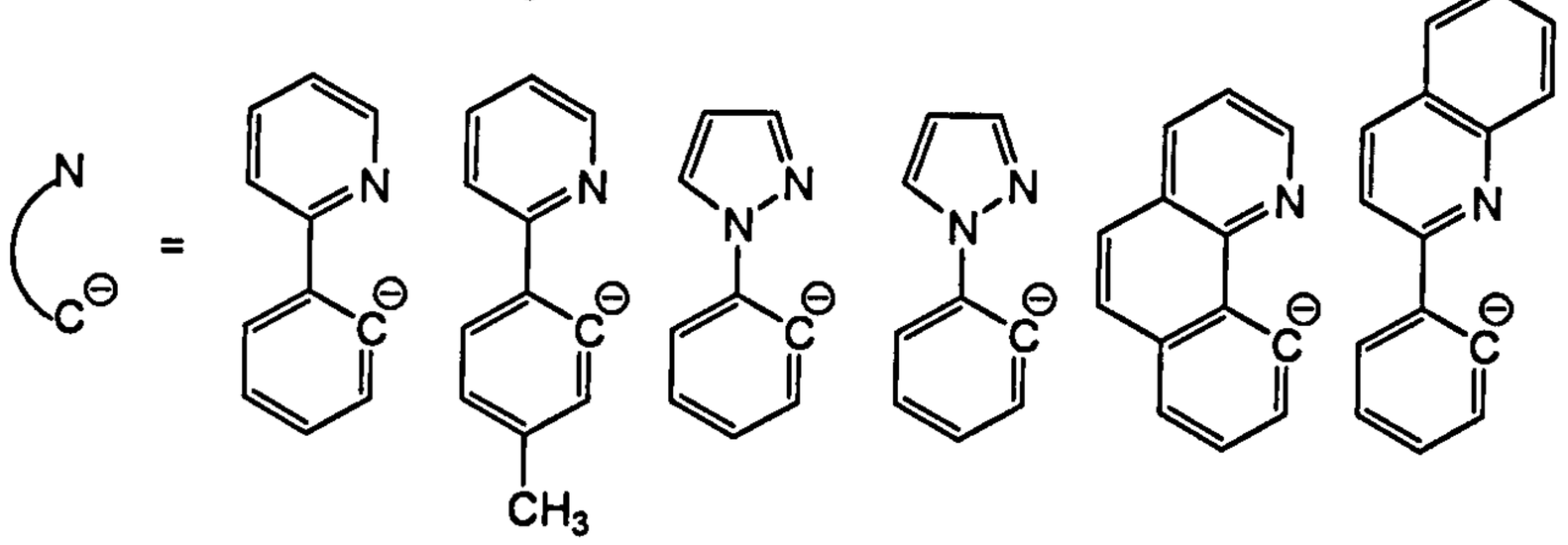

B

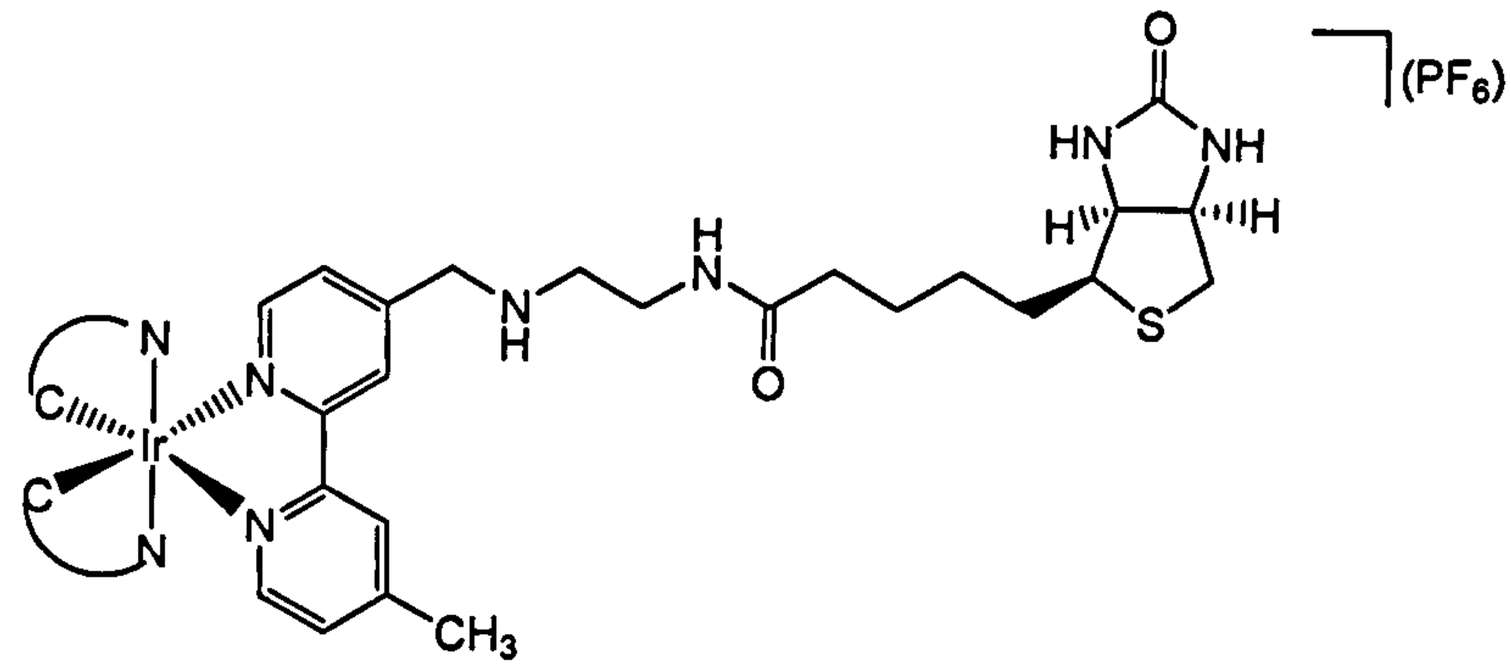

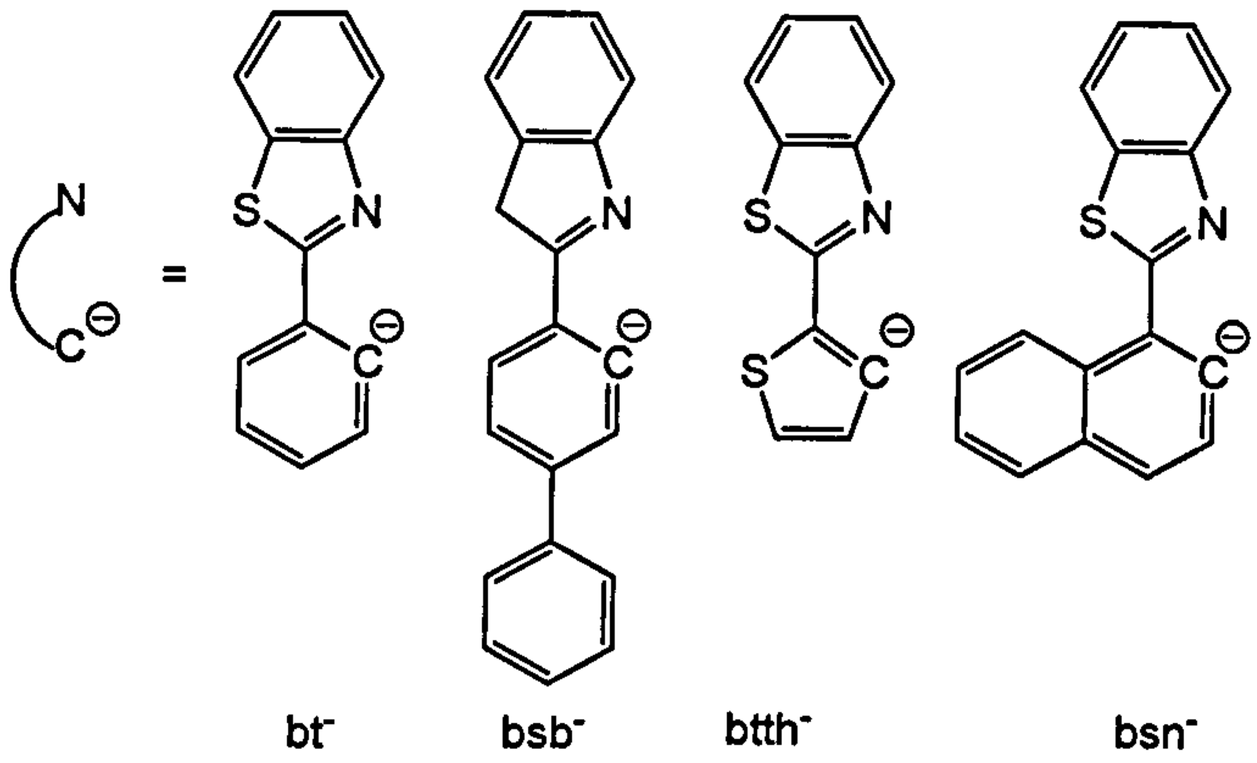

Figure 1.23 Iridium complexes reported by Lo *et al.*[76] **(A)** $[Ir(N\text{-}C)_2(bpy\text{-}CH_2NH\text{-}C_2\text{-}NH\text{-}biotin)](PF_6)$; **(B)** $[Ir(N\text{-}C)_2(bpy\text{-}CO\text{-}NH\text{-}C_6\text{-}NH\text{-}biotin)](PF_6)$.

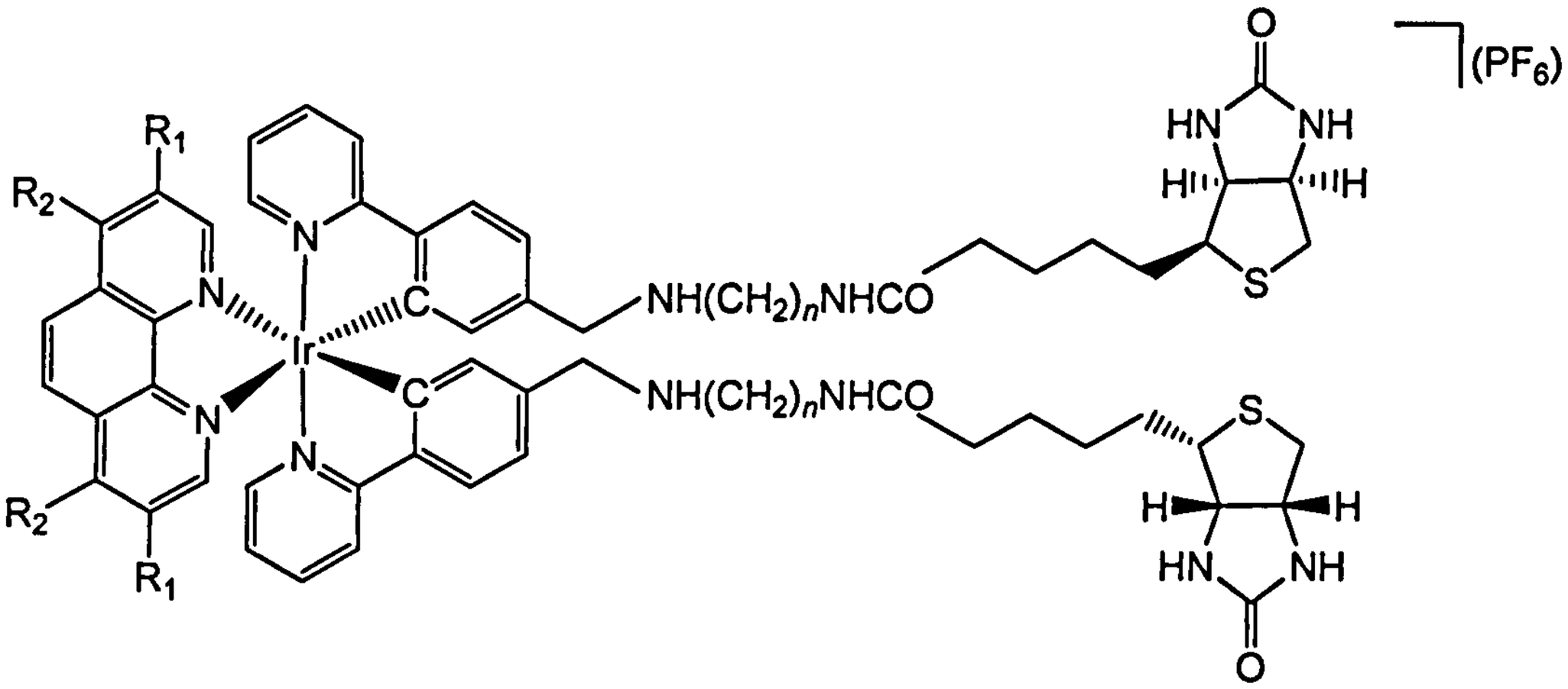

Figure 1.24 Iridium(III) diimine bis(biotin) complexes reported by Lo *et al.*[77]

Another recently reported system is shown in **Figure 1.24**, in which the iridium complex contains two biotin units[77]. The solvent dependant emission (479 – 600 nm) was assigned to a ^{3}MLCT ($d\pi(Ir) \rightarrow \pi^*$ (N-N)) excited state (with some IL ($\pi \rightarrow \pi^*$ (Me_4phen) character for the Me_4phen complex). HABA assays indicated that the complexes bound in a 2:1 complex : protein ratio and that the binding was significantly stronger than HABA unlike the complexes in **Figure 1.25**. The emission intensities of each of the complexes was enhanced and the lifetimes increased on addition of avidin. The same relationship between spacer length and emission enhancement was observed. $K_d = 3.9 \times 10^{-9}$ to 4.8×10^{-8} M, several orders of magnitude lower than biotin. The complexes with the longer spacers ($n = 6$) are able to cross-link avidin (two avidin protein molecules bound to one iridium diimine bis(biotin) complex), whereas those with shorter spacers ($n = 2$) form intramolecular adducts with the same protein molecule.

A range of probes for cytochrome $P450_{cam}$[79] have been developed by Gray and co workers for heme active sites, such as those in **Figure 1.28**[79]. The binding is sufficiently strong to allow detection of the enzyme at submicromolar concentrations[81].

Cytochrome P450 enzymes catalyse monooxygen transfer to non activated hydrocarbons under physiological conditions. $P450_{cam}$ was the first member of this family to be structurally characterised by X-ray diffraction and its biochemistry is well understood. The substrate, camphor (A), is regio- and stereospecifically hydroxylated to 5-*exo*-hydroxycamphor (B) at a heme active site. The reaction scheme is shown in **Figure 1.26.**

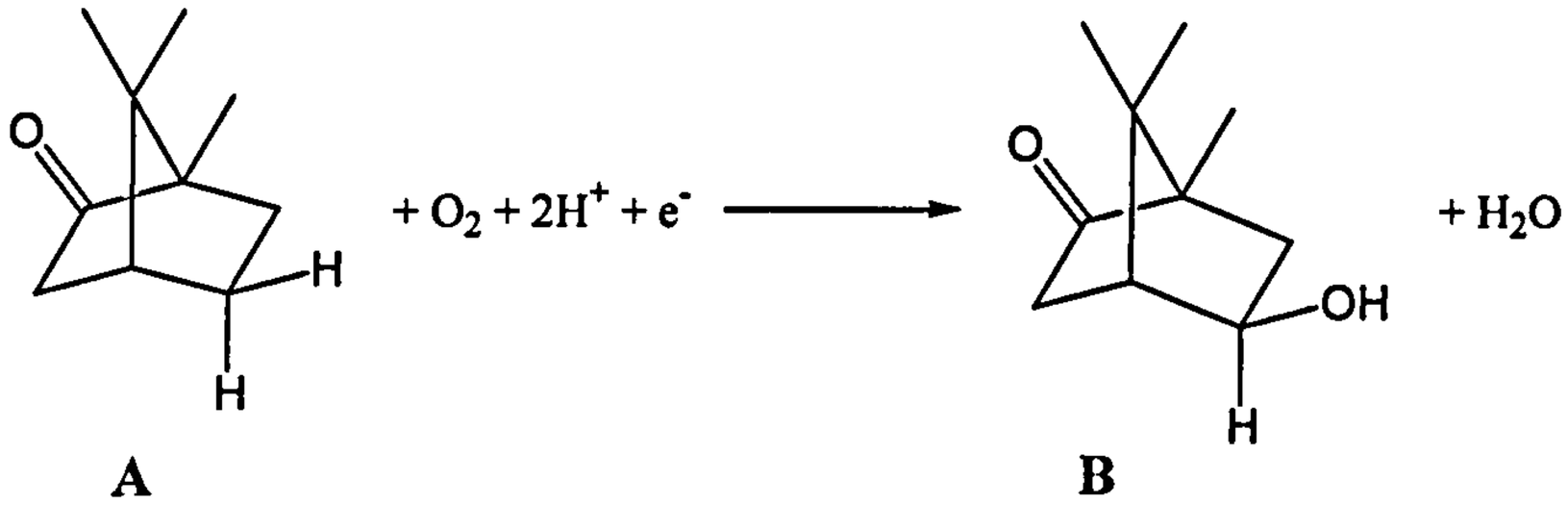

A **B**

Figure 1.26 Conversion of camphor (A) to 5-*exo*-hydroxycamphor (B) by $P450_{cam}$.

A $[Ru(bpy)_3]^{2+}$ chromophore was linked to an enzyme substrate, imidazole, adamantane or ethyl benzene, through an aliphatic spacer Ru-C_n-Im/Ad/EB, or an aromatic fluorinated spacer Ru-F_8bp-Im/Ad, (**Figure 1.27**)[82].

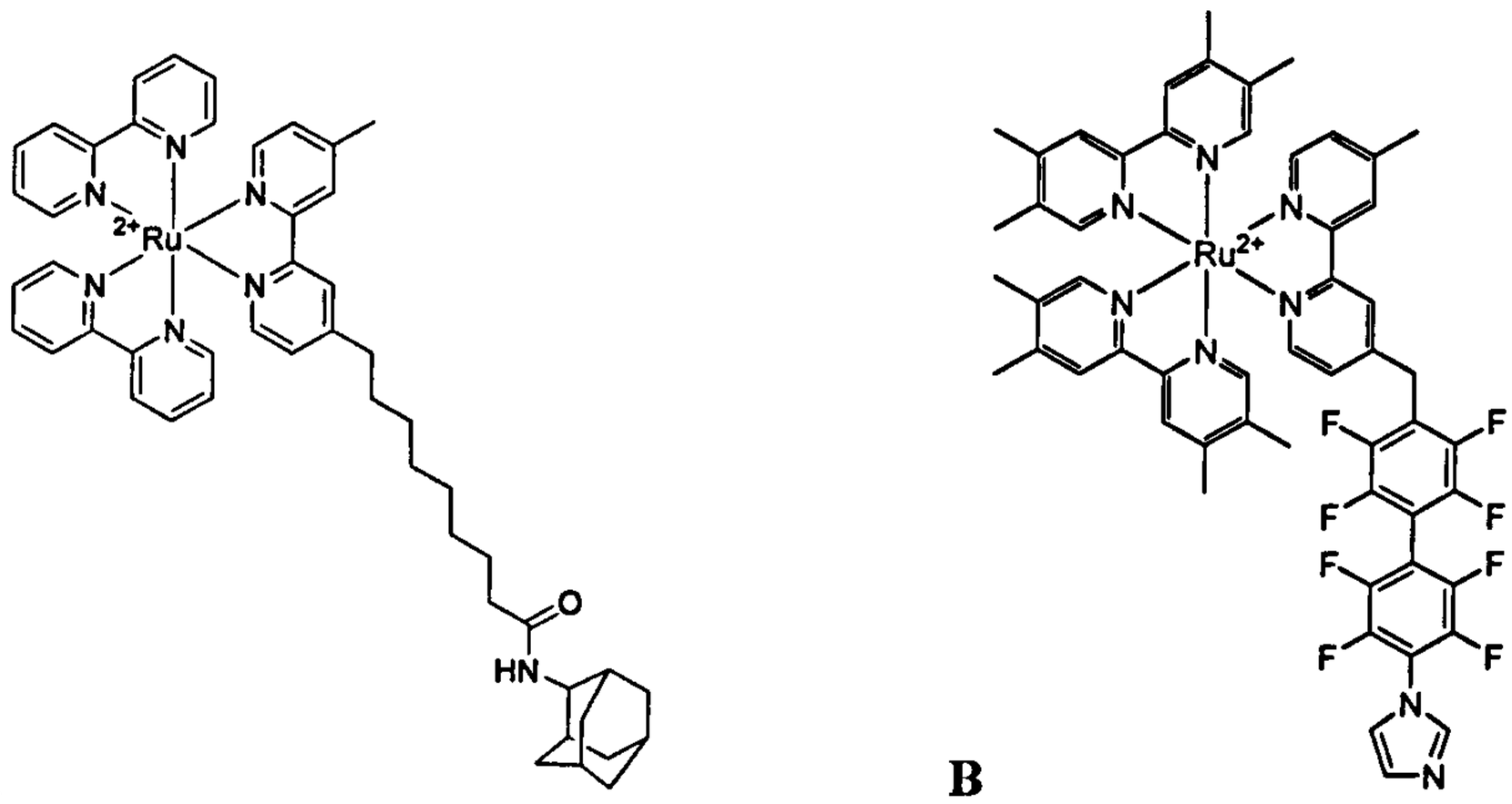

A **B**

Figure 1.27 (A) Structure of Ru-C_9-Ad and **(B)** tmRu-F_8bp-Im [79].

Firstly, binding of the probes to P450cam was signalled by quenching of the Ru^{2+} excited state (Ru^{II}*). [Ru-substrate]$^{2+}$* emission decay is normally monophasic ($k_0 = 2.1 \times 10^6\ s^{-1}$). In the presence of P450 it becomes biphasic, corresponding to the bound state, k_1 (quenched), and the free state, k_0, of the probe. The faster phase is due to energy transfer (Ru-F_8bp-Ad) or electron transfer (Ru-F_8bp-Im) to the heme. **Figure 1.28** shows the crystal structures of the bound probes with a simplified adamantane substrate.

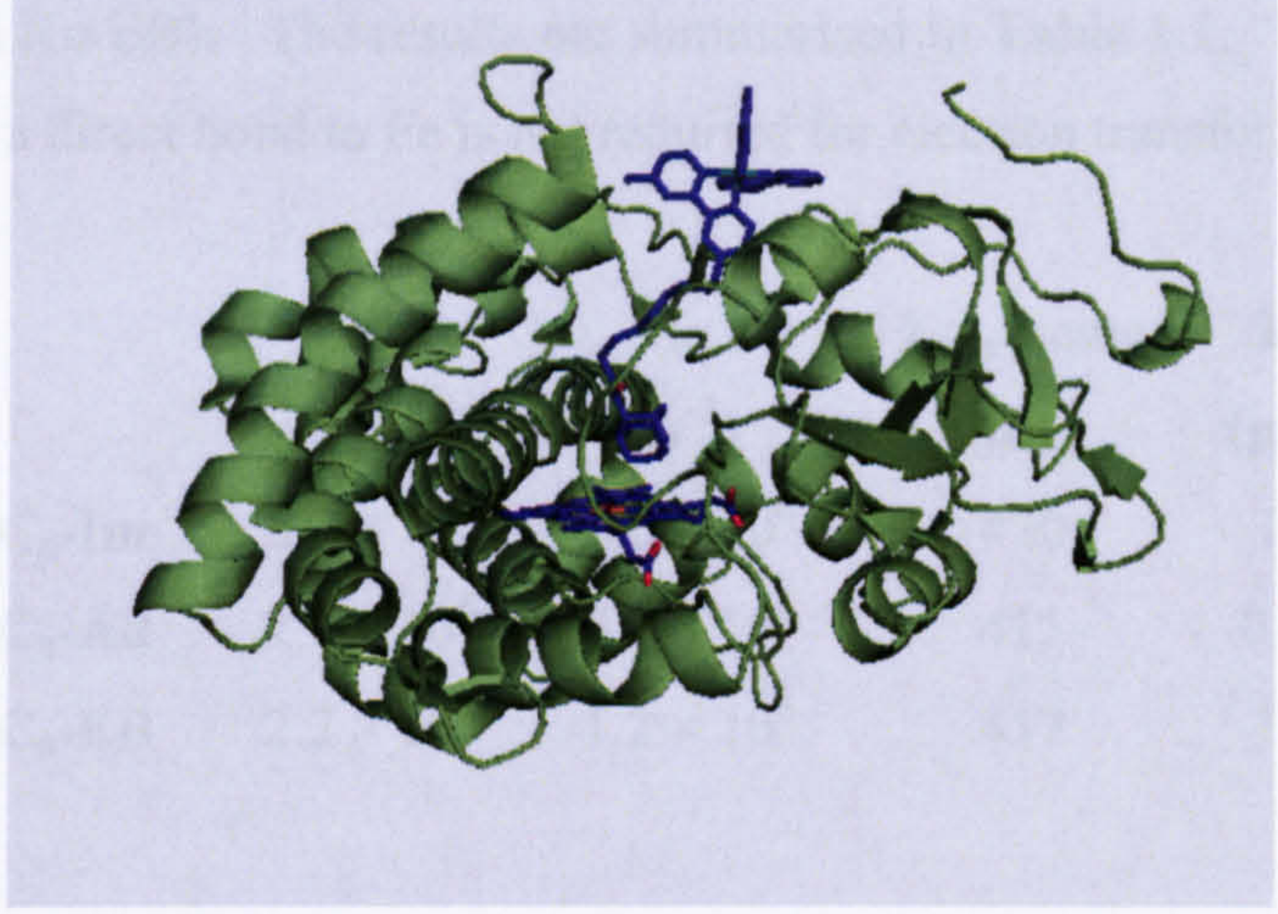

A

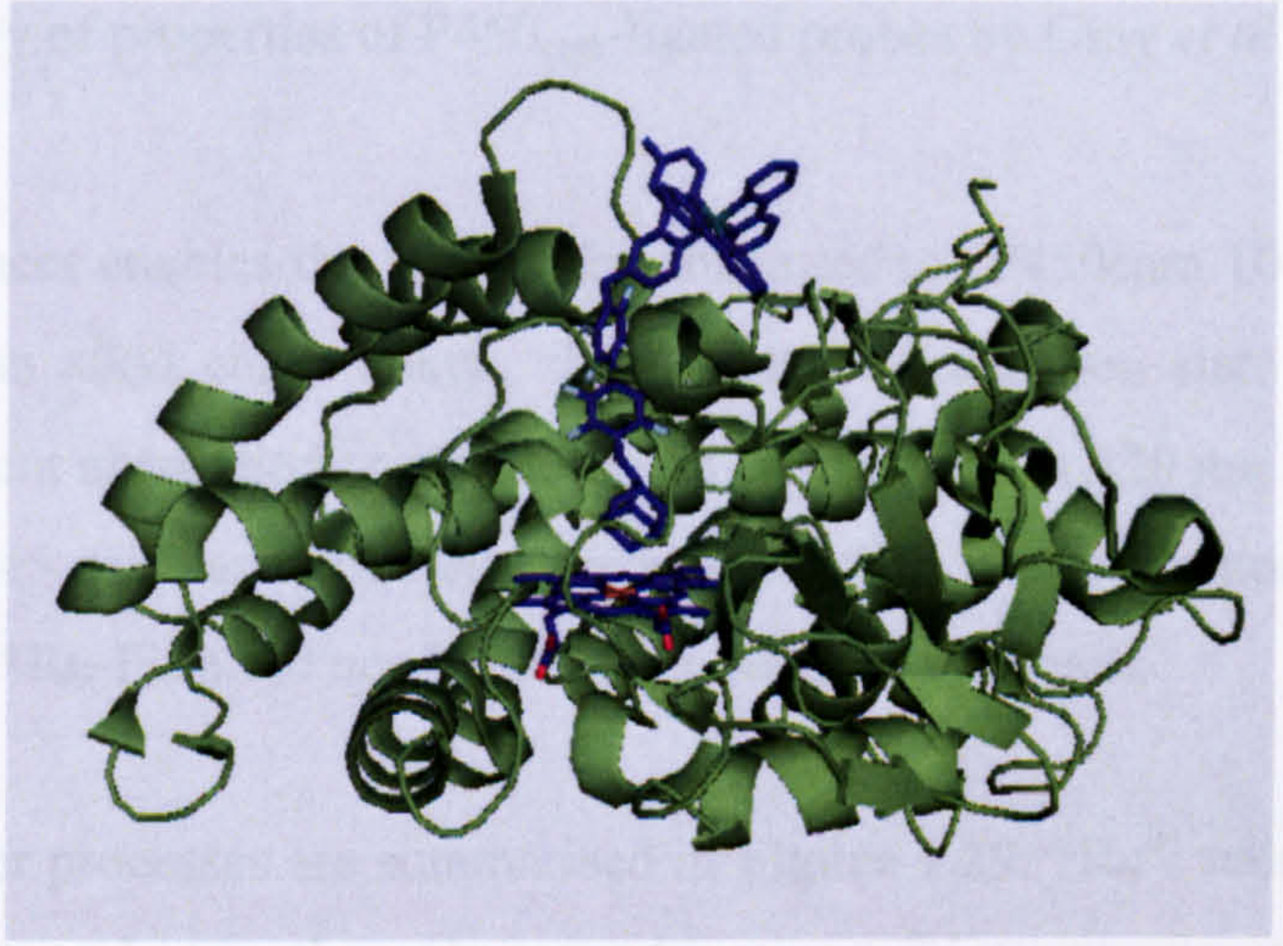

B

Figure 1.28 **(A)** Structure of Ru-C_9-Ad and **(B)** tmRu-F_8bp-Ad bound $P450_{cam}$[79]. Original in colour.

Secondly, changes to the coordination of the heme active site are indicated by a shift in the P450cam Soret band at 417 nm. For the adamantane terminated probe, a blue shift in the porphyrin absorption indicates displacement of coordinated water, whereas for imidazole formation a red shift indicates binding to the heme itself. No such shift in the Soret band absorption was observed for the ethylbenzene probe, suggesting that it binds in the active site but not directly to the heme. For probes with the aliphatic spacer, the luminescence quenching was attributed to Förster-type energy transfer ($Ru^{I} \rightarrow Fe^{III}$ for Ru-Im, $Ru^{II*} \rightarrow Fe^{III}$ for Ru-Ad and Ru-EB). The results are summarised in **Table 1.1.** The results for Ru-C_n-EB suggest that a direct bond to Fe is not required for electron transfer.

	k_0 (s^{-1})	k_1 (s^{-1})	λ_{max} heme (nm)	k_D (μM)
Ru-C_n-Im	2.2×10^6	7.0×10^6	420	1.5
Ru-C_n-Ad	2.2×10^6	7.7×10^6	415	0.69
Ru-C_n-EB	2.2×10^6	1.2×10^6	417	1.0

Table 1.1 Summary of properties of $P450_{cam}$-ligated probes by Gray *et al*[79-85].

The conjugated spacer enables the tmRu-F_8bp-Im to reduce P450cam 10^3 times faster than the Ru-wire with an alkyl chain linker. The change in oxidation state of the heme was examined by transient absorption spectroscopy where a bleach at 420 nm and an increase in optical density at 445 nm was attributed to reduction of Fe with corresponding Ru^{II} to Ru^{III} oxidation. Neither *Ru-F_8bp-Ad nor *tmRu-F_9bp reduces P450cam.

The electron transfer processes are summarised in **Figure 1.29.** $*Ru^{2+}$ reduces the heme (k_f) or decays to the ground state through a combination of intrinsic decay (k_0) and energy transfer to the heme (k_E), which decays non-radiatively to the ground state. The charge-separated state ($Ru^{3+}\cdots Fe^{2+}$) undergoes back electron transfer (k_b) or decays to form a long-lived ferrous heme (k_{sep}).

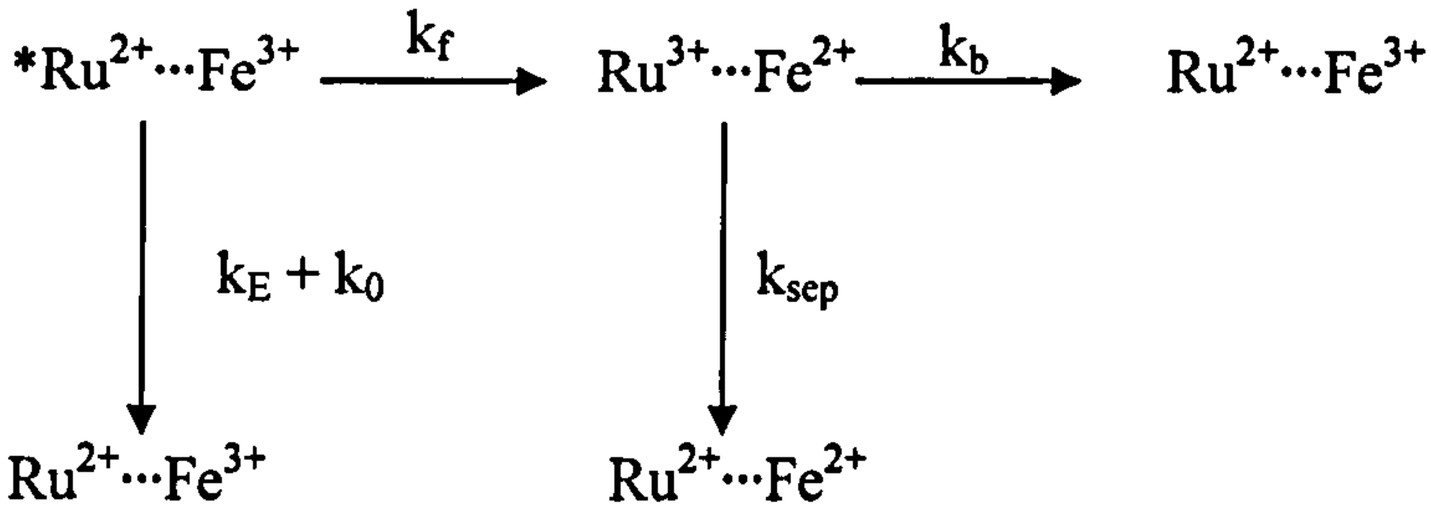

Figure 1.29 ET processes in photoexcited Ru-diimine:P450cam conjugates.

Other probes contained a dansyl fluorophore (**Figure 1.30**)[83,84]. As for the $[Ru^{II}(bpy)_3]^{2+}$ sensitiser, reduced dansyl luminescence was observed on binding to P450cam attributable to Förster type energy transfer. When the probes (D-4-Ad and D-8-Ad) were displaced by camphor (the natural substrate) the fluorescence was restored.

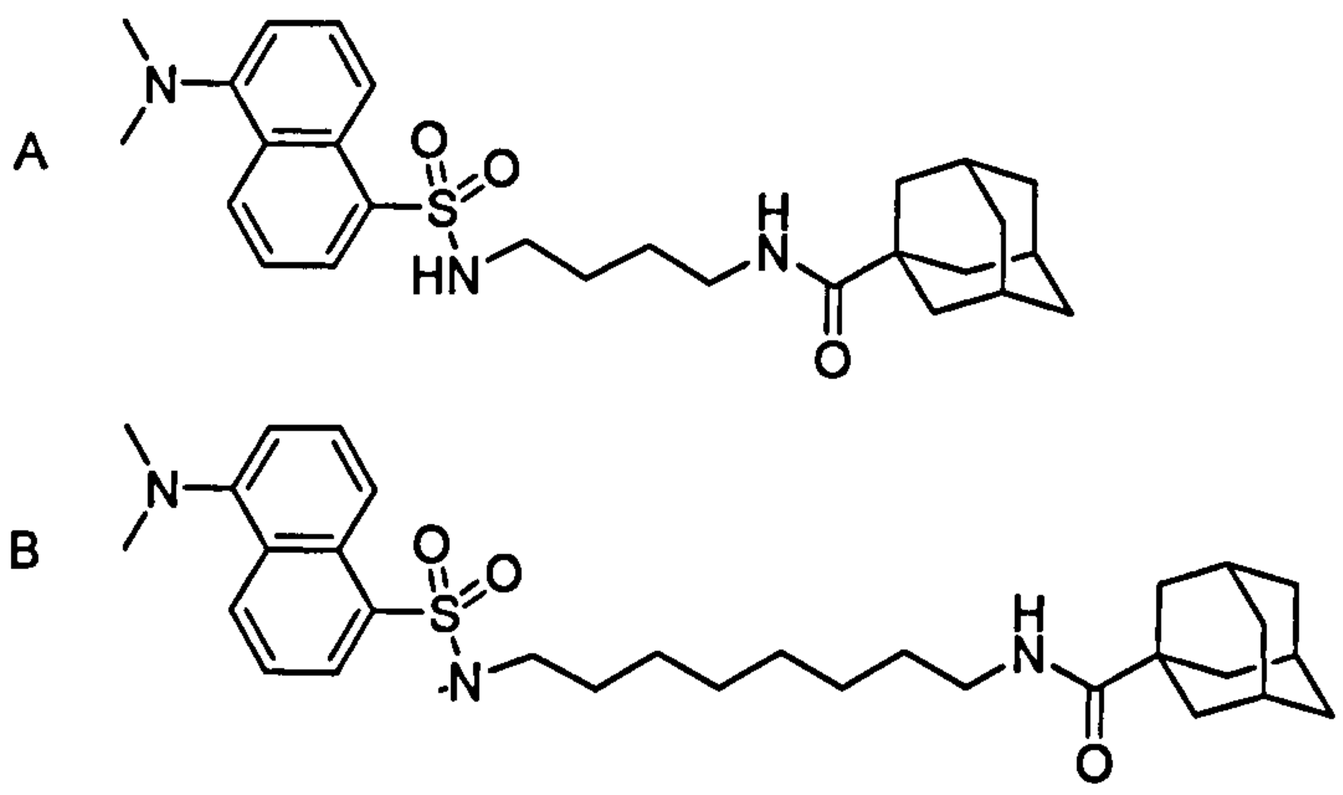

Figure 1.30 Probes reported by Gray *et al.* (**A**) D-4-Ad; (**B**) D-8-Ad.[83]

The probes were held in the active sites by hydrophobic interactions and probes of different lengths could be incorporated due to the conformational flexibility of the surrounding B', F and G helices[85]. These range from an 'open' conformation for the $[Ru^{II}(bpy)_3]^{2+}$ sensitizer, to an intermediate conformation with the dansyl fluorophore, to a 'closed' (camphor bound) form. **Figure 1.31** illustrates the dansyl probe-bound conformations of $P450_{cam}$[83]. The D-4-Ad bound channel is more open than D-8-Ad bound channel, leading to a weaker affinity

for the D-4 molecule. The The D-4-Ad probe could be used to screen for potential inhibitors since it can easily be displaced.

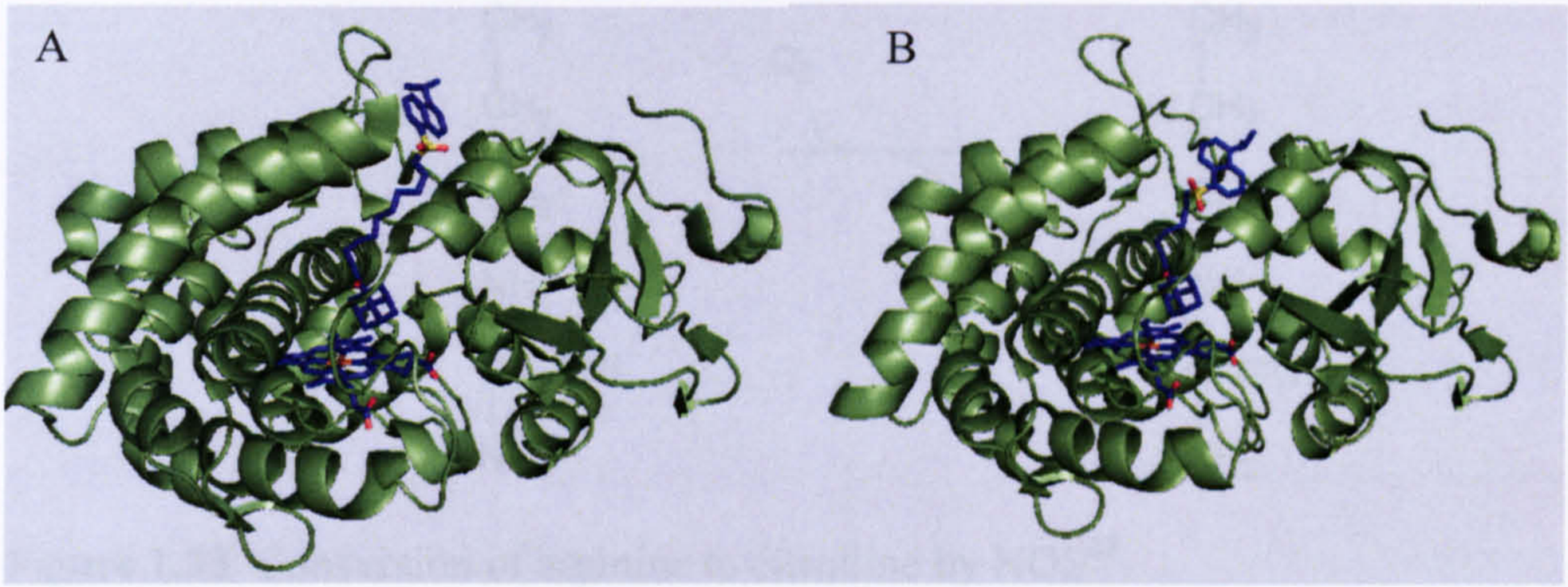

Figure 1.31 D-8-Ad[85] (A) and D-4-Ad[87] (B) bound $P450_{cam}$. Colours correspond to atoms: carbon and nitrogen: blue; sulfur: yellow; oxygen: red; zinc: orange. Original in colour.

Recently, Gray *et al.* have reported a the Re(I)(imidazole-alkyl-nitroarginine) sensistiser, shown in **Figure 1.32**, to probe the active site of nitric oxide synthase (NOS)[89]. NOSs are subdivided into cytokine-inducible (iNOS), endothelial (eNOS), and neuronal (nNOS) isozymes. Each oxidise L-arginine to the signalling molecule NO and citrulline at a heme active site (**Figure 1.33**)[88].

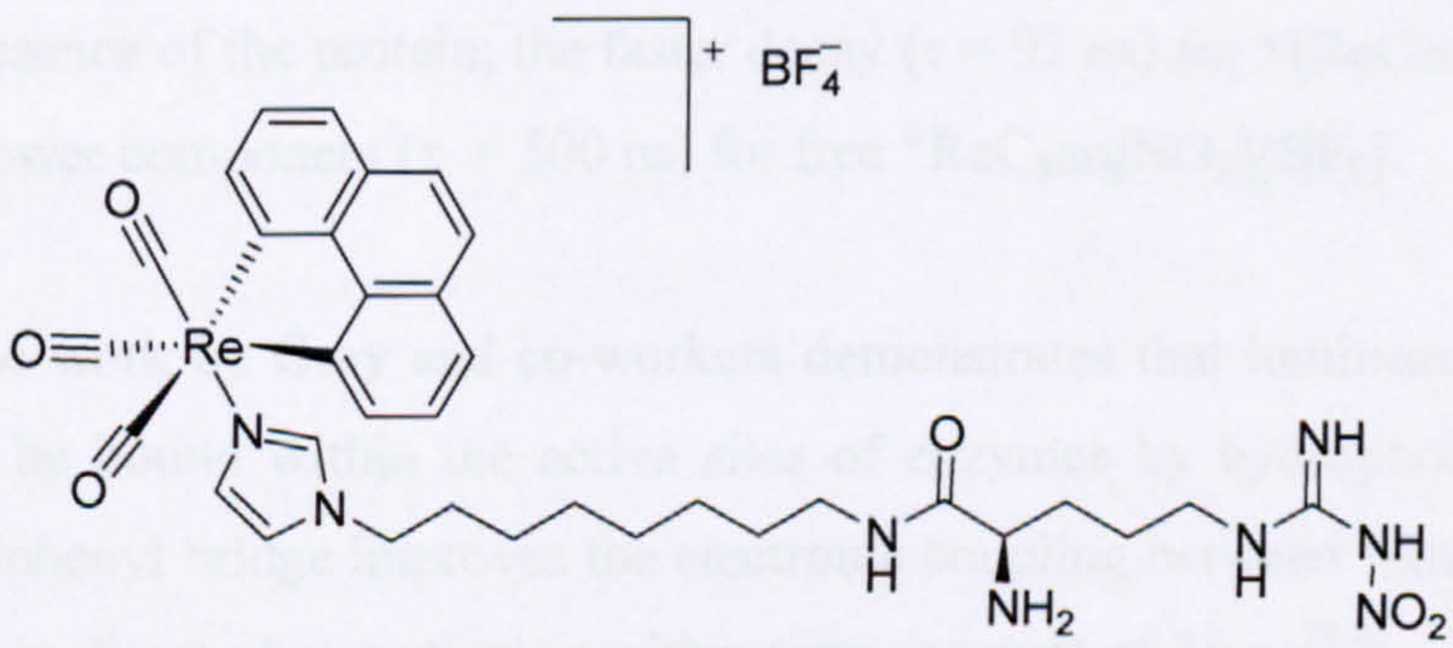

Figure 1.32 Structure of $[ReC_8argNO_2][BF_4]$ repoted by Gray *et al.*[89]

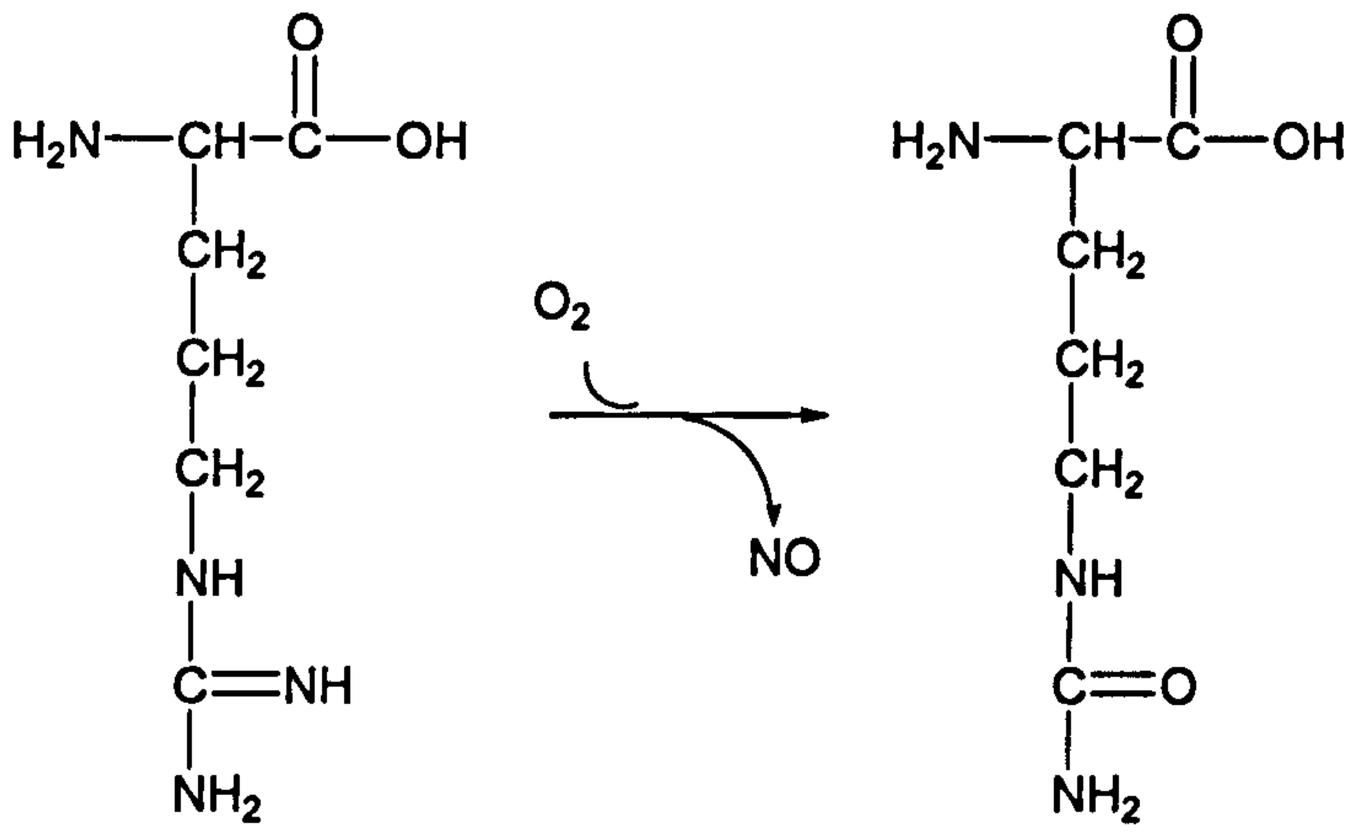

Figure 1.33 Conversion of arginine to citrulline by NOS[88].

Binding of the probe to $iNOS_{oxy}$ (inducible nitric oxide synthase with the reductase site cleaved at the interface of the two domains) caused a blue shift in the heme Soret peak from 423 nm to 390 nm which is also observed when L-arginine is added to the enzyme. This is a result of partial displacement of water from the active site, as for the $P450_{cam}$ system described above. Competitive binding studies were carried out by titrating $iNOS_{oxy}$ and different concentrations of imidazole with $[ReC_8argNO_2][BF_4]$ to show that there is competition between the probe and imidazole for the binding site. The luminescence from $[ReC_8argNO_2][BF_4]$* is quenched on addition of $iNOS_{oxy}$ and the maximum shifts from 570 nm to 550 nm. As for the probes for $P450_{cam}$, biexponential decay was observed for the probe in the presence of the protein; the faster decay (τ = 92 ns) for $*[ReC_8argNO_2]^+$ - bound $iNOS_{oxy}$; the slower component (τ = 500 ns) for free $*ReC_8argNO_2][BF_4]$.

In summary, the work by Gray and co-workers demonstrates that luminescent probes may be designed to be bound within the active sites of enzymes by hydrophobic interactions. The perfluorobiphenyl bridge improves the electronic coupling between $*Ru^{2+}(L_2)L'$ and the heme, resulting in direct photoreduction with a time constant of 36 ns[79-85]. The work by Lo and co-workers has also shown that metal complexes linked to enzyme substrates can report binding within enzyme active sites. Lo *et al.* have demonstrated that careful design of hydrophobic complexes may lead to emission enhancement rather than quenching on binding to the protein. It has also been demonstrated that whilst the changing the length of

the arm may improve the binding affinity for the probe it may simultaneously reduce the emission enhancement and therefore a compromise must be made.

1.4. Summary and Design of the Probe for Xanthine Oxidase

1.4.1. Luminophore

Porphyrins (λ_{em} = 550-750 nm) are ideal for use in photochemical devices since they have high extinction coefficients as well as tunable fluorescence emission and redox potentials. This is essential if the chromophore is to avoid the region in the spectrum dominated by the enzymes, XORs, (λ_{max} = 280 nm)[1,90]. The iron-sulfur clusters contribute absorption maxima at 420 nm, 470 nm and a shoulder at 550 nm and the absorption maxima of the flavin are at 360 and 450 nm. In addition, porphyrins can be functionalised at the periphery to suit a particular function, such as water solubility in biological systems.

1.4.2. Bridge

The bridge should provide functionalities that allow the attachment of the substrate and luminophore. Amide bonds provide a means of connection whilst being able to encourage electron transfer via superexchange[22, 67]. Other substituents may introduce hydrogen bonding within the molecule so that the system is more rigid to aid electron transfer. Aromatic groups have been shown to be particularly good bridges.

The bridge should be of a suitable length to position the substrate close to the MoCo active site. Computer modelling could be used to check the length, although computer simulation from crystal structures can be an over-simplification since enzyme active sites can often change conformation considerably on substrate binding, as demonstrated in the cases for $P450_{cam}$.

1.4.3. Substrate Analogues

The purpose of the substrate is to bind within the channel of the active site and to communicate with the molybdenum cofactor. XO has an affinity for planar aromatic substrates containing five and/or six membered rings. The substrate should be bound in the channel by hydrogen bonds and π-stacking, as for the inhibitors described earlier.

Biagi *et al.* [91] compared a series of inhibitors which were similar to xanthine or allopurinol. It was noted that the five-membered ring was more important than the six-membered ring in these complexes and therefore a reasonable initial simplification of the substrate would be pyrazole or imidazole as shown below. These should bind to the molybdenum in a similar manner to the natural substrates either through nitrogen (allopurinol) or via a carbon-oxygen bond formed by the enzyme (xanthine).

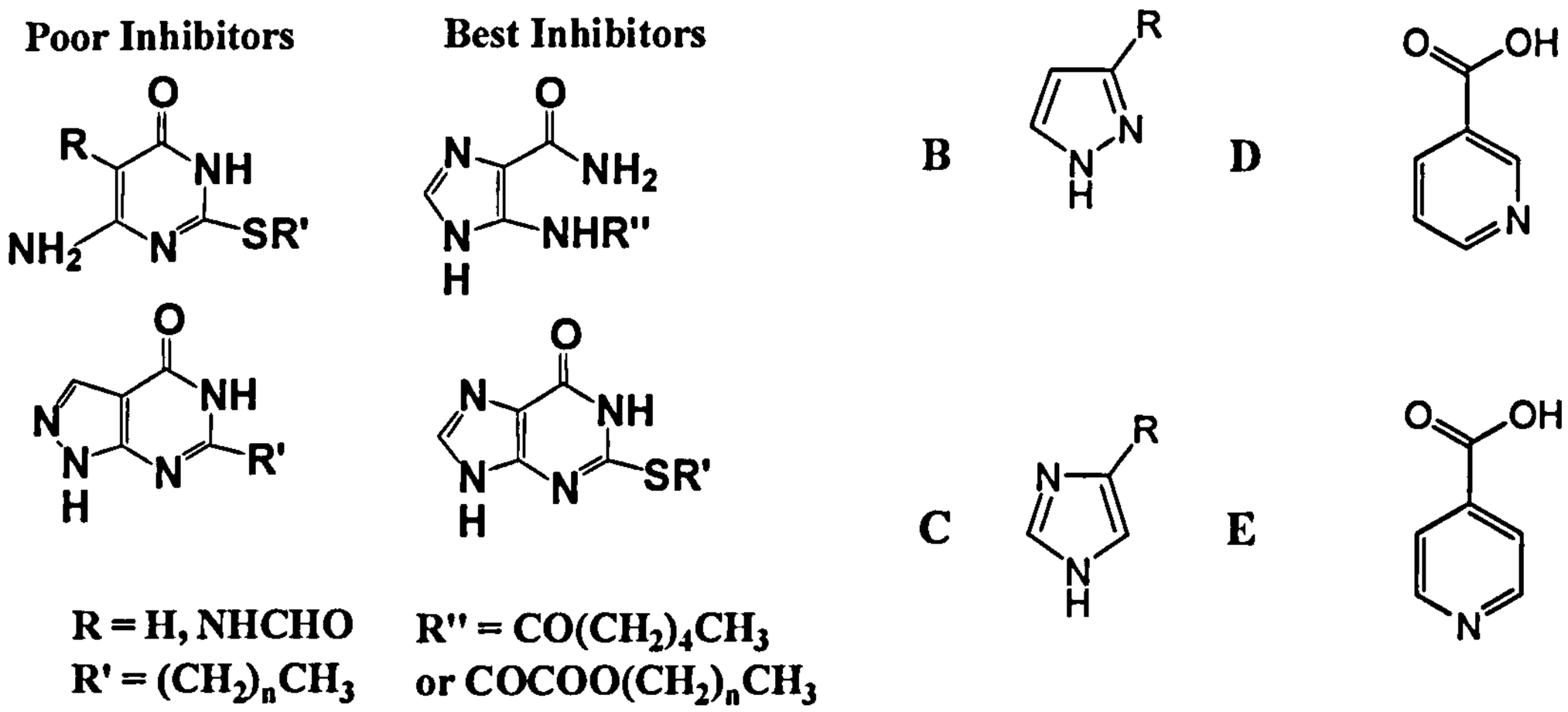

Figure 1.34 A A selection of substrates reviewed by Biagi *et al.* **Right** The simplified substrates **B** Pyrazole (Alloxanthine), **C** Imidazole (Xanthine), **D** Nicotinic acid, **E** Isonicotinic acid[91].

1.4.4. Overall system

As demonstrated by Gray *et al.*, combining a simplified substrate with a covalently attached luminophore may give rise to a novel device for reporting enzyme activity spectrophotometrically. The overall design incorporates a porphyrin luminophore, a simplified substrate and a planar bridge of the appropriate length, as shown in **Figure 1.35**.

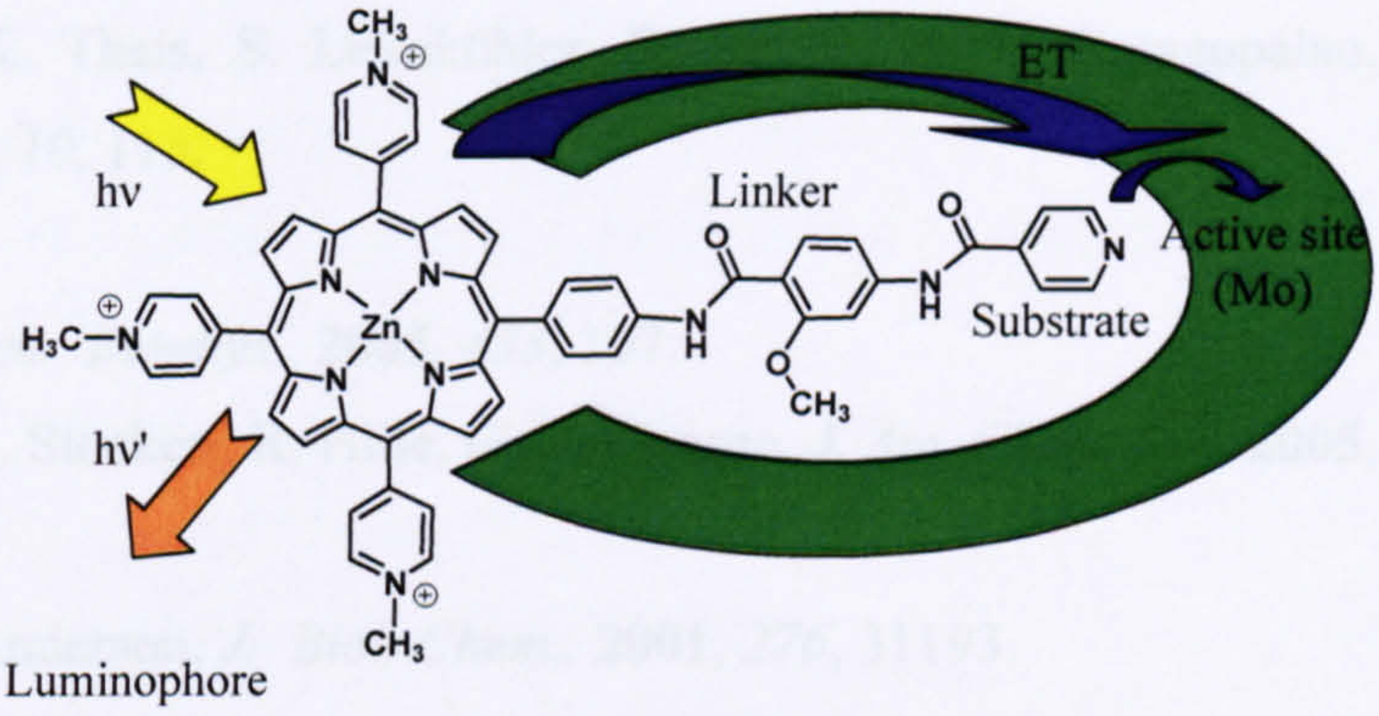

Figure 1.35 An example of a probe for XOR. Original in colour.

The following chapters will describe the synthesis and more detailed description of the components outlined above. Binding studies of the porphyrin derivatives with XO will also be described in conjunction with the important spectroscopic characteristics.

1.5. References

1. R. Hille, *Chem. Rev.* **1996**, *96*, 2757
2. J C. Enroth, B. T. Eger, K. Okamoto, T. Nishino, T. Nishino, E. F. Pai, *Proc. Nat. Acad. Sci. USA,* **2000**, *97*, 10723.
3. T. Nishino, K. Okamoto, Y. Kawaguchi, H. Hori, T. Matsumura, B. T. Eger, E. F. Pai, T. Nishino, *J. Biol. Chem.,* **2005**, *280*, 2488.
4. J. J. Truglio, K. Theis, S. Leimkühler, R. Rappa, K. V. Rajagopalan, C. Kisker, *Structure,* **2001**, *10*, 115.
5. pdb F1O4*
6. R. Hille, *Biochem. Biophys.,* **2005**, *433*, 107.
7. C. J. Doonan, A. Stockert, R. Hille, G. N. George, *J. Am. Chem. Soc.* **2005**, *127*, 4518.
8. pdb 1FIQ*
9. R. Hille, R. F. Anderson, *J. Biol. Chem.,* **2001**, *276*, 31193.
10. E. –Y. Choi, A.L.Stockert, S. Leimkühler, R. Hille, *J. Inorg. Biochem.*, **2004**. *98*, 841.
11. F. Borges, E. Fernandes, F. Roleira, *Curr. Med. Chem.,* **2002**, *9*, 195.
12. K. Okamoto, B. T. Egers, T. Nishino, S. Kondo, E. F. Pai, T. Nishino, *J. Biol. Chem.,* **2003**, *278*, 1848.
13. M. P. Keith, W. R. Gilliland, *Am. J. Med.*, **2007**, *120*, 221.
14. pdb 1N5X
15. K. Okamoto, K. Matsumoto, R. Hille, B. T. Eger, E. F. Pai, T. Nishino, *Proc. Nat. Acad. Sci. USA,* **2004**, *101*, 7931.
16. pdb 1V97*
17. K. Okamoto, A. Fukunari, T. Nishino, B. T. Eger, E. F. Pai, M. Kamezawa, I. Yamada, N. Kato, *J. Pharmacol. Exp. Ther.,* **2004**, *311*, 519.
18. pdb 1VDV*
19. T. A. Krenitsky, W.W.H., P. de Miranda, L. M. Beauchamp, H. J. Schaeffer, P. D. Whiteman, *Proc. Nat. Acad. Sci. USA*, **1984**, *8*, 3209.
20. L. Fabbrizzi and A. Poggi, *Chem. Soc. Rev.* **1995**, *24*, 197.
21. J. F. Callan, A. P. de Silva, D. C. Magria, *Tetrahedron,* **2005**, *61*, 8551.

22. V. Balzani, F. Scandola, *Supramolecular Photochemistry*, New York: Ellis Horwood, **1990**, ch2.
23. A. P. de Silva, S. A. de Silva., *J. Chem. Soc., Chem. Commun.*, **1986**, 1709.
24. V. Balzani and M. Maestri, *Catalysis by Metal Complexes,* Volume 14, *Photosensitization and Photocatalysis using Inorganic and Organometallic Compounds*, eds. K. Kalyanasundaram, M. Grätzel, Kluwer Academic Publishers, **1993**, p15-47
25. D. L. Dexter, *J. Chem. Phys.*, **1953**, *21*, 838.
26. T. Förster, *Discuss. Faraday Soc.*, **1959**, *27*, 7.
27. M. H. V Huynh, D. M. Dattlebaum, T. J. Meyer, *Coord. Chem. Rev.*, **2005**, *249*, 457.
28. A. J. Lees, *Chem. Rev.*, **1987**, *87*, 711.
29. E. M. Kober, T. J, Meyer, *Inorg. Chem.*, **1982**, *21*, 3967.
30. R. J. Watts, *J. Chem. Ed.*, **1983**, *60*, 834.
31. J. Barber, *Curr. Opin. Struct. Biol.*, **2002**, *12*, 523
32. D. LeGourriérec, M. Andersson, J. Davidsson, E. Mukhtar, L. Sun, L. Hammeström, *J. Phys. Chem. A.*, **1999**, *103*, 557.
33. F. Tani, M. Matsu-ura, S. Nakayama, Y. Naruta, *Coord. Chem. Rev.*, **2002**, *226*, 219.
34. P. J. Dandliker, F. Dierderich, A. Zingg, J. –P. Gisselbrecht, M. Gross, A. Louati, E. Sanford, *Helv. Chim. Acta*, **2004**, *80*, 1773.
35. M. R. Wasielewski, *Chem. Rev.*, **1992**, *92*, 435.
36. D. Gust, T. A. Moore, A. L. Moore, *Acc. Chem. Res.*, **1993**, *26*, 198..
37. A. Siemiarczuk, A. R. McIntosh, T.-F. Ho, M. J. Stillman, K. J. Roach, A. C. Weedon, J. R. Bolton, J. S. Connolly, *J. Am. Chem. Soc.*, **1983**, *105*, 7224.
38. G. Steinberg-Yfrach, J. –L. Rigaud, E. N. Durantini, A. L. Moore, T. A. Moore, D. Gust, *Nature*, **1998**, *392*, 479.
39. F. D'Souza, R. Chitta, S. Gadde, M. E. Zandler, A. L. McCarty, A. S. D. Sandanayaka, Y. Araki, O. Ito, *J. Phys. Chem. A.*, **2006**, *110*, 4338.
40. M. E. El-Khouly, O. Ito, P. M. Smith, F. D'Souza, *J. Photochem. Photobiol. C.*, **2004**, *5*, 79.
41. J. L. Sessler, J. Jayawickramarajah, A. Gouloumis, T. Torres, D. M. Guldi, S. Maldonado, K. J. Stevenson, *Chem. Commun.*, **2005**, 1892.

42. D. M Guldi, *Chem. Soc. Rev.*, **2002**, *31*, 22.
43. F. D'Souza, G. R. Deviprasad, M. S. Rahman, J. –P. Choi, *Inorg. Chem.*, **1999**, *38*, 2157.
44. F. D'Souza, G. R. Deviprasad, M. E. El-Khouly, M. Fujitsuka, O. Ito, *J. Am. Chem. Soc.*, **2001**, *123*, 5277.
45. D. –F. Shi, R. T. Wheelhouse, D. Sun, L. H. Hurley, *J. Med. Chem.*, **2001**, *44*, 4509.
46. R. Purello, S. Gurrieri, R. Lauceri, *Coord. Chem. Rev.*, **1999**, *190-192*, 683.
47. H.-J. Schneider, M. Wang, *J. Org. Chem. Soc.*, **1994**, *59*, 7473.
48. J. T. Groves, G. D. Fate, J. Lahiri, *J. Am Chem. Soc.*, **1994**, *116*, 5477.
49. J. Lahiri, G. D. Fate, S. B. Ungashe, J. T. Groves, *J. Am. Chem. Soc.*, **1996**, *118*, 2347.
50. M. Procházka, J. Štěpánek, P. –Y. Turpin, *Chem. Phys. Lip.*, **2004**, *132*, 145.
51. A. M. Awawdeh, H. J. Harmon, *Sensors and Actuators B*, **2005**, *106*, 234.
52. M. B. Spesia, D. Lazzeri, L. Pascual, M. Rovera, E. N. Durantini, *FEMS Immunobiology and Medical Microbiology*, **2005**, *44*, 289.
53. K. Lang, J. Mosinger, D. M. Wagnerová, *Coord. Chem. Rev.*, **2004**, *248*, 321.
54. R. J. Fiel, J. C. Howard, E. H. ark, N. Datta-Gupta, *Nucleic Acids Res.*, **1979**, *6*, 3093.
55. P. E. Strømhaug, T. O. Berg, K. Breg, P. O. Seglen, *Biochem. J.*, **1997**, *321*, 217.
56. J. N. Robinson, D. J. Cole-Hamilton, *Chem. Soc. Rev.*, **1991**, *20*, 49.
57. F. Ricceli, *J. Photochem. Photobiol. B: Biol.*, **1995**, *29*, 109.
58. R. B. Boyle, D. Dolphin, *Photochem. Photobiol.*, **1996**, *64*, 469.
59. P. Kubát, K. Lang, P. Azenbacher Jr., V. Král, B. Ehrenberg, *J. Chem. Soc., Perkin Trans.*, **2000**, *1*, 933.
60. V. V. Borovkov, M. Anikin, K. Wasa, Y. Sakata, *Photochem. PhotoBiol.*, **1996**, *63*, 477.
61. K. A. Connors, *Chem. Rev.*, **1997**, *97*, 1325.
62. K. Uekama, F. Hirayama, T. Irie, *Chem. Rev.*, **1998**, *98*, 2045.
63. F. Scandola, C. A. Bignozzi, M. T. Indelli, *Catalysis by Metal Complexes,* Volume 14, *Photosensitization and Photocatalysis using Inorganic and Organometallic Compounds*, eds. K. Kalyanasundaram, M. Grätzel, Kluwer Academic Publishers, **1993**, p161-216.

64. K. Kilså, J. Kajanus, A. N. Macpherson, J. Mårtensson, B. Albinsson, *J. Am. Chem. Soc.*, **2001**, *123*, 3069.
65. H. M. McConnell, *J. Chem. Phys.*, **1961**, *35*, 508.
66. M. U. Winters, K. Pettersson, J. Mårtensson, B. Albinsson, *Chem. Eur. J.*, **2005**, *11*, 562.
67. M. N. Paddon-Row, *Aust. J. Chem*, **2003**, *56*, 729.
68. K. Pettersson, A. Kyrychenko, E. Rönnow, T. Ljungdahl, J. Mårtensson, B. Albinsson, *J. Phys. Chem. A*, **2006**, *110*, 310.
69. K. Pettersson, J. Wiberg, T. Ljungdahl, J. Mårtensson, B. Albinsson, *J. Phys. Chem. A*, **2006**, *110*, 319..
70. S. Creager, C. J. Yu, C. Bamdad, S. O'Connor, T. MacLean, E. Lam, Y. Chong, G. T. Olsen, J. Luo, M. Gozin, J. F. Kayyem, *J. Am. Chem. Soc.*, **1999**, *121*, 1059.
71. K. Kilsa Jensen, S. B. van Berlekom, J. Kajanus, J. Mårtensson, B. Albinsson *J. Phys. Chem. A*, **1997**, *101*, 2218.
72. K. Kilså, J. Kajanus, A. N. Macpherson, J. Mårtensson, B. Albinsson, *J. Am. Chem. Soc.*, **2001**, *123*, 3069.
73. K. K. W. Lo, K. S. Sze, K. H. T. Tsang, N. Zhu, *Organometallics*, **2007**, *26*, 3440.
74. M. N. Isupov, A. A. Antson, E. J. Dodson, G. G. Dodson, I. S. Dementieva, L. N. Zakomirdina, K. W. Wilson, Z. Dauter, A. A. Lebedev, E. H. Harutyunyan, *J. Mol. Biol.*, **1998**, *276*, 603.
75. D. Carter, B. Chang, J. X. Ho, K. Keeling, Z. Krishnasami, *Eur. J. Biochem.*, **1994**, *226*, 1049.
76. K. K. W. Lo, W. K. Hui, C. K. Chung, K. H. K. Tsang, T. K. M. Lee, C. K. Li, J. S. Y. Lau, D. C. M. Ng, *Coord. Chem. Rev.*, **2006**, *250*, 1724.
77. K. K. W. Lo, J. S. Y. Lau, *Inorg. Chem.*, **2007**, *46*, 700.
78. O. Livnah, E. A. Bayer, M. Wilchek, J. L. Sussman, *Proc. Natl. Acad. Sci. U.S.A.*, **1993**, *90*, 5076.
79. I. Schlichting, J. Berendzen, K. Chu, A. M. Stock, S. A. Maves, D. E. Benson, R. M. Sweet, D. Ringe, G. A. Petsko, S. G. Sligar, *Science*, **2000**, *287*, 1615.
80. A. R. Dunn, I. J. Dmochowski, J. R. Winkler, H. B. Gray, *J. Am. Chem. Soc.*, **2003**, *125*, 12450.

81. I. J. Dmochowski, B. R. Crane, J. J. Wilker, J. R. Winkler, H. B. Gray, *Proc. Nat. Acad. Sci. USA,* **1999**, *96*, 12987.

82. J. J. Wilker, I. J. Dmochowski, J. H. Dawson, J. R. Winkler, H. B. Gray, *Angew. Chem. Int. Ed.,* **1999**, *38*, 89.

83. A.M. A. Hays, A. R. Dunn, R. Chiu, H. B. Gray, C. D. Stout, D. B. Goodin, *J. Mol. Biol.* **2004**, *344*, 455.

84. A. R. Dunn, A. M. A. Hays, D. B. Goodin, C. D. Stout, J. R. Winkler, H. B. Gray, *J. Am. Chem. Soc.*, **2002**, *124*, 10254.

85. A. R. Dunn, I. J. Dmochowski, A. M. Bilwes, H. B. Gray, B. R. Crane, *Proc. Nat. Acad. Sci. USA*, **2001**, *22*, 12420.

86. Protein databank code: 1RE9*

87. Protein databank code: 1RF9*

88. B. R. Crane, A. S. Arvai, R. Gachhui, C. Q. Wu, D. K. Gosh, E. D. Getzoff, D. J. Stuehr, J. A. Tainer, *Science*, **1997**, *278*, 425.

89. Y. H. L. Nguyen, J. R. Winkler, H. B. Gray, *J. Phys. Chem. B,* **2007**, *111*, 6628.

90. V. Massey, P. E. Brumby, H. Komai, *J. Biol. Chem.*, **1969**, *244*,1682.

91. G. Biagi, A. Costantini, L. Costantino, I. Giorgi, O. Livi, P. Pecorari, M. Rinaldi, V. Scartoni, *J. Med. Chem.* **1996**, *39*, 2529.

***Crystal structures were obtained from the protein databank (www.pdb.org) and pictures were generated using Pymol 0.99, Delano Scientific LLC, CA, USA.**

CHAPTER TWO

SYNTHESIS AND CHARACTERISATION OF SUBSTRATE-LINKER CONJUGATES

2. Synthesis and Characterisation of Substrate-Linker Conjugates

2.1. Preparation of the Substrate-Linker Conjugates

A series of substrate–linker compounds were synthesised in order to test their binding with XO. Commercially available 4–amino salicylic acid was chosen as the 'linker'. As previously described, the enzyme active site accommodates planar aromatic compounds, such as salicylic acid. The acid and amine functionalities provide a means of attachment to the luminophore and substrate by amide coupling. The methoxy group introduces a potential hydrogen bond acceptor which could bind either intramolecularly, to improve rigidity, or intermolecularly to hydrogen bond donor residues lining the channel. Some preliminary computational models were examined to assess the suitability of the compounds.

2.1.1. Computer modelling

Computer simulations of the proposed system were constructed in collaboration with Dr C. Verma. QUANTA (QUANTA98; Accelrys INC, San Diego, CA). with CHARMM [1,2] was used to calculate the likely structure of the 'docked' molecule. This provided confirmation of the depth of the channel and therefore the length of the bridging unit was decided. Residues lining the channel were examined so as to make use of any available stabilising interactions, such as hydrogen bonds, and to avoid any repulsive electrostatic interactions.

The hydrophobic residues lining the channel are clearly shown in **Figure 2.1.** Aromatic stabilisation can be inferred from the manner in which the aromatic residues are aligned with the aromatic ring of the probe molecule. Two possible hydrogen bonds can be seen from the amine of the sensor to the hydroxyl ligand of the molybdenum and the nearby Glu 802. There is also the possibility of bonding between the nitrogen lone pair of the amine and the molybdenum on displacement of the hydroxyl ligand.

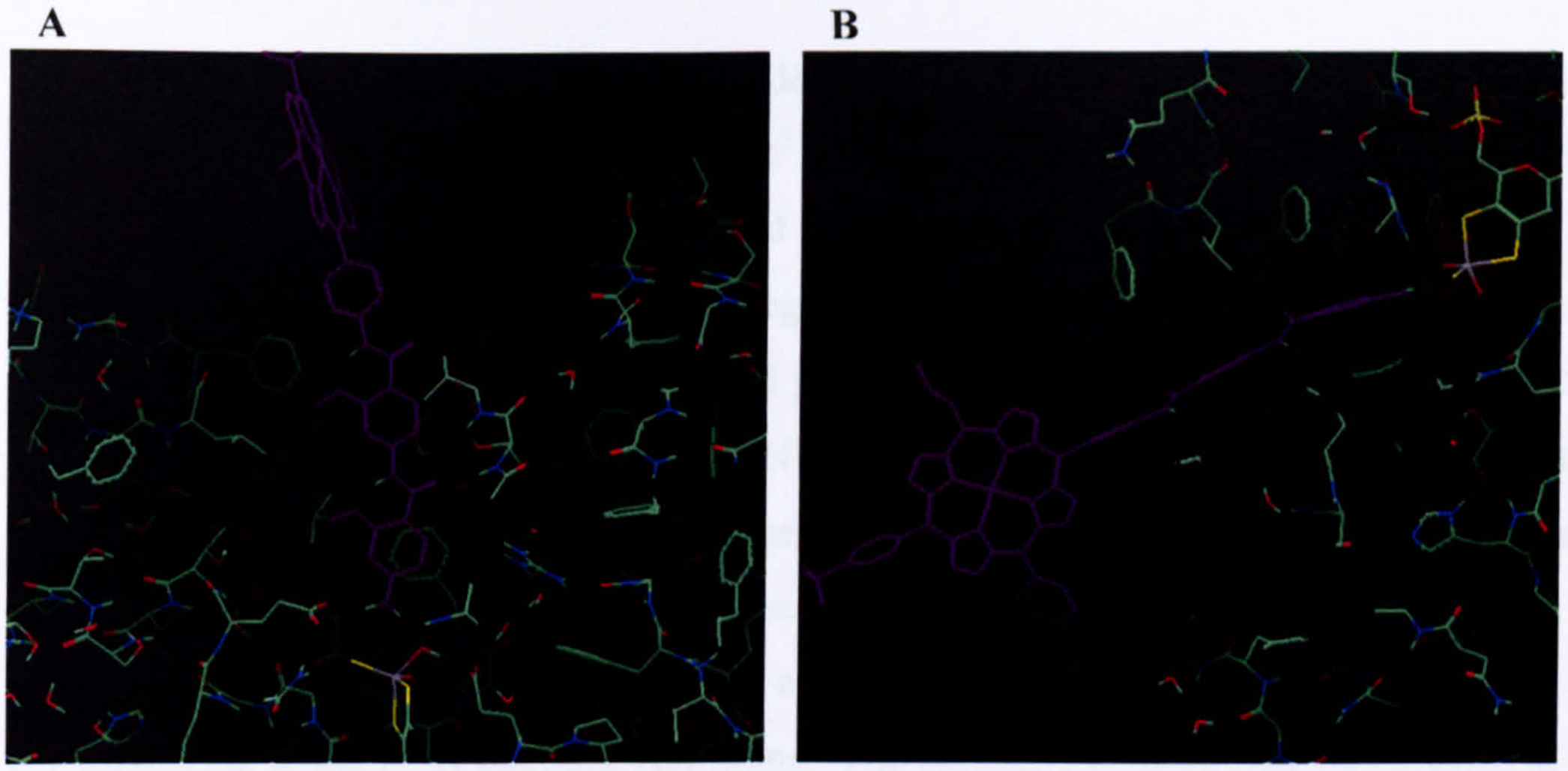

Figure 2.1 (A) Cross section of probe (purple) within XO channel. Colours correspond to atom types: Molybdenum, grey, sulfur, yellow, oxygen, red, nitrogen, blue, remaining atoms, green. (B) van der Waals' radii are shown dotted. Original in colour.

2.1.2. Methyl 4-Amino-2-methoxybenzoate, 1.

The acid group of 4–amino–2–hydroxy benzoic acid was first protected by methylation with dimethyl sulphate (**Scheme 2.1**) and then reacted with a series of acid functionalised substrates.

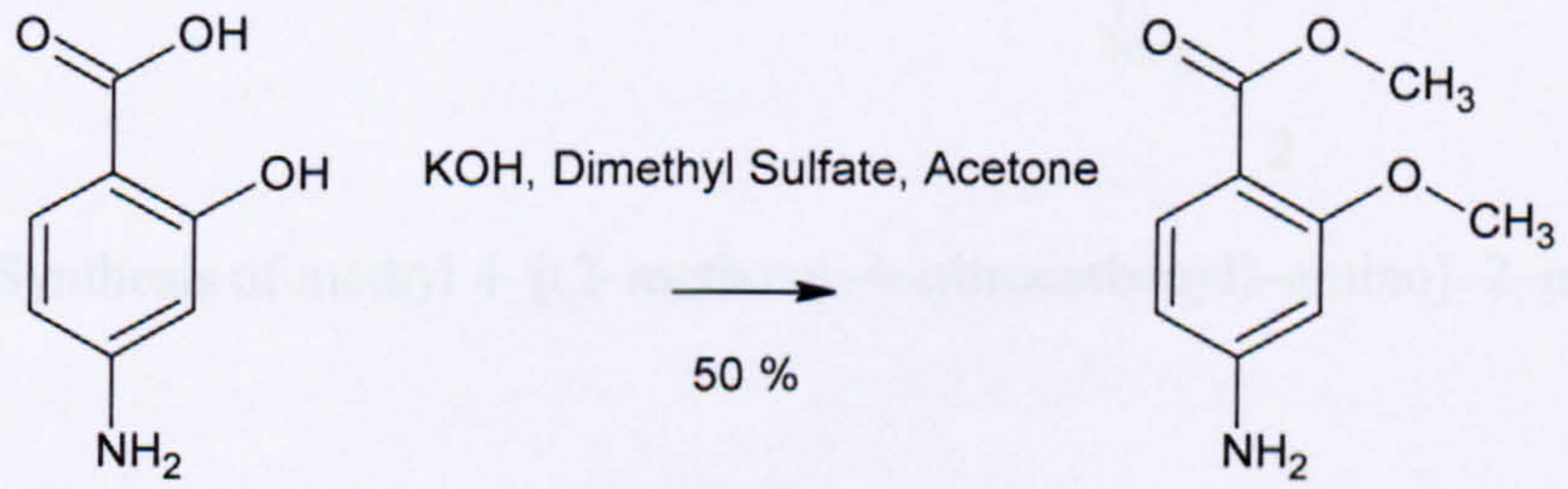

1

Scheme 2.1 Synthesis of methyl–4–amino–2–methoxy benzoate, **1**.

Compound **1** was prepared as a beige powder using the method reported by Hewlett *et al.* in a similar yield to that stated in the literature[3]. This compound was characterised by ^{1}H NMR, FTIR and EI–MS. The NMR data obtained are in good agreement with the literature. Three resonances were present in the aromatic region of the ^{1}H NMR spectrum and 6 peaks were present in the ^{13}C NMR spectrum, a broad peak at δ 4.28 corresponds to the amine protons, two singlets, at δ 3.86 and 3.83 in the ^{1}H NMR spectrum were present corresponding to the methoxy protons and two peaks were present at 55.8 and 51.5 in the ^{13}C NMR spectrum for the corresponding carbons. The FTIR spectrum contained bands at 3464 and 3362 cm^{-1} corresponding to the N–H symmetric and asymmetric stretches and at 1604 cm^{-1} corresponding to the N–H bending vibrations. The carbonyl C=O stretch was present at 1670 cm^{-1}. The mass spectrum gave the molecular ion at m/z = 181.

2.1.3. Methyl 4-[(2-methoxy-4-nitrocarbonyl)-amino]-2-methoxy benzoate, 2.

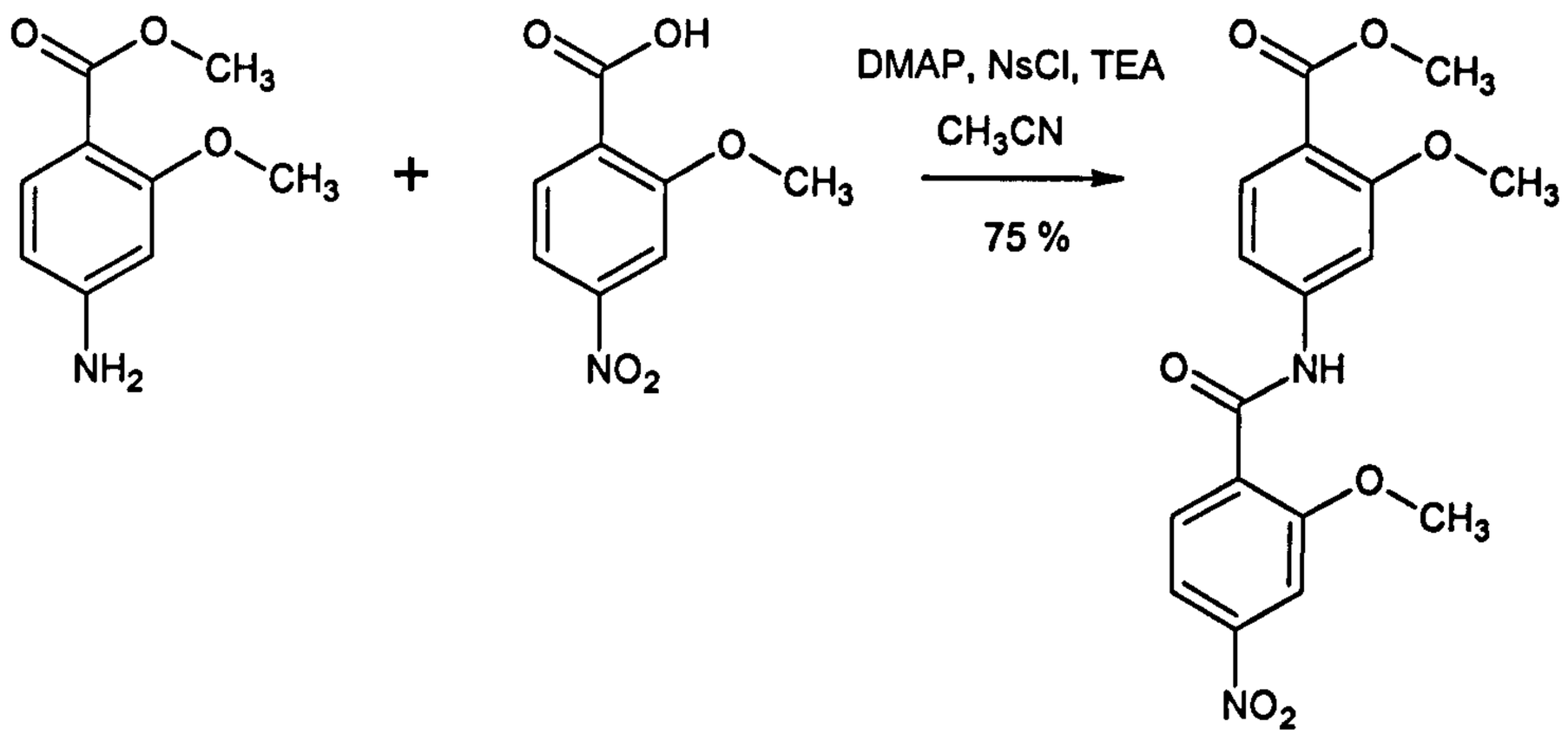

2

Scheme 2.2 Synthesis of methyl 4–[(2–methoxy–4–nitrocarbonyl)–amino]–2–methoxy benzoate, **2.**

Compound **2** was prepared by coupling **1** with 2–methoxy 4–nitrobenzoic acid (**Scheme 2.2**). These compounds were chosen in order to minimise the formation of side products. Estroff *et al.*[4] connected repeating units of a similar compound, 6-*tert*-butoxycarbonylmethoxy-5-nitro-pyridine-2-carboxylic acid, via the acid chloride, to the reduced, protected form 5-

amino-6-*tert*-butoxycarbonylmethoxy-pyridine-2-carboxylic acid methyl ester as illustrated in **Scheme 2.3**. The nitro group on the dimeric product was then reduced using hydrogen and palladium on carbon so that another repeating unit could be attached.

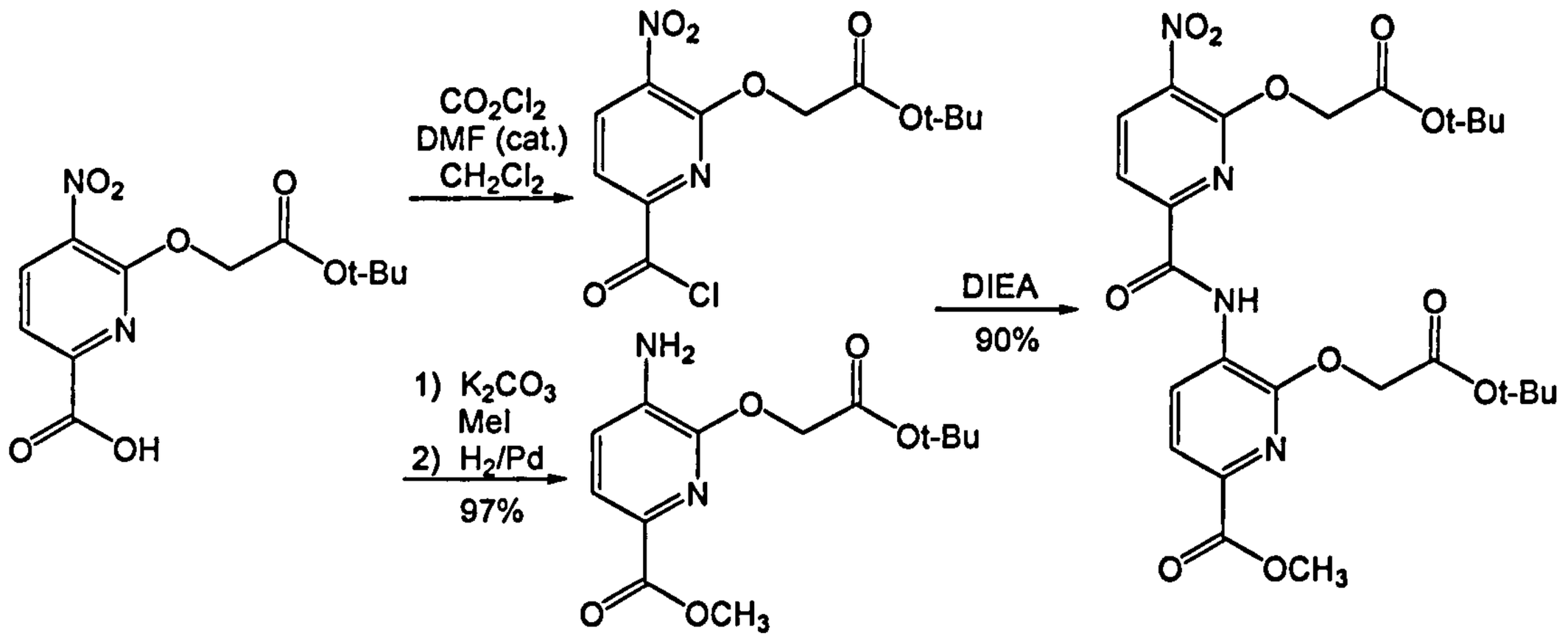

Scheme 2.3 Coupling procedure reported by Estroff *et al.*[4]

The DMAP catalysed method by Lee *et al.*[5] was found to be the most efficient route in our case. Stirring the reactants overnight under argon gave **2** as a bright yellow feathery precipitate in 75% yield.

Compound **2** was characterised by ^{1}H NMR, FTIR and EI–MS. The ^{1}H NMR spectrum in chloroform showed that the product was clean and did not require further purification after washing with cold acetonitrile. Amide bond formation was demonstrated in the ^{1}H NMR spectrum by a singlet with a relative integration of 1 at δ 9.76 corresponding to the amide proton and the FTIR spectrum contains an amide N–H stretch at 3355 and bend at 1589 cm^{-1}. The rest of the ^{1}H NMR spectrum consisted of three singlets at δ 4.20, 3.97 and 3.88 corresponding to three methoxy groups and six aromatic proton resonances. Other key peaks in the FTIR spectrum were two carbonyl peaks at 1699 and 1677 cm^{-1}, one corresponding to the ester and the other to the amide and N=O stretches at 1522 and 1357 cm^{-1}. The EI–MS corroborated this evidence by a substantial peak at m/z = 360.

^{1}H–^{1}H COSY (**Figure 2.3**) and ^{1}H–^{13}C HMQC and HMBC NMR spectra (**Figure 2.4**) were recorded to aid assignment of the spectra. d_6-DMSO was used as the solvent in order to increase the concentration and improve the signal to noise ratio in the carbon spectrum, even though this solvent broadened the proton resonances. The assignments are summarised in **Table 2.1** and **Table 2.2**; the numbers and letters correspond to those in **Figure 2.2**.

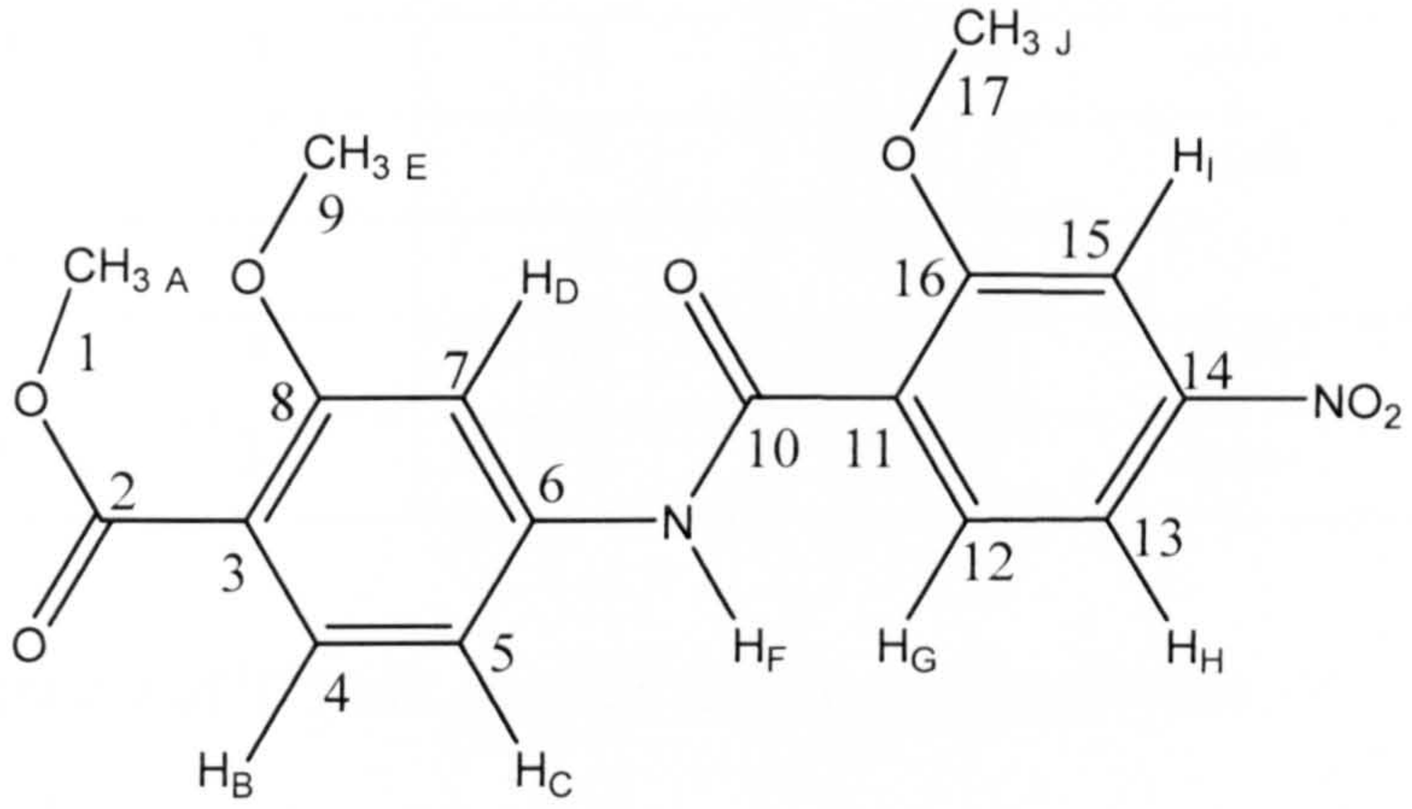

Figure 2.2 2 with atom labels: letters assigned to protons and numbers assigned to carbons.

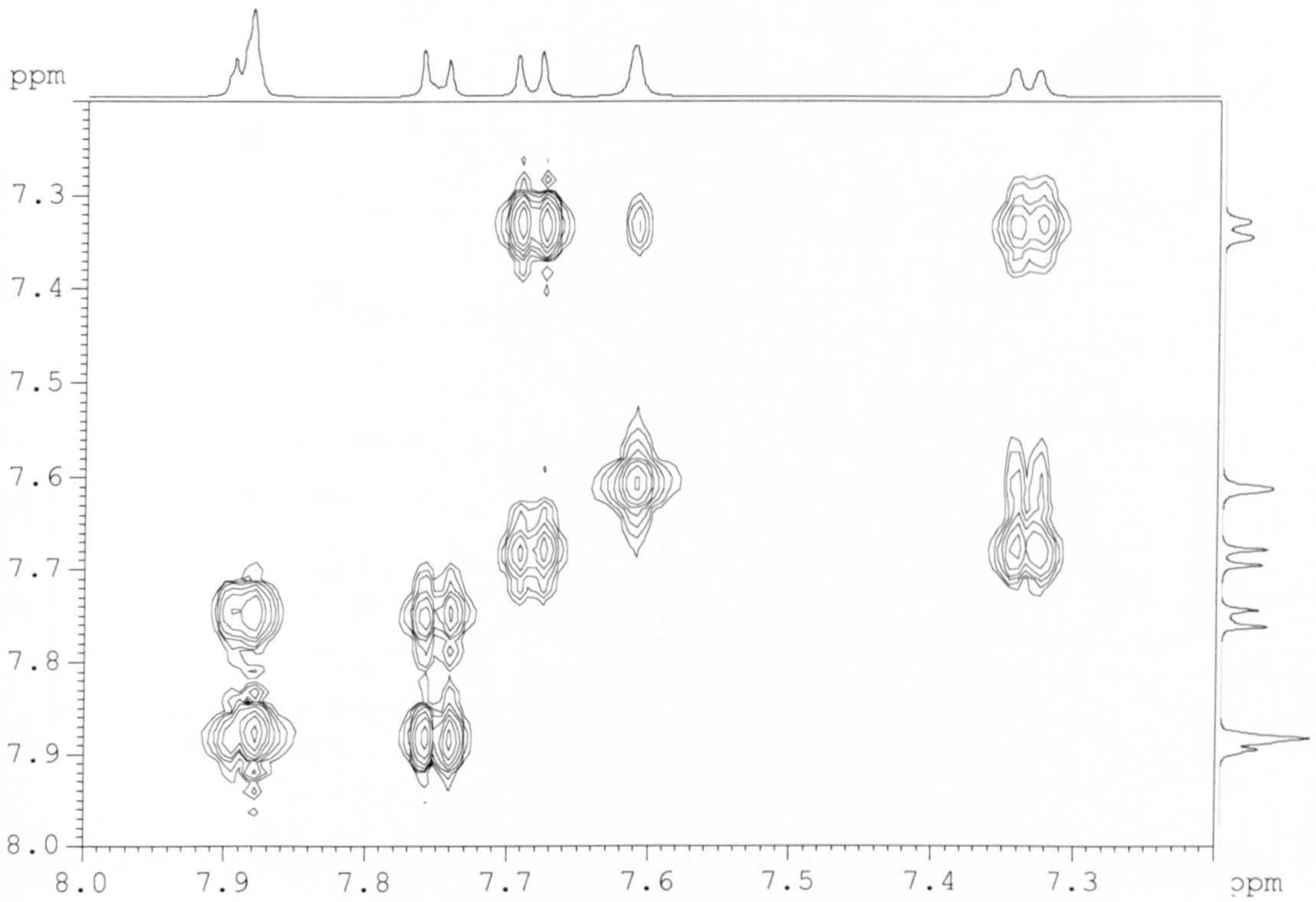

Figure 2.3 ^{1}H-^{1}H COSY spectrum of **2** in DMSO.

Label	δ	Integration	Multiplicity	Type	COSY to ^{1}H at δ
A	3.76	3	s	CH_3	none
B	7.71	1	d	CH	7.36
C	7.36	1	d	CH	7.64, 7.71
D	7.64	1	s	CH	7.36
E	3.81	3	s	CH_3	none
F	10.73	1	s	NH	none
G	7.79	1	d	CH	7.92
H, I	7.92	2	m	CH × 2	7.79
J	3.98	3	s	CH_3	none

Table 2.1 Assignment of ^{1}H NMR chemical shifts for **2** in d_6-DMSO.

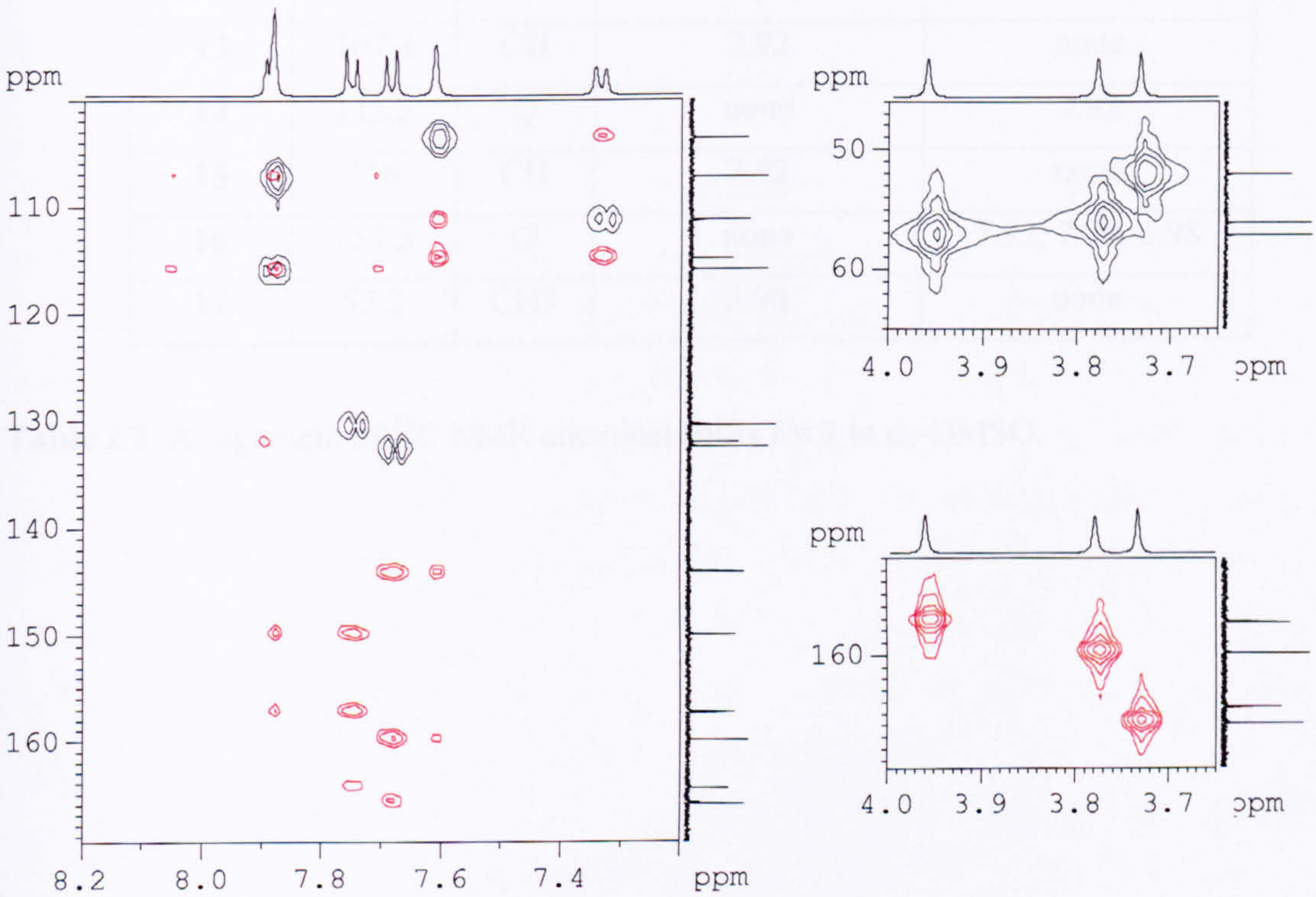

Figure 2.4 ^{1}H–^{13}C HMQC spectrum(black) and HMBC spectrum (red) of **2** in d_6-DMSO.

Label	δ	Type	HMQC to ^{1}H at δ	HMBC to ^{1}H at δ
1	52.1	CH_3	3.76	none
2	165.9	Q	none	7.71, 7.64, 3.76
3	144.2	Q	none	7.71, 7.64
4	132.6	CH	7.71	none
5	111.3	CH	7.36	7.64
6	115.0	Q	none	7.64, 7.36
7	106.7	CH	7.64	7.36
8	159.9	Q	none	7.71, 7.64, 3.81
9	56.1	CH_3	3.81	none
10	164.5	Q	none	7.92, 7.79
11	149.9	Q	none	7.92, 7.79
12	130.6	CH	7.79	7.92
13	107.3	CH	7.92	none
14	132.2	Q	none	7.92
15	116	CH	7.92	none
16	157.3	Q	none	7.92, 7.79, 3.98
17	57.2	CH3	3.98	none

Table 2.2 Assignment of ^{13}C NMR chemical shifts for **2** in d_6-DMSO.

2.1.4. 4-[(2-Methoxy-4-nitrocarbonyl)-amino]-2-methoxy benzoic acid, 3.

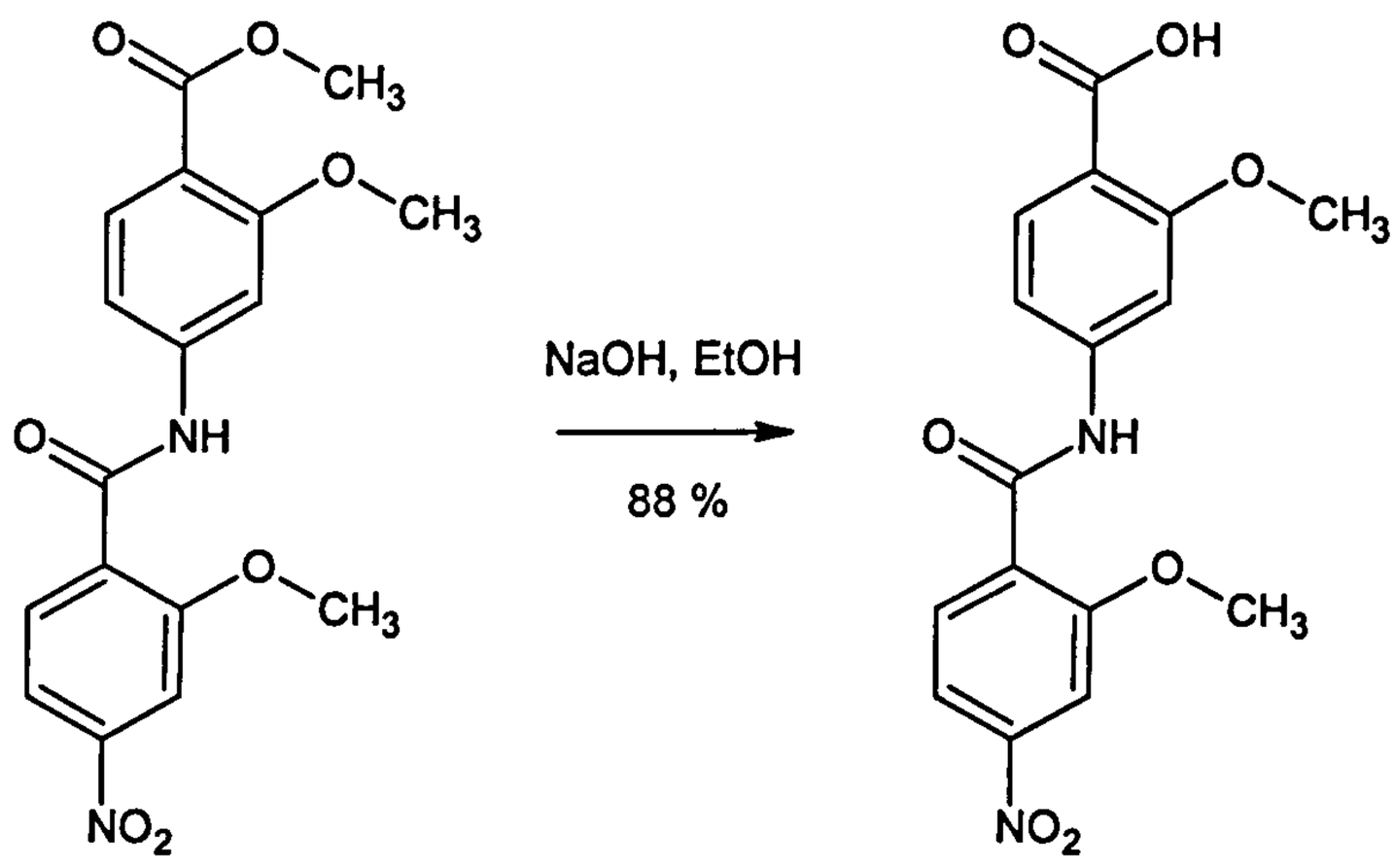

3

Scheme 2.4 Hydrolysis of **2** to give 4–[(2–methoxy–4–nitrocarbonyl)–amino]–2–methoxy benzoic acid, **3.**

Since the acid functionality is required to couple the spacer to the porphyrin, **2** was saponified by refluxing with sodium hydroxide in ethanol to give **3** as an orange solid in 88% yield (**Scheme 2.4**). The product was characterised as for **2**. The ^{1}H NMR spectrum contained a singlet at δ 11.20, shifted downfield compared to the ester, and only two singlets at δ 3.85 and 3.80 corresponding to the methoxy protons. Broad peaks were observed at 3271 cm^{-1} and 1283 cm^{-1} in the FTIR spectrum corresponding to the acid functionality. The amide N–H stretch at 3336 cm^{-1} and bend at 1592 cm^{-1} confirmed that the amide bond was unaffected. A shift to the higher frequency of 1744 cm^{-1} of one of the carbonyl stretches was the only other significant change in the spectrum. The EI–MS contained a molecular ion peak at m/z = 346, a difference of 14 (CH_2) compared to **2**.

2.1.5. Methyl 4-[(2-methoxy-4-aminocarbonyl)-amino]-2-methoxy benzoate, 4.

Reduction of **2** was also attempted since the amine functionality is required in the final probe. Reduction with stannous chloride and hydrochloric acid resulted in further hydrolysis of the ester and amide. Reaction with hydrogen and palladium on carbon also resulted in a range of products. A milder reaction was attempted with indium and ammonium chloride using the method of Pitts *et al.*[6] **(Scheme 2.5)**.

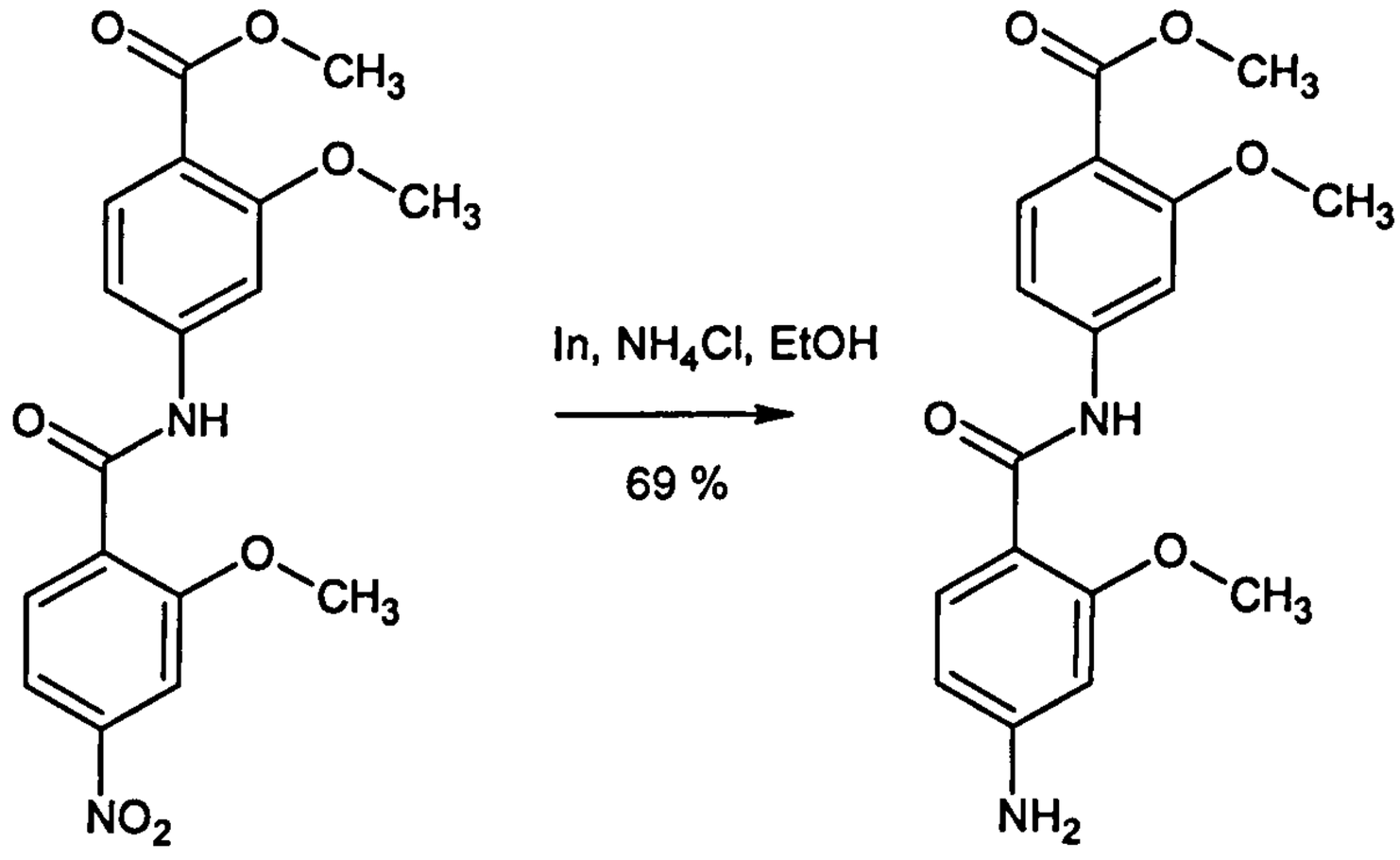

4

Scheme 2.5 Reduction of **2** to give methyl 4–[(2–methoxy–4–aminocarbonyl)–amino]–2–methoxy benzoate, **4.**

The insolubility of the product meant that Soxhlet extraction with chloroform was required to remove the inorganic impurities. Compound **4** was formed in 69% yield as a yellow solid. The ^{1}H NMR spectrum revealed that **2** had been selectively reduced to the amine with no hydrolysis of the ester. A singlet was observed at δ 5.94 corresponding to the amine protons and three singlets at δ 3.92, 3.81 and 3.75 corresponding to the methoxy protons. A singlet with at δ 9.97 was assigned as the amide proton. The full assignments are listed in **Table 2.3** and **Table 2.4**; the numbering is shown in **Figure 2.5.**

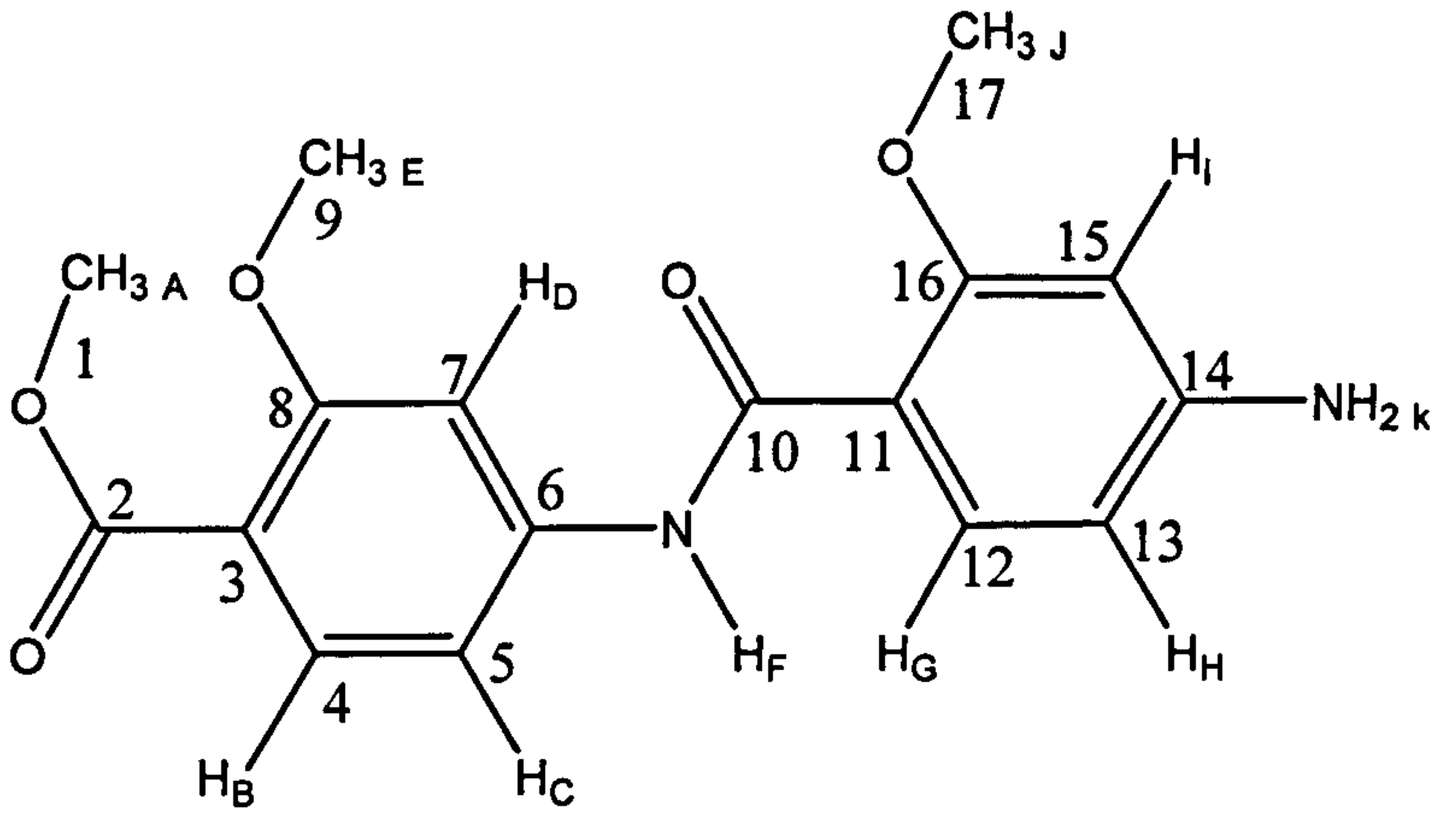

Figure 2.5 **4** with atom labels: letters assigned to protons and numbers assigned to carbons.

Label	δ	Integration	Multiplicity	Type	COSY to ^{1}H at δ
A	3.75	3	s	CH_3	none
B	7.67	1	d	CH	7.30
C	7.30	1	dd	CH	7.67, 7.70
D	7.70	1	d	CH	3.75, 7.30
E	3.82	3	s	CH_3	7.70
F	9.97	1	s	NH	none
G	7.63	1	d	CH	6.26
H	6.26	1	dd	CH	7.63, 6.30
I	6.30	1	d	CH	3.82, 6.26
J	3.92	3	s	CH_3	6.30
K	5.94	2	s	NH_2	none

Table 2.3 Assignment of ^{1}H NMR chemical shifts for **4** in d_6-DMSO.

Label	δ	Type	HMQC to ^{1}H at δ	HMBC to ^{1}H at δ
1	51.0	CH_3	3.75	none
2	164.9	Q	none	7.67, 3.75
3	143.9	Q	none	7.67, 7.70
4	131.5	CH	7.67	none
5	110.4	CH	7.3	9.97, 7.70
6	112.9	Q	none	7.70, 7.30
7	102.6	CH	7.7	9.97, 7.30
8	159.1	Q	none	7.67, 3.82
9	55.1	CH_3	3.82	none
10	163.5	Q	none	9.97, 7.63
11	153.7	Q	none	7.63, 6.30
12	132.2	CH	7.63	none
13	106.0	CH	6.26	6.30, 5.93
14	108.2	Q	none	6.30, 6.26
15	95.4	CH	6.3	6.26, 5.93
16	158.5	Q	none	7.63, 6.30, 3.92
17	55.2	CH_3	3.92	none

Table 2.4 Assignment of ^{13}C NMR chemical shifts for **4** in d_6-DMSO.

As for the previous compounds, the N–H stretch at 3340 cm^{-1} and bend at 1585 cm^{-1} confirmed the presence of the amide bond. Further evidence for successful reduction of the nitro group was provided by peaks at 3428, 3238 and 1526 cm^{-1} in the FTIR spectrum corresponding to the two stretching and one bending vibrations of the amine. The EI–MS spectrum contained a peak at m/z 330, a loss of 30 (2 × O – 2 × H) compared to **2**.

2.1.6. Methyl 4-[(nicotinoyl)-amino]-2-methoxy benzoate, 5.

Since pyridyl compounds have been shown to be suitable substrates[7,8], nicotinic acid was coupled to the linker in a similar way (**Scheme 2.6**).

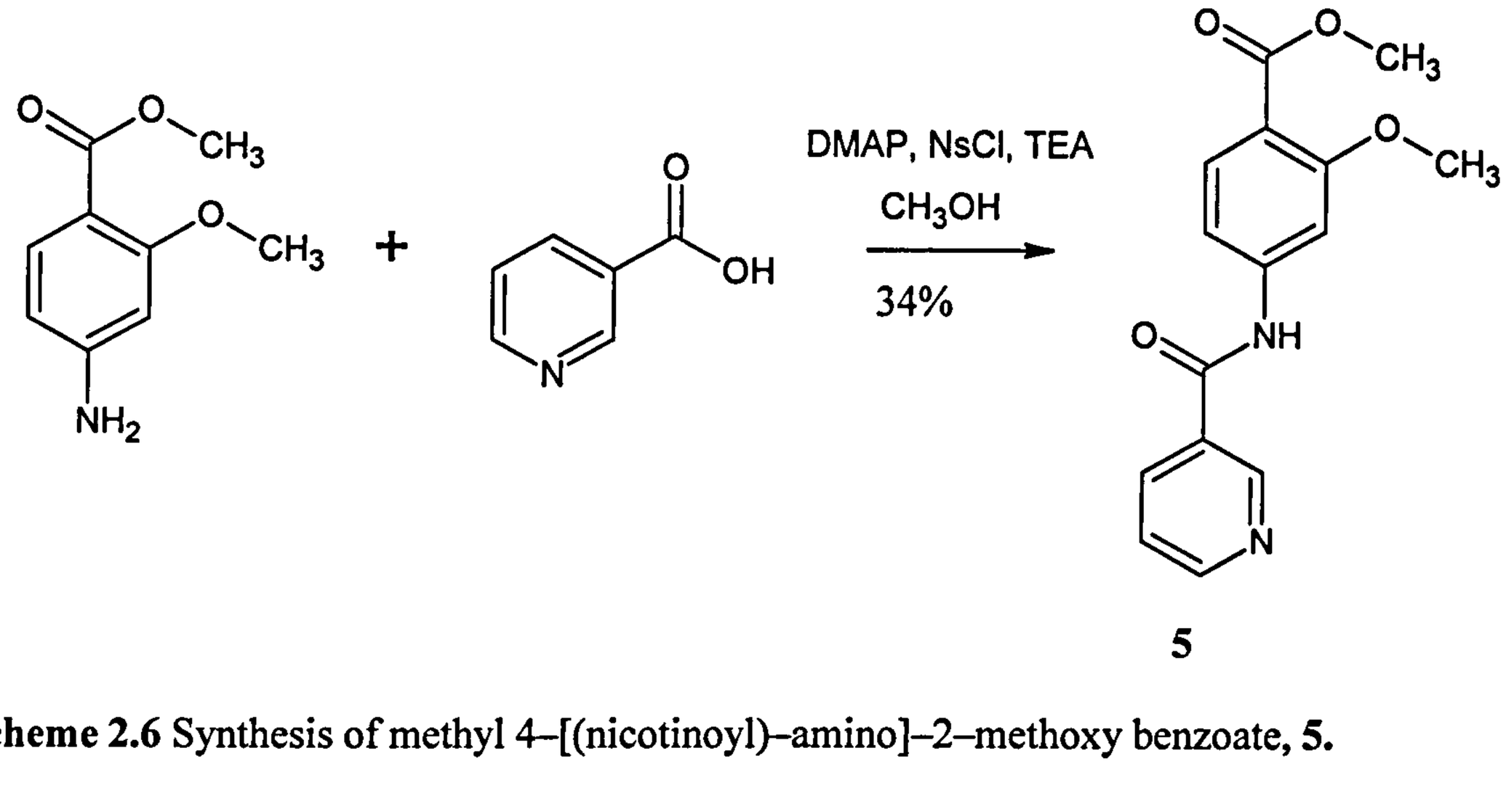

Scheme 2.6 Synthesis of methyl 4–[(nicotinoyl)–amino]–2–methoxy benzoate, **5.**

Compound **5** was purified by recrystallisation from ethyl acetate giving the pure compound in 34% yield. The ^{1}H NMR spectrum contained 4 resonances for the pyridyl protons; a singlet at δ 9.11, two doublets at 8.77 and 8.22 and a doublet of doublets at 7.44. Two singlets corresponding to the methoxy protons at δ 3.92 and 3.86 and two doublets and a doublet of doublets at δ 7.84, 7.74 and 7.06 for the phenyl protons were assigned similarly to the previous compounds. The amide proton at δ 8.77 was shifted less downfield than for the previous compounds possibly due to the absence of a hydrogen bonding methoxy group. The FTIR spectrum contained an amide N–H stretch at 3324 and a bend at 1591 cm^{-1}. The two carbonyl stretches were located at 1687 and 1670 cm^{-1}.

2.1.7. Methyl 4-[(isonicotinoyl)-amino]-2-methoxy benzoate, 6.

It would be beneficial to compare the effect of the nitrogen position on binding to XO. Therefore the isonicotinic acid derivative **6** was prepared in 40% yield after recrystallisation.

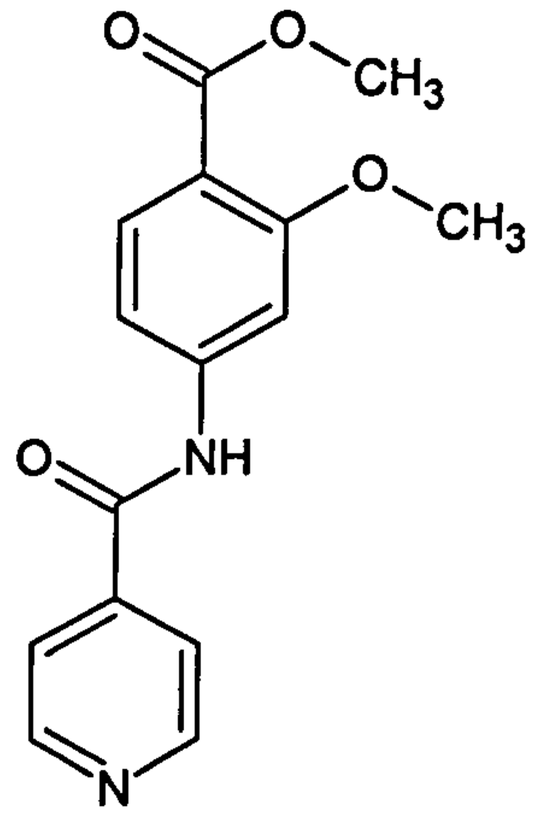

6

Figure 2.6 Methyl 4–[(isonicotinoyl)–amino]–2–methoxy benzoate, **6.**

The ^{1}H NMR spectrum for the isonicotinic acid derivative, **6**, contained only two doublets at δ 8.82 and 7.71 corresponding to the pyridyl protons. A singlet at δ 8.04 corresponded to the amide proton indicating weak hydrogen bonding, if any, in solution. The remaining aromatic resonances at δ 7.86, 7.74 and 6.99 were assigned to the phenyl protons as previously, as well as the two singlets at δ 3.94 and 3.88 to the methoxy protons. The FTIR spectrum contained an amide N–H stretch at 3342 and a bend at 1591 cm^{-1}. The two carbonyl stretches were located at 1690 and 1670 cm^{-1}. The ESI–MS for both **5** and **6** contained a molecular ion peak at *m/z* =285.0.

On slow evaporation of solvent from a concentrated solution of **6** in ethyl acetate, large transparent crystals formed. The molecular structure shown in **Figure 2.7** was determined by X-ray diffraction. The bond lengths and angles are listed in **Table 2.5.**

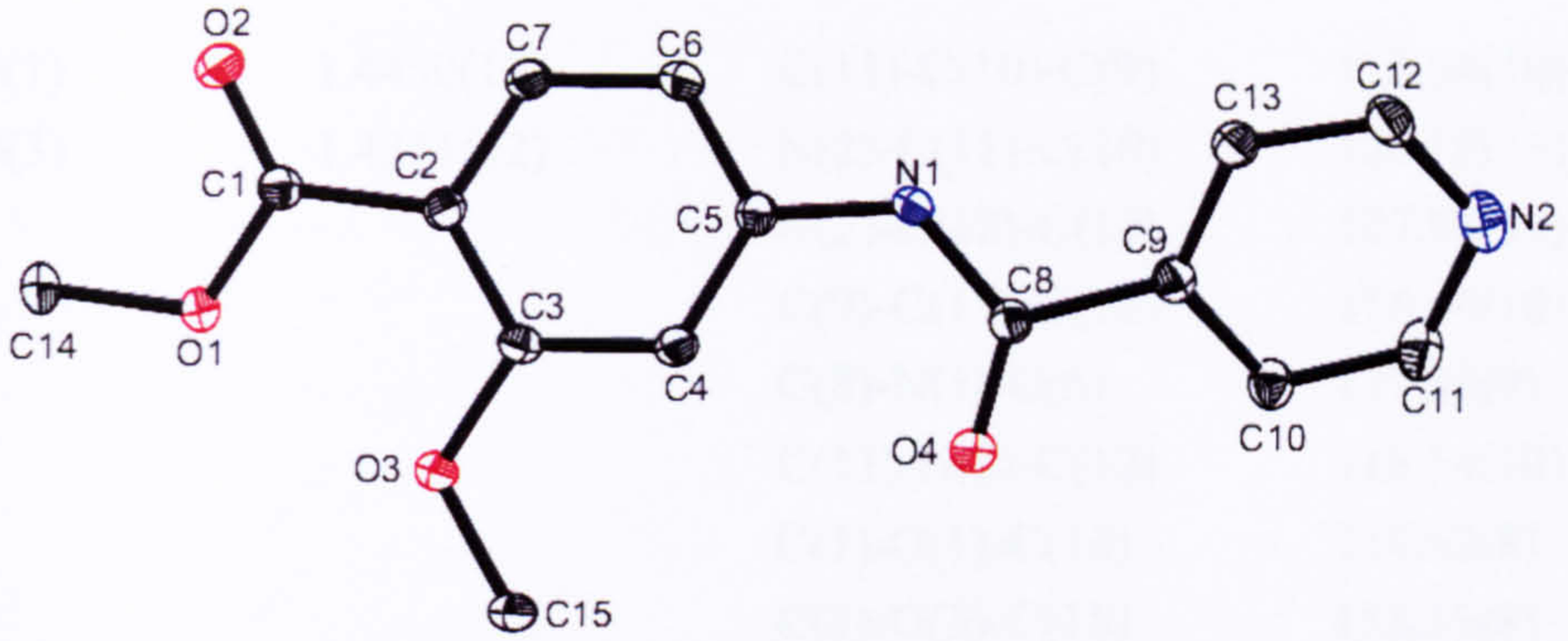

Figure 2.7 ORTEP view of **6** with 50 % thermal ellipsoids; colours correspond to atom types, carbon: black, nitrogen: blue, oxygen: red, hydrogen atoms not shown. Original in colour.

Table 2.5 Bond lengths [Å] and angles [°] for **6**.

C(1)-O(2)	1.2153(13)	O(2)-C(1)-C(2)	123.21(9)
C(1)-O(1)	1.3315(12)	O(1)-C(1)-C(2)	115.48(9)
C(1)-C(2)	1.4817(14)	C(7)-C(2)-C(3)	117.94(9)
C(2)-C(7)	1.3991(14)	C(7)-C(2)-C(1)	115.62(9)
C(2)-C(3)	1.4120(13)	C(3)-C(2)-C(1)	126.42(9)
C(3)-O(3)	1.3583(12)	O(3)-C(3)-C(4)	121.89(9)
C(3)-C(4)	1.3974(14)	O(3)-C(3)-C(2)	117.78(9)
C(4)-C(5)	1.3951(14)	C(4)-C(3)-C(2)	120.33(9)
C(5)-C(6)	1.4004(14)	C(5)-C(4)-C(3)	120.00(9)
C(5)-N(1)	1.4042(13)	C(4)-C(5)-C(6)	120.18(9)
C(6)-C(7)	1.3765(14)	C(4)-C(5)-N(1)	123.36(9)
C(8)-O(4)	1.2194(13)	C(6)-C(5)-N(1)	116.44(9)
C(8)-N(1)	1.3627(13)	C(7)-C(6)-C(5)	119.20(9)
C(8)-C(9)	1.5064(14)	C(6)-C(7)-C(2)	122.32(9)
C(9)-C(10)	1.3896(15)	O(4)-C(8)-N(1)	124.21(9)
C(9)-C(13)	1.3913(14)	O(4)-C(8)-C(9)	119.97(9)
C(10)-C(11)	1.3875(15)	N(1)-C(8)-C(9)	115.82(9)
C(11)-N(2)	1.3373(16)	C(10)-C(9)-C(13)	118.36(9)
C(12)-N(2)	1.3413(16)	C(10)-C(9)-C(8)	116.83(9)
C(12)-C(13)	1.3931(15)	C(13)-C(9)-C(8)	124.78(9)

C(14)-O(1)	1.4450(12)	C(11)-C(10)-C(9)	118.64(10)
C(15)-O(3)	1.4311(12)	N(2)-C(11)-C(10)	124.10(11)
		N(2)-C(12)-C(13)	123.88(10)
		C(9)-C(13)-C(12)	118.44(10)
		C(8)-N(1)-C(5)	127.50(9)
		C(11)-N(2)-C(12)	116.54(10)
		C(1)-O(1)-C(14)	114.62(8)
		C(3)-O(3)-C(15)	118.19(8)

Table 2.6 Torsion angles [°] for **6**.

O(2)-C(1)-C(2)-C(7)	-12.45(15)
O(1)-C(1)-C(2)-C(7)	166.31(9)
O(2)-C(1)-C(2)-C(3)	166.15(11)
O(1)-C(1)-C(2)-C(3)	-15.09(15)
C(1)-C(2)-C(3)-O(3)	2.03(15)
O(4)-C(8)-C(9)-C(10)	24.21(15)
N(1)-C(8)-C(9)-C(10)	-155.31(10)
O(4)-C(8)-C(9)-C(13)	-153.76(11)
N(1)-C(8)-C(9)-C(13)	26.72(15)
N(2)-C(12)-C(13)-C(9)	0.36(17)
O(4)-C(8)-N(1)-C(5)	4.27(17)
C(9)-C(8)-N(1)-C(5)	-176.23(9)
C(4)-C(5)-N(1)-C(8)	2.93(17)
C(6)-C(5)-N(1)-C(8)	-178.71(10)
O(2)-C(1)-O(1)-C(14)	-3.14(15)
C(2)-C(1)-O(1)-C(14)	178.07(9)
C(4)-C(3)-O(3)-C(15)	-2.42(15)
C(2)-C(3)-O(3)-C(15)	177.92(9)

As can be shown from **Figure 2.8** and **Table 2.6**, **6** is almost entirely planar apart from a small rotation around N(1)-C(8)-C(9)-C(13)of 26.72°. The dihedral angle between the fitted planes of the two aromatic rings deviates by 29.35 (0.04)° from co-planarity (see Appendix for calculation).

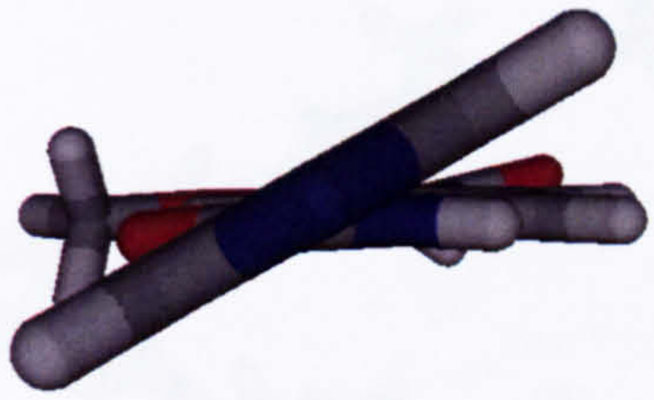

Figure 2.8 Capped-stick representation of **6** showing twist of the pyridyl group relative to the rest of the molecule. Original in colour.

A possible reason for this twist can be inferred from the higher order structure. A weak hydrogen bond between N(1) of one molecule and the ester carbonyl oxygen, O(2), on another creates a supramolecular array of criss-crossed species. The steric bulk of carbonyl oxygen and the ester group appear to cause the twist of the pyridyl group, as shown in **Figure 2.9.** The hydrogen bond lengths and angles are listed below in **Table 2.7**.

Table 2.7. Hydrogen bonds for **6** [Å and °].

D-H...A	d(D-H)	d(H...A)	d(D...A)	<(DHA)
N(1)-H(1)...O(2)#1	0.868(15)	2.062(15)	2.9257(12)	173.4(14)

Symmetry transformations used to generate equivalent atoms:

#1 -x+3/2,y-1/2,-z+3/2

Surprisingly, there seems to be the only hydrogen bond present. The pyridyl nitrogen does not act as a proton acceptor; instead it lies at some distance from any possible donors. There also does not appear to be any π-stacking between the aromatic groups as there is an 8 Å distance between each of them.

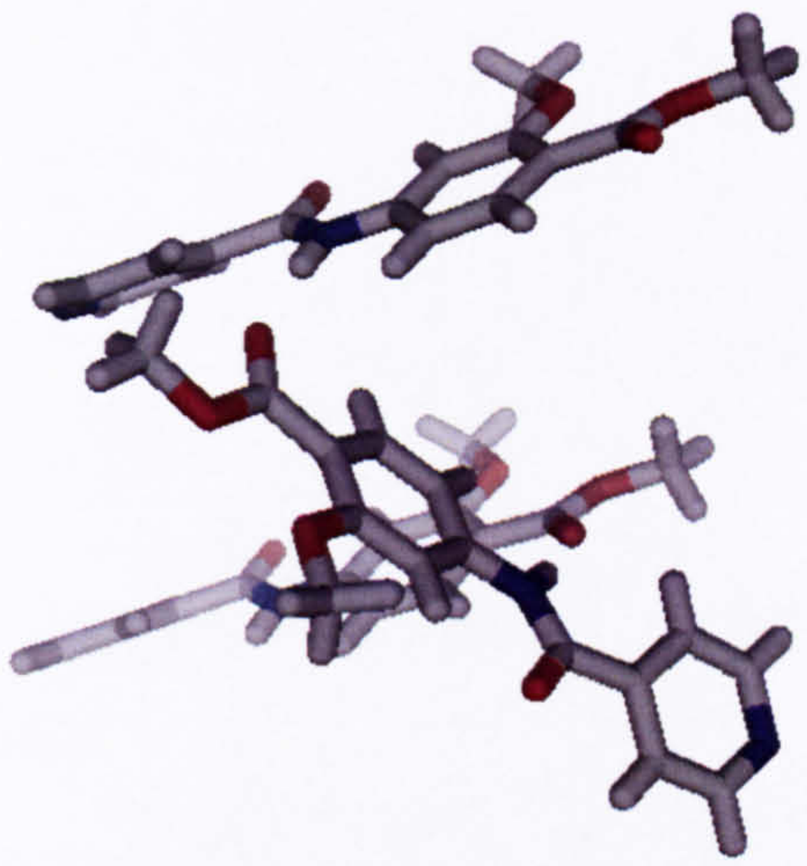

Figure 2.9 Capped-stick representation of the higher order solid state structure of **6**, colours correspond to atom types: carbon: grey; hydrogen: white; nitrogen: blue; oxygen: red. Original in colour.

This is in agreement with the spectroscopic evidence. The relatively upfield location of the NH proton at δ 8.04 in the ^{1}H NMR spectrum suggests weaker hydrogen bonding in solution than the previous compounds such as **2** for which the amide proton lies at δ 9.76.

2.2. A crystalline derivative of 2 coupled to ruthenium bis-bipyridine phenanthroline

The trimer synthesised by Estroff *et al.*[4] (was shown by X-ray diffraction to have a planar structure stabilized by intramolecular hydrogen bonds from the amide NH's to the neighbouring pyridine and alkoxy groups. The N---N and N---O bond lengths were reported

as 2.6-2.7 Å and the chemical shifts for the amide protons were shifted downfield to δ 10.12 and 10.27 in the ^{1}H NMR spectrum.

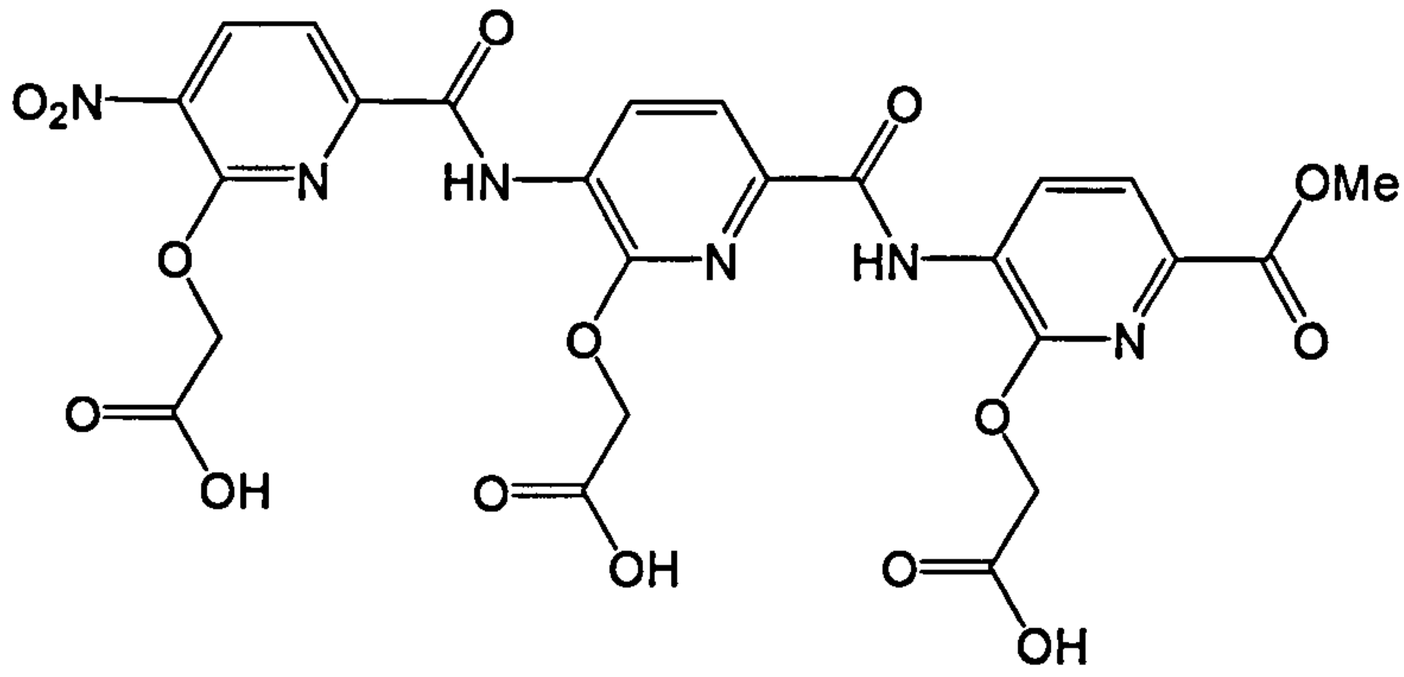

Scheme 2.7. The trimeric nitro derivative reported by Estroff *et al.*[4]

By comparison, the resonance corresponding to the amide proton of **2** is shifted downfield at δ 9.76, more towards that reported by Estroff *et al.* than that of **6** (δ 8.04), suggesting that this amide proton is involved in hydrogen bonding in solution. The single amide N–H stretch at 3355 and bend at 1589 cm^{-1} in the FTIR spectrum of **2** is not dissimilar to the corresponding frequencies at 3342 and 1591 cm^{-1} of **6** suggesting that intramolecular hydrogen bonding is present for both compounds in the solid state.

Crystals of sufficient quality for x-ray diffraction were not obtained for compound **2**. As an alternative approach, **1** was coupled to 1,10-phenanthroline-5-ylamine to give the phenanthrolinyl ligand **7**, which could be attached to a ruthenium bis bipyridyl complex to give an analogue which could be readily crystallised. X-ray diffraction was used to obtain a crystal structure for **7**, from which the hydrogen bond lengths could be measured.

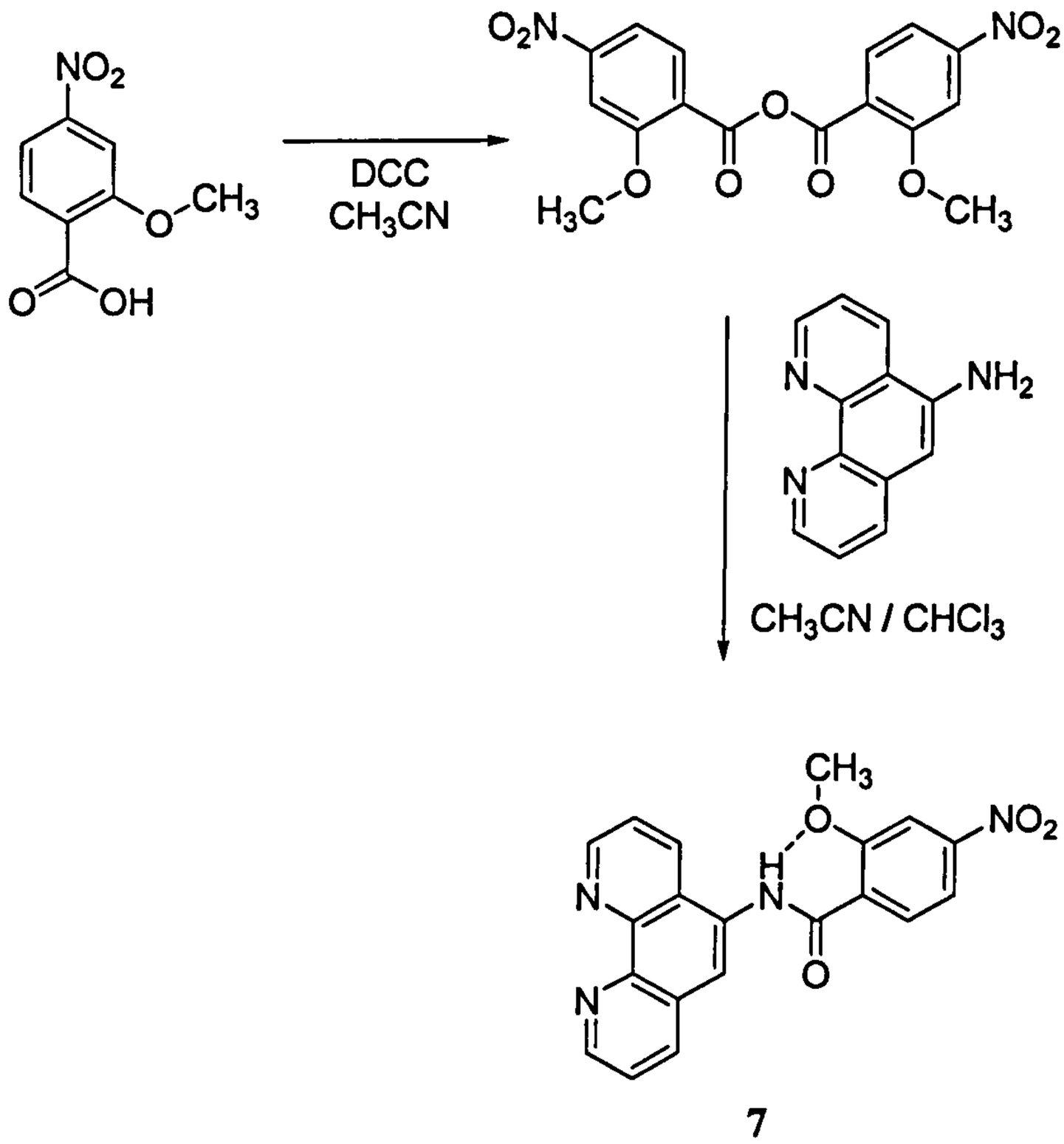

7

Scheme 2.8. Preparation of 2-methoxy-4-nitro-*N*-(1,10-phenanthrolin-5-yl)benzamide, **7**

performed by Albrighton[9].

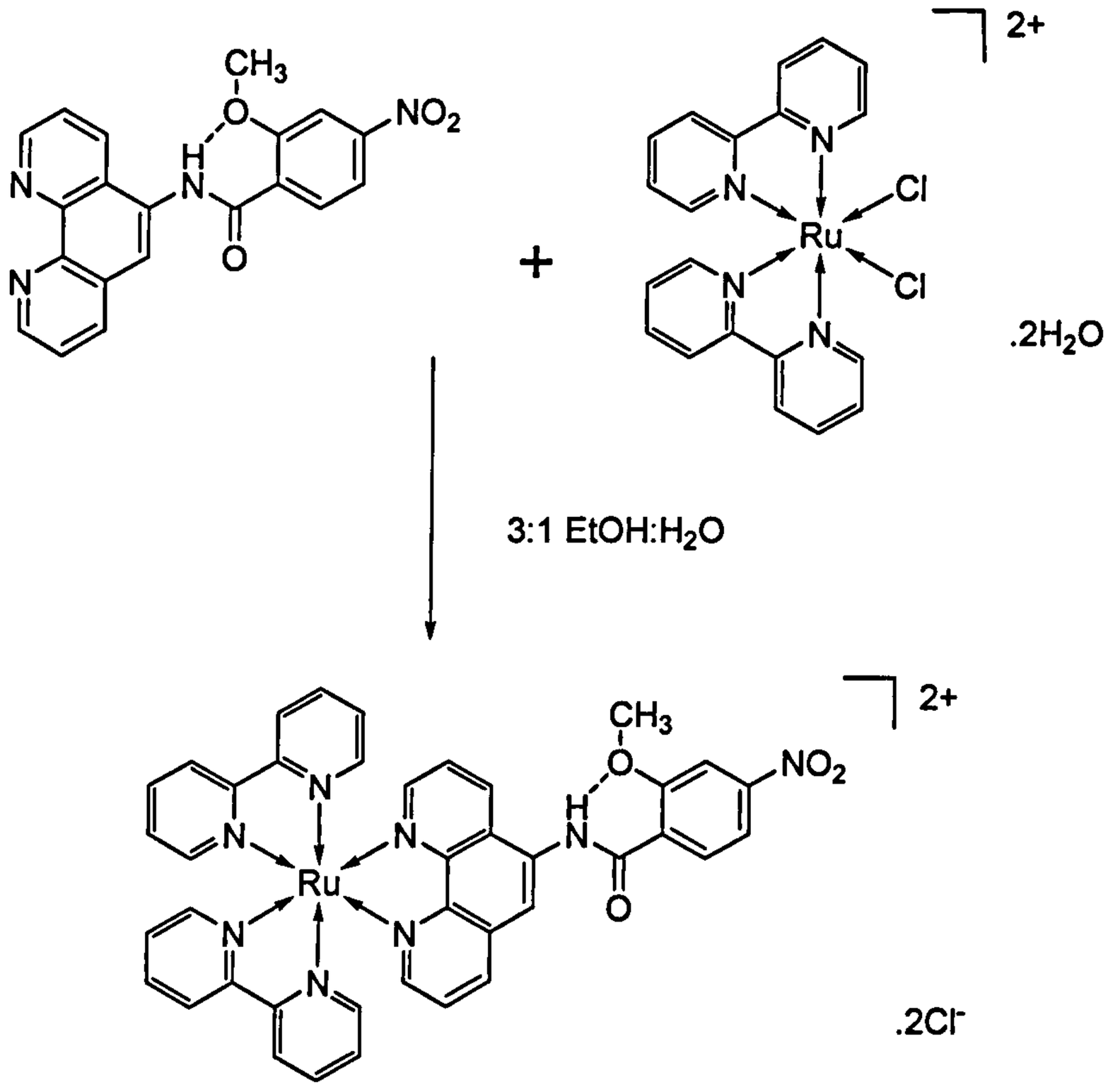

8

Scheme 2.9. Synthesis of $[Ru(bpy)_2(2\text{-methoxy-4-nitro-}N\text{-}(1,10\text{-phenanthrolin-5-yl})benzamide)]^{2+}$, $[\mathbf{8}][Cl]_2$, performed by Albrighton[9].

The synthesis was performed by Albrighton[9]. The ligand and complex both contained a downfield resonance at δ 10.3 corresponding to the amide proton and consistent with the intramolecular hydrogen bond. Subsequently, the PF_6^- salt of **8** was crystallised from acetonitrile by slow evaporation of the solvent. **Figure 2.10** shows the structure obtained by X-ray diffraction and **Table 2.8** lists selected bond lengths and angles. The ruthenium centre has octahedral geometry, typical for such complexes[10].

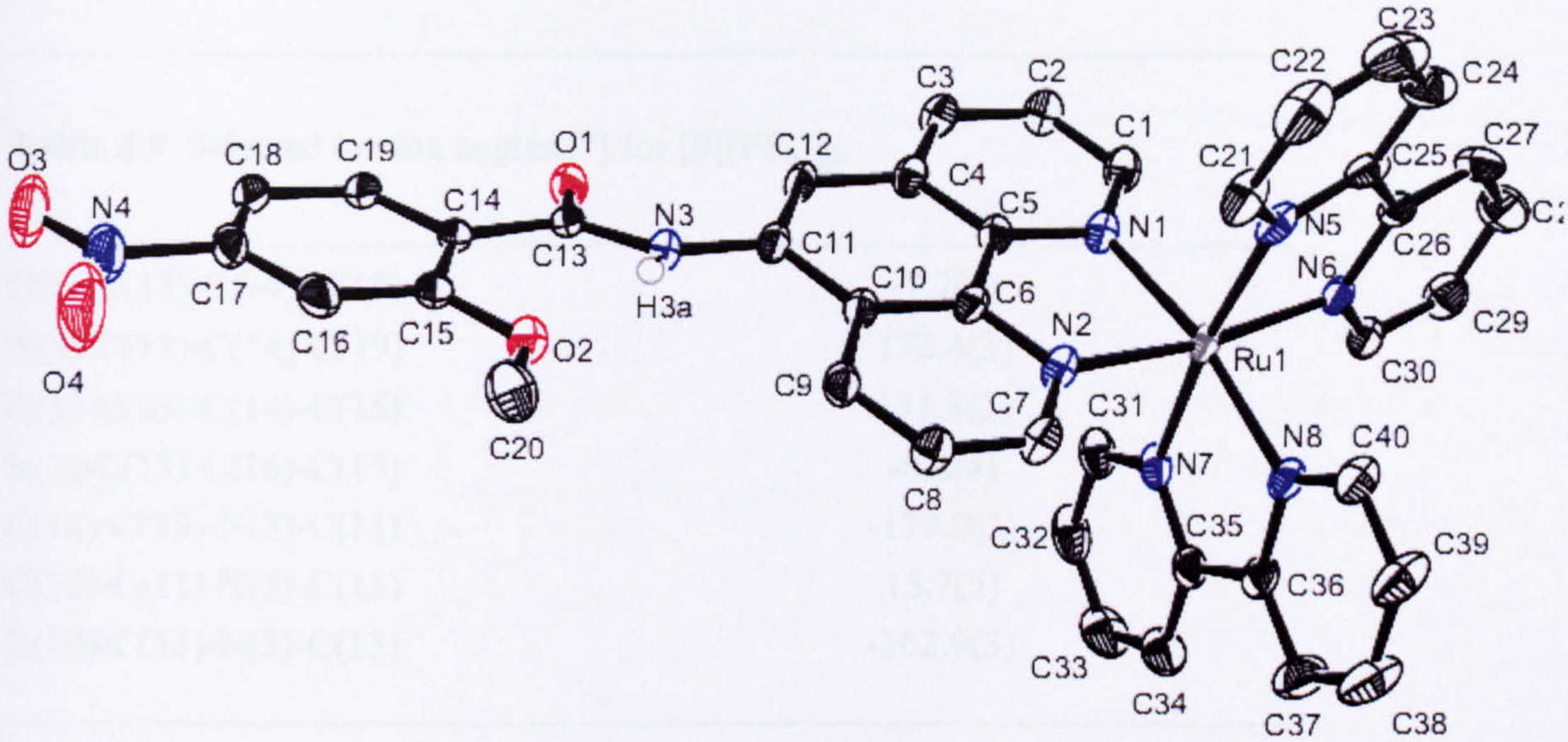

Figure 2.10 ORTEP view of [**8**][PF_6^-]$_2$ with 50 % thermal ellipsoids; colours correspond to atom types, carbon: black, nitrogen: blue, oxygen: red, ruthenium: grey, hydrogen atoms (except NH) not shown. Original in colour.

Table 2.8 Bond lengths [Å] and angles [°] in the ruthenium coordination sphere for **8**[**8**][PF_6^-]$_2$.

N(1)-Ru(1)	2.066(2)	N(6)-Ru(1)-N(8)	93.59(10)
N(2)-Ru(1)	2.071(2)	N(6)-Ru(1)-N(5)	78.80(10)
N(3)-H(3A)	0.80(4)	N(8)-Ru(1)-N(5)	95.92(10)
N(5)-Ru(1)	2.062(3)	N(6)-Ru(1)-N(7)	95.84(10)
N(6)-Ru(1)	2.059(2)	N(8)-Ru(1)-N(7)	79.04(10)
N(7)-Ru(1)	2.066(3)	N(5)-Ru(1)-N(7)	172.48(10)
N(8)-Ru(1)	2.061(3)	N(6)-Ru(1)-N(1)	93.75(9)
		N(8)-Ru(1)-N(1)	169.81(10)
		N(5)-Ru(1)-N(1)	92.43(10)
		N(7)-Ru(1)-N(1)	93.19(10)
		N(6)-Ru(1)-N(2)	171.42(10)
		N(8)-Ru(1)-N(2)	93.56(10)
		N(5)-Ru(1)-N(2)	95.75(10)
		N(7)-Ru(1)-N(2)	90.17(10)
		N(1)-Ru(1)-N(2)	79.77(10)

Table 2.9 Selected torsion angles [°] for **[8]**$[PF_6^-]_2$.

O(1)-C(13)-C(14)-C(19)	-7.7(4)
N(3)-C(13)-C(14)-C(19)	172.4(3)
O(1)-C(13)-C(14)-C(15)	171.8(3)
N(3)-C(13)-C(14)-C(15)	-8.2(4)
C(14)-C(13)-N(3)-C(11)	-179.0(3)
C(12)-C(11)-N(3)-C(13)	15.7(5)
C(10)-C(11)-N(3)-C(13)	-162.9(3)

The phenanthroline ligand is almost entirely planar, apart from two small twists either side of the planar amide bond. The torsion angles are given in **Table 2.9.** The dihedral angle between the fitted planes of the coupled aromatic ring and the phenanthroline deviates by 10.19 (0.20)° from co-planarity. The intramolecular hydrogen bond between the amide proton and the methoxy oxygen is clearly evident as expected. The bond lengths are listed in **Table 2.10** alongside the weaker hydrogen bond between the same proton and a nearby anion. The N---O bond length is much shorter for this compound than that of **2** (2.93 Å) corroborating the spectroscopic evidence.

Table 2.10 Hydrogen bonds for **[8]**$[PF_6^-]_2$ [Å and °].

D-H...A	d(D-H)	d(H...A)	d(D...A)	<(DHA)
N(3)-H(3A)...O(2)	0.80(4)	1.97(4)	2.662(3)	144(3)
N(3)-H(3A)...F(4)#1	0.80(4)	2.60(4)	3.097(4)	121(3)

The higher order solid state structure contains pairs of complexes surrounded by counter ions (not shown), as in **Figure 2.11**. The pairs are held together by π-π-stacking interactions. The intermolecular distance between the oxygen atom positioned over the centre of the π-electrons of the aromatic rings and the centroid itself is 3.4 Å for both the coupled ring to the amide carbonyl (O1) and the phenanthroline to the nitro oxygen (O4). This short distance suggests significant parallel-displaced aromatic-aromatic interactions[11].

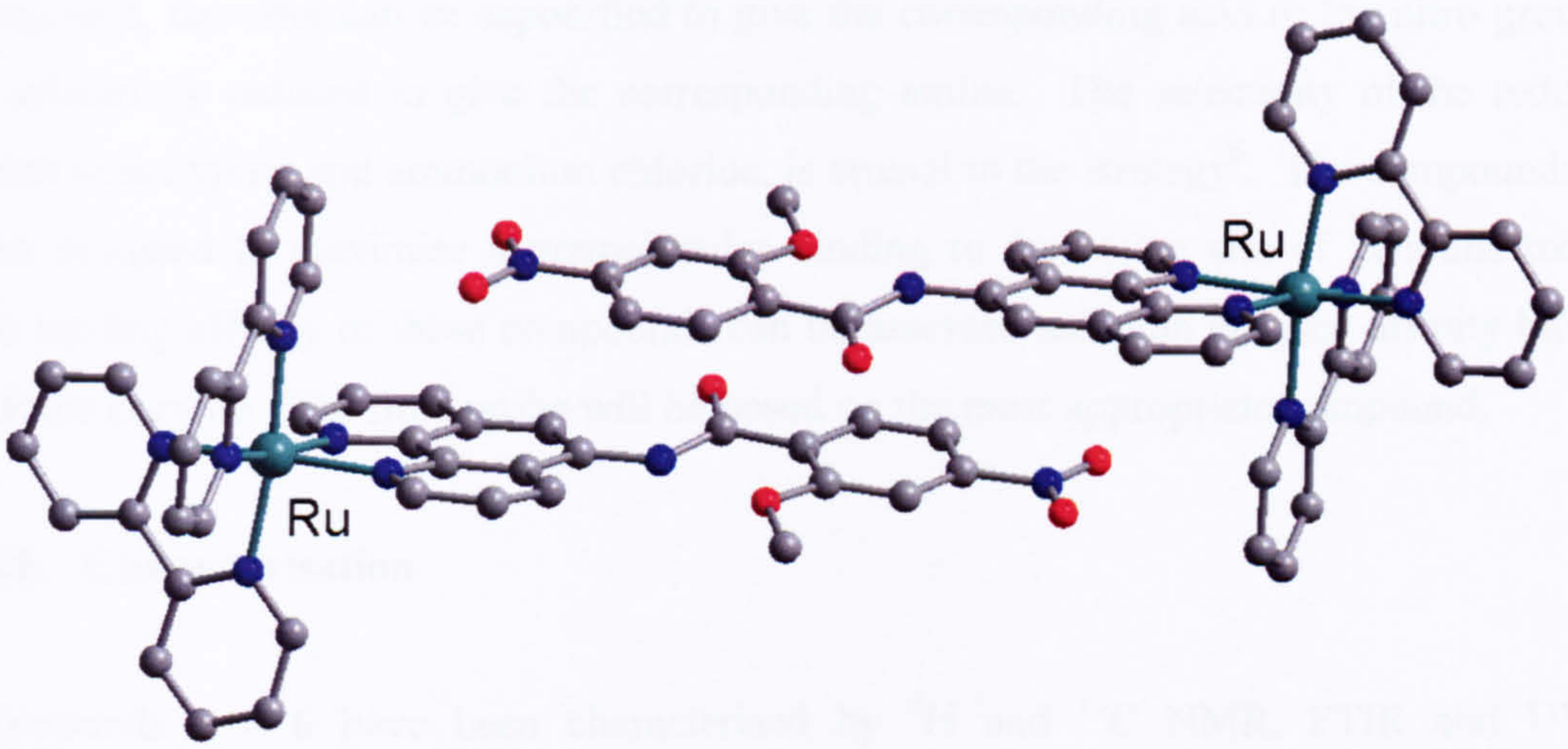

Figure 2.11 Ball and stick representation of [**8**][PF_6^-]$_2$, colours according to atom types, carbon: grey, nitrogen: blue, oxygen: red, ruthenium green (hydrogen not shown). Original in colour.

2.3. Summary

2.3.1. Synthesis

A number of linker-substrate compounds have been prepared using peptide coupling. A synthetic strategy to build up compounds of different lengths has been developed whereby an ester protected aniline derivative has been coupled with a nitro protected benzoic acid derivative. The most successful method found to couple aromatic acids and amines such as these was the DMAP catalysed method developed by Lee *et al.*[2]. In order to couple a third compound, the ester can be saponified to give the corresponding acid or the nitro group can be selectively reduced to give the corresponding amine. The selectivity of the reduction, which uses indium and ammonium chloride, is crucial to the strategy[6]. The compounds have been designed to maximise supramolecular binding to the active site of xanthine oxidase. The binding affinity of these compounds can be assessed using an enzyme affinity bioassay with the enzyme. The final probe will be based on the most appropriate compound.

2.3.2. Characterisation

Compounds **1 – 6** have been characterised by ^{1}H and ^{13}C NMR, FTIR and UV-Vis spectroscopy and electron ionisation or electrospray mass spectrometry. Full assignment of the NMR spectra was aided by 2D experiments, $^{1}H - ^{1}H$ COSY, $^{1}H - ^{13}C$ HMQC and HMBC. A successful coupling reaction was indicated by a solvent dependent downfield signal corresponding to the amide NH. The signal was located more downfield for compounds **2-4** than for compounds **5** and **6** due to the presence of hydrogen bonding in solution.

The intramolecular hydrogen bond between the methoxy oxygen of the linker to a neighbouring amide proton was confirmed by X-ray diffraction of a ruthenium bis bipyridyl complex which could be readily crystallised. The H…O bond distance was measured to be 1.97 Å, appropriate for a hydrogen bond.

The remaining functional groups were identified from the FTIR spectrum. The ester carbonyls (**1, 2, 4, 5, 6**) were located around 1670-1700 cm^{-1}, the acid carbonyl (**3**) was located at higher frequency at 1744 cm^{-1} and the amide carbonyls at slightly lower frequency, 1630 – 1680 cm^{-1} (**2 – 6**). The NH stretch for each was at 3320 – 3355 cm^{-1}, the amide NH deformation was around 1585 - 1595 and the amine (**1, 4**) NH deformation was at lower frequency at 1525 - 1565 cm^{-1}. The nitro antisymmetric stretch (**2, 3**) was located at 1522 cm^{-1} and the symmetric stretch at 1357 cm^{-1}. The acid OH stretch (**3**) was located at 3271 cm^{-1}, and bend at 1283 cm^{-1}.

Each of the compounds contained strong absorption bands in the UV region of the spectrum.

For compounds **1 – 4**, the M^+ ion was observed in EI-MS, and fragmenting mostly occurred by cleavage of the amide bond. In the ESI-MS the $M + H^+$ adducts were observed for compounds **2 – 6**.

2.4. References

1. B.R. Brooks, R. E. Bruccoleri, B. D. Olafson, D. J. States, S. Swaminathan, M. Karplus, *J. Comput. Chem.*, **1983**, *2*, 187.
2. A.D. MacKerell Jr., D. Bashford, M. Bellott, R. L. Dunbrack, J. D. Evanseck, M. J. Field, S. Fischer, J. Gao, H. Guo, S. Ha, D. Joseph-McCarthy, L. Kuchnir, K. Kuczera, F. T. K. Lau, C. Mattos, S. Michnick, T. Ngo, D. T. Nguyen, B. Prodhom, W. E. Reiher III, B. Roux, M. Schlenkrich, J. C. Smith, R. Stote, J. Straub, M. Watanabe, J. Wiorkiewicz-Kuczera, D. Yin, M. Karplus, *J. Phys. Chem. B*, **1998**, *18*, 3586.
3. W. A. Hewlett, T. de Paulis, N. S. Mason, D. E. Schmidt, B. L. Trivedi, Z. –J. Zhang, M. H. Ebert, *Chem. Pharm. Bull.*, **1997**, *45*, 2079.
4. L. A. Estroff, C. D. Incarvito, A. D. Hamilton, *J. Am. Chem. Soc.*, **2004**, *126*, 2.
5. J. C. Lee, Y. H. Cho., H. K. Lee, S. H. Cho, *Synth. Commun.*, **1995**, *25*, 2877.
6. M. R. Pitts, J. R. Harrison, C. J. Moody, *J. Chem. Soc., Perkin Trans. 1*, **2001**, 977.
7. K. Okamoto, K. Matsumoto, R. Hille, B. T. Eger, E. F. Pai, T. Nishino, *PNAS* 2004, *101*, 7931.
8. G. Biagi, A. Costantini, L. Costantino, I. Giorgi, O. Livi, P. Pecorari, M. Rinaldi, V. Scartoni, *J. Med. Chem.* 1996, *39*, 2529.
9. C. Albrighton, MChem. Year 4 Project Report, **2006**. *An MChem student under my guidance.*
10. D. P. Rillema, D. S. Jones, H. A. Levy, *J. Chem. Soc.*, Chem. Comm. **1979**, 849.
11. C. Janiak, *J. Chem. Soc., Dalton Trans.*, **2000**, 3885.

CHAPTER THREE

TETRAPHENYL PORPHYRIN DERIVATIVES

3. Tetraphenyl Porphyrin Derivatives

3.1. Synthesis

The synthesis of porphyrins is typically achieved by the Adler-Longo method of heating benzaldehyde and pyrrole in propionic acid at reflux in air[6]. By this method tetraphenyl porphyrin (TPP) can be prepared in around 20% yield (**Scheme 3.1**). Variation of the aldehyde enables porphyrins with different substituents at the 5, 10, 15 and 20 positions to be synthesised. Unsymmetrical porphyrins can be obtained in this way by using two different benzaldehydes. However, a statistical distribution of products is obtained which must be separated and therefore limits the overall yield[2].

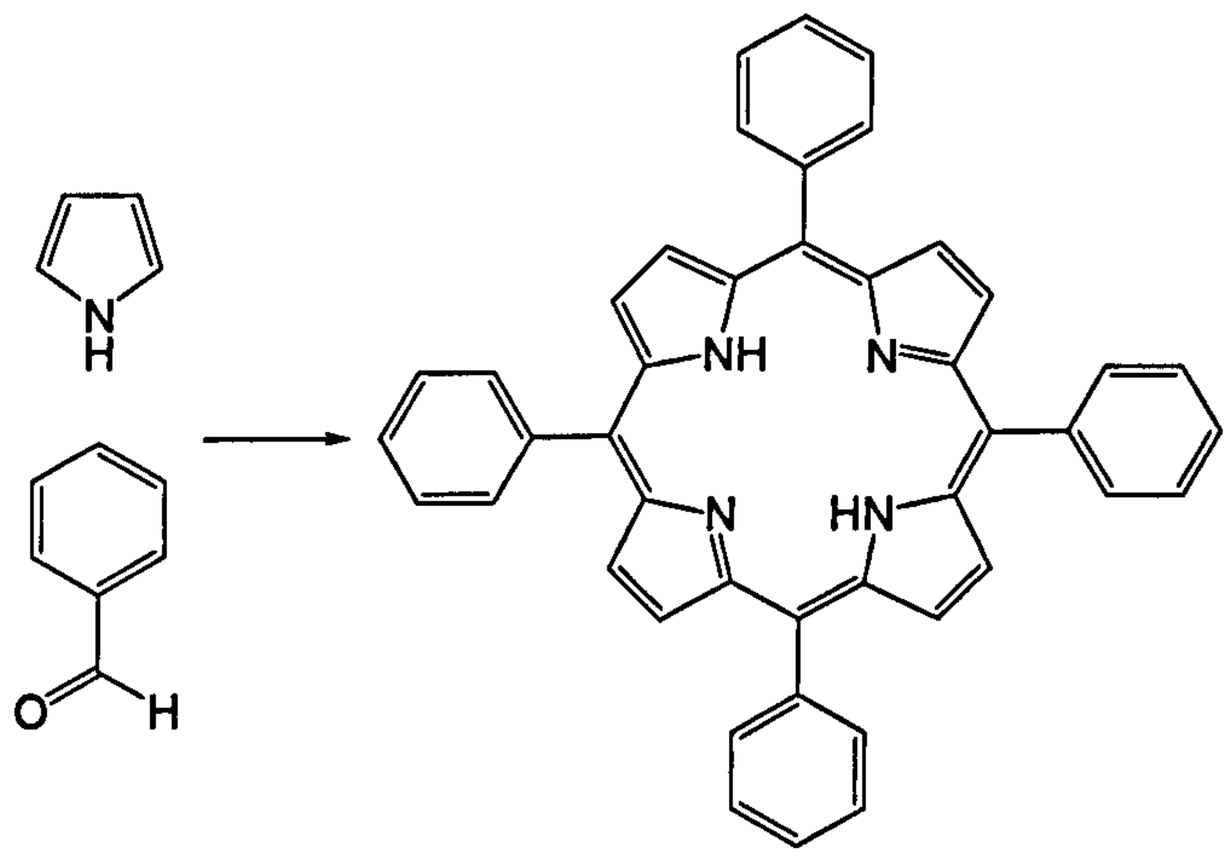

Scheme 3.1 Formation of tetraphenyl porphyrin by the Adler-Longo method[6].

The Lindsey method enables synthesis of porphyrins from more sensitive aldehydes in smaller quantities but much higher yields (35-40%)[3]. Pyrrole, benzaldehyde, triethyl orthoacetate (water scavenger) and boron trifluoride (catalyst) are reacted at room temperature in chloroform under nitrogen (**Scheme 3.2**). After an hour, equilibrium between the staring materials and tetraphenylporphyrinogen is established at which point the oxidant 2,3,5,6-tetrachlorobenzoquinone is added and the reaction heated at reflux. The oxidant irreversibly converts the porphyrinogen to porphyrin. The purification is more facile since the tarry by-products, which contaminate the products from the Adler-Longo procedure, are not present. However, a high dilution of the reaction mixture (10^{-2} M) is required which limits the scale. The advantage of the Lindsey method is that porphyrins with ortho and pyrrole substituents can be obtained.

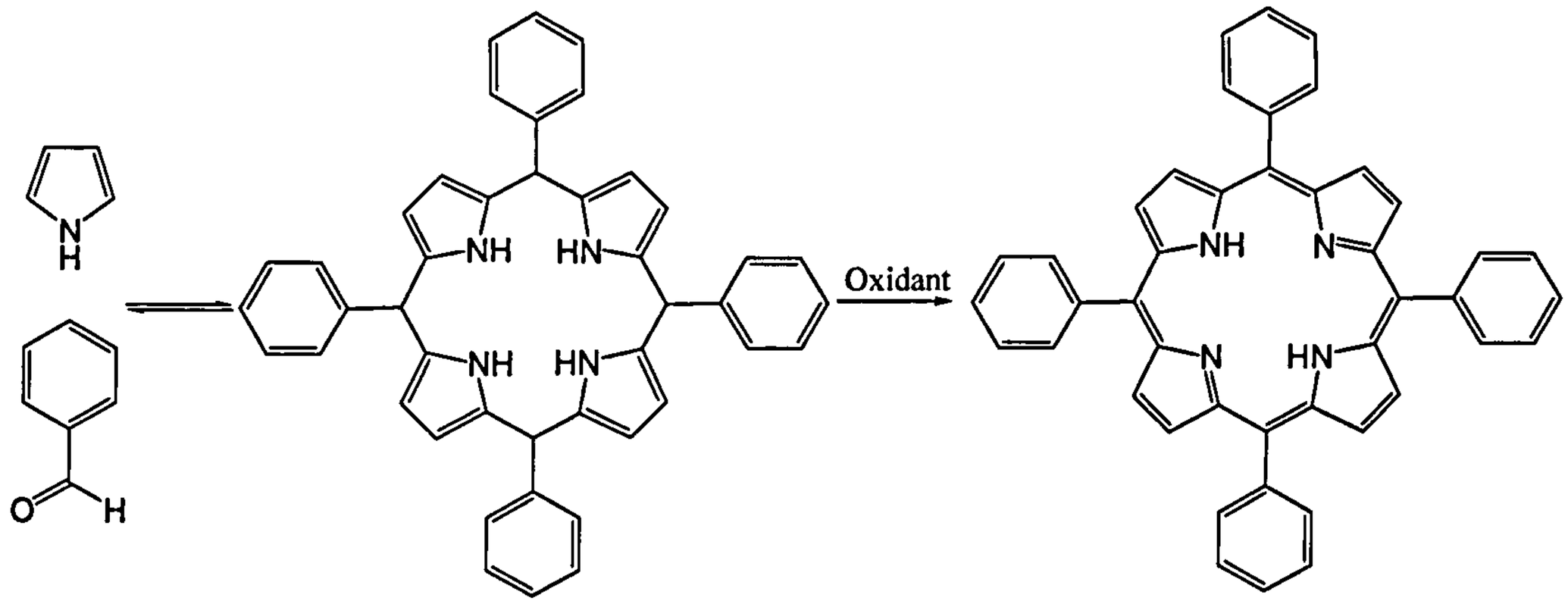

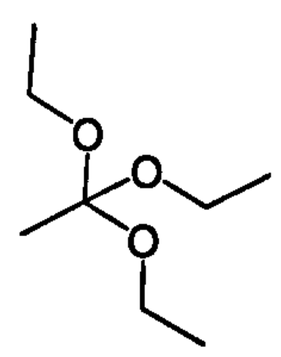

triethyl orthoacetate

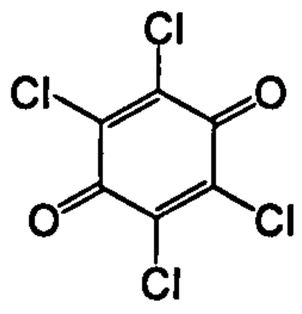

tetrachlorobenzoquinone

Scheme 3.2 Formation of tetraphenyl porphyrin by the Lindsey method[2].

A thorough review by Shanmugathasan *et al.* describes several other routes including the '2 + 2' route whereby two dipyrromethanes are condensed and the '3 + 1' route, condensation of a tripyrrane and a diformyl pyrrole, which enable the preparation of more highly substituted porphyrins[2].

A far simpler route to monofunctionalised porphyrins is to perform substitution reactions around a pre-formed porphyrin periphery.

3.1.1. 5-(4-Aminophenyl)-10,15,20-triphenylporphyrin, 9.

Previous work at York on the synthesis of porphyrin derivatives[5,6] involved the selective monofunctionalisation of commercially available TPP according to the method by Kruper *et al.*[7] (**Scheme 3.3**).

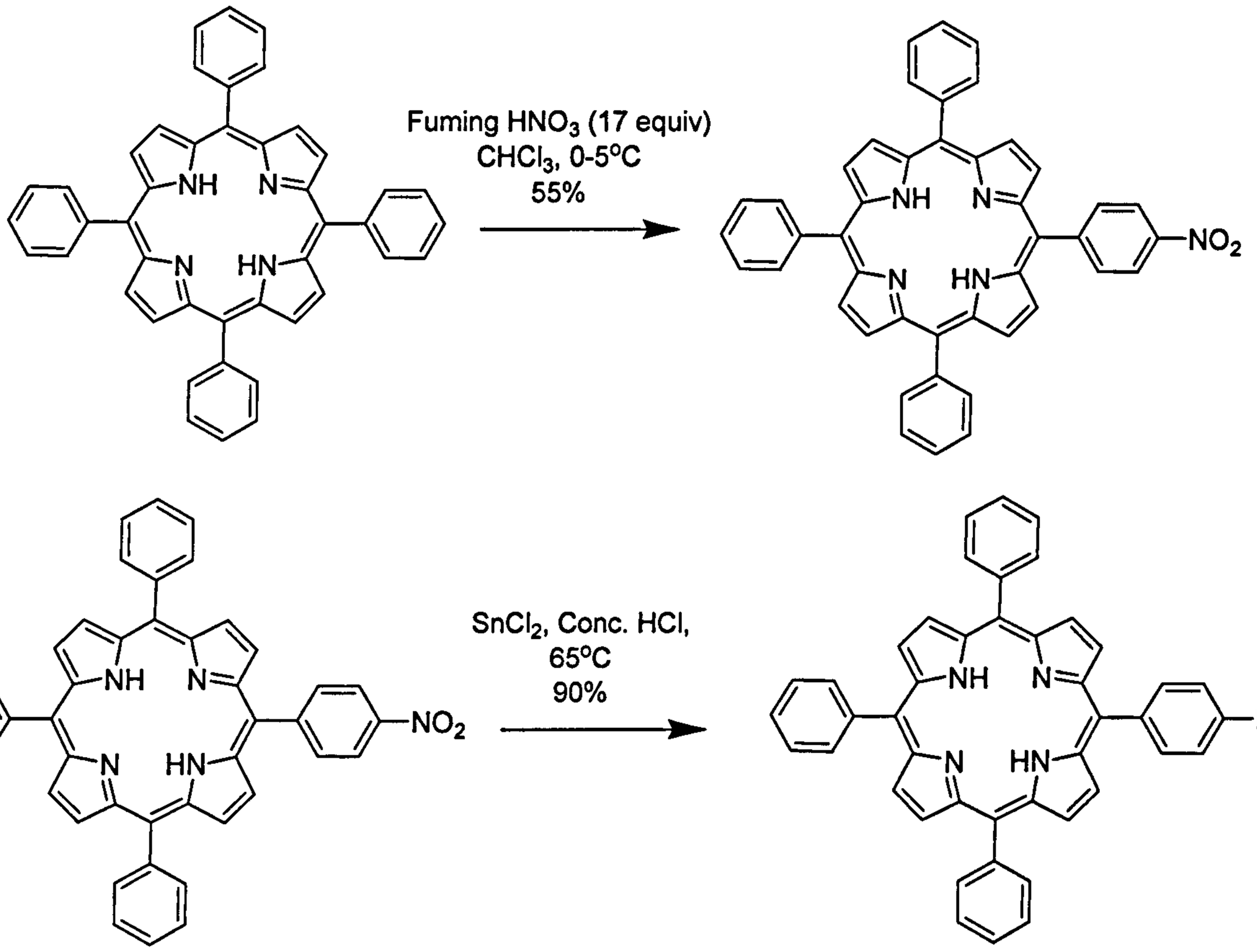

Scheme 3.3 Preparation of free-base 5–(4–aminophenyl)–10,15,20–triphenyl porphyrin, **9**, according to the method by Kruper *et al.*[7]

This is a simpler route to prepare asymmetrically functionalised porphyrins than the traditional mixed condensation routes described above[3]. The advantage is that this method avoids the lengthy purification required, can be carried out on a relatively large scale and improves the yield substantially.

In this research, the porphyrin was functionalised according to the improved method by Luguya *et al.*, whereby TPP was stirred with sodium nitrite in trifluoroacetic acid at room temperature for a few minutes[8]. This gave the *para* nitrated porphyrin, which was reduced by tin (II) chloride in hydrochloric acid to the corresponding amino porphyrin (**9**) (**Scheme 3.4**).

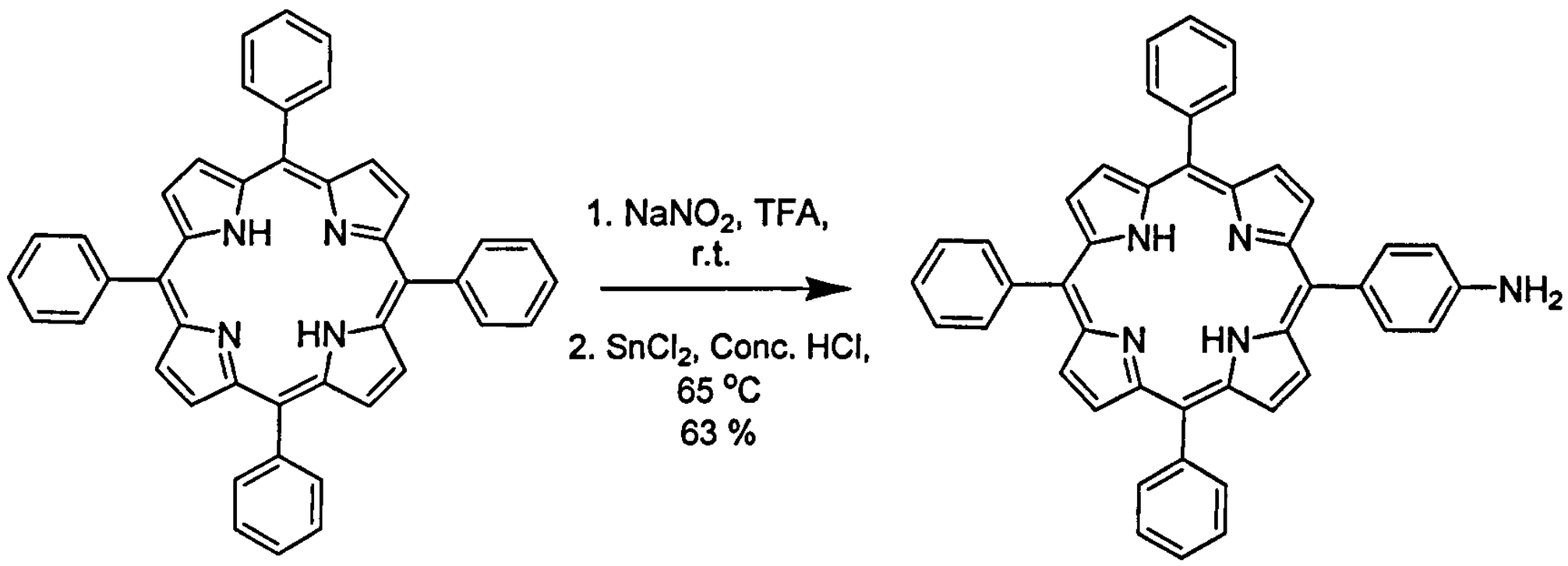

9

Scheme 3.4 Preparation of **9** according to the method by Luguya *et al.*[8]

Treatment of TPP in trifluoroacetic acid with sodium nitrite leads to stepwise selective nitration of the aryl groups at the *para* position in moderate conditions which enables the mono functionalised porphyrin to be obtained with little damage to the macrocycle. Preparation of 5–(4–nitrophenyl)–10,15,20–triphenylporphyrin (**8**) proceeded as in **Scheme 3.4**, and was monitored by tlc. The reaction was quenched after a few minutes, as soon as a second spot from the dinitroporphyrin was observed. This eased isolation of the product, which was achieved by column chromatography eluting with dichloromethane. Unreacted TPP, the first band to elute, was recovered and reused. **8** was then reduced to the amino porphyrin **9** as above with 86% yield (63% overall). **8** and **9** were characterised by ^{1}H NMR, FTIR and EI–MS. The data obtained agreed with the literature.

3.1.2. Coupling of the Linker

Unfortunately the poor solubility of the acid, **3**, (Chapter 2) meant that coupling to the porphyrin was not achieved using standard coupling techniques [6, 9, 10]. However, coupling of 2–methoxy 4–nitrobenzoic acid to **9** was achieved in excellent yield by the anhydride method[11]. Therefore the strategy of coupling the linker, reducing the nitro group to give the amine followed by a second coupling step was developed in order to build up probes of different lengths and which could easily be modified to improve binding to the enzyme **(Scheme 3.5)**.

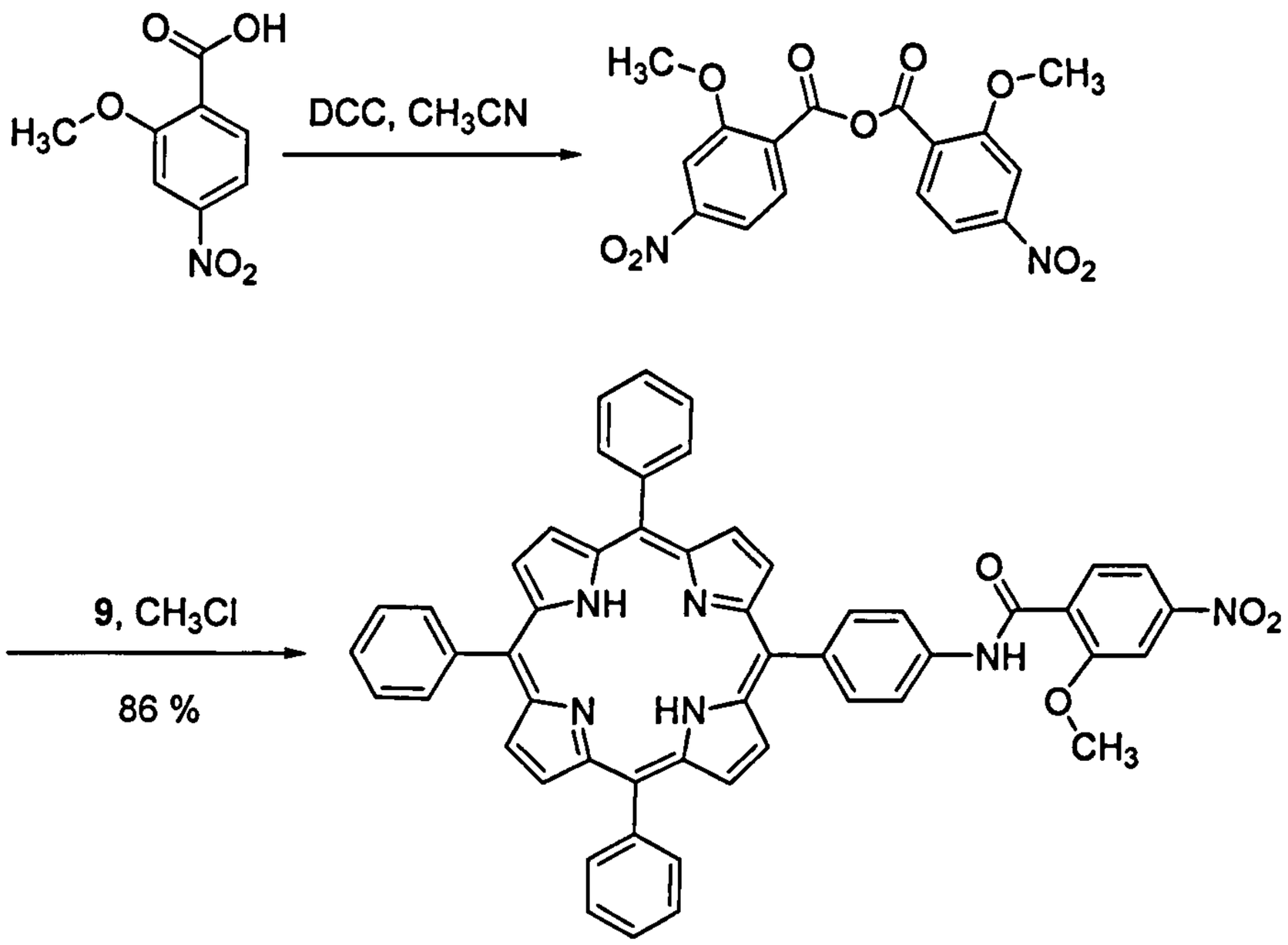

10

Scheme 3.5 Coupling of spacer to luminophore, **9**, to give **10**.

Stirring 2–methoxy 4–nitrobenzoic acid in a solution of dicyclohexylcarbodiimide in dry acetonitrile gave the acid anhydride which, once the insoluble urea byproduct had been removed by filtration, was heated under reflux with the porphyrin **9** in 50:50 v/v acetonitrile/chloroform. This produced free base 5-[4-[(2-methoxy-4-nitro-phenylcarbonyl)-amino] phenyl]-10,15,20-triphenyl porphyrin **10**, which was purified by column chromatography over silica, in 86% yield. Zinc was then inserted to give **11 (Section 3.1.6.)**.

3.1.3. Reduction of the Linker

The nitro group was reduced selectively using the method shown in **Scheme 3.6**, which was described previously[6].

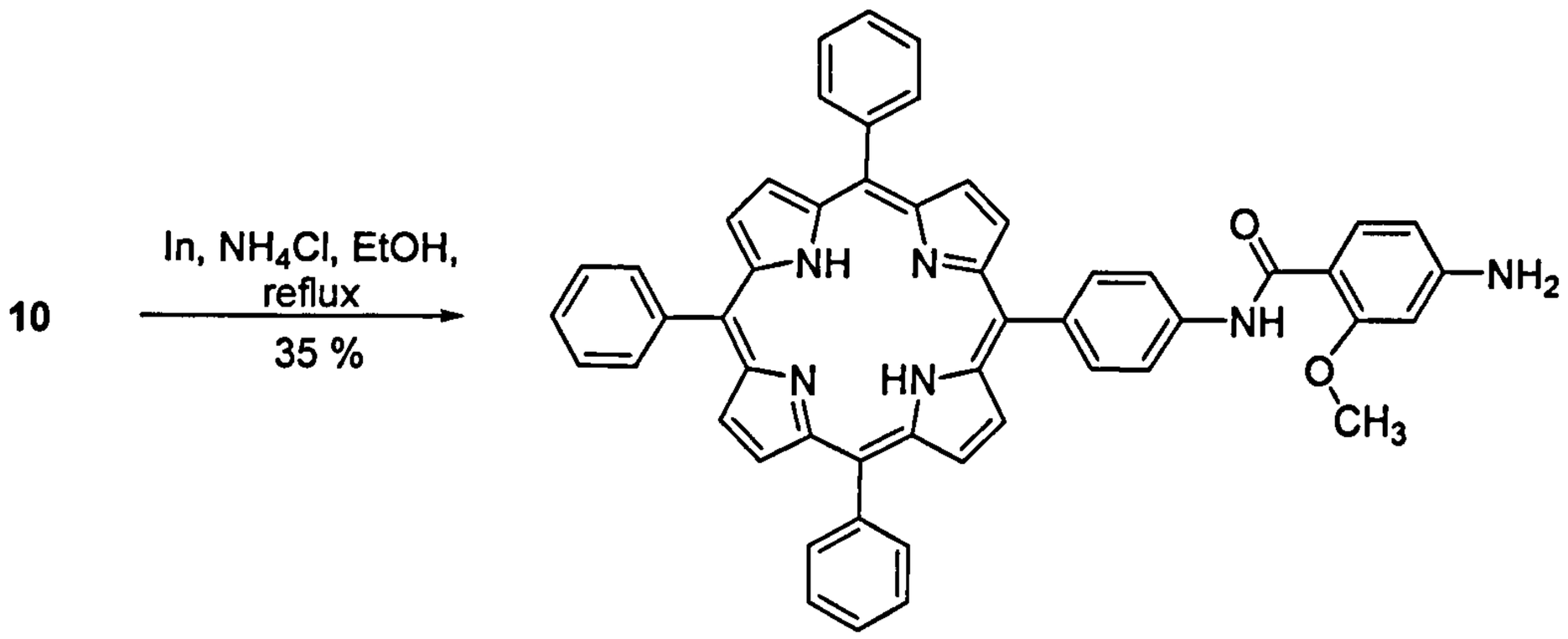

12

Scheme 3.6 Reduction of nitro group to give **12.**

The ESI–MS of the reduced porphyrin contained peaks corresponding to the indium coordinated porphyrin at *m/z* = 891.5 (57 %) and with methanol at *m/z* = 922.5 (100%). Therefore the porphyrin was stirred in 5% sulfuric acid in trifluoroacetic acid to remove the metal. This further purification step, in addition to the poor solubility of the product, reduced the yield to 35%. Zinc was inserted into **12** to give **13 (Section 3.1.6.)**.

3.1.4. Coupling of the Substrate-Analogue

The whole procedure was repeated to link a second unit. **14** was prepared in 78% yield in the same way as **10**, by heating **12** with the acid anhydride. **14** was poorly soluble in most common laboratory solvents, precipitating from DMSO and chloroform solutions on standing. The solubility was improved by incorporating zinc to give **15 (Section 3.1.6)**.

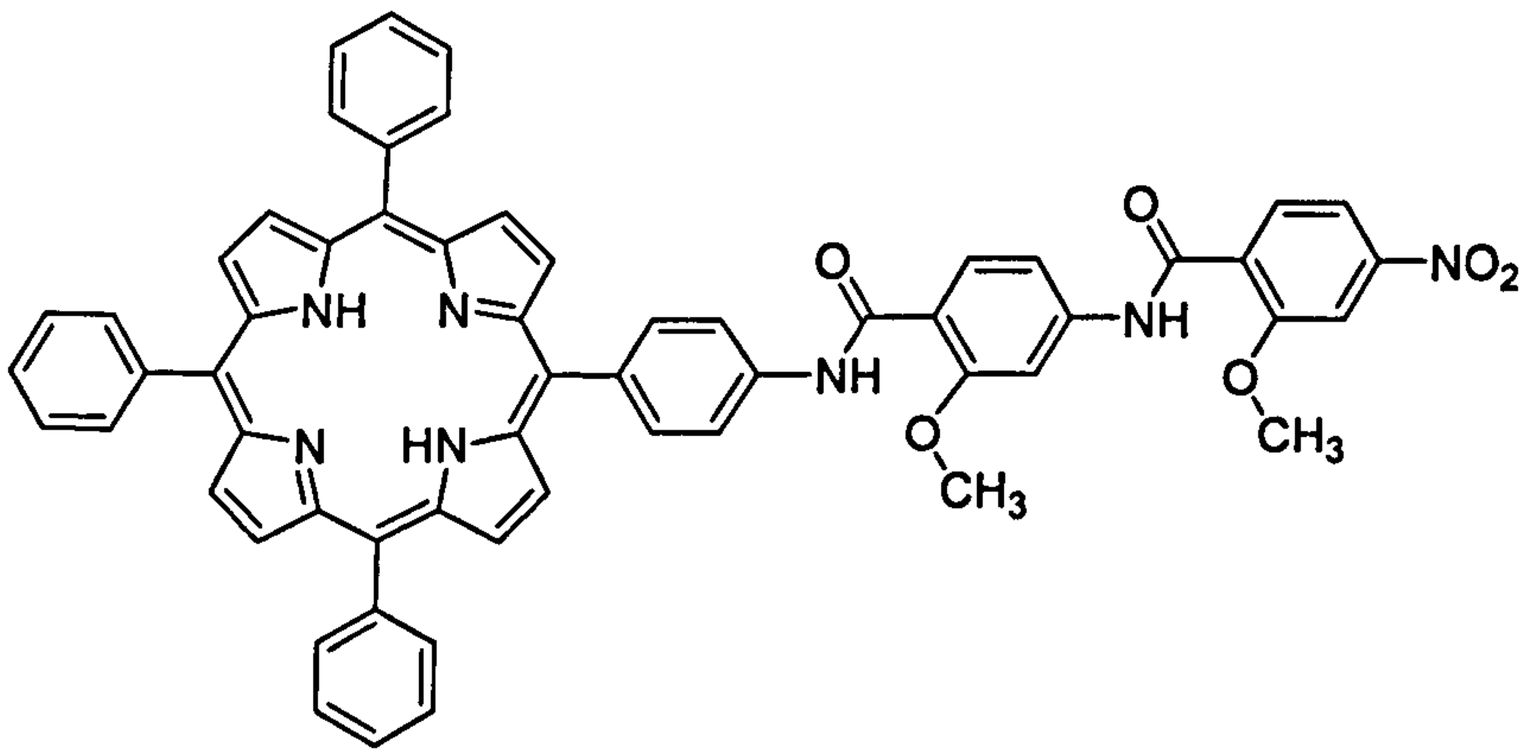

14

3.1.5. Reduction of the Substrate-Analogue

Compound **14** was reduced with indium and ammonium chloride to give **16** in a similar yield to **12** (30%). Preparation of the zinc derivative **17** is described in the following section.

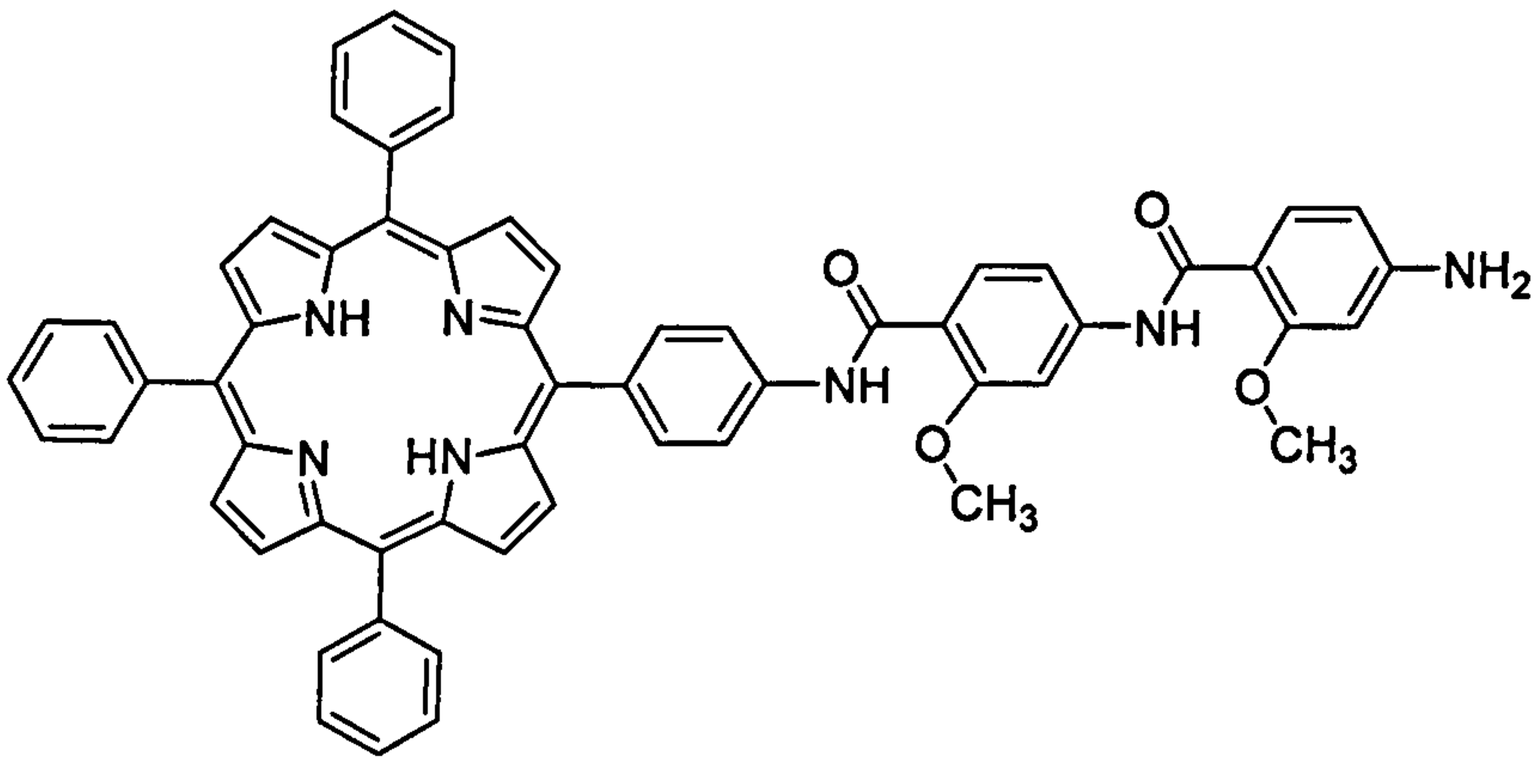

16

3.1.6. Insertion of Zinc

The desired metalloporphyrins were prepared by heating a solution of free base porphyrin in dichloromethane and methanol with zinc acetate dihydrate at reflux. The progress of the reaction can be monitored by UV–visible spectroscopy where a change from four Q–bands to two is observed. The zinc porphyrins were then purified by column chromatography over silica, eluting with chloroform and methanol to reduce the aggregation in solution.

Compounds **10, 12, 14,** and **16** were heated at reflux with zinc acetate as described previously to give zinc porphyrins **11** (80%), **13,** (94%), **15** (90%) and **17** (83%).

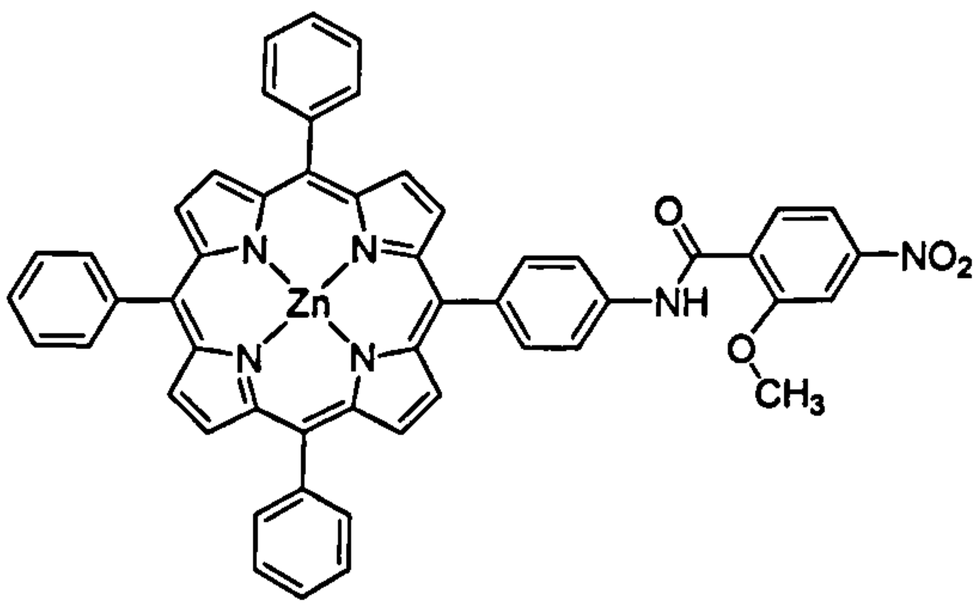

11

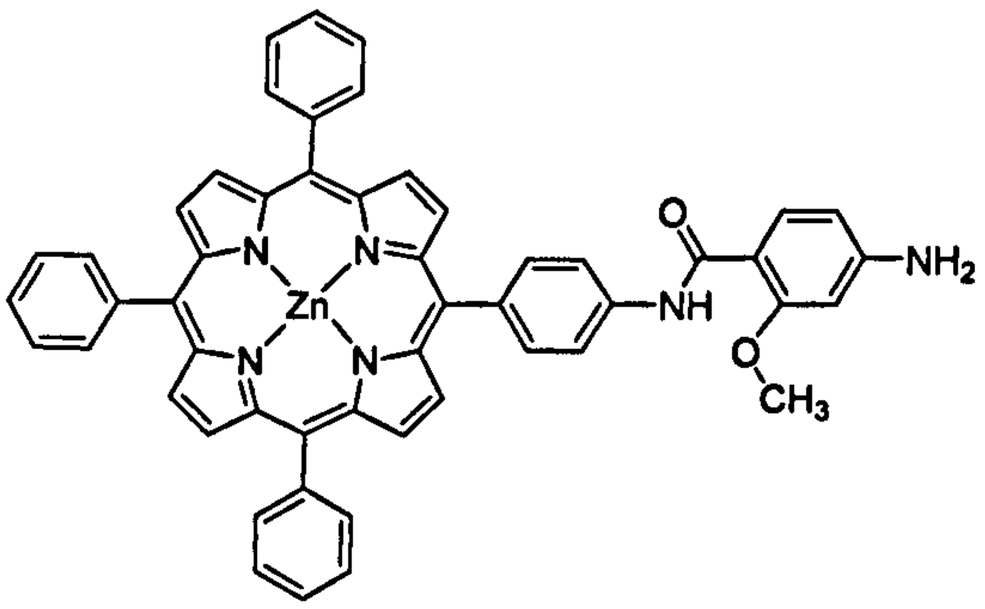

13

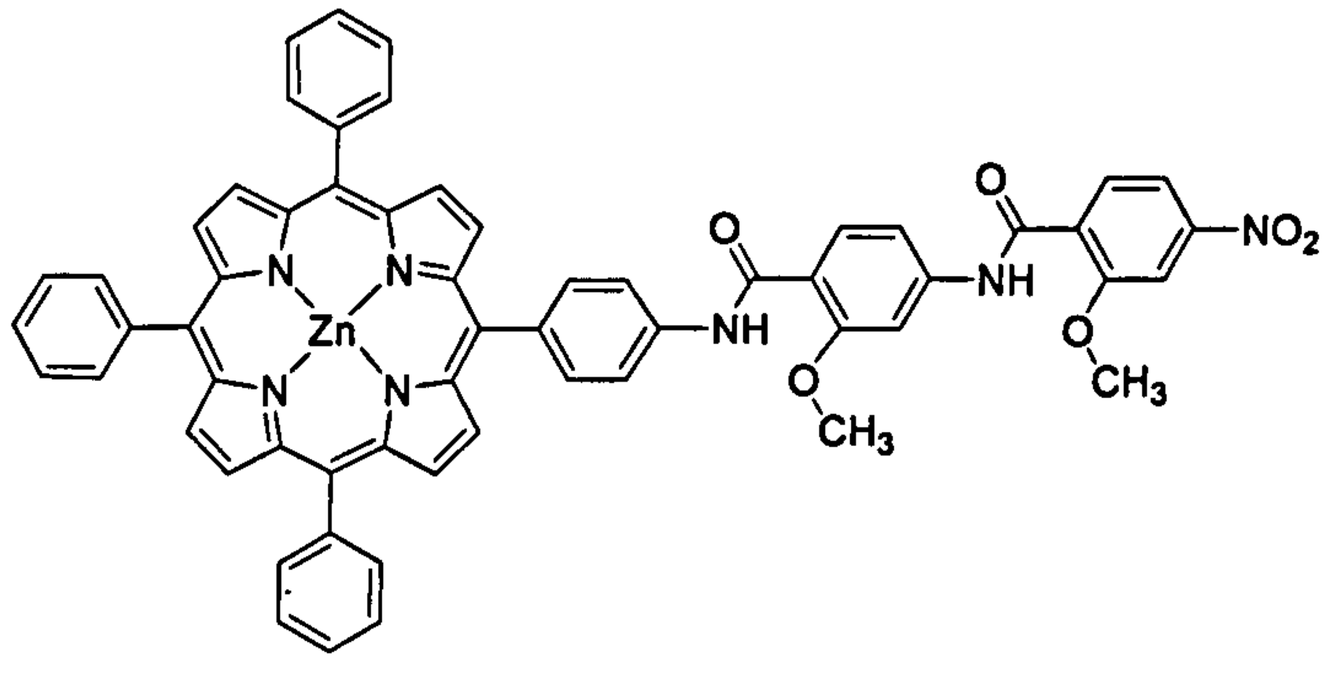

15

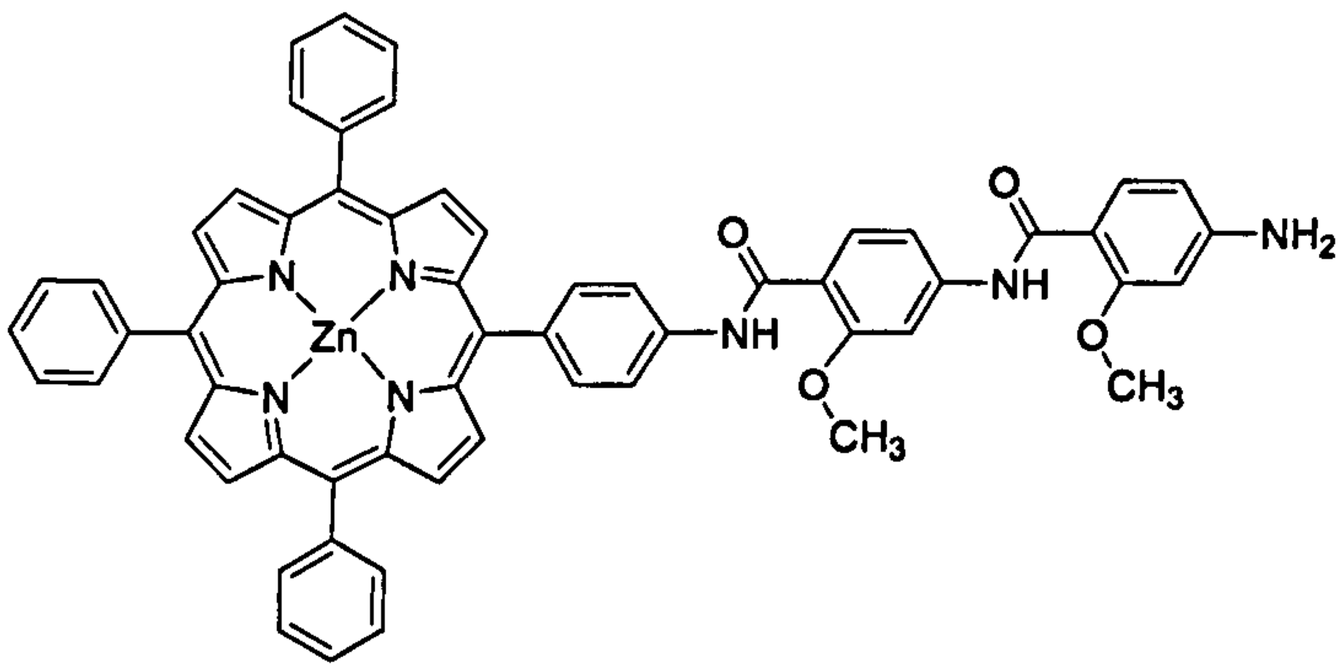

17

There is an increased tendency for zinc porphyrins to aggregate in solution and therefore the solubility of each decreased with respect to the free base porphyrins in organic solvents. However, solubility in coordinating solvents such as methanol improved. Such aggregation was demonstrated by substantial broadening of the peaks in the ^{1}H NMR spectra of **13**. Addition of a drop of d_5-pyridine disrupted this, causing sharpening of the peaks. The presence of aggregates was also observed in the electrospray ionisation mass spectrum of **13**. A peak at $m/z = 1682.9$ corresponds to $2M - H^+$.

3.2. Characterisation

Porphyrins **10 – 17** have been characterised by NMR, FTIR, UV-Vis and ESI-MS.

The characterisation of **9** by NMR, FTIR, UV-Vis and ESI-MS has been reported in the literature[5, 6, 7, 8] and the data for the compound synthesised here are in good agreement with the previously reported data.

3.2.1. NMR Spectroscopy

The porphyrins **10 - 17** were characterised using 1D ^{1}H and ^{13}C NMR and 2D ^{1}H - ^{1}H COSY and ^{1}H - ^{13}C HMQC and HMBC experiments.

The ^{1}H NMR spectra each contained several characteristic features. The signal with the furthest downfield shift at $\delta \sim 10$ corresponded to the amide resonance (G) (**Figure 3.1**) and was indicative of a successful coupling reaction. The resonance was sharp and shifted further downfield than had been observed for porphyrins synthesised previously in the group ($\delta \sim 8.5$[5, 6]) suggesting the presence of hydrogen bonding. The porphyrin pyrrole resonances were located at $\delta \sim 8.9$. These resonances appeared as two doublets each corresponding to two protons and one singlet corresponding to four protons. The singlet can be assigned to the four (D) protons that experience *pseudo*-D_{4h} symmetry. The doublets (D', D'') are shifted downfield with the biggest shift for D'' due to its proximity to the functionalised phenyl group which has a stronger ring current. The resolution varied depending on the compound and solvent and therefore they have been treated as one multiplet in most cases to ease assignment. The porphyrin phenyl *ortho*-protons (C, E) were assigned to the two doublets with integration 2 (E) and 6 (C) at $\delta \sim 8.2$ - 8.3. The *meta*-protons closest to the amide (F) were assigned to the doublet due to two protons, slightly upfield at $\delta \sim 8.1$. The *meta*- and *para*-protons (A, B) appear as a multiplet further upfield at $\delta \sim 7.7 - 7.9$ since they are further away from the field generated by the porphyrin ring current than C. The shifts of the remaining aromatic protons on the linker and substrate phenyl groups depend on their environment; most upfield for amine, most downfield for nitro. The methoxy protons located at $\delta \sim 4.0 - 4.3$ are similarly affected by nature of the neighbouring groups. The spectra for the free base porphyrins each contain a resonance between $\delta \sim -2.5$ and -2.3 which are absent for the zinc porphyrins. These are assigned to the inner N-H protons shifted upfield by the porphyrin ring current.

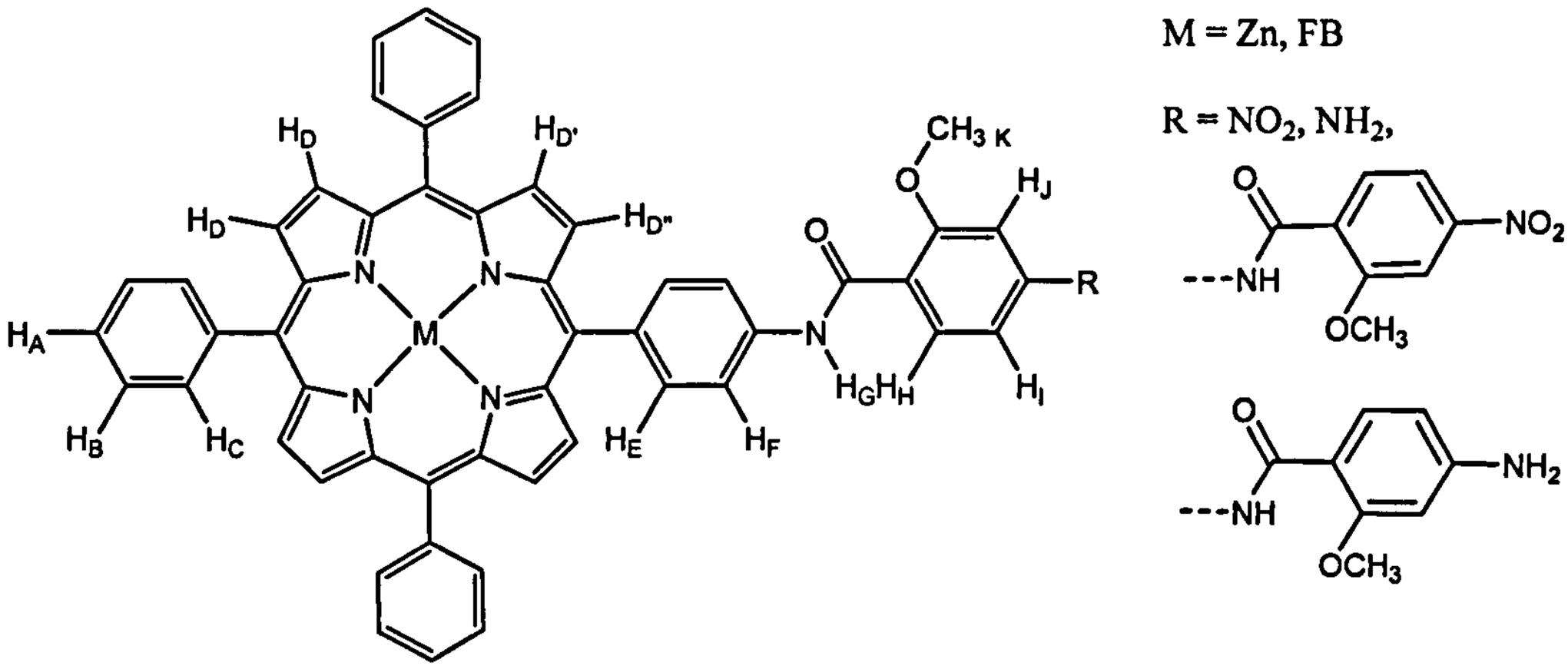

Figure 3.1 Labelling of significant porphyrin protons (FB = free-base).

The ^{13}C NMR spectra were similar for each compound. The type of carbon was determined by DEPT 45, 90 and 135 experiments. A broad signal at δ 130 - 135 was observed in the spectra for the free base porphyrins, which was assigned to the β-pyrrolic carbons. Sharp resonances in the same region were observed for the zinc porphyrins.

2D experiments were used to aid assignment of the ^{1}H and ^{13}C NMR spectra. The ^{1}H-^{1}H COSY spectra contained cross-peaks between neighboring protons three bonds apart. Weak 'W coupling' was observed between protons (I and J) four bonds apart. CH and CH_3 carbons were assigned from the ^{1}H – ^{13}C HMQC spectra which contained cross peaks between carbons and protons one bond apart. Quaternary carbons were assigned from the ^{1}H – ^{13}C HMBC spectra which contained cross peaks for carbons and protons two to four bonds apart. The spectra for the zinc porphyrins contained cross peaks between the β-pyrrolic protons and carbons whereas the spectra for the free base porphyrins did not. Since the zinc porphyrins were more soluble and therefore produced better spectra, apart from **10**, the zinc porphyrins will be discussed in more detail.

3.2.1.1. Free Base 5-[4-[(2-Methoxy-4-nitro-phenylcarbonyl)-amino] phenyl]-10,15,20-triphenyl Porphyrin, 10.

As for the compounds in Chapter 2, the ^{1}H NMR spectrum of **10** in $CDCl_3$ showed a singlet at δ 9.99 assigned to the amide proton (G), a singlet at δ 4.31 due to the methoxy protons (K) and a singlet at δ –2.74 assigned to the inner N–H protons (L) of the porphyrin (**Figure 3.2**).

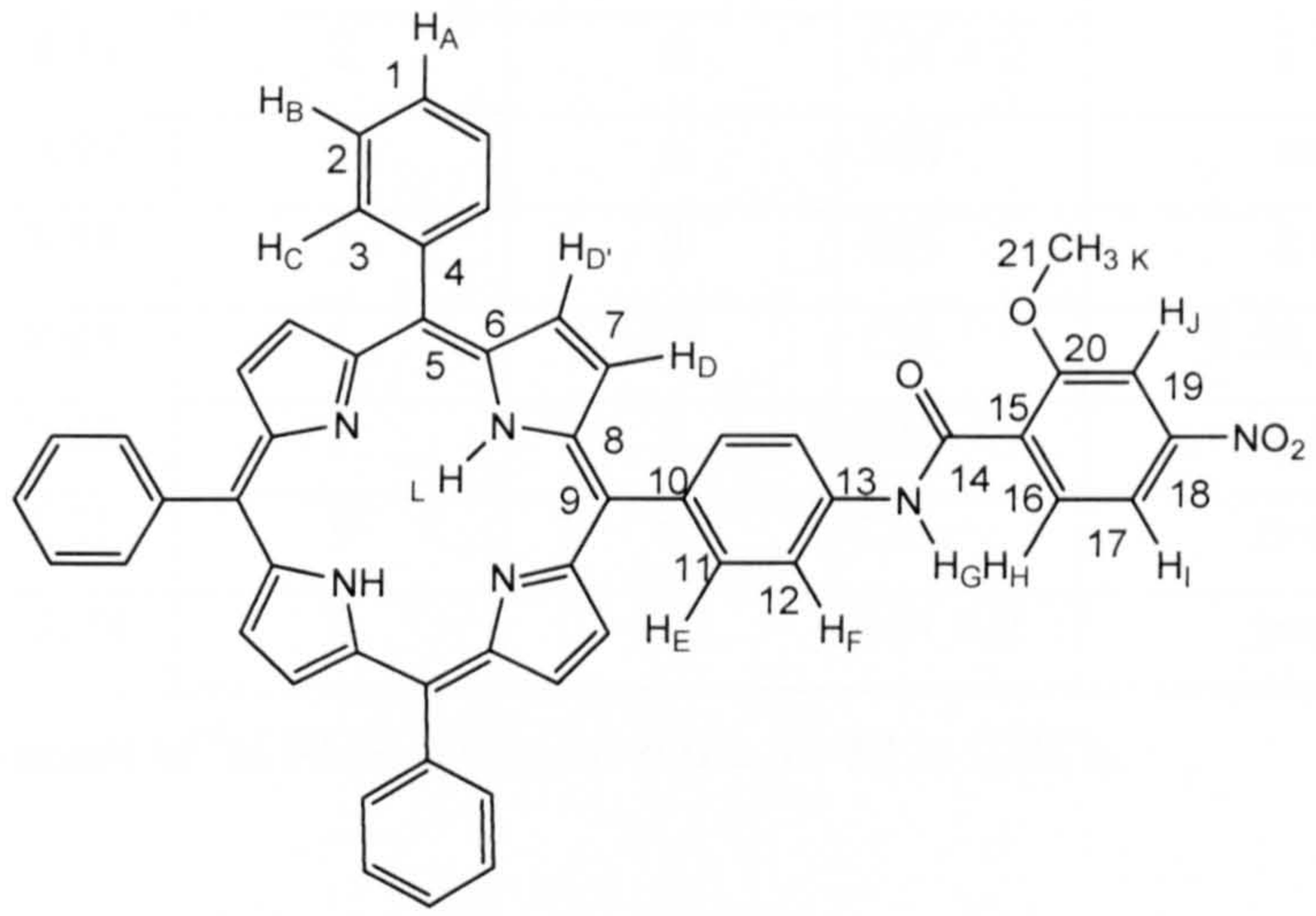

Figure 3.2 10 with atom labels: letters assigned to protons and numbers assigned to carbons.

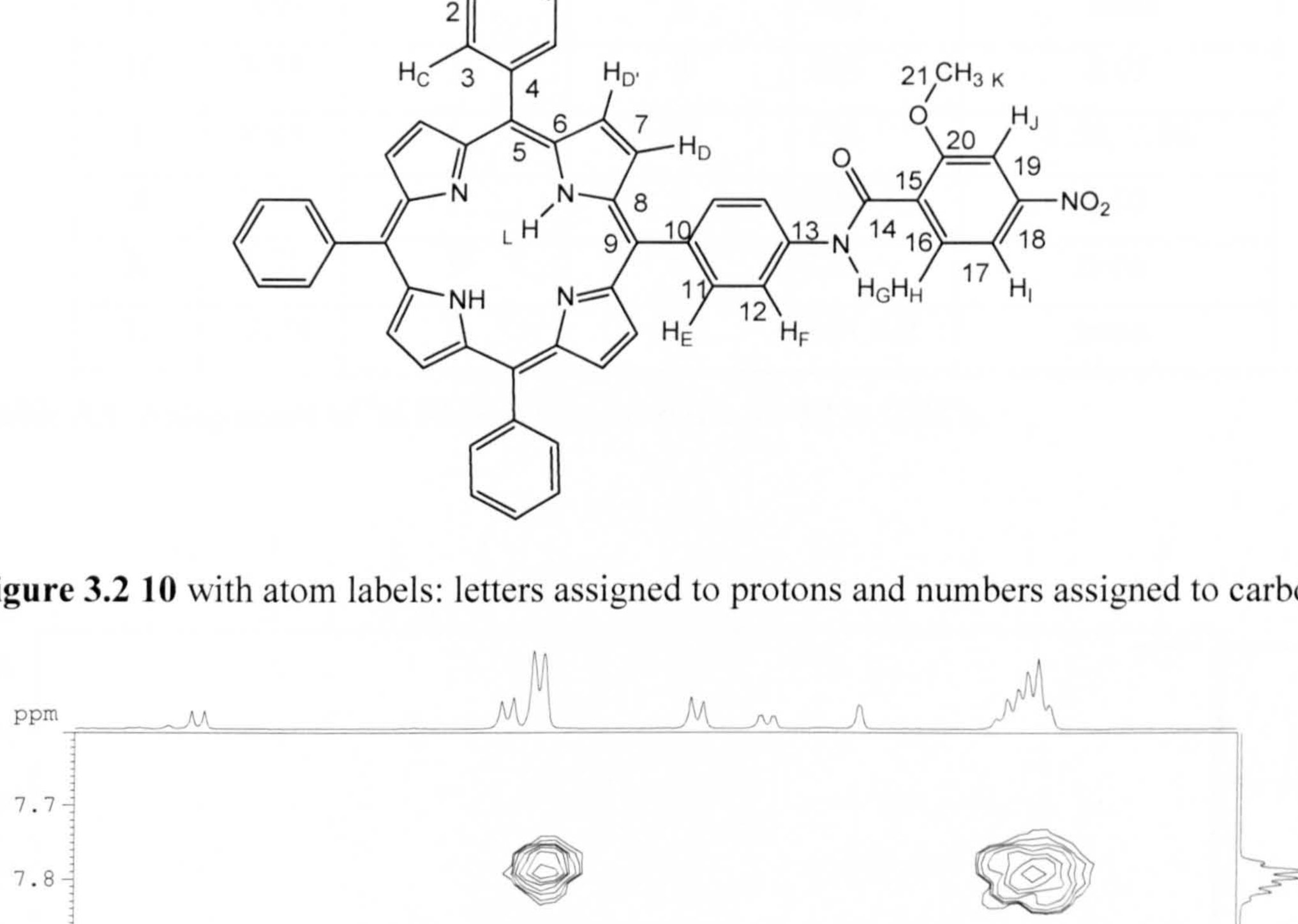

Figure 3.3 ^{1}H–^{1}H COSY spectrum of **10** in $CDCl_3$.

Label	δ	Integration	Multiplicity	Type	COSY to ^{1}H at δ
A	7.78	3	M	CH × 3	8.26
B	7.79	6	D	CH × 6	8.26
C	8.26	6	D	CH × 6	7.78, 7.79
D	8.89	8	M	CH × 8	none
E	8.29	2	D	CH × 2	8.11
F	8.11	2	d	CH × 2	8.29
G	9.99	1	s	NH	none
H	8.58	1	d	CH	8.05
I	8.05	1	dd	CH	8.58, 7.96
J	7.96	1	s	CH	8.05
K	4.31	3	s	CH_3	none
L	–2.74	2	s	NH × 2	none

Table 3.1 Assignment of ^{1}H NMR chemical shifts for **10** in $CDCl_3$.

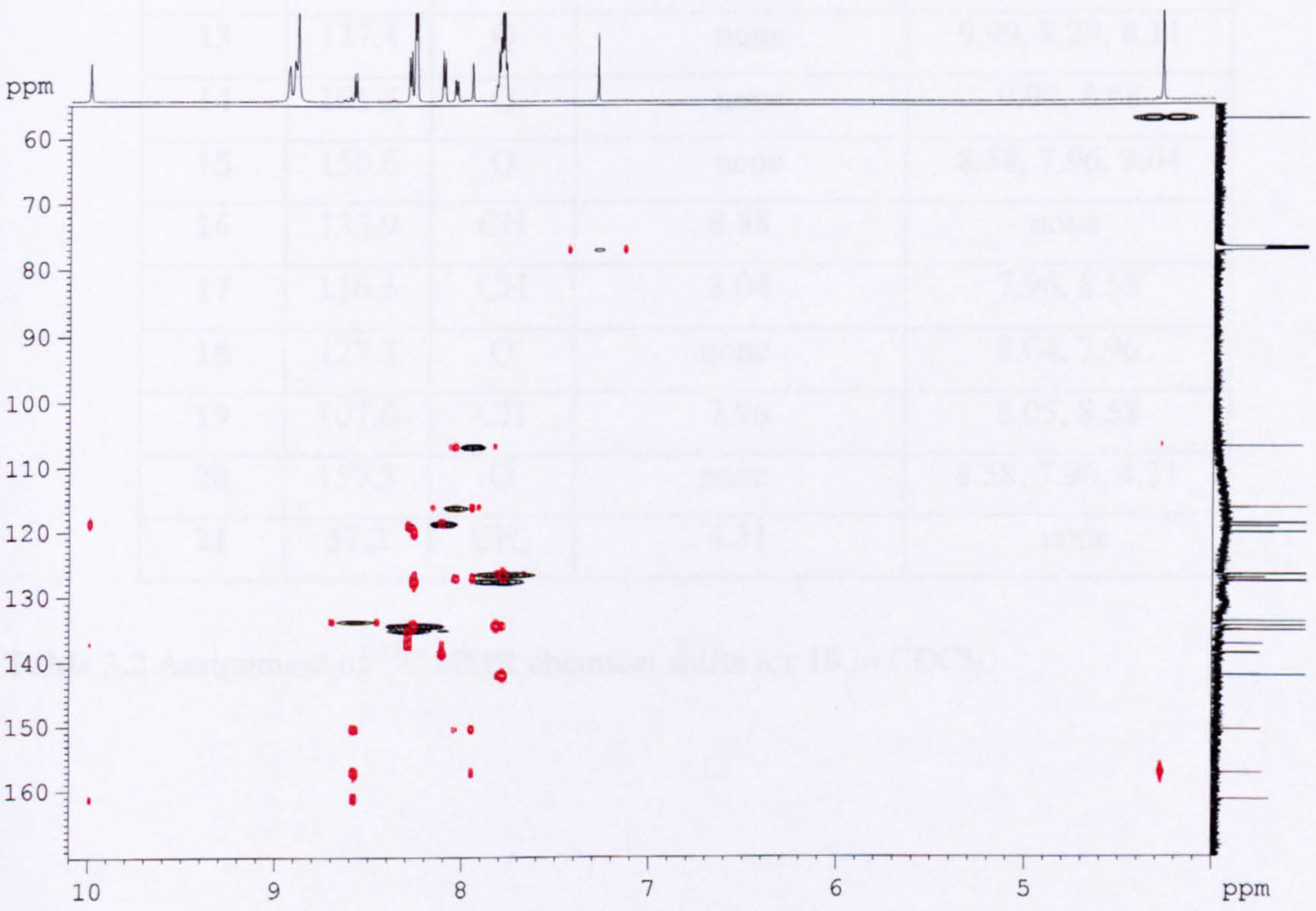

Figure 3.4 ^{1}H-^{13}C HMQC (black) and HMBC (red) spectra of **10** in $CDCl_3$. Original in colour.

The crowded aromatic region was assigned by comparison with the spectra of the starting compounds and from the $^{1}H - {}^{1}H$ correlation spectra (**Figure 3.3, Table 3.1**). The carbon assignments are listed in **Table 3.2.**

Label	δ	Type	HMQC to ^{1}H at δ	HMBC to ^{1}H at δ
1	126.7	CH	7.78	7.79, 8.26
2	127.8	CH	7.79	8.26
3	134.6	CH	8.26	7.78, 7.79
4	120.2	Q	none	8.26
5	142.2	Q	none	7.79
6	142.1	Q	none	7.78
8	120.3	Q	none	8.89
9	138.8	Q	none	8.11
10	119.3	Q	none	8.29
11	135.3	CH	8.29	8.11
12	118.9	CH	8.11	9.99, 8.29
13	137.4	Q	none	9.99, 8.29, 8.11
14	161.5	Q	none	9.99, 8.58
15	150.6	Q	none	8.58, 7.96, 8.04
16	133.9	CH	8.58	none
17	116.5	CH	8.04	7.96, 8.58
18	127.3	Q	none	8.04, 7.96
19	107.0	CH	7.96	8.05, 8.58
20	157.3	Q	none	8.58, 7.96, 4.31
21	57.2	CH_3	4.31	none

Table 3.2 Assignment of ^{13}C NMR chemical shifts for **10** in $CDCl_3$.

3.2.1.2. Zinc 5-[4-[(2-Methoxy-4-nitro-phenylcarbonyl)-amino] phenyl]-10,15,20-triphenyl Porphyrin, 11.

The ^{1}H NMR spectrum of **11** in d_8-THF contained a peak at δ 10.11 for the N–H proton (G) and a peak at δ 4.24 for the methoxy protons. The phenyl protons of the coupled unit were assigned at δ 8.26, 8.01 and 7.98. In $CDCl_3$, which is non-coordinating, the N–H proton (G) was shifted upfield with respect to that measured in the coordinating solvent, d_8-THF, whereas the remaining protons remained relatively unchanged. The ^{1}H and ^{13}C assignments are listed in **Table 3.3** and **Table 3.4**; the numbering system is shown in **Figure 3.5.**

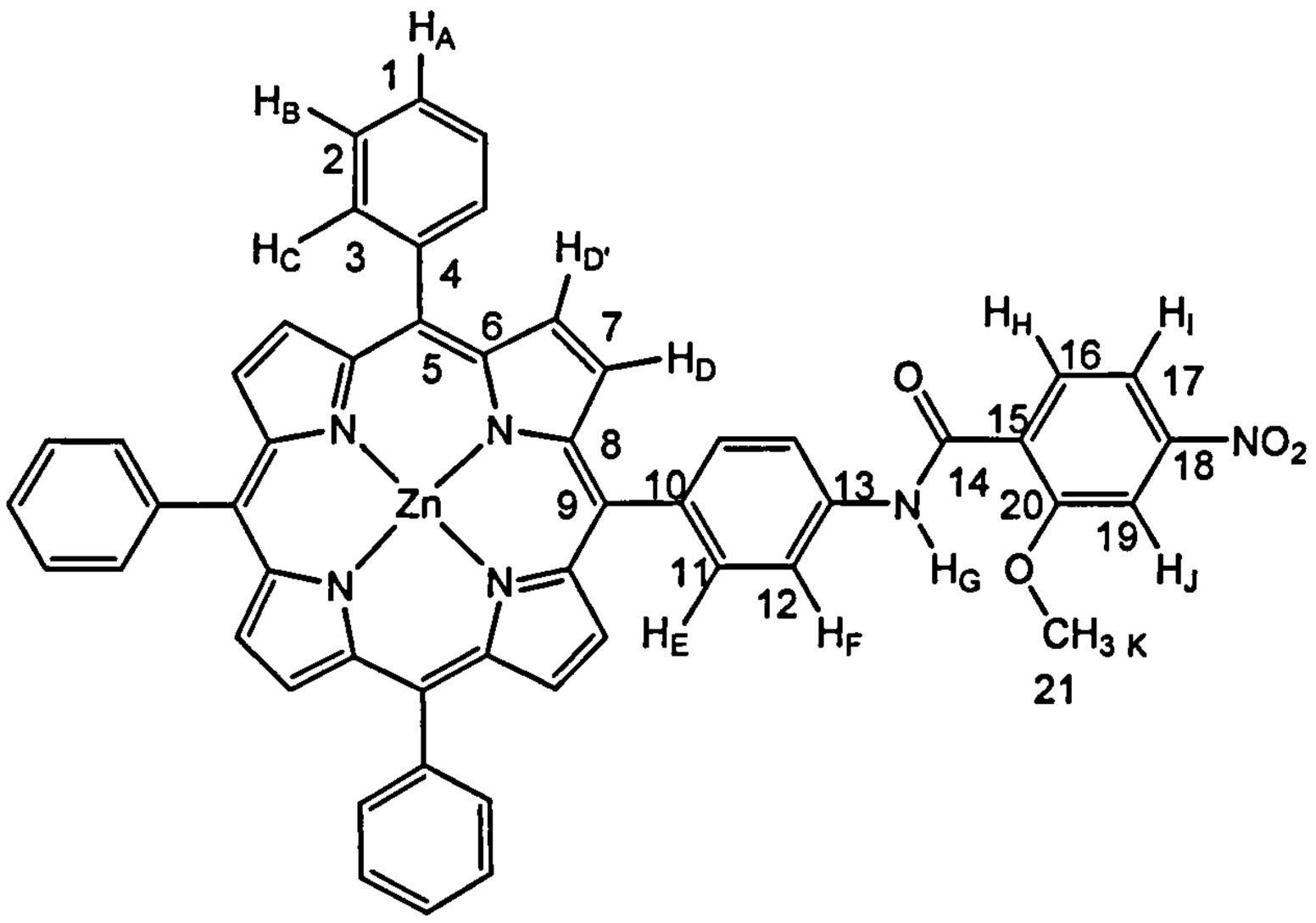

Figure 3.5 11 with atom labels: letters assigned to protons and numbers assigned to carbons.

Label	δ	Integration	Multiplicity	Type	COSY to ^{1}H at δ
A, B	7.75	9	m	CH × 9	8.25
C, E	8.25	8	m	CH × 8	7.75, 8.01
D	8.96	8	m	CH × 8	none
F, I	8.01	3	m	CH × 3	8.25, 8.46
G	9.93	1	s	NH	none
H	8.46	1	d	CH	8.01
J	7.95	1	s	CH	8.01
K	4.27	3	s	CH_3	none

Table 3.3 Assignment of ^{1}H NMR chemical shifts for **11** in $CDCl_3$.

Label	δ	Type	HMQC to ^{1}H at δ	HMBC to ^{1}H at δ
1	126.3	CH	7.7	none
2	127.1	CH	7.7	8.17
3	134.6	CH	8.17	7.7
4	143.7	Q	none	7.7
5	150.1	Q	none	7.79, 8.92, 8.84
6	120.6	Q	none	8.92, 8.84, 8.17
7	131.8	CH	8.92	none
7	131.6	CH	8.83	none
8	120.4	Q	none	none
9	150.3	Q	none	none
10	138.1	Q	none	8.14
11	135.2	CH	8.14	none
12	118.3	CH	8.00	8.14, 8.00
13	138.9	Q	none	8.00
14	163.9	Q	none	8.19, 6.25
15	151.6	Q	none	8.19, 6.25
16	134.5	CH	8.19	none
17	108.1	CH	6.41	6.25
18	112.1	Q	none	6.41, 6.25, 4.07
19	97.4	CH	6.25	6.41, 4.07
20	159.2	Q	none	8.19, 6.25, 6.41, 4.07
21	56.1	CH_3	4.07	none

Table 3.4 Assignment of ^{13}C NMR chemical shifts for **11** in $CDCl_3$.

3.2.1.3. Zinc 5-[4-[(2-Methoxy-4-amino-phenylcarbonyl)-amino] phenyl] - 10,15,20-triphenyl Porphyrin, 13.

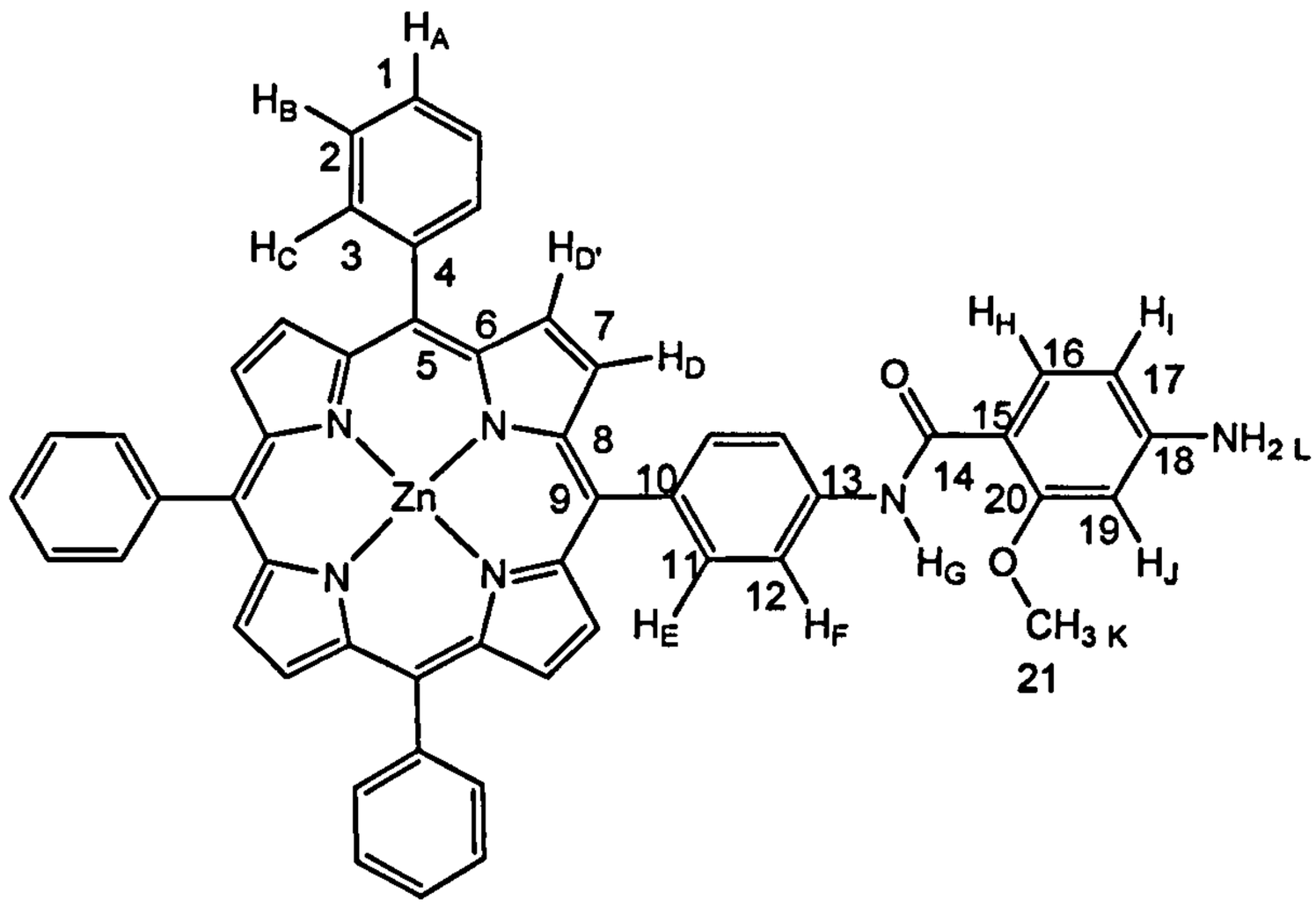

Figure 3.6 13 with atom labels: letters assigned to protons and numbers assigned to carbons.

Label	δ	Integration	Multiplicity	Type	COSY to ^{1}H at δ
A, B	7.70	9	m	CH × 9	8.17
C	8.17	6	d	CH × 6	7.70
D **D'** **D''**	8.92 8.84 8.83	2 2 4	d d s	CH × 8	8.84 8.92
E	8.14	2	d	CH × 2	8.00
F	8.00	2	d	CH × 2	8.14
G	10.01	1	s	NH	none
H	8.19	1	d	CH	6.41
I	6.41	1	dd	CH	6.25, 8.19
J	6.25	1	s	CH	6.41, 4.07
K	4.04	3	s	CH_3	none
L	4.07	2	s	NH_2	6.25

Table 3.5 Assignment of ^{1}H NMR chemical shifts for **13** in $CDCl_3$, d_5-pyridine.

The ^{1}H NMR spectrum of **13** contained a peak at δ 10.01 for the N–H proton and a peak at δ 4.04 for the methoxy protons. The phenyl protons of the coupled unit were assigned at δ 8.19, 6.41 and 6.25 (**Table 3.5**). The carbon assignments are listed in **Table 3.6** and the numbering system is shown in **Figure 3.6.**

Label	δ	Type	HMQC to ^{1}H at δ	HMBC to ^{1}H at δ
1	126.3	CH	7.7	none
2	127.1	CH	7.7	8.17
3	134.6	CH	8.17	7.7
4	143.7	Q	none	7.7
5	150.1	Q	none	7.79, 8.92, 8.84
6	120.6	Q	none	8.92, 8.84, 8.17
7	131.8	CH	8.92	none
7	131.6	CH	8.83	none
8	120.4	Q	none	none
9	150.3	Q	none	none
10	138.1	Q	none	8.14
11	135.2	CH	8.14	none
12	118.3	CH	8.00	8.14, 8.00
13	138.9	Q	none	8.00
14	163.9	Q	none	8.19, 6.25
15	151.6	Q	none	8.19, 6.25
16	134.5	CH	8.19	none
17	108.1	CH	6.41	6.25
18	112.1	Q	none	6.41, 6.25, 4.07
19	97.4	CH	6.25	6.41, 4.07
20	159.2	Q	none	8.19, 6.25, 6.41, 4.07
21	56.1	CH_3	4.07	none

Table 3.6 Assignment of ^{13}C NMR chemical shifts for **13** in $CDCl_3$, d_5-pyridine.

3.2.1.4. Zinc 5-[4-{(2-Methoxy-4-[(2-methoxy-4-nitro-phenylcarbonyl)-amino]-phenyl carbonyl)-amino} phenyl]-10,15,20-triphenyl Porphyrin, 15.

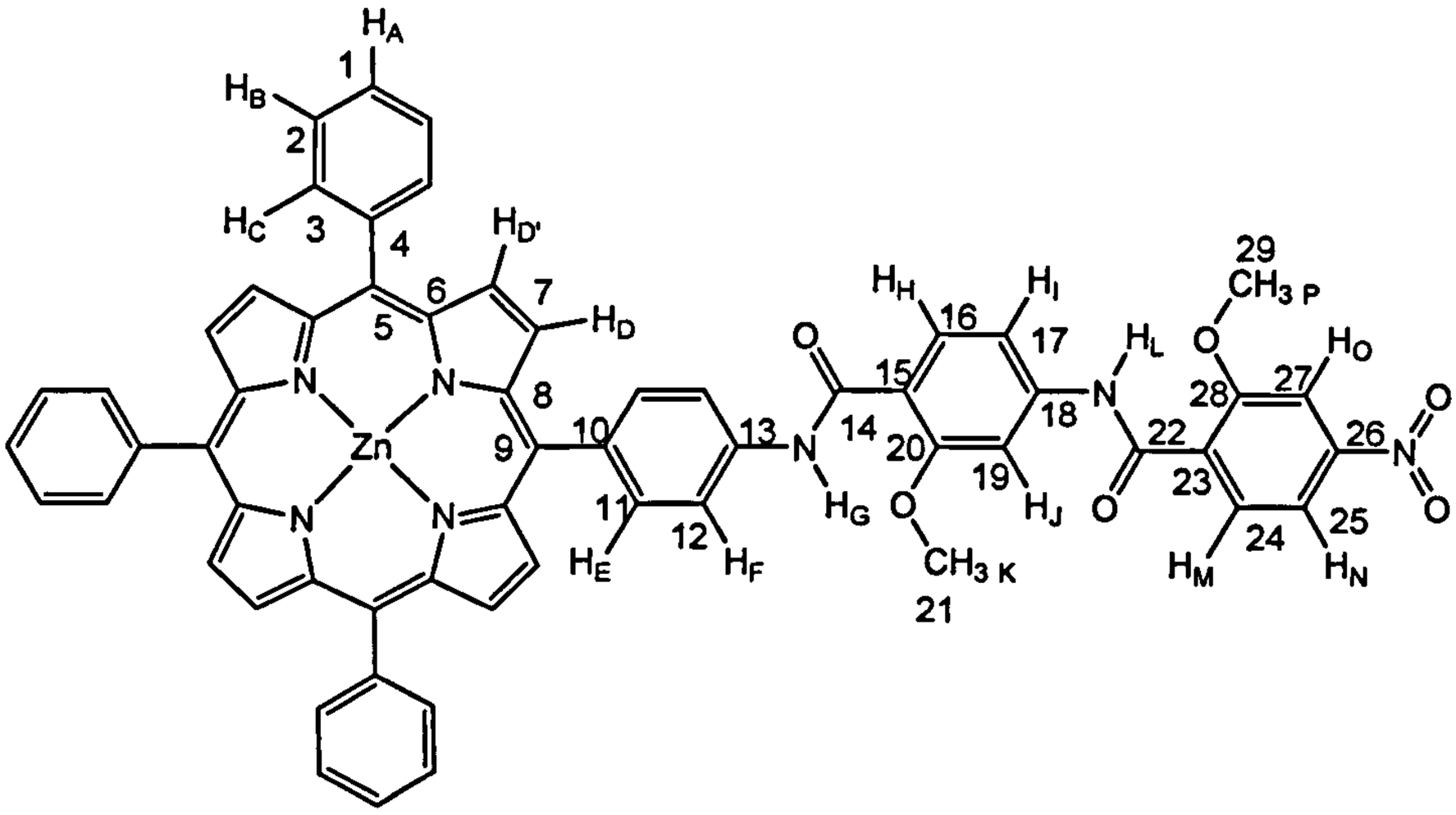

Figure 3.7 **15** with atom labels: letters assigned to protons and numbers assigned to carbons.

Label	δ	Integration	Multiplicity	Type	COSY to ^{1}H at δ
A, B	7.75	9	m	CH × 9	8.21
C, E	8.21	6	m	CH × 8	7.75, 8.04
D	8.94	8	m	CH × 8	none
F	8.04	2	d	CH × 2	8.21
G	10.14	1	s	NH	none
H	8.34	1	d	CH	6.91, 8.24
I	6.91	1	d	CH	8.34, 8.24
J	8.24	1	s	CH	8.34
K	4.24	3	s	CH_3	none
L	9.86	1	s	NH	none
M	8.42	1	d	CH	8
N	8.00	1	d	CH	8.42, 7.9
O	7.90	1	s	CH	8
P	4.21	3	s	CH_3	none

Table 3.7 Assignment of ^{1}H NMR chemical shifts for **15** in $CDCl_3$, d_5-pyridine.

The ^{1}H NMR spectrum of **15** contained peaks at δ 10.15 and 9.96 for the N–H protons and a peak at δ 4.22 and 4.14 for the methoxy protons. These signals were distinguished by their respective coupling to carbon atoms on different ring systems in the HMQC and HMBC spectra. The phenyl protons of the coupled units were assigned at δ 8.36, 8.23, 7.93, 7.83, 7.19 and 6.94 (**Table 3.7**). The carbon assignments are listed in **Table 3.8** and the numbering system is shown in **Figure 3.7**.

Label	δ	Type	HMQC to ^{1}H at δ	HMBC to ^{1}H at δ
1	126.5	CH	7.75	7.75
2	127.5	CH	7.75	8.21
3	134.5	CH	8.21	8.21,7.75
4	121.1	Q	none	8.21
5	143.0	Q	none	7.75
6	150.3	Q	none	8.94
7	132.0	CH	8.94	none
8	150.2	Q	none	8.94
9	137.9	Q	none	8.21
10	120.6	Q	none	8.21
11	135.1	Q	none	8.21
12	118.5	CH	8.04	10.14
13	138.8	Q	none	8.04
14	163.1	Q	none	8.34
15	142.3	Q	none	8.34, 8.24
16	134.4	Q	none	none
17	112.7	CH	6.91	8.24, 9.86
18	117.8	Q	none	8.24, 6.91
19	103.8	CH	8.24	9.86, 6.91
20	158.4	Q	none	8.34, 8.24, 4.24
21	56.6	CH_3	4.24	none
22	161.5	Q	none	8.42
23	150.8	Q	none	8.42, 7.9
24	131.9	Q	none	none

25	116.5	CH	8.oo	7.90
26	126.7	Q	none	8.00, 7.90
27	107.1	CH	7.90	none
28	157.3	Q	none	8.42, 7.91, 4.21
29	57.3	CH_3	4.21	none

Table 3.8 Assignment of ^{13}C NMR chemical shifts for **15** in $CDCl_3$, d_5-pyridine.

3.2.1.5. Zinc 5-[4-{(2-Methoxy-4-[(2-methoxy-4-amino-phenylcarbonyl)-amino]-phenylcarbonyl)-amino} phenyl]-10,15,20-triphenyl Porphyrin, 17.

The ^1H NMR spectrum of **17** contained peaks at δ 10.08 and 9.74 for the N–H protons and a peak at δ 4.17 and 3.65 for the methoxy protons. The phenyl protons of the coupled units were assigned at δ 8.24, 8.13, 6.85, 7.51, 4.79 and 4.54, the latter three shifted upfield due to the amine function. ^1H NMR spectra for both **15** and **17** did not contain peaks at negative δ, demonstrating that the inner protons have been displaced by zinc. The ^1H and ^{13}C assignments are listed in **Table 3.9** and **Table 3.10**; the numbering system is shown in **Figure 3.8.**

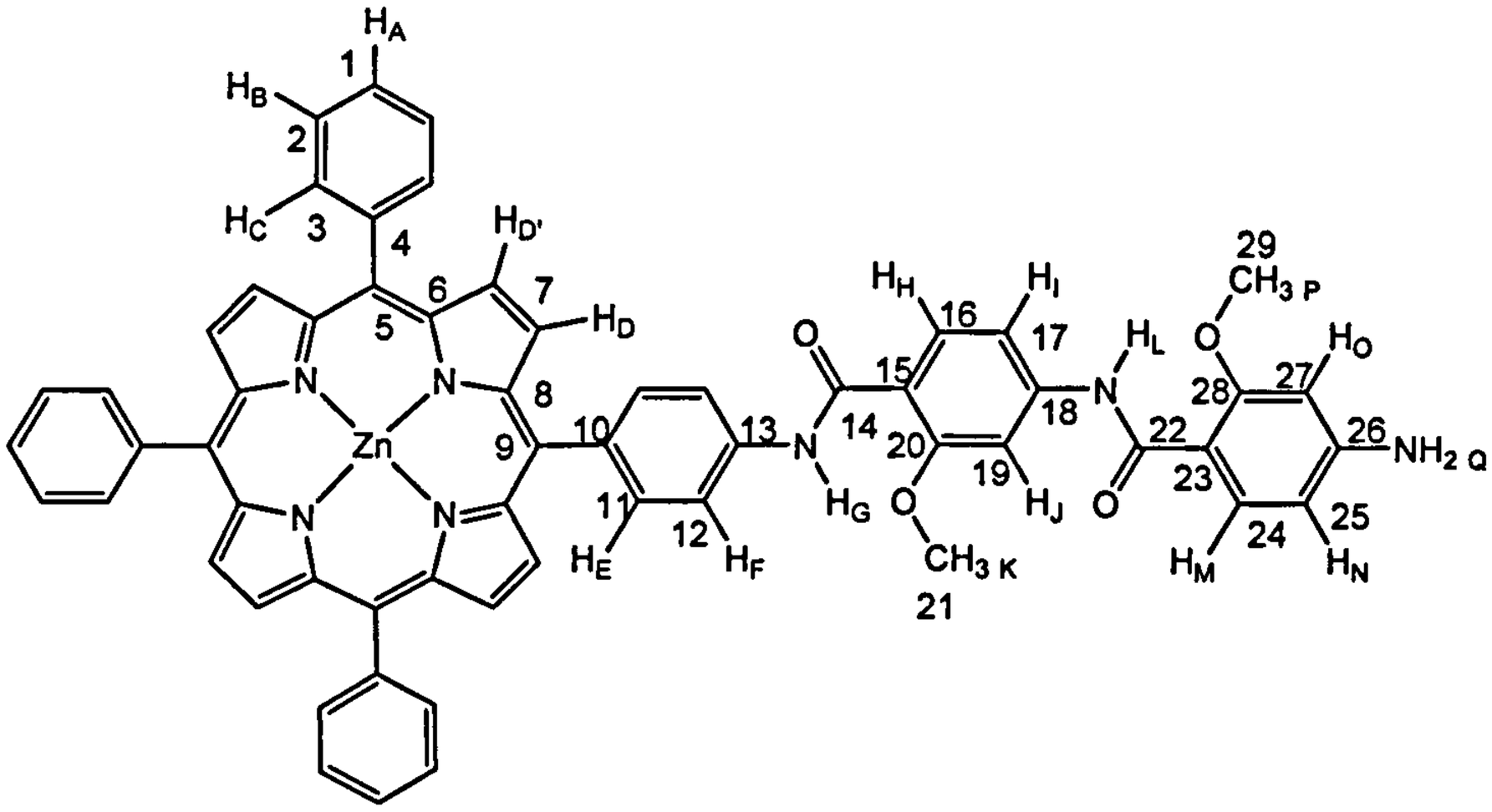

Figure 3.8 **17** with atom labels: letters assigned to protons and numbers assigned to carbons.

Label	δ	Integration	Multiplicity	Type	COSY to ^{1}H at δ
A, B	7.75	9	m	CH × 9	8.22
C	8.22	6	m	CH × 6	7.75
D	8.95	2	d	CH × 2	8.91
D', "	8.91	6	m	CH × 6	8.95
E	8.09	2	d	CH × 2	7.91
F	7.91	2	d	CH × 2	8.13, 8.09
G	10.08	1	s	NH	none
H	8.24	1	d	CH	6.85
I	6.85	1	dd	CH	8.24, 8.13
J	8.13	1	s	CH	7.91
K	4.17	3	s	CH_3	none
L	9.74	1	s	NH	none
M	7.51	1	d	CH	4.79
N	4.79	1	d	CH	7.51
O	4.54	1	s	CH	none
P	3.65	3	s	CH_3	none

Table 3.9 Assignment of ^{1}H NMR chemical shifts for **17** in $CDCl_3$, d_5-pyridine.

Label	δ	Type	HMQC to ^{1}H at δ	HMBC to ^{1}H at δ
1	126.6	CH	7.75	none
2	127.4	CH	7.75	8.22
3	134.6	CH	8.22	7.75, 8.22
4	126.5	Q	none	7.75
5	143.1	Q	none	7.75
6	150.0	Q	none	8.91
7	131.9	CH	8.91	8.95
8	120.9	Q	none	none
9	137.8	Q	none	8.09
10	120.8	Q	none	8.09, 8.22
11	135.4	CH	8.09	8.13
12	118.6	CH	7.91	10.08, 8.09
13	138.5	Q	none	7.91
14	163.6	Q	none	none
15	143.6	Q	none	8.13
16	132.9	CH	8.24	none
17	112.4	CH	6.85	9.74, 8.13
18	116.4	Q	none	6.85, 8.13
19	103.4	CH	8.13	6.85, 9.74
20	158.4	Q	none	4.17
21	56.6	CH_3	4.17	none
22	163.4	Q	none	none
23	150.4	Q	none	none
24	132.1	CH	8.95	8.91
25	97.2	CH	4.79	none
26	127.4	Q	none	none
27	108.0	Q	none	none
28	157.9	Q	none	3.65
29	55.8	CH_3	3.65	none

Table 3.10 Assignment of ^{13}C NMR chemical shifts for **17** in $CDCl_3$, d_5-pyridine.

3.2.2. Infrared Spectroscopy

The solid state infrared spectra of compounds **10-17** showed the same characteristic absorption bands. Broad bands at ~ 3300-3400 cm^{-1} were typical of an N-H stretch. The sharper N-H deformations were located at ~ 1590-1650 cm^{-1}. Characteristically strong bands for the carbonyl stretches were observed at ~ 1675-1650 cm^{-1}. Sharp bands at ~ 2925 and 3025 cm^{-1} correspond to an asymmetric and symmetric stretch of the methoxy C-H bonds. These were matched by the corresponding asymmetric and symmetric deformations at ~ 1470 and 1400 cm^{-1}. Compounds **10, 11, 14** and **15** contained peaks at ~ 1530 and 1340 cm^{-1} typical of the asymmetric and symmetric stretching frequencies of a nitro group. The spectra for each were unsurprisingly crowded in the region 1200-1000 cm^{-1} were the C-N, C-O and C-C vibrations would be located[13]. The significant peaks in the infrared spectra of compounds **10 – 17** are summarised in **Table 3.11.**

Compound	10	11	12	13	14	15	16	17
C=O stretch	1677	1675	1655	1629	1676 1624	1675 1650	1662	1665
N=O stretch	1529 1347	1526 1340			1527 1346	1525 1341		
N-H stretch	3448	3432	3437 3341	3434 3379	3422 3328	3443 3364	3446 3357	3430 3361
N-H bend	1591	1594	1591 1519	1594 1522	1584	1588	1584 1517	1585 1519

Table 3.11 Summary of infrared absorption frequencies in cm^{-1} for compounds **10-11.**

3.2.3. Electrospray Mass Spectrometry

The majority of compounds followed the typical ionisation pathway for ESI-MS and the $M + H^+$ adduct was observed in the positive ion spectrum while the $M - H^+$ ion was observed in the negative ion spectrum. For zinc porphyrins **11** and **17** the oxidation product M^+ was detected. For each of the zinc porphyrins the typical isotope pattern was observed.

Compound	Molecular Mass	Observed +ve ion *m/z*	Assignment	Observed –ve ion *m/z*	Assignment
10	808.9	809.5	$M + H^+$	807.4	$M - H^+$
11	870.2	870.3	M^+		
12	778.3	779.4	$M + H^+$	777.3	$M - H^+$
13	840.2	841.0	$M + H^+$	839.1	$M - H^+$
14	957.3	958.4	$M + H^+$	956.2	$M - H^+$
15	1019.2	1020.3	$M + H^+$	1018.4	$M - H^+$
16	927.4	928.4	$M + H^+$		
17	989.3	989	M^+	988	$M - H^+$

Table 3.12 Summary of molecular ion peaks *m/z* for **10 – 11.** Peaks are calculated for ^{12}C, ^{64}Zn and ^{14}N.

3.2.4. Ground State Electronic Spectroscopy

The absorption spectra of the free-base porphyrins[14,15] contain a strong Soret or B band at 420 nm, four weaker Q bands at 500-700 nm and some weaker bands at higher energy (N, L, M bands). The zinc porphyrins have similar spectra except for a 10 nm red-shift of the Soret band and a reduction to two Q bands between 550-625 nm.

For metalloporphyrins with D_{4h} symmetry (such as ZnTPP) the LCAO-MO four orbital model by Gouterman provides an explanation of the origin of the transitions[16].

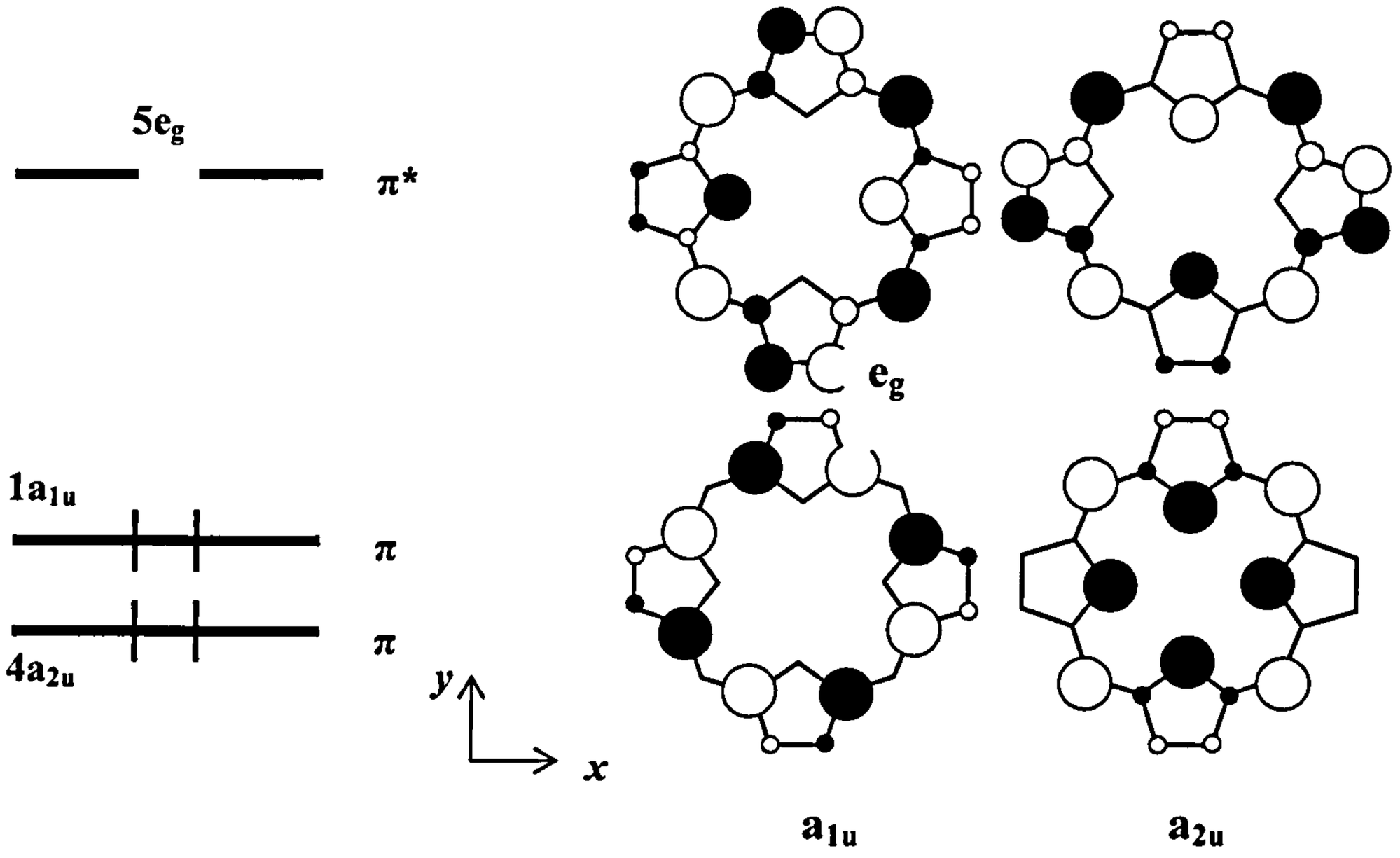

Figure 3.9 Left: The ground state electronic configuration $(a_{1u})^2(a_{2u})^2$; **Right:** The four 'Gouterman' orbitals[16,18].

The B and Q bands are strong and low in energy since they arise from allowed $\pi \rightarrow \pi^*$ transitions. The ground state electronic configuration is shown in **Figure 3.9**; the first excited state has either the $^1(a_{1u},e_g)$ or the $^1(a_{2u},e_g)$ configuration, according to MO theory[16]. The result is two degenerate pairs of states (Q_x, Q_y, B_x, B_y). The bands are split into one strong transition (B band) and one weak transition (Q band) due to a strong electronic interaction between the dipole transition moments which add to give the Soret band and nearly cancel to give the Q band. The Q band is split due to vibrations of these states (0-0, 0-1). The free-base porphyrins are not fully symmetrical and therefore the Q band splits into Q_x and Q_y, each with fundamental harmonics (0-0) and harmonics (0-1).

3.2.4.1. Free-base Porphyrins

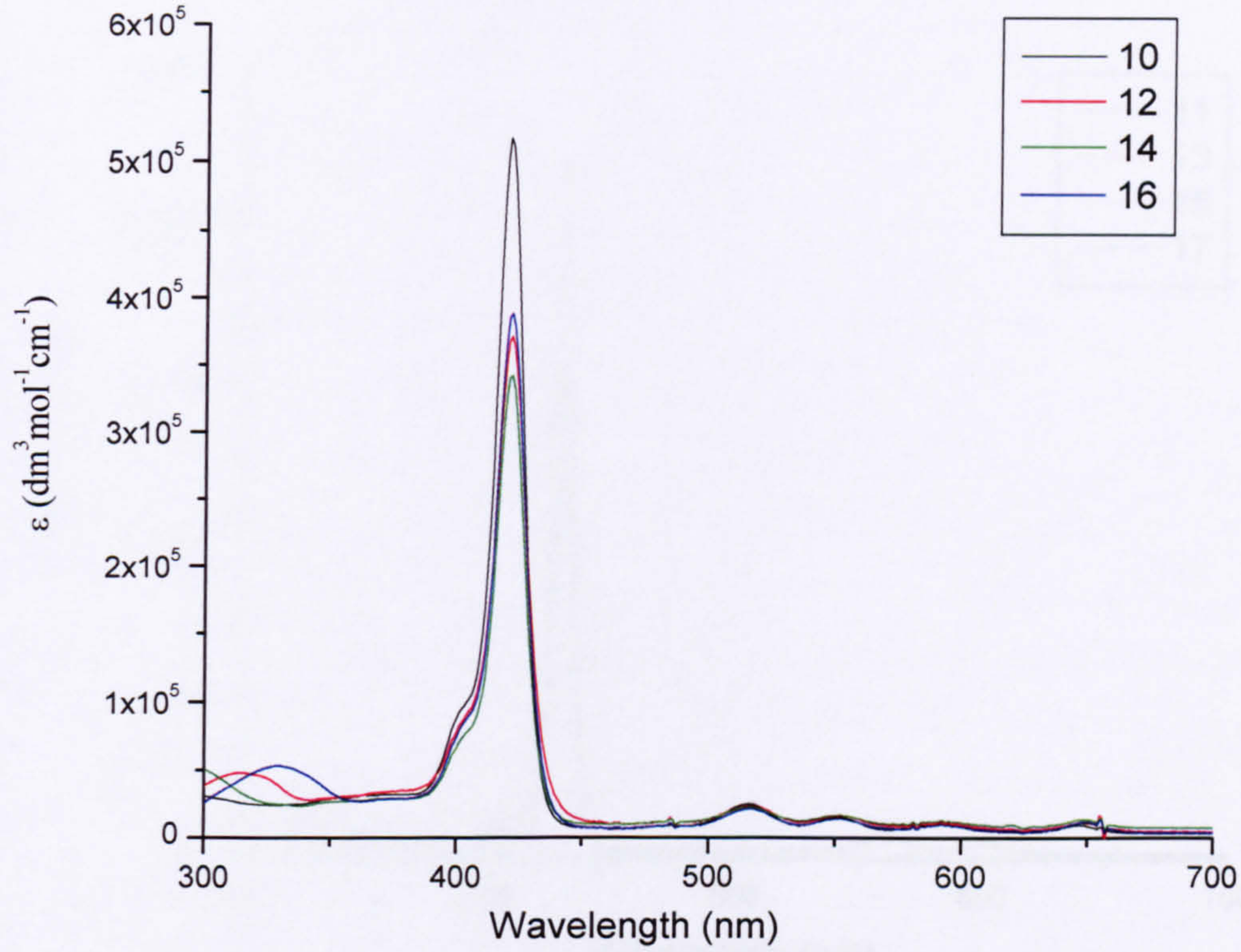

Figure 3.10 Ground state electronic absorption spectra of **10, 12, 14** and **16** in DMSO. Original in colour.

Figure 3.10 shows the absorption spectra of the free base tetraphenyl porphyrin derivatives, **10-16**.

There is little change in λ_{max} for each band but there is some variation in extinction coefficient of the Soret band. The free base porphyrins were poorly soluble in other solvents.

3.2.4.2. Zinc Porphyrins

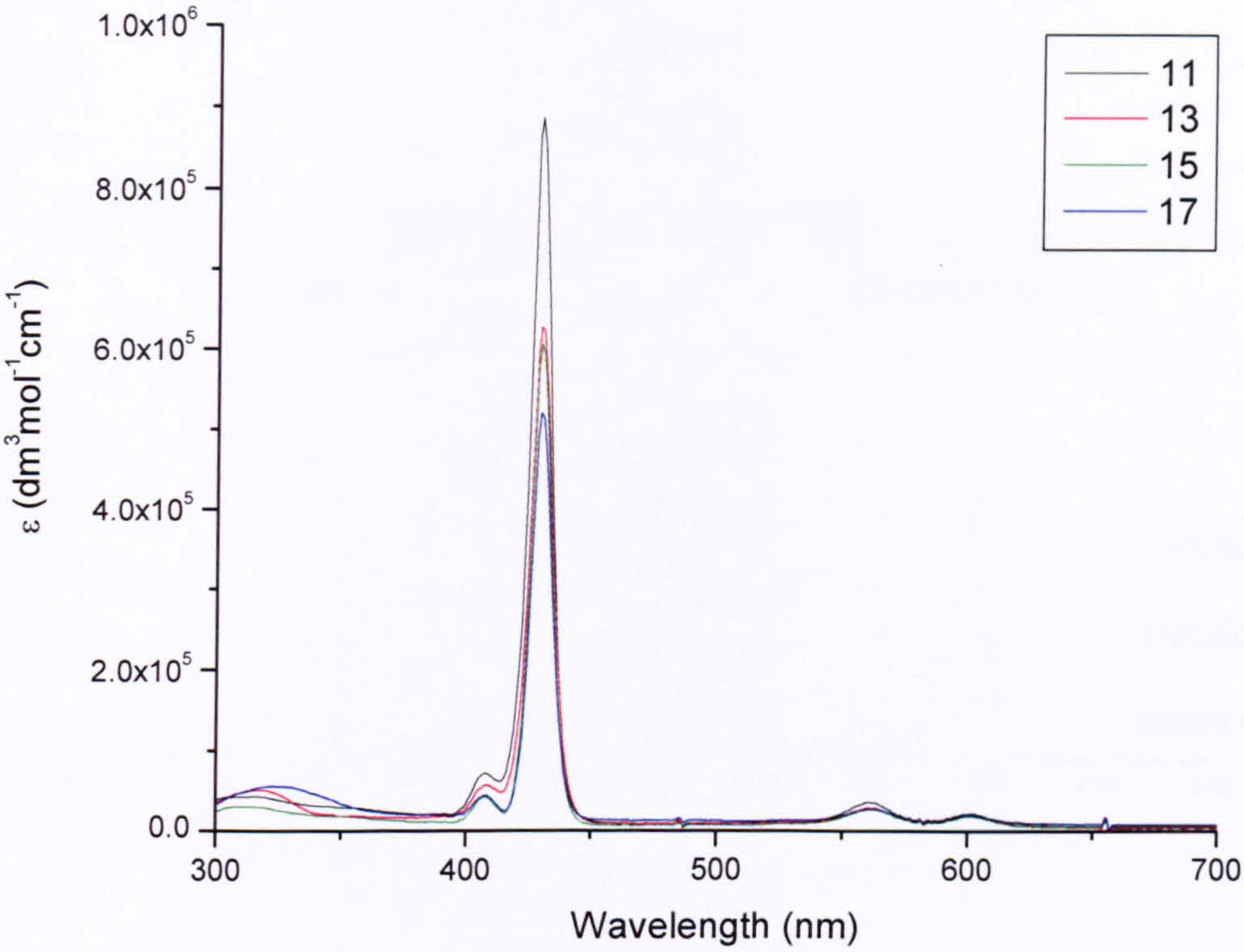

Figure 3.11 Ground state electronic absorption spectra of **11, 13, 15** and **17** in DMSO. Original in colour.

Figure 3.11 shows the absorption spectra for zinc tetraphenyl porphyrin derivatives **11-17**. Typically, a reduction of four Q-bands to two can be seen, with a slight narrowing of the Soret band. There is little difference between each spectrum apart from the slight difference in absorption coefficient as was observed for the free base porphyrins. A plot of absorption intensity against concentration gave a straight line suggesting the absence of aggregates at this micromolar concentration range.

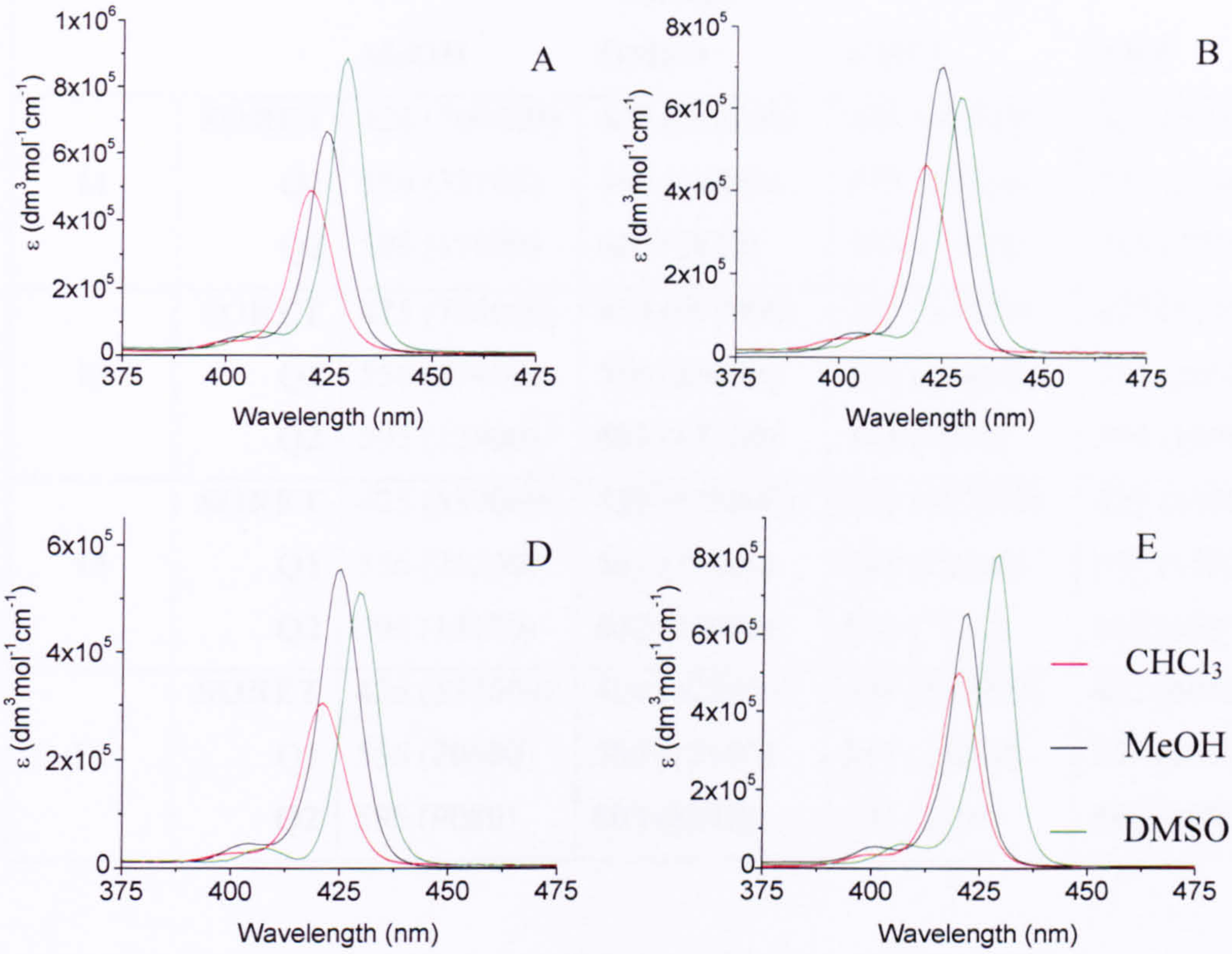

Figure 3.12 Solvent dependence of the electronic absorption spectra of **11** (A), **13** (B), **17** (D) and ZnTPP (E). Original in colour.

Figure 3.12 shows the solvent dependence of the Soret bands of the zinc tetraphenyl porphyrin derivatives compared with ZnTPP itself. Each exhibits the characteristic red shift of the absorption maxima with increasing polarity of the solvent[18]. The Q-bands behave in the same way. This is a consequence of coordination to the metal by the solvent resulting in a five coordinate species. Nappa and Valentine concluded that the red shift was a predominantly dependant on the amount of negative charge transferred from the ligand to the porphyrin ring via the metal[19]. The extinction coefficients of the longer probes (**15** and **17**) are lower but the trend follows that of the shorter ones (**11** and **13**).

		Solvent			
		MeOH	**DMSO**	**$CHCl_3$**	**THF**
11	**SORET**	424 (709000)	429 (573000)	420 (607000)	422 (649000)
	Q1	556 (32100)	560 (14800)	547 (25200)	557 (20400)
	Q2	596 (15900)	602 (5810)	584 (7400)	595 (7730)
13	**SORET**	425 (748000)	429 (597000)	421 (502000)	422 (514000)
	Q1	556 (27400)	560 (25400)	548 (24400)	557 (20000)
	Q2	595 (12900)	603 (17100)	584 (7030)	595 (10900)
15	**SORET**	425 (539000)	429 (525000)	421 (507000)	422 (40000)
	Q1	556 (26200)	561 (19400)	548 (22900)	557 (1180)
	Q2	596 (14100)	602 (10900)	584 (7170)	597 (459)
17	**SORET**	425 (537000)	429 (477000)	421 (343000)	422 (495000)
	Q1	556 (20600)	560 (12100)	547 (16200)	557 (19700)
	Q2	595 (9080)	603 (8140)	583 (2700)	596 (10400)

Table 3.13 Summary of porphyrin Q and Soret absorption maxima in nm (ε in $dm^3mol^{-1}cm^{-1}$) for zinc porphyrins **11 - 17**

3.2.5. Steady State Fluorimetry

Since steady state fluorimetry will be used to probe binding of the porphyrin to the XO active site, it is necessary to first fully characterise the spectroscopic properties of the porphyrin compounds. Spectra shown in the same graph were obtained from solutions optically matched at the excitation wavelength.

3.2.5.1. Free Base Porphyrins

Figure 3.13 shows the emission spectra for the free base porphyrins **10 – 16**. There is little difference between each. The relative quantum yields for the longer probes, **14** and **16**, were slightly larger than for the shorter ones, **10** and **12**. There is a very small blue shift associated with the nitro compounds, **10** and **14**, compared to the amines, **12** and **16**.

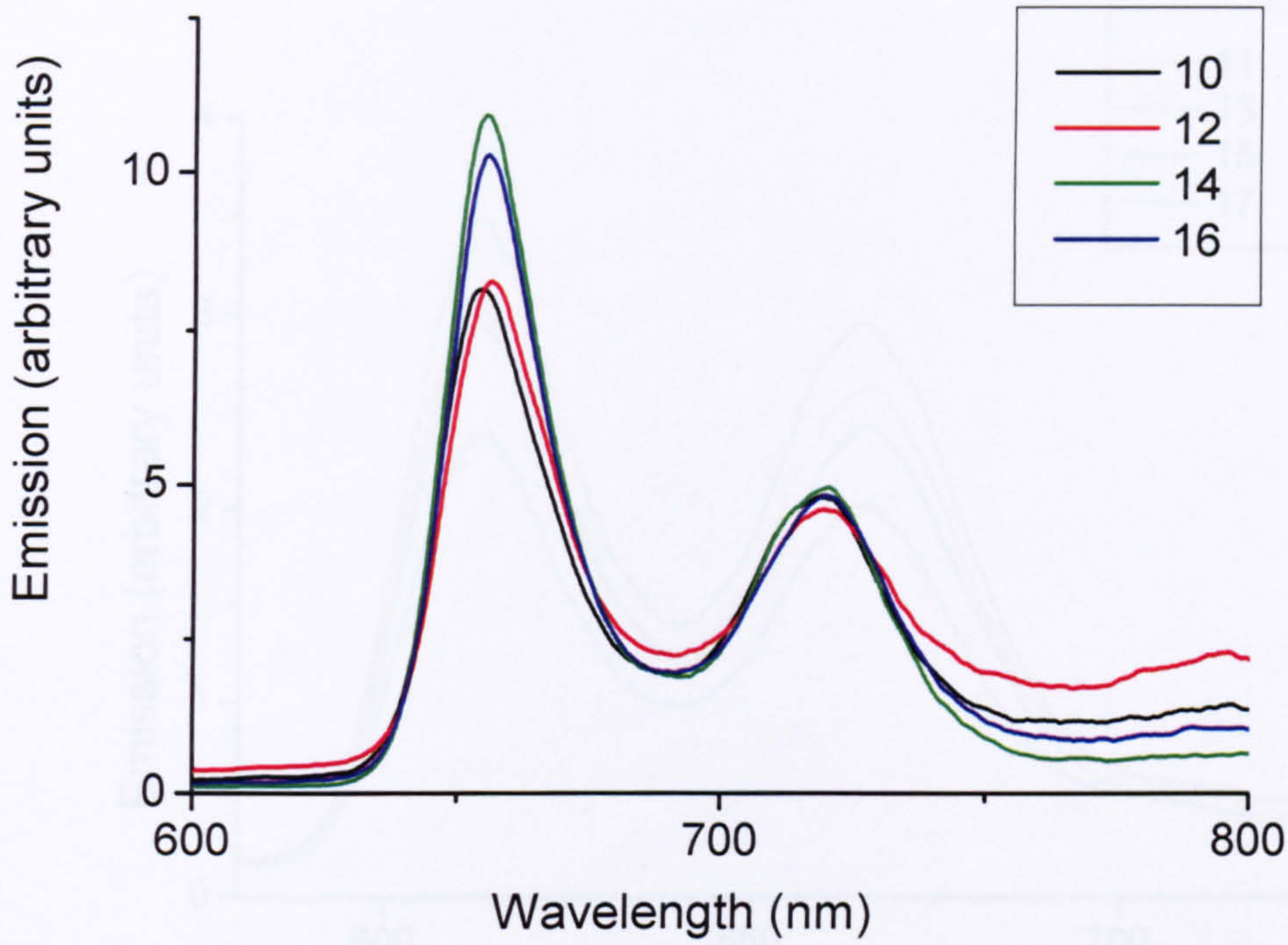

Figure 3.13 Emission spectra for free base porphyrins **10** – **16** in DMSO, λ_{ex} = 420 nm. Original in colour.

3.2.5.2. Zinc Porphyrins

Zinc porphyrins emit strongly from the first singlet-excited state. Porphyrins can be fluorescent, phosphorescent, luminescent or radiationless. Typically zinc porphyrins decay by fluorescence ($\varphi_{fl} \sim 0 - 2 \times 10^{-3}$, decay rate $k_{fl} \sim 6.0$ ns) from the lowest excited state (^1Q (π-π^*)) [14].

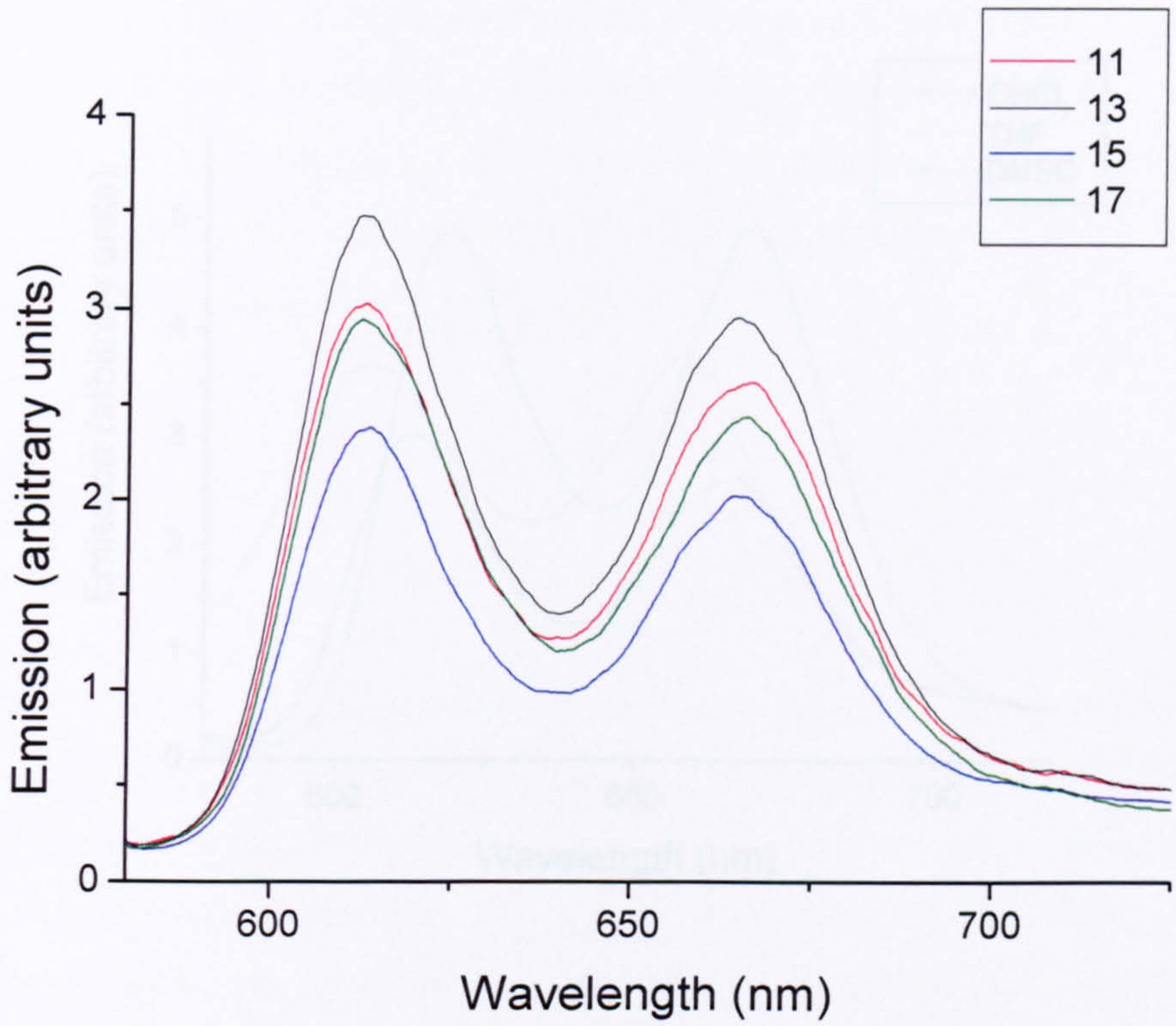

Figure 3.14 Emission spectra of zinc porphyrins **11** – **17** in DMSO. Original in colour.

Each of the zinc porphyrins displayed similar emission spectra (**Figure 3.14**). As for the free base porphyrins, the spectra for the nitro porphyrins (**11** and **15**) had lower emission intensity than the amino derivatives (**13** and **17**) and the spectra for the longer probes (**15** and **17**) were lower in intensity than those for the shorter ones (**11** and **13**).

A

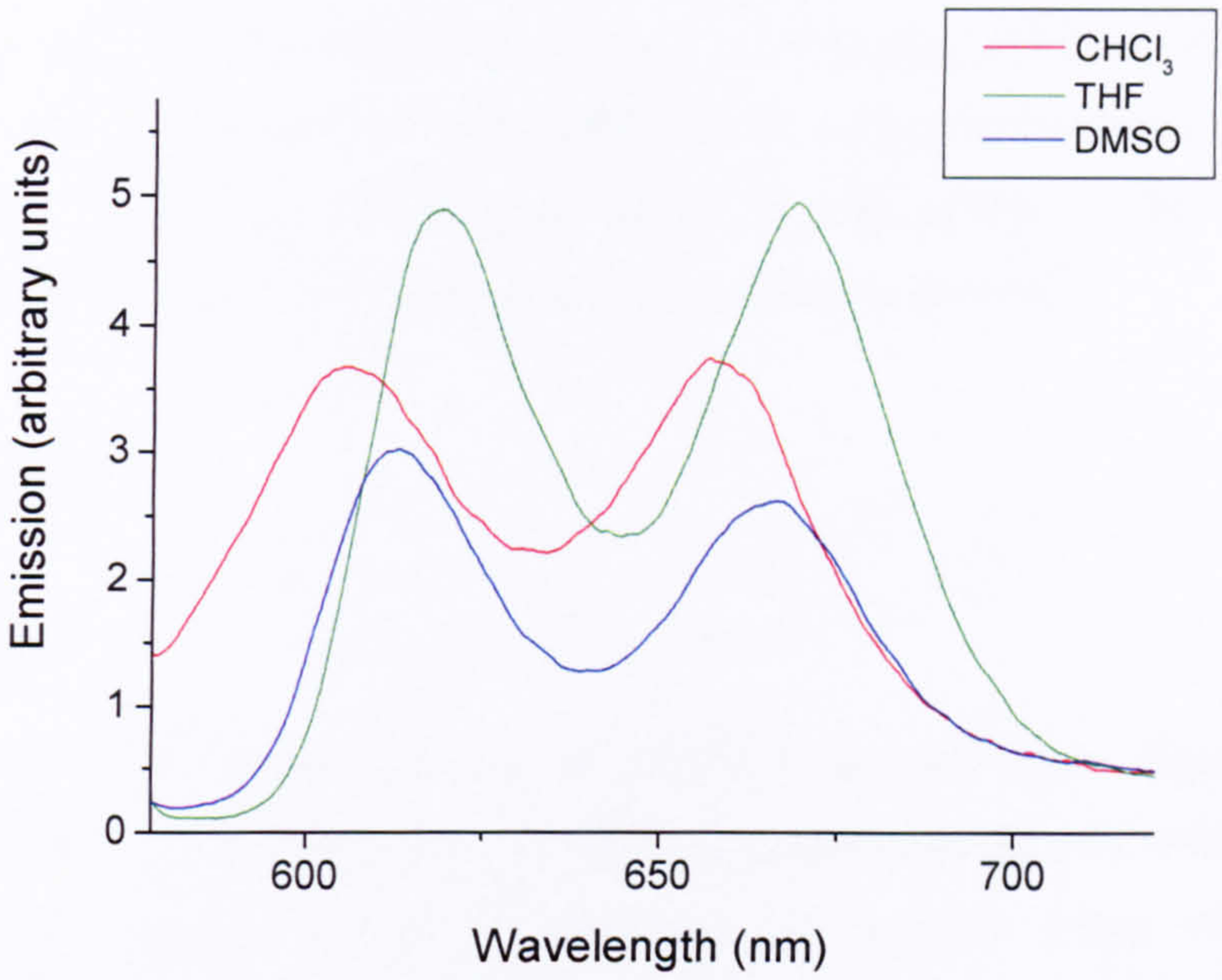

B

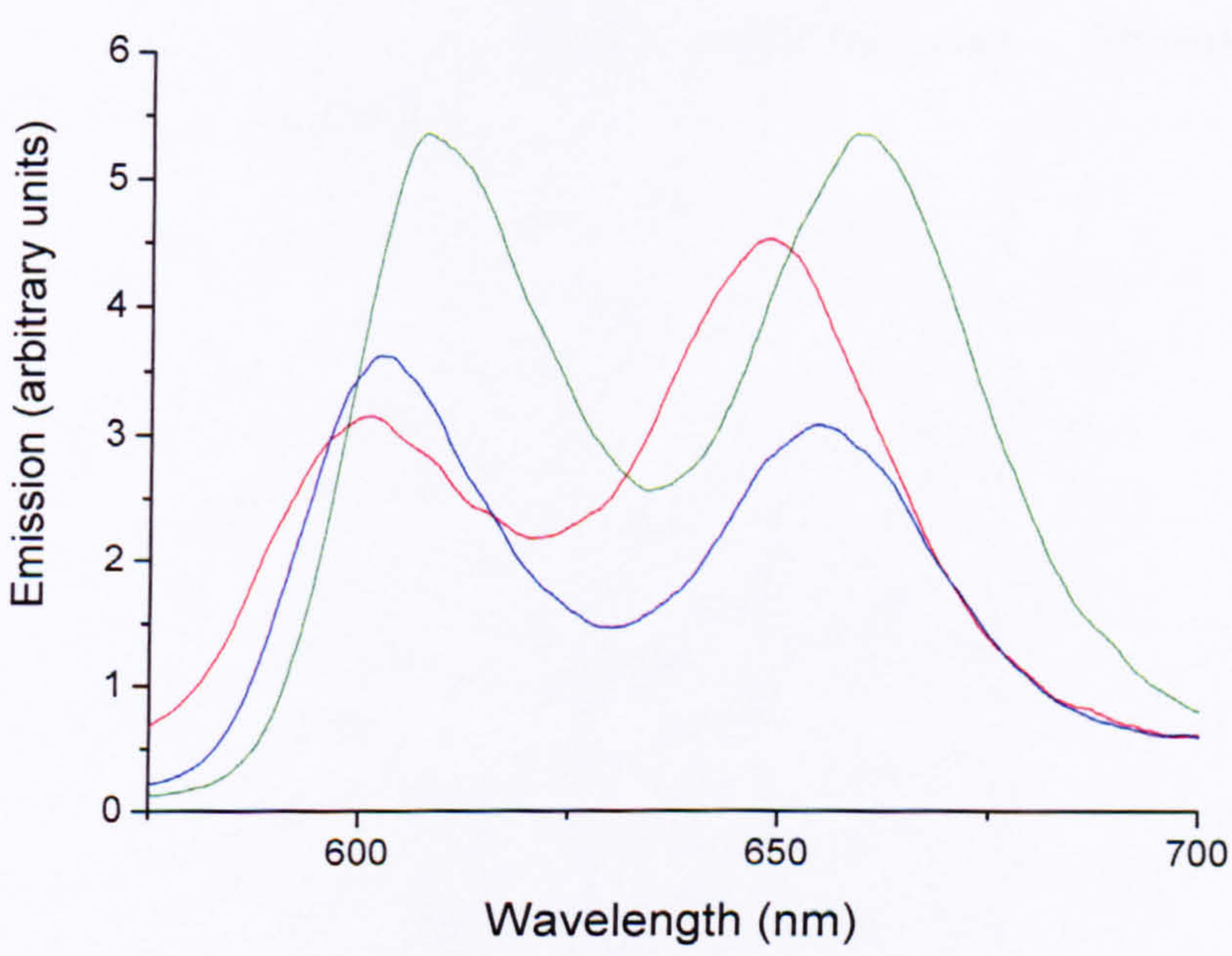

Figure 3.15 Emission spectra for (**A**) **15** and (**B**) **17** in different solvents. Original in colour.

The emission spectra for the zinc porphyrins were solvent dependant as observed for the absorption spectra. **Figure 3.15** shows the emission spectra for **15** and **17** in coordinating (dimethyl sulfoxide and tetrahydrofuran) and non coordinating solvents (chloroform). The emission bands were most intense for the porphyrins in tetrahydrofuran and significantly red shifted compared with the corresponding bands in chloroform. This is a result of coordination of the solvent to zinc, forming a five-coordinate species[14].

3.3. Summary

3.3.1. Synthesis

Tetraphenyl porphyrin derived probes of different lengths have been prepared by systematically coupling 5-(4-aminophenyl)-10,15,20-triphenylporphyrin, with 2-methoxy-4-nitrobenzoic acid, followed by selective reduction of the nitro group with indium and ammonium chloride then repetition to give 5-[4-{(2-methoxy-4-[(2-methoxy-4-amino-phenylcarbonyl)-amino]-phenylcarbonyl)-amino} phenyl]-10,15,20-triphenyl porphyrin. The zinc analogues were prepared by heating the free base porphyrins with zinc acetate in methanol. Each compound was successfully purified by column chromatography. The synthesis is summarised in **Scheme 3.7.**

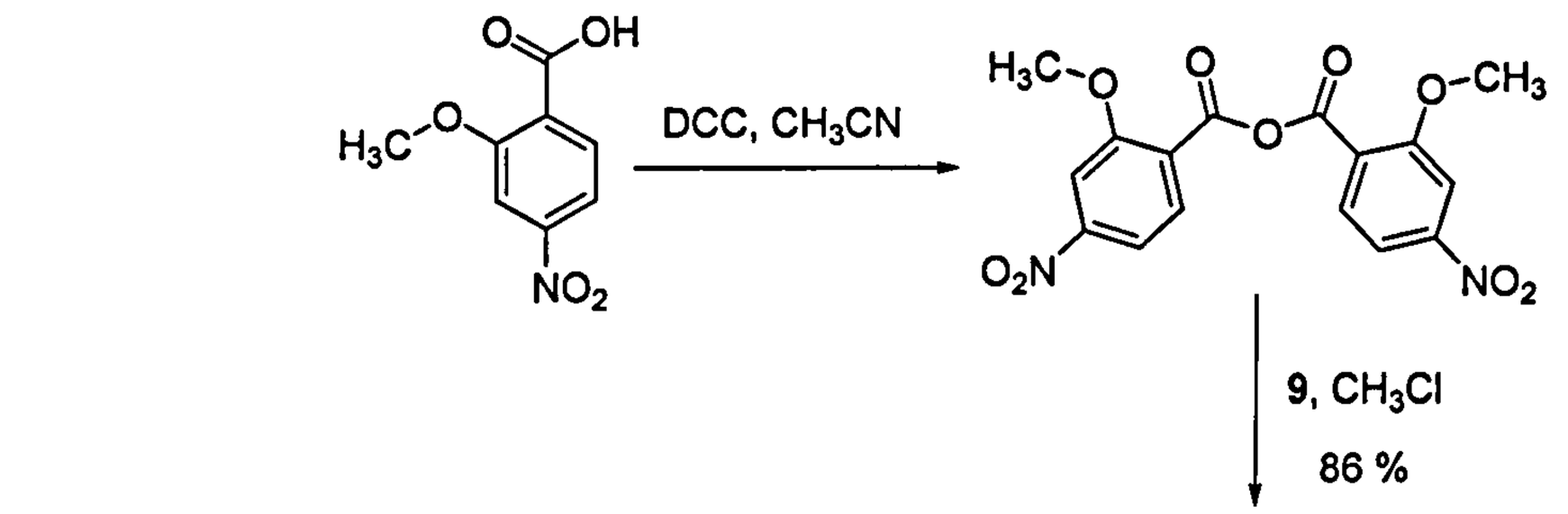
DCC, CH3CN
9, CH3Cl
86 %
ZnOAc2, NH4Cl
80%
11
10
In, NH4Cl, EtOH,
reflux
35%
ZnOAc2, NH4Cl
94%
13
12

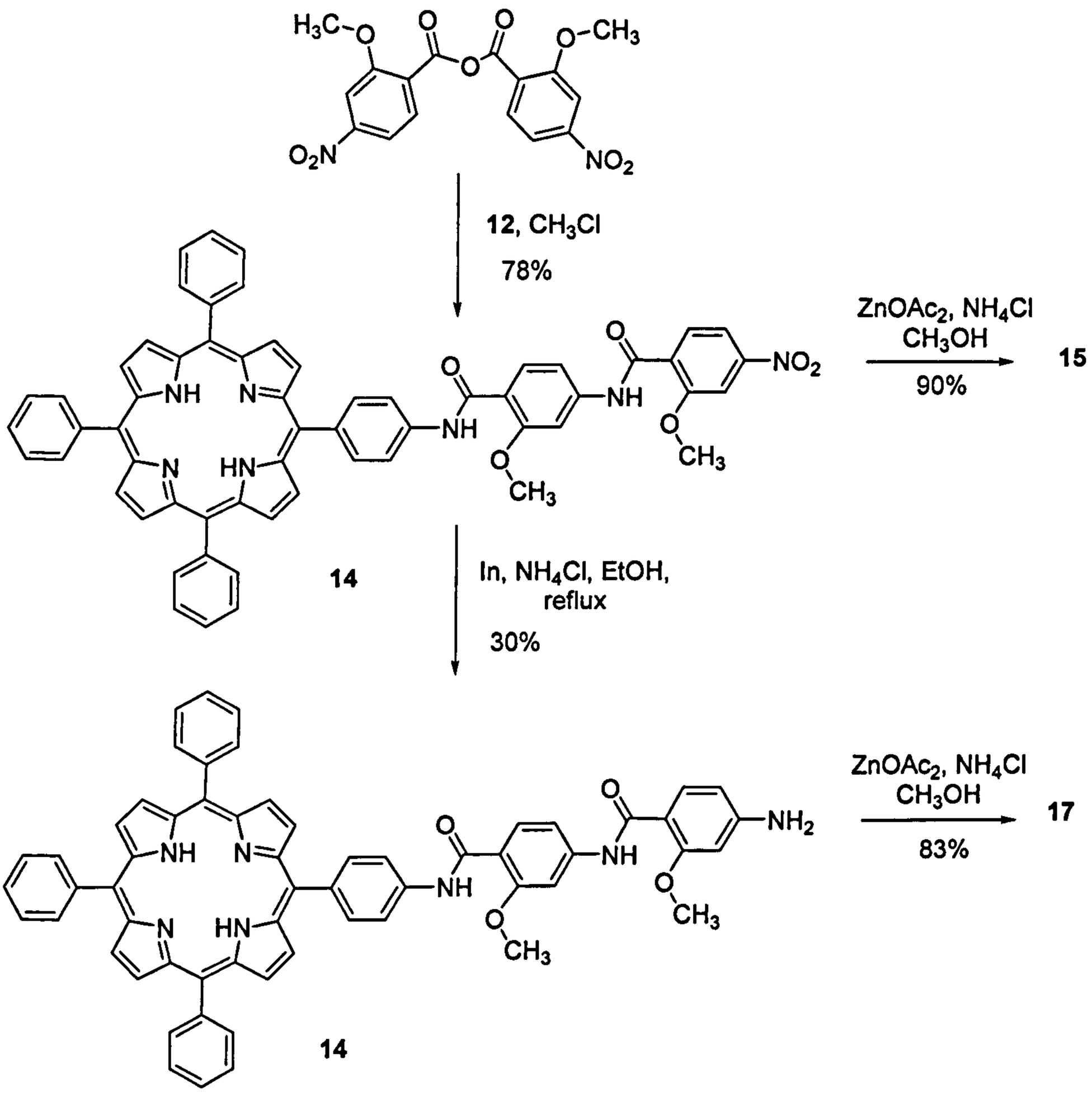

Scheme 3.7 Total synthesis of porphyrins **10 – 17**

3.3.2. Characterisation

Porphyrins **10 – 17** were characterised by ^{1}H, ^{13}C NMR, FTIR and UV-Vis spectroscopy and ESI-MS.

In the ^{1}H NMR spectra signals characteristic of a porphyrin were observed. For each amide bond a signal at $\delta \sim 10$ was observed and for each methoxy group a chemical shift at $\delta \sim 4$ was present. In the ^{13}C spectra the methoxy carbons were located at $\delta \sim 55$. The aromatic carbons were located at $\delta \sim 100 - 150$ and the most downfield chemical shifts at $\delta \sim 160 - 170$ were assigned to the carbonyls. The spectra were fully assigned using 2D experiments including ^{1}H-^{1}H COSY, ^{1}H-^{13}C HMQC and HMBC carried out on the zinc porphyrins.

Aggregation was observed in the NMR and ESI mass spectra for the amines **13** and **17.** Deuterated pyridine was added to the samples to disrupt this and resulted in sharpening of the signals.

For each of the porphyrins a molecular ion peak was observed corresponding to $M + H^+$ except for two of the zinc porphyrins, **11** and **17,** which contained molecular ions at M^+ corresponding to the oxidised compounds.

The infrared spectra contained the same characteristic absorption bands for each porphyrin. Notably the carbonyl stretch, N-H stretch and deformation and for compounds **10, 11, 14** and **15** the N=O symmetric and asymmetric stretch were all assigned.

Each porphyrin displayed solvent dependent absorption bands in the visible region. The extinction coefficient of the intense Soret band varied with the nature of the functional groups i.e. nitro or amine, but λ_{max} did not vary. The extinction coefficients for the zinc porphyrin were higher than for the free base porphyrins.

3.4. References

1. A. D. Adler, F. R. Longo, J. D. Finarelli, J. Goldmacher, J, Assour, L. Korsakoff, *J. Org. Chem.*, **1967**, *32*, 476.
2. S. Shanmugathasan, C. Edwards, R. W. Boyle, *Tetrahedron*, **2000**, 56, 1025.
3. J. S. Lindsey, S. Prathapan, T. E. Johnson, R. W. Waner, *Tetrahedron*, **1994**, *50*, 8941.
4. J. S. Lindsey, I. C. Schreiman, H. C. Hsu, P. C. Kearney, A. M. Marguerettaz, *J. Org. Chem.*, **1987**, *52*, 827.
5. A. Gabrielsson, Ph.D. Thesis, University of York, **2002**.
6. C. J. Aspley, Ph.D. Thesis, University of York, **2000**.
7. W. J. Kruper, T. A. Chamberlin, M. Kochanny, *J. Org. Chem.*, **1989**, *54*, 2753.
8. R. Luguya, L. Jaquinod, F. R. Fronczek, M. G. H. Vicente, K. M. Smith, *Tetrahedron*, **2004**, *60*, 2757.
9. K. Okamoto, S. Fukuzumi, *J. Phys. Chem.*, **2005**, *109*, 7713.
10. K. L. Dombi, C. Richert, *Molecules*, **2004**, *5*, 1265.
11. S. Deroo, E. Defrancq, C. Moucheron, A. Kirsch-De Mesmaeker, P. Dumy, *Tetrahedron Lett.*, **2003**, *44*, 8379.
12. M. R. Pitts, J. R. Harrison, C. J. Moody, *J. Chem. Soc., Perkin Trans. 1*, **2001**, 977.
13. D. H. Williams, I. Fleming, 'Spectroscopic Methods in Organic Chemistry', 5th Ed., McGraw-Hill, 1997.
14. K. Kalyanasundaram, 'Photochemistry of Polypyridine and Porphyrin Complexes', Academic Press Limited, 1992.
15. 'The Porphyrins', ed. D. Dolphin. Aademic Press, New York, 1978-1979.
16. M. Gouterman, *J. Chem. Phys.*, **1959**, *30*, 1139.
17. E. G. Bàerends, G. Ricciardi, A. Rosa, S. J. A. Van Gisbergen, *Coord. Chem. Rev.*, **2002**, *230*, 5.
18. I. Baraldi, A. Carnevali, G. Ponterini, D. Vanossi, *J. Mol. Struct. (Theochem)*, **1995**, *333*, 121.
19. M. Nappa, J. S. Valentine, *J. Am. Chem. Soc.*, **1978**, 5075.

CHAPTER FOUR

WATER-SOLUBLE PORPHYRIN DERIVATIVES

4. Water-Soluble Porphyrin Derivatives

Water-solubility is essential for biological applications. Consequently, the synthetic procedure described in chapter 3 was applied to a porphyrin that was subsequently derivatised to produce a charged periphery.

4.1. Synthesis

Initially, coupling 5-(-4-aminophenyl)-10, 15, 20-tris (4-sulfonatophenyl)-porphyrin illustrated in **Figure 4.1** to the linker was attempted.

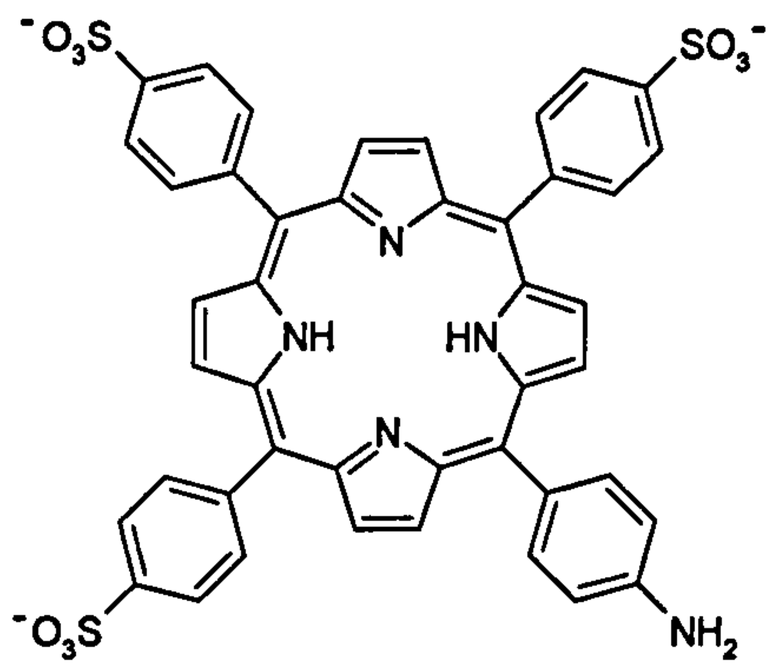

Figure 4.1 5-(-4-aminophenyl)-10, 15, 20-tris (4-sulfonatophenyl)-porphyrin reported by Kruper *et al*[1].

Computer modelling (Chapter 2) had shown that regions of opposite charge criss-cross the opening of the channel. It is therefore possible for the sulfonate groups of the planar porphyrin to be aligned along the electropositive domains as shown in **Figure 4.2**. This would minimise electrostatic repulsion between the enzyme surface and a negatively charged porphyrin.

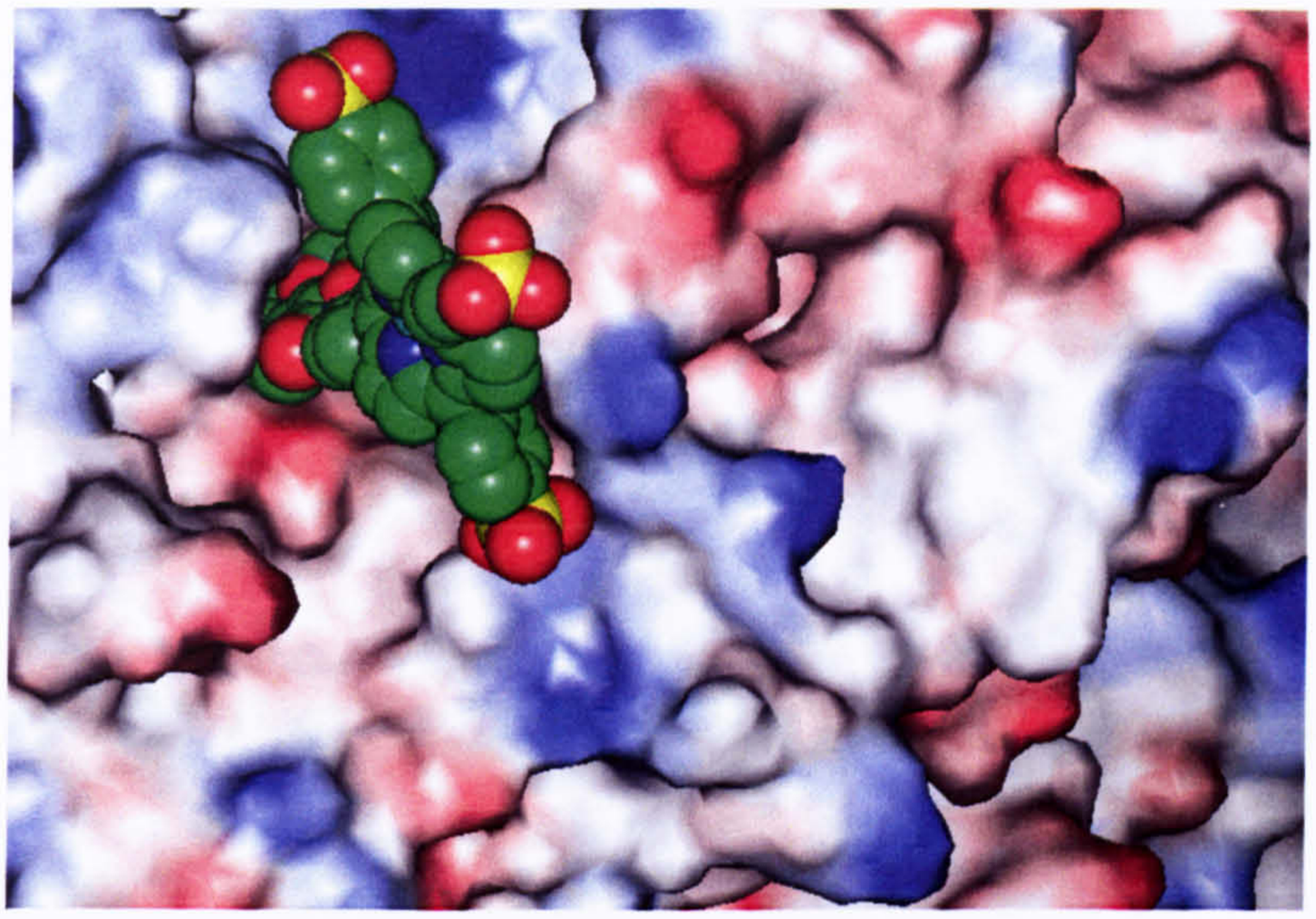

Figure 4.2 Enzyme surface with exposed sulfonated porphyrin. Red and blue shading corresponds to negative and positive electrostatics of surface residues respectively. Original in colour.

Unfortunately the reaction was unsuccessful with both the sodium and more soluble ammonium salts and such a reaction was not found in the literature.

Several commercially available water-soluble porphyrins were initially investigated (**Figure 4.3**). Tetracarboxyphenyl porphyrin (TCPP) was chosen since the carboxyl groups could be coupled to the amine function of the linker. However, this porphyrin had limited solubility in water, preferring basic solution. Tetraaminophenyl porphyrin was found to be soluble in acidic solution as was tetrapyridyl porphyrin. However, these could be methylated to give the water soluble tetracationic porphyrins (TAPP and TMPyP). The advantage of tetracationic porphyrins is that they are found to be water soluble over the whole pH range and do not suffer from the aggregation phenomena associated with tetraanionic porphyrins like TPPS[3].

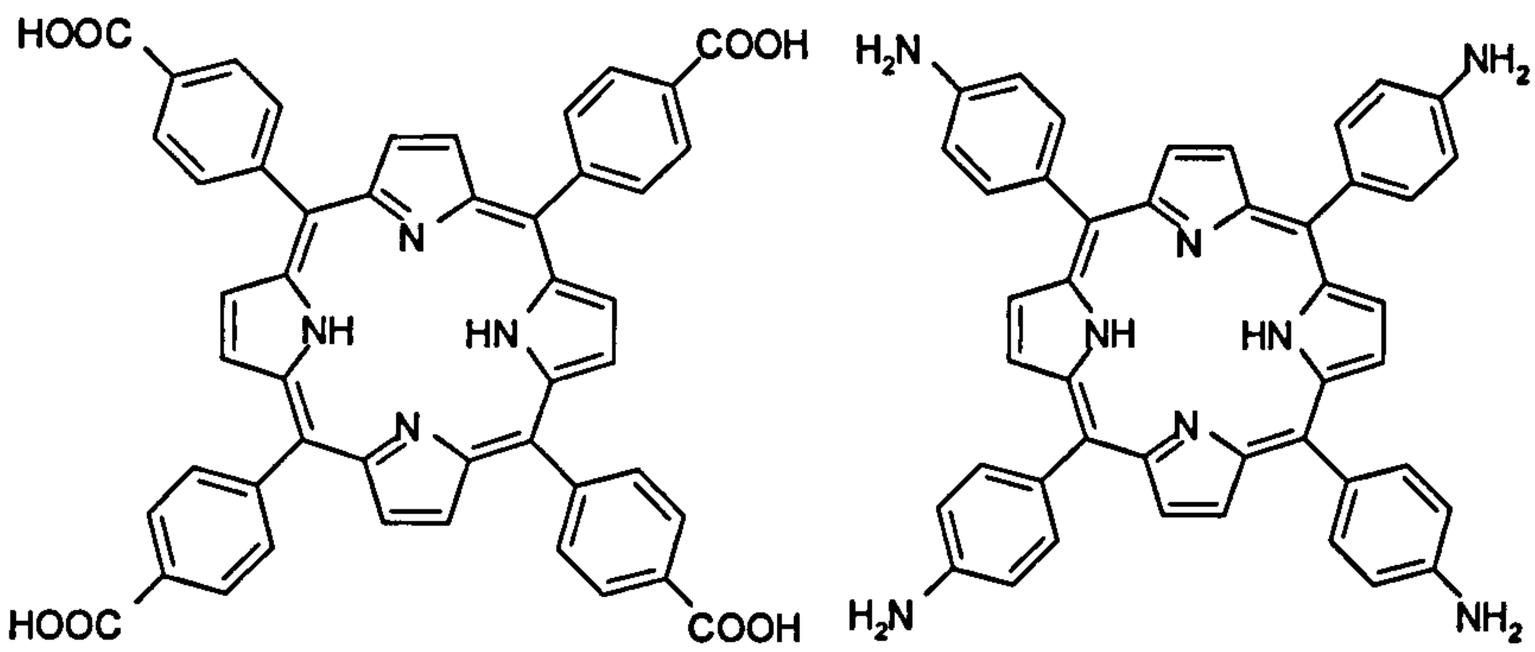

TCPP **Tetra (4-aminophenyl) porphyrin**

Figure 4.3 Commercially available porphyrins

Li *et al.* have synthesised a series of *meso*-5, 10, 15-tris(*N*-methyl-4-pyridiniumyl)-20-(4-alkylamidophenyl) porphyrins shown in **Figure 4.4** for use as DNA photomodifiers[4].

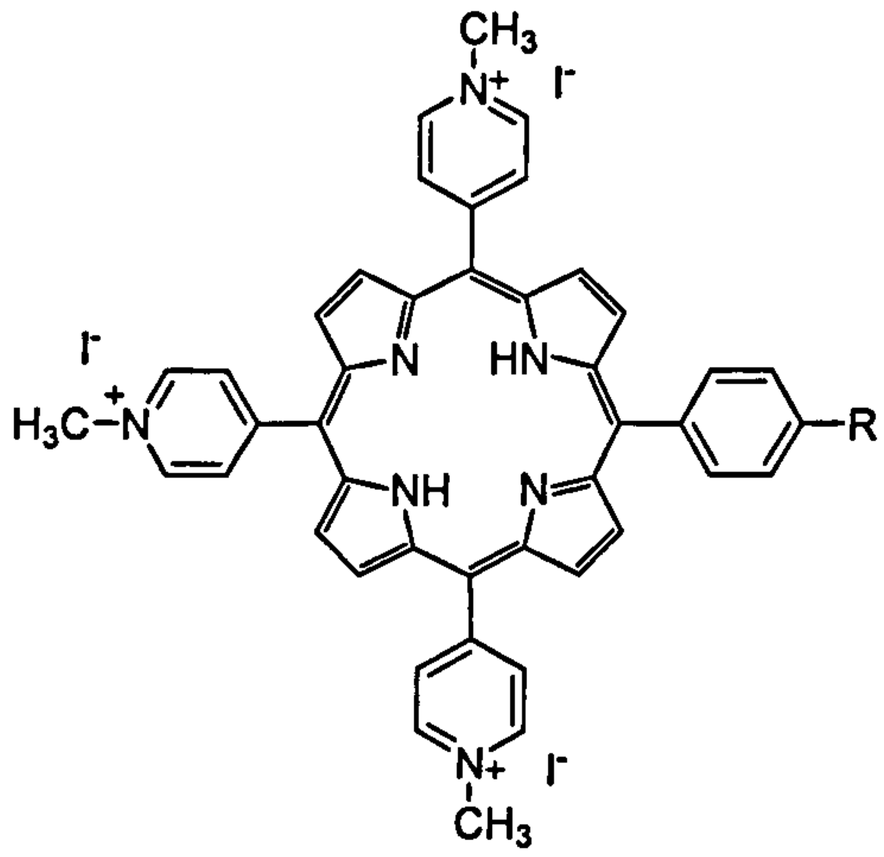

1 R = NH_2
2 R = $NHCOCH_3$
3 R = $NHCO(CH_2)_6CH_3$
4 R = $NHCO(CF_2)_6CF_3$
5 R = $NHCO(CH_2)_{14}CH_3$
6 R = $NHCOCH=CH_2$

Figure 4.4 Porphyrins reported by Li *et al*[4].

Whilst some success was achieved at mono-functionalising tetra(4-aminophenyl) porphyrin, the pyridyl and pyridiniumyl porphyrins were found to be easier to handle. Therefore the approach was taken whereby 5, 10, 15-tris(4-pyridyl)-20-(4-aminophenyl)porphyrin, prepared using the method described by Li *et al.*, was coupled to 2-methoxy-4-nitrobenzoic acid using the DCC mediated method described for TPP derivatives.

4.1.1 5, 10, 15-tris(4-pyridyl)-20-(4-aminophenyl)porphyrin, 19.

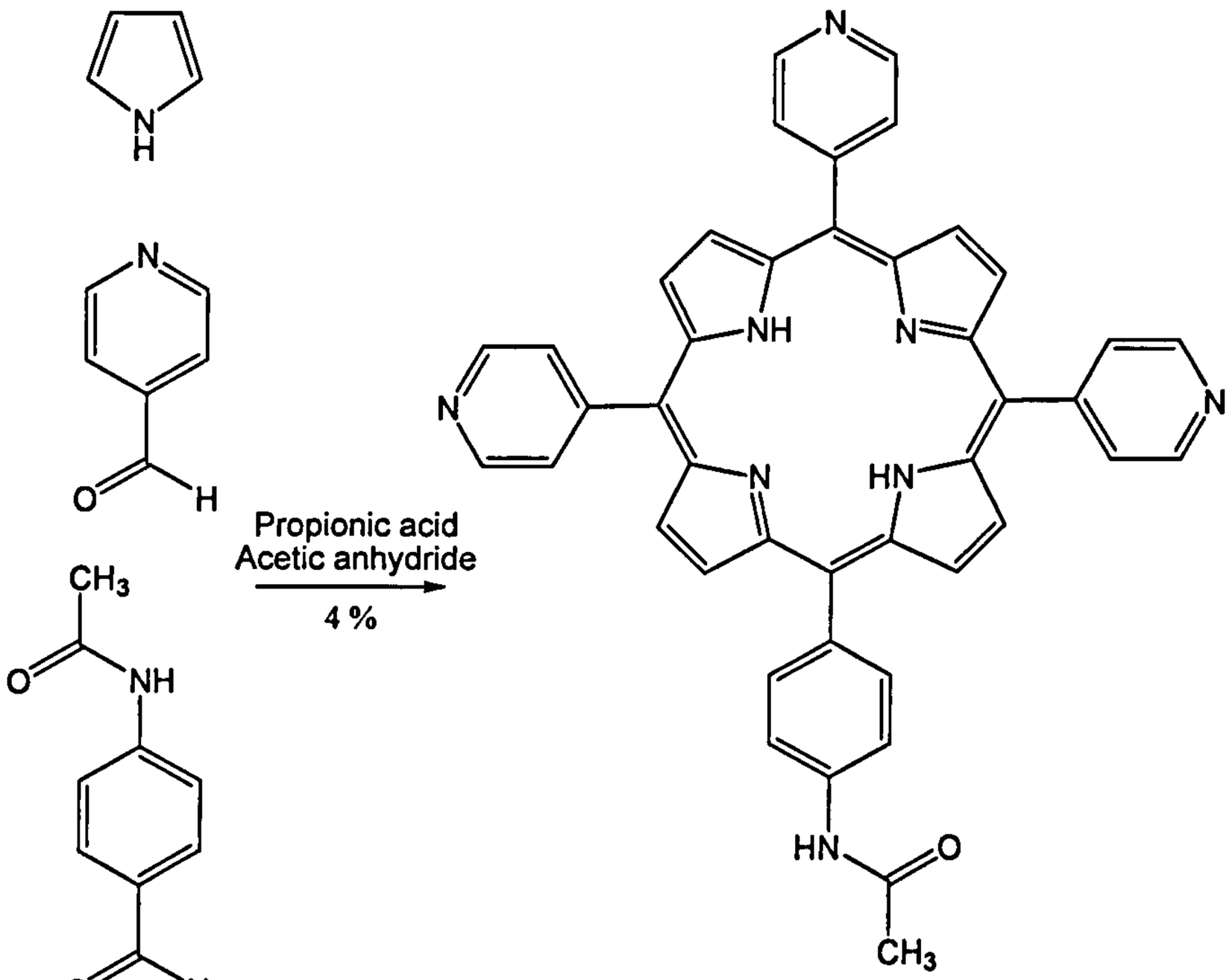

18

Scheme 4.1 Preparation of free base m*eso*-5-10,15,-tris(4-pyridyl)-20-(4-acetamidophenyl)porphyrin, **18**, reported by Li *et al.*[4]

Free base m*eso*-5-10,15,-tris(4-pyridyl)-20-(4-acetamidophenyl)porphyrin, **18**, was prepared by the Alder-Longo method as described by Li *et al.* [4] in 4.2% yield, a little lower than described by the authors (5%) due to the extra purification steps added. To ease purification by column chromatography, the tarry black residue resulting from the reaction illustrated in **Scheme 4.1** was washed with methanol using Soxhlet apparatus for up to one week to remove the polymeric material. The remaining residue was dissolved in dichloromethane and passed through a short plug of Florisil® eluting with chloroform-methanol (10:1, v/v) to remove any remaining polymer[149].

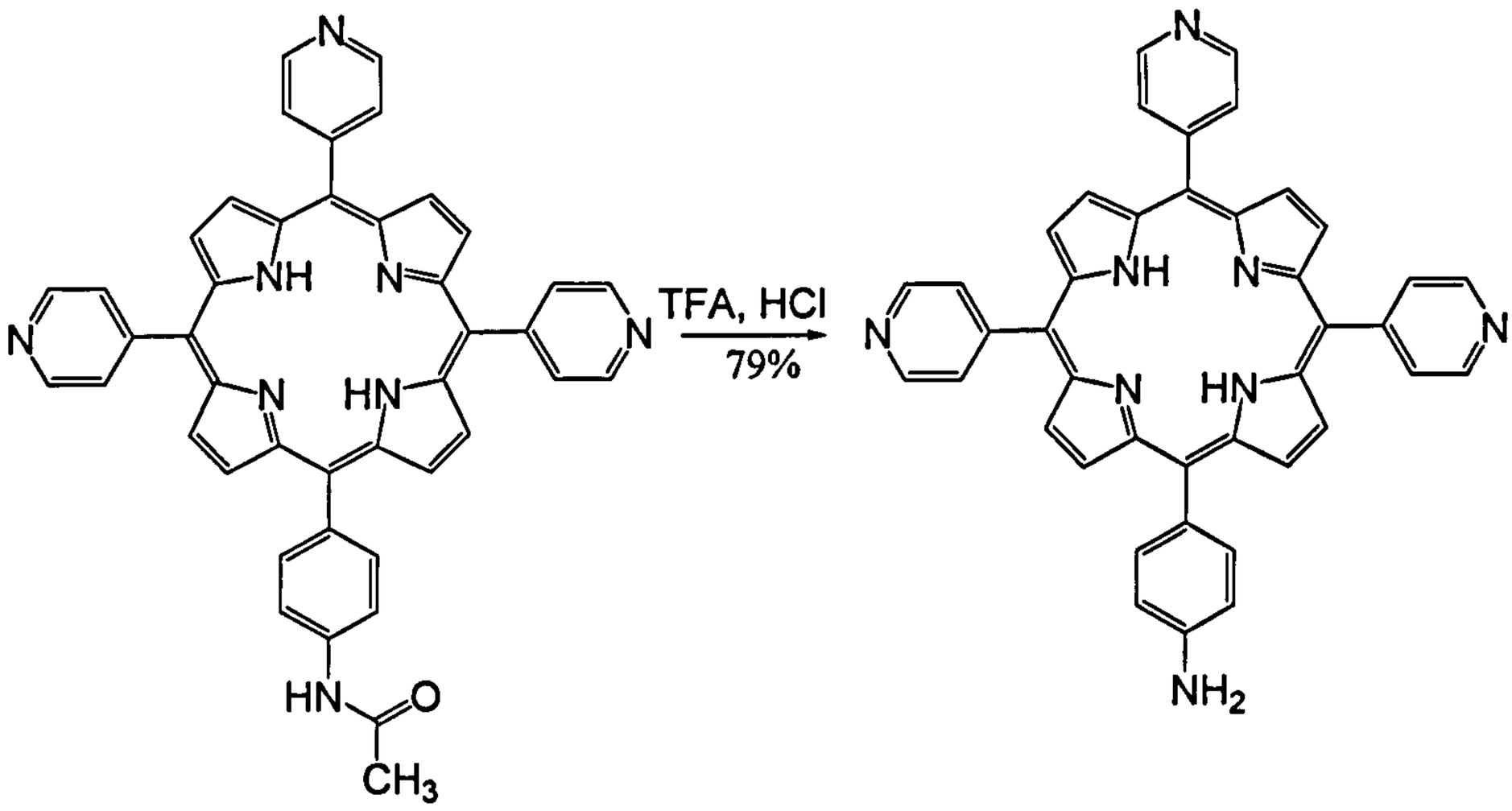

19

Scheme 4.2 Preparation of free base 5,10,15-tris(4-pyridyl)-20-(4-aminophenyl)porphyrin, **19**, described by Li *et al.*[149]

Compound **18** was deprotected by heating a 1:1 trifluoroacetic acid, hydrochloric acid solution of the porphyrin at 80°C for 36 h, followed by neutralisation of the cold solution with aqueous ammonia (**Scheme 4.2**). Amine **19** was purified by column chromatography over silica, eluting with chloroform-methanol (80:1, v/v). The yield was comparable to that reported by the authors (80%).

4.1.2 Coupling of the linker

Compound **20** was prepared using the anhydride procedure described for **10** as illustrated in **Scheme 4.3.** Purification was aided by extracting **20** into dilute hydrochloric acid and washing the green aqueous layer with dichloromethane. This enabled removal of the unreacted organic reagents and, moreover, the urea byproduct which was difficult to remove from the TPP derivatives. The acid was neutralised with ammonia solution and the purple precipitate was extracted with chloroform and purified further by column chromatography. The yield was 79% for this step, a little lower than for **10.**

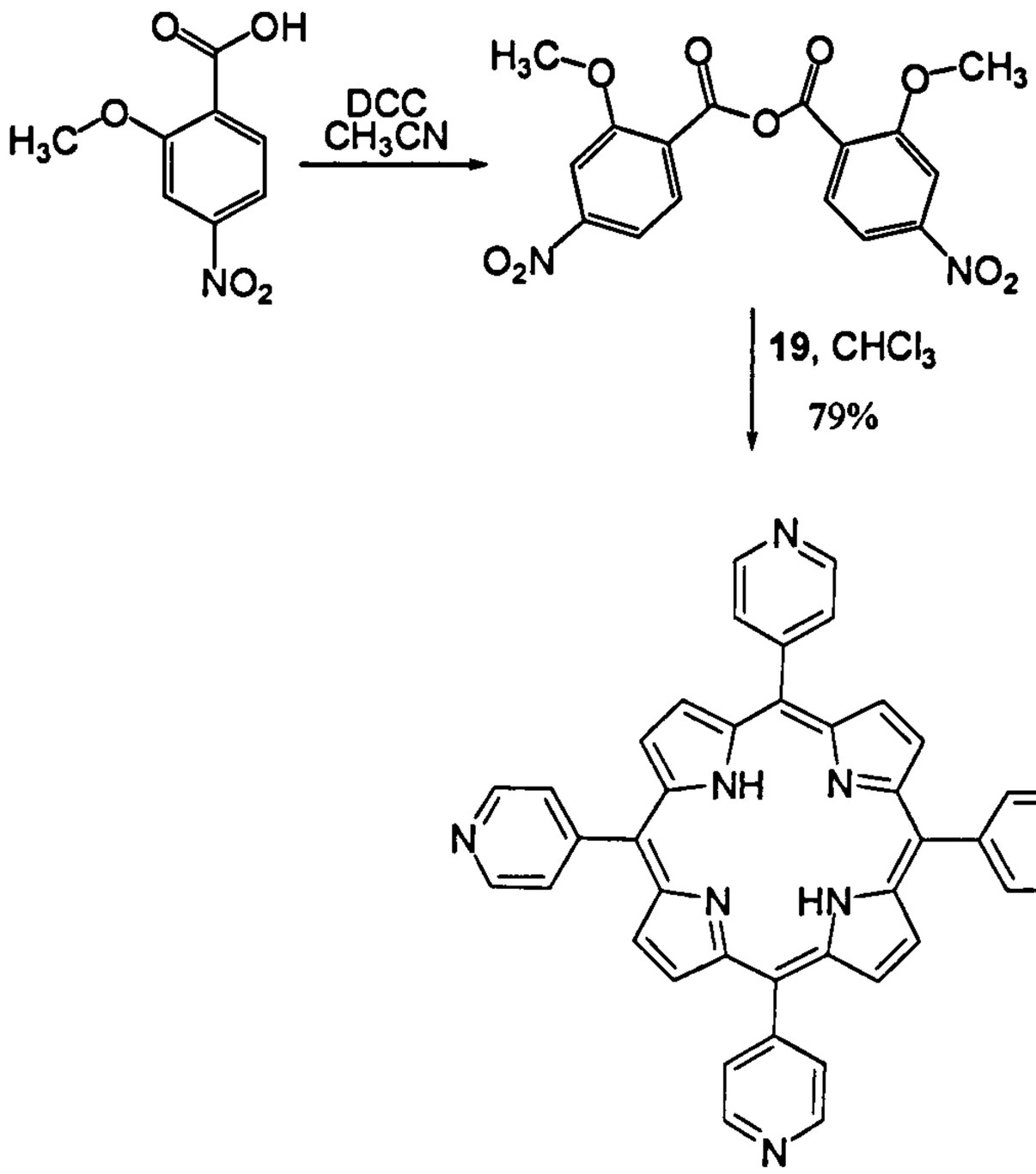

20

Scheme 4.3 Preparation of free base 5,10,15-tris(4-pyridyl)-20-[4-[(2-methoxy-4-nitro-phenylcarbonyl)-amino] phenyl] porphyrin, **20**.

4.1.3 *N*-methylation

Nitro compound **20** was methylated with methyl iodide as described by Li *et al.* and illustrated in **Scheme 4.4**. Having stirred the DMF solution of **20** with an excess of methyl iodide overnight, the solvent was evaporated and the porphyrin dried in a vacuum oven for a few days. No further purification was carried out. Methylation in all three positions was shown to be complete by ^{1}H NMR spectroscopy and ESI-MS (chapter 7). The iodide salt was reasonably soluble in water and ethanol.

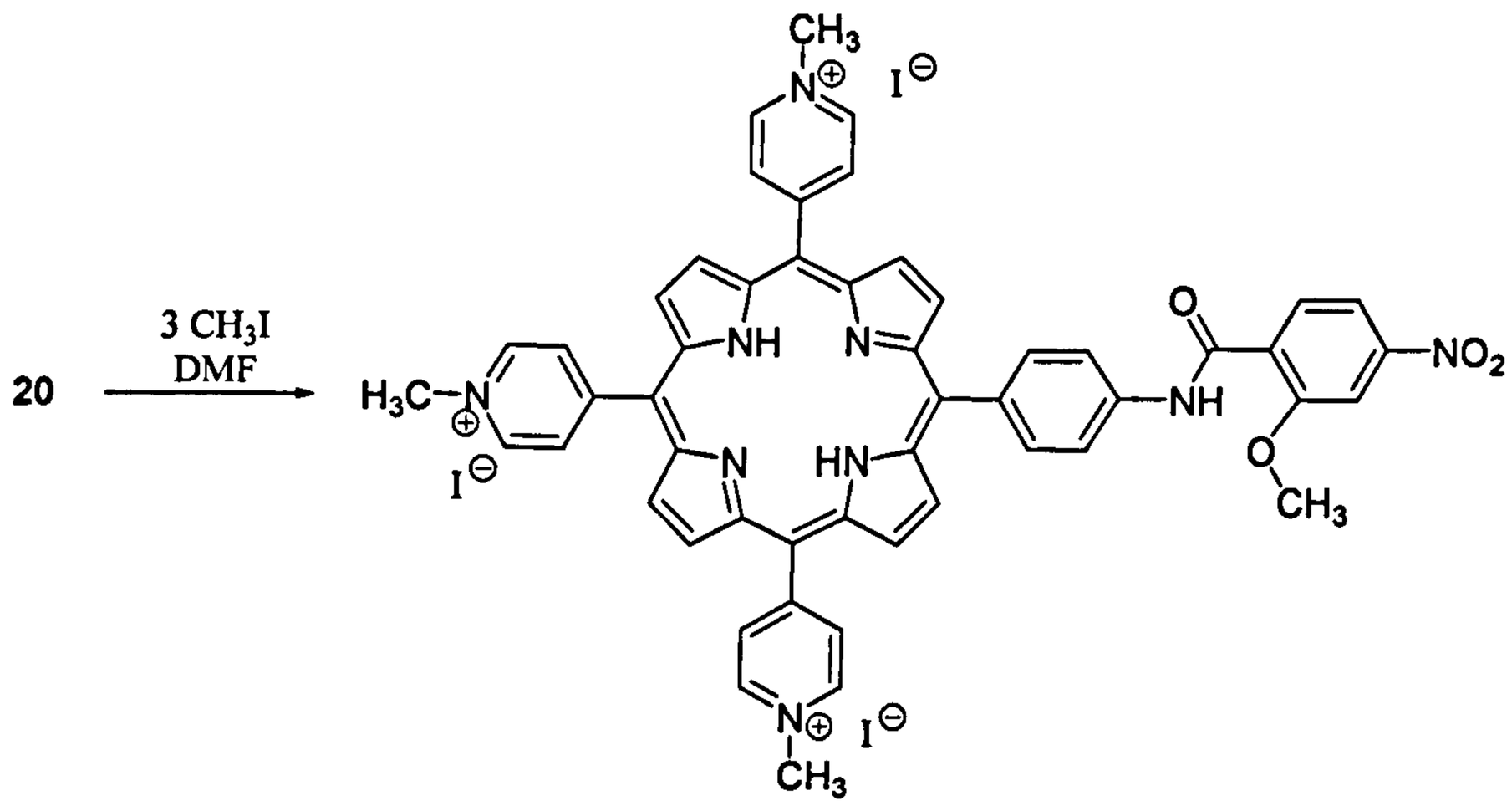

Scheme 4.4 Preparation of free base 5,10,15-tris(*N*-methyl-4-pyridiniumyl)-20-[4-[(2-methoxy-4-nitro-phenylcarbonyl)-amino] phenyl] porphyrin tris iodide, **21**, described by Li *et al.*[149]

4.1.4 Reduction of the linker

21 was reduced with indium and ammonium chloride as for the TPP derivatives, as illustrated in **Scheme 4.5**. The reaction mixture was acidified slightly to enable filtration through Celite®. The solvent was removed and the residue taken up in water. Ammonium hexafluorophosphate solution in water was added dropwise until **[22]**$[PF_6]_3$ precipitated. The yield for this step was 64%, an improvement over the TPP derivatives, probably due to the increased solubility of the halide salts in ethanol and water. The ^{1}H NMR spectrum and ESI-MS indicated that the free base compound, not the indium porphyrin, was present at this stage. Water solubility of the compound could be achieved by conversion to the chloride salt. Compound **[22]**$[PF_6]_3$ was dissolved in acetonitrile and tetrabutyl or tetraethyl ammonium chloride solution in acetonitrile added dropwise until the chloride salt **[22]**$[Cl]_3$ precipitated. The product could be further purified by passing an aqueous solution through Sephadex G-10 size exclusion gel and/or precipitation from an aqueous or methanolic solution by addition of acetone.

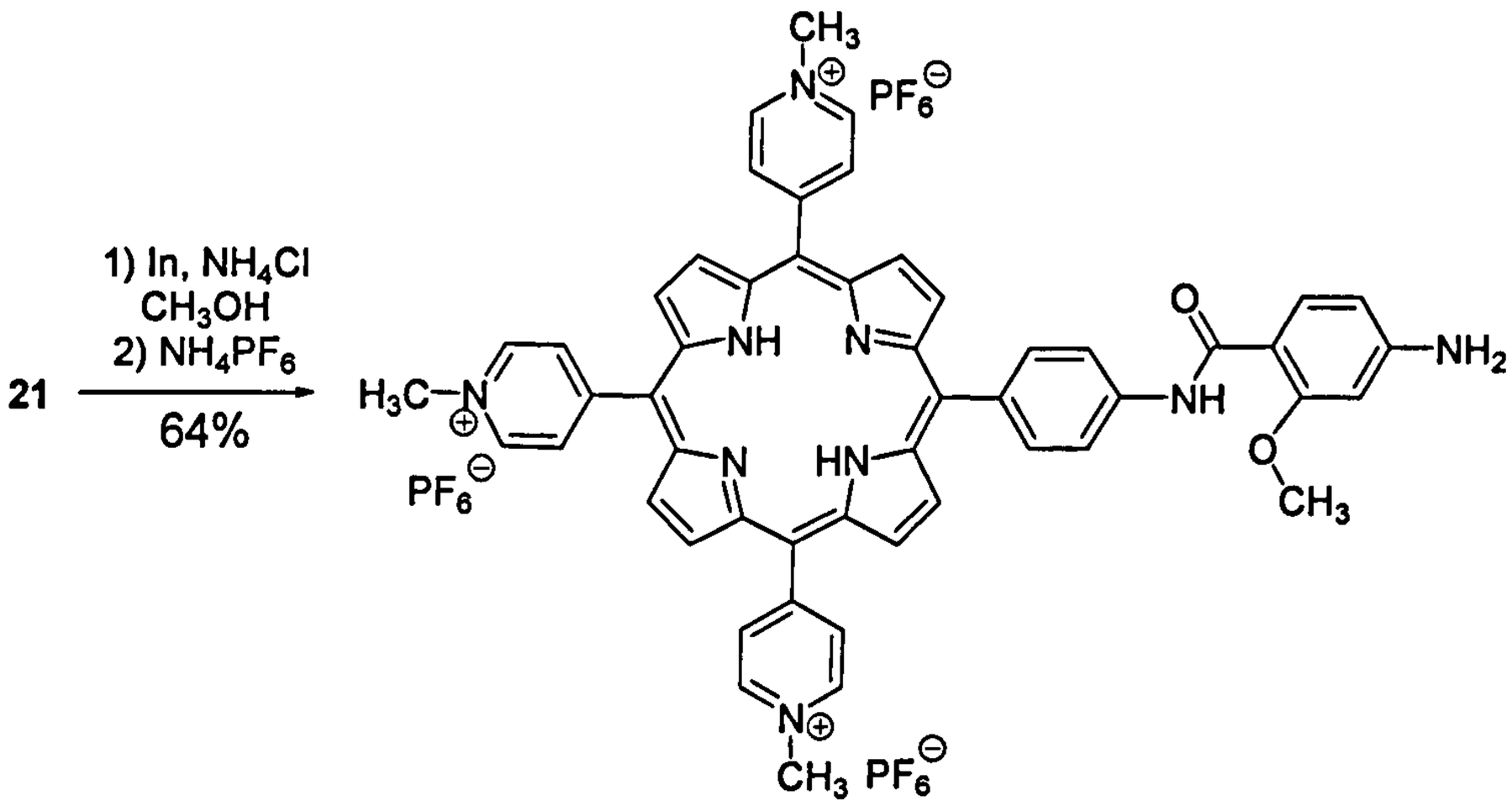

Scheme 4.5 Preparation of free base 5,10,15-tris(*N*-methyl-4-pyridiniumyl)-20-[4-[(2-methoxy-4-amino-phenylcarbonyl)-amino] phenyl] porphyrin, **[22]**$[PF_6]_3$.

4.1.5 Coupling of the substrate

Isonicotinic acid anhydride was chosen as the substrate since the linker-substrate complex, **6**, had an appropriate IC_{50} for this application (chapter 5). Isonicotinic acid itself was not sufficiently soluble in the solvents appropriate for the DCC mediated method used so far. The acid chloride and DMAP catalysed reaction were inappropriate since triethylammonium chloride is produced which would exchange anions with **[22]**$[PF_6]_3$, precipitating the porphyrin from acetonitrile before the reaction had gone to completion. Therefore commercially available isonicotinic acid anhydride was used directly, as illustrated in **Scheme 4.6**.

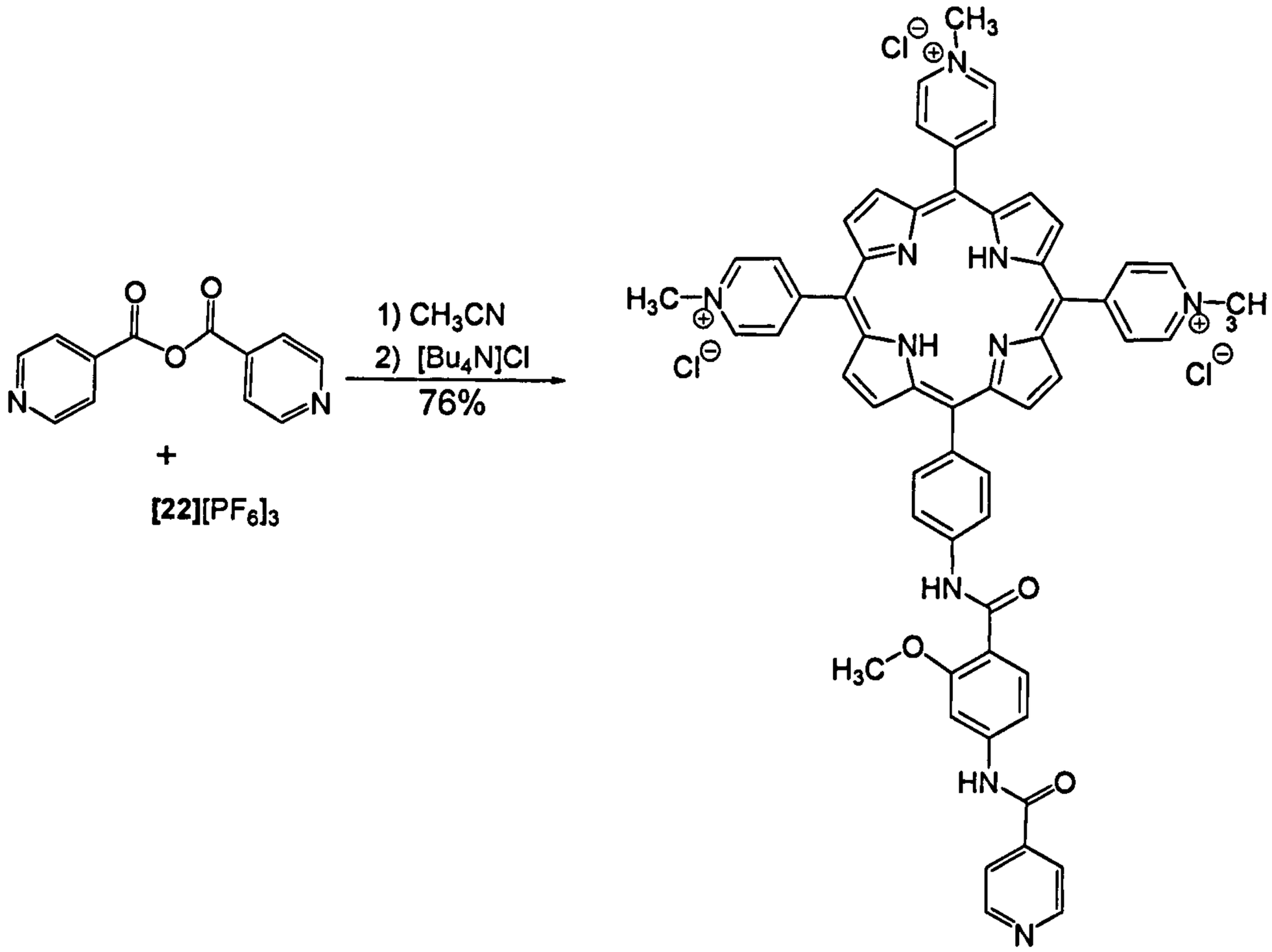

Scheme 4.6 Preparation of free base 5,10,15-tris(*N*-methyl-4-pyridiniumyl)-20-[4-{(2-methoxy-4-[(pyridine-4-carbonyl)-amino]-phenylcarbonyl)-amino} phenyl]-porphyrin, **[24]**$[Cl]_3$.

As for **[22]**$[Cl]_3$, the compound could be further purified by passing an aqueous solution through Sephadex G-10 size exclusion gel and/or precipitation from an aqueous or methanolic solution by addition of acetone. The overall yield after purification was 76 %.

4.1.6 Insertion of zinc

The porphyrins were metallated by a similar method to the TPP derivatives. Following the procedure reported by Myatani *et al.*[7], free base porphyrins **[22]**$[Cl]_3$ and **[24]**$[Cl]_3$ were heated at reflux with ten equivalents of zinc acetate dihydrate in methanol for two hours. As

previously, the progress of the reaction could be monitored by UV-Vis spectroscopy. The metalloporphyrins were purified by addition of ammonium hexafluorophosphate solution to precipitate **[23]**$[PF_6]_3$ and **[25]**$[PF_6]_3$ accordingly, enabling unreacted zinc acetate and other inorganic byproducts to be washed off with water. The water soluble derivatives could be re-obtained by adding tetrabutylammonium chloride to the acetonitrile solution as previously. **[23]**$[Cl]_3$ and **[25]**$[Cl]_3$ (**Figure 4.5**) could then be purified by gel permeation chromatography through Sephadex LH-20, eluting with methanol.

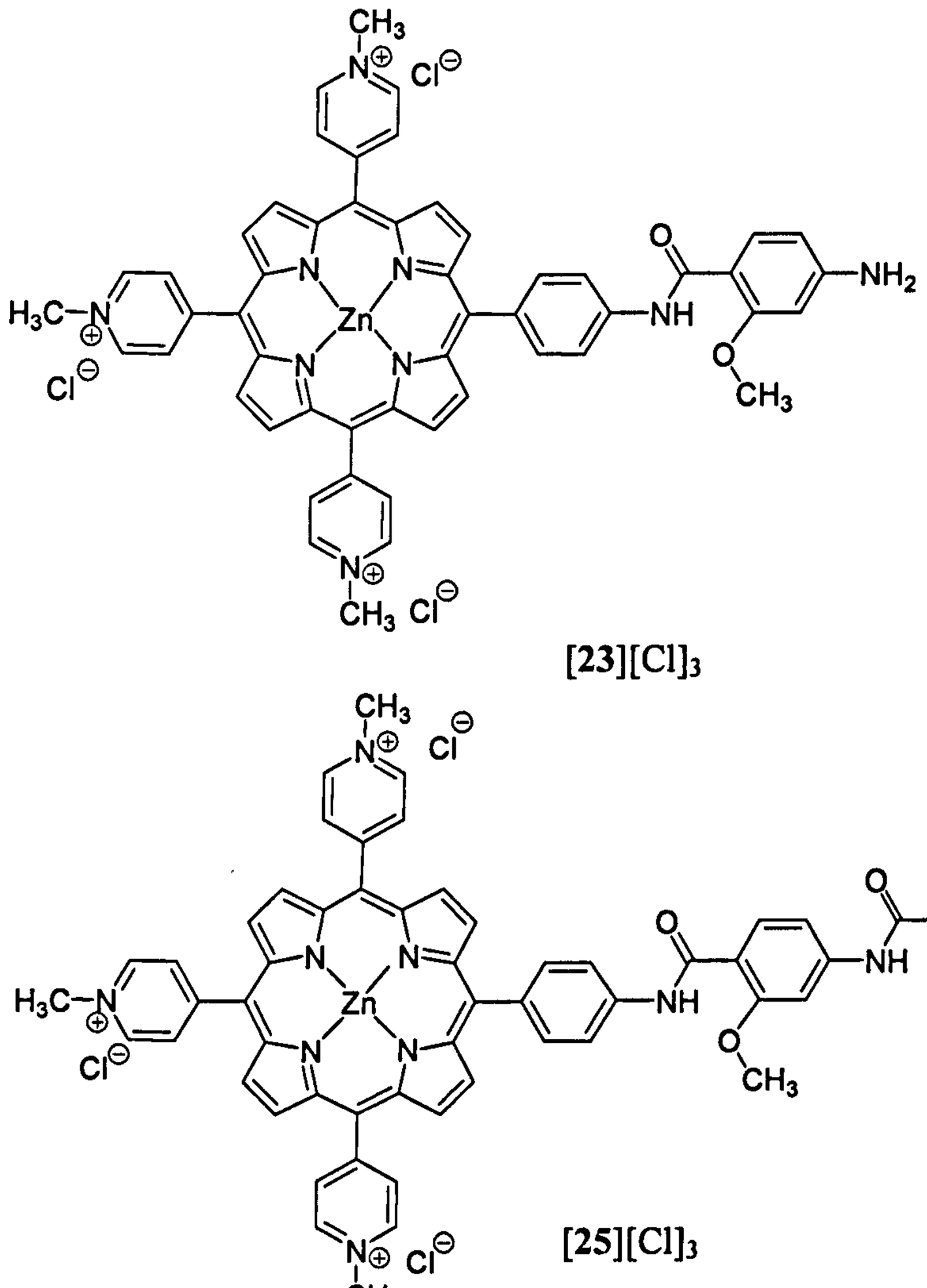

4.2

Figure 4.5 Water-soluble metalloporphyrins **[23]**$[Cl]_3$ and **[25]**$[Cl]_3$.

4.2. Characterisation

Porphyrins **18 – 25** have been characterised by NMR, FTIR and UV-Vis spectrometry and by ESI-MS.

The characterisation of **18** and **19** by NMR, FTIR and UV-Vis spectrometry and by ESI-MS has been reported in the literature[4] and the compounds synthesised here are mostly in good agreement with the previously reported data. However, there was a discrepancy between the ^{1}H NMR data reported by Li *et al.* for **18** and that characterised here and for completion the characterisation data for each compound, including **18** and **19**, will be discussed for comparison.

4.2.1 NMR spectroscopy

As for the TPP derivatives, porphyrins **18 - 25** were characterised using 1D ^{1}H and ^{13}C NMR and 2D ^{1}H - ^{1}H COSY and ^{1}H - ^{13}C HMQC and HMBC experiments. The spectra were similar to those of the TPP derivatives with some characteristic differences which will be discussed. The spectra of the water-soluble porphyrins were run using d_6-DMSO as the solvent since protic solvents such as D_2O and CD_3OD exchange with the NH protons so they cannot be observed. Despite broadening of the peaks, the spectra were of higher quality for the chloride salts in d_6-DMSO than the PF_6^- salts in CD_3CN.

4.2.1.1. Free base m*eso*-5-10,15,-tris(4-pyridyl)-20-(4-acetamidophenyl) porphyrin, 18.

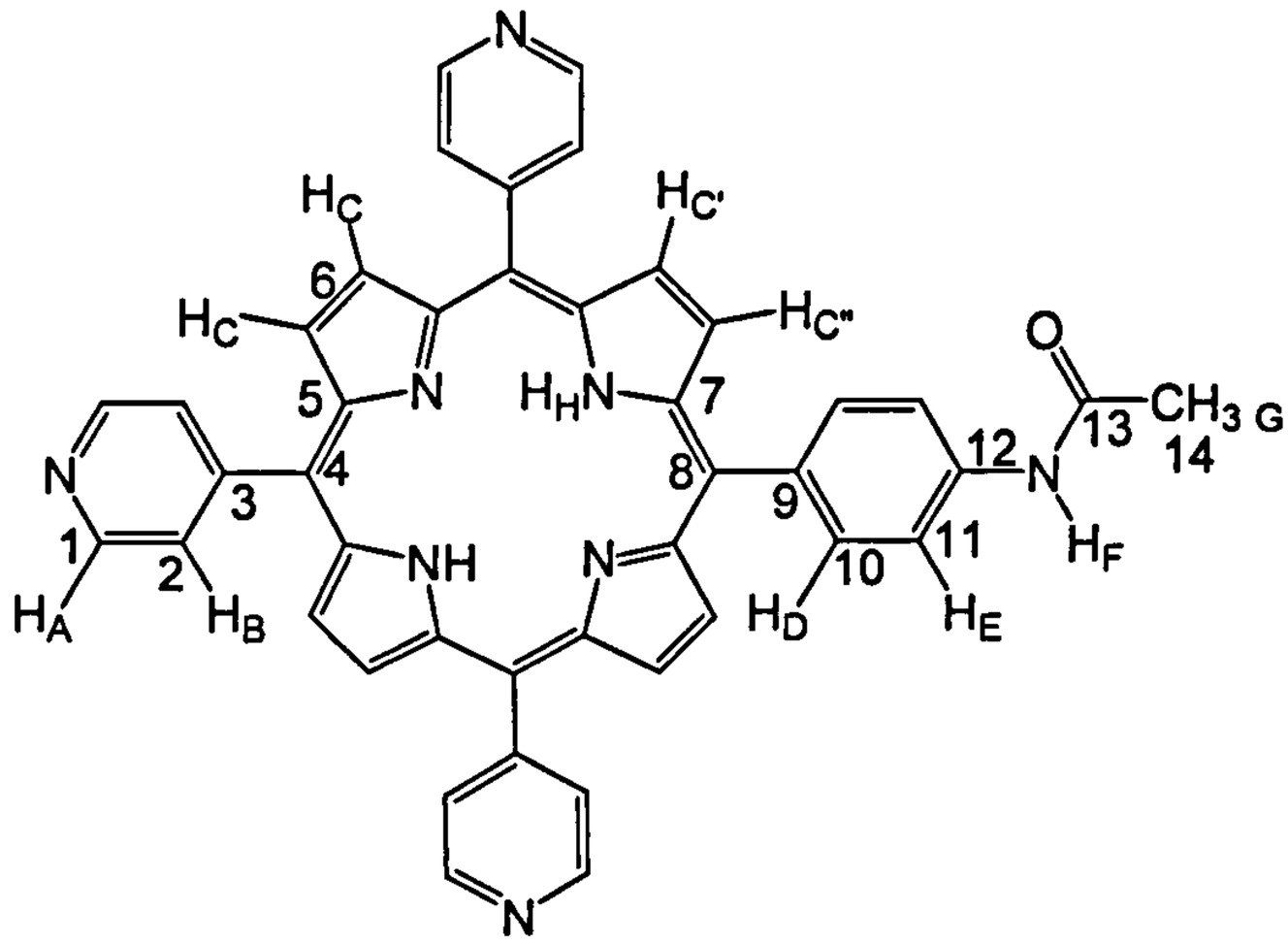

Figure 4.6 18 with atom labels: letters assigned to protons and numbers assigned to carbons.

Label	δ	Integration	Multiplicity	Type	COSY to ^{1}H at δ	Lit[4]
A	9.05	6	m	CH × 6	8.14	9.05
B, D	8.14	8	m	CH × 8	7.94, 9.05	8.10, 8.00
C	8.84 8.94 8.81	4 2 2	s d d	CH × 8 CH × 2 CH × 2	none 8.81 8.94	8.85 9.05
E	7.94	2	d	CH × 2	8.14	7.10
F	7.74	1	s	NH	none	none
G	2.38	3	s	CH_3	none	1.95
H	–2.89	2	s	NH × 2	none	-2.95

Table 4.1 Assignment of ^{1}H NMR chemical shifts for **18** in $CDCl_3$.

Table 4.1 lists the ^{1}H NMR signals for the spectra of **18** in $CDCl_3$ along side those reported by Li *et al.*[4] in the same solvent. The numbering system is shown in **Figure 4.6.** Some of the

signals reported here appear to be shifted downfield relative to those reported in the literature. Li *et al.* did not report a signal corresponding to the amide NH. For this reason the spectra were fully assigned using 2D experiments as for the novel compounds to prove the structure. The carbon assignments are listed in **Table 4.2.**

Label	δ	Type	HMQC to ^{1}H at δ	HMBC to ^{1}H at δ
1	148.5	CH	9.05	8.14
2	129.4	CH	8.14	9.05
3	117.5	Q	none	8.14
4	117.1	Q	none	8.14
5	150.1	Q	none	9.05
7	150.0	Q	none	9.05
8	138.1	Q	none	8.14
9	121.2	Q	none	8.14
10	135.2	CH	8.14	8.14
11	118.2	CH	7.94	7.74
12	137.4	Q	none	7.94
13	168.8	Q	none	2.38
14	24.9	CH_3	2.38	none

Table 4.2 Assignment of ^{13}C NMR chemical shifts for **18** in $CDCl_3$.

Despite the differences between the proton spectrum reported here and that published by Li *et al.*, the compound has been more thoroughly investigated in this work, including two dimensional experiments and ^{13}C NMR spectra. Compound **18** has also been characterised by ESI-MS, infra-red and UV-Vis spectroscopy (see experimental), and the corresponding data agree with the proposed structure. These data were not published by Li *et al.* for comparison.

4.2.1.2. Free base 5,10,15-tris(4-pyridyl)-20-(4-aminophenyl)porphyrin, 19.

The ^{1}H NMR spectrum for **19** agreed with the published data[4].

4.2.1.3. Free base 5,10,15-tris(4-pyridyl)-20-[4-[(2-methoxy-4-nitro-phenyl carbonyl)-amino] phenyl] porphyrin, 20.

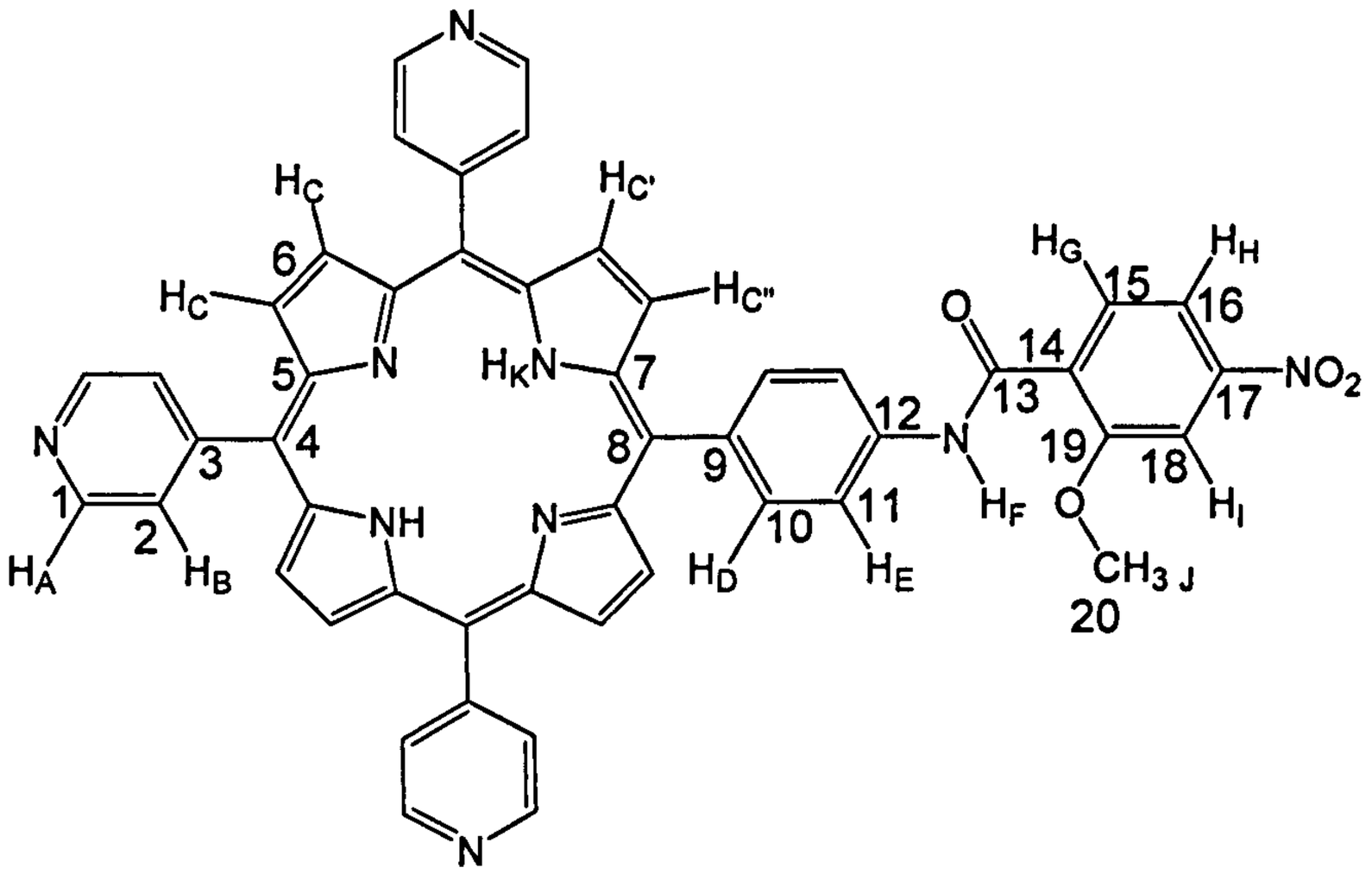

Figure 4.7 **20** with atom labels: letters assigned to protons and numbers assigned to carbons.

Label	δ	Integration	Multiplicity	Type	COSY to ^{1}H at δ	10
A	9.05	6	d	CH × 6	8.17	7.78
B	8.17	6	d	CH × 6	9.05	8.26
C	8.85 8.97	6 2	m d	CH × 6 CH × 2	8.97 8.85	8.89
D	8.23	2	d	CH × 2	8.11	8.29
E	8.11	2	d	CH × 2	8.23	8.11
F	10.02	1	s	NH	none	9.99
G	8.58	1	d	CH	8.04	8.58
H	8.04	1	dd	CH	7.98, 8.58	8.05
I	7.98	1	d	CH	8.04	7.96
J	4.29	3	s	CH_3	none	4.31
K	–2.88	2	s	NH × 2	none	-2.74

Table 4.3 Assignment of ^{1}H NMR chemical shifts for **20** in $CDCl_3$.

The ^{1}H NMR spectrum was similar to the spectrum for **10** discussed in chapter 2 (**Table 4.3**). The porphyrin signals are located at similar chemical shifts. The pyridyl protons are shifted downfield relative to the phenyl protons of **10**. The inner NH protons are shifted upfield relative to those of **10**. The protons for the coupled linker have almost identical chemical shifts to those for **10**. For compound **18** the amide NH proton was located at δ 7.74. The downfield chemical shift corresponding to the amide NH protons ($\delta_F \sim 10$) for **10** and **20** suggests hydrogen bonding as was discussed in chapters 2 and 3.

Label	δ	Type	HMQC to ^{1}H at δ	HMBC to ^{1}H at δ
1	148.3	CH	9.05	8.17
2	129.4	CH	8.17	9.05
3	117.5	Q	none	8.17
4	117.1	Q	none	none
5	150.2	Q	none	none
7	150.1	Q	none	none
8	138.0	Q	none	none
9	121.1	Q	none	8.23
10	135.3	CH	8.23	none
11	119.1	CH	8.11	4.29
12	137.9	Q	none	8.23, 8.11
13	161.6	Q	none	8.58
14	150.8	Q	none	8.58, 7.98
15	134.0	CH	8.58	none
16	116.6	CH	8.04	7.98
17	127.3	Q	none	8.04, 7.98
18	107.1	CH	7.98	none
19	157.4	Q	none	4.29, 8.58, 7.98
20	57.3	CH_3	4.29	none

Table 4.4 Assignment of ^{13}C NMR chemical shifts for **20** in $CDCl_3$.

As for the ^{1}H NMR spectrum, the ^{13}C NMR spectrum for **20** was similar to that of **10** except for the pyridyl carbons which were located more downfield than the phenyl carbons of **10** **(Table 4.4).**

4.2.1.4. Free base 5,10,15-tris(*N*-methyl-4-pyridiniumyl)-20-[4-[(2-methoxy-4-nitro-phenylcarbonyl)-amino] phenyl] porphyrin tris iodide, 21.

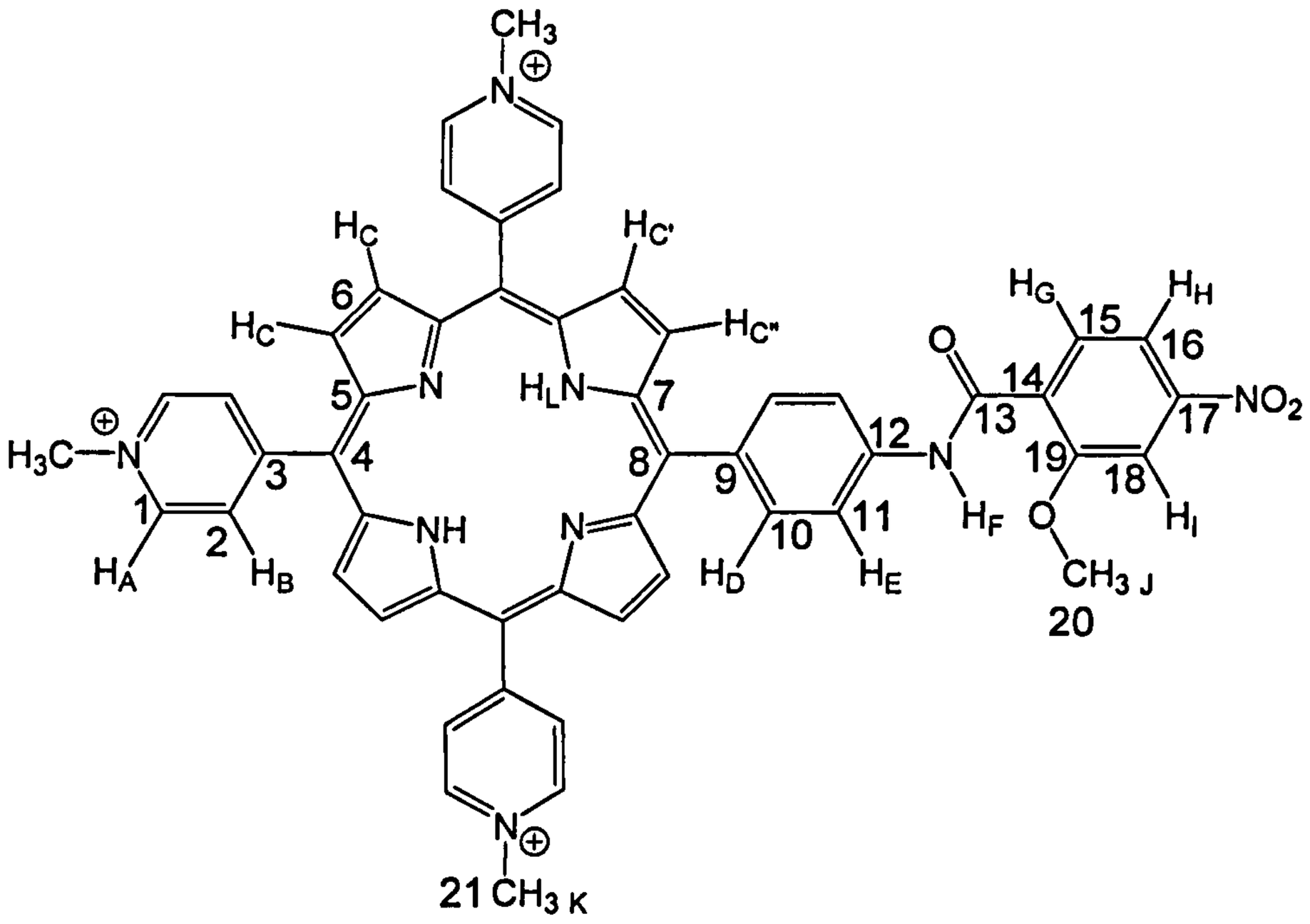

Figure 4.8 21 with atom labels: letters assigned to protons and numbers assigned to carbons.

Table 4.5 lists the ^{1}H chemical shifts for **21** and the numbering system is shown in **Figure 4.8.** In general the signals for **21** were broader than for the previous spectra due to the solvent. The amide NH proton was shifted considerably downfield and the inner protons were shifted considerably upfield relative to **20,** due to hydrogen bonding with the solvent[6]. The pyridyl protons, **A** and **B,** and porphyrin protons, **C,** were shifted downfield due to their proximity to the positive charge. The phenyl protons of the bridge were present at similar chemical shift as in the ^{1}H NMR spectrum of **21.**

Label	δ	Integration	Multiplicity	Type	COSY to ^{1}H at δ
A	9.49	6	d	CH × 6	4.73, 9.01
B	9.01	6	m	CH × 8	9.49
C	9.18 9.10	8	m	CH × 8	none
D, E	8.25	4	m	CH × 4	none
F	10.92	1	s	NH	none
G	7.94	1	m	CH	none
H	8.03	1	m	CH	7.94
I	8.03	1	s	CH	8.03
J	4.12	3	s	CH_3	none
K	4.73	9	s	CH_3 × 3	9.49
L	–2.98	2	s	NH × 2	none

Table 4.5 Assignment of ^{1}H NMR chemical shifts for **21** in d_6-DMSO.

Label	δ	Type	HMQC to ^{1}H at δ	HMBC to ^{1}H at δ
1	144.7	CH	9.49	4.73, 9.49, 9.01
2	132.6	CH	9.01	9.49, 9.18, 9.01
3	115.8	Q	none	9.01
4	115.0	Q	none	none
5	157.1	Q	none	none
7	157.0	Q	none	9.49
8	139.7	Q	none	8.25
9	123.2	Q	none	none
10	135.4	CH	8.25	none
11	118.7	CH	8.25	10.92
12	136.2	Q	none	8.25
13	164.5	Q	none	10.92

14	150.0	Q	none	8.03
15	130.6	CH	7.94	none
16	116.2	CH	8.03	none
17	127.6	Q	none	none
18	107.5	CH	8.03	none
19	157.4	Q	none	4.12, 8.04, 7.94
20	57.3	CH_3	4.12	none
21	48.5	CH_3	4.73	9.49

Table 4.6 Assignment of ^{13}C NMR chemical shifts for **21** in d_6-DMSO.

The signals in the ^{13}C NMR spectra were not shifted to the extent of the protons (**Table 4.6**). The strong resonance at δ 48.5 was assigned to the pyridinium methyl groups (**21**).

4.2.1.5. Free base 5,10,15-tris(*N*-methyl-4-pyridiniumyl)-20-[4-[(2-methoxy-4-amino-phenylcarbonyl)-amino] phenyl] porphyrin, 22.

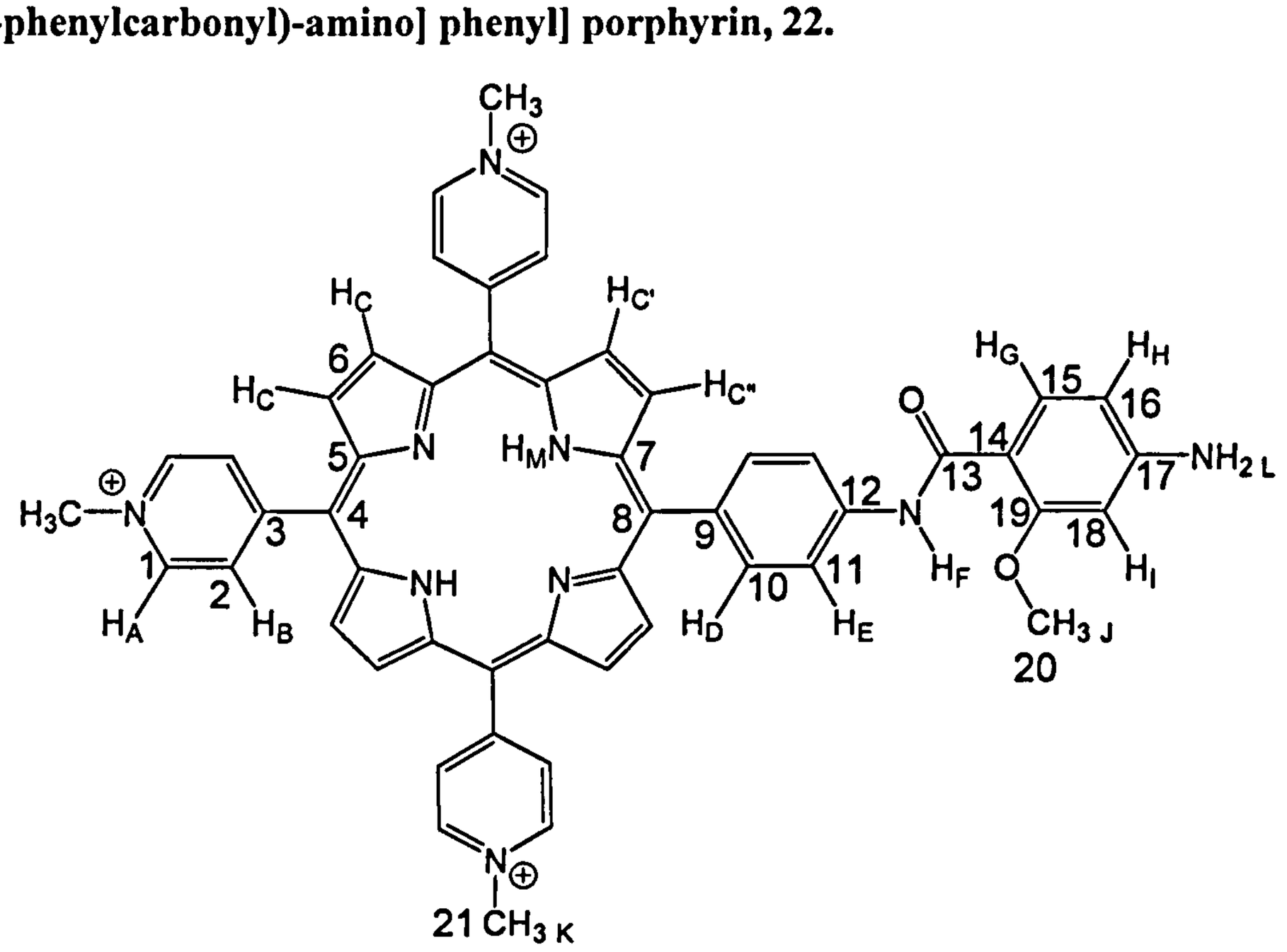

Figure 4.9 22 with atom labels: letters assigned to protons and numbers assigned to carbons.

Label	δ	Integration	Multiplicity	Type	COSY to ^{1}H at δ
A	9.53	6	m	CH × 6	4.73, 9.00
B	9.00	6	m	CH × 6	9.53
C	9.13	8	m	CH × 8	none
D	8.21	2	d	CH × 2	8.19
E	8.19	2	d	CH × 2	8.21
F	10.21	1	s	NH	none
G	7.74	1	d	CH	6.33
H	6.33	1	dd	CH	7.74, 6.40
I	6.40	1	d	CH	6.33
J	4.01	3	s	CH_3	none
K	4.73	9	s	CH_3 × 3	9.53
L	5.97	2	br s	NH_2	none
M	-2.99	2	s	NH × 2	none

Table 4.7 Assignment of ^{1}H NMR chemical shifts for **[22]**$[Cl]_3$ in d_6-DMSO.

On reduction of the nitro group the chemical shifts for the porphyrin protons remained unchanged (**Table 4.7**). The protons on the linker, including the amide proton and the methoxy protons, were shifted upfield significantly as for the TPP derivatives. The amine protons were located at δ 5.97, which is more downfield than **12** because of hydrogen bonding to the solvent.

Label	δ	Type	HMQC to ^{1}H at δ	HMBC to ^{1}H at δ
1	144.7	CH	9.53	4.73, 9, 9.53
2	132.6	CH	9.00	9.53
3	115.8	Q	none	none
4	114.9	Q	none	none
5	157.1	Q	none	none
7	157.0	Q	none	9.53
8	140.3	Q	none	8.19
9	123.6	Q	none	none
10	135.4	CH	8.21	none
11	118.8	CH	8.24	10.21
12	135.7	Q	none	8.21
13	164.7	Q	none	none
14	154.6	Q	none	7.74
15	133.2	CH	7.74	none
16	107.0	CH	6.33	6.4
17	109.7	Q	none	6.33, 6.4
18	96.6	CH	6.40	none
19	159.6	Q	none	4.01, 7.74
20	56.3	CH_3	4.01	none
21	48.3	CH_3	4.73	9.53

Table 4.8 Assignment of ^{13}C NMR chemical shifts for **[22]**$[Cl]_3$ in d_6-DMSO.

As for the ^{1}H NMR spectrum, the ^{13}C resonances were unchanged for the porphyrin carbons and shifted upfield for the linker carbons, 14-19 (**Table 4.8**).

4.2.1.6. Free base 5,10,15-tris(*N*-methyl-4-pyridiniumyl)-20-[4-{(2-methoxy-4-[(pyridine-4-carbonyl)-amino]-phenylcarbonyl)-amino} phenyl]-porphyrin, 24.

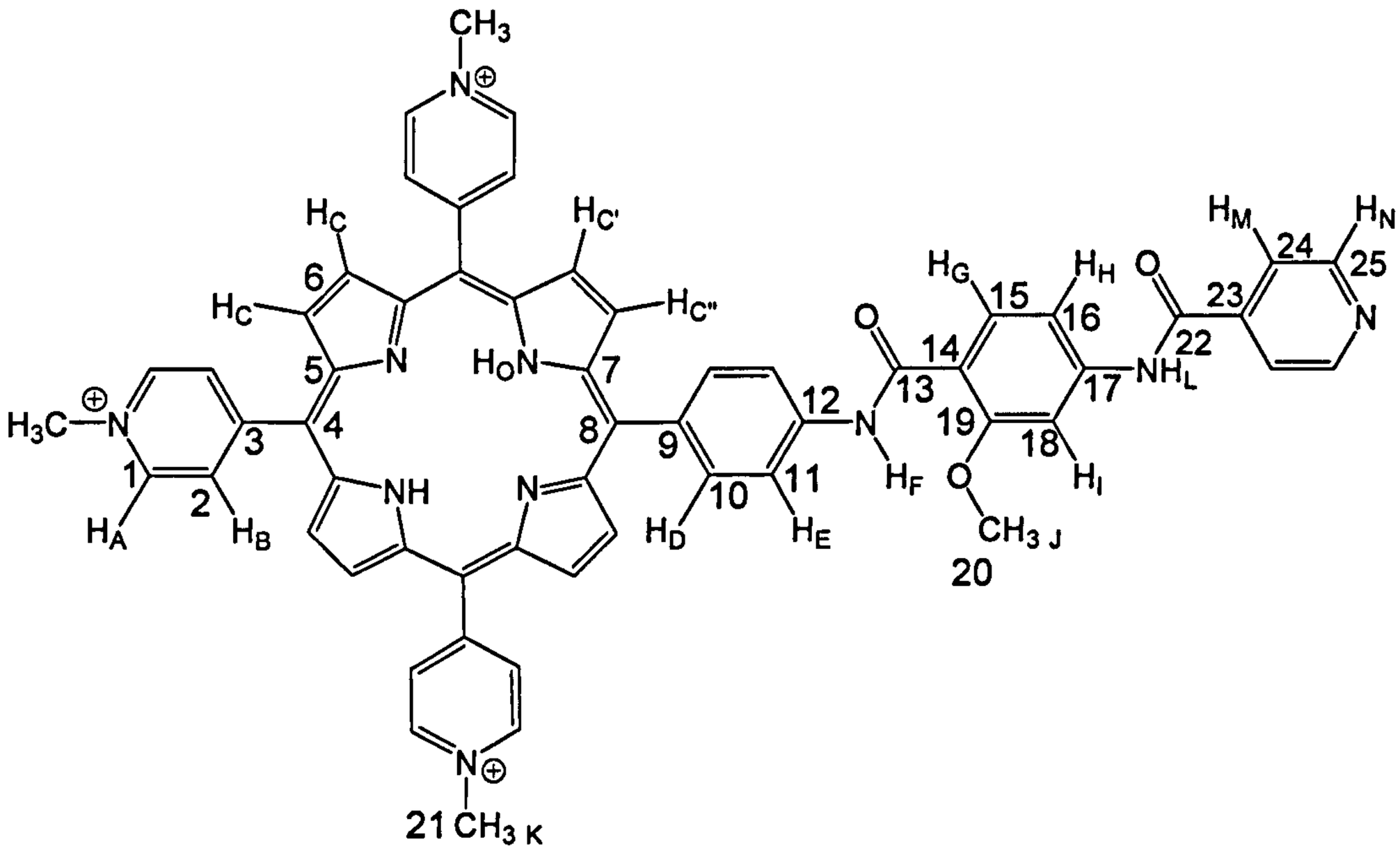

Figure 4.10 24 with atom labels: letters assigned to protons and numbers assigned to carbons.

The ^{1}H NMR chemical shifts for **[24]**[Cl]$_3$ are listed in **Table 4.9.** The numbering scheme is shown in **Figure 4.10**. The additional doublets at δ 8.35 and overlapping with B at δ 9.01 correspond to the pyridyl protons. Two amide signals are located at δ 11.35 and 10.58. F is shifted further upfield due to hydrogen bonding to the neighbouring methoxy compared to L for which there is no neighbouring hydrogen bond acceptor. L is shifted upfield compared to that recorded for **6** (δ 8.04, chapter 2) possibly due to hydrogen bonding to the solvent (**6** was recorded in $CDCl_3$).

Label	δ	Integration	Multiplicity	Type	COSY to ^{1}H at δ
A	9.55	6	m	CH × 6	4.75,9.01
B, M	9.01	8	m	CH × 8	9.55
C	9.10	8	m	CH × 8	none
D	8.29	2	d	CH × 2	8.23
E	8.23	2	d	CH × 2	8.23
F	11.35	1	s	NH	none
G	7.87	1	s	CH	7.72
H	7.72	1	d	CH	7.87
I	7.95	1	s	CH	none
J	4.06	3	s	CH_3	none
K	4.75	9	s	CH_3 × 3	9.55
L	10.58	1	s	NH	none
N	8.35	2	d	CH	9.01
O	–2.95	2	d	NH × 2	none

Table 4.9 Assignment of ^{1}H NMR chemical shifts for **[24]**$[Cl]_3$ in d_6-DMSO.

4.2.2 Zinc Porphyrins

4.2.2.1. Zinc 5,10,15-tris(*N*-methyl-4-pyridiniumyl)-20-[4-[(2-methoxy-4-amino-phenylcarbonyl)-amino] phenyl] porphyrin, 23.

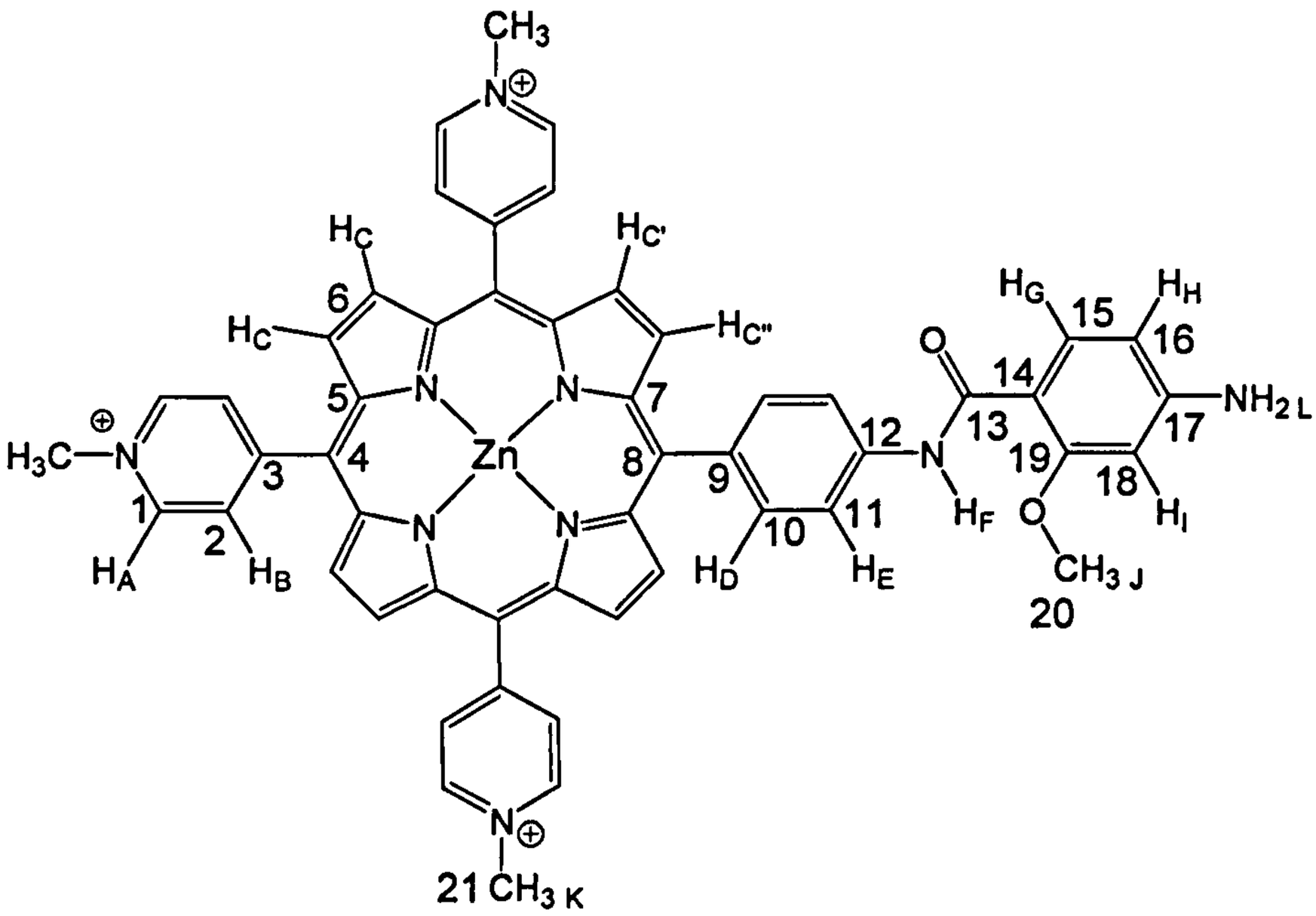

Figure 4.11 23 with atom labels: letters assigned to protons and numbers assigned to carbons.

On addition of zinc, the chemical shifts for the linker protons remained unchanged (**Table 4.10**). The protons on the porphyrin itself were shifted slightly. The signals were too broad to enable assignment from the 2D ^{13}C-^{1}H experiments. However, the majority of the peaks were unaffected by chelation of zinc. From the comparison with the spectra for the free-base compound (**Table 4.8**), these are likely to be the linker carbon resonances (see experimental).

Label	δ	Integration	Multiplicity	Type	COSY to ^{1}H at δ
A	9.41	6	m	CH × 6	4.70, 8.88
B	8.88	6	m	CH × 6	8.98
C	8.98	8	m	CH × 8	none
D	8.17	2	d	CH × 2	8.10
E	8.10	2	d	CH × 2	8.17
F	10.18	1	s	NH	none
G	7.76	1	s	CH	6.33
H	6.32	1	d	CH	7.76
I	6.39	1	s	CH	none
J	4.02	3	s	CH_3	none
K	4.70	9	s	CH_3 × 3	8.98
L	5.95	2	br s	NH_2	none

Table 4.10 Assignment of ^{1}H NMR chemical shifts for **[23]**$[Cl]_3$ in d_6-DMSO.

4.2.2.2. Zinc 5,10,15-tris(*N*-methyl-4-pyridiniumyl)-20-[4-{(2-methoxy-4-[(pyridine-4-carbonyl)-amino]-phenylcarbonyl)-amino} phenyl]-porphyrin, 25.

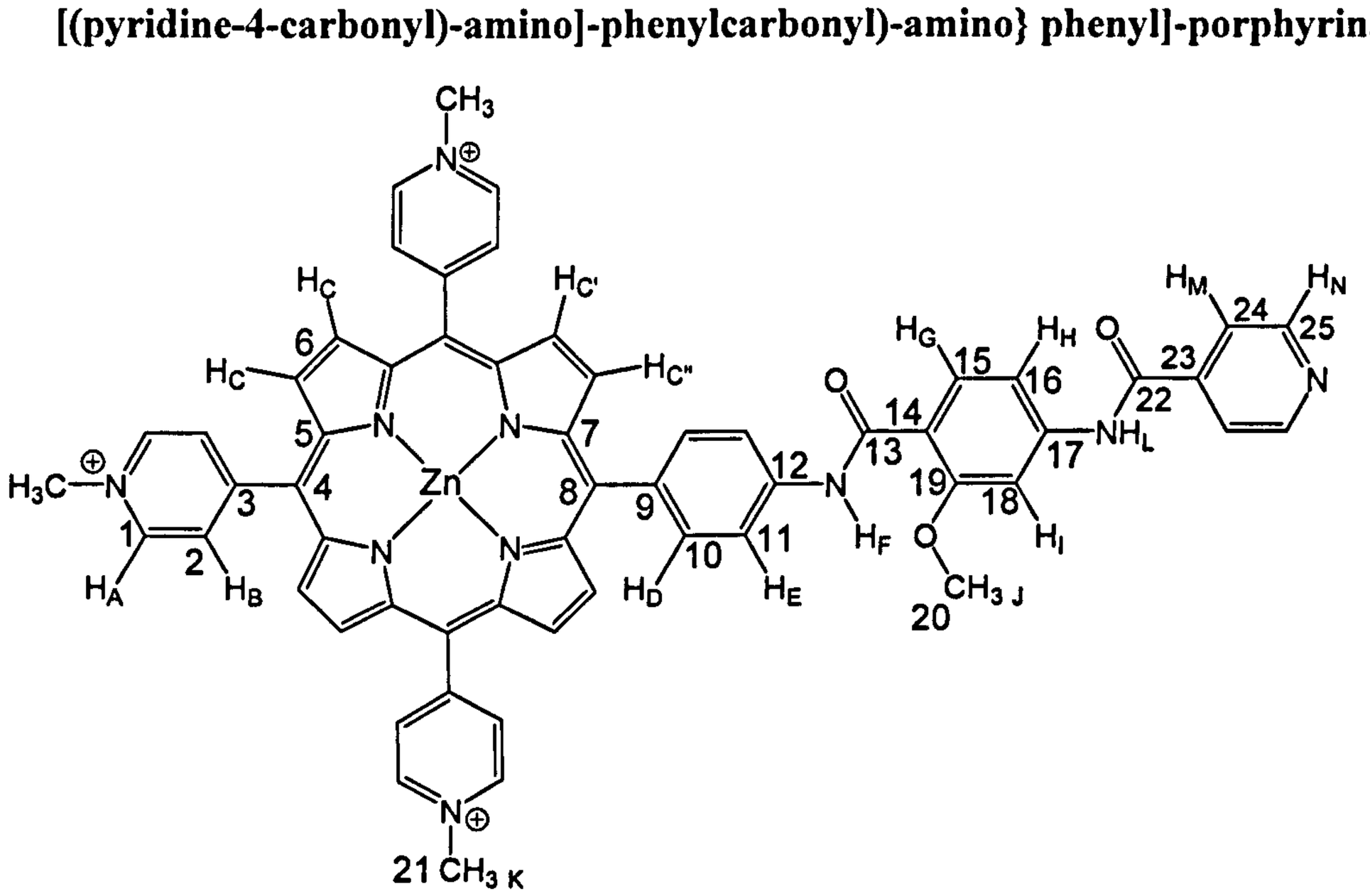

Figure 4.12 25 with atom labels: letters assigned to protons and numbers assigned to carbons.

As for **23**, the resonances for the porphyrin protons were shifted slightly on incorporation of zinc (**Table 4.11**). However, the chemical shifts for the linker protons were also shifted upfield, possibly due to interaction of the pyridyl group on the linker interacting with the metal centre. As for the previous compound (**23**) the resonances were too broad to enable assignments of the ^{13}C signals by HMQC and HMBC experiments. However, the majority of signals were not greatly affected by chelation of zinc (see experimental).

Label	δ	Integration	Multiplicity	Type	COSY to ^{1}H at δ
A	9.48	6	m	CH × 6	4.75,8.92
B	8.92	6	m	CH × 6	8.47
C	9.00	8	m	CH × 8	none
D	8.23	2	d	CH × 2	8.14
E	8.14	2	d	CH × 2	8.23
F	11.18	1	s	NH	none
G	7.82	1	s	CH	7.69
H	7.69	1	d	CH	7.82
I	7.91	1	s	CH	none
J	4.05	3	s	CH_3	none
K	4.75	9	s	CH_3 × 3	9.48
L	10.98	1	s	NH	none
M	8.81	2	d	CH	7.99
N	7.99	2	d	CH	8.81

Table 4.11 Assignment of ^{1}H NMR chemical shifts for **[25]**$[Cl]_3$ in d_6-DMSO.

4.2.3 Infrared spectroscopy

The infrared spectra of **18 – 25** were similar to those of the TPP derivatives. Each contained broad bands at ~ 3300-3400 cm^{-1} corresponding to N-H stretching modes. The sharper N-H deformations were located at ~ 1590-1650 cm^{-1}. These bands are located at lower frequency for **20** and **21**, which may posess intramolecular hydrogen bonds, than those for **18** which can

only hydrogen bond intermolecularly. Compounds **24** and **25** contain one amide neighbouring a methoxy group which may hydrogen bond intramolecularly to the amide proton, and one which is not and can only hydrogen bond intermolecularly. As a result, a low frequency and a higher frequency deformation are observed as for the amine dervatives (**22, 23**). The carbonyl stretch for compound **18** was observed at 1671 cm^{-1}. The corresponding stretching frequencies for compounds **20 – 25** were red shifted (~1630 cm^{-1}) due to intramolecular hydrogen bonding which causes the carbon-oxygen bond to have more single bond character (**Scheme 4.7**).

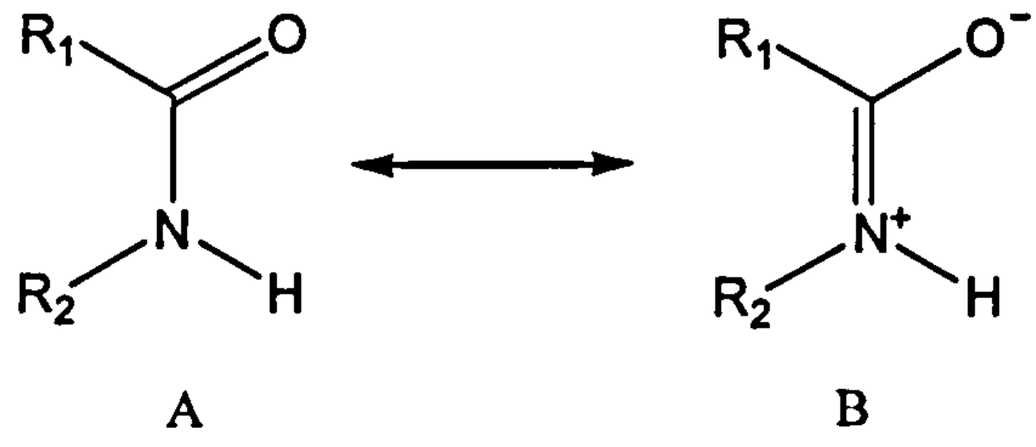

Scheme 4.7 Possible amide resonance structures. Hydrogen bonding favours **B**.

Sharp bands at ~ 2925 and 2850 cm^{-1} correspond to an asymmetric and symmetric stretch of the methoxy C-H bonds. These were matched by the corresponding asymmetric and symmetric deformations at ~ 1470 and 1350 cm^{-1}. Compounds **20** and **21** contained peaks at ~ 1520 and 1340 cm^{-1} typical of the asymmetric and symmetric stretching frequencies of a nitro group. The significant peaks in the infrared spectra of compounds **18 – 25** are summarised in **Table 4.12.**

Compound	18	19	20	21	22	23	24	25
C=O stretch	1671		1638	1638	1636	1636	1636	1637
N=O stretch			1522 1346	1521 1346				
N-H stretch	3432	3439 3321	3429	3430	3426	3428	3421	3443
N-H bend	1594	1593	1589	1589	1597 1509	1602 1508	1597 1521	1594 1526

Table 4.12 Summary of infrared absorption frequencies (KBr pressed disk in cm^{-1} for compounds **18-25.**

4.2.4 Electrospray mass spectrometry

As for the TPP derivatives, the $M + H^+$ adduct was observed for most of the compounds (**Table 4.13**). The spectra for the pyridyl porphyrins also contained peaks for the $[M + 2H^+]$ and $[M + 3H^+]$ adducts (see experimental). A different ionisation pathway was observed for **21**. A peak at *m/z* = 856 corresponding to reduction of the porphyrin, possibly by iodide ($M^{3+} + 2e^-$), was observed. Porphyrins **22** and **23** were already charged and therefore the corresponding M^{3+} ions were observed.

Compound	Molecular Mass	Observed +ve ion *m/z*	Assignment
18	674	675	$M + H^+$
19	632	633	$M + H^+$
20	811	812	$M + H^+$
21	856	856	M^+
22	826	275	M^{3+}
23	888	296	M^{3+}
24	931	310	M^{3+}
25	993	331	M^{3+}

Table 4.13 Summary of molecular ion peaks *m/z* for **18 – 25.**

4.2.5 Ground state electronic spectroscopy

4.2.5.1. Free-base porphyrins

Table 4.14 lists the Soret and Q bands with corresponding extinction coefficients for the porphyrin absorption bands for the free base porphyrins **20 – 22,** and **24.** The spectra for each were characteristic of free base porphyrins. The Soret and Q_x bands of **20** are located closer to those of TMPyP than **21,** the methylated derivative, whereas the Q_y bands are located

closer to those of **21**. The difference in the Q_y bands between **20** and TMPyP could be a result of the substituent in the *yz* plane of **20** compared to the D_{2h} symmetry of TMPyP **(Figure 4.13)**.

Compound	S		Q1		Q2		Q3		Q4	
	λ_{max}	E	λ_{max}	ε	λ_{max}	ε	λ_{max}	ε	λ_{max}	ε
20*	422	167000	516	8210	552	4140	590	2710	647	1790
TMPyP	422	235000	518	16300	554	6430	585	7520	640	2000
21	431	142000	524	12300	564	7710	592	6350	649	2630
22	429	124000	522	9780	564	8750	595	5840	653	3510
24	434	117000	524	11600	566	11800	598	8120	620	6520

Table 4.14 Summary of porphyrin Q and Soret (S) absorption maxima in nm and ε in $dm^3mol^{-1}cm^{-1}$ for free base porphyrins TMPyP, **21**, **[22]**$[Cl]_3$ and **[24]**$[Cl]_3$ in 0.5 mM potassium phosphate buffer, pH 7.5. * **20** in chloroform.

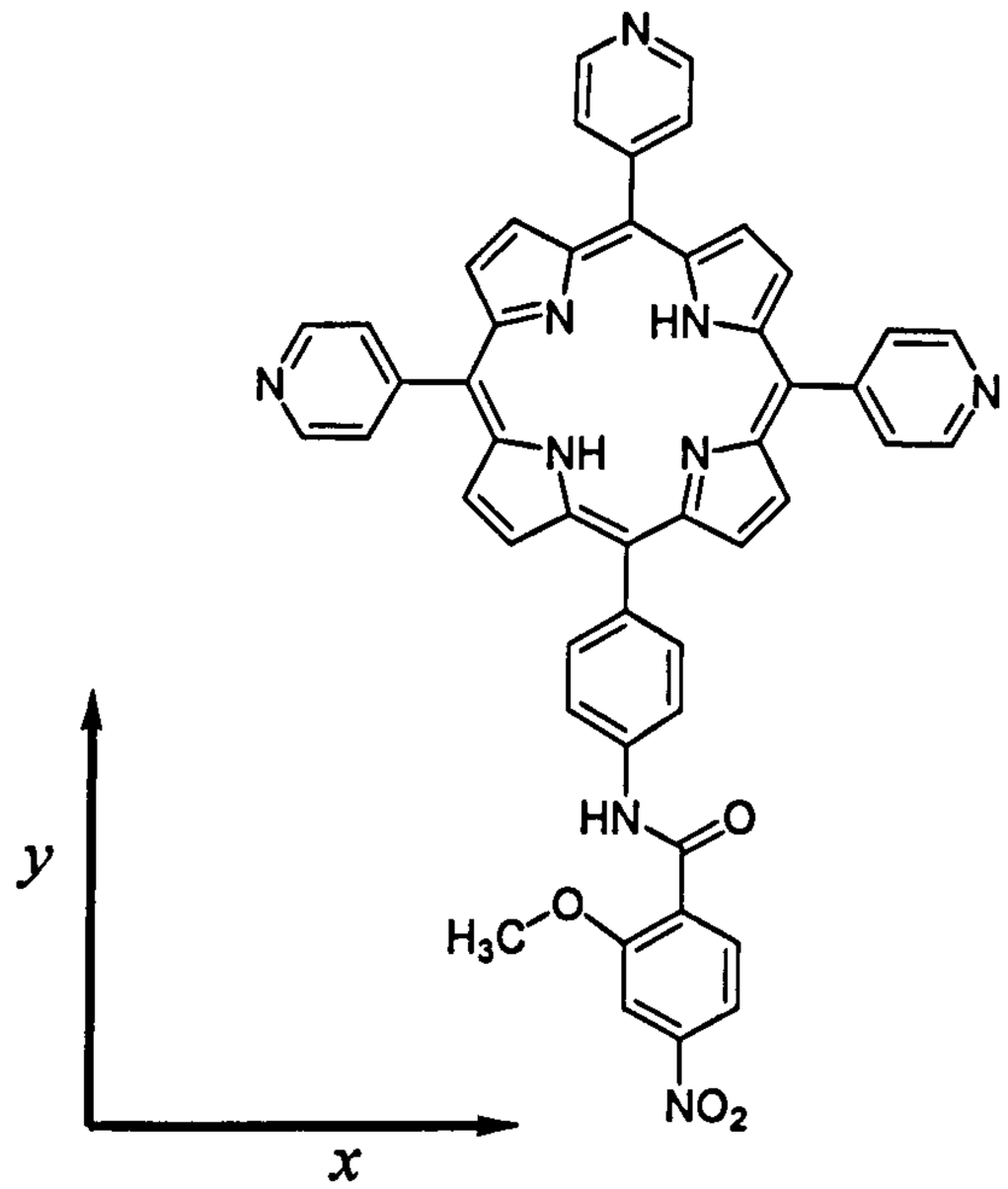

Figure 4.13 20 with labelled axes.

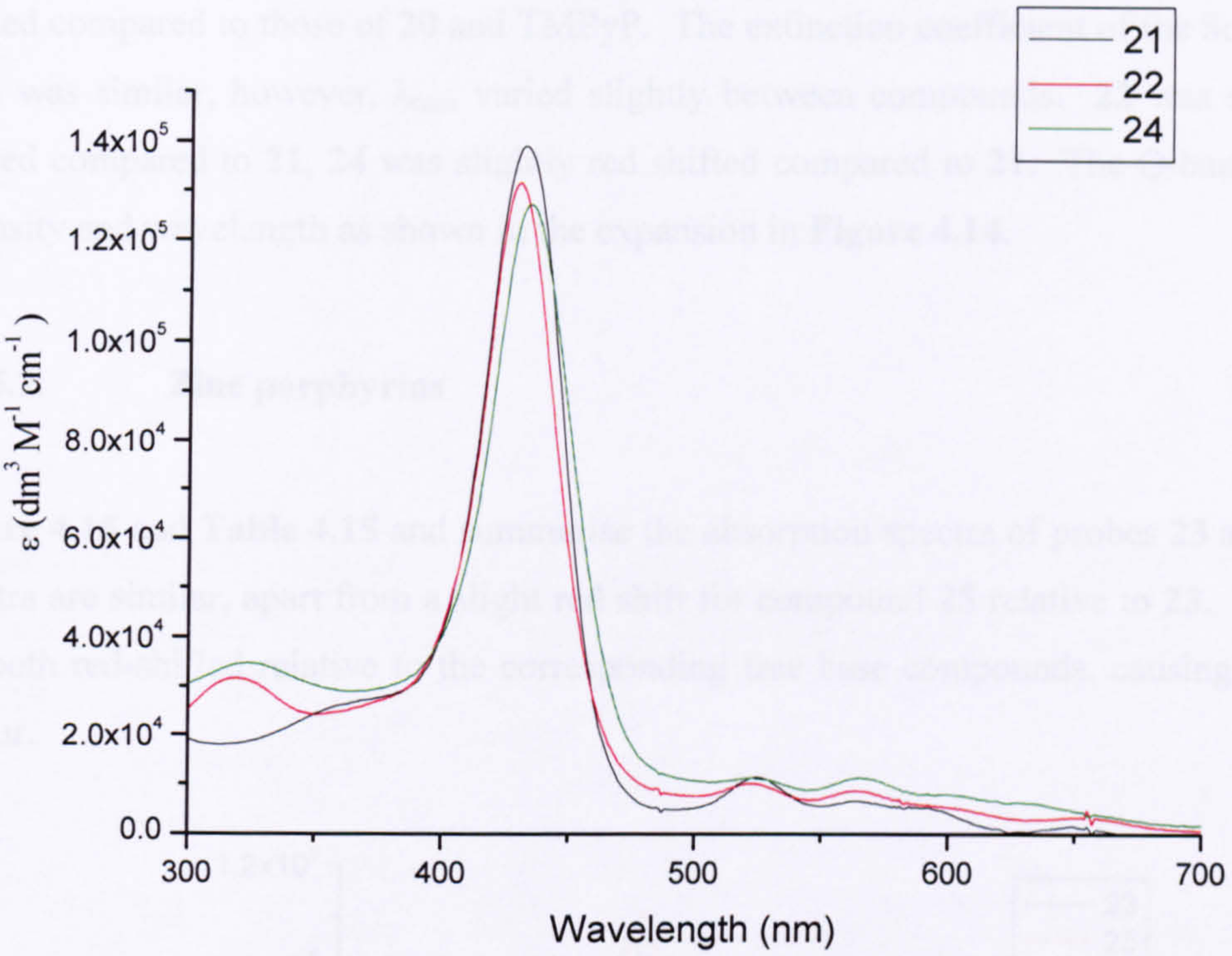

Figure 4.14 Ground state electronic absorption spectra of **21, 22** and **24** in 50mM potassium phosphate buffer, pH 7.5. Bottom: expansion to show the Q-bands. Original in colour.

The absorption spectra for **21**, **22** and **24** shown in **Figure 4.14** were all substantially red-shifted compared to those of **20** and TMPyP. The extinction coefficient of the Soret band for each was similar, however, λ_{max} varied slightly between compounds. **22** was slightly blue shifted compared to **21**, **24** was slightly red shifted compared to **21**. The Q-bands varied in intensity and wavelength as shown in the expansion in **Figure 4.14**.

4.2.5.2. Zinc porphyrins

Figure 4.15 and **Table 4.15** and summarise the absorption spectra of probes **23** and **25**. The spectra are similar, apart from a slight red shift for compound **25** relative to **23**. The spectra are both red-shifted relative to the corresponding free base compounds, causing their green colour.

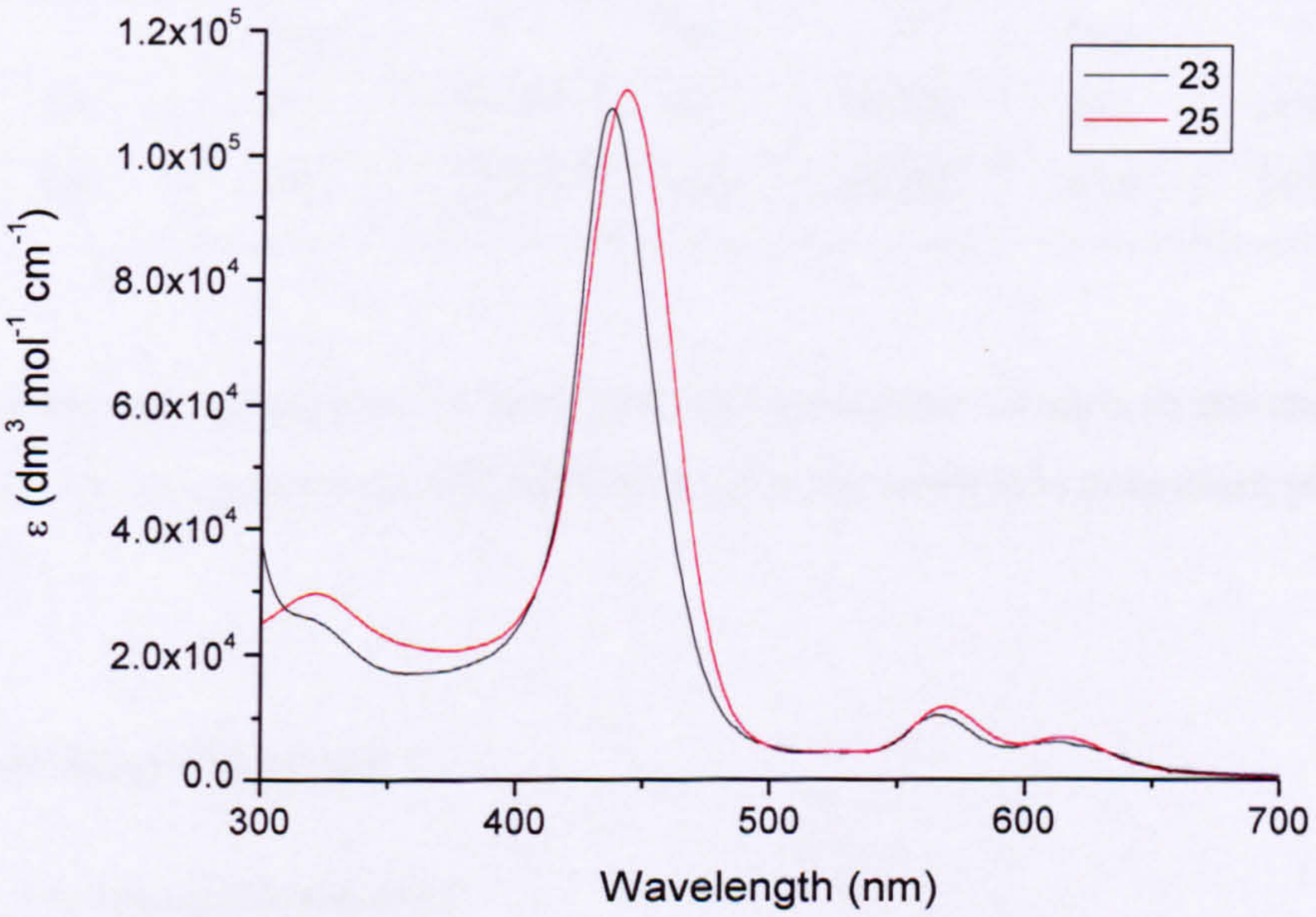

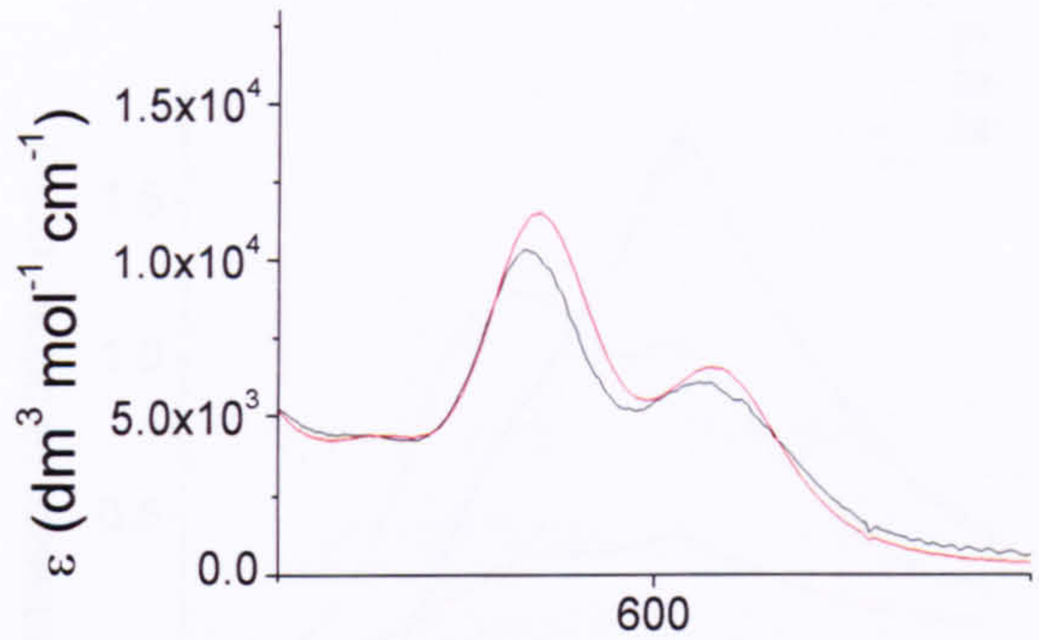

Figure 4.15 Ground state electronic absorption spectra of [**23**][Cl]$_3$ and [**25**][Cl]$_3$ in 50 mM potassium phosphate buffer, pH 7.5. Bottom: expansion to show the Q-bands. Original in colour

Compound	S		Q1		Q2	
	λ_{max}	ε	λ_{max}	ε	λ_{max}	ε
23	436	108000	565	10300	615	6040
25	442	110000	569	11500	614	6520

Table 4.15 Summary of porphyrin Q and Soret (S) absorption maxima in nm and ε in $dm^3mol^{-1}cm^{-1}$ for zinc porphyrins [**23**][Cl]$_3$ and [**25**][Cl]$_3$ in 50 mM potassium phosphate buffer, pH 7.5.

4.2.6 Steady State Fluorimetry

4.2.6.1. Free-base porphyrins

Figure 4.16 shows the emission spectrum of free base porphyrins **21,** [**22**][Cl]$_3$ and [**24**][Cl]$_3$. Spectra shown in the same graph are obtained from solutions optically matched at the excitation wavelength. The emission spectrum of **21** was similar to that of TMPyP in shape and λ_{max}; the quantum yield was 50% of that of TMPyP. The quantum yields of **22** and **24** were much lower and the spectra contained a more intense shoulder at shorter wavelength.

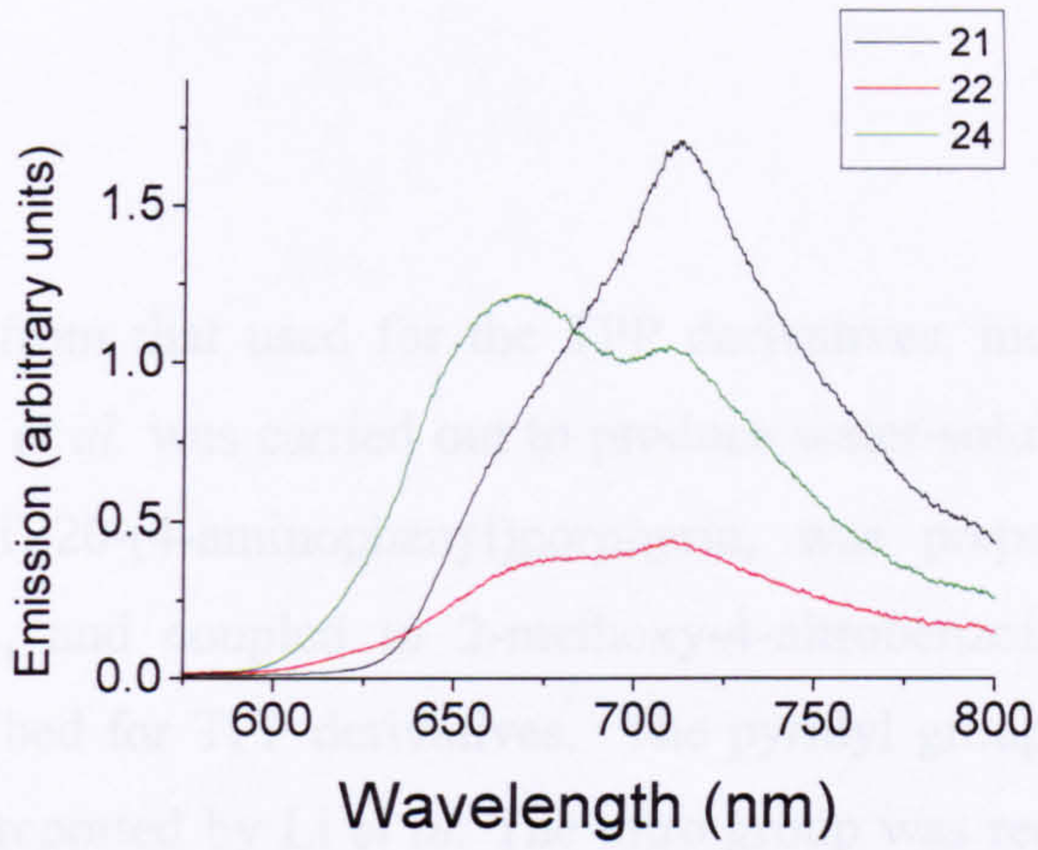

Figure 4.16 Corrected and optically matched emission spectra for **21,** [**22**][Cl]$_3$ and [**24**][Cl]$_3$ in 50mM potassium phosphate buffer, pH 7.5. λ_{ex} = 420 nm. Original in colour.

4.2.6.2. Zinc porphyrins

The emission spectra for the zinc porphyrins **23** and **25** are shown in **Figure 4.17**. The spectra are similar in intensity and λ_{max}. The spectra are blue-shifted and more intense relative to the free base derivatives.

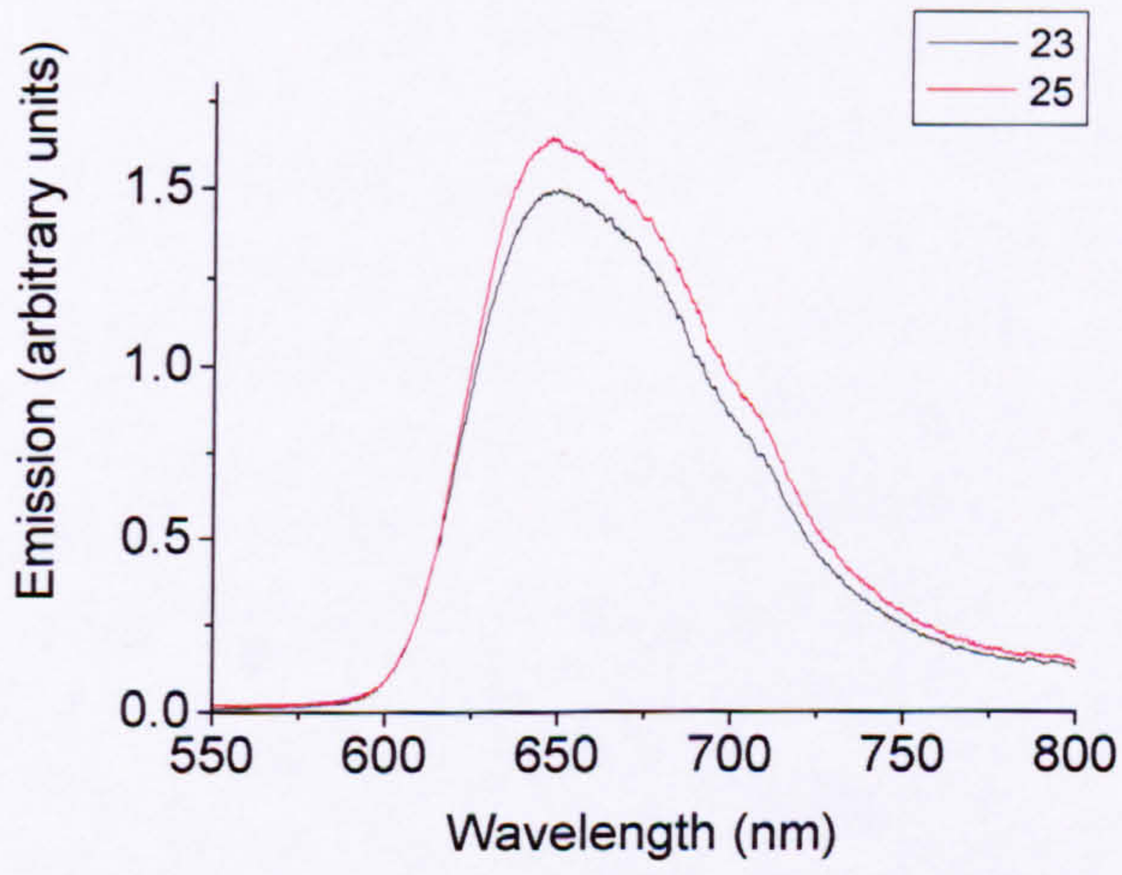

Figure 4.17 Corrected and optically matched emission spectra for [**23**][Cl]$_3$ and [**25**][Cl]$_3$ in 50mM potassium phosphate buffer, pH 7.5. λ_{ex} = 435 nm.

4.3 Summary

4.3.1 Synthesis

A procedure modified from that used for the TPP derivatives, incorporating some of the methods reported by Li *et al.* was carried out to produce water-soluble porphyrins **21** to **25**. 5, 10, 15-tris(4-pyridyl)-20-(4-aminophenyl)porphyrin, was prepared using the method described by Li *et al*., and coupled to 2-methoxy-4-nitrobenzoic acid using the DCC mediated method described for TPP derivatives. The pyridyl groups were then methylated using methyl iodide as reported by Li *et al.* The nitro group was reduced using indium and ammonium chloride and the substrate was coupled to the resulting amine. Indium was not introduced to the pyridinium porphyrin since the electron withdrawing groups reduce the basicity of the pyrrole nitrogens. Anion exchange was used to modify the solubility of the porphyrins and to purify the compounds at each stage. The application of the synthetic procedure (peptide coupling of a nitro substituted benzoic acid derivative to an amino porphyrin, reduction to give the amine, followed by coupling to a second unit) to both hydrophobic (TPP) and hydrophilic (TMPyP) porphyrins demonstrated the versatility of the reactions involved. A summary is illustrated in **Scheme 4.8**.

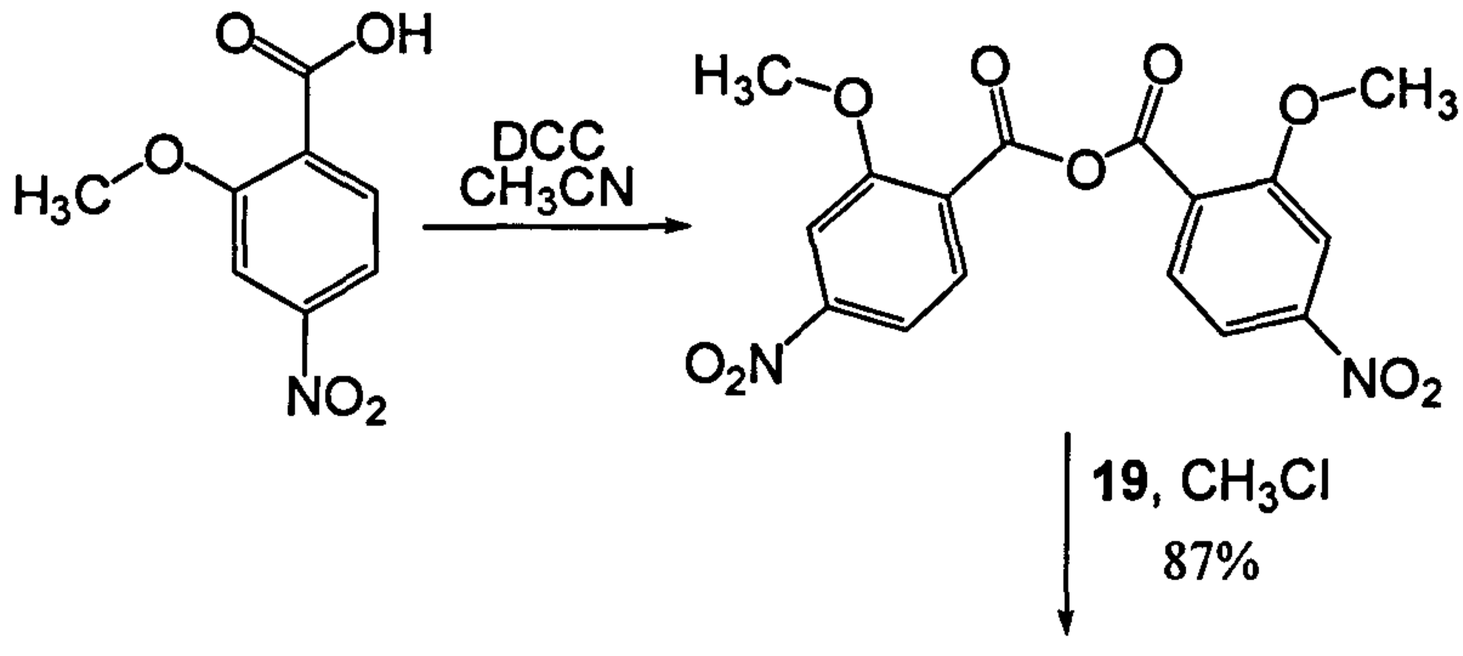

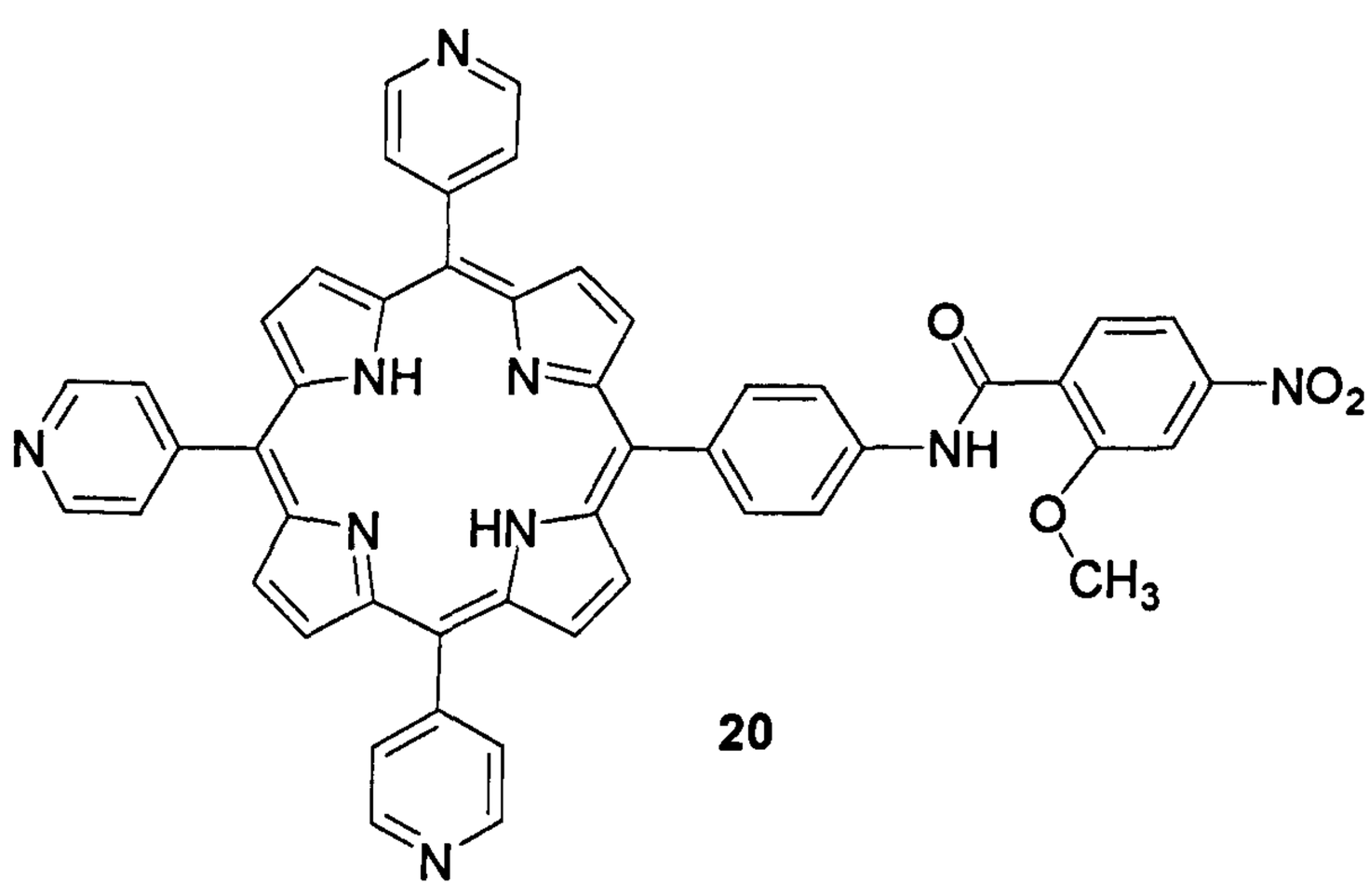

20

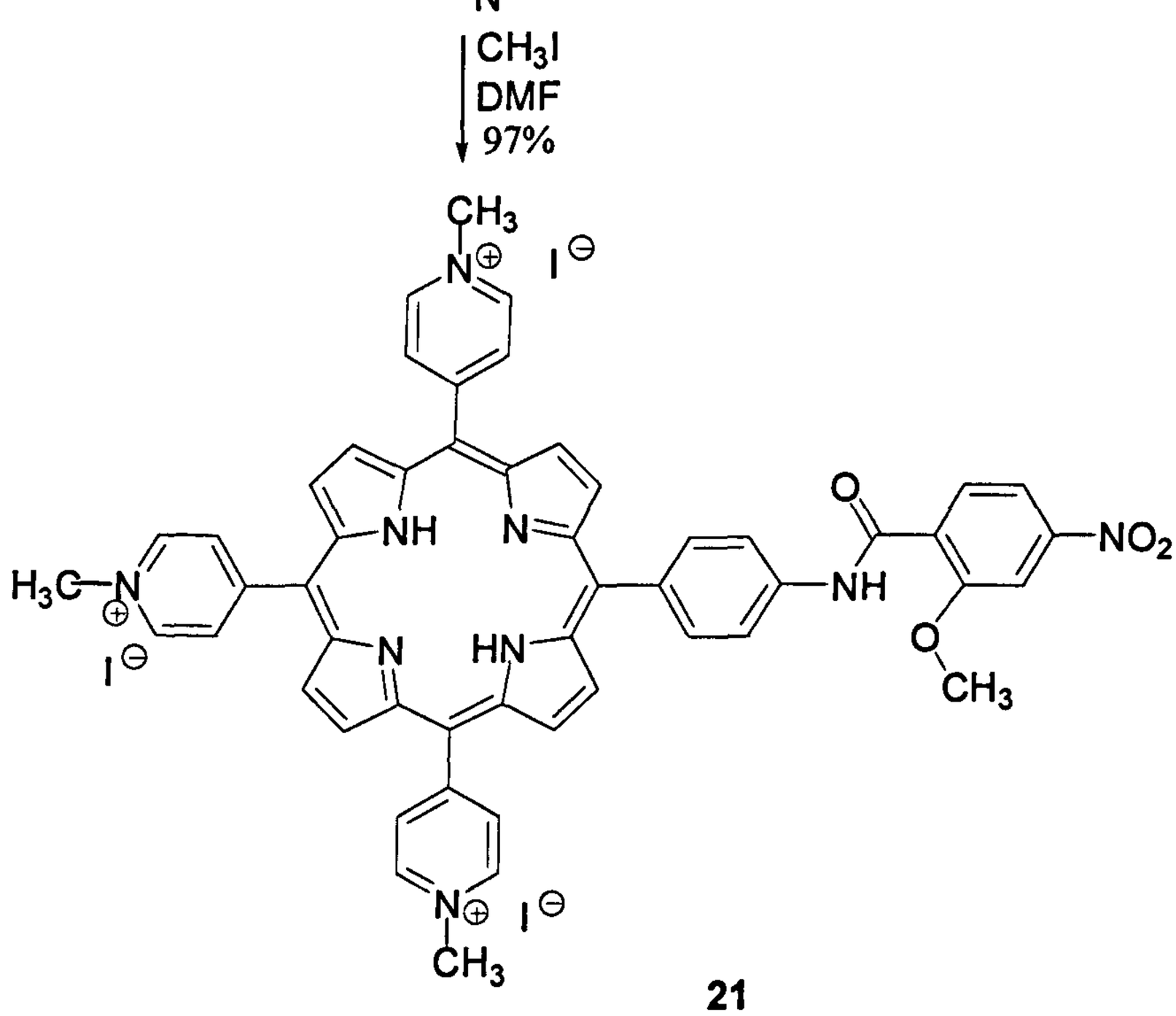

21

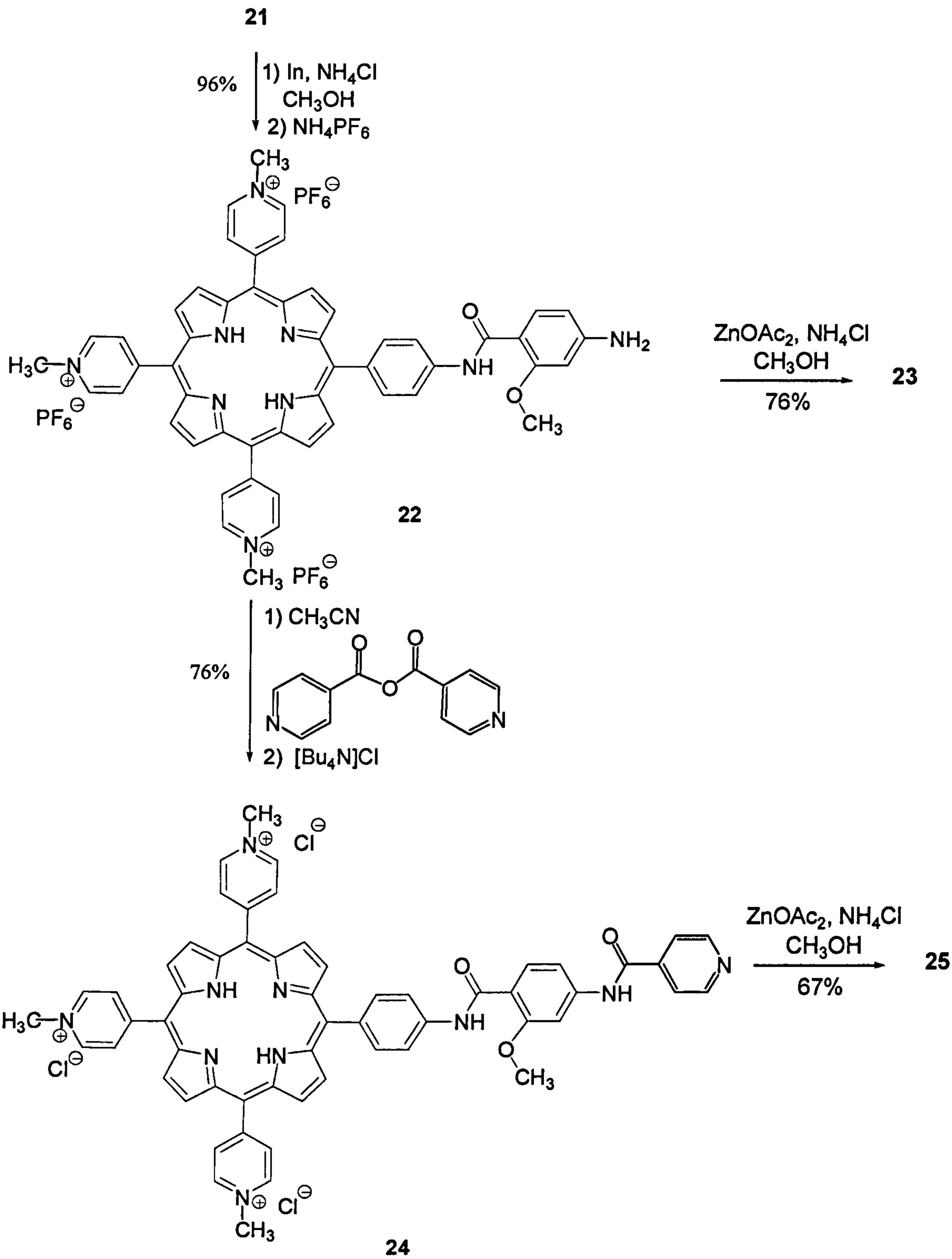

Scheme 4.8 Synthesis of water-soluble probe **25**.

4.3.2 Characterisation

Porphyrins **18 – 25** were characterised by ^{1}H, ^{13}C NMR, FTIR and UV-Vis spectroscopy and ESI-MS.

The ^{1}H and ^{13}C NMR spectra were similar to those for the TPP derivatives. ^{1}H-^{1}H COSY, ^{1}H-^{13}C HMQC and HMBC experiments were carried out to enable full assignment of the ^{1}H and ^{13}C spectra.

For each of the porphyrins, a molecular ion peak was observed corresponding to $M + H^{+}$ for compounds **18 – 20** and for the water-soluble porphyrins **22 – 25** the M^{3+} molecular ion was observed. The exception was compound **21** which appeared to be reduced, possibly by the iodide counter ions, for which a peak corresponding to the singly charged molecular ion ($M^{3+} + 2e^{-}$) was observed.

The infrared spectra contained the same characteristic absorption bands for each porphyrin. Notably the carbonyl stretch, N-H stretch and deformation and for compounds **20** and **21** the N=O symmetric and asymmetric stretch were assigned.

Each porphyrin displayed intense absorption bands in the visible region. The extinction coefficient and λ_{max} of the intense Soret band as well as the Q-bands varied significantly with the nature of the functional groups i.e. nitro, amine vs pyridine. In contrast to the TPP derivatives, the extinction coefficients for the zinc porphyrin were lower than those of the free base porphyrins, possibly as a result of coordination to water.

Compounds **18 – 25** each gave broad emission bands between 600 and 800 nm upon excitation at 420 nm. The quantum yields were lower than that of TMPyP but were sufficiently high to compete with absorption from XO in assay conditions.

4.4 References

1. W. J. Kruper, T. A. Chamberlin, M. Kochanny, *J. Org. Chem.*, **1989**, *54*, 2753.
2. P. Hambright, *The Porphyrin Handbook, 18 Chemistry of Water Soluble Porphyrins*; K. M Kadish, K. M Smith, R. Guilard, Eds., Volume 3 / Inorganic, Organometallic and Coordination Chemistry, 2000, Academic Press.
3. C. R. Lefley, PhD Thesis, **1994**, University of York.
4. H. Li, O. S. Fedorova, A. N. Grachev, W. R. Trumble, G. A. Bohach, L. Czuchajowski, *Biochim. Biophys. Acta*, **1997**, *1354*, 252.
5. M. Gardner, A. J. Guerin, C. A. Hunter, U. Michelsen, C. Roger, *New J. Chem.*, **1999**, 309.
6. A. Gabrielsson, PhD Thesis, **2002**, University of York.
7. R. Miyatani, Y. Amao, *Photochem. Photobiol. Sci.*, **2004**, *3*, 681.

CHAPTER FIVE

ENZYME INIBITION STUDIES

5 Enzyme Inhibition Studies

5.1 Introduction

In order to compare the binding affinity of the compounds prepared, enzyme affinity bioassays were carried out. Understanding the kinetics of the enzyme of interest is essential when selecting the appropriate conditions for the bioassay. Therefore, some of the fundamentals will be discussed so as to highlight some general considerations and more specific issues relating to the XO activity assay.

5.1.1 Historical Overview

Early kinetic studies of unireactant enzymes led to the general rate equations shown below, (1), for the following reaction:

$$E + S \underset{k_{-1}}{\overset{k_1}{\rightleftharpoons}} ES \xrightarrow{k_p} E + P$$

Where E is the free enzyme, S is the free substrate, ES is the enzyme substrate complex and P is the free product.

The Henri equation[1]:

$$\upsilon = \frac{K[S]}{1 + [S]/K_S} \qquad (1)$$

[S] = a fixed enzyme concentration

υ = initial velocity at the given [S]

= $d[P] / dt$ or $-d[S] / dt$

k_p = rate constant for the breakdown of ES to E + P

K_S = the dissociation constant of the ES complex

= k_{-1} / k_1 = [E][S] / [ES]

K = a constant, characteristic of the enzyme preparation

= $k_p[E]_t / K_S$

$[E]_t$ = the total concentration of enzyme

= [E] + [ES]

The Henri equation can be applied to a reaction for which a number of assumptions are valid.

1) E is a catalyst.
2) E and S react rapidly to form ES (k_1 is fast).
3) Only a single S and a single ES are involved and ES breaks down directly to form free E and P.
4) E, S, and ES are at equilibrium: $k_{-1} >> k_p$.
5) [S] >> [E]: the formation of an ES complex does not alter [S].
6) The overall rate of the reaction is limited by the breakdown of the ES complex to form E and P.
7) The velocity is measured during the very early stages of the reaction so that the reverse reaction is insignificant.

To summarise, only the early components of the reaction are assumed to be at equilibrium. This is known as the rapid (quasi-) equilibrium assumption. Due to assumption 3, the rate is proportional to [ES], the only product forming species. This enables a kinetic expression to be obtained from an equilibrium expression ($[E]_t$ = [E] + [ES]). Equation (1) is more commonly known in the form below (3):

The Michaelis-Menten equation[1]:

$$\upsilon = \frac{k_p [E]_t [S]}{K_S + [S]} \qquad (2)$$

$$\upsilon = k_p[ES]$$

$$k_p[E]_t = V_{max}$$

$$\frac{\upsilon}{V_{max}} = \frac{[S]}{K_S + [S]} \qquad (3)$$

V_{max} = the limiting maximal velocity that would be observed when all the enzyme is present as ES.

Therefore, providing assumption 4 holds, exact steady state treatment can be avoided and a simple kinetic system can be used to model the mechanism of the enzyme.

Van Slyke derived a similar equation (4) based on the assumptions that the overall reaction occurred in two irreversible steps and that the time taken for the overall reaction was the sum of the times for each step.

$$E + S \xrightarrow{k_1} ES \xrightarrow{k_p} E + P$$

$$\upsilon = \frac{k_p [E]_t [S]}{K + [S]} \qquad (4)$$

This equation differs from the previous equations since K is the ratio of forward rate constants (k_p/k_1) instead of the equilibrium constant.

A generalized method was derived by Briggs and Haldane. This approach does not require ES to be in equilibrium with E and S (assumption 4), nor the irreversible reactions (Van Slyke). Instead it allows [ES] to be obtained from steady-state equations instead of equilibrium expressions.

$$E + S \xrightarrow{k_1} ES$$

$$ES \xrightarrow{k_{-1}} E + S$$

$$ES \xrightarrow{k_p} E + P$$

$$\left(+ \frac{d[ES]}{dt} \right) = k_1 [E] [S]$$

$$\left(- \frac{d[ES]}{dt} \right) = k_{-1} [ES] + k_p [ES] = (k_{-1} + k_p) [ES]$$

Within a very short time after starting the reaction, ES builds up to a near constant ('steady-state') level. At this point ES is formed at the same rate as it decomposes. As the ratio of $[S]_0/[E]_t$ (where $[S]_0$ is the initial substrate concentration) increases, the steady state assumption becomes more valid since the time taken to reach steady state conditions decreases and the duration under those conditions increases. Therefore, this approximation is appropriate for *in vitro* enzyme studies performed using a catalytic [E].

$$\left(+\frac{d[ES]}{dt}\right) = \left(-\frac{d[ES]}{dt}\right) \quad \text{or} \quad \frac{d[ES]}{dt} = 0$$

$$k_1[E]\,[S] = k_{-1}\,[ES] + k_p\,[ES] = (k_{-1} + k_p)\,[ES]$$

$$[ES] = \frac{k_1\,[S]}{(k_{-1} + k_p)}\,[E]$$

As for the previous approach:

$$\upsilon = k_p[ES]$$

$$\frac{\upsilon}{[E]_t} = \frac{k_p[ES]}{[E] + [ES]}$$

$$\frac{\upsilon}{k_p[E]_t} = \frac{\dfrac{k_1\,[S]}{(k_{-1} + k_p)}\,[E]}{[E] + \dfrac{k_1\,[S]}{(k_{-1} + k_p)}\,[E]}$$

$$k_p[E]_t = V_{max}$$

$$\frac{\upsilon}{V_{max}} = \frac{\dfrac{k_1\,[S]}{(k_{-1} + k_p)}}{1 + \dfrac{k_1\,[S]}{(k_{-1} + k_p)}}$$

$$K_m = \frac{k_{-1} + k_p}{k_1}$$

$$\frac{\upsilon}{V_{max}} = \frac{[S]}{K_m + [S]} \qquad (5)$$

K_m is the Michaelis constant. It is a dynamic or pseudo-equilibrium constant which expresses the relationship between the actual steady-state concentrations rather than the equilibrium concentrations. When $k_{-1} >> k_p$, $K_m \sim k_{-1} / k_1 \sim K_S$ (the dissociation constant for ES). When $k_{-1} << k_p$, $K_m \sim k_p / k_1$ (a kinetic constant). When more complex systems are examined, the final equation has the same form as that derived for rapid equilibrium conditions or steady-state conditions described here. The differences are the definitions of K_m and V_{max} with respect to the rate constants.

5.1.2 Significance of K_m[1]

- K_m relates the velocity of an enzyme-catalysed reaction to the substrate concentration:

$$\upsilon = \frac{[S]}{K_m + [S]} V_{max} \qquad (6)$$

- K_m is numerically equivalent to the substrate concentration that yields half-maximal velocity:

when $[S] = K_m$

$$\upsilon = \frac{K_m}{K_m + K_m} V_{max} = 1/2\ V_{max} \qquad (7)$$

- K_m is a means of comparing enzymes e.g. deduce those which are structurally different but catalyse the same reaction.
- K_m is a means of determining assay conditions where [S]>> K_m, from which V_{max} and $[E]_t$ can be estimated.
- Monitoring the effects of different compounds on K_m is a means of identifying new inhibitors/activators for a particular enzyme.

The last point is the basis of enzyme affinity bioassays whereby an inhibitor is added to a solution of an enzyme and a known substrate. The effect on the observed value of K_m compared to the inhibitor-free reaction indicates the relative binding strength of the inhibitor. Since K_m is required in order to choose the appropriate [S] in the assay, it must be calculated for the XO catalysed reaction.

5.1.3 Plotting υ against [S]

Figure 5.1 shows a plot of υ vs. [S] for an enzyme-catalysed reaction which obeys Michaelis-Menten kinetics. The curvature is fixed and independent of K_m and V_{max}. There are three distinct regions which have different reaction orders.

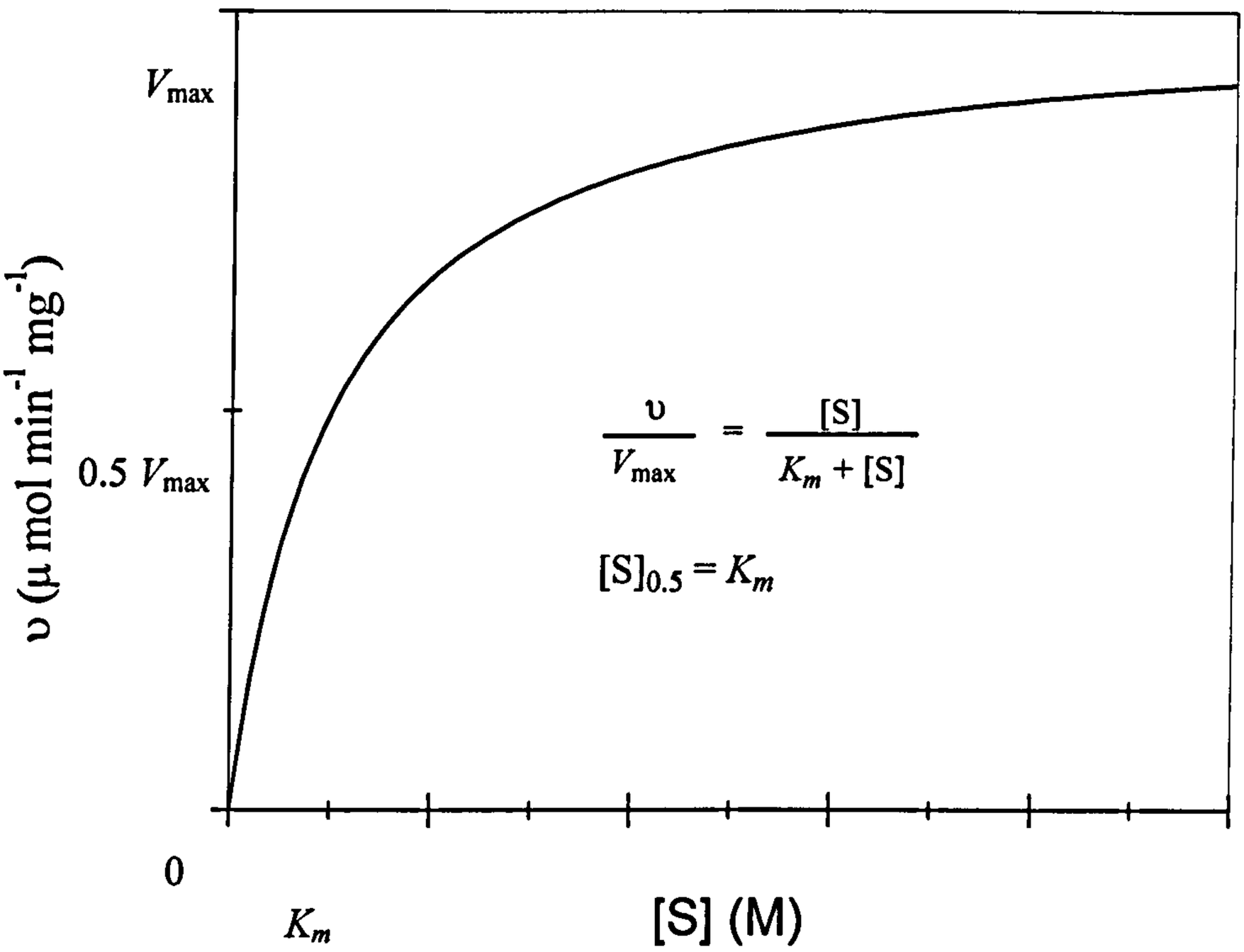

Figure 5.1 υ vs. [S] plot for a reaction obeying Michealis-Menten kinetics: $(V_{max} - \upsilon)(K_m + [S]) = K_m - V_{max}$[1,2]

5.1.3.1 First-Order Region

At low substrate concentrations ([S] < 0.01 K_m), the curve is approximately linear (υ proportional to [S]) (**Figure 5.2**)

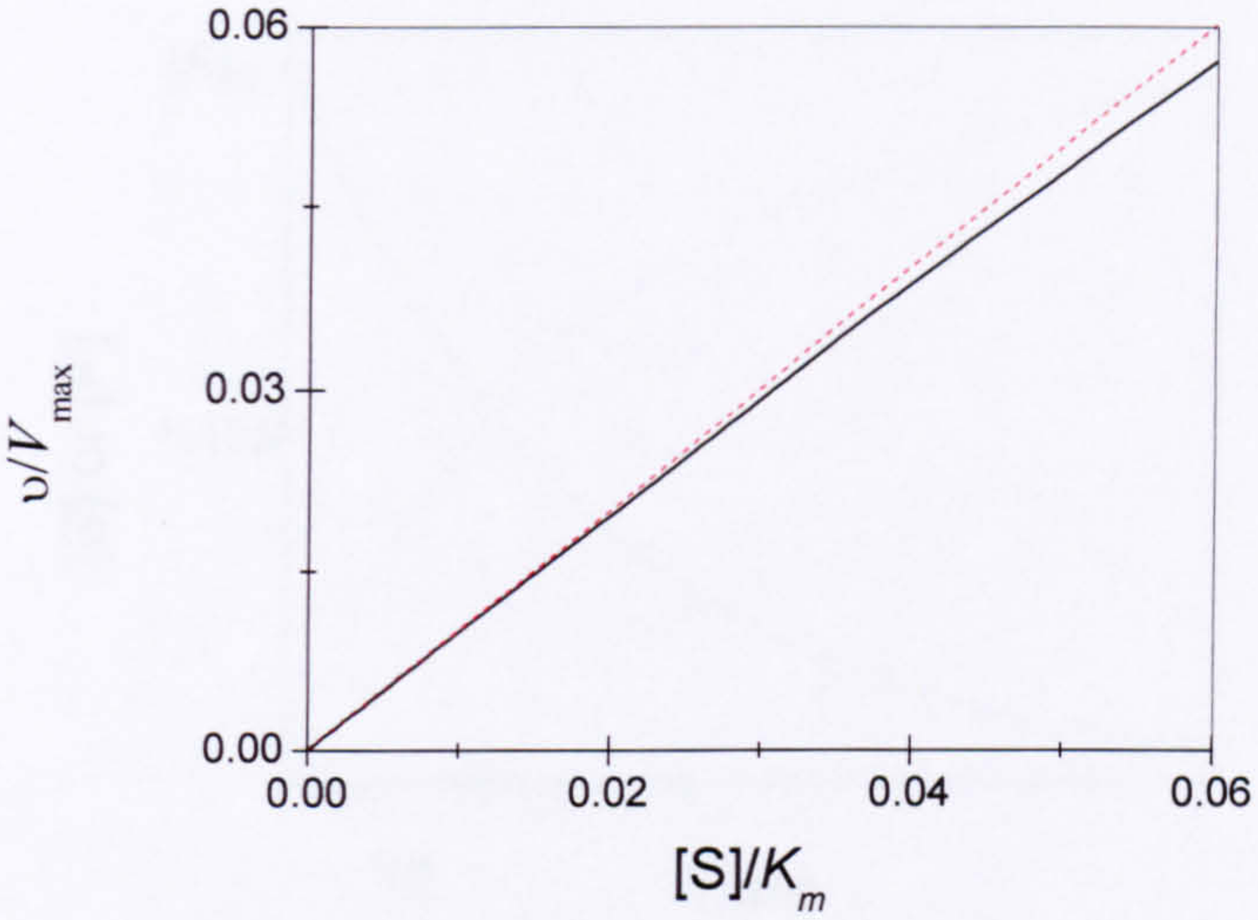

Figure 5.2 Black: υ vs. [S] plot where [S] << K_m; **Red**: true first-order behaviour[1].

This is because when [S] << K_m, [S] in the denominator in equation (6) can be ignored:

$$\upsilon \sim \frac{[S]}{K_m} V_{max} \quad \text{or} \quad \upsilon \sim k\,[S] \tag{8}$$

k = first order rate constant = V_{max}/K_m (min^{-1}) (K_m in moles x 1^{-1}, υ in moles x 1^{-1} x min^{-1})

i.e. k is the fraction of substrate converted to product per unit of time (e.g. minutes).

The integrated form of the first order rate equation can be used to determine the amount of substrate used or product formed at time t.

$$[S] = [S]_0 e^{-kt} \tag{9}$$

A plot of [S] or [P] vs. time is shown in **Figure 5.3**.

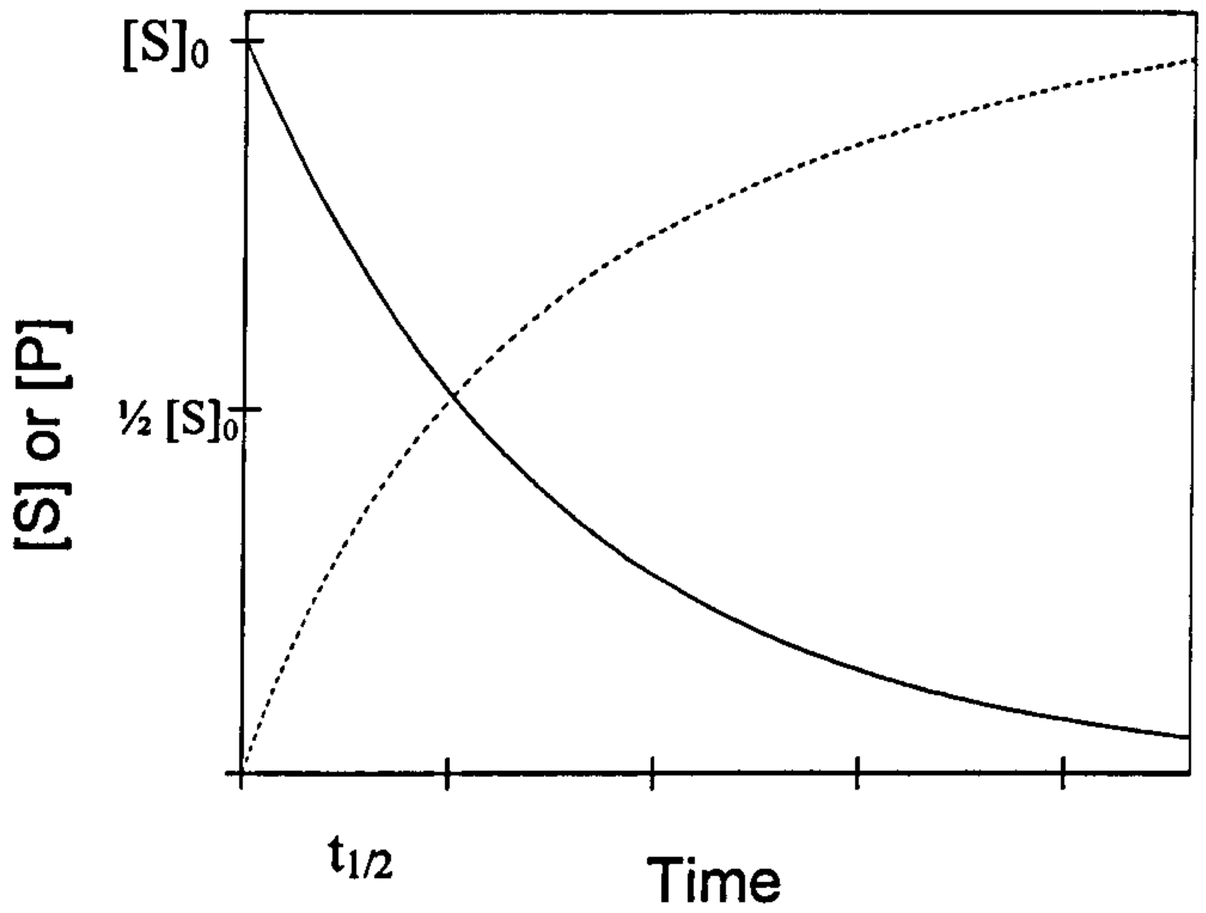

Figure 5.3 Plot of [S] (solid line) and [P] (dashed line) vs. time for the first-order region of the velocity curve[1].

A linear plot can be obtained by taking log [S] vs. time as shown in **Figure 5.4**.

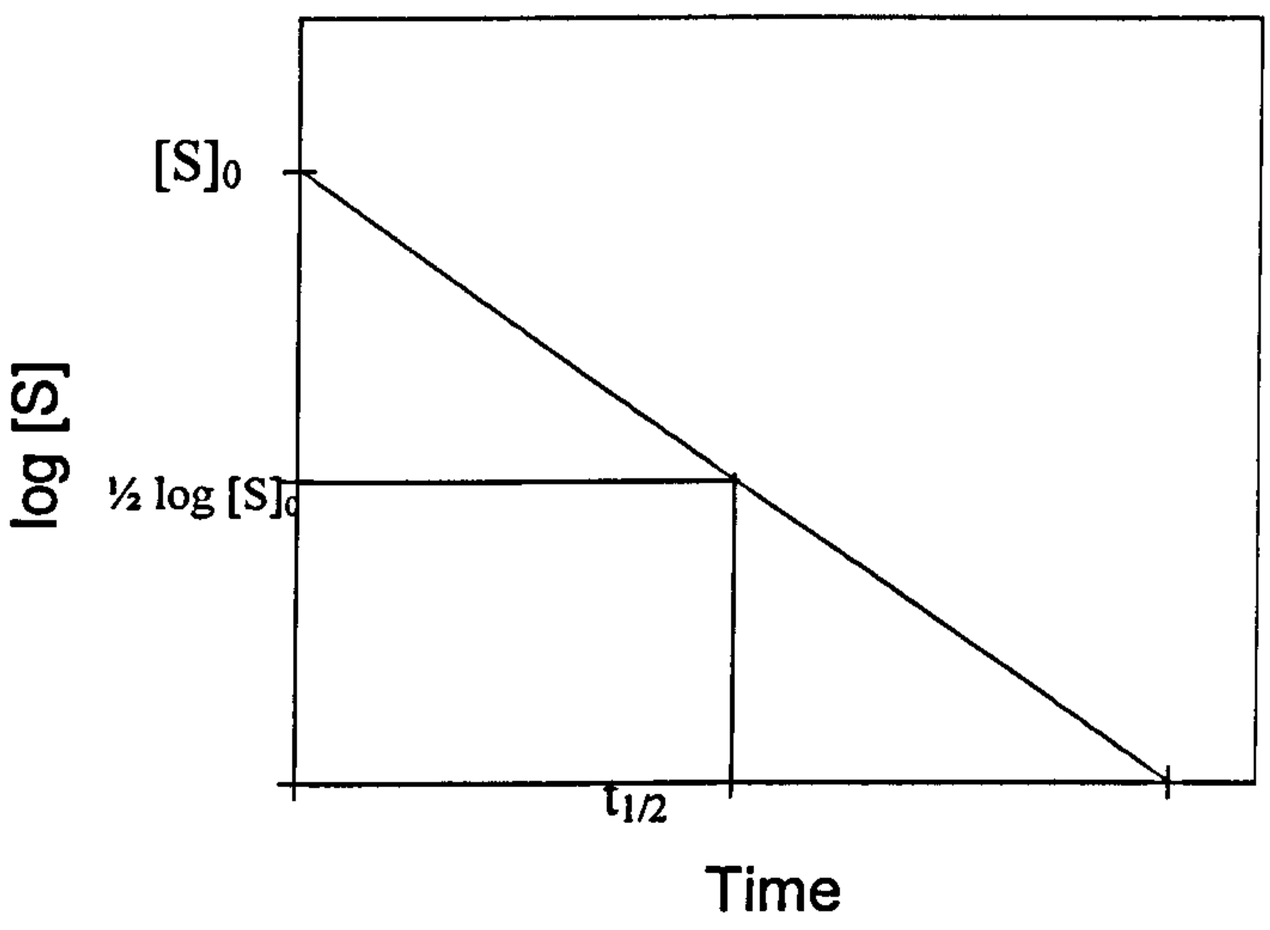

Figure 5.4 Semilog plot of the integrated first-order velocity equation[1].

5.1.3.2 Zero-Order Region

At very high substrate concentrations ([S] > 100 K_m), υ is approximately independent of [S]. At this point the enzyme may be described as 'saturated' (**Figure 5.5**).

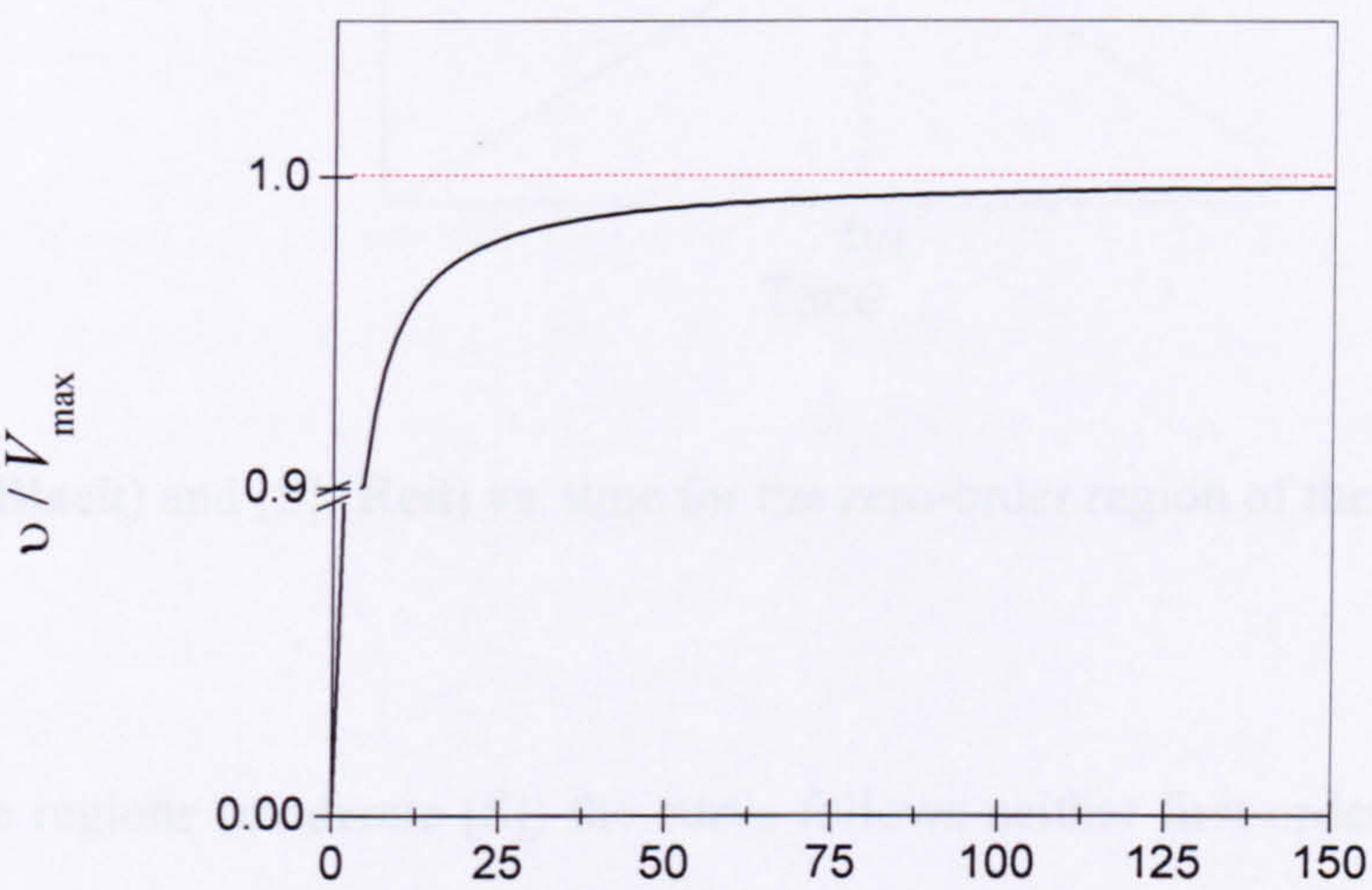

Figure 5.5 Black: υ vs. [S] plot where [S] > K_m; **Red:** true zero-order behaviour[1,2].

This is because when [S]>>K_m the denominator of the Michaelis-Menten equation (5) may be ignored.

$$\upsilon \sim \frac{V_{max}[S]}{[S]} \quad \text{or} \quad \upsilon \sim V_{max} \qquad (10)$$

A plot of [S] vs. time in the zero-order region of the velocity curve is shown in **Figure 5.6**.

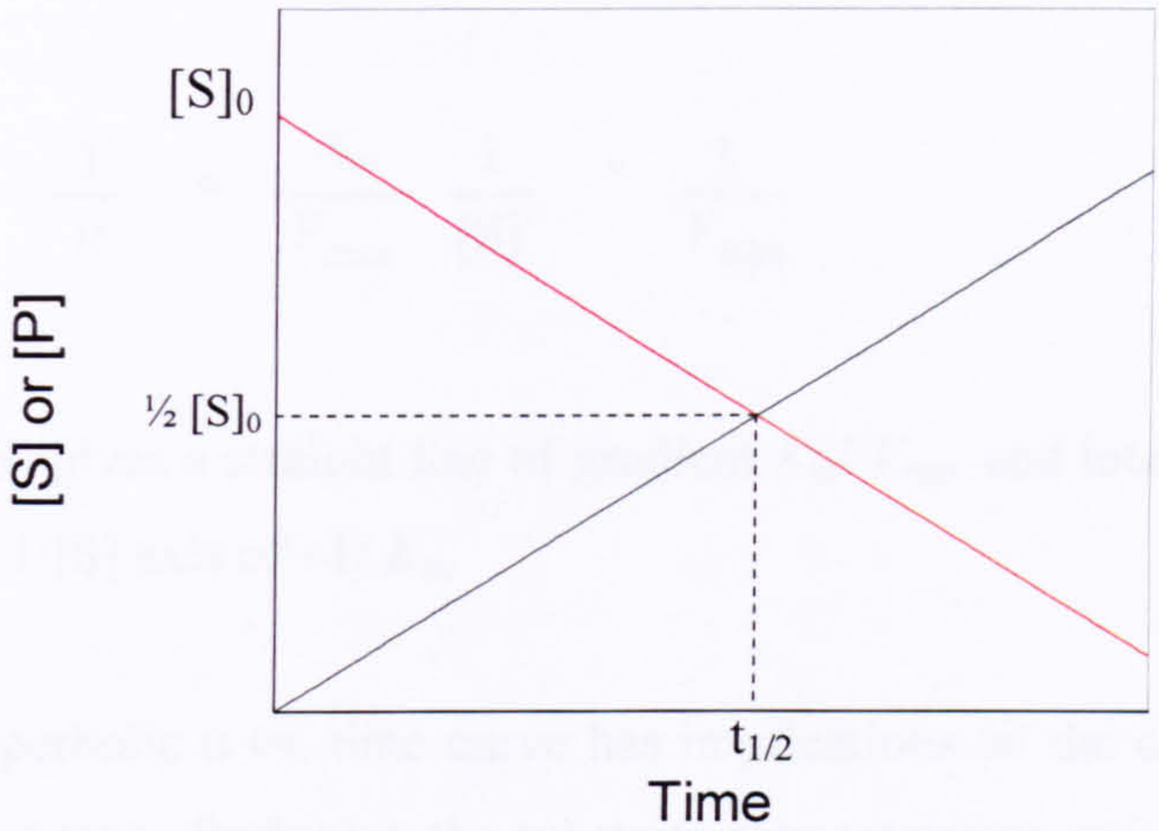

Figure 5.6 [P] (**Black**) and [S] (**Red**) vs. time for the zero-order region of the velocity curve[1].

In between these regions (moderate [S]) the curve follows neither first-order nor zero-order kinetics.

The hyperbolic υ vs. time curve makes determination of K_m and V_{max} impossible (they are asymptotes of the υ vs. [S] hyperbolic curve). There are number of different ways of rearranging the Michaelis-Menten equation in order to simplify the estimation of K_m.

A plot of υ vs. log[S] according to equation (11) gives a sigmoidal curve. At the point of inflection [S] = K_m.

$$\log\left(\frac{V_{max}}{\upsilon} - 1\right) = \log K_m - \log [S] \qquad (11)$$

When $\upsilon = 0.5\ V_{max}$

$V_{max}/\ \upsilon\text{-}1 = 1$

$\log\ (V_{max}/\ \upsilon\text{-}1) = 0$

$\log [S] = \log K_m$ or **$[S] = K_m$**

The Lineweaver-Burk plot is based on the rearrangement of the Michaelis-Menten equation to give a linear form.

$$\frac{1}{\upsilon} = \frac{K_m}{V_{max}} \frac{1}{[S]} + \frac{1}{V_{max}} \qquad (12)$$

A plot of 1/υ vs. 1/[S] gives a straight line of gradient K_m/ V_{max} and intercept on the 1/υ axis of $1/ V_{max}$ and on the 1/[S] axis of $-1/ K_m$.

The nature of the hyperbolic υ vs. time curve has implications on the conditions chosen for the assay. For a Lineweaver-Burk plot, the substrate concentrations must be carefully chosen to be in the intermediate range (0.3-0.7 V_{max}), of similar magnitude to K_m, and chosen to give evenly spaced reciprocals. For the sigmoidal plot, log[S] should be evenly spaced.

5.1.4 Turnover Rate

V_{max} varies with enzyme concentration and enzyme concentration can be difficult to measure. Also, the true value of V_{max} is impossible to determine experimentally (even at [S] = 10 K_m, υ < 10 % V_{max}[2]). Therefore a means of describing the turnover rate of an enzyme in an assay cannot be described in terms of V_{max}. Instead, catalytic activity is often defined in terms of 'units' (U). One unit is the amount of enzyme required to catalyse the transformation of one μmol of substrate into products in one minute under defined conditions (usually 25°C, pH 7.5)[1, 2].

5.1.5 Measuring Enzyme Inhibition

Inhibitors reduce the rate of an enzyme catalysed reaction[1, 2]. Therefore they can be used as drugs, such as allopurinol as an inhibitor of XO. Irreversible inhibitors (catalytic poisons) reduce the enzyme activity to zero. Reversible inhibitors proceed by either a competitive (increased K_m), non-competitive (decreased V_{max}), uncompetitive (decreased V_{max} and K_m) or a mixed (combination) inhibition mechanism. In these situations the enzyme-inhibitor

complex has no activity. Partial inhibition occurs when some activity is retained by the enzyme-inhibitor complex. Competitive inhibition occurs when the enzyme and substrate compete for the same site. In this situation, the inhibition constant, K_i is a true equilibrium constant (13).

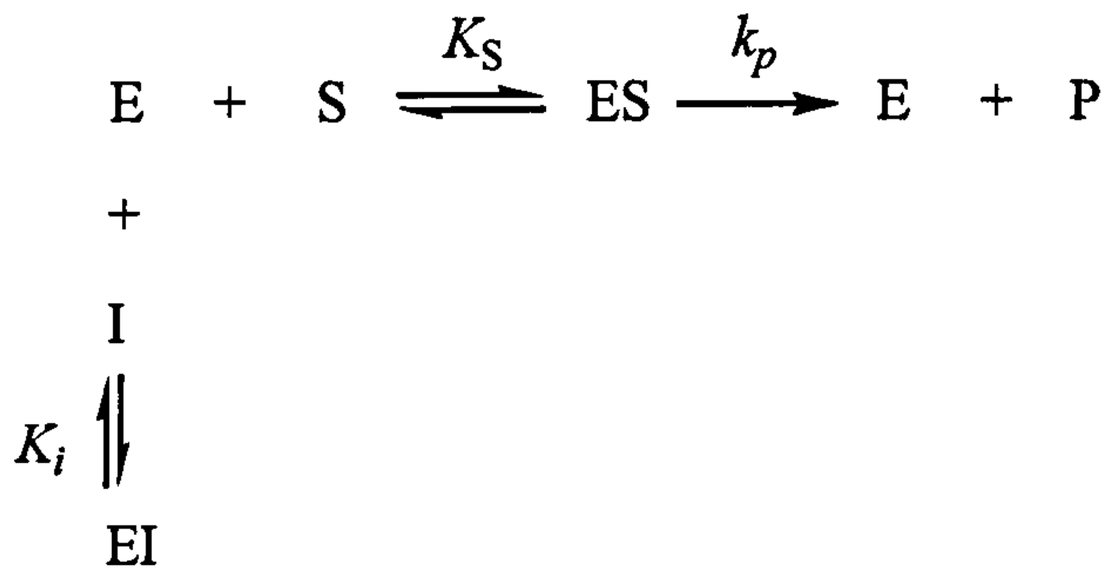

$$K_i = [E]\,[I] / [EI] \qquad (13)$$

$$\frac{\upsilon_i}{\upsilon_0} = \frac{[I]}{[I] + K_i\,(1 + [S]/K_m)}$$

υ_i = initial velocity in the absence of an inhibitor

υ_0 = initial velocity in the presence of an inhibitor at the same [S] as υ_i

5.1.5.1 The IC50

$[I]_{0.5}$ is the concentration of inhibitor required to reduce the rate of the reaction by 50 %.

$$[I]_{0.5} = (1 + [S]/K_m)\,K_i \qquad (14)$$

A plot of $(1-\upsilon_i/\upsilon_0)$, the percentage inhibition, vs. log [I] gives a sigmoidal curve. The point of inflection can be determined by non-linear regression analysis and is known as the IC_{50}. The IC_{50} is the half maximal inhibitory concentration, $[I]_{0.5}$. It is dependent on enzyme concentration and therefore the assay conditions must be stated and values are usually quoted relative to a standard or well-characterised inhibitor.

5.1.5.2 The Double Reciprocal Plot

An alternative method of comparing the effectiveness of an inhibitor uses the double reciprocal plot described previously (**Figure 5.7**).

$$\frac{1}{\upsilon} = \frac{K_m}{V_{max}}\left(1 + \frac{[I]}{K_i}\right)\frac{1}{[S]} + \frac{1}{V_{max}} \qquad (15)$$

For a competitive system the intercept on the $1/\upsilon$ axis remains $1/ V_{max}$ but the gradient increases by the factor in the brackets (equation 15) as [I] increases and the intercept on the 1/[S] axis moves towards the origin. K_i can be extrapolated from a replot, as shown in **Figure 5.8**[1].

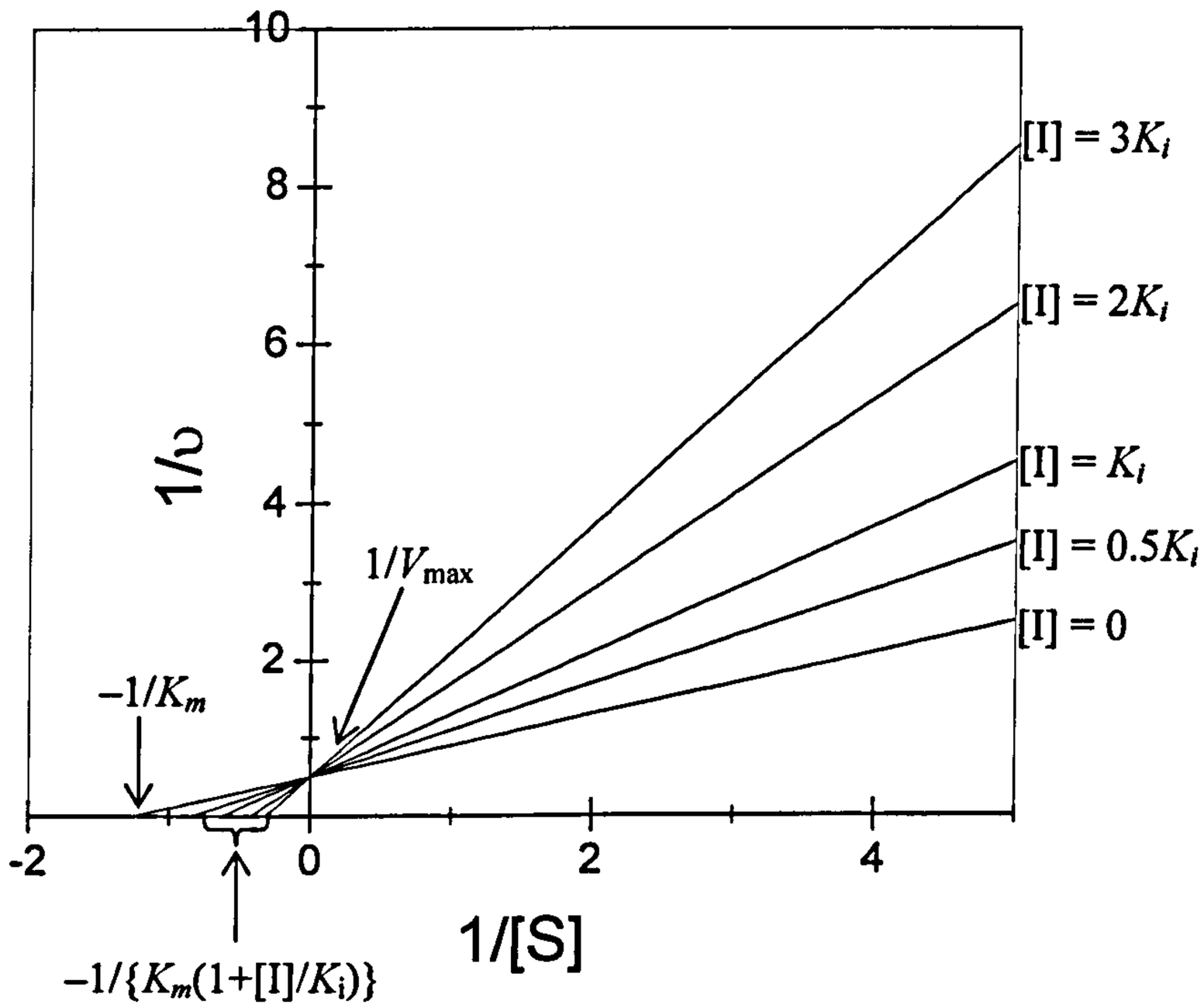

Figure 5.7 $1/\upsilon$ vs. 1/[S] in the presence of different concentrations of a competitive inhibitor[1].

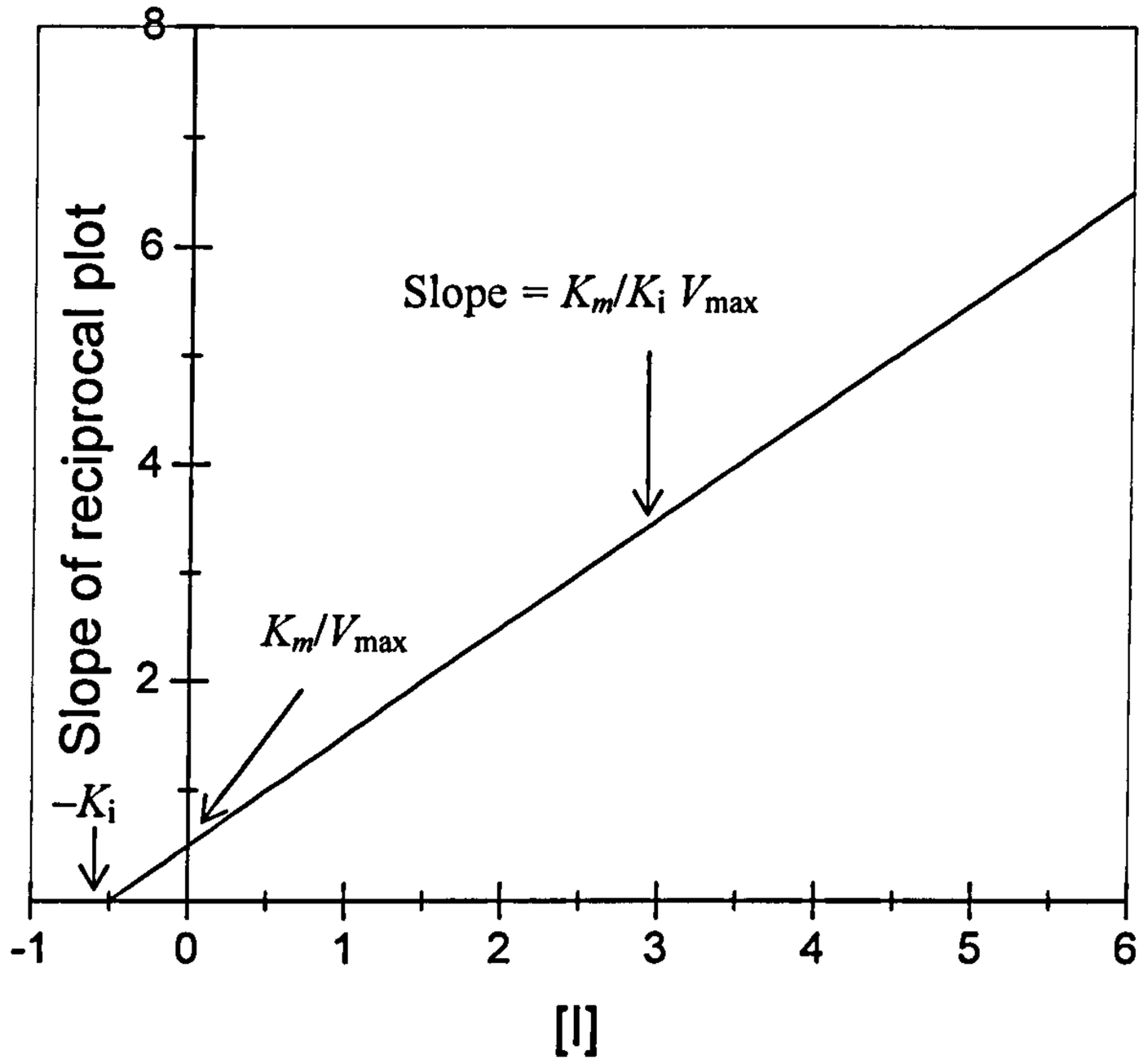

Figure 5.8 Replots of slope (**Figure 5.7**) vs. [I]

The conditions for the double-reciprocal plot must be carefully chosen. The concentration range must be in the intermediate region of the υ vs. [S] curve (**Figure 5.1**). If [S] is in the zero-order region the intercept on the *x* axis will be too low (K_m deceptively high) and if [S] is in the first order region the intercept will be too close to the *y* axis (K_m deceptively low). These restrictions may make the Lineweaver-Burk plot an unsuitable method for determining K_i in some circumstances. Also, the nature of the double-reciprocal plot means that experimental errors are amplified. The slope of the plot is affected most at larger values of 1/[S] for which the rates are slowest and the experimental error greatest.

5.1.6 Summary and Choice of Conditions

Whilst the double-reciprocal plot method provides more information on the inhibition mechanism, the IC_{50} plot is a quick and simple method of comparing potential inhibitors. It also can be used without the extensive prior information required for the Lineweaver-Burk plot. Therefore for the purpose of this study, a selection of compounds was screened for inhibitory activity using the IC_{50} plot.

The rate of formation of uric acid was measured spectrophotometrically at 295 nm using the method of Sweeney *et al.* with modifications[3]. Typical spectra are shown in **Figure 5.9**.

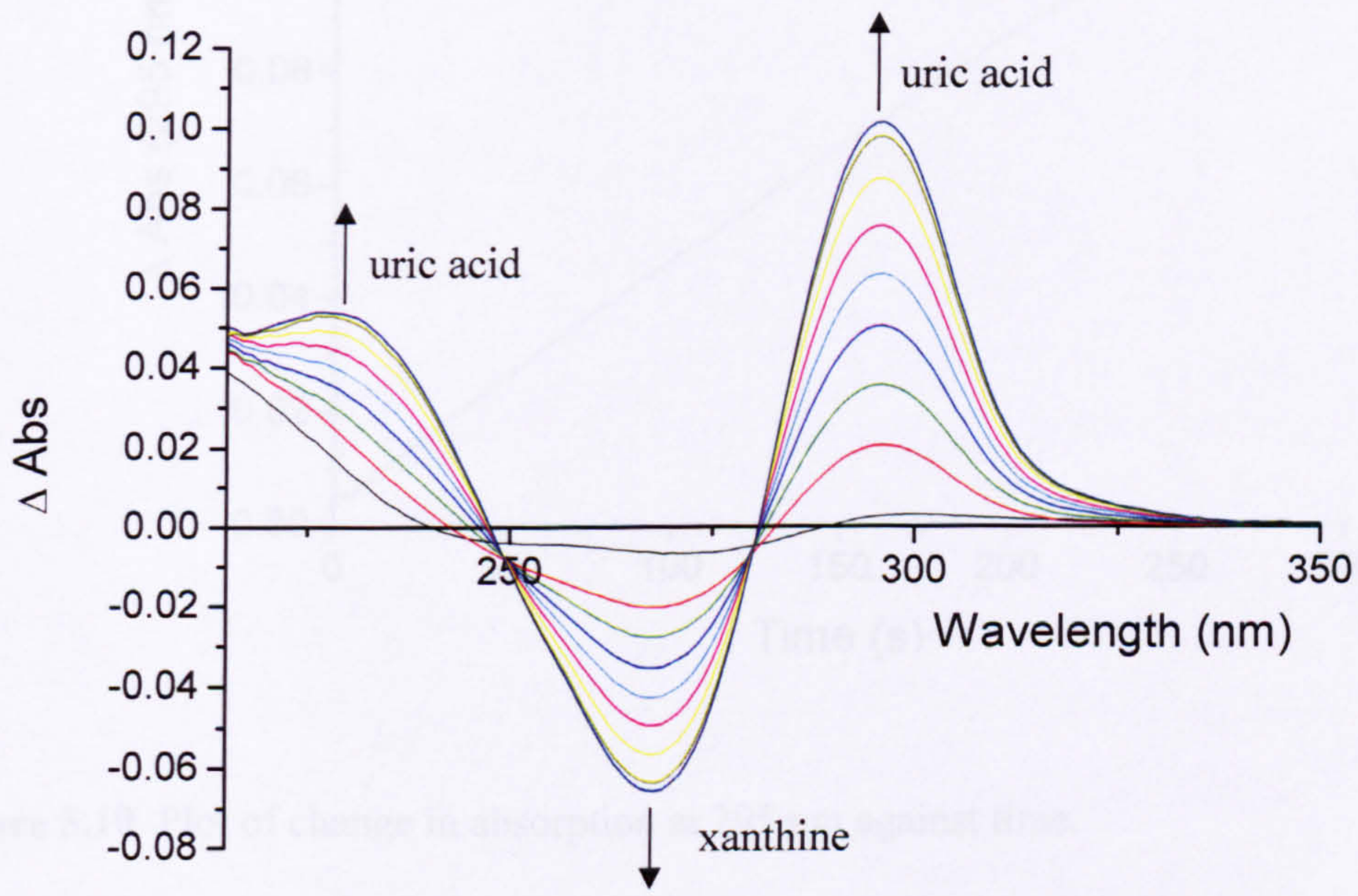

Figure 5.9 Difference spectra recorded at different times throughout a typical xanthine oxidase bioassay.

All solutions were freshly prepared and stored in an ice bath before use. 100 µl enzyme solution (3 U ml^{-1}) in phosphate buffer (50 mM, pH 7.5) was added to a 2900 µl solution of xanthine and inhibitor in phosphate buffer (50 mM, pH 7.5, 25 °C) giving a final assay concentration of 0.050 mM xanthine (saturated) and 0.1 units enzyme. The reaction mixture

was stirred and maintained at 25 °C for the duration of the reaction (10 minutes). A blank was run in the absence of the inhibitor and a control reaction was carried out in the absence of XO. Three replicates were recorded for each [I]. The stock solutions of inhibitors that were not water soluble were made up in dimethyl sulfoxide. The final concentration of dimethyl sulfoxide (1%) was not sufficient to affect the assay. In those cases the control reactions were carried out with 1% dimethyl sulfoxide in the final assay.

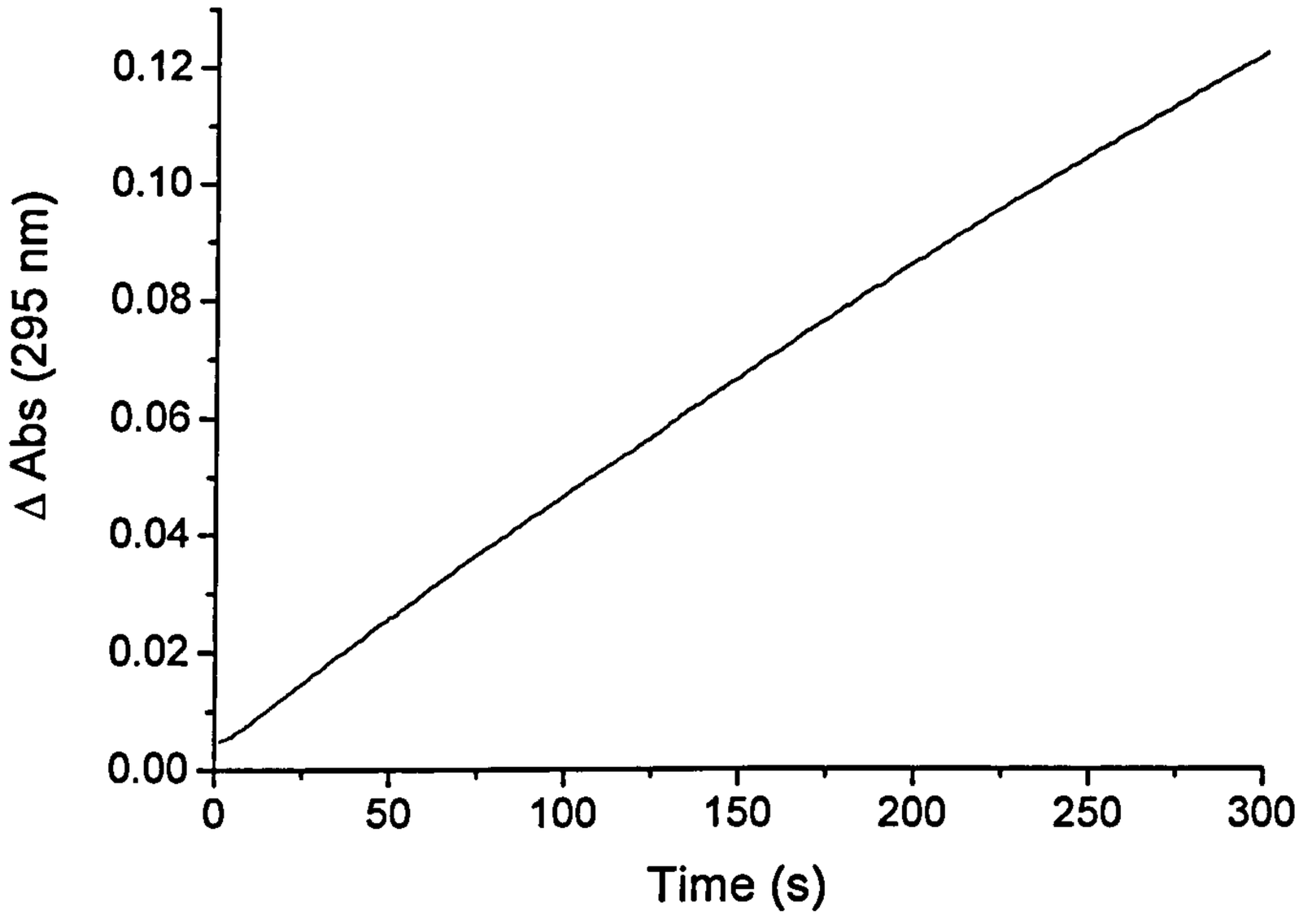

Figure 5.10 Plot of change in absorption at 295 nm against time.

The initial rate of formation of uric acid (absorption at 295 nm) (**Figure 5.10**) was plotted against log [I]. The IC_{50} was calculated using the sigmoidal fit tool in Origin 6.1 (OriginLab Coporation, Northampton, MA). Some of the inhibitors were not sufficiently soluble at concentrations that gave close to 100% inhibition. In those cases, the upper limit was fixed at 100%. λ_{max} for the inhibitors was recorded over time to ensure no degradation reaction was taking place.

5.2 The Determination of the IC_{50} of Allopurinol

In order to provide a means of comparison with literature data, the IC_{50} of allopurinol was measured as a control experiment.

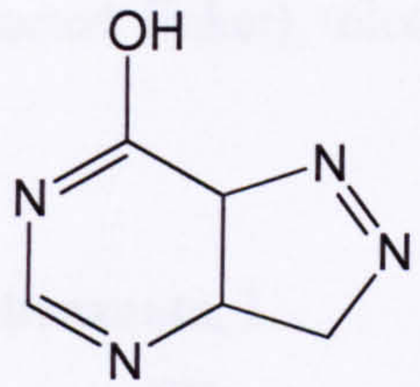

allopurinol

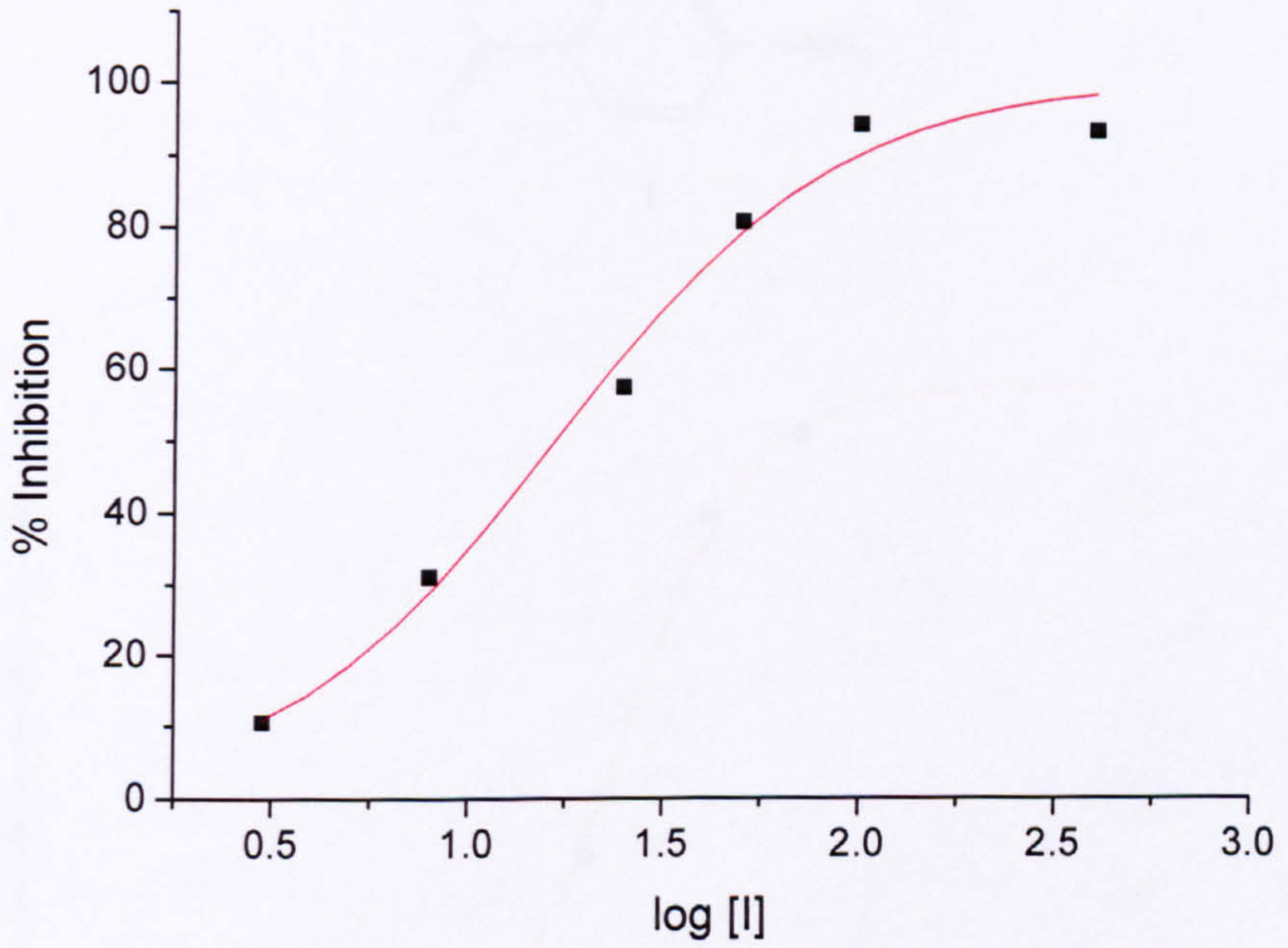

Figure 5.11 Plot of % inhibition vs. log [I] ([I] in μM) where I = allopurinol. $IC_{50} = 17.3 \pm 4.5$ μM. $\chi^2 = 0.00434$, $R^2 = 0.974$.

As expected, the point of inflection at 50% inhibition gave a value in the micromolar region (**Figure 5.11**)[4].

5.3 IC_{50} of Substrate-analogues and Linkers

A number of substrate analogues and linkers were tested as potential inhibitors of XO. Below are the results obtained for methyl 4-amino-2-methoxybenzoate (the linker), 4-amino-2-methoxybenzoic acid (the deprotected linker), nicotinic acid, isonicotinic acid and 4-imidazolecarboxylic acid.

5.3.1 Methyl 4-Amino-2-methoxybenzoate, 1.

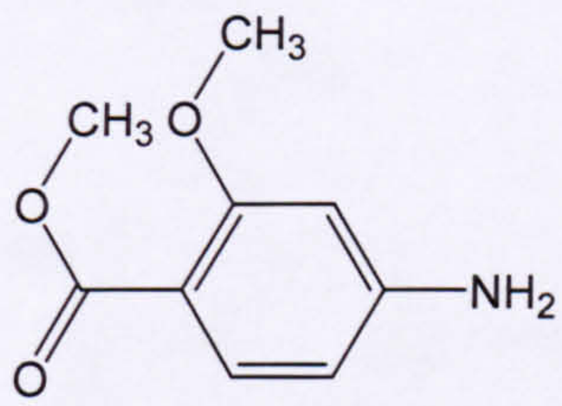

1

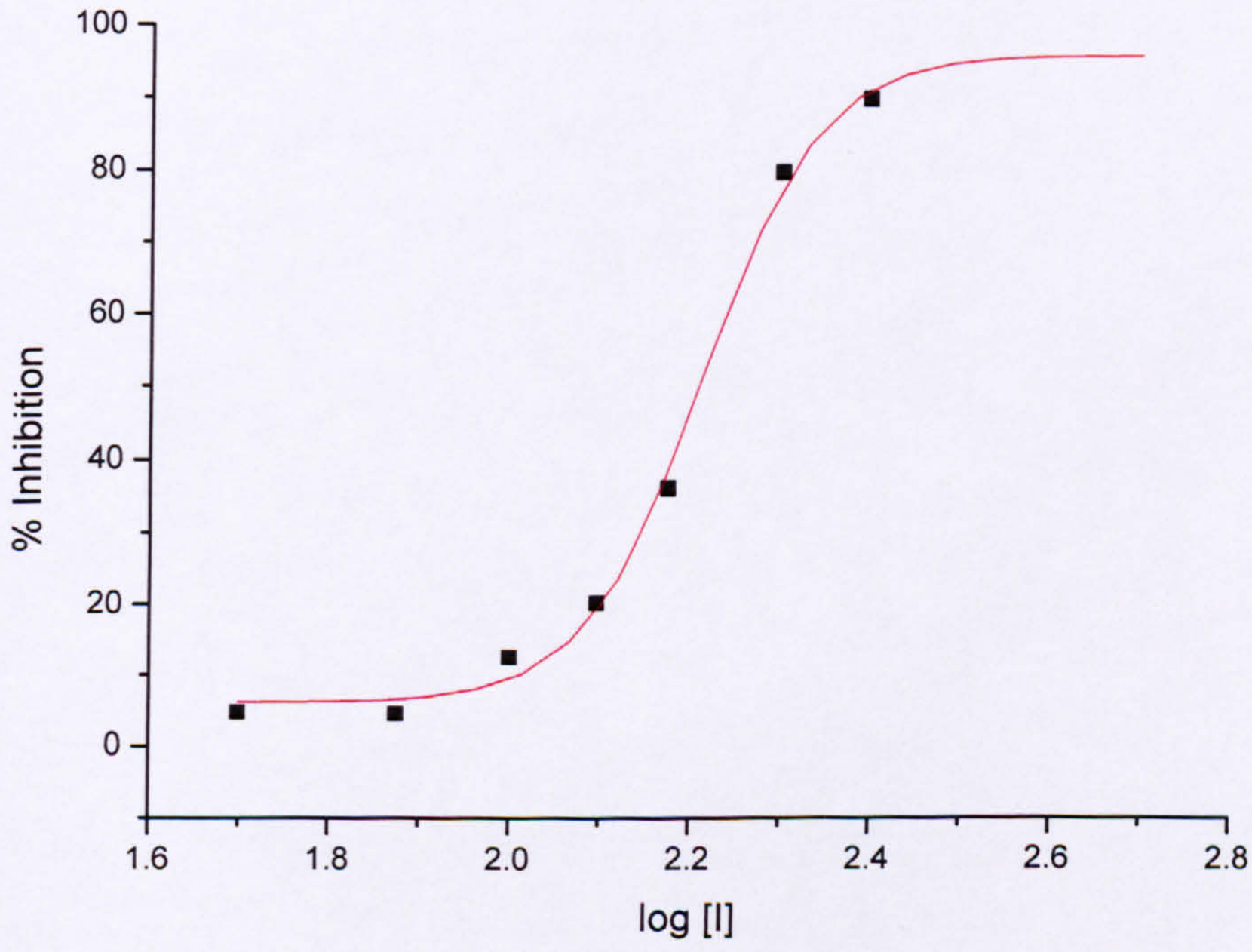

Figure 5.12 Plot of % inhibition vs. log [I] ([I] in μM) where I = **1**. $IC_{50} = 163 \pm 5$ μM. $\chi^2 = 10.1$, $R^2 = 0.996$.

1 inhibited the production of uric acid with an IC_{50} of 163 ± 5 μM (**Figure 5.12**). This is a reasonable value, suggesting that the aromatic linker can be accommodated in the active site. The moderate value is appropriate for a probe since it is sufficient to be measured. The binding, however, is sufficiently weak so that the compound can be displaced by a successful drug candidate with a higher IC_{50} value, such as allopurinol. Modification of the structure, such as attachment of the substrate, should improve the binding affinity.

5.3.2 4-Amino-2-methoxybenzoic Acid.

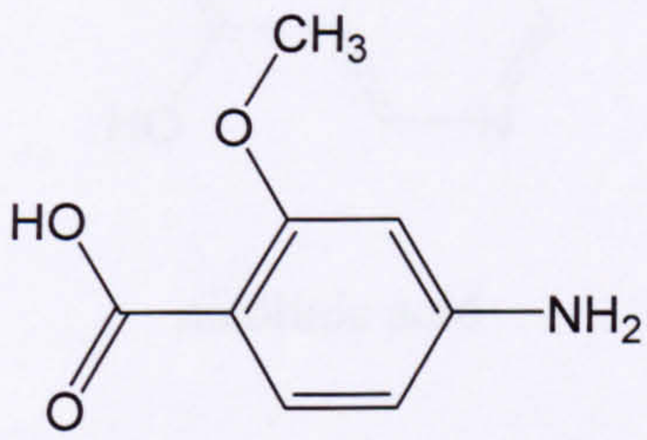

4-amino-2-methoxybenzoic acid

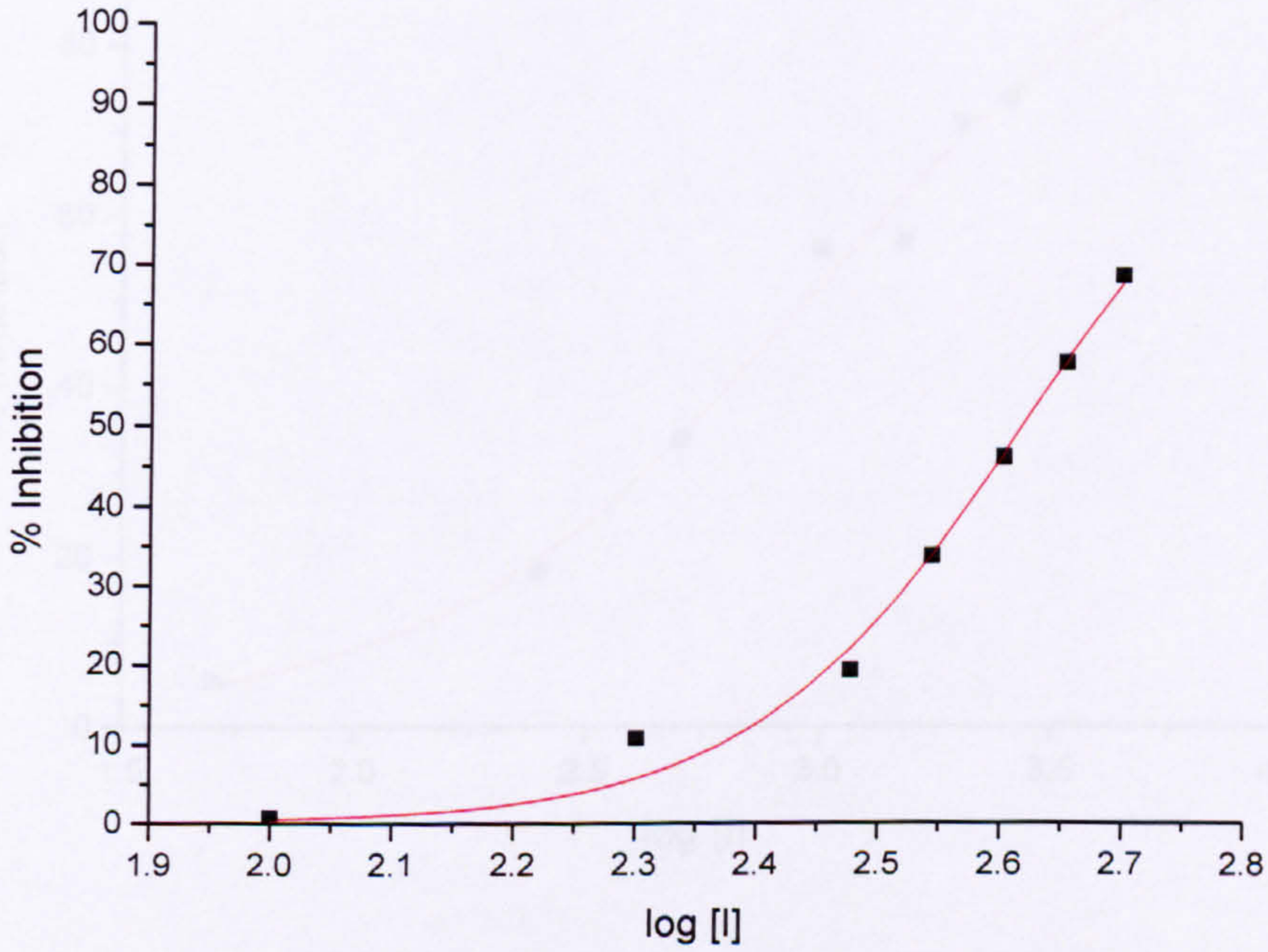

Figure 5.13 Plot of % inhibition vs. log [I] ([I] in μM) where I = 4-amino-2-methoxybenzoic acid. IC_{50} = 416 ± 5 μM. χ^2 = 7.26, R^2 = 0.996.

The IC_{50} of 4-amino-2-methoxybenzoic acid (**Figure 5.13**) was higher than that of the ester, **1**. This suggests that the acid functionality is less likely to be accommodated in the active site than the ester. The acid is likely to be deprotonated and anionic (the pKa of benzoic acids ~ 4-5), whereas the enzyme is known to accommodate neutral substrates. Alternatively, hydrogen-bonding may cause aggregation of the compound in solution.

5.3.3 Nicotinic acid.

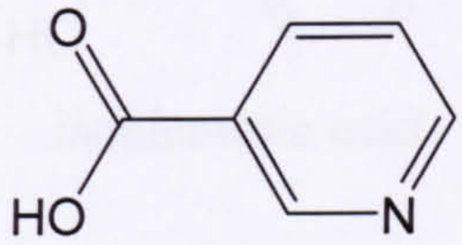

nicotinic acid

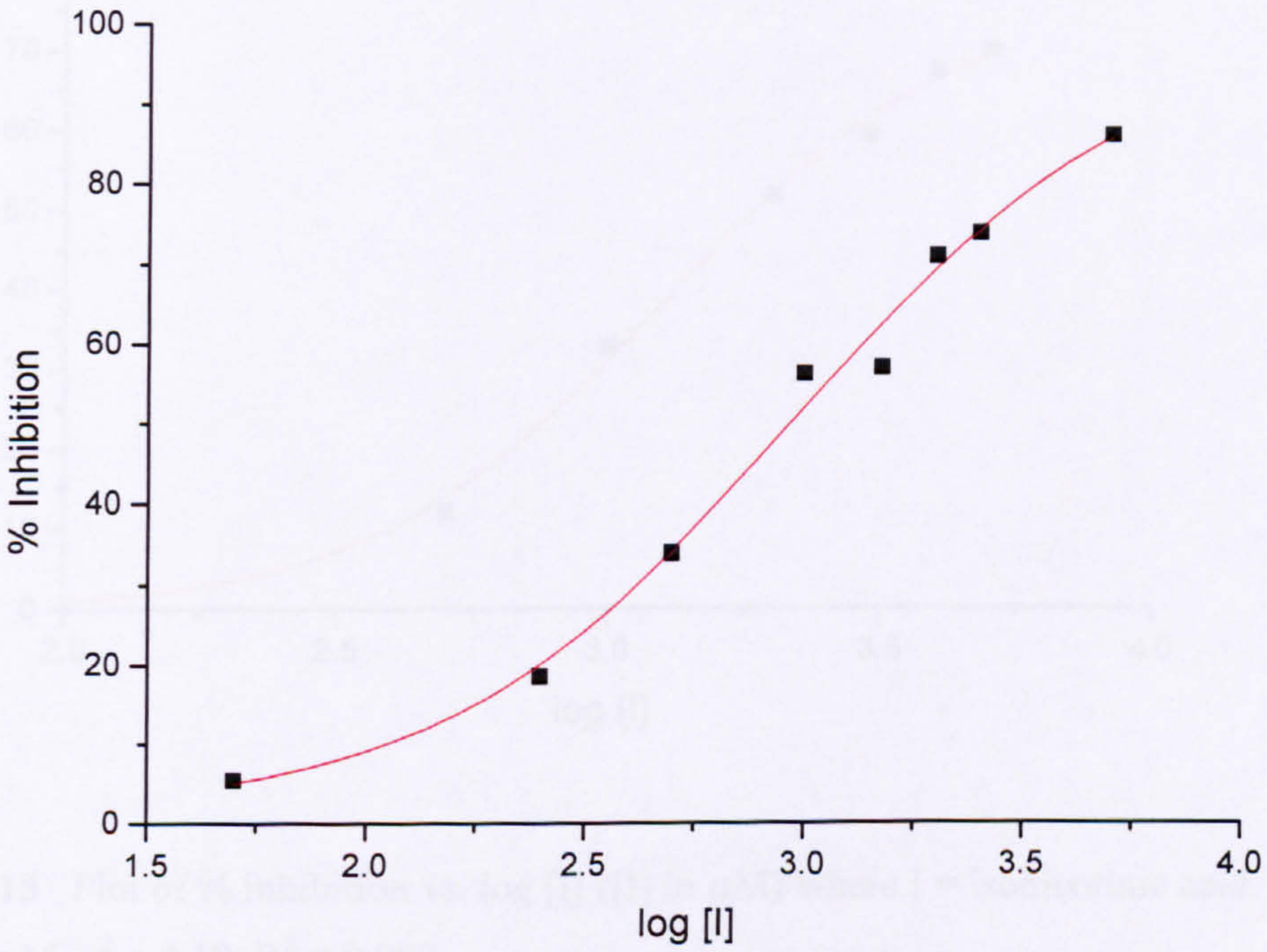

Figure 5.14 Plot of % inhibition vs. log [I] ([I] in μM) where I = nicotinic acid. IC_{50} = 946 ± 1 μM. $\chi^2 = 13.3$, $R^2 = 0.991$.

The IC_{50} for nicotinic acid (**Figure 5.14**) is twice as large as 4-amino-2-methoxybenzoic acid. As for the previous compound, the acid functionality may be the reason for the relatively low affinity.

5.3.4 Isonicotinic acid.

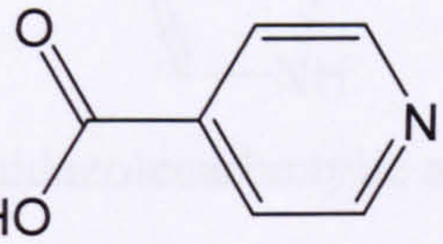

isonicotinic acid

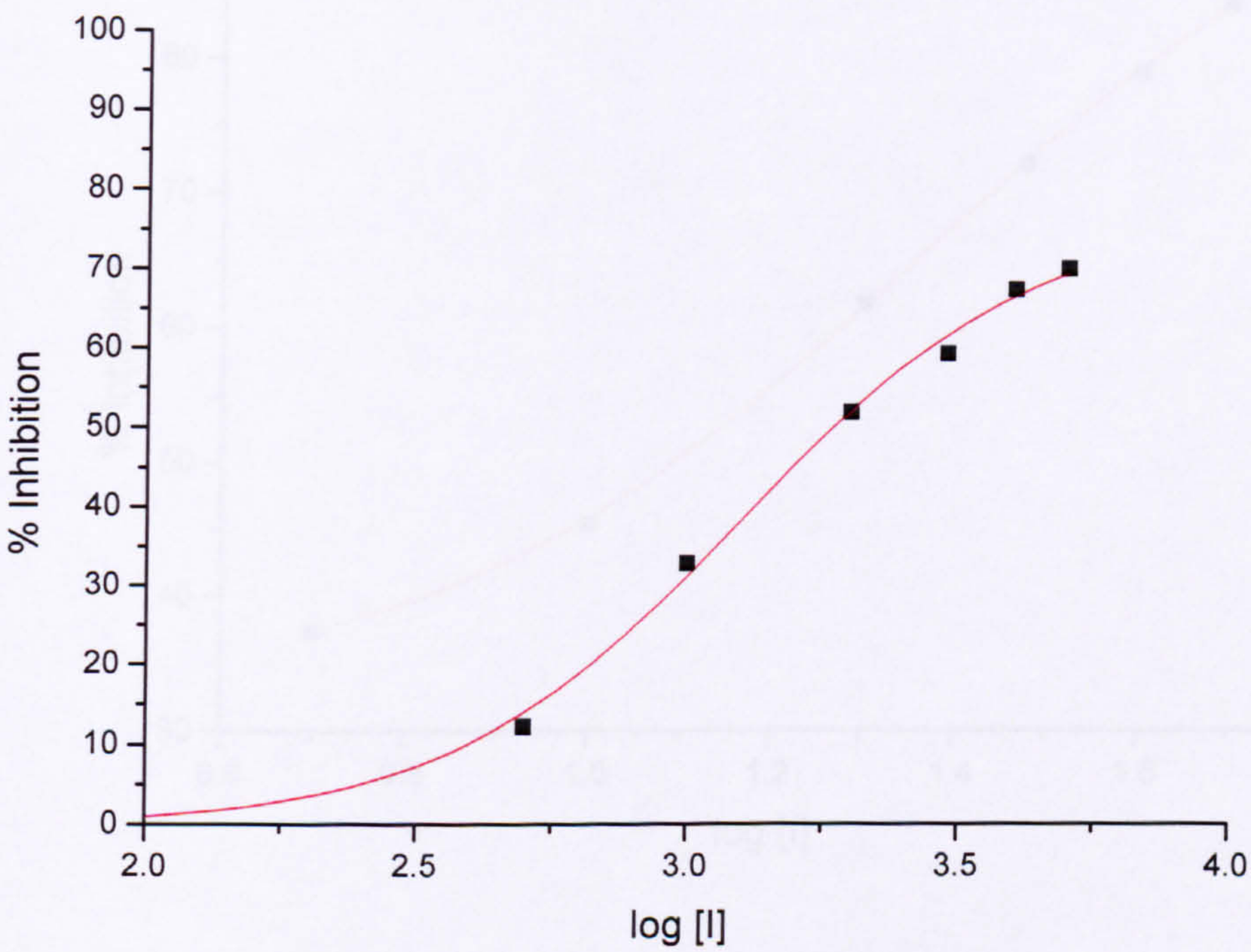

Figure 5.15 Plot of % inhibition vs. log [I] ([I] in μM) where I = isonicotinic acid. IC_{50} = 1269 ± 1 μM. $\chi^2 = 4.10$, $R^2 = 0.997$.

The IC_{50} for isonicotinic acid (**Figure 5.15**) was slightly higher than for nicotinic acid.

5.3.5 4-Imidazolecarboxylic Acid.

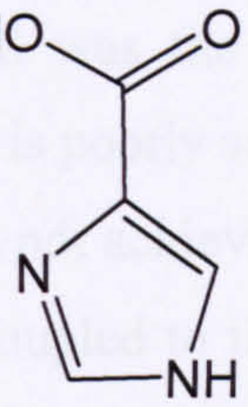

4-imidazolecarboxylic acid

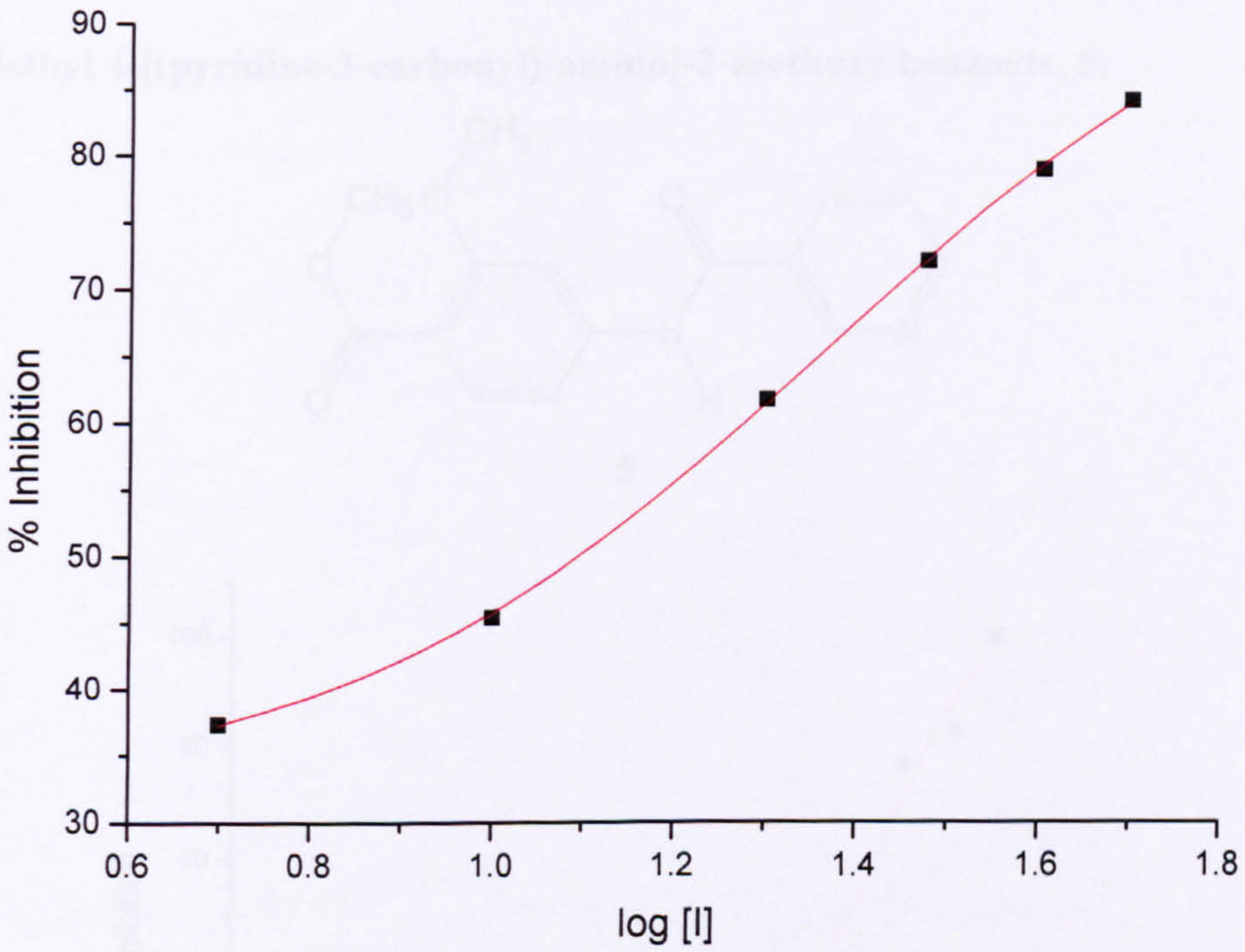

Figure 5.16 Plot of % inhibition vs. log [I] ([I] in μM) where I = 4-imidazolecarboxylic acid. $IC_{50} = 23.6 \pm 1.4$ μM. $\chi^2 = 0.196$, $R^2 = 0.999$.

The IC_{50} of 4-imidazole carboxylic acid was relatively low (**Figure 5.16**) despite the acid functiontionality. This is in agreement with the data reported by Biagi *et al.*[5] who suggest that a simplified substrate with a five-membered ring rather than a six-membered ring would have a higher binding affinity for XO.

5.4 The Determination of the IC_{50} Values of the Substrate-Linker Conjugates

The IC_{50} of 4-imidazole carboxylic acid was the most promising of all the substrates-analogues tested, however, the compound is poorly soluble in most solvents and therefore the coupling of the substrate to the linker was not achieved in a reasonable yield. The remaining 'substrate-analogues' were successfully coupled to the linker (chapter 2). Of these only the nicotinic and isonicotinic acid derivatives were sufficiently soluble at the required concentrations for inhibition.

5.4.1 Methyl 4-[(pyridine-3-carbonyl)-amino]-2-methoxy benzoate, 5.

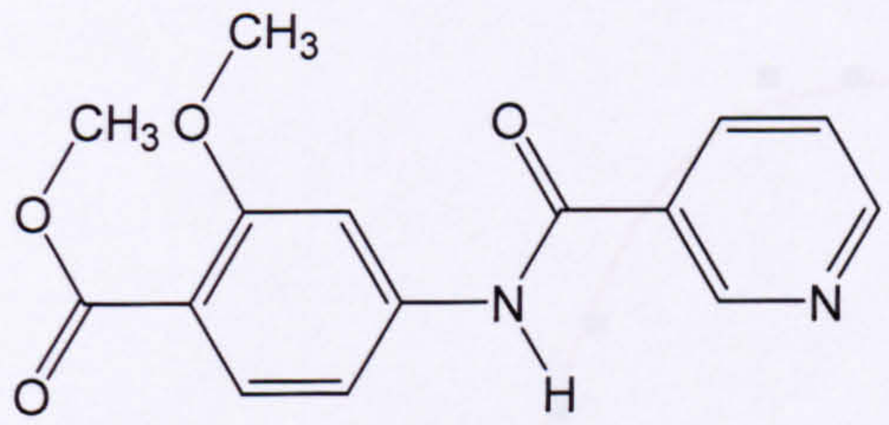

5

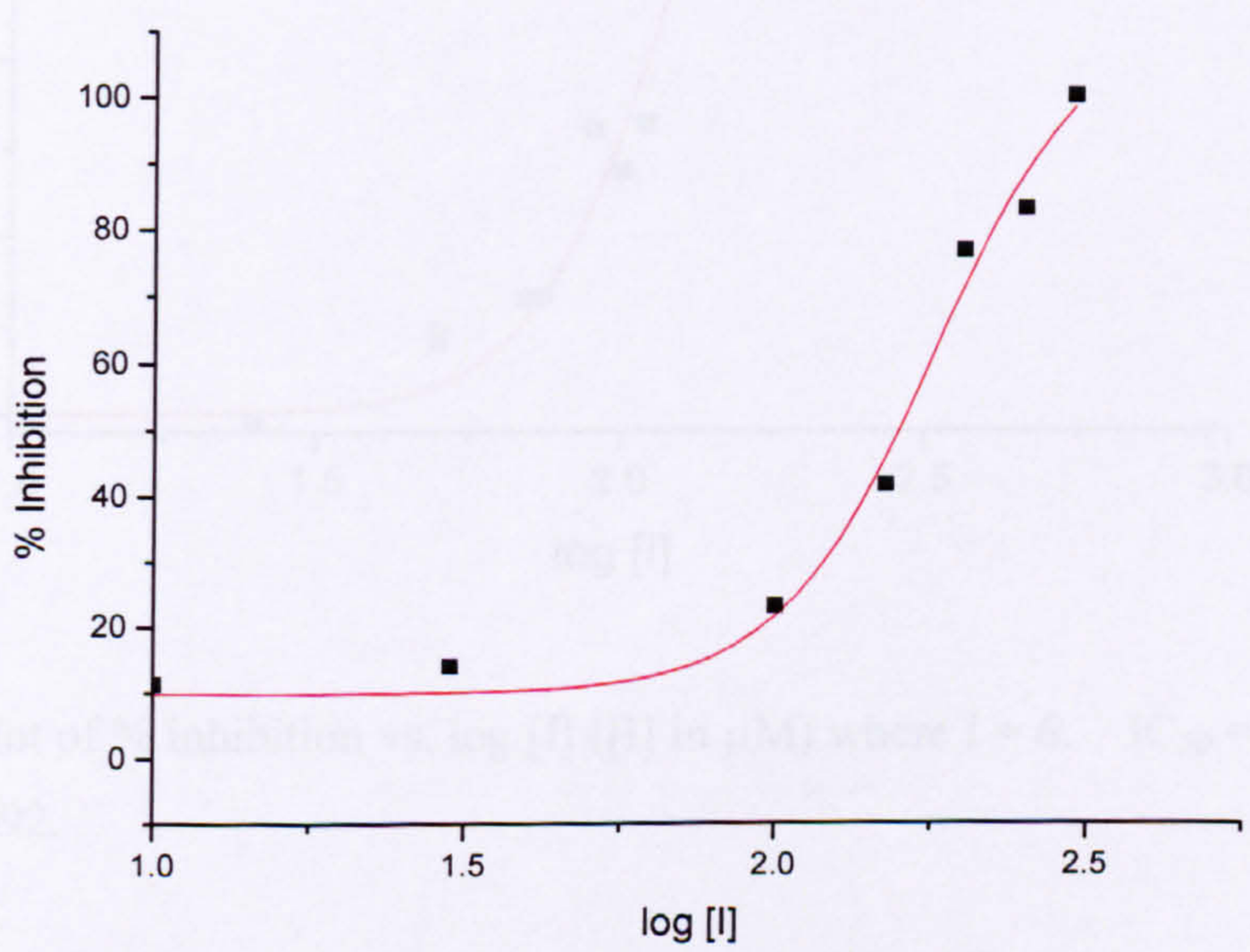

Figure 5.17 Plot of % inhibition vs. log [I] ([I] in μM) where I = **5**. $IC_{50} = 179 \pm 1$ μM. $\chi^2 = 35.1$, $R^2 = 0.986$.

The IC_{50} of **5** (**Figure 5.17**) was much lower than that of nicotinic acid and closer to that of the linker, **1**.

5.4.2 Methyl 4-[(pyridine-4-carbonyl)-amino]-2-methoxy benzoate, 6.

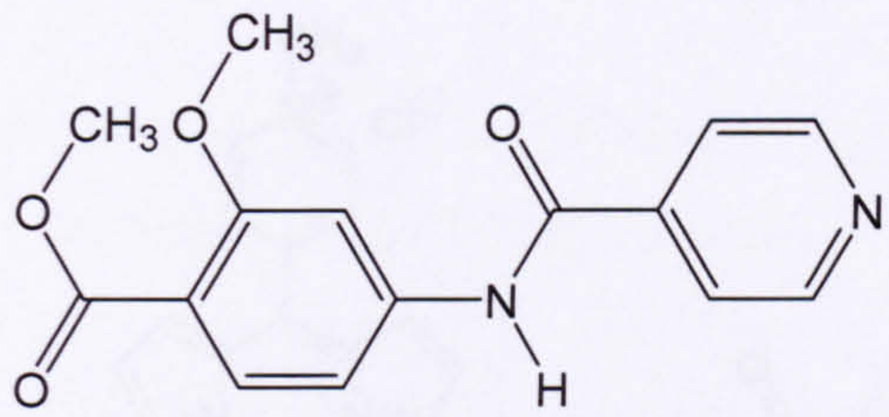

6

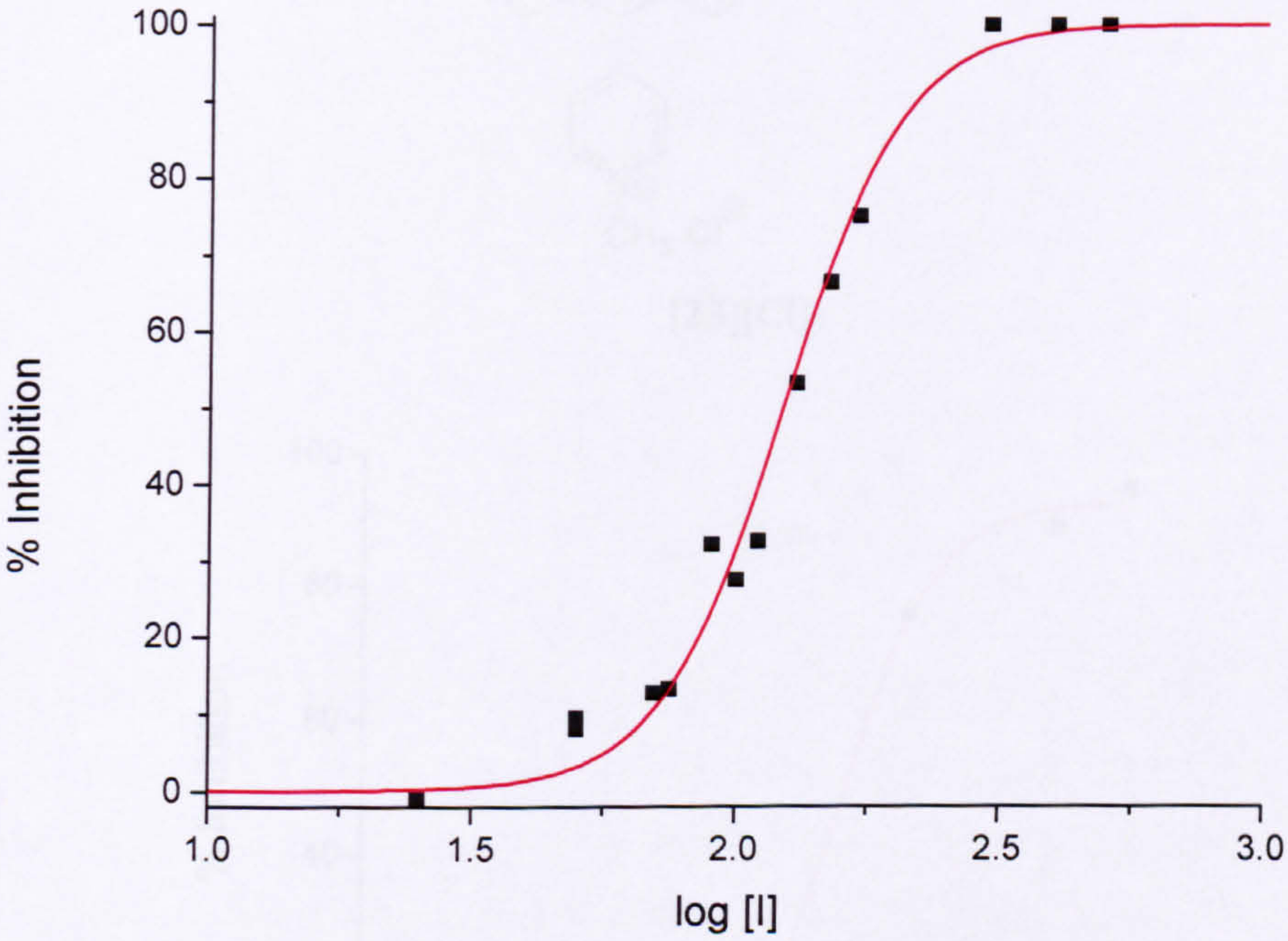

Figure 5.18 Plot of % inhibition vs. log [I] ([I] in μM) where I = **6**. $IC_{50} = 130 \pm 1$ μM. $\chi^2 = 14.5$, $R^2 = 0.992$.

The IC_{50} of **6** (**Figure 5.18**) was not only lower than that of isonicotinic acid, but also the linker, **1**, and the nicotinic acid derivative, **5**. This was the most promising substrate-linker conjugate and therefore isonicotinic acid was chosen as the substrate-analogue over nicotinic acid.

5.5 The Determination of the IC_{50} Values of the Probe Molecules

5.5.1 Zinc 5,10,15-tris(*N*-methyl-4-pyridiniumyl)-20-[4-[(2-methoxy-4-amino-phenylcarbonyl)-amino] phenyl] porphyrin, [23][Cl]$_3$.

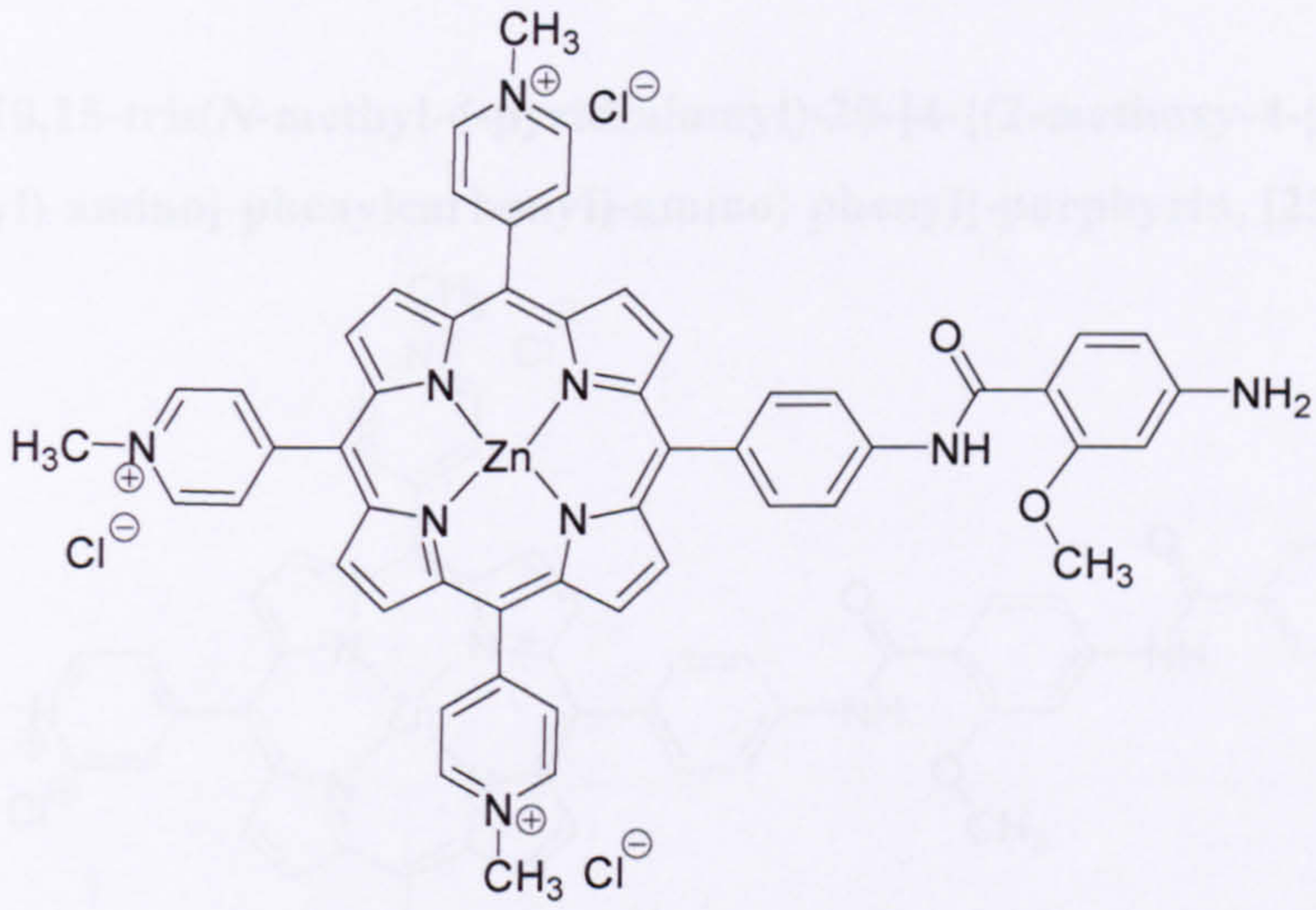

[**23**][Cl]$_3$

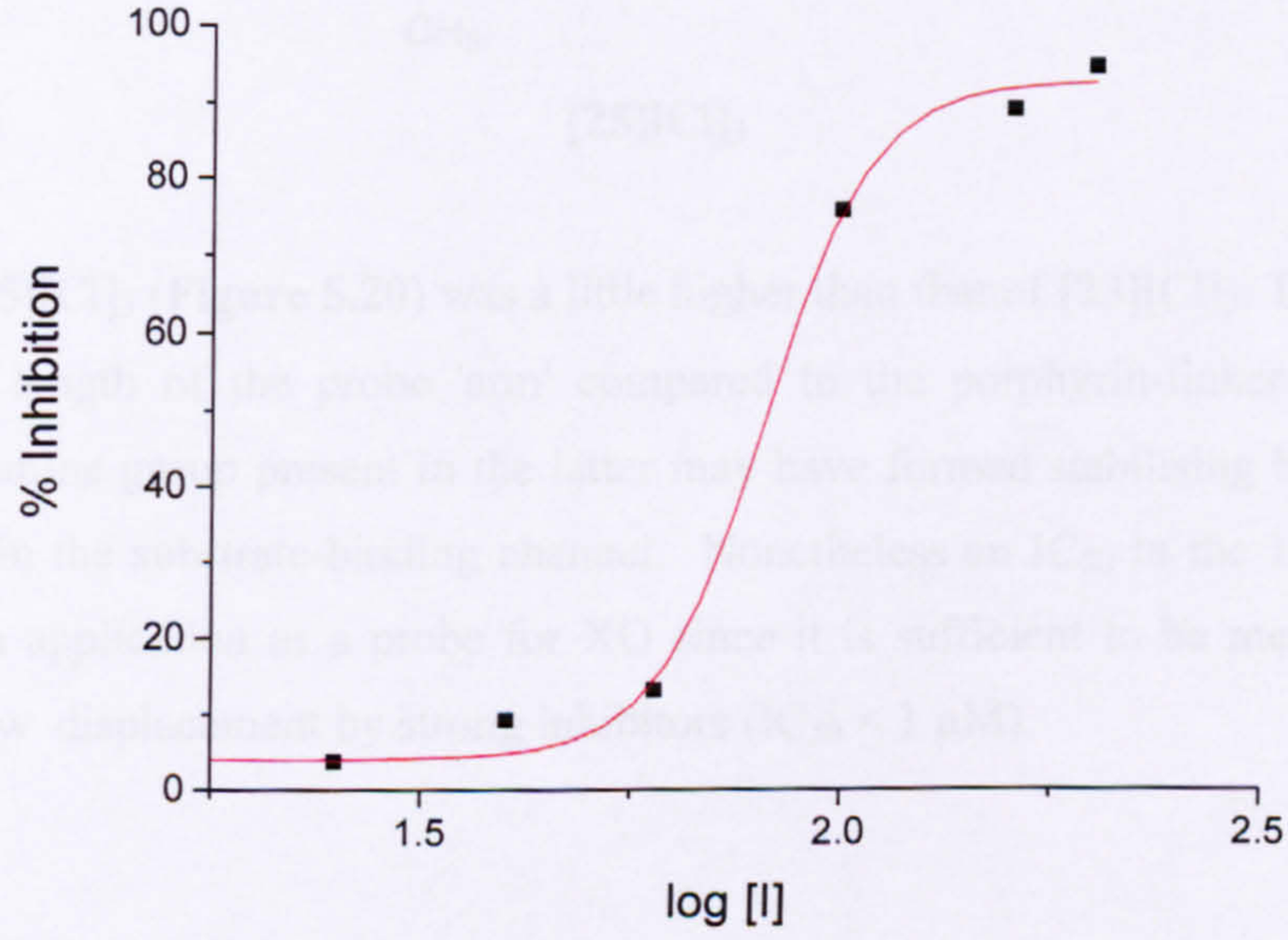

Figure 5.19 Plot of % inhibition vs. log [I] ([I] in μM) where I = [**23**][Cl]$_3$. IC_{50} = 81.2 ± 3.6 μM. χ^2 = 0.0017, R^2 = 0.997.

The IC_{50} of **[23][Cl]$_3$** (**Figure 5.19**) was approximately five times that of allopurinol, suggesting that the porphyrin-linker conjugate already has a reasonable affinity for xanthine oxidase. The value was half that of the linker alone, possibly due to improved water-solubility and additional interactions of the porphyrin with the enzyme surface.

5.5.2 Zinc 5,10,15-tris(*N*-methyl-4-pyridiniumyl)-20-[4-{(2-methoxy-4-[(pyridine-4-carbonyl)-amino]-phenylcarbonyl)-amino} phenyl]-porphyrin, [25][Cl]$_3$.

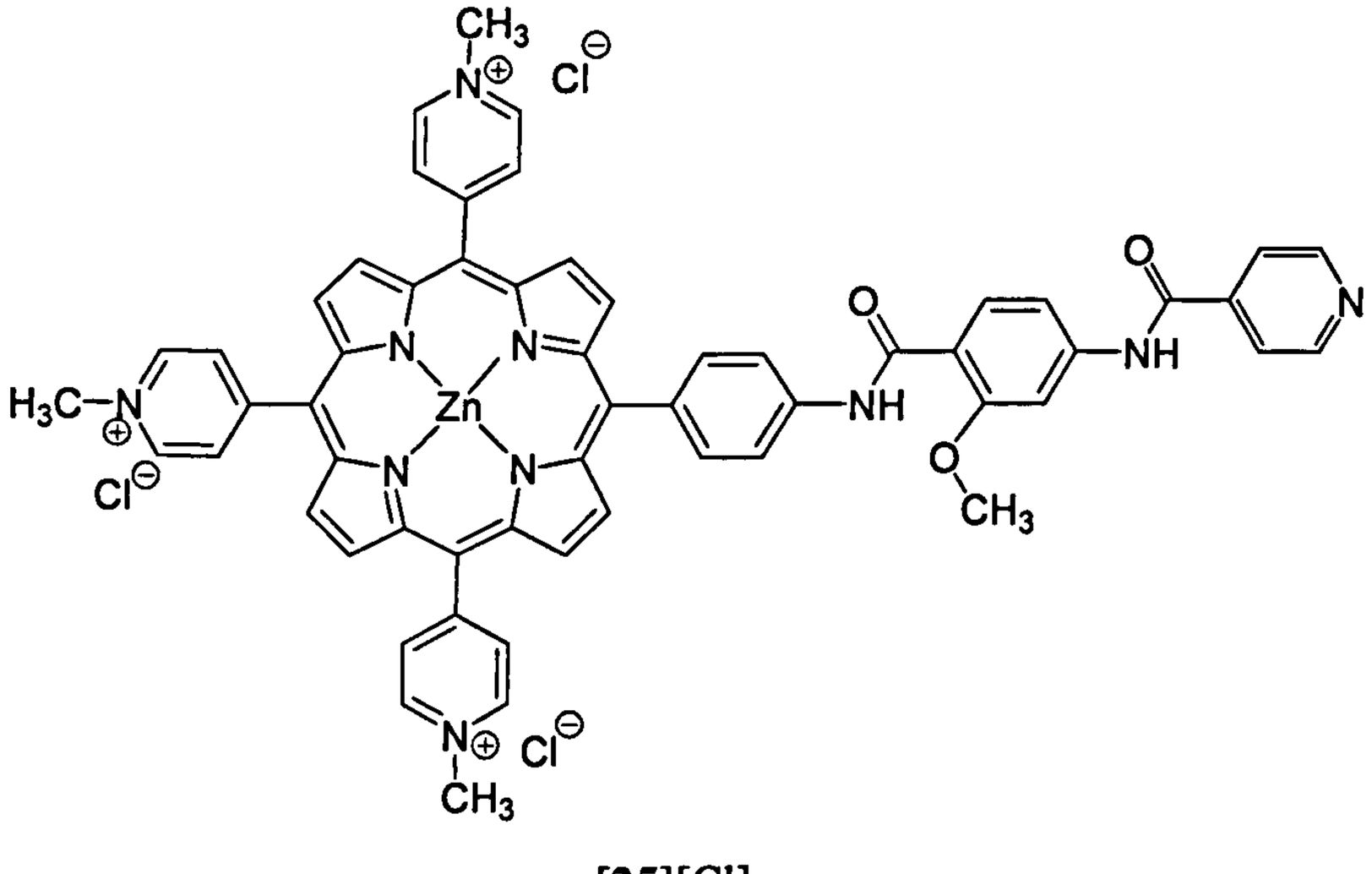

[25][Cl]$_3$

The IC_{50} of **[25][Cl]$_3$** (**Figure 5.20**) was a little higher than that of **[23][Cl]$_3$**. This may be due to the longer length of the probe 'arm' compared to the porphyrin-linker compound. In addition, the amine group present in the latter may have formed stabilising hydrogen bonds with residues in the substrate-binding channel. Nonetheless an IC_{50} in the 100 μM scale is suitable for an application as a probe for XO since it is sufficient to be measured but low enough to allow displacement by strong inhibitors (IC_{50} < 1 μM).

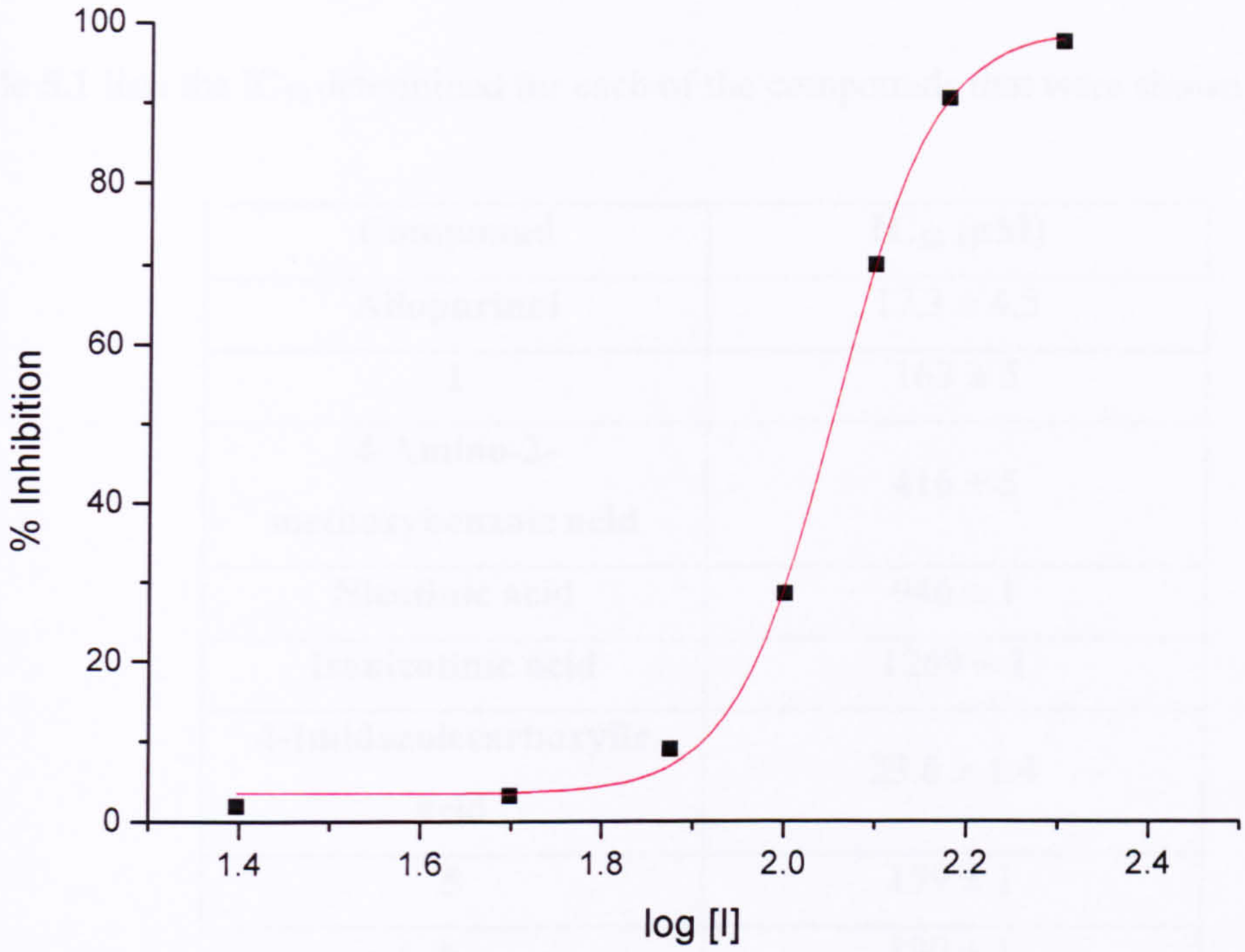

Figure 5.20 Plot of % inhibition vs. log [I] ([I] in μM) where I = [**25**][Cl]$_3$. IC_{50} = 113 ± 1 μM. χ^2 = 2.66, R^2 = 0.999.

5.5.3 Summary of IC_{50} Data

Table 5.1 lists the IC_{50} determined for each of the compounds that were shown to inhibit XO.

Compound	IC_{50} (μM)
Allopurinol	17.3 ± 4.5
1	163 ± 5
4-Amino-2-methoxybenzoic acid	416 ± 5
Nicotinic acid	946 ± 1
Isonicotinic acid	1269 ± 1
4-Imidazolecarboxylic acid	23.6 ± 1.4
5	179 ± 1
6	130 ± 1
[23][Cl]$_3$	81.2 ± 3.6
[25][Cl]$_3$	113 ± 1

Table 5.1 IC_{50} values for each of the compounds with XO.

5.6 Binding Constant, K_i.

Since the IC_{50} is dependent on the conditions of the assay, of which there is a great variation across published data, the binding constant, K_i was calculated from equation 14.

$$[I]_{0.5} = (1 + [S]/K_m)\, K_i \qquad (14)$$

K_m was estimated for each assay using the double-reciprocal plot method described earlier (**Figure 5.21** and **Figure 5.22**).

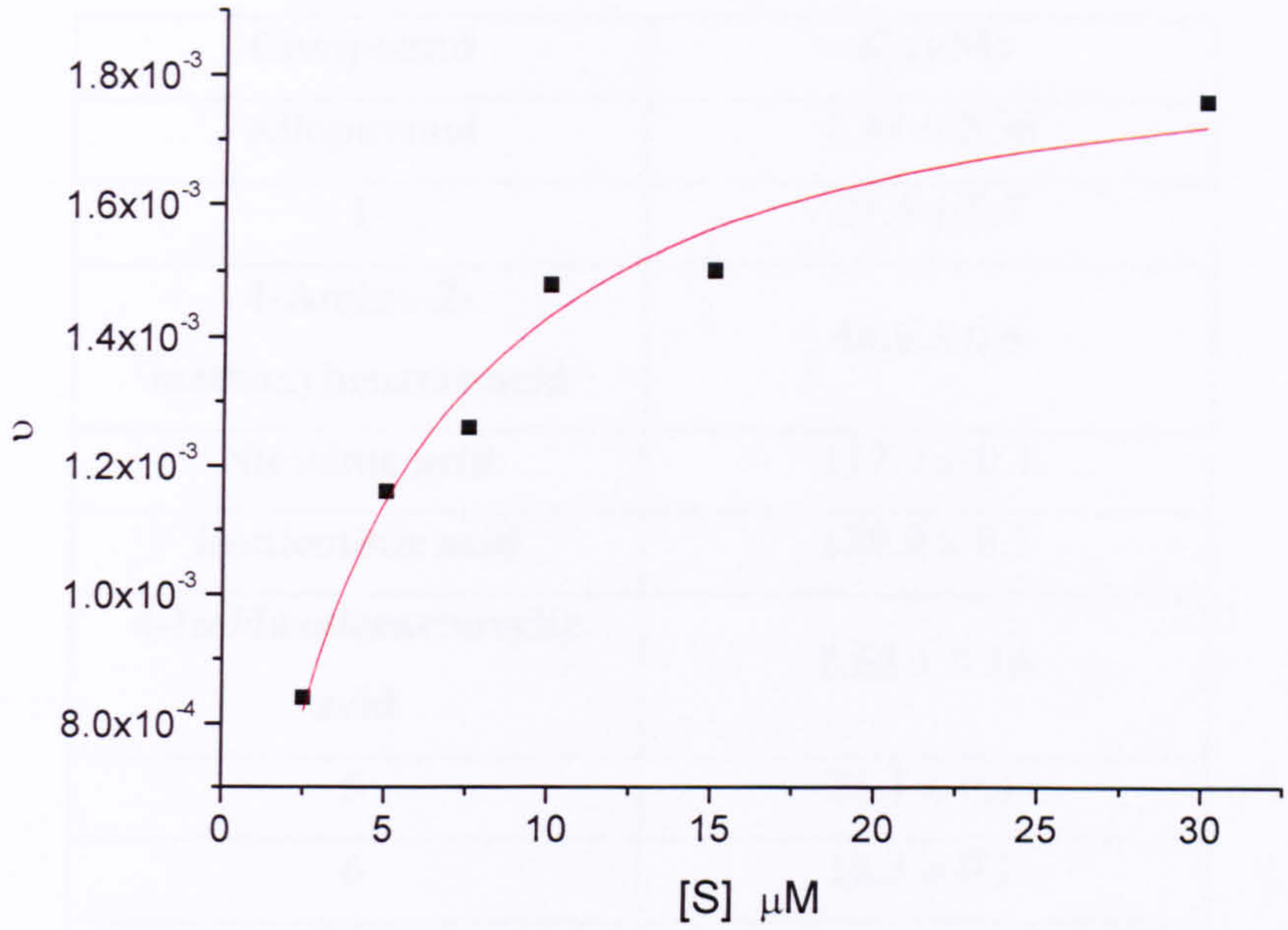

Figure 5.21 Example plot of υ against [S] in the concentration range used to determine K_m.

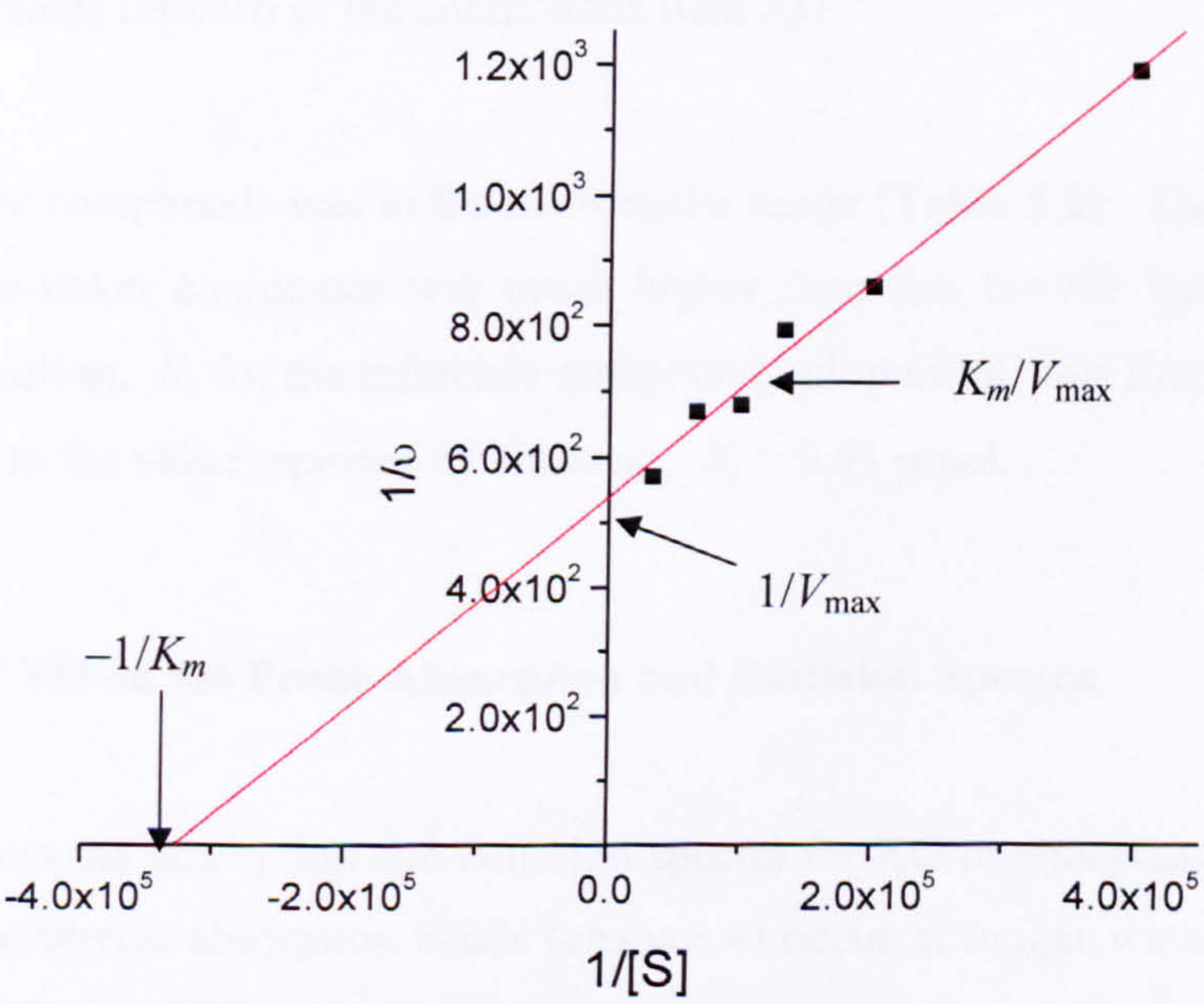

Figure 5.22 Example plot of 1/ υ against 1/[S] used to determine K_m. [S] in μM. $1/V_{max}$ = 537, K_m/V_{max} = 0.00164, K_m = 3.05 μM.

Compound	K_i (μM)
Allopurinol	1.37 ± 0.36
1	21.5 ± 0.7
4-Amino-2-methoxybenzoic acid	48.6 ± 0.6
Nicotinic acid	112.9 ± 0.1
Isonicotinic acid	139.9 ± 0.1
4-Imidazolecarboxylic acid	2.63 ± 0.16
5	25.1 ± 0.1
6	18.3 ± 0.1
[23][Cl]$_3$	11.4 ± 0.5
[25][Cl]$_3$	31.9 ± 0.3

Table 5.2 K_i values for each of the compounds with XO.

K_i for each of the compounds was in the micromolar range (**Table 5.2**). The binding affinity for the substrate-linker conjugates was much higher than that for the linker and substrate analogues themselves. K_i for the reference compound, allopurinol, was found to be 1.4 ± 0.4 μmol compared to the value reported by Ho *et al.*, K_i = 0.91 μmol.

5.7 Affects of XO on the Probe Absorption and Emission Spectra

Figure 5.23 shows the absorption and emission spectra for XO in phosphate buffer (50 mM, pH 7.5). The porphyrin absorption bands (chapter 4) occur at longer wavelength than λ_{max} for the enzyme (**Figure 5.23 (A)**). Similarly the emission bands are at longer wavelength for porphyrins **22 - 25** than that of XO (**Figure 5.23 (B)**). These properties are essential for an efficient probe.

A

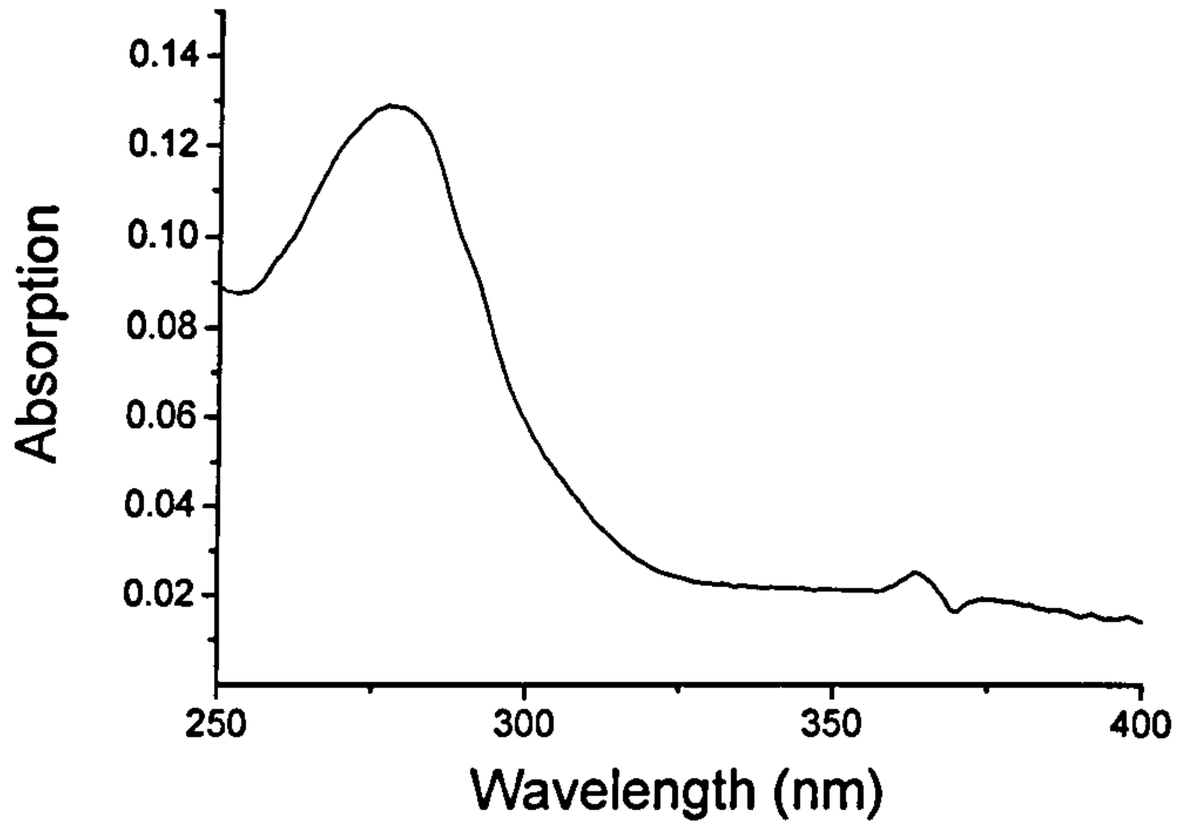

B

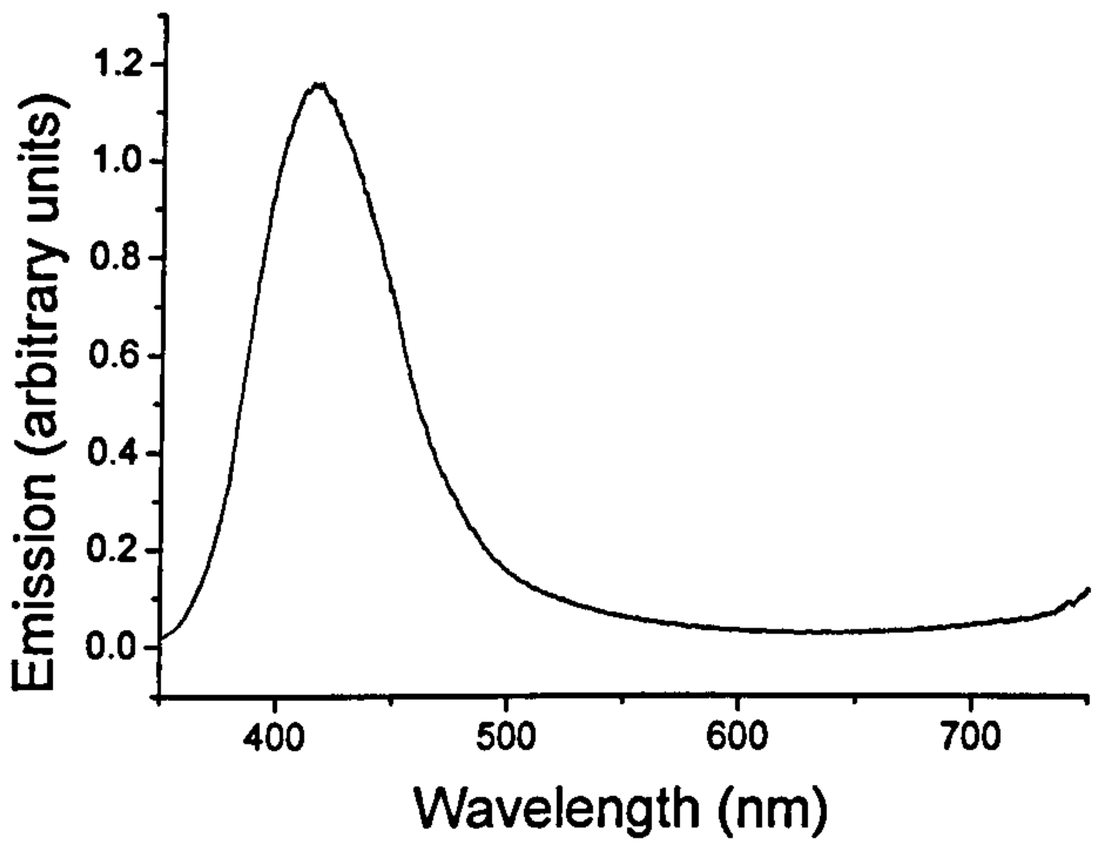

Figure 5.23 **(A)** Absorption spectra for XO; **(B)** emission spectra for XO (λ_{ex} = 280 nm)

10μl XO (bovine milk, grade III, 22 mg ml^{-1}, 1.30 U ml^{-1}) was added to each of the water-soluble porphyrins, **22 – 24**. In each case the absorption decreased by ~ 30 % and was accompanied by a small red-shift (1-3 nm) (**Figure 5.24 (A)**). This was matched by a 30 % decrease in emission intensity (**Figure 5.24 (B)**). . This shows that the porphyrin does report the presence of XO by a change in luminescence and absorption.

A

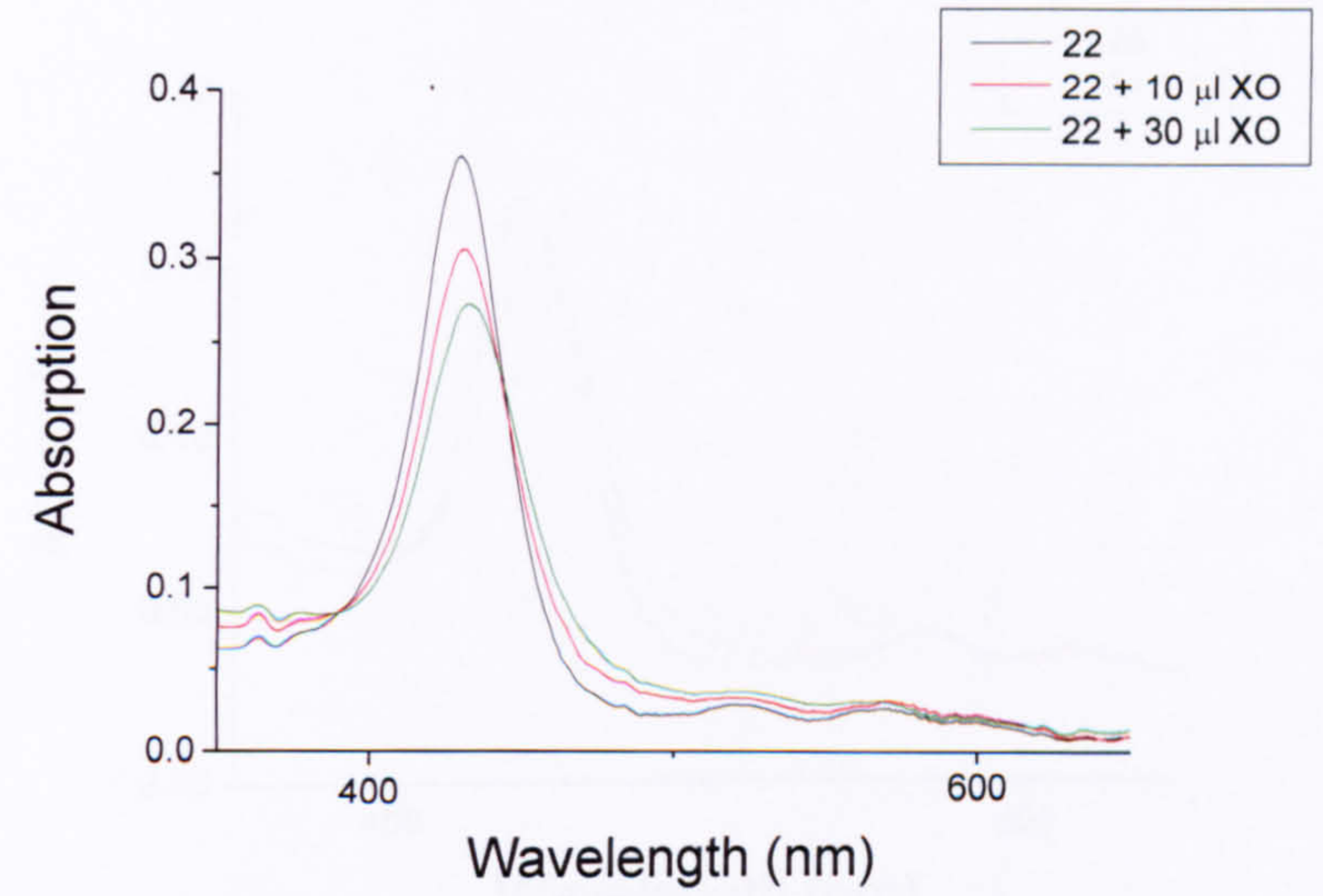

B

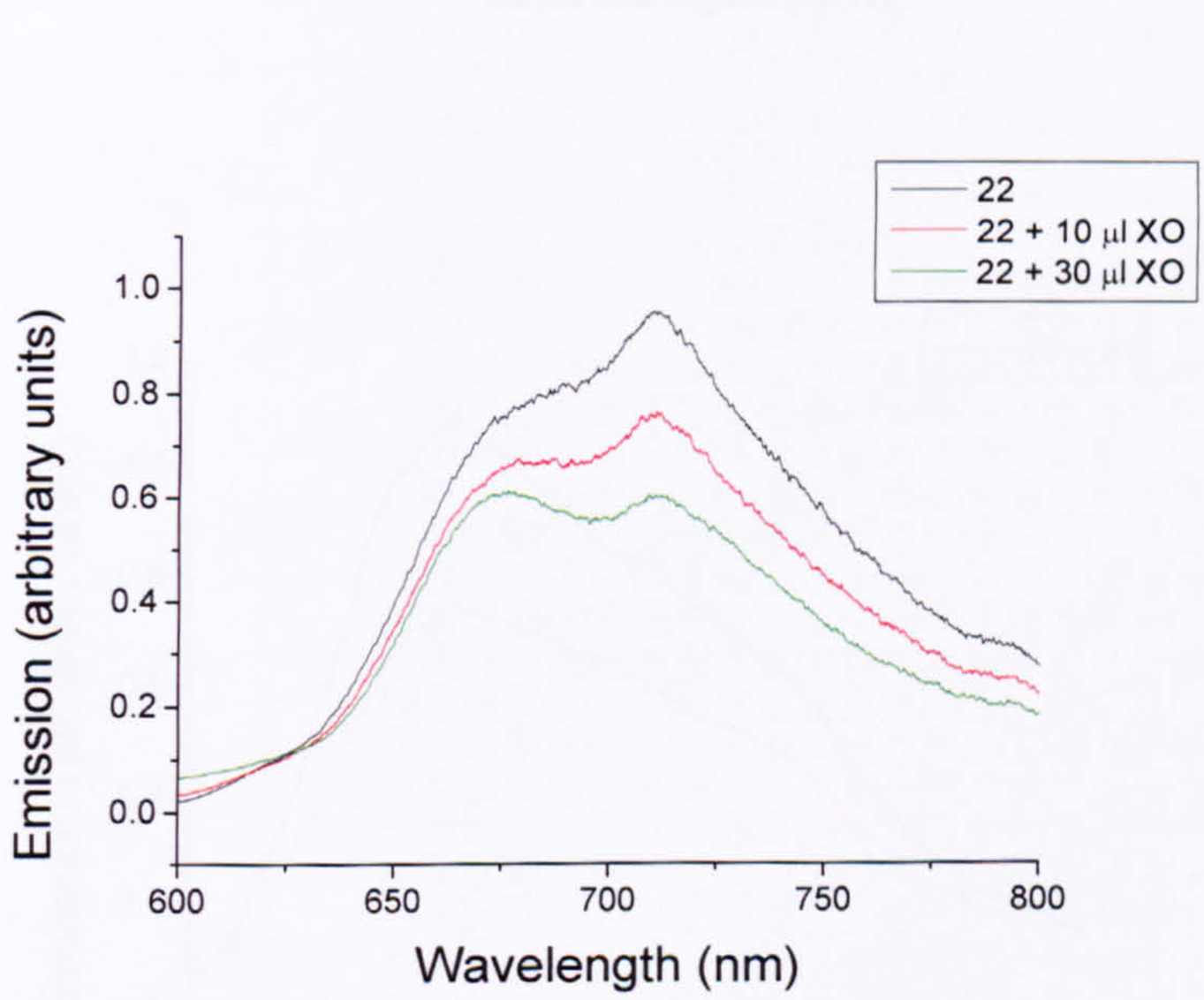

Figure 5.24 Effect of adding XO to [**22**][Cl]$_3$ in phosphate buffer pH 7.5; **(A)** absorption spectra; **(B)** corrected emission spectra (λ_{ex} = 420 nm).

The absorption spectrum for [**25**][Cl]$_3$ was more substantially red-shifted on addition of XO (441 – 446 nm). The quantum yield was also reduced by 25 %.

A

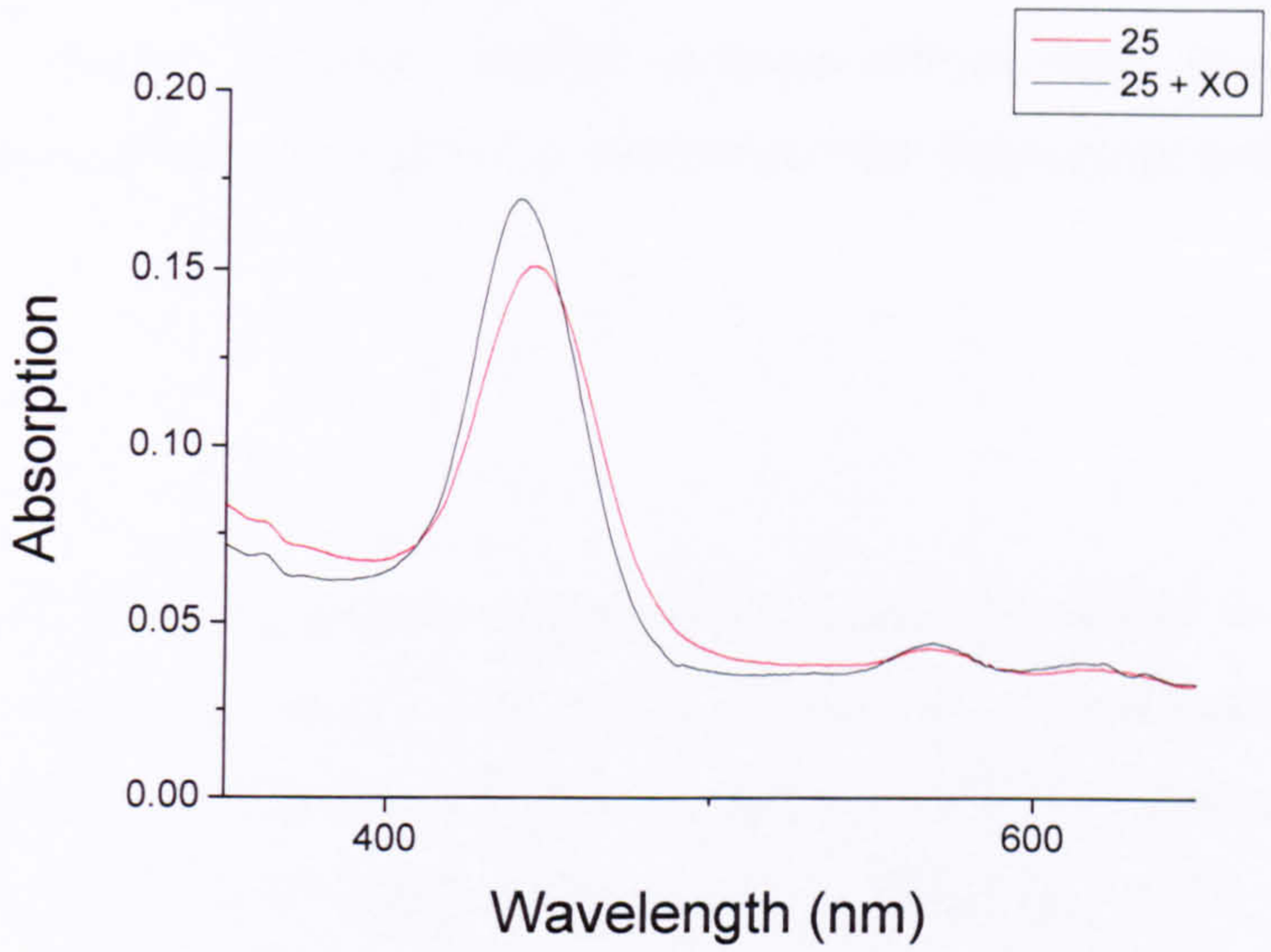

B

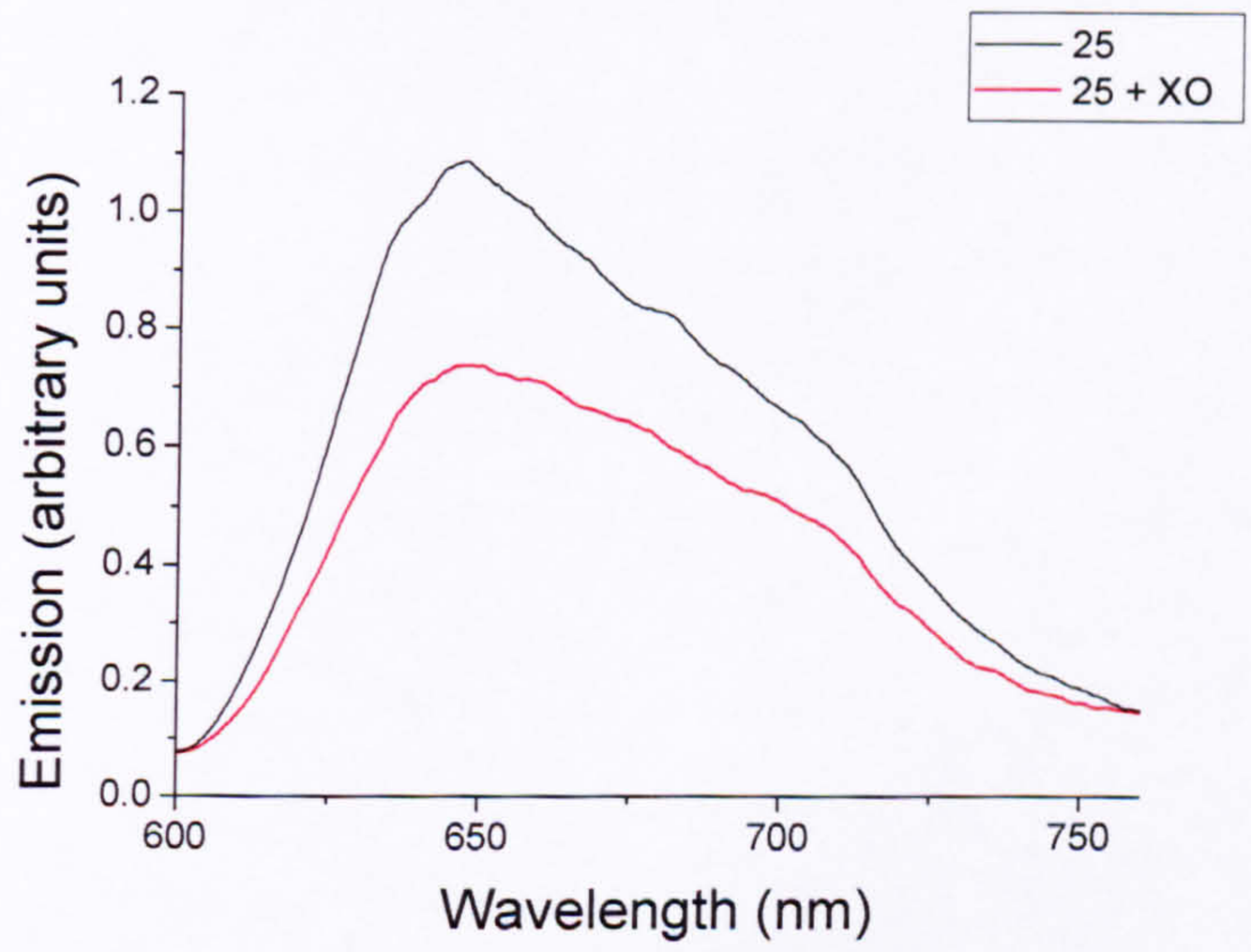

Figure 5.25 Effect of adding XO to [**25**][Cl]$_3$ in phosphate buffer pH 7.5; **(A)** absorption spectra; **(B)** corrected emission spectra (λ_{ex} = 570 nm).

Addition of allopurinol did not result in restoration of the luminescence. Therefore it has not been conclusively proven that the quenching is due to binding to the active site and not just to the enzyme surface. However, neither of these effects were observed for TMPyP, suggesting that the quenching is not due to interaction with the enzyme surface alone.

5.8 Summary

The IC_{50} for the substrate-analogues and substrate-linker conjugates in xanthine oxidase affinity assays were measured by spectrophotometric rate determinations. The values obtained were used to aid design of the final compound, **[25]**$[Cl]_3$. Each of the compounds had a binding affinity, K_i, in the micromolar range. For **[23]**$[Cl]_3$, the $K_i = 11.4 \pm 0.5$ μM is lower than that of **[25]**$[Cl]_3$ ($K_i = 31.9 \pm 0.3$ μM). However **[25]**$[Cl]_3$ has the potential to bind closer to the molybdenum active site than **[23]**$[Cl]_3$. The absorption spectra for the probe, **[25]**$[Cl]_3$, was red-shifted in the presence of XO and the quantum yield was 25 % lower than in the absence of the enzyme.

5.9 References

1. I. H Segel, 'Enzyme Kinetics', John Wiley & Sons, 1975.
2. A. Cornish-Bowden, 'Fundamentals of Enzyme Kinetics', Butterworth & Co Ltd., 1979.
3. A.P. Sweeney, S.G. Wyllie, R.A. Shalliker, J.L. Markham, *J. Ethnopharmacology,* **2001**, *75*, 273.
4. P. Pacher, A. Nivorozhkin, C. Szabó, *Pharmacological Reviews*, **2006**, *58*, 87.
5. G. Biagi, A. Costantini, L. Costantino, I. Giorgi, O. Livi, P. Pecorari, M. Rinaldi, V. Scartoni, *J Med Chem* **1996**, *39*, 2529.
6. C. Y. Ho, A. J. Clifford, *J. Nutrition*, **1976**, *106*, 1600.
7. T. Spector, D. G. Johns, *J. Biol. Chem.*, **1970**, *245*, 5079.
8. J. Hunt, V. Massey, *J. Biol. Chem.*, **1992**, *26*, 21479.

CHAPTER SIX

CONCLUSIONS AND FUTURE WORK

6. Conclusions and Future Work

6.1 Conclusions

Water-soluble zinc porphyrin derived probes, which report binding to xanthine oxidase (XO), have been prepared. The probes are composed of a porphyrin luminophore, a linker and a substrate.

The porphyrin luminophore absorbed strongly in the visible region of the electromagnetic spectrum where there is little competition between the flavin and XO. The chloride salts of the pyridinium derivatives were highly water-soluble, which is required for the XO affinity bioassay. There is also a possibility for interaction of the cationic groups with the charged surface of the protein. Zinc was incorporated to give an electron donating metalloporphyrin. Electron transfer from the metalloporphyrin to the molybdenum cofactor active site on coordination of the probes would result in quenching of the luminescence and therefore signal binding.

4-amino-2-methoxybenzoic acid was chosen as the linker since it is aromatic and contains possible hydrogen bond donor and acceptor substituents. Therefore, it can be stabilized within the hydrophobic channel leading to the active site. The neutral ester derivative (**1**) was shown to bind to XO with $K_i = 21.5 \pm 0.7$ μM.

The enzyme catalyses oxidation of aromatic, nitrogen containing heterocycles. Isonicotinic acid was shown to bind to the enzyme with $K_i = 112.9 \pm 0.1$ μM. However, when coupled to the linker (**6**) the binding was improved to $K_i = 18.3 \pm 0.1$ μM, making it a suitable choice as the substrate.

A straightforward strategy was used to sequentially couple the aromatic units using peptide chemistry. The need for amine protecting groups was avoided by using the corresponding nitro compound and selectively reducing the coupled species with indium and ammonium

chloride to give the amine. This procedure was suitable for preparing the simple substrate-linker compounds in addition to neutral and cationic porphyrin-linker, extended porphyrin-linker-substrate compounds and extended ruthenium polypyridyl complexes.

A range of standard characterisation techniques were used to identify the compounds, including NMR, FTIR, UV-visible absorption, luminescence spectroscopy and mass spectrometry. The compounds displayed behaviour characteristic of porphyrins, such as high extinction coefficients and stability, which are necessary for this application. The NMR and FTIR spectra indicated the presence of intra molecular hydrogen bonding which was confirmed by x-ray crystallography. Aggregation of the porphyrin compounds was occasionally observed in the NMR and mass spectra. At the low concentrations used in the xanthine oxidase assays and fluorescence studies, aggregation was not observed in the UV-Vis absorption spectra.

Enzyme affinity bioassays were carried out on the porphyrin compounds to investigate their ability to bind to XO. The porphyrin-linker compound, **23**, had a lower IC_{50} than the linker (**1**) alone. This could be due to a combination of improved water solubility compared to compound **1** and the cationic periphery lining up with the anionic residues around the channel. Since compound **23** was not displaced by allopurinol (IC_{50} 17 μM, K_i 1.37 μM) the channel may be blocked by the porphyrin, preventing access. ZnTMPyP did not inhibit XO and, therefore, inhibition by compound **23** is likely to be associated coordination of the amine with an amino acid residue within or close to the channel.

Compound **25** had a lower affinity for XO (IC_{50} = 113 ± 1 μM, K_i = 31.9 ± 0.3 μM) than compounds **23** and **1**. Despite its weaker binding to XO, the longer probe should approach more closely or bind directly to the active site molybdenum. As a result there is more opportunity for quenching of the luminescence by electron transfer. Indeed, addition of XO to an aqueous solution of **[25]**$[Cl]_3$ did cause quenching of the porphyrin emission and a red shift in the absorption spectrum. The K_i is in the low micromolar region which is suitable for use in screening for XO inhibitors, where the displacement of the probe by active analytes (such as febuxostat $K_i \sim$ nM) would restore the porphyrin luminescence.

6.2 Future work

4-Imidazolecarboxylic acid had the highest affinity for XO (K_i = 2.63 ± 0.16 μM). If this substrate could be coupled to the porphyrin-linker compound the resulting probe could bind more tightly to XO than **[25]**$[Cl]_3$. The synthetic procedure has been shown to be highly versatile; enabling synthesis of tetraphenyl porphyrin derivatives as well as water-soluble trimethylpyridiniumyl porphyrins. Further modification of the linker and substrate-analogue, such as substitution of 4-imidazolecarboxylic acid for isonicotinic acid, should be reasonably straightforward. Likewise, derivatisation around the porphyrin periphery is not restricted to methylation of the pyridyl nitrogens.

Further investigation using a more rigorously purified enzyme solution should give more informative results. Nonetheless, the probe has been shown to bind to XO and to report interaction with the protein by a change in the absorption and luminescence properties as anticipated. The preliminary studies introduced here should provide the foundation for more extensive analysis of the kinetics involved and an indication of how the system can be improved. Such experiments could include transient absorption spectroscopy where the lifetimes of the excited state intermediates could be measured and used to confirm electron transfer from the porphyrin to the molybdenum cofactor.

Further studies need to be carried out with a pure solution of XO. The enzyme solution purchased, whilst the highest grade available, is a mixture of active and inactive enzyme, which contains, amongst other impurities, free flavin. Titrations with pure XO should give more reliable results. In addition, further investigation of the required incubation time should be completed. Inhibition by allopurinol is known to be time dependent (~ 2 hours for maximal inhibition) due to the time taken to form alloxanthine and this is not unusual. The spectra did not appear to vary over one hour but it would be desirable to measure the spectra over a longer time, maintained at a cool temperature to avoid degradation of the enzyme, with pure XO. Co-crystallisation of the probe with XO would give more structural information and assist with improvements to the system.

CHAPTER SEVEN

EXPERIMENTAL

7. Experimental

7.1. General Methods

Chemicals came from the following suppliers: triethylamine, sodium carbonate, ammonium chloride, nicotinic acid (BDH); tetraphenylporphyrin (H_2TPP) (Frontier Scientific); 4-aminosalicylic acid, 2-methoxy-4-nitrobenzoic acid, indium powder (100 mesh), tetrabutyl ammonium chloride, 4-acetamidobenzaldehyde, methyl iodide, nicotinic acid anhydride, sodium nitrite, imidazole-4-carboxylic acid, isonicotinic acid, potassium bromide, potassium phosphate, trifluoroacetic acid, EDTA (0.1 M in water), Celite®, Florisil®, xanthine oxidase (bovine milk, grade III, 22 mg ml^{-1}, 1.30 U ml^{-1}) (Sigma-Aldrich); ammonium carbonate, tin dichloride dihydrate, zinc (II) acetate, tetrabutylammonium hexafluorophosphate, allopurinol (Avocado); DCC (Acros Organics); ammonium hexafluorophosphate (Fluorochem) pyridine-4-carboxaldehyde, propionic acid, acetic anhydride, pyrrole, xanthine (Alfa Aesar) magnesium sulfate, sodium hydroxide, potassium hydroxide, dimethyl sulfate, sodium hydrogen carbonate, sodium carbonate, sodium sulfate, sodium chloride, hydrochloric acid (Fisher); ammonia solution (Fisons); silica gel 60, DMAP (Fluka); NsCl (Lancaster); Sephadex G-10 (Sigma); TLC plates F_{254} (Merck), $[TMPyP][OTs]_4$ kindly donated by Prof. John Lindsey-Smith.

Solvents for general use were obtained from Fisher and dried over calcium hydride (triethylamine, acetonitrile, chloroform) or Drierite ® (Aldrich) (acetone), distilled and stored under argon. Dichloromethane was dried using a PURE SOLV 400 solvent purification system[3].

All reactions were carried out under an argon atmosphere unless otherwise stated. Deuterated solvents were obtained from Aldrich or Cambridge Isotope Laboratories.

7.2. Physical Measurements

UV-Visible Spectra were recorded on an Agilent 8453 diode-array spectrophotometer. Infra-red spectra were recorded on a Unicam RS 10 000E FTIR instrument. EI and FAB Mass Spectra were recorded on a VG Auto-Spec mass spectrometer, ESI-MS on a Finnigan LCQ instrument. NMR spectra were recorded on a Bruker AMX 300, Bruker AMX 500 or Bruker DMX 600 spectrometer. Fluorescence spectra were recorded on a Hitachi F-4500 fluorescence spectrometer. Samples were measured using a 10 mm pathlength and constant slit width. The instrument was corrected for the wavelength dependent response of the detector system. For quantum yield determination the absorption at and above the excitation wavelength was below 0.1 absorbance units.

Diffraction data were collected at 110 K on a Bruker Smart Apex diffractometer with Mo-Kα radiation (λ = 0.71073 Å) using a SMART CCD camera. Diffractometer control, data collection and initial unit cell determination was performed using "SMART" (v5.625 Bruker-AXS). Frame integration and unit-cell refinement software was carried out with "SAINT+" (v6.22, Bruker AXS). Absorption corrections were applied by SADABS (v2.03, Sheldrick). Structures were solved by direct methods using SHELXS-97 (Sheldrick, 1997) and refined by full-matrix least squares using SHELXL-97 (Sheldrick, 1997). All non-hydrogen atoms were refined anisotropically. Hydrogen atoms were placed using a "riding model" and included in the refinement at calculated positions.

7.3. Synthesis

Methyl 4-Amino-2-methoxybenzoate, 1.

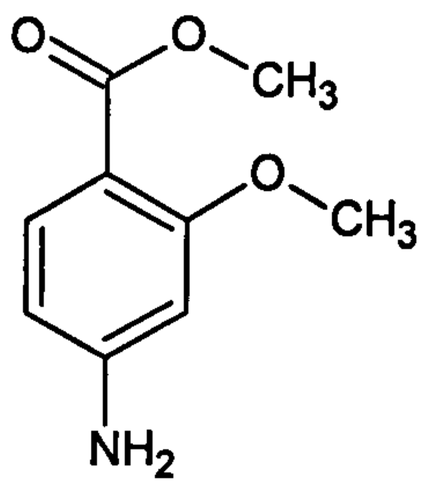

1

4-Aminosalicylic acid (10.0 g, 65 mmol) was dissolved in acetone (200 cm^3). Pellets of potassium hydroxide (9.2 g, 143 mmol) were added followed by dropwise addition of dimethyl sulfate (19.5 g, 155 mmol) at 25 °C. Stirring was continued at room temperature for 2.5 hours. The solvent was removed and the residue was diluted with water (150 cm^3), extracted with ethyl acetate (2 × 150 cm^3), washed with 5% sodium hydrogen carbonate solution (2 × 25 cm^3) and dried with sodium sulfate. Evaporation of the solvent to 70 cm^3 gave **1** as a beige powder (5.0 g, 33 mmol, 45%).

Rf (ethyl acetate): 0.65. **Melting Point:** 149-151 °C.

^{1}H NMR δ_H (500 MHz; solvent $CDCl_3$): 7.74 (1H, d, J = 8.4 Hz, C-6 phenyl), 6.23 (1H, dd, J = 8.5, 2.1 Hz, C-5 phenyl), 6.22 (1H, d, J = 2.1 Hz, C-3 phenyl), 4.18 (2H, br s, NH_2), 3.86 (3H, s, OCH_3), 3.83 (3H, s, OCH_3) ppm.

^{13}C{^{1}H} NMR δ_C (125 MHz; solvent $CDCl_3$): 166.3, 161.8, 152.1, 134.3, 109.1, 106.5, 97.8, 55.8, 51.5 ppm.

EI-MS: m/z = 181 (M^+, 39%), 164 (5), 150 (100), 135 (6), 120 (9), 107 (12), 92 (10), 79 (10), 65 (8), 52 (8), 44 (18).

FTIR (KBr pressed disc) ν_{max} /cm^{-1}: 3464s, 3363s, 3256w, 3219w, 3024w, 3006w, 2971w, 2950m, 2841w, 1673s, 1628s, 1611s, 1593s, 1565s, 1513 m, 1470s, 1435s, 1344s, 1274s br,

1220s, 1183m, 1141s, 1090m, 1030m, 973w, 957w, 837m, 828m, 772m, 702w, 654w, 641w, 551w, 474w.

UV-Vis: λ_{max}/nm (DMSO) 282 (ε/dm^3 mol^{-1} cm^{-1} 15600), 303 (16900).

Methyl 4-[(2-methoxy-4-nitro-phenylcarbonyl)-amino]-2-methoxy benzoate, 2.

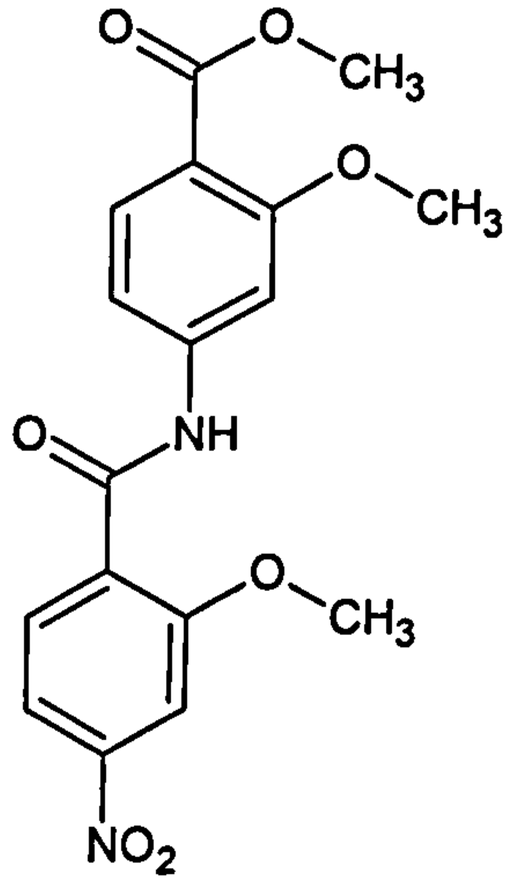

2

Triethylamine (1.67 cm^3, 12.0 mmol) was added to a stirred solution of (1.00 g, 6.0 mmol), DMAP (0.14 g, 1.2 mmol) NsCl (1.34 g, 6.0 mmol) in acetonitrile (60 cm^3) under argon. The solution was stirred for 20 minutes at which point a solution of methyl 4-amino-2-methoxybenzoate **1** (1.24 g, 6.8 mmol) in acetonitrile (10 cm^3) was added under an ice bath. Stirring was continued for 24 hours until a yellow precipitate developed. The reaction mixture was concentrated by 50% and then filtered. The feathery yellow powder was washed thoroughly with cold acetonitrile and dried under vacuum to give **2** (1.63 g, 4.5 mmol, 75%).

Melting Point: 185-190 °C

^{1}H NMR δ_H (500 MHz; solvent $CDCl_3$): 9.76 (1H, s, NH), 8.43 (1H, d, J = 8.6 Hz, phenyl), 7.98 (1H, d, J = 8.6 Hz, phenyl), 7.92 (1H, s, phenyl), 7.87 (1H, s, phenyl), 7.85 (1H, d, J =

8.3 Hz, phenyl), 6.88 (1H, d, J = 8.3 Hz, phenyl), 4.20 (3H, s, OCH_3), 3.97 (3H, s, OCH_3), 3.88 (3H, s, OCH_3) ppm.

$^{13}C\{^1H\}$ NMR δ_C (125 MHz; solvent $CDCl_3$): 166.0, 161.6, 160.7, 157.4, 150.8, 142.8, 133.7, 132.8, 127.0, 116.5, 115.6, 111.35, 107.1, 104.1, 57.3, 56.2, 52.0 ppm.

EI-MS: m/z = 360 (M^+, 63%), 329 (18), 180 (100), 150 (21), 134 (33), 122 (8), 107 (6), 91 (5), 63 (8), 40 (61).

HR ESI-MS: For $C_{17}H_{17}N_2O_7$ ($M + H^+$), observed mass 361.1044, calculated 361.1030, difference 1.4 mDa.

FTIR (KBr pressed disc) ν_{max} /cm^{-1}: 3470br w, 3355m, 3202w, 3155w, 3123w, 3103w, 3011w, 2978m, 2944m, 2880w, 2840w, 2804w, 2758w, 2740w, 2678m, 2625w, 2605w, 2530w, 2493m, (1719m), 1699s, 1677s, 1590s, 1533br s, 1472m, 1459m, 1439m, 1413m, 1357s, 1294s, 1265s, 1256s, 1237s, 1194m, 1175m, 1152s, 1124m, 1113m, 1083s, 1036s, 1020m, 967w, 868s, 858s, 823w, 806s, 769s, 736s, 697 m, 659s, 632m.

UV-Vis: λ_{max}/nm (DMSO) 275 (ε/dm^3 mol^{-1} cm^{-1} 13900), 302 (10000), 340 (5280).

4-[(2-methoxy-4-nitro-phenylcarbonyl)-amino]-2-methoxy benzoic acid, 3.

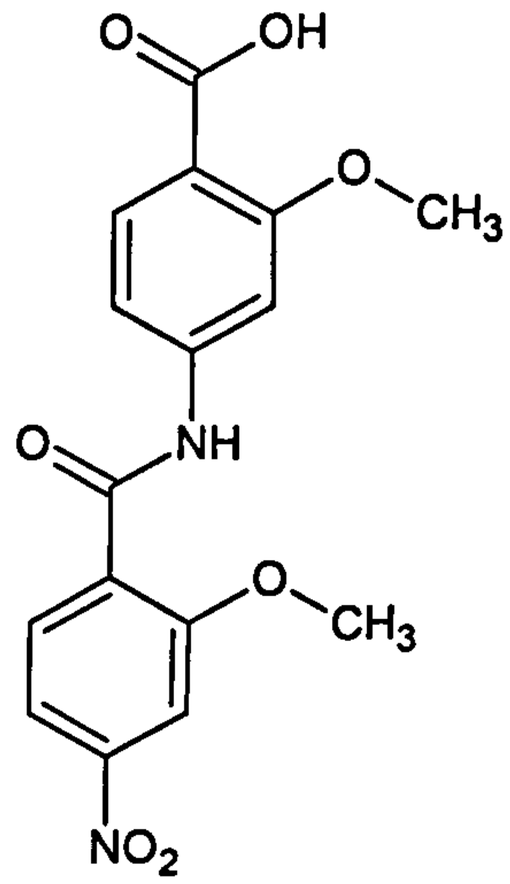

3

2M sodium hydroxide, (1.5 cm^3, 3 mmol) was added to a solution of methyl 4-[(2-methoxy-4-nitro-phenylcarbonyl)-amino]-2-methoxybenzoate **2** (1.00 g, 2.8 mmol) in ethanol (50 cm^3) and heated at reflux for 40 minutes under argon. The solvent was evaporated and the residue taken up in hot water and filtered. 12 M hydrochloric acid was added to alter the solution to pH 3. Cooling gave **3** as a feathery, pale orange solid (0.85 g, 2.5 mmol, 88%).

Melting Point: > 250 °C

^{1}H NMR δ_H (300 MHz; solvent DMSO): 11.20 (1H, s, NH), 8.35 (1H, d, J = 8.4 Hz, phenyl), 8.14 (1H, s, phenyl), 8.12 (1H, s, phenyl) 7.93 (1H, dd, J = 1.9, 8.4 Hz, phenyl), 7.78 (1H. d, J = 2.0 Hz, phenyl), 7.64 (1H, dd, J =1.8, 8.5 Hz, phenyl), 3.85 (3H, s, OCH_3), 3.80 (3H, s, OCH_3) ppm.

^{13}C{^{1}H} NMR δ_C (75 MHz; solvent DMSO): 166.5, 163.9, 159.4, 156.8, 149.4, 143.4, 132.3, 131.8, 130.0, 115.5, 110.7, 106.8, 103.0, 56.7, 55.6 ppm.

EI-MS: *m/z* =346 (M^+, 56%), 180 (100), 150 (6), 134 (32), 122 (7).

HR ESI-MS: For $C_{16}H_{15}N_2O_7$ ($M + H^+$), observed mass 347.0877, calculated 347.0874, difference 0.3 mDa.

FTIR (KBr pressed disc) ν_{max} /cm^{-1}: 3336s, 3270 br m, 3120w, 3100w, 2998w, 2957w, 2851w, 1744 s, 1679s, 1592s, 1520s, 1460m, 1415m, 1353s, 1283m, 1266m, 1238s, 1170m, 1150m, 1126m, 1111w, 1079m, 1013s, 966m, 878s, 859s, 805s, 970s, 734s, 661s

Methyl 4-[(2-methoxy-4-amino-phenylcarbonyl)-amino]-2-methoxy benzoate, 4.

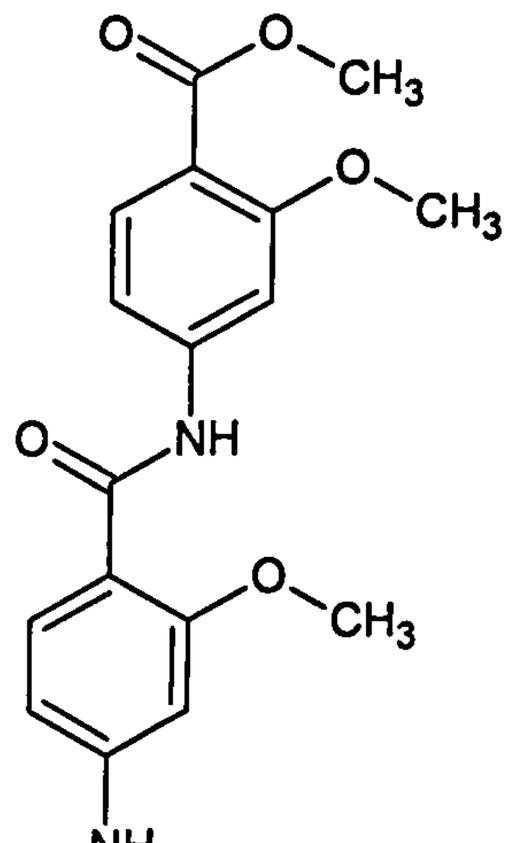

4

Methyl 4-[(2-methoxy-4-nitro-phenylcarbonyl)-amino]-2-methoxybenzoate **3** (0.90 g, 2.5 mmol), was dissolved in 100 cm^3 methanol. Saturated ammonium chloride solution (3 cm^3), and indium powder (100 mesh, 2.0 g), were added and the solution stirred for 72 h under reflux until the reaction was complete by tlc (dichloromethane/methanol v/v 5:1). The reaction mixture was evaporated to dryness and the solid residue extracted with chloroform using Sohxlet apparatus to yield **4** as an orange solid. (0.62 g, 1.9 mmol, 69%)

Melting Point: > 250 °C

^{1}H NMR δ_H (500 MHz; solvent DMSO): 9.97 (1H, s, NH, exchangeable with D_2O), 7.70 (1H, d, J = 1.4 Hz, phenyl), 7.67 (1H, d, J = 8.8 Hz, phenyl), 7.63 (1H, d, J = 8.3 Hz, phenyl) 7.30 (1H, dd, J = 1.9, 8.8 Hz, phenyl), 6.30 (1H. d, J = 1.9 Hz, phenyl), 6.26 (1H, dd, J =1.9,

8.8 Hz, phenyl), 5.93 (2H, s, NH_2), 3.92 (3H, s, OCH_3), 3.82 (3H, s, OCH_3), 3.75 (3H, s, OCH_3) ppm.

$^{13}C\{^1H\}$ NMR δ_C (175 MHz; solvent DMSO): 164.9, 163.5, 159.1, 158.5, 153.7, 143.9, 132.2, 131.5, 112.9, 110.4, 108.2, 106.0, 102.6, 95.4, 55.2, 55.1, 51.0 ppm.

EI-MS: *m/z* =330 (M^+, 25%), 299 (8), 164 (12), 150 (100), 107 (5).

HR ESI-MS: For $C_{17}H_{19}N_2O_5$ ($M + H^+$), observed mass 331.1293, calculated 331.1288, difference 0.5 mDa.

FTIR (KBr pressed disc) ν_{max} /cm^{-1}: 3427m, 3340s, 3238m, 3155w, 3121w, 3084w, 3009w, 2946w, 2913w, 2865w, 2834w, 1714s, 1637m, 1609s, 1585s, 1528br s, 1467m, 1448m, 1432m, 1408m, 1339m, 1329s, 1244br s, 1214w, 1205w, 1186w, 1175w, 1157m, 1085m, 1031m, 975w, 861w, 838w, 821w, 764m, 747w, 696w, 678w, 665w, 548w, 525w.

UV-Vis: λ_{max}/nm (DMSO) 329 (ε/dm^3 mol^{-1} cm^{-1} 27000).

Methyl 4-[(pyridine-3-carbonyl)-amino]-2-methoxy benzoate, 5.

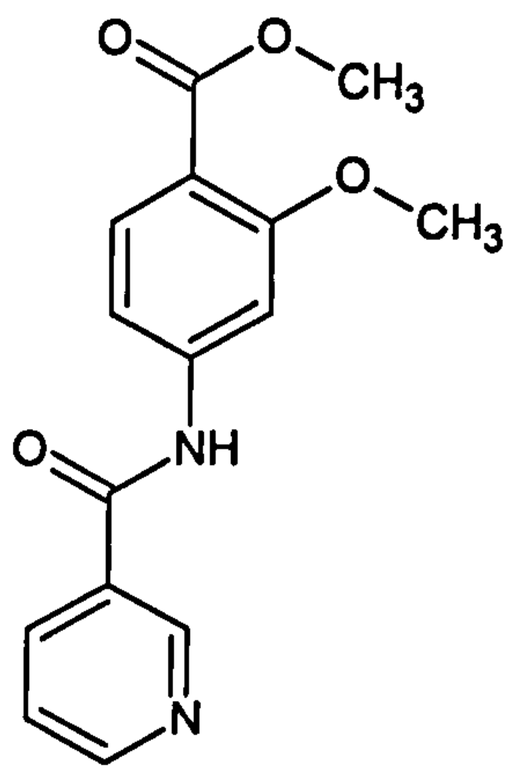

5

Triethylamine (0.7 cm^3, 5.0 mmol) was added to a stirred solution of nicotinic acid (0.31 g, 2.5 mmol), DMAP (0.061 g, 0.50 mmol) NsCl (0.55 g, 2.5 mmol) in acetonitrile (30 cm^3) under argon. The solution was stirred for 20 minutes at which point a solution of methyl 4-

amino-2-methoxybenzoate, **1** (0.50 g, 2.8 mmol) in acetonitrile (10 cm^3) was added under an ice bath. Stirring was continued for 24 hours until the reaction was complete by tlc (ethyl acetate). The reaction mixture was concentrated and extracted into 2M hydrochloric acid. The acid solution was washed with ethyl acetate, neutralised with sodium hydrogen carbonate and the resulting precipitate re-extracted into ethyl acetate. The organic fraction was washed with sodium hydrogen carbonate, water and brine and dried over magnesium sulfate. The solvent was removed *in vacuo* to give **5** as a pale yellow powder (0.27 g, 0.94 mmol, 34 %).

Rf (ethyl acetate): 0.32 **Melting Point:** 144 -146 °C

^{1}H NMR δ_H (300 MHz; solvent $CDCl_3$): 9.11 (1H, s, pyridyl), 8.77 (1H, d, J = 6.0 Hz, pyridyl), 8.33 (1H, s, NH), 8.22 (1H, d, J = 7.3 Hz, pyridyl) 7.85 (1H, d, J = 8.6 Hz, phenyl), 7.72 (1H, d, J = 1.8 Hz, phenyl), 7.44 (1H, dd, J = 4.6, 7.7 Hz, pyridyl), 7.04 (1H, dd, J = 1.7, 8.6, phenyl), 3.91 (3H, s, OCH_3), 3.87 (3H, s, OCH_3) ppm.

^{13}C{^{1}H} NMR δ_C (75 MHz; solvent $CDCl_3$): 166.4, 164.5, 160.1, 152.6, 147.9, 143.0, 136.5, 133.4, 130.0, 124.4, 116.1, 111.4, 104.1, 56.5, 52.4 ppm.

ESI-MS: *m/z* =285.0 ($M - H^+$, 100%).

HR ESI-MS: For $C_{15}H_{15}N_2O_4$ ($M + H^+$), observed mass 287.1025, calculated 287.1026, difference 0.1 mDa.

FTIR (KBr pressed disc) ν_{max} /cm^{-1}: 3401w, 3342s, 3199w, 3150w, 3127w, 3090w, 3056w, 3039w, 3012w, 2964w, 2935w, 2913w, 2863w, 2837w, 1687s, 1663s, 1593s, 1532s, 1479w, 1466m, 1448m, 1429m, 1406s, 1341w, 1298s, 1257s, 1202w, 1187w, 1173w, 1147m, 1117w, 1090m, 1026m, 976w, 958w, 886w, 860m, 839w, 827w, 780m, 734w, 704, 682w, 640w, 620w, 583w.

UV-Vis: λ_{max}/nm (DMSO) 284 (ε/dm^3 mol^{-1} cm^{-1} 14000) 308 (13000).

Methyl 4-[(pyridine-4-carbonyl)-amino]-2-methoxy benzoate, 6.

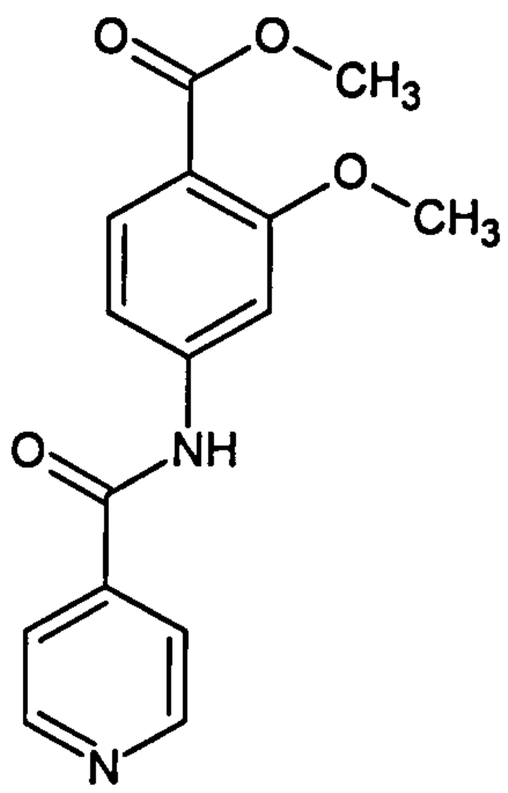

6

The procedure above was carried out using isonicotinic acid to give **6** as a pale yellow powder (0.30 g, 1.0 mmol, 40 %).

Rf (ethyl acetate): 0.30

Melting Point: 196-197 °C

^{1}H NMR δ_H (300 MHz; solvent $CDCl_3$): 8.82 (2H, dd, *J* = 4.5, 1.6 Hz, pyridyl), 8.04 (1H, s, NH), 7.86 (1H, d, *J* = 8.5 Hz, phenyl), 7.74 (1H, d, *J* = 1.8 Hz, phenyl) 7.71 (2H, dd, *J* = 1.5, 4.4 Hz, pyridyl), 6.99 (1H. dd, *J* = 1.9, 8.5, phenyl), 3.94 (3H, s, OCH_3), 3.88 (3H, s, OCH_3) ppm.

^{13}C{^{1}H} NMR δ_C (75 MHz; solvent $CDCl_3$): 166.3, 164.3, 161.0, 151.3, 142.7, 141.9, 133.4, 121.3, 116.3, 111.3, 104.0, 56.6, 52.4 ppm.

ESI-MS: *m/z* =285.0 (M - H^+, 100%).

HR ESI-MS: For $C_{15}H_{15}N_2O_4$ (M + H^+), observed mass 287.1023, calculated 287.1026, difference 0.3 mDa.

FTIR (KBr pressed disc) ν_{max}/cm^{-1}: 3468 br w, 3324s, 3199w, 3128w, 3098w, 3064w, 3049, 3031w, 3001w, 2954w, 2934w, 2919w, 2833w, 1690s, 1670s, 1591s, 1532s, 1467m, 1451m, 1413s, 1340m, 1297s, 1259s, 1206w, 1179w, 1147m, 1094m, 1068w, 1029m, 992w, 977w, 96m, 893w, 860m, 848m, 829w, 781m, 756m, 694m, 663w, 644w, 547w.

UV-Vis: λ_{max}/nm (DMSO) 280 (ε/dm^3 mol^{-1} cm^{-1} 18000), 305 (14000).

5-(4-aminophenyl)-10,15,20-triphenylporphyrin, 9[1].

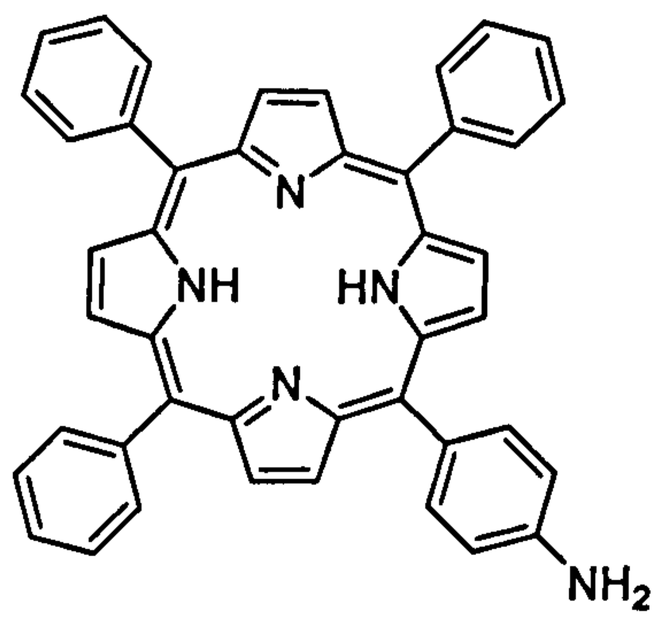

9

Sodium nitrite (1.0 g, 14.5 mmol) was added to a solution of 5, 10, 15, 20-tetraphenylporphyrin (5.0 g, 8.15 mmol) in trifluoroacetic acid (500 cm^3) and the reaction was stirred at room temperature until the reaction was complete by tlc (3 mins). The reaction was quenched by pouring into cold water (5000 cm^3). The mixture was extracted with dichloromethane (6 × 1000 cm^3), which was washed with saturated sodium hydrogen carbonate and water, then dried over sodium sulfate. The solvent was removed *in vacuo* and the mixture was purified on a plug of silica (Si-60, dichloromethane). The solvent was removed and the purple product was dissolved in hydrochloric acid (500 cm^3). Tin dichloride dihydrate (11.0 g, 48.8 mmol) was added with stirring and the reaction was heated to 65 °C for 1 h under argon. The reaction mixture was poured into cold water (5000 cm^3) and neutralized with ammonia solution (pH 8). The suspension was extracted with dichloromethane until colourless. The organic layer was died over sodium sulfate, concentrated *in vacuo*, and purified by column chromatography (Si-60, dichloromethane) to give **9** (3.21 g, 5.14 mmol, 63 %).

R_f (Chloroform) = 0.23

^{1}H NMR δ_H (500 MHz; solvent $CDCl_3$): 9.01 (2H, d, *J* = 4.6 Hz, β-pyrrole), 8.91 (6H, s, β-pyrrole), 8.29 (6H, m, *o*-phenyl), 8.05 (2H, d, *J* = 8.3 Hz, *o*-aminophenyl), 7.81 (9H, m, *m*-/*p*-phenyl), 7.07 (2H, d, *J* = 8.3 Hz *m*-aminophenyl), 4.00 (2H, br s, NH_2), -2.66 (2H, br s, inner NH) ppm.

^{13}C{^{1}H} NMR δ_H (125 MHz; solvent $CDCl_3$): 146.2, 142.5, 142.4, 135.9, 134.8, 132.6, 128.0, 126.9, 126.8, 121.1, 120.2, 113.7 ppm.

FAB-MS: *m/z* = 630 (M^+, 52%), 535 (9), 503 (5), 474 (6), 461 (16), 429 (10), 401 (6), 355 (7), 327 (14), 281 (23), 267 (14), 221 (26), 207 (38), 191 (19), 177 (8), 147 (100)

FTIR (KBr pressed disc) ν_{max} /cm^{-1}: 3455br w, 3317w, 3051w, 3023w, 1619m, 1510m, 1470m, 1440m, 1349m, 1261m, 1177m, 965s, 844s, 731m, 700m.

UV-Vis: λ_{max}/nm ($CHCl_3$) 419 (ε/dm^3 mol^{-1} cm^{-1} 439000), 516 (26900), 552 (15600), 590 (9960), 647 (8680).

Free base 5-[4-[(2-methoxy-4-nitro-phenylcarbonyl)-amino] phenyl]-10,15,20-triphenyl porphyrin, 10.

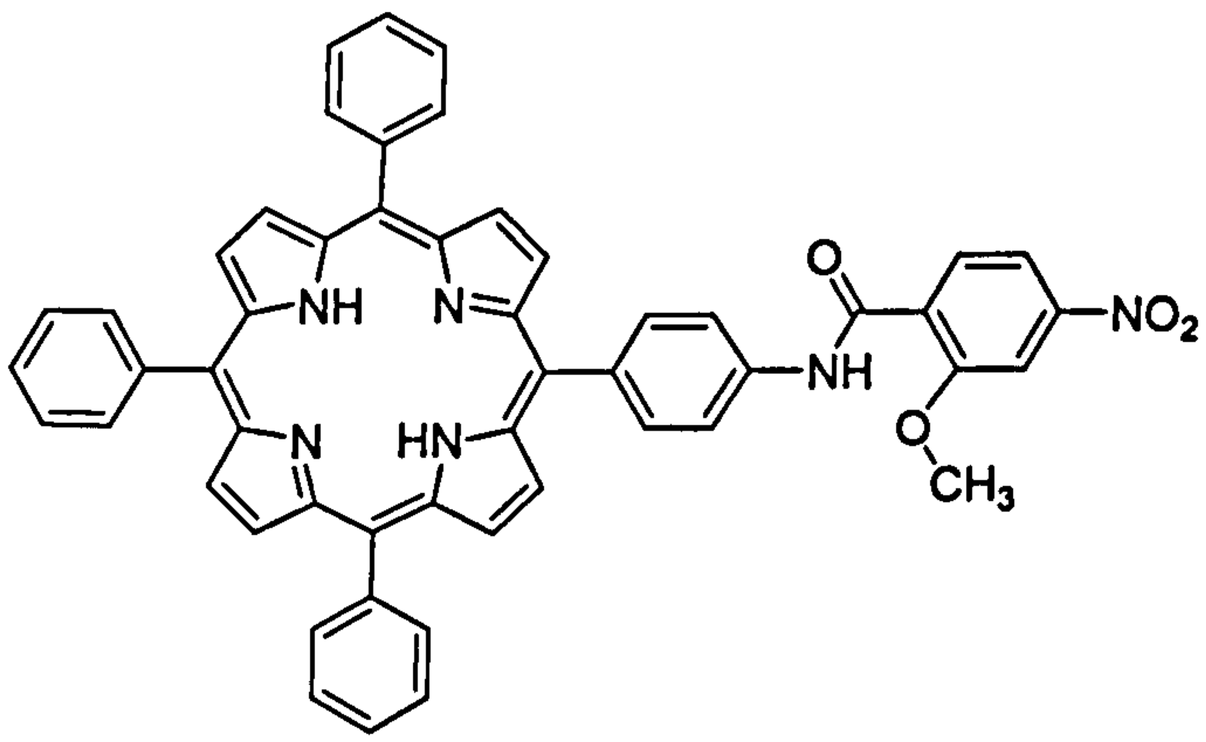

10

Dicyclohexylcarbodiimide (1.00 g, 4.85 mmol) was added to a stirred solution of 2-methoxy-4-nitrobenzoic acid (0.80 g, 4.05 mmol) in acetonitrile (25 cm^3) at 0 °C. After 15 minutes the reaction was brought to room temperature and stirred until the reaction was complete by tlc (10:1 chloroform:acetonitrile v/v) (~24 h). The solution was filtered and the solid by-product was washed thoroughly with acetonitrile and the washings added to the filtrate. Removal of the solvent yielded a pale yellow solid, which was used without any further purification. The anhydride residues were taken up in acetonitrile (20 cm^3) and added dropwise to an ice cold solution of free base 5-(4-aminophenyl)-10,15,20-triphenylporphyrin, **9** (0.40 g, 0.635 mmol) in chloroform with stirring. The reaction was heated at reflux for 48 h. The solvent was removed and the purple residue was extracted into dichloromethane and washed with 2 M sodium hydroxide (3 × 250 cm^3), water and brine. The organic fraction was dried over sodium sulfate and the solution was then concentrated *in vacuo* and purified by column chromatography (Si-60, 10:1 chloroform:acetonitrile v/v) to give **10** (0.44 g, 0.544 mmol, 86 %).

Rf (10:1 chloroform:acetonitrile v/v): 0.86.

^{1}H NMR δ_H (500 MHz; solvent $CDCl_3$): 9.99 (1H, s, NH), 8.89 (8H, m, β-pyrrole), 8.58 (1H, d, J = 8.4 Hz, phenyl), 8.29 (2H, d, J = 8.0 Hz, *o*-aminophenyl) 8.26 (6H, m, *o*-phenyl), 8.11 (2H, d, J = 8.2 Hz, *m*-aminophenyl) 8.05 (1H, dd, J = 2.3, 8.8 Hz, phenyl), 7.78 (9H, m, *m*-/ *p*-phenyl), 7.96 (1H, d, J = 2.0 Hz, phenyl), 4.31 (3H, s, OCH_3), -2.74 (2H, br s, inner NH) ppm.

^{13}C{^{1}H} NMR δ_C (176 MHz; solvent $CDCl_3$): 161.5, 157.3, 150.6, 142.2, 142.1 138.8, 137.4, 135.3, 134.6, 133.9, 127.8, 127.3, 126.7, 120.3, 120.2, 119.3, 118.9, 116.5, 107.0, 57.2, ppm.

ESI-MS: m/z = 809.5 ($M + H^+$, 100%), 807.4 ($M - H^+$, 100%).

HR ESI-MS: For $C_{52}H_{37}N_6O_4$ ($M + H^+$), observed mass 809.2895, calculated 809.2871, difference 2.4 mDa.

FTIR (ATR) ν_{max} /cm^{-1}: 1676s, 1589s, 1521s, 1471s, 1440m, 1400m, 1344s, 1311m, 1259s, 1177m, 1156m, 1101br s, 1056m, 1022s, 1002s, 981s, 964s, 867m, 798s, 750m, 728s, 699s.

FTIR (KBr pressed disc) ν_{max} /cm^{-1}: 3448br w, 3374br w, 3316br w, 3083w, 3061w, 3026m, 2924s, 2852w.

UV-Vis: λ_{max}/nm (DMSO) 420 (ε/dm^3 mol^{-1} cm^{-1} 511000), 518 (20800), 552 (11200), 592 (6130), 647 (5560).

Zinc 5-[4-[(2-methoxy-4-nitro-phenylcarbonyl)-amino] phenyl]-10,15,20-triphenyl porphyrin, 11.

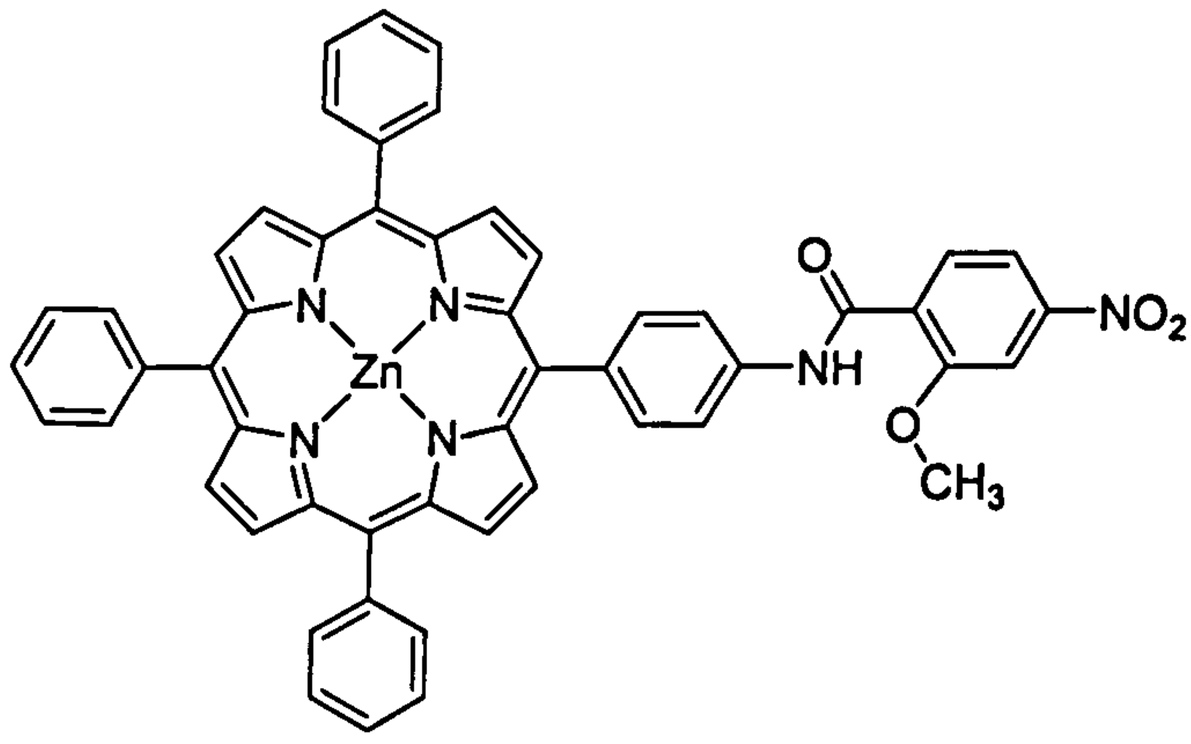

11

Free base 5-[4-[(2-methoxy-4-nitro-phenylcarbonyl)-amino] phenyl]-10,15,20-triphenyl porphyrin, **10** (0.16 g, 0.20 mmol) and zinc acetate dihydrate (0.20 g, 0.90 mmol) were dissolved in chloroform and methanol (25 cm^3, 5:1, v/v) and heated at reflux for 1 h. The reaction mixture was cooled, diluted with dichloromethane (100 cm^3) and washed with EDTA solution (2 g in 200 cm^3 10 % sodium carbonate solution), water (3 × 200 cm^3), dried over sodium sulfate and the solvent removed *in vacuo*. The residue was purified by column chromatography (Si-60, 10:1 chloroform:acetonitrile v/v) to give **11** (0.14 g, 0.16 mmol, 80 %).

Rf (10:1 chloroform:acetonitrile v/v): 0.88.

^{1}H NMR δ_H (500 MHz; solvent THF): 10.11 (1H, s, NH), 8.86 (8H, m, β-pyrrole, *o*-aminophenyl), 8.26 (1H, d, J = 9.9 Hz, phenyl), 8.22 (10H, m, *o*-phenyl, *m*-aminophenyl), 8.01 (1H, d, J = 1.8 Hz, phenyl), 7.98 (1H, dd, J = 8.6, 2.2 Hz, phenyl), 7.77 (9H, m, *m*-/ *p*-phenyl), 4.24 (3H, s, OCH_3) ppm.

^{13}C{^{1}H} NMR δ_C (125 MHz; solvent THF): 161.9, 157.6, 150.4, 142.4, 142.3, 138.9, 137.8, 134.9, 134.3, 132.2, 129.6, 127.7, 126.6, 120.0, 119.9, 119.7, 118.0, 115.5, 106.8, 56.4, ppm.

ESI-MS: m/z = 870.3 (M^+, 100%).

HR ESI-MS: For $C_{52}H_{34}N_6O_4Zn$ (M^+), observed mass 870.1929, calculated 870.1928, difference 0.1 mDa.

FTIR (ATR) ν_{max} /cm^{-1}: 1675s, 1591s, 1525s, 1486s, 1439m, 1406m, 1339s, 1312m, 1259s, 1205s, 1178m, 1156m, 1084s, 1018m, 1001s, 993s, 864m, 796s, 753m, 734m, 717m, 701s, 660m.

FTIR (KBr pressed disc) ν_{max} /cm^{-1}: 3432br w, 3084w, 3063w, 3026m, 2926m, 2852w.

UV-Vis: λ_{max}/nm (DMSO) 429 (ε/dm^3 mol^{-1} cm^{-1} 573000), 560 (14800), 552 (5810).

Free base 5-[4-[(2-methoxy-4-amino-phenylcarbonyl)-amino] phenyl]-10,15,20-triphenyl porphyrin, 12.

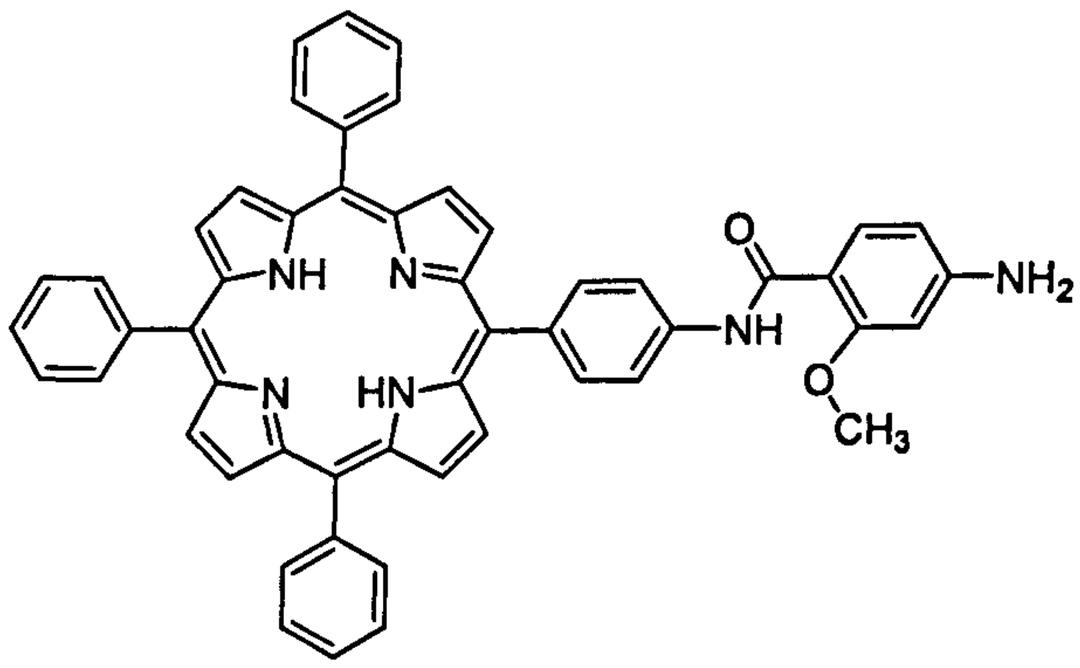

12

Free base 5-[4-[(2-methoxy-4-nitro-phenylcarbonyl)-amino] phenyl]-10,15,20-triphenyl porphyrin, **10** (1.1 g, 1.4 mmol), was dissolved in 100 cm^3 ethanol. Saturated ammonium chloride solution (1.6 cm^3), and indium powder (100 mesh, 1.1 g), were added and the solution stirred for 72 h under reflux until the reaction was complete by tlc (dichloromethane/acetonitrile v/v 5:1). The reaction mixture was evaporated to dryness and the solid residue extracted with chloroform using Sohxlet apparatus. The solvent was removed *in vacuo* give a green/purple solid. This was taken up in the minimum amount of 5 % sulfuric acid in trifluoroacetic acid and stirred at room temperature for 15 min. The solution was carefully neutralised with ice cold saturated sodium carbonate solution and the porphyrin was extracted with chloroform. The organic layer was separated, dried over sodium sulfate, concentrated *in vacuo* and purified by passing through a short silica column (Si-60, 10:1 chloroform:acetonitrile v/v) to give **12** (0.37 g, 0.48 mmol, 35 %).

Rf (10:1 chloroform:acetonitrile v/v): 0.41.

^{1}H NMR δ_H (500 MHz; solvent $CDCl_3$): 10.05 (1H, s, NH), 8.85 (8H, m, β-pyrrole), 8.22, (1H, d, phenyl), 8.19 (6H, m, *o*-phenyl), 8.17 (2H, d, *o*-aminophenyl), 8.04 (2H, d, J = 8.4 Hz, *m*-aminophenyl), 7.74 (9H, m, *m*-/ *p*-phenyl), 6.45 (1H, dd, J = 2.5, 8.4 Hz, phenyl), 6.32 (1H, d, J = 2.5 Hz, phenyl), 4.12 (3H, s, OCH_3), -2.78 (2H, br s, inner NH) ppm.

^{13}C{^{1}H} NMR δ_C (176 MHz; solvent $CDCl_3$): 161.5, 157.3, 150.6, 142.1, 138.8, 137.4, 135.3, 134.6, 133.8, 128.0, 127.3, 126.7, 120.3, 119.4, 118.7, 118.2, 117.4, 116.6, 107.1, 57.5 ppm.

ESI-MS: m/z = 779.4 ($M + H^+$, 100%), 777.3 ($M - H^+$, 100%).

HR ESI-MS: For $C_{52}H_{39}N_6O_2$ ($M + H^+$), observed mass 779.3102, calculated 779.3129, difference 2.7 mDa.

FTIR (ATR) ν_{max} /cm^{-1}: 1663m, 1595s, 1516s, 1472s, 1441m, 1400m, 1349m, 1309s, 1270s, 1245s, 1206m, 1178s, 1156m, 1134s, 1094m, 1072m, 1029s, 1002s, 981s, 965s, 877m, 847m, 827m, 799s, 726s, 701s, 658s.

FTIR (KBr pressed disc) ν_{max} /cm^{-1}: 3437br m, 3341br m, 3056w, 3017w, 2975w, 2938w, 2924m, 2899w.

UV-Vis: λ_{max}/nm (DMSO) 421 (ε/dm^3 mol^{-1} cm^{-1} 368000), 518 (19800), 552 (12300), 592 (7140), 648 (8100).

Zinc 5-[4-[(2-methoxy-4-amino-phenylcarbonyl)-amino] phenyl] -10,15,20-triphenyl porphyrin, 13.

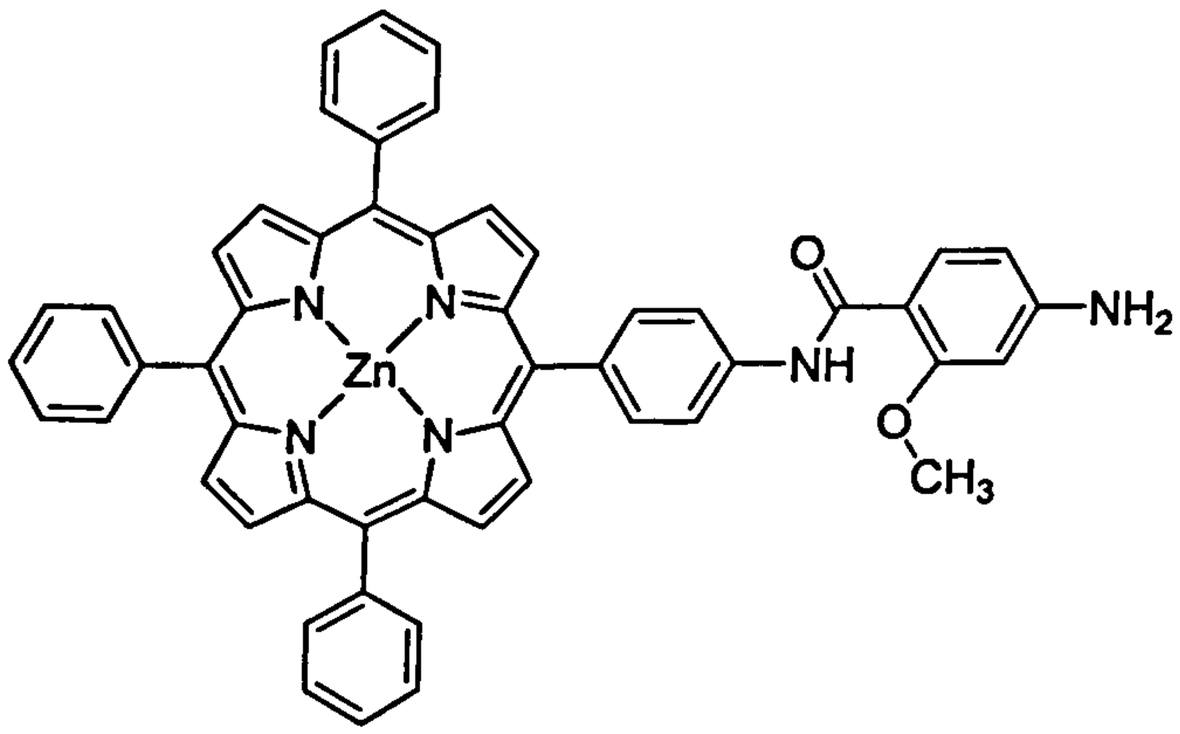

13

Free base 5-[4-[(2-methoxy-4-amino-phenylcarbonyl)-amino] phenyl]-10,15,20-triphenyl porphyrin, **12** (0.060 g, 0.077 mmol) and zinc acetate dihydrate (0.080 g, 0.36 mmol) were dissolved in chloroform and methanol (10 cm^3, 5:1, v/v) and heated at reflux for 1 h. The reaction mixture was cooled, diluted with dichloromethane (40 cm^3) and washed with EDTA solution (1 g in 100 cm^3 10 % sodium carbonate solution), water (3 × 100 cm^3), dried (Na$_2SO_4$) and the solvent removed *in vacuo*. The residue was purified by column chromatography (Si-60, 50:1 chloroform:methanol v/v) to give **13** (0.060 g, 0.072 mmol, 94 %).

Rf (50:1 chloroform:methanol v/v): 0.5.

^{1}H NMR δ_H (500 MHz; solvent $CDCl_3$, d_6-pyridine): 10.01 (1H, s, NH), 8.92 (2H, d, J = 4.25 Hz, *o*-aminophenyl), 8.84 (6H, m, β-pyrrole), 8.19 (1H, d, J = 8.3 Hz, phenyl), 8.17 (6H, m, *o*-phenyl,), 8.14 (2H, d, *o*-aminophenyl) 8.00 (2H, d, J = 8.1 Hz, *m*-aminophenyl), 7.70 (9H, m, *m-/ p*-phenyl), 6.41 (1H, dd, J = 2.1, 8.5 Hz, phenyl), 6.25 (1H, d, J = 1.9 Hz, phenyl), 4.07 (2H, s, NH_2), 4.04 (3H, s, OCH_3) ppm.

^{13}C{^{1}H} NMR δ_C (125 MHz; solvent $CDCl_3$): 163.9, 159.2, 151.6, 150.3, 150.1, 143.7, 138.1, 138.9, 135.2, 134.6, 134.5, 131.8, 131.6, 127.1, 126.3, 120.6, 120.4, 118.3, 112.1, 108.1, 97.4, 56.1 ppm.

ESI-MS: m/z = 839.1 (M - H^+, 100%), 1682.9 (2M – H^+, 43%).

HR ESI-MS: For $C_{52}H_{37}N_6O_2Zn$ (M + H^+), observed mass 841.2282, calculated 841.2264, difference 1.8 mDa.

FTIR: (ATR) ν_{max} /cm^{-1}: 1629m, 1594s, 1559m, 1521s, 1490s, 1458m, 1441m, 1339m, 1313s, 1275s, 1259s, 1244s, 1205s, 1176s, 1142m, 1096m, 1066s, 1029s, 1001s, 993s, 828m, 809s, 796s, 760s, 752s, 732s, 717s, 700s, 660s, 644s.

FTIR: (KBr pressed disc) ν_{max} /cm^{-1}: 3434br m, 3379br m, 3124w, 3094w, 3053w, 3018w, 2924w, 2850w.

UV-Vis: λ_{max}/nm (DMSO) 429 (ε/dm^3 mol^{-1} cm^{-1} 597000), 560 (25400), 603 (17100).

Free base 5-[4-{(2-methoxy-4-[(2-methoxy-4-nitro-phenylcarbonyl)-amino]-phenylcarbonyl)-amino} phenyl]-10,15,20-triphenyl porphyrin, 14.

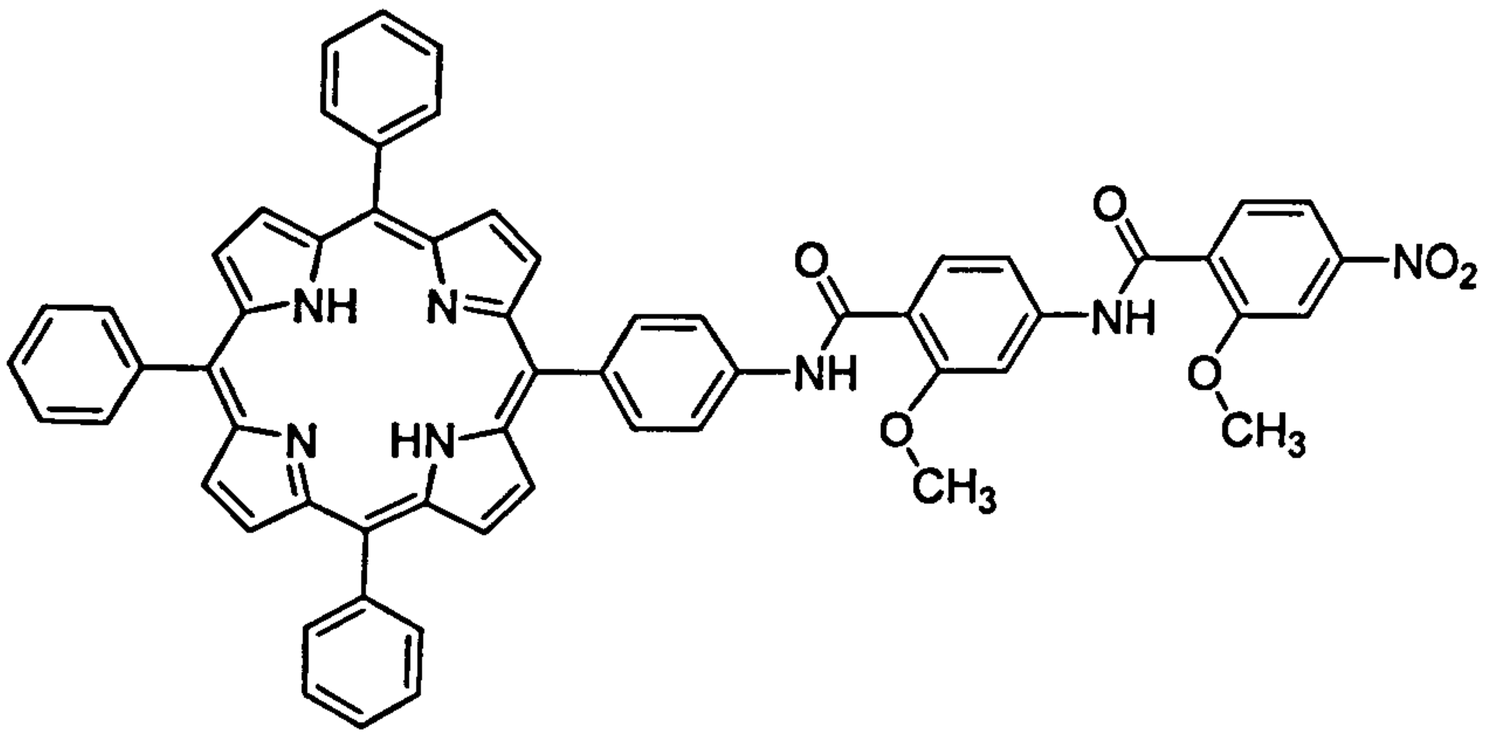

14

Dicyclohexylcarbodiimide (0.50 g, 2.42 mmol) was added to a stirred solution of 2-methoxy-4-nitrobenzoic acid (0.40 g, 2.03 mmol) in acetonitrile (15 cm^3) at 0°C. After 15 minutes the reaction was brought to room temperature and stirred until the reaction was complete by tlc (10:1 chloroform:acetonitrile v/v) (~24 h). The solution was filtered and the solid by-product was washed thoroughly with acetonitrile and the washings added to the filtrate. Removal of the solvent gave a pale yellow solid which was used without any further purification. The anhydride residues were taken up in acetonitrile (20 cm^3) and added dropwise to an ice cold solution of free base 5-[4-[(2-methoxy-4-amino-phenylcarbonyl)-amino] phenyl]-10,15,20-triphenyl porphyrin, **12** (0.25g, 0.32 mmol) in chloroform with stirring. The reaction was heated at reflux for 48 h. The solvent was removed and the purple residue was extracted into dichloromethane and washed with 2 M sodium hydroxide (3 × 250 cm^3), water and brine. The organic fraction was dried over sodium sulfate and the solution was then concentrated *in vacuo* and purified by column chromatography (Si-60, 10:1 chloroform:acetonitrile v/v) to give **14** (0.24g, 0.25 mmol, 78 %).

Rf (10:1 chloroform:acetonitrile v/v): 0.71.

^{1}H NMR δ_H (500 MHz; solvent $CDCl_3$): 10.18 (1H, s, NH), 9.91 (1H, s, NH), 8.87 (8H, m, β-pyrrole), 8.47 (1H, d, J = 8.7 Hz, phenyl), 8.42 (1H, d, J = 8.4 Hz, phenyl), 8.28 (1H, d, J = 1.8 Hz, phenyl), 8.21 (8H, m, *o*-phenyl), 8.08 (1H, d, J = 8.4 Hz, phenyl), 8.00 (2H, d, J = 2.4, 9.0 Hz, *m*-aminophenyl), 7.93 (1H, d, J = 1.5 Hz, phenyl), 7.74 (9H, m, *m*-/ *p*-phenyl), 6.94 (1H, dd, J = 2.1, 8.4 Hz, phenyl), 4.26 (3H, s, OCH_3), 4.23 (3H, s, OCH_3), -2.79 (2H, s, inner NH) ppm.

^{13}C{^{1}H} NMR δ_C (125 MHz; solvent $CDCl_3$): 163.3, 161.6, 158.4, 157.1, 150.7, 149.4, 149.3, 142.1, 138.9, 138.1, 137.4, 136.0, 134.6, 134.4, 133.8, 130.1, 128.4, 126.3, 126.2, 120.2, 119.7, 118.4, 117.1, 116.2, 115.0, 107.5. 103.0, 57.2, 56.6 ppm.

ESI-MS: m/z = 956.2 ($M - H^+$), 958.4 ($M + H^+$).

HR ESI-MS: For $C_{60}H_{44}N_7O_6$ ($M + H^+$), observed mass 958.3323, calculated 958.3348, difference 2.5 mDa.

FTIR: (ATR) ν_{max} /cm^{-1}: 1676s, 1624s, 1584s, 1559m, 1521s, 1473m, 1414m, 1346s, 1312s, 1263s, 1243s, 1176s, 1140m, 1089m, 1026m, 965s, 800s, 737s, 702s, 657w, 641w.

FTIR: (KBr pressed disc) ν_{max} /cm^{-1}: 3422br m, 3328br m, 2928m, 2850m.

UV-Vis: λ_{max}/nm (DMSO) 421 (ε/dm^3 mol^{-1} cm^{-1} 383000), 516 (37600), 552 (30100), 592 (24800), 648 (25100).

Zinc 5-[4-{(2-methoxy-4-[(2-methoxy-4-nitro-phenylcarbonyl)-amino]-phenyl carbonyl)-amino} phenyl]-10,15,20-triphenyl porphyrin, 15.

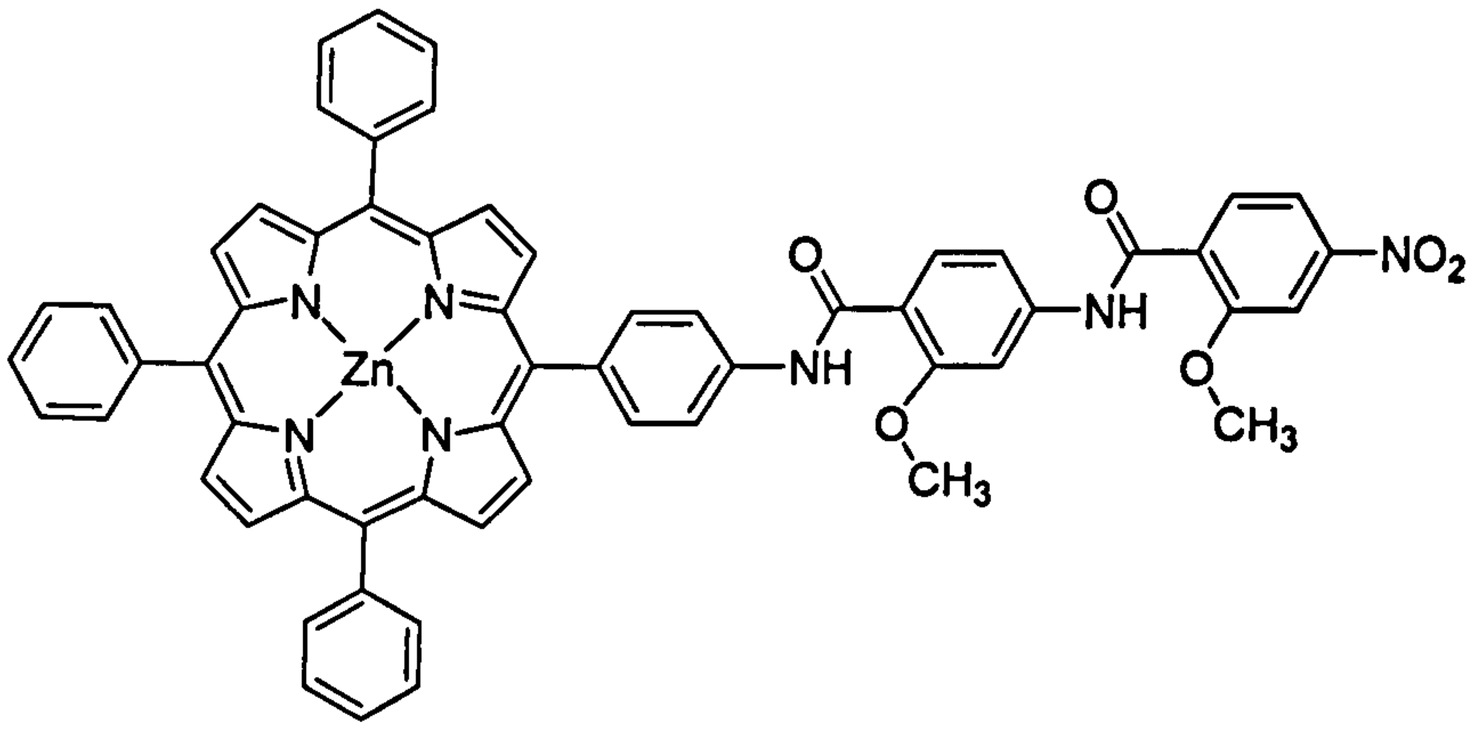

15

Free base 5-[4-{(2-methoxy-4-[(2-methoxy-4-nitro-phenylcarbonyl)-amino]-phenylcarbonyl)-amino} phenyl]-10,15,20-triphenyl porphyrin, **14** (0.10 g, 0.10 mmol) and zinc acetate dihydrate (0.20 g, 0.90 mmol) were dissolved in chloroform and methanol (30 cm^3, 5:1, v/v) and heated at reflux for 1 h. The reaction mixture was cooled, diluted with dichloromethane (50 cm^3) and washed with EDTA solution (1 g in 100 cm^3 10 % sodium carbonate solution), water (3 × 100 cm^3), dried (Na_2SO_4) and the solvent removed *in vacuo*. The residue was purified by column chromatography (Si-60, 50:1 chloroform:acetonitrile, v/v) to give **15** (0.092 g, 0.090 mmol, 90 %).

Rf (50:1 chloroform:acetonitrile v/v): 0.68.

^{1}H NMR δ_H (500 MHz; solvent $CDCl_3$): 10.14 (1H, s, NH), 9.86 (1H, s, NH), 8.94 (8H, m, β-pyrrole), 8.42 (1H, d, J = 8.4 Hz, phenyl), 8.34 (1H, d, J = 8.4 Hz, phenyl), 8.24 (1H, s, phenyl), 8.21 (8H, m, *o*-phenyl, *o*-aminophenyl), 8.04 (2H, d, J = 8.0 Hz, *m*-aminophenyl), 8.00 (1H, d, 8.0 Hz, phenyl), 7.90 (1H, s, phenyl), 7.75 (9H, m, *m*-/ *p*-phenyl), 6.91 (1H, d, J = 7.0 Hz, phenyl), 4.24 (3H, s, OCH_3), 4.21 (3H, s, OCH_3) ppm.

$^{13}C\{^1H\}$ NMR δ_C (125 MHz; solvent $CDCl_3$): 163.1, 161.5, 158.4, 157.3, 150.8, 150.3, 150.2, 143.0, 142.3, 138.8, 137.9, 135.1, 134.5, 134.4, 132.0, 131.9, 127.5, 126.7, 126.5, 121.1, 120.6, 118.5, 117.8, 116.5, 112.7, 107.1, 103.8, 57.3, 56.6 ppm.

ESI-MS: *m/z* = 1018.4 ($M - H^+$), 1020.3 ($M + H^+$).

HR ESI-MS: For $C_{60}H_{42}N_7O_6Zn$ ($M + H^+$), observed mass 1020.2442, calculated 1020.2483, difference 4.0 mDa.

FTIR: (KBr pressed disc) ν_{max} /cm^{-1}: 3443br s, 3364br s, 3115w, 3051w, 3019w, 2851w, 1675br m, 1650m, 1588br s, 1526br s, 1486m, 1463m, 1450m, 1441m, 1409m, 1341s, 1313m, 1262m, 1240m, 1204m, 1179m, 1138m, 1097m, 1071m, 1025m, 1003s, 994s, 970w, 868w, 797s, 753m, 735m, 718m, 702s, 660w.

UV-Vis: λ_{max}/nm (DMSO) 429 (ε/dm^3 mol^{-1} cm^{-1} 525000), 561 (19400), 602 (10900).

Free base 5-[4-{(2-methoxy-4-[(2-methoxy-4-amino-phenylcarbonyl)-amino]-phenylcarbonyl)-amino} phenyl]-10,15,20-triphenyl porphyrin, 16.

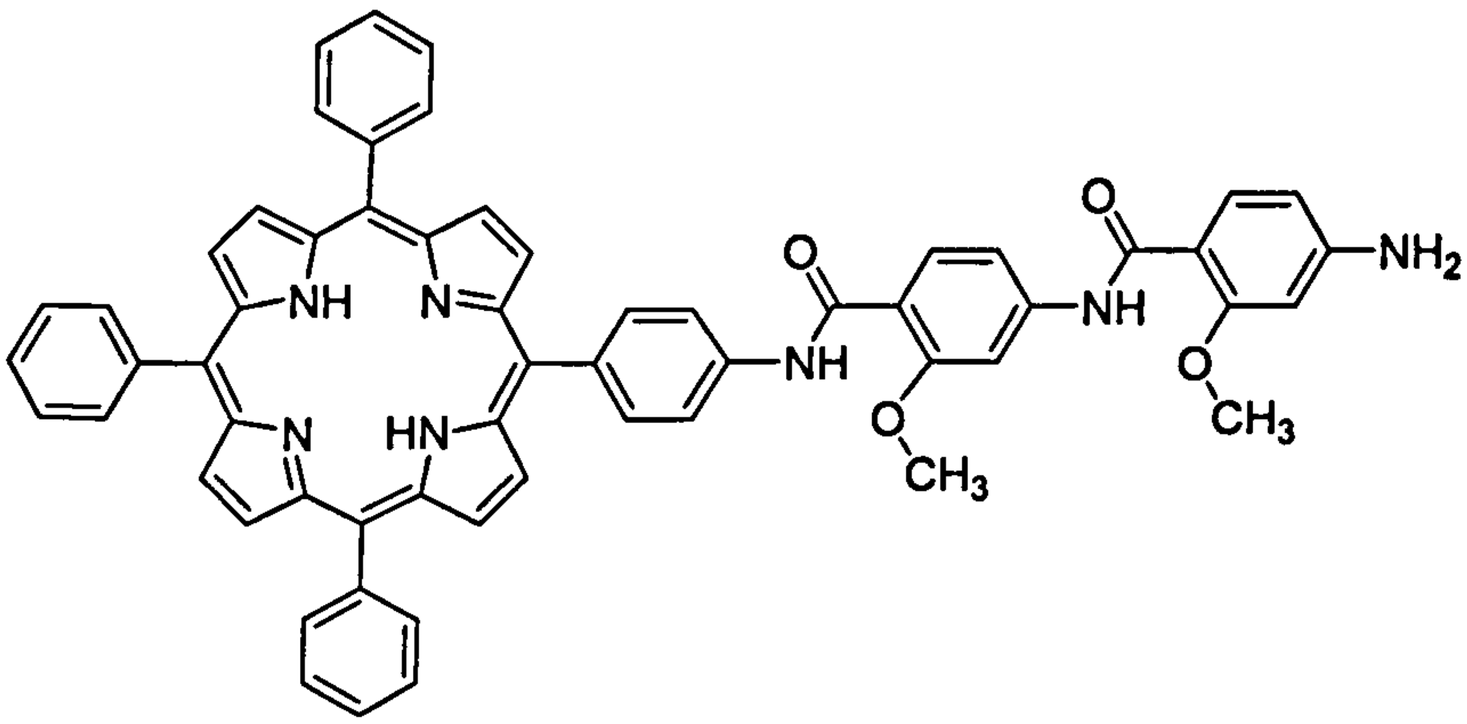

16

Free base 5-[4-{(2-methoxy-4-[(2-methoxy-4-nitro-phenylcarbonyl)-amino]-phenylcarbonyl)-amino} phenyl]-10,15,20-triphenyl porphyrin, **14** (0.050 g, 0.050 mmol), was dissolved in 200 cm^3 ethanol. Saturated ammonium chloride solution (0.3 cm^3), and indium powder (100 mesh, 0.050 g), were added and the solution stirred for 72 h under reflux until the reaction was complete by tlc (chloroform/acetonitrile v/v 5:1). The reaction mixture was evaporated to dryness and the solid residue extracted with chloroform using Sohxlet apparatus. The solvent was removed *in vacuo* give a green/purple solid. This was taken up in the minimum amount of 5 % sulfuric acid in trifluoroacetic acid and stirred at room temperature for 15 min. The solution was carefully neutralised with ice cold saturated sodium carbonate solution and the porphyrin was extracted with chloroform. The organic layer was separated, dried over sodium sulfate, concentrated *in vauo* and purified by passing through a short silica column (Si-60, chloroform, 10:1 chloroform:acetonitrile v/v) to give **16** (0.015 g, 0.015 mmol, 30 %).

Rf (10:1 chloroform:acetonitrile v/v): 0.42.

^{1}H NMR δ_H (700 MHz; solvent $CDCl_3$): 10.22 (1H, s, NH), 10.01 (1H, s, NH), 8.92 (2H, d, J = 6.0 Hz, β-pyrrole), 8.83 (6H, m, β-pyrrole), 8.39 (1H, s, phenyl), 8.36 (1H, d, J = 8.5 Hz, phenyl) 8.21 (8H, m, *o*-phenyl, *o*-aminophenyl), 8.10 (1H, d, J = 8.5 Hz, phenyl), 8.09 (2H, d, J = 8.0 Hz, *m*-aminophenyl), 7.75 (9H, m, *m*-/ *p*-phenyl), 6.84 (1H, dd, J = 1.8, 8.0 Hz, phenyl), 6.84 (1H, dd, J = 8.5, 1.8 Hz, phenyl), 6.43 (1H, d, J = 8.5 Hz, phenyl), 6.27 (1H, d, J = 1.8 Hz, phenyl), 4.24 (3H, s, OCH_3), 4.12 (2H, s, NH_2), 4.06 (3H, s, OCH_3) ppm.

^{13}C{^{1}H} NMR δ_C (125 MHz; solvent $CDCl_3$): 164.0, 163.5, 158.9, 158.2, 149.4, 144.5, 142.1, 138.3, 136.4 134.9, 134.3, 127.7, 127.4, 126.4, 125.9, 122.1, 119.7, 118.4, 116.8, 112.2, 108.0, 103.1, 97.1, 56.3, 56.1 ppm.

ESI-MS: m/z = 928.4 ($M + H^+$)

HR ESI-MS: For $C_{60}H_{46}N_7O_4$ ($M + H^+$), observed mass 928.3592, calculated 928.3606, difference 1.4 mDa.

FTIR (KBr pressed disc) ν_{max} /cm^{-1}: 3446br s, 3356br s, 3040w, 3018w, 2960w, 2926w, 2840w, 2685w, 2589w, 2520w, 1662br m, 1584br s, 1517br s, 1468m, 1441w, 1401m, 1349w, 1311m, 1286m, 1243br s, 1209m, 1178m, 1163w, 1155w, 1131m, 1104w, 1072w, 1027m, 1001w, 980w, 956s, 876w, 848w, 826w, 800s, 747m, 730m, 701s, 657w.

UV-Vis: λ_{max}/nm (DMSO) 421 (ε/dm^3 mol^{-1} cm^{-1} 403000), 516 (21700), 552 (14200), 595 (8500), 649 (11000).

Zinc 5-[4-{(2-methoxy-4-[(2-methoxy-4-amino-phenylcarbonyl)-amino]-phenylcarbonyl)-amino} phenyl]-10,15,20-triphenyl porphyrin, 17.

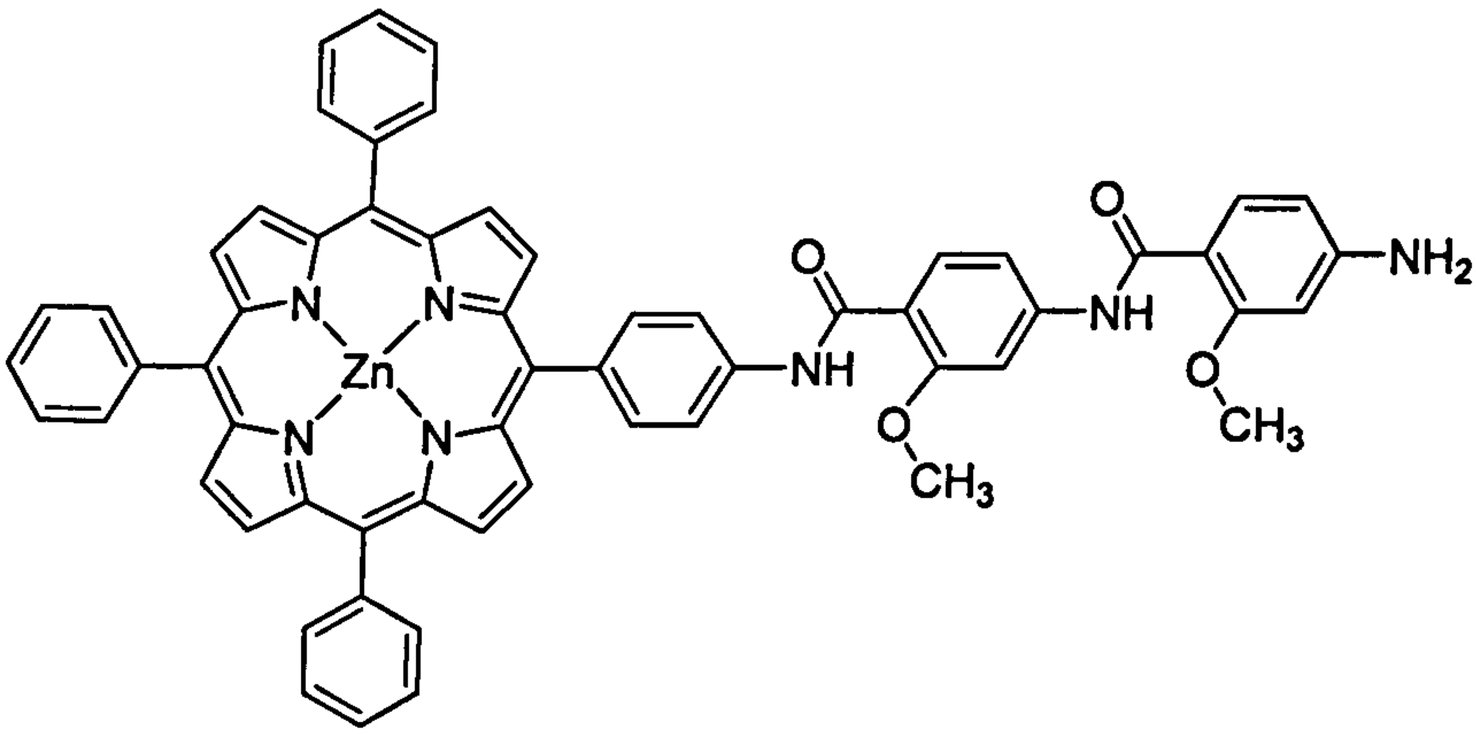

17

Free base 5-[4-{(2-methoxy-4-[(2-methoxy-4-amino-phenylcarbonyl)-amino]-phenylcarbonyl)-amino} phenyl]-10,15,20-triphenyl porphyrin, **16** (0.24 g, 0.24 mmol) and zinc acetate dihydrate (0.4 g, 1.8 mmol) were dissolved in chloroform and methanol (25 cm^3, 5:1, v/v) and heated at reflux for 1 h. The reaction mixture was cooled, diluted with chloroform (100 cm^3) and washed with EDTA solution (2 g in 200 cm^3 10 % sodium carbonate solution), water (3 × 100 cm^3), dried (Na_2SO_4) and the solvent removed *in vacuo*. The residue was purified by column chromatography (Si-60, 50:1 chloroform:methanol v/v) to give **17** (0.20 g, 0.20 mmol, 83 %).

Rf (50:1 chloroform:methanol v/v): 0.19.

^{1}H NMR δ_H (500 MHz; solvent $CDCl_3$, d_5-pyridine): 10.08 (1H, s, NH), 9.74 (1H, s, NH), 8.91 (8H, m, β-pyrrole), 8.24 (1H, d, phenyl), 8.22 (6H, m, *o*-phenyl), 8.13 (1H, s, phenyl), 8.09 (2H, d, J = 8.5 Hz, *o*-aminophenyl), 7.91 (2H, d, J = 8.5 Hz, *m*-aminophenyl), 7.75 (9H, m, *m*-/ *p*-phenyl), 7.51 (1H, d, J = 8.5 Hz, phenyl), 6.85 (1H, dd, J = 8.5, 1.8 Hz, phenyl), 4.79 (1H, d, J = 8.5 Hz, phenyl), 4.54 (1H, s, phenyl), 4.17 (3H, s, OCH_3), 3.65 (3H, s, OCH_3) ppm.

^{13}C{^{1}H} NMR δ_C (125 MHz; solvent $CDCl_3$, d_5-pyridine): 163.6, 163.4, 158.4, 157.9, 150.4, 150.0, 143.6, 143.1, 138.5, 137.8, 135.4, 134.6, 132.9, 132.1, 131.9, 127.4, 127.4, 126.6, 126.5, 120.9, 120.8, 118.6, 116.4, 112.4, 108.0, 103.4, 97.2, 56.6, 55.8 ppm.

ESI-MS: m/z = 989 (M^+, 100%), 988 ($M - H^+$, 100%).

HR ESI-MS: For $C_{60}H_{44}N_7O_4Zn$ ($M + H^+$), observed mass 990.2675, calculated 990.2741, difference 6.6 mDa.

FTIR: ν_{max} /cm^{-1} 1521s (NH_2), 1594s (NH), 1629m (CO).

FTIR: (KBr pressed disc) ν_{max} /cm^{-1}: 3430br m, 3361br m, 3051w, 3021w, 2922m, 2852m, 1665m, 1585br s, 1519br s, 1466m, 1450m, 1441m, 1403m, 1339m, 1312m, 1285m, 1244br s, 1204m, 1178m, 1131m, 1069m, 1027m, 1002s, 994s, 797s, 753m, 717m, 702m, 661w, 535w.

UV-Vis: λ_{max}/nm (DMSO) 429 (ε/dm^3 mol^{-1} cm^{-1} 477000), 560 (12100), 603 (8140).

Free base m*eso*-5-10,15,-tris(4-pyridyl)-20-(4-acetamidophenyl)porphyrin, 18[2].

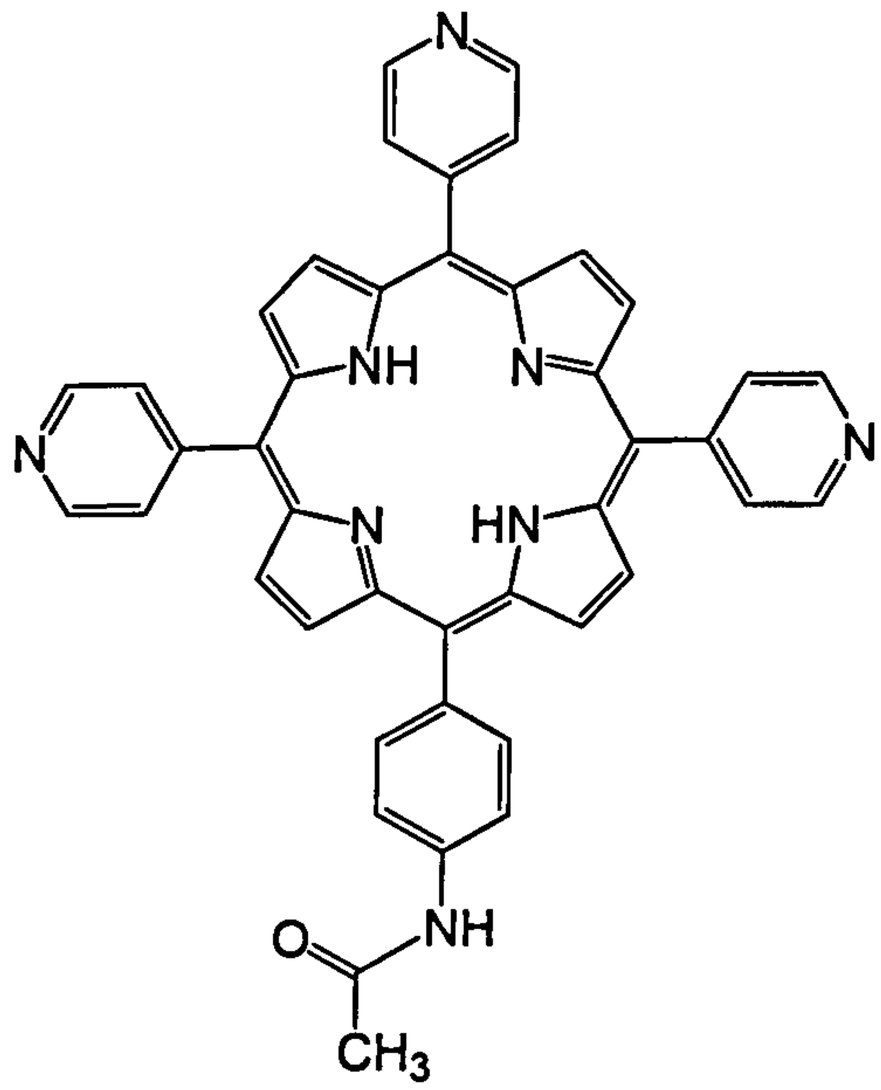

18

Pyridine-4-carboxaldehyde (16.07 g, 0.175 mol) and 4-acetamidobenzaldehyde (8.16 g, 0.05 mol) were dissolved in propionic acid (600 cm^3) and acetic anhydride (20 cm^3) and heated to reflux under nitrogen. Pyrrole (13.42 g, 0.225 mol) in propionic acid (60 cm^3) was added to the hot solution dropwise without heating. The final solution was heated at reflux for 1 h in air. The solvent was removed *in vacuo* to give a purple sticky residue. This was poured into ice-water (1500 cm^3) and neutralised with aqueous ammonia solution to give a black solid. The solid was filtered, dried and extracted three times with chloroform. The solvent was removed *in vacuo* and the resulting dry solid was extracted with methanol using Soxhlet apparatus for 1 week. The remaining purple residue was passed through Florisil® (short plug, 10:1 dichloromethane:methanol v/v). The solvent was removed and the crude product was purified by column chromatography (Si-60, 60:1 chloroform:methanol v/v) to give **18** as the major fraction (fifth) (1.41 g, 2.09 mmol, 4.2 %).

^{1}H NMR δ_H (500 MHz; solvent $CDCl_3$): 9.05 (6H, m, *m*-pyridyl), 8.98 (2H, d, J = 8.9 Hz, β-pyrrole), 8.94 (4H, s, β-pyrrole), 8.81 (2H, d, J = 8.8 Hz, β-pyrrole), 8.15 (8H, m, *o*-pyridyl, *o*-aminophenyl), 7.94 (2H, d, *m*-aminophenyl), 7.74 (1H, s, NH), 2.38 (3H, s, OCH_3), -2.89 (2H, s, inner NH) ppm.

$^{13}C\{^1H\}$ NMR δ_C (125 MHz; solvent $CDCl_3$): 168.8, 150.1, 150.0, 148.1, 148.4, 138.1, 137.4, 135.2, 129.4, 129.4, 121.2, 118.2, 117.5, 117.1, 24.9 ppm.

ESI-MS: *m/z* = 675 ($M + H^+$, 25%), 338 ($M + 2H^+$, 100%), 225 ($M + 3H^+$, 30%).

HR ESI-MS: For $C_{43}H_{30}N_8O$ ($M + H^+$), observed mass 675.2638, calculated 675.2615, difference 2.3 mDa.

FTIR: (KBr pressed disc) ν_{max} /cm^{-1} 3432 br m, 3315m, 3096w, 3028m, 2970, 2922m, 2848w, 2708w, 2608w, 1671m, 1594s, 1559w, 1526m, 1508m, 1473m, 1402m, 1384m, 1351m, 1313m, 1294w, 1255w, 1227w, 1181w, 1155w, 1112w, 1068m, 1022w, 997w, 981w, 970s, 882m, 851m, 799s, 728s, 660m, 642w.

UV-Vis: λ_{max}/nm ($CHCl_3$) 419 (ε/dm^3 mol^{-1} cm^{-1} 99200), 515 (4880), 550 (2100) 592 (1860), 648 (1430).

Free base 5,10,15-tris(4-pyridyl)-20-(4-aminophenyl)porphyrin, 19[2].

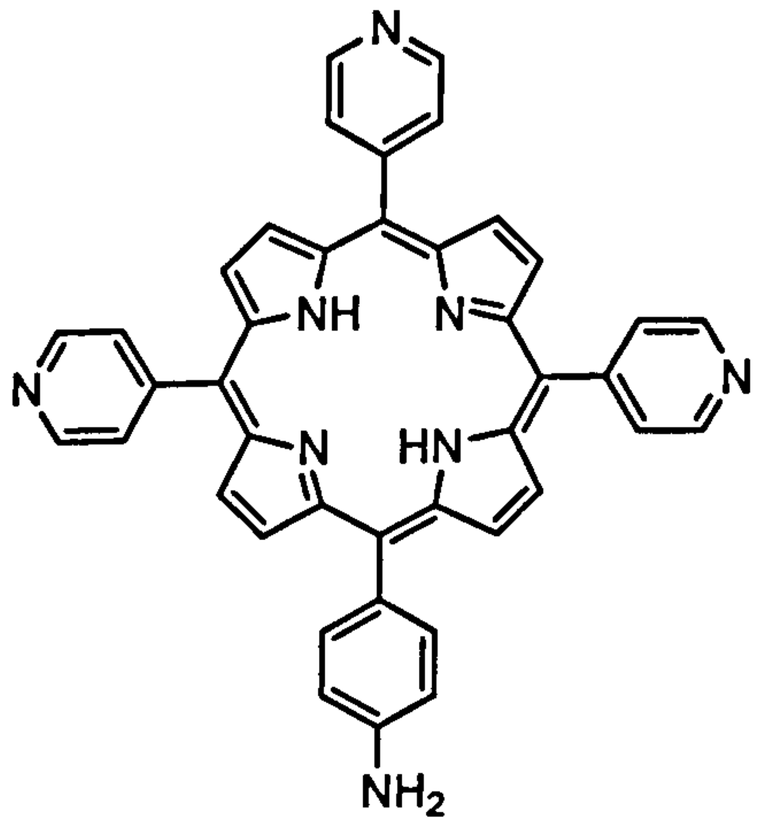

19

Free base *meso*-5,10,15-tris(4-pyridyl)-20-(4-acetamidophenyl)-porphyrin, **18** (0.10 g, 0.15 mmol,) was dissolved in trifluoroacetic acid (10 cm^3) and concentrated hydrochloric acid (10 cm^3). The solution was heated and stirred at 80°C for 36 h. The pH of the resulting solution was adjusted to 9.0 with dilute cold aqueous ammonia solution. The solution was extracted with chloroform (3 × 50 cm^3). The chloroform extracts were combined, washed with 10% sodium hydrogen carbonate solution and water and dried over magnesium sulfate. The solvent was removed *in vacuo* and the residue was purified by column chromatography (Si-60, chloroform: methanol, 80:1 v/v) to give **19** (0.074 g, 0.12 mol, 79 %).

^{1}H NMR δ_H (300 MHz; solvent $CDCl_3$): 9.05 (8H, m, *m*-pyridyl, β-pyrrole), 8.83 (6H, m, β-pyrrole), 8.16 (6H, m, *o*-pyridyl), 7.98 (2H, d, J = 8.0 Hz, *o*-aminophenyl), 7.08 (2H, d, J = 7.0 Hz, *m*-aminophenyl), 1.89 (2H, br s, NH_2), -2.86 (2H, s, inner NH) ppm.

^{13}C{^{1}H} NMR δ_C (75 MHz; solvent $CDCl_3$): 150.3, 150.2, 148.4, 146.6, 135.9, 131.7, 131.2, 129.5, 122.7, 118.8, 116.74, 113.65 ppm.

ESI-MS: m/z = 633 ($M + H^+$, 100%).

HR ESI-MS: For $C_{41}H_{29}N_8$ ($M + H^+$), observed mass 633.2507, calculated 633.2510, difference 0.3 mDa.

FTIR: (KBr pressed disc) ν_{max} /cm^{-1} 3439 br m, 3321m, 3200w, 3135w, 3026w, 2957w, 2922w, 2852w, 2712w, 2611 w, 2535w, 1721w, 1613m, 1593s, 1561w, 1540w, 1511w, 1473w, 1404w, 1384w, 1351w, 1292w, 1257w, 1215w, 1178w, 1157w, 1070w, 1058w, 1027w, 982w, 970m, 882w, 837w, 802s, 784w, 732m, 660w, 642w.

UV-Vis: λ_{max}/nm ($CHCl_3$) 420, 516, 552, 592, 649.

Free base 5,10,15-tris(4-pyridyl)-20-[4-[(2-methoxy-4-nitro-phenylcarbonyl)-amino] phenyl] porphyrin, 20.

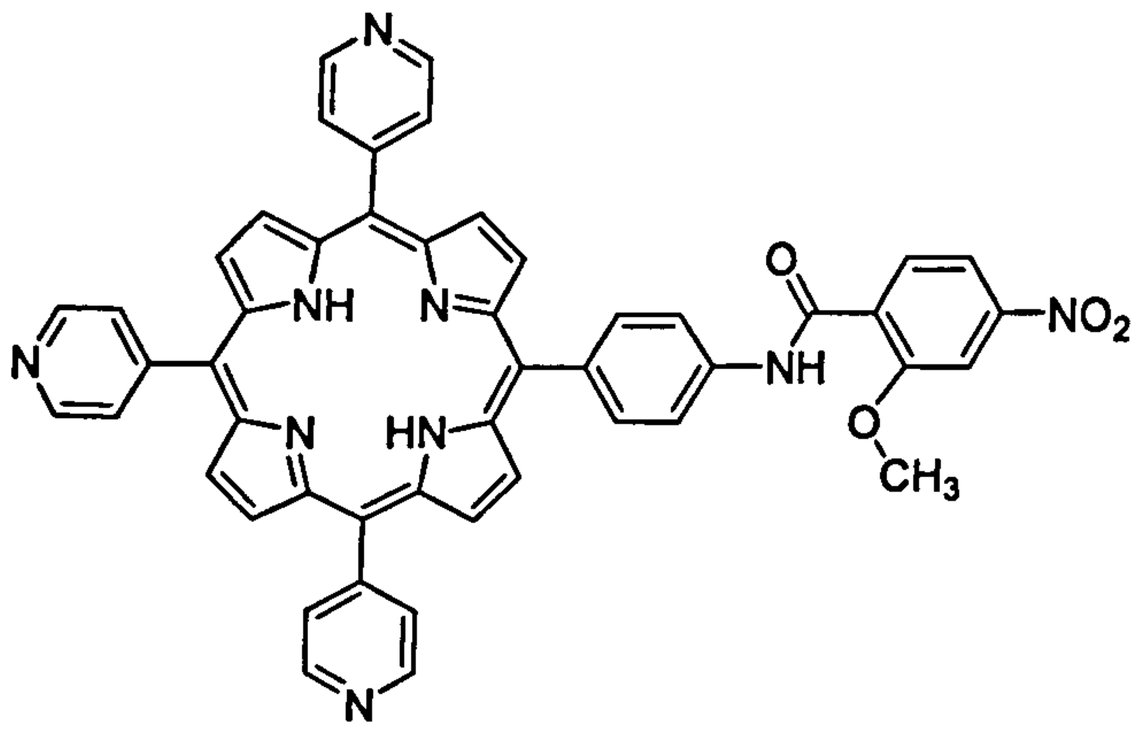

20

Dicyclohexylcarbodiimide (1.4 g, 6.8 mmol) was added to a stirred solution of 2-methoxy-4-nitrobenzoic acid (1.2 g, 6.1 mmol) in acetonitrile (25 cm^3) at 0 °C. After 15 minutes the reaction was brought to room temperature and stirred until the reaction was complete by tlc (10:1 chloroform:acetonitrile v/v) (~24 h). The solution was filtered and the solid by-product was washed thoroughly with acetonitrile and the washings added to the filtrate. Removal of the solvent yielded a pale yellow solid, which was used without any further purification. The anhydride residues were taken up in acetonitrile (20 cm^3) and added dropwise to an ice cold solution of free base 5,10,15-tris(4-pyridyl)-20-(4-aminophenyl)porphyrin, **19** (0.64 g, 1.01 mmol) in chloroform with stirring. The reaction was heated at reflux for 48 h. The solvent was removed and the purple residue was extracted into 1 M hydrochloric acid and washed with chloroform (3 × 100 cm^3). The green solution was neutralised with ammonia solution and the purple precipitate was extracted with chloroform. The organic fraction was dried over sodium sulfate and the solution was then concentrated *in vacuo* and purified by column chromatography (Si-60, 10:1 chloroform:methanol v/v) to give **20** (0.71 g, 0.88 mmol, 87 %).

^{1}H NMR δ_H (500 MHz; solvent $CDCl_3$): 10.02 (1H, s, NH), 9.05 (6H, d, *o*-pyridyl), 8.97 (2H, d, β-pyrrole), 8.85 (6H, m, β-pyrrole), 8.58 (1H, d, J = 8.6 Hz, phenyl), 8.23 (2H, d, J = 8.5 Hz, *o*-aminophenyl), 8.17 (6H, d, J = 8.7 Hz *m*-pyridyl), 8.11 (2H, d, J = 8.5 Hz, *m*-

aminophenyl), 8.04 (1H, dd, J = 2.0, 8.5 Hz, phenyl), 7.98 (1H, d, J = 2.0 Hz, phenyl), 4.29 (3H, s, OCH_3), -2.88 (2H, br s, inner NH) ppm.

$^{13}C\{^1H\}$ NMR δ_C (176 MHz; solvent $CDCl_3$): 161.6, 157.4, 150.8, 150.2, 150.1, 148.3, 138.0, 137.9, 135.3, 134.0, 129.4, 127.3, 121.1, 119.1, 117.5, 117.1, 116.6, 107.1, 57.3 ppm.

ESI-MS: m/z = 812.3 ($M + H^+$, 100%), 406.6 ($M + 2H^+$, 15%).

HR ESI-MS: For $C_{49}H_{34}N_9O_4$ ($M + H^+$), observed mass 812.2708, calculated 812.2728, difference 2.1 mDa.

FTIR (KBr pressed disc) ν_{max} /cm^{-1}: 3429br m, 3314m, 3077w, 3023w, 2925w, 2854w, 2756w, 2615w, 2536w, 2400w, 2349w, 1716w, 1662m, 1638s, 1589m, 1567w, 1522s, 1480w, 1459m, 1401m, 1383w, 1346m, 1321m, 1279w, 1251m, 1210w, 1182s, 1158w, 1123w, 1085m, 1018m, 999m, 981m, 968s, 897w, 885m, 856m, 801s, 729s, 664w, 639w.

UV-Vis: λ_{max}/nm (DMSO) 422 (ε/dm^3 mol^{-1} cm^{-1} 167000), 516 (8210), 552 (4140), 590 (2710), 647 (1790).

Free base 5,10,15-tris(*N*-methyl-4-pyridiniumyl)-20-[4-[(2-methoxy-4-nitro-phenylcarbonyl)-amino] phenyl] porphyrin tris iodide, 21.

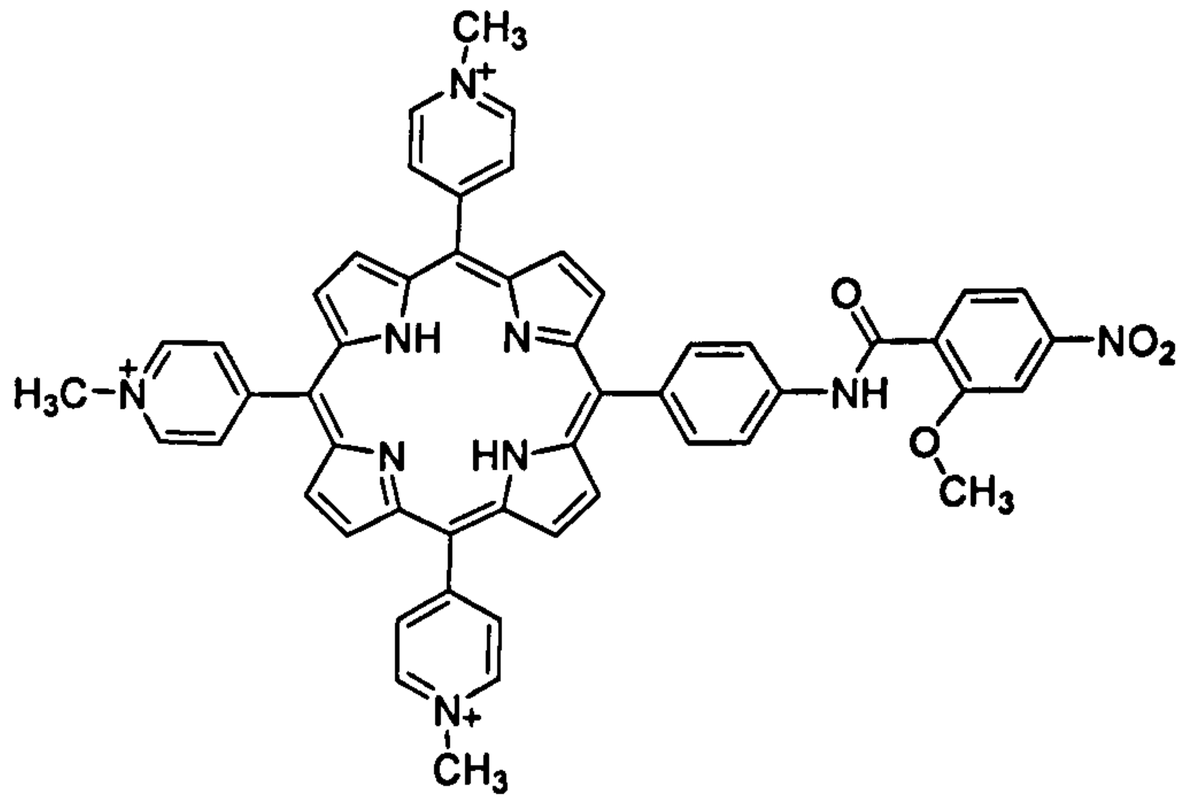

21

Free base 5,10,15-tris(4-pyridyl)-20-[4-[(2-methoxy-4-nitro-phenylcarbonyl)-amino] phenyl] porphyrin, **20**, (0.067g, 0.082 mmol) was dissolved in dimethylformide (5 cm^3). Excess methyl iodide (0.1 cm^3) was added and the solution was stirred at room temperature for 12 h. The solvent was removed *in vacuo* to give **21** which was dried in a vacuum oven at 70°C for 48 h (0.11 g, 0.086 mmol, 96 %).

^{1}H NMR δ_H (500 MHz; solvent d_6-DMSO): 10.92 (1H, s, NH), 9.49 (6H, d, *m*-pyridyl), 9.01 (6H, m, *o*-pyridyl), 9.18 (4H, s, β-pyrrole), 9.10 (4H, m, β-pyrrole), 8.25 (4H, m, *o, m*-aminophenyl), 8.03 (2H, m, phenyl), 7.94 (1H, m, phenyl), 4.73 (9H, s, NCH_3), 4.12 (3H, s, OCH_3), -2.88 (2H, br s, inner NH) ppm.

^{13}C{^{1}H} NMR δ_C (176 MHz; solvent $CDCl_3$): 164.5, 157.4, 157.1, 157.0, 150.0, 144.7, 139.7, 136.2, 135.4, 132.6, 130.6, 127.6, 123.2, 118.7, 116.2, 115.8, 115.0, 107.5, 57.3, 48.5 ppm.

ESI-MS: *m/z* = 856.3 ($M^{3+} + 2e^-$, 25%), 427.7 ($M^{3+} - H^+$, 15%).

HR ESI-MS: For $C_{52}H_{41}N_9O_4$ ($M^{3+} - H^+$), observed mass 427.6627, calculated 427.6635, difference 0.8 mDa.

FTIR (KBr pressed disc) ν_{max}/cm^{-1}: 3430br m, 3314w, 3077w, 3023br m, 2925br m, 2854w, 2756w, 2615w, 2536w, 2400w, 2349w, 1662m, 1638s, 1589m, 1567w, 1521s, 1479w, 1459m, 1401m, 1383w, 1346m, 1322m, 1279w, 1251m, 1210w, 1182s, 1158w, 1123w, 1083m, 1018m, 999m, 981m, 968s, 897w, 885m, 856m, 801s, 719s, 664m, 639m.

UV-Vis: λ_{max}/nm (pH 7.5 phosphate buffer) 431 (ε/dm^3 mol^{-1} cm^{-1} 142000), 524 (12300), 564 (7710), 592 (6350), 649 (2630).

Free base 5,10,15-tris(*N*-methyl-4-pyridiniumyl)-20-[4-[(2-methoxy-4-amino-phenylcarbonyl)-amino] phenyl] porphyrin, 22.

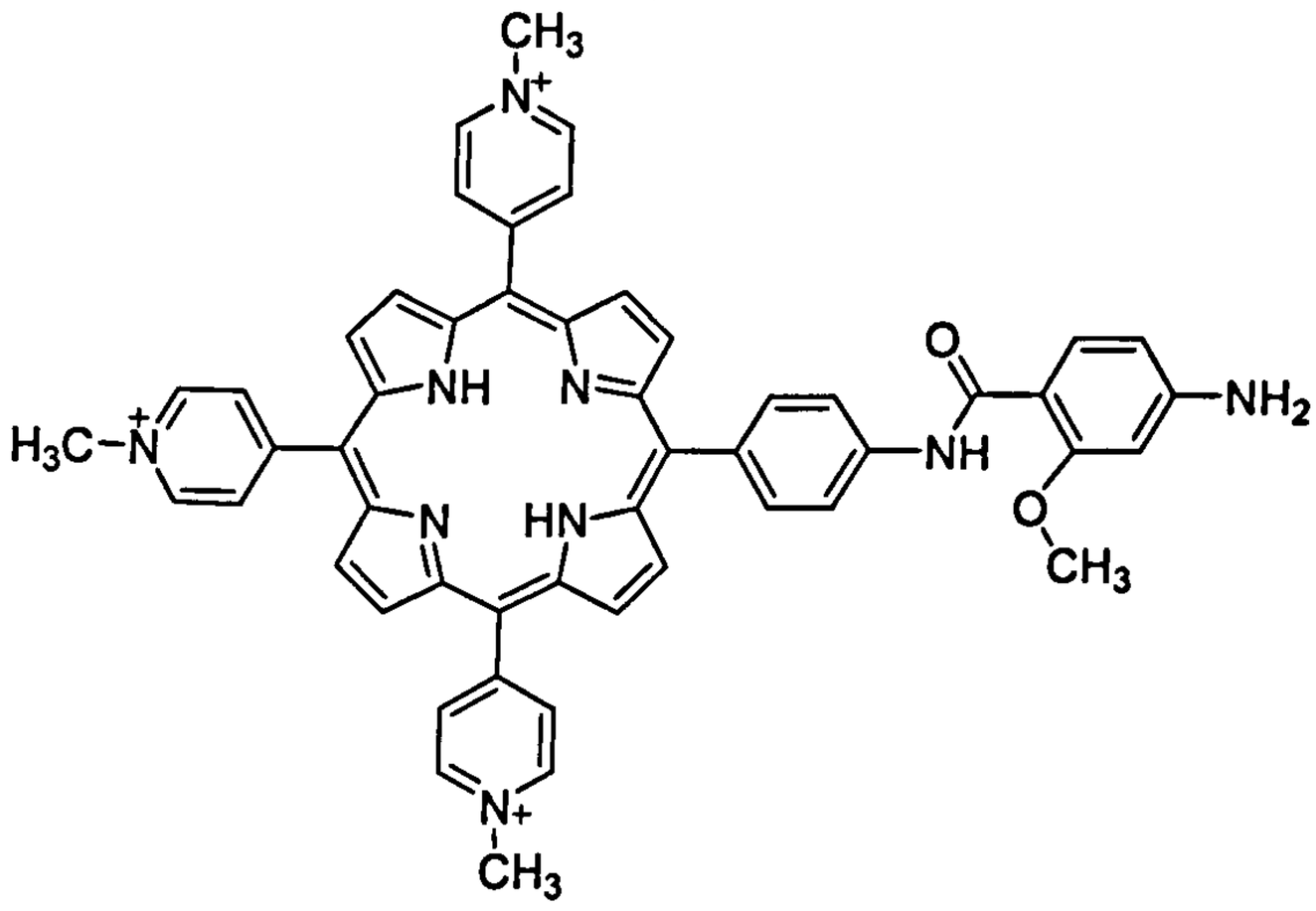

22

Free base 5,10,15-tris(*N*-methyl-4-pyridiniumyl)-20-[4-[(2-methoxy-4-nitro-phenylcarbonyl)-amino] phenyl] porphyrin tris iodide, **21** (0.10 g, 0.082 mmol), was dissolved in 25 cm^3 ethanol. Saturated ammonium chloride solution (0.1 cm^3), and indium powder (100 mesh, 0.05 g), were added and the solution stirred for 72 h under reflux. The reaction mixture was diluted with water, adjusted to pH 3 with 0.1 M hydrochloric acid and filtered through celite. The solvent was removed *in vacuo* give a green/purple solid. The crude porphyrin was taken up in water and ammonium hexafluorophosphate added to precipitate the **22** as the hexafluorophosphate salt. This was filtered, washed with cold water and dried to give [**22**][PF_6]$_3$ (0.070 g, 0.055 mmol, 64 %).

To obtain the water soluble chloride salt, tetrabutyl ammonium chloride solution in acetonitrile was added dropwise to an acetonitrile solution of the [**22**][PF_6]$_3$ precipitate the [**22**][Cl]$_3$. This was further purified by passing an aqueous solution through Sephadex G10 size exclusion gel and precipitation from aqueous solution by addition of acetone.

^{1}H NMR δ_H (500 MHz; solvent d_6-DMSO): 10.21 (1H, s, NH), 9.53 (6H, d, *m*-pyridyl), 9.13 (8H, m, β-pyrrole), 9.00 (6H, m, *o*-pyridyl), 8.21 (2H, d, J = 8.2 Hz, *m*-aminophenyl), 8.19 (2H, d, J = 8.2 Hz, *o*-aminophenyl), 7.74 (1H, d, J = 9.0 Hz, phenyl), 6.40 (1H, d, J = 1.9

Hz, phenyl), 6.33 (1H, dd, J = 9.0, 1.9 Hz, phenyl) 4.73 (9H, s, NCH_3), 4.01 (3H, s, OCH_3), -2.99 (2H, br s, inner NH) ppm.

$^{13}C\{^1H\}$ NMR δ_C (176 MHz; solvent $CDCl_3$): 164.7, 159.6, 157.1, 157.0, 154.6, 144.7, 140.3, 135.7, 135.4, 133.2, 132.9, 132.6, 123.6, 118.8, 115.8, 114.9, 109.7, 107.0, 96.6, 56.3, 48.3 ppm.

ESI-MS: m/z = 412.7 ($M^{3+} - H^+$, 15%), 275.5 (M^{3+}, 100%), 206.8 ($M^{3+} + H^+$, 10%)

HR ESI-MS: For $C_{52}H_{44}N_6O_2$ (M^{3+}), observed mass 275.4526, calculated 275.4534, difference 0.8 mDa.

FTIR (ATR) ν_{max} /cm^{-1}: 1636s, 1597s, 1588s, 1559m, 1509s, 1468s, 1460s, 1400m, 1359w, 1349w, 1329w, 1312s, 1271s, 1245s, 1211m, 1182s, 1155m, 1136m, 1094m, 1054w, 1024s, 1014s, 998m, 968s, 945w, 927w, 883m, 853s, 793s, 764s, 710s, 663s.

FTIR (KBr pressed disc) ν_{max} /cm^{-1}: 3426br s, 2961w, 2926w, 2855m, 1638 s, 1599s, 1590s, 1511s, 1463s, 1400m, 1384s, 1311s, 1271s, 1244s, 1210m, 1182sm 1135m, 1094m, 1052w, 1023s, 1014s, 999m, 981w, 968s, 885w, 821m, 797s, 763m, 729m, 710s. 672m.

UV-Vis: λ_{max}/nm (DMSO) 429 (ε/dm^3 mol^{-1} cm^{-1} 124000), 522 (9780), 564 (8750), 595 (5840), 653 (3510).

Zinc 5,10,15-tris(*N*-methyl-4-pyridiniumyl)-20-[4-[(2-methoxy-4-amino-phenylcarbonyl)-amino] phenyl] porphyrin, 23.

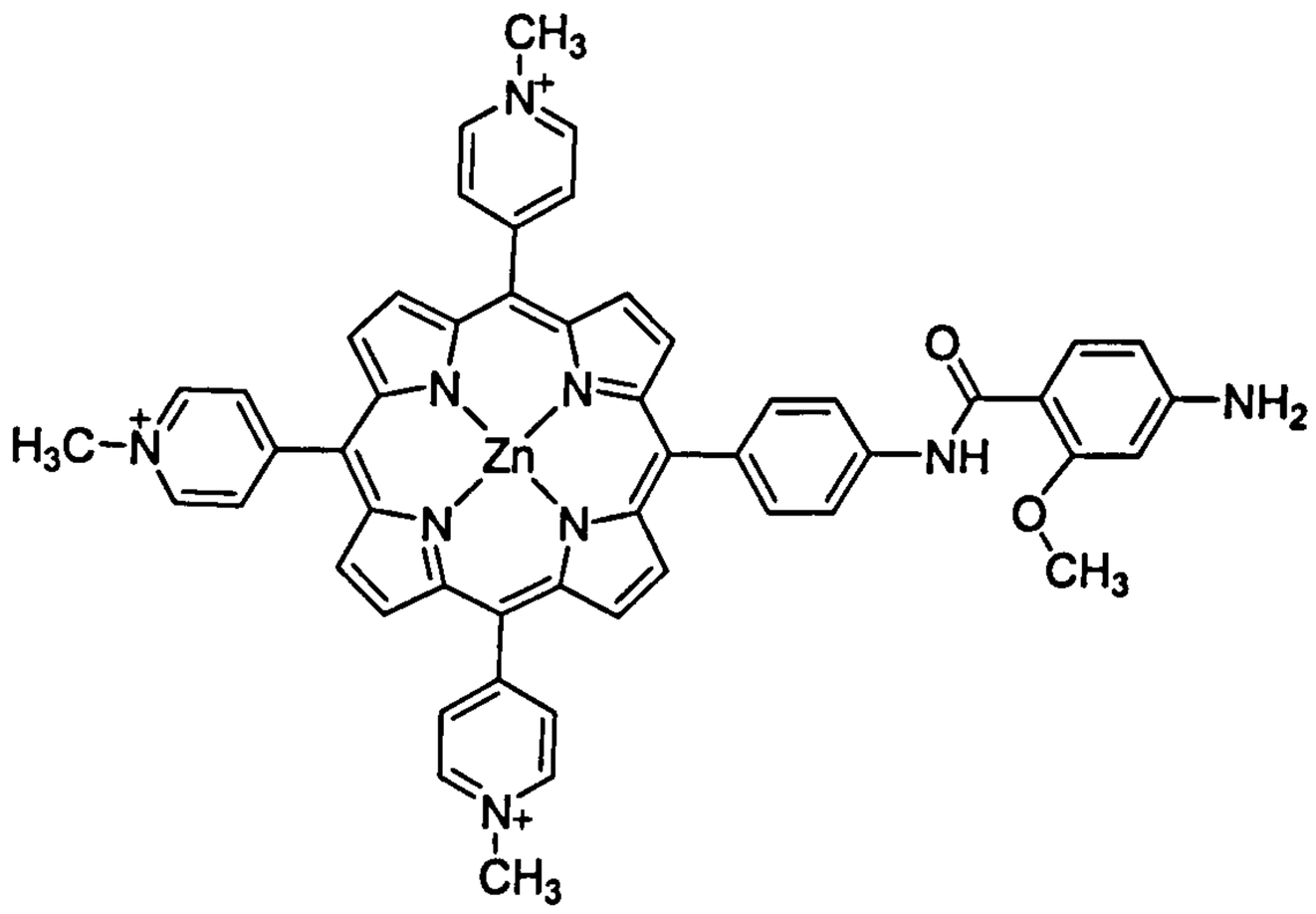

23

Free base 5,10,15-tris(*N*-methyl-4-pyridiniumyl)-20-[4-[(2-methoxy-4-amino-phenylcarbonyl)-amino] phenyl] porphyrin, **22** (0.050 g, 0.054 mmol) and zinc acetate dihydrate (0.11 g, 0.50 mmol) were dissolved in ethanol (25 cm^3) and heated at reflux for 2 h. The reaction mixture was cooled and diluted with water (50 cm^3). Ammonium hexafluorophosphate was added to precipitate the **23** as the hexafluorophosphate salt, **[23]**$[PF_6]_3$ (0.058 g, 0.044 mmol, 82%). This was filtered, washed with cold water and dried. To obtain the water soluble chloride salt, tetrabutyl ammonium chloride solution in acetonitrile was added dropwise to an acetonitrile solution of the **[23]**$[PF_6]_3$ to precipitate the **[23]**$[Cl]_3$. This was further purified by passing a methanol solution through Sephadex LH20 size exclusion gel and precipitation from aqueous solution by addition of acetone to give **[23]**$[Cl]_3$ (0.040 g, 0.041 mmol, 76 %).

^{1}H NMR δ_H (600 MHz; solvent d_6-DMSO): 10.18 (1H, s, NH), 9.41 (6H, m, *m*-pyridyl), 8.98 (8H, m, β-pyrrole), 8.88 (6H, m, *o*-pyridyl), 8.17 (2H, d, J = 6.0 Hz, *m*-aminophenyl), 8.10 (2H, d, J = 6.0 Hz, *o*-aminophenyl), 7.76 (1H, d, J = 7.5 Hz, phenyl), 6.39 (1H, s, phenyl), 6.32 (1H, d, J = 7.5 Hz, phenyl) 5.95 (2H, br s, NH_2), 4.70 (9H, s, N^+CH_3), 4.02 (3H, s, OCH_3) ppm.

$^{13}C\{^1H\}$ NMR δ_C (150 MHz; solvent d_6-DMSO): 164.6, 159.0, 154.6, 150.1, 148.8, 148.6, 148.3, 144.1, 135.0, 133.8, 133.2, 132.6, 132.4, 131.9, 123.8, 115.9, 118.5, 113.9, 109.7, 106.9, 96.6, 56.3, 48.2 ppm.

HR ESI-MS: For $C_{52}H_{42}N_9O_2Zn$ (M^{3+}), observed mass 296.0891, calculated 296.0912, difference 2.1 mDa.

FTIR: (KBr pressed disc) ν_{max} /cm^{-1}: 3428 br m, 3110w, 3044w, 2963w, 2921m, 2851m, 1636s, 1602s, 1559w, 1518s, 1508s, 1457m, 1400w, 1385m, 1359w, 1341w, 1311w, 1264m, 1241m, 1202w, 1182m, 1129m, 1108w, 1093m, 1016m, 992s, 855w, 797s, 759m, 713m, 673m.

UV-Vis: λ_{max}/nm (pH 7.5 phosphate buffer) 436 (ε/dm^3 mol^{-1} cm^{-1} 107000), 565 (11200), 615 (6890).

Free base 5,10,15-tris(*N*-methyl-4-pyridiniumyl)-20-[4-{(2-methoxy-4-[(pyridine-4-carbonyl)-amino]-phenylcarbonyl)-amino} phenyl]-porphyrin, 24.

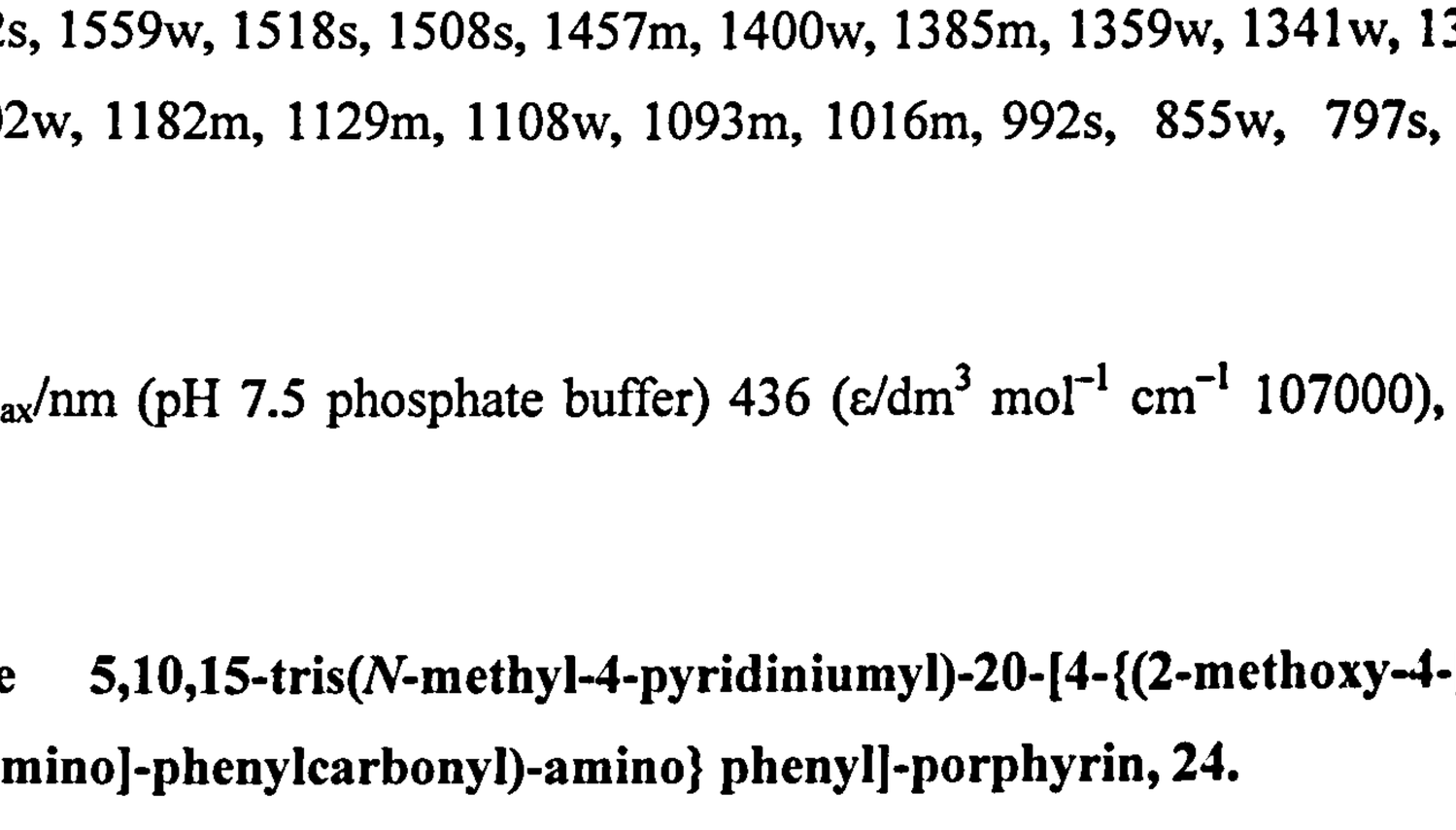

24

The isonicotinic acid anhydride (0.050 g, 0.18 mmol) was taken up in acetonitrile (50 cm^3) and added dropwise to an ice cold solution of free base 5,10,15-tris(*N*-methyl-4-pyridiniumyl)-20-[4-[(2-methoxy-4-aminocarbonyl)-amino] phenyl] porphyrin tris pentafluorophosphate, **[22]**$[PF_6]_3$ (0.068 g, 0.054 mmol) in acetonitrile with stirring. The reaction was heated at reflux for 48 h. Tetrabultylammonium chloride solution in acetonitrile was added dropwise to the cool solution until a precipitate of **[24]**$[Cl]_3$ formed. This was filtered, washed with acetonitrile and dried. The product was further purified by passing an aqueous solution through Sephadex G10 size exclusion gel and precipitating from aqueous solution by addition of acetone to give **[24]**$[Cl]_3$ (0.043 g, 0.041 mmol, 76 %).

^{1}H NMR δ_H (600 MHz; solvent d_6-DMSO): 11.35 (1H, s, NH), 10.58 (1H, s, NH), 9.55 (6H, m, *m*-pyridyl), 9.10 (8H, m, β-pyrrole), 9.01 (8H, m, *o*-pyridyl, *m*-pyridyl), 8.35 (2H, d, J = 5.3 Hz, *o*-pyridyl), 8.29 (2H, d, J = 7.8 Hz, *m*-aminophenyl), 8.23 (2H, d, J = 7.9 Hz, *o*-aminophenyl), 7.95 (1H, s, phenyl), 7.87 (1H, d, J = 8.6 Hz, phenyl), 7.72 (1H, d, J = 8.6, phenyl) 4.75 (9H, s, NCH_3), 4.06 (3H, s, OCH_3), –2.95 (2H, br s, inner NH) ppm.

^{13}C{^{1}H} NMR δ_C (150 MHz; solvent CD_3CN): 164.0, 163.4, 159.4, 158.3, 149.6, 148.3, 144.0, 143.4, 138.7, 138.4, 135.2, 132.8, 132.7, 132.3, 131.6, 123.8, 121.3, 118.7, 118.3, 114.9, 114.0, 112.2, 103.4, 56.3, 48.4 ppm.

ESI-MS: m/z = 465.2 ($M^{3+} - H^+$, 10%), 310.5 (M^{3+}, 100%).

HR ESI-MS: For $C_{58}H_{47}N_{10}O_3$ (M^{3+}), observed mass 310.4596, calculated 310.4605, difference 0.9 mDa.

FTIR: (KBr pressed disc) ν_{max} /cm^{-1}: 3421s, 3109w, 3018w, 2958w, 2917w, 2837w, 1636br s, 1559w, 1539w, 1521m, 1506m, 1521m, 1507m, 1475w, 1457w, 1437w, 1401s, 1384s, 1323w, 1260w, 1232w, 1213w, 1182w, 1145w, 1090m, 1072m, 1026s, 964w, 882w, 856w, 794m, 763m, 698m, 668s, 659w, 617w.

UV-Vis: λ_{max}/nm (pH 7.5 phosphate buffer) 434 (ε/dm^3 mol^{-1} cm^{-1} 117000), 524 (11600), 566 (11800), 598 (8120), 620 (6520).

Zinc 5,10,15-tris(*N*-methyl-4-pyridiniumyl)-20-[4-{(2-methoxy-4-[(pyridine-4-carbonyl)-amino]-phenylcarbonyl)-amino} phenyl]-porphyrin, 25.

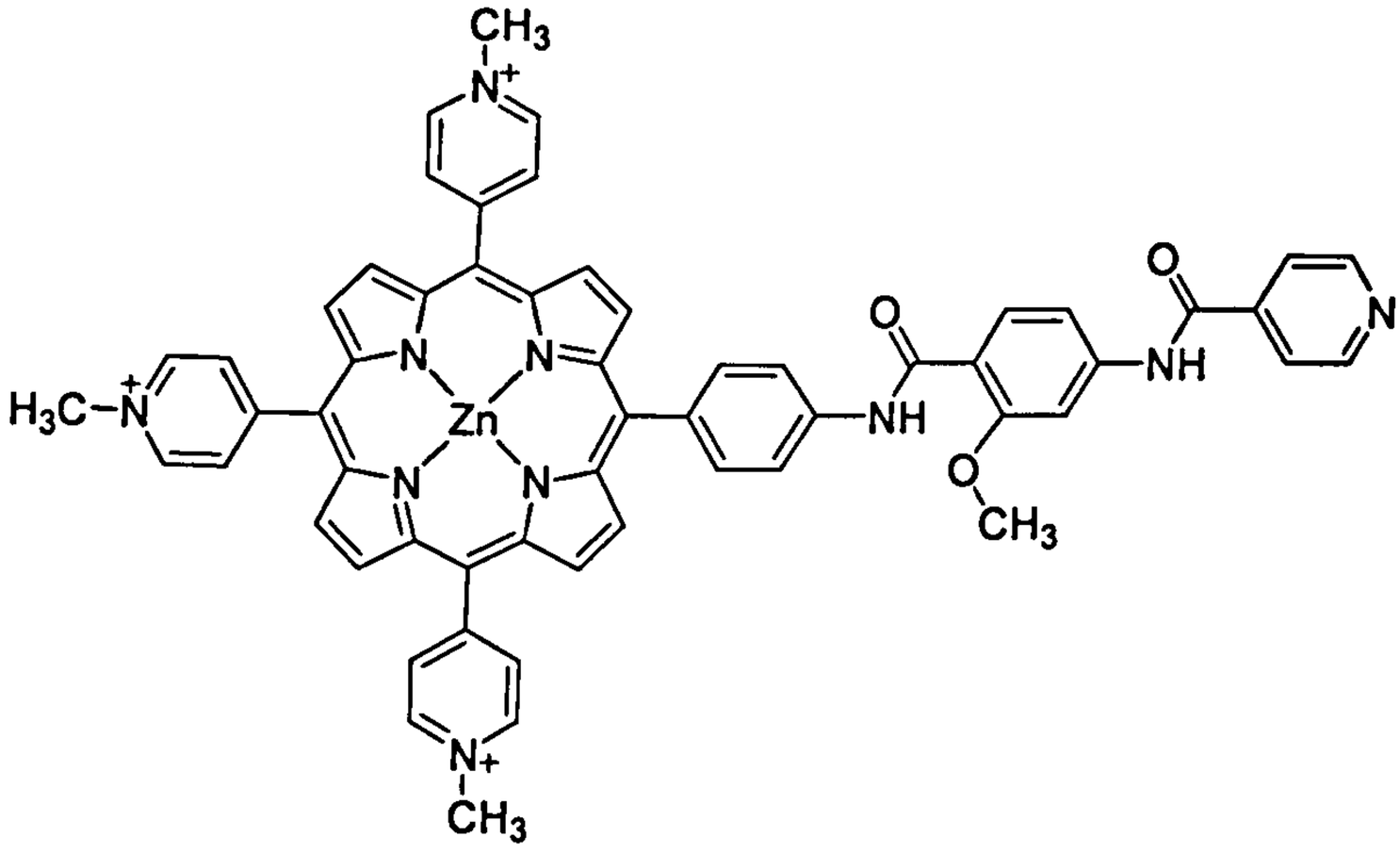

25

Free base 5,10,15-tris(*N*-methyl-4-pyridiniumyl)-20-[4-{(2-methoxy-4-[(pyridine-4-carbonyl)-amino]-phenylcarbonyl)-amino} phenyl]-porphyrin, **24** (0.043 g, 0.041 mmol) and zinc acetate dihydrate (0.075 g, 0.41 mmol) were dissolved in methanol (25 cm^3) and heated at reflux for 2 h. The reaction mixture was cooled and diluted with water (50 cm^3). Ammonium hexafluorophosphate was added to precipitate the **25** as the hexafluorophosphate salt. This was filtered, washed with cold water and dried. To obtain the water soluble chloride salt, tetrabutyl ammonium chloride solution in acetonitrile was added dropwise to an acetonitrile solution of the **[25]**$[PF_6]_3$ giving a precipitate of **[25]**$[Cl]_3$. This was further purified by passing a methanol solution through Sephadex LH20 size exclusion gel and precipitation from aqueous solution by addition of acetone to give **[25]**$[Cl]_3$ (0.030 g, 0.028 mmol, 67 %).

^{1}H NMR δ_H (600 MHz; solvent d_6-DMSO): 11.18 (1H, s, NH), 10.98 (1H, s, NH), 9.47 (6H, m, *m*-pyridyl), 9.00 (8H, m, β-pyrrole), 8.92 (6H, m, *o*-pyridyl), 8.81 (2H, d, J = 6.0 Hz, *m*-

pyridyl), 8.23 (2H, d, J = 8.2 Hz, *m*-aminophenyl), 8.14 (2H, d, J = 8.2 Hz, *o*-aminophenyl), 7.99 (2H, d, J = 6.0 Hz, *o*-pyridyl), 7.91 (1H, s, phenyl), 7.82 (1H, d, J = 8.2 Hz, phenyl), 7.69 (1H, d, J = 8.2, phenyl) 4.75 (9H, s, NCH_3), 4.05 (3H, s, OCH_3) ppm.

$^{13}C\{^1H\}$ NMR δ_C (150 MHz; solvent d_6-DMSO): 164.8, 164.7, 159.0, 157.6, 150.9, 150.8, 148.6, 148.3, 144.1, 142.0, 137.5, 135.0, 133.8, 132.8, 131.8, 131.2, 126.6, 123.7, 122.2, 118.5, 115.9, 115.0, 112.8, 104.4, 55.6, 48.1 ppm.

ESI-MS: m/z = 496 (M^{2+}, 100%), 331 (M^{3+}, 80%).

HR ESI-MS: For $C_{58}H_{45}N_1O_3Zn$ (M^{3+}), observed mass 331.0971, calculated 331.0984, difference 1.2 mDa.

FTIR (KBr pressed disc) ν_{max} /cm^{-1}: 3443br w, 3116w, 3043w, 2963w, 2920w, 2849w, 1637s, 1594m, 1526m, 1514w, 1461m, 1453m, 1402m, 1384s, 1342w, 1314m, 1288w, 1262w, 1247w, 1185m, 1129w, 1092m, 1019w, 994s, 853w, 797s, 750w, 715w, 673w, 616w.

UV-Vis: λ_{max}/nm (DMSO) 442 (ε/dm^3 mol^{-1} cm^{-1} 111000), 569 (12500), 614 (7520).

Enzyme assay of XO

50 mM Potassium phosphate buffer, pH 7.5.

Potassium phosphate, monobasic, anhydrous (1.36 g, 10 mmol) was dissolved in deionised water (190 cm^3). A solution of EDTA (0.1 M, 0.2 cm^3) was added and the pH of the solution was adjusted to 7.5 at 25 °C with 1M potassium hydroxide solution. The volume of the solution increased to 200 cm^3 with deionised water.

0.15 mM Solution of Xanthine

Xanthine (2.3 mg, 0.015 mmol) was dissolved in the minimum volume of aqueous potassium hydroxide (1 M). The solution was diluted to 90 cm^3 with deionised water and the pH was adjusted to 7.5 with dilute hydrochloric acid. The solution was made up to 100 cm^3 with deionised water.

Solution of Xanthine Oxidase

17 µl of a stock solution of xanthine oxidase (bovine milk, grade III, 22 mg ml^{-1}, 1.30 U ml^{-1}) was diluted to 5 cm^3 with 50 mM potassium phosphate buffer and stored over ice.

References

1. R. Luguya, L. Jaquinod, F. R. Fronczek, M. G. H. Vicente, K. M. Smith, *Tetrahedron*, **2004**, *60*, 2757.
2. H. Li, O. S. Fedorova, A. N. Grachev, W. R. Trumble, G. A. Bohach, L. Czuchajowski, *Biochimica et Biophysica Acta*, **1997**, *1354*, 252.
3. A. B. Pangborn, M. A. Giardello, R. H. Grubbs, R. K. Rosen, F. J. Timmers, *Organometallics*, **1996**, *15*, 1518.

APPENDIX 1

APPENDIX 1

Table 1. Crystal data and structure refinement for **6**.

Empirical formula	C15 H14 N2 O4	
Formula weight	286.28	
Temperature	110(2) K	
Wavelength	0.71073 Å	
Crystal system	Monoclinic	
Space group	P2(1)/n	
Unit cell dimensions	a = 13.6031(9) Å	a= 90°.
	b = 8.0726(5) Å	b= 118.0610(10)°.
	c = 13.6339(9) Å	g = 90°.
Volume	1321.17(15) $Å^3$	
Z	4	
Density (calculated)	1.439 Mg/m^3	
Absorption coefficient	0.106 mm^{-1}	
F(000)	600	
Crystal size	0.37 x 0.32 x 0.22 mm^3	
Theta range for data collection	1.74 to 28.30°.	
Index ranges	-18<=h<=18, -10<=k<=10, -18<=l<=18	
Reflections collected	13200	
Independent reflections	3270 [R(int) = 0.0194]	
Completeness to theta = 28.30°	99.7 %	
Absorption correction	Semi-empirical from equivalents	
Max. and min. transmission	0.980 and 0.906	
Refinement method	Full-matrix least-squares on F^2	
Data / restraints / parameters	3270 / 0 / 196	
Goodness-of-fit on F^2	1.033	
Final R indices [I>2sigma(I)]	R1 = 0.0364, wR2 = 0.0979	
R indices (all data)	R1 = 0.0403, wR2 = 0.1011	
Largest diff. peak and hole	0.377 and -0.186 $e.Å^{-3}$	

Table 2. Atomic coordinates (x 10^4) and equivalent isotropic displacement parameters ($Å^2$x 10^3) for **6**. U(eq) is defined as one third of the trace of the orthogonalized U^{ij} tensor.

	x	y	z	U(eq)
C(1)	6631(1)	5650(1)	9285(1)	16(1)
C(2)	7553(1)	4646(1)	9308(1)	15(1)
C(3)	8545(1)	4194(1)	10262(1)	14(1)
C(4)	9367(1)	3290(1)	10158(1)	16(1)
C(5)	9207(1)	2819(1)	9108(1)	15(1)
C(6)	8217(1)	3230(1)	8158(1)	17(1)
C(7)	7420(1)	4141(1)	8271(1)	17(1)
C(8)	11022(1)	1408(1)	9716(1)	16(1)
C(9)	11745(1)	626(1)	9280(1)	16(1)
C(10)	12541(1)	-502(1)	9972(1)	19(1)
C(11)	13221(1)	-1256(1)	9600(1)	24(1)
C(12)	12423(1)	180(2)	7970(1)	22(1)
C(13)	11692(1)	990(1)	8259(1)	19(1)
C(14)	5753(1)	6860(2)	10225(1)	22(1)
C(15)	9652(1)	4173(2)	12242(1)	23(1)
N(1)	10010(1)	1967(1)	8933(1)	16(1)
N(2)	13176(1)	-943(1)	8616(1)	24(1)
O(1)	6638(1)	5833(1)	10259(1)	20(1)
O(2)	5898(1)	6252(1)	8440(1)	27(1)
O(3)	8667(1)	4674(1)	11268(1)	19(1)
O(4)	11354(1)	1500(1)	10715(1)	25(1)

Table 3. Bond lengths [Å] and angles [°] for **6**.

C(1)-O(2)	1.2153(13)
C(1)-O(1)	1.3315(12)
C(1)-C(2)	1.4817(14)
C(2)-C(7)	1.3991(14)
C(2)-C(3)	1.4120(13)
C(3)-O(3)	1.3583(12)
C(3)-C(4)	1.3974(14)
C(4)-C(5)	1.3951(14)
C(4)-H(4)	0.9500
C(5)-C(6)	1.4004(14)
C(5)-N(1)	1.4042(13)
C(6)-C(7)	1.3765(14)
C(6)-H(6)	0.9500
C(7)-H(7)	0.9500
C(8)-O(4)	1.2194(13)
C(8)-N(1)	1.3627(13)
C(8)-C(9)	1.5064(14)
C(9)-C(10)	1.3896(15)
C(9)-C(13)	1.3913(14)
C(10)-C(11)	1.3875(15)
C(10)-H(10)	0.9500
C(11)-N(2)	1.3373(16)
C(11)-H(11)	0.9500
C(12)-N(2)	1.3413(16)
C(12)-C(13)	1.3931(15)
C(12)-H(12)	0.9500
C(13)-H(13)	0.9500
C(14)-O(1)	1.4450(12)
C(14)-H(14A)	0.9800
C(14)-H(14B)	0.9800
C(14)-H(14C)	0.9800
C(15)-O(3)	1.4311(12)
C(15)-H(15A)	0.9800
C(15)-H(15B)	0.9800

C(15)-H(15C)	0.9800
N(1)-H(1)	0.868(15)
O(2)-C(1)-O(1)	121.30(9)
O(2)-C(1)-C(2)	123.21(9)
O(1)-C(1)-C(2)	115.48(9)
C(7)-C(2)-C(3)	117.94(9)
C(7)-C(2)-C(1)	115.62(9)
C(3)-C(2)-C(1)	126.42(9)
O(3)-C(3)-C(4)	121.89(9)
O(3)-C(3)-C(2)	117.78(9)
C(4)-C(3)-C(2)	120.33(9)
C(5)-C(4)-C(3)	120.00(9)
C(5)-C(4)-H(4)	120.0
C(3)-C(4)-H(4)	120.0
C(4)-C(5)-C(6)	120.18(9)
C(4)-C(5)-N(1)	123.36(9)
C(6)-C(5)-N(1)	116.44(9)
C(7)-C(6)-C(5)	119.20(9)
C(7)-C(6)-H(6)	120.4
C(5)-C(6)-H(6)	120.4
C(6)-C(7)-C(2)	122.32(9)
C(6)-C(7)-H(7)	118.8
C(2)-C(7)-H(7)	118.8
O(4)-C(8)-N(1)	124.21(9)
O(4)-C(8)-C(9)	119.97(9)
N(1)-C(8)-C(9)	115.82(9)
C(10)-C(9)-C(13)	118.36(9)
C(10)-C(9)-C(8)	116.83(9)
C(13)-C(9)-C(8)	124.78(9)
C(11)-C(10)-C(9)	118.64(10)
C(11)-C(10)-H(10)	120.7
C(9)-C(10)-H(10)	120.7
N(2)-C(11)-C(10)	124.10(11)
N(2)-C(11)-H(11)	117.9
C(10)-C(11)-H(11)	118.0

N(2)-C(12)-C(13)	123.88(10)
N(2)-C(12)-H(12)	118.1
C(13)-C(12)-H(12)	118.1
C(9)-C(13)-C(12)	118.44(10)
C(9)-C(13)-H(13)	120.8
C(12)-C(13)-H(13)	120.8
O(1)-C(14)-H(14A)	109.5
O(1)-C(14)-H(14B)	109.5
H(14A)-C(14)-H(14B)	109.5
O(1)-C(14)-H(14C)	109.5
H(14A)-C(14)-H(14C)	109.5
H(14B)-C(14)-H(14C)	109.5
O(3)-C(15)-H(15A)	109.5
O(3)-C(15)-H(15B)	109.5
H(15A)-C(15)-H(15B)	109.5
O(3)-C(15)-H(15C)	109.5
H(15A)-C(15)-H(15C)	109.5
H(15B)-C(15)-H(15C)	109.5
C(8)-N(1)-C(5)	127.50(9)
C(8)-N(1)-H(1)	118.5(10)
C(5)-N(1)-H(1)	113.8(10)
C(11)-N(2)-C(12)	116.54(10)
C(1)-O(1)-C(14)	114.62(8)
C(3)-O(3)-C(15)	118.19(8)

Symmetry transformations used to generate equivalent atoms:

Table 4. Anisotropic displacement parameters ($Å^2 x\ 10^3$) for **6**. The anisotropic displacement factor exponent takes the form: $-2p^2[\ h^2\ a^{*2}U^{11} + ... + 2\ h\ k\ a^*\ b^*\ U^{12}\ ]$

	U^{11}	U^{22}	U^{33}	U^{23}	U^{13}	U^{12}
C(1)	14(1)	17(1)	16(1)	0(1)	8(1)	-1(1)
C(2)	14(1)	17(1)	15(1)	1(1)	7(1)	0(1)
C(3)	15(1)	17(1)	12(1)	0(1)	7(1)	-1(1)
C(4)	13(1)	19(1)	13(1)	1(1)	5(1)	0(1)
C(5)	14(1)	17(1)	16(1)	0(1)	7(1)	0(1)
C(6)	17(1)	22(1)	12(1)	-1(1)	6(1)	1(1)
C(7)	14(1)	22(1)	13(1)	2(1)	5(1)	1(1)
C(8)	15(1)	17(1)	16(1)	-1(1)	8(1)	0(1)
C(9)	14(1)	17(1)	17(1)	-3(1)	8(1)	-3(1)
C(10)	19(1)	19(1)	22(1)	2(1)	12(1)	0(1)
C(11)	23(1)	20(1)	33(1)	4(1)	17(1)	4(1)
C(12)	20(1)	30(1)	20(1)	-5(1)	12(1)	-3(1)
C(13)	15(1)	25(1)	16(1)	-2(1)	7(1)	-1(1)
C(14)	20(1)	25(1)	22(1)	-2(1)	11(1)	7(1)
C(15)	18(1)	36(1)	12(1)	1(1)	6(1)	5(1)
N(1)	14(1)	22(1)	11(1)	-2(1)	6(1)	1(1)
N(2)	23(1)	25(1)	30(1)	-4(1)	17(1)	-1(1)
O(1)	19(1)	25(1)	16(1)	1(1)	9(1)	8(1)
O(2)	21(1)	42(1)	18(1)	9(1)	10(1)	13(1)
O(3)	16(1)	28(1)	12(1)	-1(1)	6(1)	4(1)
O(4)	22(1)	37(1)	14(1)	0(1)	6(1)	10(1)

Table 5. Hydrogen coordinates (x 10^4) and isotropic displacement parameters ($Å^2$x 10^3) for **6**.

	x	y	z	U(eq)
H(4)	10035	2996	10802	19
H(6)	8096	2886	7444	21
H(7)	6757	4436	7622	20
H(10)	12618	-752	10686	23
H(11)	13750	-2044	10072	28
H(12)	12386	439	7273	26
H(13)	11170	1773	7770	23
H(14A)	5847	7997	10031	33
H(14B)	5778	6852	10956	33
H(14C)	5033	6427	9666	33
H(15A)	9683	2961	12286	34
H(15B)	9638	4623	12902	34
H(15C)	10309	4592	12204	34
H(1)	9794(12)	1722(18)	8241(13)	25(4)

Table 6. Torsion angles [°] for **6**.

O(2)-C(1)-C(2)-C(7)	-12.45(15)
O(1)-C(1)-C(2)-C(7)	166.31(9)
O(2)-C(1)-C(2)-C(3)	166.15(11)
O(1)-C(1)-C(2)-C(3)	-15.09(15)
C(7)-C(2)-C(3)-O(3)	-179.40(9)
C(1)-C(2)-C(3)-O(3)	2.03(15)
C(7)-C(2)-C(3)-C(4)	0.94(15)
C(1)-C(2)-C(3)-C(4)	-177.63(10)
O(3)-C(3)-C(4)-C(5)	179.86(9)
C(2)-C(3)-C(4)-C(5)	-0.48(15)
C(3)-C(4)-C(5)-C(6)	-0.87(16)
C(3)-C(4)-C(5)-N(1)	177.43(9)
C(4)-C(5)-C(6)-C(7)	1.73(16)
N(1)-C(5)-C(6)-C(7)	-176.68(9)
C(5)-C(6)-C(7)-C(2)	-1.28(16)
C(3)-C(2)-C(7)-C(6)	-0.05(16)
C(1)-C(2)-C(7)-C(6)	178.67(10)
O(4)-C(8)-C(9)-C(10)	24.21(15)
N(1)-C(8)-C(9)-C(10)	-155.31(10)
O(4)-C(8)-C(9)-C(13)	-153.76(11)
N(1)-C(8)-C(9)-C(13)	26.72(15)
C(13)-C(9)-C(10)-C(11)	-2.17(15)
C(8)-C(9)-C(10)-C(11)	179.72(10)
C(9)-C(10)-C(11)-N(2)	1.39(18)
C(10)-C(9)-C(13)-C(12)	1.36(15)
C(8)-C(9)-C(13)-C(12)	179.31(10)
N(2)-C(12)-C(13)-C(9)	0.36(17)
O(4)-C(8)-N(1)-C(5)	4.27(17)
C(9)-C(8)-N(1)-C(5)	-176.23(9)
C(4)-C(5)-N(1)-C(8)	2.93(17)
C(6)-C(5)-N(1)-C(8)	-178.71(10)
C(10)-C(11)-N(2)-C(12)	0.30(17)
C(13)-C(12)-N(2)-C(11)	-1.20(17)
O(2)-C(1)-O(1)-C(14)	-3.14(15)

C(2)-C(1)-O(1)-C(14)	178.07(9)
C(4)-C(3)-O(3)-C(15)	-2.42(15)
C(2)-C(3)-O(3)-C(15)	177.92(9)

Symmetry transformations used to generate equivalent atoms:

Table 7. Hydrogen bonds for **6** [Å and °].

D-H...A	d(D-H)	d(H...A)	d(D...A)	<(DHA)
N(1)-H(1)...O(2)#1	0.868(15)	2.062(15)	2.9257(12)	173.4(14)

Symmetry transformations used to generate equivalent atoms:

#1 -x+3/2,y-1/2,-z+3/2

APPENDIX 2

APPENDIX 2

Table 1. Crystal data and structure refinement for **[8]**[PF_6^-]$_2$.

Empirical formula	C44.66 H37 F12 N10.33 O4 P2 Ru	
Formula weight	1173.40	
Temperature	110(2) K	
Wavelength	0.71073 Å	
Crystal system	Triclinic	
Space group	P-1	
Unit cell dimensions	a = 11.9956(10) Å	a = 69.116(2)°.
	b = 14.3953(12) Å	b = 78.306(2)°.
	c = 14.9670(12) Å	g = 80.187(2)°.
Volume	2350.9(3) $Å^3$	
Z	2	
Density (calculated)	1.658 Mg/m^3	
Absorption coefficient	0.506 mm^{-1}	
F(000)	1183	
Crystal size	0.23 x 0.15 x 0.15 mm^3	
Theta range for data collection	1.52 to 28.31°.	
Index ranges	-13<=h<=15, -19<=k<=14, -19<=l<=16	
Reflections collected	16853	
Independent reflections	11445 [R(int) = 0.0217]	
Completeness to theta = 28.31°	98.3 %	
Absorption correction	Semi-empirical from equivalents	
Max. and min. transmission	0.927 and 0.787	
Refinement method	Full-matrix least-squares on F^2	
Data / restraints / parameters	11445 / 15 / 759	
Goodness-of-fit on F^2	1.025	
Final R indices [I>2sigma(I)]	R1 = 0.0498, wR2 = 0.1164	
R indices (all data)	R1 = 0.0626, wR2 = 0.1232	
Largest diff. peak and hole	1.453 and -1.003 $e.Å^{-3}$	

Table 2. Atomic coordinates (x 10^4) and equivalent isotropic displacement parameters ($Å^2$x 10^3)for **[8]**[PF_6^-]$_2$. U(eq) is defined as one third of the trace of the orthogonalized U^{ij} tensor.

	x	y	z	U(eq)
C(1)	4951(3)	8228(2)	5075(2)	26(1)
C(2)	3914(3)	8809(2)	5229(2)	27(1)
C(3)	3780(3)	9309(2)	5877(2)	27(1)
C(4)	4689(2)	9244(2)	6372(2)	22(1)
C(5)	5694(2)	8644(2)	6182(2)	21(1)
C(6)	6632(2)	8532(2)	6674(2)	20(1)
C(7)	8440(3)	7740(2)	6956(2)	27(1)
C(8)	8474(3)	8256(2)	7582(2)	27(1)
C(9)	7565(3)	8917(2)	7760(2)	24(1)
C(10)	6594(2)	9070(2)	7304(2)	21(1)
C(11)	5552(2)	9707(2)	7471(2)	21(1)
C(12)	4637(2)	9766(2)	7033(2)	23(1)
C(13)	4613(3)	10654(2)	8560(2)	22(1)
C(14)	4826(3)	11181(2)	9209(2)	24(1)
C(15)	5877(3)	11173(2)	9497(2)	26(1)
C(16)	5938(3)	11714(2)	10092(2)	32(1)
C(17)	4936(4)	12237(2)	10396(2)	35(1)
C(18)	3895(3)	12257(2)	10139(2)	35(1)
C(19)	3853(3)	11718(2)	9552(2)	29(1)
C(20)	7901(3)	10675(3)	9392(3)	38(1)
C(21)	8791(3)	8852(2)	4311(3)	35(1)
C(22)	9332(3)	9477(3)	3441(3)	49(1)
C(23)	9178(3)	9402(3)	2588(3)	50(1)
C(24)	8514(3)	8705(3)	2599(3)	39(1)
C(25)	8002(3)	8091(2)	3486(2)	26(1)
C(26)	7331(2)	7288(2)	3583(2)	24(1)
C(27)	7062(3)	7106(3)	2805(2)	35(1)
C(28)	6474(3)	6301(3)	2962(3)	40(1)
C(29)	6180(3)	5680(3)	3907(3)	33(1)
C(30)	6461(3)	5897(2)	4653(2)	25(1)

C(31)	5500(3)	5999(3)	7088(2)	30(1)
C(32)	5092(3)	5200(3)	7860(3)	39(1)
C(33)	5862(4)	4417(3)	8259(3)	43(1)
C(34)	7010(4)	4436(3)	7900(2)	37(1)
C(35)	7375(3)	5252(2)	7124(2)	26(1)
C(36)	8575(3)	5335(2)	6653(2)	26(1)
C(37)	9485(3)	4644(3)	6991(3)	40(1)
C(38)	10581(4)	4791(3)	6502(3)	49(1)
C(39)	10748(3)	5610(3)	5677(3)	43(1)
C(40)	9820(3)	6271(2)	5368(3)	31(1)
N(1)	5824(2)	8128(2)	5544(2)	22(1)
N(2)	7546(2)	7869(2)	6506(2)	23(1)
N(3)	5549(2)	10219(2)	8112(2)	22(1)
N(4)	4993(4)	12790(2)	11048(2)	49(1)
N(5)	8131(2)	8172(2)	4336(2)	26(1)
N(6)	7008(2)	6696(2)	4507(2)	22(1)
N(7)	6615(2)	6033(2)	6721(2)	24(1)
N(8)	8745(2)	6154(2)	5851(2)	24(1)
O(1)	3636(2)	10632(2)	8457(2)	29(1)
O(2)	6795(2)	10607(2)	9195(2)	26(1)
O(3)	4108(3)	13239(2)	11322(2)	61(1)
O(4)	5914(4)	12742(3)	11306(3)	77(1)
Ru(1)	7324(1)	7176(1)	5565(1)	19(1)
C(41)	1914(5)	4725(4)	-268(5)	76(2)
C(42)	1378(5)	4602(4)	696(4)	70(2)
N(9)	2322(7)	4790(6)	-1072(6)	149(3)
C(43A)	8973(11)	839(9)	4686(8)	45(3)
C(44A)	9170(20)	1662(15)	3759(12)	97(9)
N(10A)	8794(10)	338(7)	5473(8)	49(3)
C(43B)	7679(13)	3201(14)	2904(12)	63(5)
C(44B)	8485(15)	2470(30)	2550(20)	152(18)
N(10B)	7074(14)	3713(19)	3260(20)	164(12)
C(43C)	8450(15)	2248(13)	3268(15)	290(30)
C(44C)	7804(19)	2880(20)	2489(15)	227(15)
N(10C)	8943(15)	1742(15)	3868(14)	310(20)
F(1)	6791(3)	3683(2)	6131(2)	71(1)

F(2)	7647(5)	2551(3)	5428(2)	164(3)
F(3)	5977(3)	2253(2)	6476(2)	93(1)
F(4)	7625(2)	1342(2)	6884(2)	74(1)
F(5)	6782(2)	2471(2)	7576(2)	48(1)
F(6)	8410(3)	2782(2)	6559(3)	88(1)
P(1)	7203(1)	2522(1)	6502(1)	40(1)
F(7A)	10952(17)	1586(14)	10577(15)	96(6)
F(8A)	9083(14)	1619(10)	10669(10)	78(3)
F(9A)	9077(14)	2779(8)	9264(11)	75(4)
F(10A)	10980(11)	2703(12)	9083(11)	84(4)
F(7B)	11189(9)	1958(13)	10262(12)	71(4)
F(8B)	9376(17)	1649(8)	10957(11)	80(5)
F(9B)	8743(11)	2742(11)	9635(14)	78(4)
F(10B)	10505(19)	3107(15)	8987(9)	122(6)
F(11)	9864(3)	3108(2)	10403(2)	72(1)
F(12)	10122(2)	1383(2)	9490(2)	71(1)
P(2)	9992(1)	2265(1)	9931(1)	36(1)

Table 3. Bond lengths [Å] and angles [°] for **[8]**[PF_6^-]$_2$.

C(1)-N(1)	1.335(4)	C(17)-N(4)	1.480(4)
C(1)-C(2)	1.403(4)	C(18)-C(19)	1.376(4)
C(1)-H(1)	0.9500	C(18)-H(18)	0.9500
C(2)-C(3)	1.371(4)	C(19)-H(19)	0.9500
C(2)-H(2)	0.9500	C(20)-O(2)	1.442(4)
C(3)-C(4)	1.412(4)	C(20)-H(20A)	0.9800
C(3)-H(3)	0.9500	C(20)-H(20B)	0.9800
C(4)-C(5)	1.400(4)	C(20)-H(20C)	0.9800
C(4)-C(12)	1.427(4)	C(21)-N(5)	1.346(4)
C(5)-N(1)	1.376(4)	C(21)-C(22)	1.395(5)
C(5)-C(6)	1.422(4)	C(21)-H(21)	0.9500
C(6)-N(2)	1.372(4)	C(22)-C(23)	1.371(7)
C(6)-C(10)	1.407(4)	C(22)-H(22)	0.9500
C(7)-N(2)	1.332(4)	C(23)-C(24)	1.377(6)
C(7)-C(8)	1.397(4)	C(23)-H(23)	0.9500
C(7)-H(7)	0.9500	C(24)-C(25)	1.392(4)
C(8)-C(9)	1.369(4)	C(24)-H(24)	0.9500
C(8)-H(8)	0.9500	C(25)-N(5)	1.360(4)
C(9)-C(10)	1.413(4)	C(25)-C(26)	1.467(4)
C(9)-H(9)	0.9500	C(26)-N(6)	1.358(4)
C(10)-C(11)	1.454(4)	C(26)-C(27)	1.389(5)
C(11)-C(12)	1.364(4)	C(27)-C(28)	1.382(5)
C(11)-N(3)	1.402(4)	C(27)-H(27)	0.9500
C(12)-H(12)	0.9500	C(28)-C(29)	1.388(5)
C(13)-O(1)	1.219(4)	C(28)-H(28)	0.9500
C(13)-N(3)	*1.363(4)*	*C(29)-C(30)*	1.376(4)
C(13)-C(14)	1.509(4)	*C(29)-H(29)*	*0.9500*
C(14)-C(19)	1.398(4)	C(30)-N(6)	1.351(4)
C(14)-C(15)	1.410(5)	C(30)-H(30)	0.9500
C(15)-O(2)	1.355(4)	C(31)-N(7)	1.342(4)
C(15)-C(16)	1.395(4)	C(31)-C(32)	1.383(5)
C(16)-C(17)	1.390(5)	C(31)-H(31)	0.9500
C(16)-H(16)	0.9500	C(32)-C(33)	1.367(6)
C(17)-C(18)	1.372(6)	C(32)-H(32)	0.9500

C(33)-C(34)	1.375(6)	C(43A)-C(44A)	1.4754(19)
C(33)-H(33)	0.9500	C(44A)-H(44A)	0.9800
C(34)-C(35)	1.384(4)	C(44A)-H(44B)	0.9800
C(34)-H(34)	0.9500	C(44A)-H(44C)	0.9800
C(35)-N(7)	1.360(4)	C(43B)-N(10B)	1.1374(19)
C(35)-C(36)	1.473(4)	C(43B)-C(44B)	1.4711(19)
C(36)-N(8)	1.360(4)	C(44B)-H(44D)	0.9800
C(36)-C(37)	1.389(5)	C(44B)-H(44E)	0.9800
C(37)-C(38)	1.380(6)	C(44B)-H(44F)	0.9800
C(37)-H(37)	0.9500	C(43C)-N(10C)	1.1362(17)
C(38)-C(39)	1.377(6)	C(43C)-C(44C)	1.4701(17)
C(38)-H(38)	0.9500	C(44C)-H(44G)	0.9800
C(39)-C(40)	1.376(5)	C(44C)-H(44H)	0.9800
C(39)-H(39)	0.9500	C(44C)-H(44I)	0.9800
C(40)-N(8)	1.350(4)	F(1)-P(1)	1.586(3)
C(40)-H(40)	0.9500	F(2)-P(1)	1.575(3)
N(1)-Ru(1)	2.066(2)	F(3)-P(1)	1.595(3)
N(2)-Ru(1)	2.071(2)	F(4)-P(1)	1.612(3)
N(3)-H(3A)	0.80(4)	F(5)-P(1)	1.564(2)
N(4)-O(3)	1.221(5)	F(6)-P(1)	1.581(3)
N(4)-O(4)	1.225(5)	F(7A)-P(2)	1.616(13)
N(5)-Ru(1)	2.062(3)	F(8A)-P(2)	1.549(14)
N(6)-Ru(1)	2.059(2)	F(9A)-P(2)	1.545(10)
N(7)-Ru(1)	2.066(3)	F(10A)-P(2)	1.578(10)
N(8)-Ru(1)	2.061(3)	F(7B)-P(2)	1.556(11)
C(41)-N(9)	1.180(9)	F(8B)-P(2)	1.575(11)
C(41)-C(42)	1.416(8)	F(9B)-P(2)	1.616(11)
C(42)-H(42A)	0.9800	F(10B)-P(2)	1.589(11)
C(42)-H(42B)	0.9800	F(11)-P(2)	1.580(3)
C(42)-H(42C)	0.9800	F(12)-P(2)	1.601(3)
C(43A)-N(10A)	1.1399(19)		

C(25)-C(24)-H(24)	120.5	C(37)-C(36)-C(35)	123.8(3)
N(5)-C(25)-C(24)	121.6(3)	C(38)-C(37)-C(36)	119.5(3)
N(5)-C(25)-C(26)	115.0(3)	C(38)-C(37)-H(37)	120.3
C(24)-C(25)-C(26)	123.4(3)	C(36)-C(37)-H(37)	120.3
N(6)-C(26)-C(27)	121.1(3)	C(39)-C(38)-C(37)	119.2(3)
N(6)-C(26)-C(25)	114.9(3)	C(39)-C(38)-H(38)	120.4
C(27)-C(26)-C(25)	124.0(3)	C(37)-C(38)-H(38)	120.4
C(28)-C(27)-C(26)	120.1(3)	C(40)-C(39)-C(38)	119.2(3)
C(28)-C(27)-H(27)	120.0	C(40)-C(39)-H(39)	120.4
C(26)-C(27)-H(27)	120.0	C(38)-C(39)-H(39)	120.4
C(27)-C(28)-C(29)	118.5(3)	N(8)-C(40)-C(39)	122.4(3)
C(27)-C(28)-H(28)	120.7	N(8)-C(40)-H(40)	118.8
C(29)-C(28)-H(28)	120.7	C(39)-C(40)-H(40)	118.8
C(30)-C(29)-C(28)	119.1(3)	C(1)-N(1)-C(5)	117.7(2)
C(30)-C(29)-H(29)	120.5	C(1)-N(1)-Ru(1)	128.9(2)
C(28)-C(29)-H(29)	120.5	C(5)-N(1)-Ru(1)	113.06(19)
N(6)-C(30)-C(29)	122.8(3)	C(7)-N(2)-C(6)	117.9(3)
N(6)-C(30)-H(30)	118.6	C(7)-N(2)-Ru(1)	128.4(2)
C(29)-C(30)-H(30)	118.6	C(6)-N(2)-Ru(1)	113.66(19)
N(7)-C(31)-C(32)	122.5(3)	C(13)-N(3)-C(11)	126.6(3)
N(7)-C(31)-H(31)	118.7	C(13)-N(3)-H(3A)	111(3)
C(32)-C(31)-H(31)	118.7	C(11)-N(3)-H(3A)	122(3)
C(33)-C(32)-C(31)	118.3(3)	O(3)-N(4)-O(4)	124.1(3)
C(33)-C(32)-H(32)	120.8	O(3)-N(4)-C(17)	117.8(4)
C(31)-C(32)-H(32)	120.8	O(4)-N(4)-C(17)	118.1(4)
C(32)-C(33)-C(34)	120.2(3)	C(21)-N(5)-C(25)	118.6(3)
C(32)-C(33)-H(33)	119.9	C(21)-N(5)-Ru(1)	126.0(2)
C(34)-C(33)-H(33)	119.9	C(25)-N(5)-Ru(1)	115.3(2)
C(33)-C(34)-C(35)	119.2(4)	C(30)-N(6)-C(26)	118.4(3)
C(33)-C(34)-H(34)	120.4	C(30)-N(6)-Ru(1)	126.1(2)
C(35)-C(34)-H(34)	120.4	C(26)-N(6)-Ru(1)	115.3(2)
N(7)-C(35)-C(34)	121.0(3)	C(31)-N(7)-C(35)	118.7(3)
N(7)-C(35)-C(36)	115.1(3)	C(31)-N(7)-Ru(1)	126.1(2)
4)-C(35)-C(36)	123.9(3)	C(35)-N(7)-Ru(1)	115.2(2)
N(8)-C(36)-C(37)	121.2(3)	C(40)-N(8)-C(36)	118.5(3)
N(8)-C(36)-C(35)	115.0(3)	C(40)-N(8)-Ru(1)	126.0(2)

C(36)-N(8)-Ru(1)	115.2(2)	F(5)-P(1)-F(1)	90.79(14)
C(15)-O(2)-C(20)	118.3(3)	F(2)-P(1)-F(1)	90.4(2)
N(6)-Ru(1)-N(8)	93.59(10)	F(6)-P(1)-F(1)	88.87(17)
N(6)-Ru(1)-N(5)	78.80(10)	F(5)-P(1)-F(3)	88.51(18)
N(8)-Ru(1)-N(5)	95.92(10)	F(2)-P(1)-F(3)	92.0(3)
N(6)-Ru(1)-N(7)	95.84(10)	F(6)-P(1)-F(3)	178.4(2)
N(8)-Ru(1)-N(7)	79.04(10)	F(1)-P(1)-F(3)	91.38(18)
N(5)-Ru(1)-N(7)	172.48(10)	F(5)-P(1)-F(4)	88.95(15)
N(6)-Ru(1)-N(1)	93.75(9)	F(2)-P(1)-F(4)	89.9(2)
N(8)-Ru(1)-N(1)	169.81(10)	F(6)-P(1)-F(4)	90.89(18)
N(5)-Ru(1)-N(1)	92.43(10)	F(1)-P(1)-F(4)	179.65(19)
N(7)-Ru(1)-N(1)	93.19(10)	F(3)-P(1)-F(4)	88.85(17)
N(6)-Ru(1)-N(2)	171.42(10)	F(9A)-P(2)-F(8A)	89.1(7)
N(8)-Ru(1)-N(2)	93.56(10)	F(9A)-P(2)-F(7B)	159.1(7)
N(5)-Ru(1)-N(2)	95.75(10)	F(8A)-P(2)-F(7B)	111.4(7)
N(7)-Ru(1)-N(2)	90.17(10)	F(9A)-P(2)-F(8B)	108.6(7)
N(1)-Ru(1)-N(2)	79.77(10)	F(8A)-P(2)-F(8B)	23.1(7)
N(9)-C(41)-C(42)	176.2(7)	F(7B)-P(2)-F(8B)	92.2(7)
C(41)-C(42)-H(42A)	109.5	F(9A)-P(2)-F(10A)	91.2(6)
C(41)-C(42)-H(42B)	109.5	F(8A)-P(2)-F(10A)	166.1(7)
H(42A)-C(42)-H(42B)	109.5	F(7B)-P(2)-F(10A)	67.9(7)
C(41)-C(42)-H(42C)	109.5	F(8B)-P(2)-F(10A)	160.1(7)
H(42A)-C(42)-H(42C)	109.5	F(9A)-P(2)-F(11)	96.0(6)
H(42B)-C(42)-H(42C)	109.5	F(8A)-P(2)-F(11)	97.8(5)
N(10A)-C(43A)-C(44A)	167.6(11)	F(7B)-P(2)-F(11)	85.4(6)
N(10B)-C(43B)-C(44B)	174(2)	F(8B)-P(2)-F(11)	83.6(6)
C(43B)-C(44B)-H(44D)	109.5	F(10A)-P(2)-F(11)	96.1(4)
C(43B)-C(44B)-H(44E)	109.5	F(9A)-P(2)-F(10B)	69.3(7)
H(44D)-C(44B)-H(44E)	109.5	F(8A)-P(2)-F(10B)	158.3(8)
C(43B)-C(44B)-H(44F)	109.5	F(7B)-P(2)-F(10B)	90.3(7)
H(44D)-C(44B)-H(44F)	109.5	F(8B)-P(2)-F(10B)	166.2(12)
H(44E)-C(44B)-H(44F)	109.5	F(10A)-P(2)-F(10B)	26.9(6)
N(10C)-C(43C)-C(44C)	179(2)	F(11)-P(2)-F(10B)	83.1(8)
F(5)-P(1)-F(2)	178.7(3)	F(9A)-P(2)-F(12)	85.4(6)
F(5)-P(1)-F(6)	89.92(18)	F(8A)-P(2)-F(12)	80.9(5)
F(2)-P(1)-F(6)	89.6(3)	F(7B)-P(2)-F(12)	93.7(6)

F(8B)-P(2)-F(12)	94.7(6)	F(12)-P(2)-F(7A)	86.1(5)
F(10A)-P(2)-F(12)	85.3(4)	F(9A)-P(2)-F(9B)	22.0(7)
F(11)-P(2)-F(12)	177.99(18)	F(8A)-P(2)-F(9B)	71.5(8)
F(10B)-P(2)-F(12)	98.7(8)	F(7B)-P(2)-F(9B)	170.8(7)
F(9A)-P(2)-F(7A)	171.4(9)	F(8B)-P(2)-F(9B)	88.4(7)
F(8A)-P(2)-F(7A)	88.6(9)	F(10A)-P(2)-F(9B)	111.5(6)
F(7B)-P(2)-F(7A)	23.1(8)	F(11)-P(2)-F(9B)	85.5(4)
F(8B)-P(2)-F(7A)	71.1(7)	F(10B)-P(2)-F(9B)	87.0(6)
F(10A)-P(2)-F(7A)	89.0(7)	F(12)-P(2)-F(9B)	95.4(4)
F(11)-P(2)-F(7A)	92.5(5)	F(7A)-P(2)-F(9B)	159.5(7)
F(10B)-P(2)-F(7A)	113.0(7)		

Table 4. Anisotropic displacement parameters ($Å^2 x\ 10^3$) for [**8**][PF_6^-]$_2$. The anisotropic displacement factor exponent takes the form: $-2\pi^2[\ h^2\ a^{*2}U^{11} + \ldots + 2\ h\ k\ a^*\ b^*\ U^{12}\ ]$

	U^{11}	U^{22}	U^{33}	U^{23}	U^{13}	U^{12}
C(1)	24(2)	28(2)	31(2)	-16(1)	-1(1)	-6(1)
C(2)	22(2)	31(2)	34(2)	-16(1)	-5(1)	-3(1)
C(3)	22(1)	27(2)	33(2)	-14(1)	-2(1)	0(1)
C(4)	20(1)	21(1)	25(1)	-10(1)	2(1)	-4(1)
C(5)	22(1)	19(1)	22(1)	-9(1)	3(1)	-5(1)
C(6)	20(1)	16(1)	24(1)	-8(1)	0(1)	-2(1)
C(7)	23(2)	25(2)	37(2)	-16(1)	-3(1)	1(1)
C(8)	23(2)	29(2)	33(2)	-15(1)	-6(1)	-1(1)
C(9)	29(2)	22(1)	23(1)	-11(1)	-1(1)	-4(1)
C(10)	22(1)	19(1)	21(1)	-9(1)	1(1)	-3(1)
C(11)	25(1)	18(1)	22(1)	-10(1)	3(1)	-3(1)
C(12)	22(1)	21(1)	26(1)	-13(1)	2(1)	2(1)
C(13)	31(2)	15(1)	16(1)	-4(1)	-2(1)	2(1)
C(14)	38(2)	15(1)	15(1)	-4(1)	-1(1)	0(1)
C(15)	41(2)	16(1)	16(1)	-3(1)	-1(1)	-2(1)
C(16)	55(2)	22(2)	21(1)	-5(1)	-7(1)	-9(1)

C(17)	69(3)	16(1)	18(1)	-7(1)	-1(2)	-7(2)
C(18)	59(2)	19(1)	18(1)	-6(1)	2(1)	4(1)
C(19)	44(2)	19(1)	18(1)	-5(1)	-1(1)	5(1)
C(20)	39(2)	46(2)	37(2)	-19(2)	-7(2)	-10(2)
C(21)	27(2)	25(2)	52(2)	-17(2)	11(2)	-7(1)
C(22)	38(2)	27(2)	71(3)	-14(2)	18(2)	-14(2)
C(23)	36(2)	34(2)	54(2)	7(2)	12(2)	-2(2)
C(24)	29(2)	35(2)	36(2)	3(2)	2(1)	1(1)
C(25)	20(1)	18(1)	32(2)	-3(1)	-1(1)	4(1)
C(26)	21(1)	21(1)	24(1)	-5(1)	-2(1)	4(1)
C(27)	38(2)	34(2)	25(2)	-2(1)	-13(1)	5(2)
C(28)	45(2)	46(2)	34(2)	-15(2)	-18(2)	-2(2)
C(29)	33(2)	31(2)	41(2)	-17(2)	-10(1)	-2(1)
C(30)	25(2)	22(1)	28(2)	-11(1)	-1(1)	-1(1)
C(31)	33(2)	32(2)	28(2)	-15(1)	6(1)	-13(1)
C(32)	47(2)	41(2)	32(2)	-19(2)	16(2)	-23(2)
C(33)	66(3)	32(2)	28(2)	-5(2)	4(2)	-22(2)
C(34)	57(2)	26(2)	27(2)	-7(1)	1(2)	-13(2)
C(35)	37(2)	21(1)	22(1)	-11(1)	-1(1)	-6(1)
C(36)	34(2)	18(1)	29(2)	-12(1)	-2(1)	-3(1)
C(37)	46(2)	22(2)	45(2)	-6(2)	-9(2)	4(2)
C(38)	39(2)	31(2)	66(3)	-8(2)	-9(2)	11(2)
C(39)	27(2)	29(2)	64(3)	-13(2)	3(2)	5(1)
C(40)	28(2)	23(2)	39(2)	-11(1)	3(1)	-1(1)
N(1)	21(1)	21(1)	26(1)	-12(1)	2(1)	-4(1)
N(2)	21(1)	19(1)	29(1)	-12(1)	-1(1)	-2(1)
N(3)	24(1)	21(1)	24(1)	-12(1)	-2(1)	-2(1)
N(4)	88(3)	29(2)	33(2)	-18(1)	-3(2)	-12(2)
N(5)	20(1)	16(1)	37(2)	-8(1)	4(1)	1(1)
N(6)	21(1)	18(1)	25(1)	-9(1)	1(1)	1(1)
N(7)	30(1)	25(1)	22(1)	-14(1)	3(1)	-8(1)
N(8)	26(1)	17(1)	29(1)	-11(1)	0(1)	-1(1)
O(1)	29(1)	34(1)	26(1)	-15(1)	-4(1)	7(1)
O(2)	30(1)	25(1)	27(1)	-13(1)	-5(1)	-2(1)
O(3)	95(3)	45(2)	50(2)	-36(2)	9(2)	-7(2)
O(4)	100(3)	78(3)	84(3)	-64(2)	-24(2)	1(2)

Ru(1)	19(1)	16(1)	24(1)	-10(1)	2(1)	-3(1)
C(41)	52(3)	65(3)	105(5)	-31(3)	14(3)	-17(3)
C(42)	96(4)	45(3)	82(4)	-27(3)	-44(3)	10(3)
N(9)	140(6)	142(6)	179(7)	-99(6)	83(6)	-83(5)
C(43A)	33(7)	47(7)	77(10)	-43(7)	-11(7)	-8(5)
C(44A)	51(10)	101(13)	136(15)	-74(12)	63(11)	-19(9)
N(10A)	57(7)	39(6)	64(7)	-27(5)	-24(6)	2(5)
C(43B)	36(8)	110(15)	57(9)	-46(10)	8(7)	-20(9)
C(44B)	24(9)	330(50)	160(30)	-170(30)	-12(13)	29(16)
N(10B)	73(12)	230(30)	290(30)	-220(30)	-23(16)	-10(14)
C(43C)	120(20)	190(20)	580(60)	-270(30)	240(30)	-139(19)
C(44C)	150(20)	270(30)	160(20)	-20(20)	53(16)	31(19)
N(10C)	103(14)	450(40)	570(40)	-490(40)	209(19)	-175(19)
F(1)	119(3)	33(1)	55(2)	10(1)	-38(2)	-19(1)
F(2)	364(7)	110(3)	41(2)	-46(2)	66(3)	-158(4)
F(3)	122(3)	67(2)	97(2)	16(2)	-78(2)	-47(2)
F(4)	72(2)	36(1)	107(2)	-36(2)	38(2)	-18(1)
F(5)	82(2)	32(1)	26(1)	-8(1)	0(1)	-13(1)
F(6)	57(2)	63(2)	143(3)	-39(2)	18(2)	-32(2)
P(1)	65(1)	33(1)	26(1)	-12(1)	3(1)	-23(1)
F(7A)	133(12)	85(9)	115(11)	-70(8)	-102(9)	52(7)
F(8A)	134(8)	66(5)	38(5)	-14(4)	6(5)	-50(5)
F(9A)	87(9)	43(4)	85(7)	14(4)	-65(6)	6(4)
F(10A)	70(6)	99(8)	95(8)	-51(7)	32(5)	-51(5)
F(7B)	32(4)	100(10)	103(9)	-61(8)	-32(4)	20(4)
F(8B)	133(11)	37(4)	43(6)	-5(4)	34(6)	-16(5)
F(9B)	47(5)	75(6)	146(11)	-72(8)	-46(6)	15(4)
F(10B)	129(12)	131(11)	57(5)	35(6)	4(7)	-49(9)
F(11)	79(2)	54(2)	101(2)	-42(2)	-37(2)	9(1)
F(12)	60(2)	97(2)	84(2)	-61(2)	-28(2)	8(2)
P(2)	32(1)	44(1)	32(1)	-9(1)	-10(1)	-5(1)

Table 5. Hydrogen coordinates (x 10^4) and isotropic displacement parameters ($Å^2$x 10^3) for $[8][PF_6^-]_2$.

	x	y	z	U(eq)
H(1)	5037	7891	4619	31
H(2)	3309	8856	4886	33
H(3)	3077	9699	5991	32
H(7)	9078	7281	6847	33
H(8)	9130	8148	7885	33
H(9)	7587	9269	8184	29
H(12)	3951	10164	7171	28
H(16)	6642	11725	10284	38
H(18)	3230	12627	10358	41
H(19)	3139	11711	9374	35
H(20A)	8070	11373	9119	57
H(20B)	8489	10264	9096	57
H(20C)	7897	10435	10093	57
H(21)	8892	8907	4903	42
H(22)	9800	9947	3441	58
H(23)	9528	9831	1989	60
H(24)	8408	8644	2012	47
H(27)	7282	7535	2164	42
H(28)	6276	6176	2435	48
H(29)	5791	5113	4036	40
H(30)	6261	5466	5297	30
H(31)	4969	6546	6807	36
H(32)	4298	5196	8106	47
H(33)	5602	3857	8787	51
H(34)	7547	3895	8179	45
H(37)	9353	4075	7553	48
H(38)	11214	4333	6732	59
H(39)	11496	5718	5326	52
H(40)	9940	6830	4794	37
H(3A)	6120(30)	10320(30)	8230(20)	21(9)

H(42A)	783	4150	877	105
H(42B)	1030	5253	744	105
H(42C)	1950	4318	1132	105
H(44A)	9397	1387	3228	145
H(44B)	9788	2025	3773	145
H(44C)	8471	2121	3660	145
H(44D)	8229	2405	1996	228
H(44E)	8513	1820	3068	228
H(44F)	9249	2699	2351	228
H(44G)	8003	3570	2273	341
H(44H)	6981	2875	2729	341
H(44I)	7997	2629	1944	341

Table 6. Torsion angles [°] for **[8]**[PF_6^-]$_2$.

N(1)-C(1)-C(2)-C(3)	0.7(5)
C(1)-C(2)-C(3)-C(4)	0.7(5)
C(2)-C(3)-C(4)-C(5)	-1.1(4)
C(2)-C(3)-C(4)-C(12)	177.8(3)
C(3)-C(4)-C(5)-N(1)	0.0(4)
C(12)-C(4)-C(5)-N(1)	-178.9(3)
C(3)-C(4)-C(5)-C(6)	-178.8(3)
C(12)-C(4)-C(5)-C(6)	2.3(4)
N(1)-C(5)-C(6)-N(2)	-4.0(4)
C(4)-C(5)-C(6)-N(2)	174.9(3)
N(1)-C(5)-C(6)-C(10)	176.9(3)
C(4)-C(5)-C(6)-C(10)	-4.2(4)
N(2)-C(7)-C(8)-C(9)	0.5(5)
C(7)-C(8)-C(9)-C(10)	0.1(5)
N(2)-C(6)-C(10)-C(9)	1.2(4)
C(5)-C(6)-C(10)-C(9)	-179.8(3)
N(2)-C(6)-C(10)-C(11)	-176.3(3)
C(5)-C(6)-C(10)-C(11)	2.7(4)
C(8)-C(9)-C(10)-C(6)	-0.9(4)
C(8)-C(9)-C(10)-C(11)	176.5(3)
C(6)-C(10)-C(11)-C(12)	0.7(4)
C(9)-C(10)-C(11)-C(12)	-176.6(3)
C(6)-C(10)-C(11)-N(3)	179.3(3)
C(9)-C(10)-C(11)-N(3)	2.0(4)
N(3)-C(11)-C(12)-C(4)	178.9(3)
C(10)-C(11)-C(12)-C(4)	-2.6(4)
C(5)-C(4)-C(12)-C(11)	1.1(4)
C(3)-C(4)-C(12)-C(11)	-177.7(3)
O(1)-C(13)-C(14)-C(19)	-7.7(4)
N(3)-C(13)-C(14)-C(19)	172.4(3)
O(1)-C(13)-C(14)-C(15)	171.8(3)
N(3)-C(13)-C(14)-C(15)	-8.2(4)
C(19)-C(14)-C(15)-O(2)	176.7(3)
C(13)-C(14)-C(15)-O(2)	-2.7(4)

C(19)-C(14)-C(15)-C(16)	-1.5(4)
C(13)-C(14)-C(15)-C(16)	179.0(3)
O(2)-C(15)-C(16)-C(17)	-177.2(3)
C(14)-C(15)-C(16)-C(17)	1.0(4)
C(15)-C(16)-C(17)-C(18)	-0.4(5)
C(15)-C(16)-C(17)-N(4)	178.5(3)
C(16)-C(17)-C(18)-C(19)	0.5(5)
N(4)-C(17)-C(18)-C(19)	-178.4(3)
C(17)-C(18)-C(19)-C(14)	-1.1(5)
C(15)-C(14)-C(19)-C(18)	1.6(4)
C(13)-C(14)-C(19)-C(18)	-178.9(3)
N(5)-C(21)-C(22)-C(23)	0.6(6)
C(21)-C(22)-C(23)-C(24)	-1.2(6)
C(22)-C(23)-C(24)-C(25)	0.5(6)
C(23)-C(24)-C(25)-N(5)	0.8(5)
C(23)-C(24)-C(25)-C(26)	-176.5(3)
N(5)-C(25)-C(26)-N(6)	-4.6(4)
C(24)-C(25)-C(26)-N(6)	172.8(3)
N(5)-C(25)-C(26)-C(27)	177.3(3)
C(24)-C(25)-C(26)-C(27)	-5.2(5)
N(6)-C(26)-C(27)-C(28)	-1.2(5)
C(25)-C(26)-C(27)-C(28)	176.8(3)
C(26)-C(27)-C(28)-C(29)	-1.0(5)
C(27)-C(28)-C(29)-C(30)	1.4(5)
C(28)-C(29)-C(30)-N(6)	0.4(5)
N(7)-C(31)-C(32)-C(33)	-0.1(5)
C(31)-C(32)-C(33)-C(34)	0.5(5)
C(32)-C(33)-C(34)-C(35)	-0.6(5)
C(33)-C(34)-C(35)-N(7)	0.3(5)
C(33)-C(34)-C(35)-C(36)	-177.3(3)
N(7)-C(35)-C(36)-N(8)	-3.3(4)
C(34)-C(35)-C(36)-N(8)	174.4(3)
N(7)-C(35)-C(36)-C(37)	176.2(3)
C(34)-C(35)-C(36)-C(37)	-6.1(5)
N(8)-C(36)-C(37)-C(38)	0.0(5)
C(35)-C(36)-C(37)-C(38)	-179.5(3)

C(36)-C(37)-C(38)-C(39)	-1.4(6)
C(37)-C(38)-C(39)-C(40)	1.0(7)
C(38)-C(39)-C(40)-N(8)	0.8(6)
C(2)-C(1)-N(1)-C(5)	-1.7(4)
C(2)-C(1)-N(1)-Ru(1)	171.0(2)
C(4)-C(5)-N(1)-C(1)	1.3(4)
C(6)-C(5)-N(1)-C(1)	-179.8(3)
C(4)-C(5)-N(1)-Ru(1)	-172.5(2)
C(6)-C(5)-N(1)-Ru(1)	6.3(3)
C(8)-C(7)-N(2)-C(6)	-0.2(5)
C(8)-C(7)-N(2)-Ru(1)	-179.5(2)
C(10)-C(6)-N(2)-C(7)	-0.7(4)
C(5)-C(6)-N(2)-C(7)	-179.8(3)
C(10)-C(6)-N(2)-Ru(1)	178.7(2)
C(5)-C(6)-N(2)-Ru(1)	-0.3(3)
O(1)-C(13)-N(3)-C(11)	1.0(5)
C(14)-C(13)-N(3)-C(11)	-179.0(3)
C(12)-C(11)-N(3)-C(13)	15.7(5)
C(10)-C(11)-N(3)-C(13)	-162.9(3)
C(18)-C(17)-N(4)-O(3)	-0.2(5)
C(16)-C(17)-N(4)-O(3)	-179.2(3)
C(18)-C(17)-N(4)-O(4)	177.3(4)
C(16)-C(17)-N(4)-O(4)	-1.7(5)
C(22)-C(21)-N(5)-C(25)	0.7(5)
C(22)-C(21)-N(5)-Ru(1)	178.1(3)
C(24)-C(25)-N(5)-C(21)	-1.4(4)
C(26)-C(25)-N(5)-C(21)	176.1(3)
C(24)-C(25)-N(5)-Ru(1)	-179.0(2)
C(26)-C(25)-N(5)-Ru(1)	-1.5(3)
C(29)-C(30)-N(6)-C(26)	-2.5(4)
C(29)-C(30)-N(6)-Ru(1)	173.3(2)
C(27)-C(26)-N(6)-C(30)	2.9(4)
C(25)-C(26)-N(6)-C(30)	-175.3(2)
C(27)-C(26)-N(6)-Ru(1)	-173.4(2)
C(25)-C(26)-N(6)-Ru(1)	8.5(3)
C(32)-C(31)-N(7)-C(35)	-0.2(4)

C(32)-C(31)-N(7)-Ru(1)	179.4(2)
C(34)-C(35)-N(7)-C(31)	0.1(4)
C(36)-C(35)-N(7)-C(31)	177.8(3)
C(34)-C(35)-N(7)-Ru(1)	-179.6(2)
C(36)-C(35)-N(7)-Ru(1)	-1.8(3)
C(39)-C(40)-N(8)-C(36)	-2.2(5)
C(39)-C(40)-N(8)-Ru(1)	171.6(3)
C(37)-C(36)-N(8)-C(40)	1.7(5)
C(35)-C(36)-N(8)-C(40)	-178.7(3)
C(37)-C(36)-N(8)-Ru(1)	-172.7(3)
C(35)-C(36)-N(8)-Ru(1)	6.9(3)
C(16)-C(15)-O(2)-C(20)	-8.5(4)
C(14)-C(15)-O(2)-C(20)	173.3(3)
C(30)-N(6)-Ru(1)-N(8)	81.6(2)
C(26)-N(6)-Ru(1)-N(8)	-102.5(2)
C(30)-N(6)-Ru(1)-N(5)	176.9(3)
C(26)-N(6)-Ru(1)-N(5)	-7.2(2)
C(30)-N(6)-Ru(1)-N(7)	2.3(2)
C(26)-N(6)-Ru(1)-N(7)	178.2(2)
C(30)-N(6)-Ru(1)-N(1)	-91.3(2)
C(26)-N(6)-Ru(1)-N(1)	84.6(2)
C(40)-N(8)-Ru(1)-N(6)	84.8(3)
C(36)-N(8)-Ru(1)-N(6)	-101.3(2)
C(40)-N(8)-Ru(1)-N(5)	5.7(3)
C(36)-N(8)-Ru(1)-N(5)	179.6(2)
C(40)-N(8)-Ru(1)-N(7)	-180.0(3)
C(36)-N(8)-Ru(1)-N(7)	-6.0(2)
C(40)-N(8)-Ru(1)-N(1)	-139.2(5)
C(36)-N(8)-Ru(1)-N(1)	34.7(7)
C(40)-N(8)-Ru(1)-N(2)	-90.5(3)
C(36)-N(8)-Ru(1)-N(2)	83.5(2)
C(21)-N(5)-Ru(1)-N(6)	-172.9(3)
C(25)-N(5)-Ru(1)-N(6)	4.6(2)
C(21)-N(5)-Ru(1)-N(8)	-80.4(3)
C(25)-N(5)-Ru(1)-N(8)	97.1(2)
C(21)-N(5)-Ru(1)-N(1)	93.8(3)

C(25)-N(5)-Ru(1)-N(1)	-88.8(2)
C(21)-N(5)-Ru(1)-N(2)	13.8(3)
C(25)-N(5)-Ru(1)-N(2)	-168.7(2)
C(31)-N(7)-Ru(1)-N(6)	-82.9(2)
C(35)-N(7)-Ru(1)-N(6)	96.7(2)
C(31)-N(7)-Ru(1)-N(8)	-175.5(3)
C(35)-N(7)-Ru(1)-N(8)	4.1(2)
C(31)-N(7)-Ru(1)-N(1)	11.2(3)
C(35)-N(7)-Ru(1)-N(1)	-169.2(2)
C(31)-N(7)-Ru(1)-N(2)	91.0(2)
C(35)-N(7)-Ru(1)-N(2)	-89.5(2)
C(1)-N(1)-Ru(1)-N(6)	7.8(3)
C(5)-N(1)-Ru(1)-N(6)	-179.2(2)
C(1)-N(1)-Ru(1)-N(8)	-128.2(5)
C(5)-N(1)-Ru(1)-N(8)	44.8(6)
C(1)-N(1)-Ru(1)-N(5)	86.7(3)
C(5)-N(1)-Ru(1)-N(5)	-100.3(2)
C(1)-N(1)-Ru(1)-N(7)	-88.3(3)
C(5)-N(1)-Ru(1)-N(7)	84.7(2)
C(1)-N(1)-Ru(1)-N(2)	-177.9(3)
C(5)-N(1)-Ru(1)-N(2)	-4.88(19)
C(7)-N(2)-Ru(1)-N(8)	9.9(3)
C(6)-N(2)-Ru(1)-N(8)	-169.4(2)
C(7)-N(2)-Ru(1)-N(5)	-86.4(3)
C(6)-N(2)-Ru(1)-N(5)	94.3(2)
C(7)-N(2)-Ru(1)-N(7)	89.0(3)
C(6)-N(2)-Ru(1)-N(7)	-90.4(2)
C(7)-N(2)-Ru(1)-N(1)	-177.8(3)
C(6)-N(2)-Ru(1)-N(1)	2.8(2)

Symmetry transformations used to generate equivalent atoms:

Table 7. Hydrogen bonds for **[8]**$[PF_6^-]_2$ [Å and °].

D-H...A	d(D-H)	d(H...A)	d(D...A)	<(DHA)
N(3)-H(3A)...O(2)	0.80(4)	1.97(4)	2.662(3)	144(3)
N(3)-H(3A)...F(4)#1	0.80(4)	2.60(4)	3.097(4)	121(3)

Symmetry transformations used to generate equivalent atoms:
#1 x,y+1,z